Cranfield University

Angela Marie Knepper

Examination of Three Candidate Technologies for High-Lift Devices on an Aircraft Wing

School of Engineering

PhD

Cranfield University

College of Aeronautics

Department of Aerospace Sciences

PhD

Academic Year 2005

Angela Marie Knepper

Examination of Three Candidate Technologies for High-Lift Devices on an Aircraft Wing

Supervisor: Professor Kevin P Garry

December 2005

Abstract

A research programme was initiated to examine three candidate high-lift technologies, which would, if implemented, simplify the mechanical complexity of the multiple component trailing-edge devices traditionally employed on civil transport aircraft. Experimental studies were undertaken with the aim of examining each technology in terms of its potential to favourably influence boundary layer development and improve the aerodynamic characteristics of a high-lift configuration.

Preliminary studies of triangular serrated geometries, at the trailing edge of a modified flat plate, highlighted that the ability of the serrations to favourably influence the flow field development over an aft positioned single slotted flap was critically dependent upon the flap lap/gap and deflection angle. Under the test conditions, the serrations were most effective at low flap deflection angles, particularly serrations with a length corresponding to 13% flap chord. Extending these studies to a representative high-lift configuration significantly limited the range of flap laps/gaps and deflection angles over which the serrations were favourable. Furthermore, oil flow visualisation provided evidence of wake structures emanating from serration vertices, corroborating earlier hypotheses and suggesting the flow mechanism by which serrations favourably influenced boundary layer development over the upper surface of the downstream flap.

Experiments indicated that when optimised, blowing tangentially from a slot at the trailing edge of the main element over the upper surface of a flap within a three-element high-lift configuration, provided a highly effective means of preventing boundary layer separation and increasing lift. This was corroborated by oil flow visualisation and computational simulations. Maintaining the same momentum coefficient and blowing through discrete orifices at the trailing edge of the main element, proved highly favourable, heightening the increment in lift in comparison to the corresponding tangential slot blowing configuration. Hence, the mass flow rate could be reduced in comparison to the tangential slot blowing configuration, without compromising the aerodynamic performance.

Acknowledgements

Firstly, I would like to express my heartfelt gratitude to Rachel, Paul, Jonny and Lewis Foster. Thank you for inviting me into your family and allowing me to be part of the furniture. Thank-you for Wednesday night tea, for salt dough and sparklers, for chocolate crispy cakes and searching for Christmas trees. Most of all, thank you for your friendship, for your endless support and encouragement, for the laughter and for the wonderful memories your family have given me.

I would like to thank the friends that I have made during my time at Cranfield, especially Jenny Roberts, Jason Hill, Faye Andrews, Jason Bennett and Lolli Mankazana. Words cannot express my gratitude for all the encouragement and support you have given me over the years. Thank you for bringing laughter and smiles into my days.

I would like to extend my heartfelt thanks to Hannah Danson and Joanne Cruickshank for always being there for me, ready with a listening ear and warm words of encouragement. Quite simply, thank you for being true friends.

I would also like to express my sincere appreciation to my father, Michael Knepper, for his support and encouragement. Words cannot express the depth of my gratitude – all I can simply say is a heartfelt thank-you.

Finally, to those who I have not mentioned directly but have been friendly faces who have taken the time to show me that there is light at the end of the wind-tunnel…….thank-you! ☺

Contents

Table of Figures

Notation

c	chord
c_{flap}	flap chord
c_{main}	main element chord
c_{slat}	slat chord
C_a	axial force coefficient
C_d	drag coefficient per unit span
C_{D0}	drag coefficient at zero lift
C_{dp}	profile drag coefficient (Jones' method of wake integration)
C_l	lift coefficient per unit span
ΔC_l	incremental lift coefficient
$C_{l\alpha=0°}$	lift at zero incidence
C_{lmax}	maximum lift coefficient
C_n	normal force coefficient
C_p	pressure coefficient
C_{pmin}	minimum pressure coefficient
C_{PB}	mean coefficient of base pressure
d/c	depth-to-chord ratio
d_{TE}	trailing-edge thickness
d_{TE}/c	trailing-edge-thickness-to-chord ratio
d_{TE}/t	trailing-edge-thickness-to-maximum-profile-thickness ratio
H	total pressure
l	length of serration
l/c	length-to-chord ratio
l/δ_{TE}	serration-length-to-total-trailing-edge-boundary-layer-thickness ratio
L/D	lift-to-drag ratio
$(L/D)_{max}$	maximum lift-to-drag ratio
$\dot{m}$	mass flow rate
M_∞	freestream Mach number
p	static pressure
q_∞	freestream dynamic pressure
Re	Reynolds number
V_{jet}	velocity of jet of blown air
α	angle of incidence
α_{stall}	stall angle of incidence
δ_f	flap deflection angle
δ_{fstall}	stall angle for the flap
δ_{TE}	trailing edge boundary layer thickness
$(\delta_{us}/\delta_{ls})$	upper-to-lower-surface-trailing-edge-boundary-layer-thickness ratio
C_μ	momentum coefficient per unit span
$C_{\mu crit}$	critical momentum coefficient

Schematics for Test Configurations

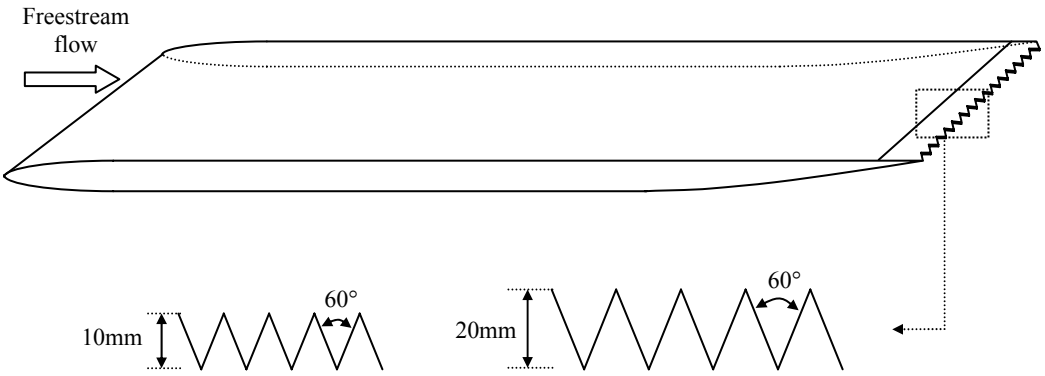

Modified Flat Plate with a Plain, 10mm or 20mm 60° Triangular Serrated Trailing Edge

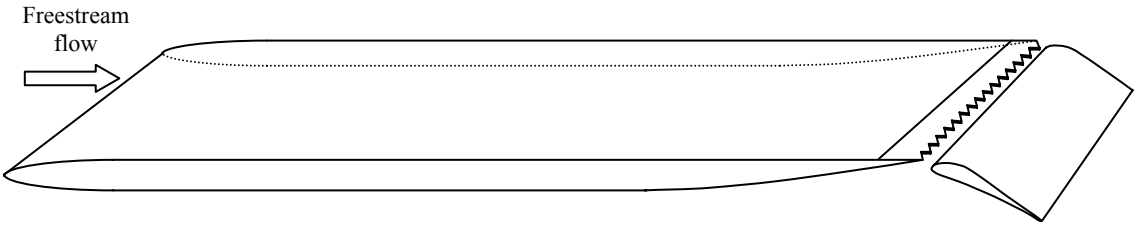

Modified Flat Plate with a Plain, 10mm or 20mm 60° Triangular Serrated Trailing Edge, Upstream of a Single Slotted Trailing Edge Flap

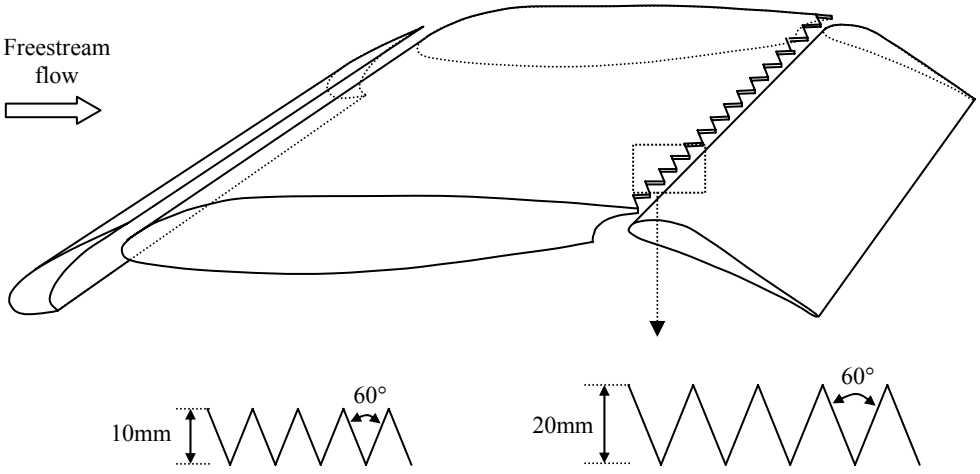

Multi-Element High-Lift Configuration with Plain, 10mm or 20mm 60° Triangular Serrations at the Trailing Edge of the Main Element

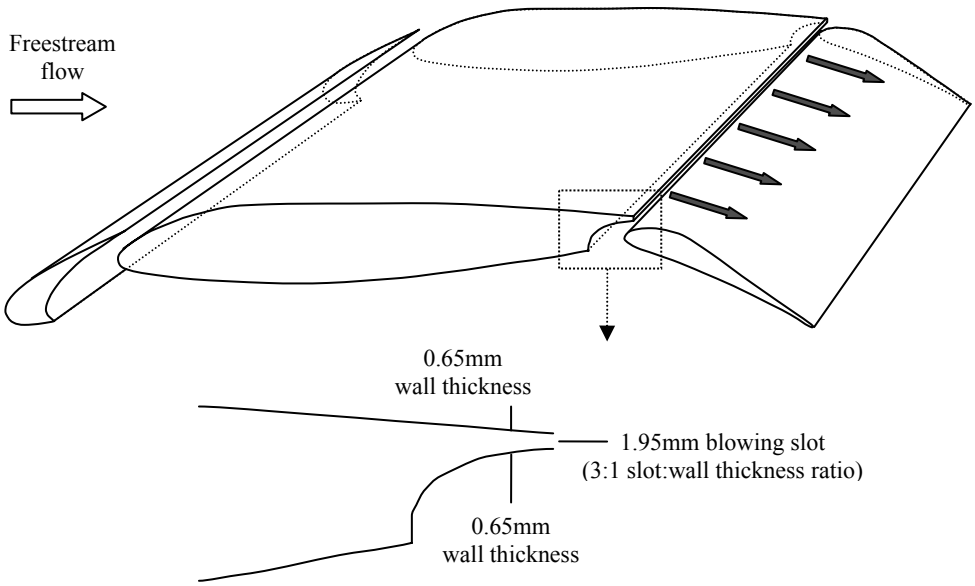

Multi-Element High-Lift Configuration with Air Blown Tangentially from a Slot at the Trailing Edge of the Main Element

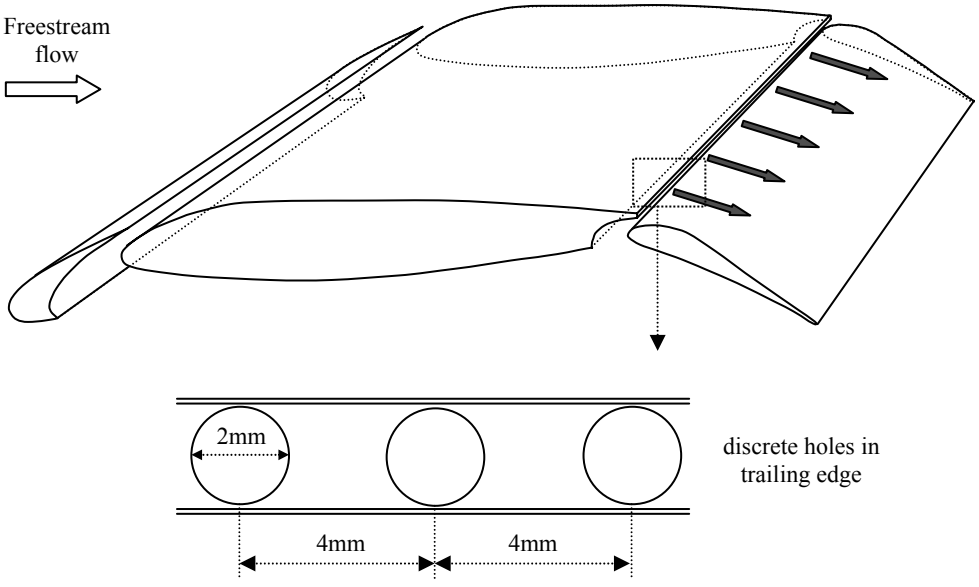

Multi-Element High-Lift Configuration with Air Blown Tangentially from Discrete Holes at the Trailing Edge of the Main Element

1 Introduction

1.1 General Introduction

Aircraft design is typically driven by customer requirements, which reflect the aircraft's proposed primary mission and include such aspects as aircraft range, takeoff and landing distances/speeds, maximum velocity and payload specifications. Of particular importance to the design of civil transport aircraft are economic and safety considerations (Dillner, May, and McMasters, 1984). Low production and maintenance costs necessitate simple designs and product reliability, whilst intrinsic to the operational requirements is the ability for the aircraft to conduct all aspects of its mission in compliance with the stipulated airworthiness requirements. Accordingly, by virtue of the dominant design specifications, civil transport aircraft are optimised for cruise conditions. Thus, in order to satisfy the takeoff and landing phases of the flight envelope, in-flight modification to the aircraft is required.

An aircraft normally encounters its lowest flight velocities at takeoff and landing. Takeoff and landing speeds are defined relative to and marginally in excess of the stalling speed, i.e. the lowest speed at which an aircraft can fly in straight and level flight. Whilst it is advantageous that the stalling speed be as small as possible, this necessitates that the maximum lift force attainable be increased. However, the maximum lift force generated is governed by the geometric design and thus, in order to augment the lifting properties of a wing at takeoff and landing, additional high-lift devices must be implemented to temporarily modify the wing geometry without unduly impeding the performance at cruise conditions.

High-lift devices employed on conventional civil transport aircraft have, for the most part, remained largely unaltered since the mid-1900s. The mechanical high-lift systems are essentially based upon single or multiple-slotted retractable elements which, when combined with the Fowler flap concept, increase the effective camber, angle of incidence and wing area. Whilst deploying a triple-slotted Fowler flap in conjunction with a leading-edge device maximises the lift force achievable from a purely mechanical high-lift system, such complexity has a detrimental effect upon the design, production and maintenance costs, as well as increasing the weight penalty arising from the hydraulic actuation systems necessary for device deployment.

Subsequent progression towards mechanically simpler high-lift systems is impeded by the attendant degradation in aerodynamic performance (Lin, Robinson, and McGhee, 1992). In reducing the number of flap elements from two or three to one, additional methods of boundary layer control are required to attenuate or prevent premature boundary layer separation over the upper surface of the flap and hence, reduce or negate the attendant loss in lift and increase in drag. Methods of boundary layer control are typically characterised by whether or not additional power from the propulsive unit is required and are termed active or passive, accordingly.

One such method of active boundary layer control comprises blowing air tangentially from a slot over the upper surface of a deployed trailing edge flap. Extensive studies have shown tangential slot blowing to be an effective means of boundary layer control, delaying or even eliminating trailing edge boundary layer separation. However, the momentum of the blown air required to sustain boundary layer attachment is typically minimised by optimising the geometric parameters of the aerofoil or wing, particularly the flap profile, the position of the flap relative to the slot and the slot height. Investigations thus far have not considered modifying the geometric shape of the orifice through which the blown air is ejected, highlighting a novel method of active boundary layer control with the potential to reduce the momentum of air required to prevent boundary layer separation.

Passive boundary layer control is also frequently utilised on aircraft, typically in the form of vortex generators. Comprehensive investigations have shown that optimised device geometries generate streamwise vortices, which promote increased mixing and hence, transfer high-energy fluid from the outer boundary layer to the near surface region, subsequently delaying or eliminating boundary layer separation, with an attendant reduction in drag and increment in lift (Lin, Robinson, and McGhee, 1992). However, vortex generators are rendered ineffective if positioned aft of the point of boundary layer separation. Accordingly, with flow separation on multi-element aerofoils critically dependent upon configuration geometry and flight conditions, optimisation of vortex generators necessitates detailed analysis of the flow field development for all applicable phases within the flight envelope.

Streamwise vortices have also been shown to emanate from triangular serrations positioned at the lower surface leading edge of a single element aerofoil, promoting upper surface boundary layer attachment (Soderman, 1972). Whilst optimised serrated geometries at the trailing edge of a single element have also exhibited favourable effects

upon the aerodynamic characteristics (Vijgen, van Dam, Holmes, and Howard, 1989), the effect of trailing edge serrations on an aft positioned single slotted flap has been limited to a predominantly qualitative analysis of the developing wake (Brennan, 2002). However, the limited data suggests that triangular serrations have the potential to effectively delay boundary layer separation and a comprehensive investigation is required to evaluate the effectiveness of this novel method of passive boundary layer control within a high-lift configuration.

Thus, clear scope is evident in terms of developing potential methods of active or passive boundary layer control, which would, if implemented, simplify the mechanically complex high-lift systems traditionally employed in present day civil transport aircraft.

1.2 Overview of Aims and Objectives

This research was conducted in conjunction with the HELIX project, a European collaboration initiated by a European Union Framework V Programme, investigating innovative high-lift aerodynamic concepts.

The aim of this research was to conduct a detailed examination of three candidate high-lift technologies, which would, if implemented, simplify the mechanical complexity of the multiple component trailing-edge high-lift devices traditionally employed on civil transport aircraft.

Accordingly, the following objectives were identified:

- Conduct a detailed investigation into the effect of triangular serrations, implemented at the trailing edge of a modified flat plate, on the aerodynamic characteristics of an aft positioned single slotted flap;
- Accordingly, establish a set of aerodynamic data quantifying the influence of triangular serrations on the flow field developing over an aft single slotted flap for a comprehensive range of flap lap/gap and deflection angles;
- Conduct an in-depth study into the effect of implementing triangular serrated geometries at the trailing edge of a main element, upstream of a single slotted flap, on the flow field development and resultant aerodynamic forces over the multi-element aerofoil, which was representative of a mechanically feasible high-lift configuration, i.e. demonstrating a cove geometry over the aft region of

the main element lower surface, facilitating mechanical retraction of the trailing-edge high-lift device in cruise conditions;

- Examine the potential of triangular serrations as a means of passive boundary layer control within a high-lift configuration;
- Evaluate the effect of blowing air tangentially from a slot at the trailing edge of the main element over the upper surface of a single slotted flap within a three-element high-lift configuration;
- Augment the aforesaid wind-tunnel data with a two-dimensional computational simulation investigating the effect of blowing air tangentially from a slot at the trailing edge of the main element over the upper surface of a single slotted flap within a three-element high-lift configuration;
- Investigate whether aerodynamic benefits can be achieved by modifying the geometry at the trailing edge of the main element, through which the air was ejected over the upper surface of a trailing-edge flap within a three-element high-lift configuration, which would enable the momentum of the blown air to be reduced.

1.3 Thesis Structure

Comprising ten chapters, this thesis details the experimental investigations and computational simulations of three candidate high-lift technologies. Following the initial introduction to the subject matter in the present chapter, Chapter 2 provides a comprehensive critical review of the previous research conducted on high-lift devices and methods of boundary layer control pertinent to the present study. Specifically, the available literature on serrated geometries is comprehensively reviewed in order to justify the development and evaluation of serrations within the present context of a high-lift configuration. In addition, an overview of tangential slot blowing literature is provided, selecting references which highlight the critical parameters influencing the effectiveness of the tangential blowing, together with those demonstrative of the effect of blowing boundary layer control upon the aerodynamic characteristics and performance attributes of a high-lift configuration. Chapter 3 details the experimental methodology, with a description of the experimental setup, model, instrumentation and subsequent analysis provided for each element of the test programme.

Chapter 4 through to Chapter 9 discuss the experimental and computational results. Specifically, Chapter 4 examines the experiments conducted on a modified flat plate with triangular serrations implemented at the trailing edge. The influence of triangular

serrations on the flow field developing over a single slotted flap aft of the modified flat plate over a comprehensive range of flap lap/gap and deflection angles is discussed in Chapter 5. Chapter 6 examines the influence of triangular serrations on the developing flow field when positioned at the trailing edge of a main element upstream of a single slotted flap within a representative multi-element high-lift configuration. In Chapter 7, conventional tangential slot blowing is implemented on three distinct multi-element high-lift configurations and the subsequent results are discussed. The corresponding computational simulation of tangential slot blowing within a single high-lift configuration is compared to the experimental data in Chapter 8. Chapter 9 examines whether benefits can be achieved by modifying the geometry through which the air is blown. Finally, Chapter 10 contains the overall conclusions for the research programme and provides recommendations for future work.

2 Review of Previous Literature

This chapter provides a review of the previous research conducted on serrated geometries and tangential slot blowing, pertinent to the present study.

2.1 Overview of Mechanical High-Lift Developments

High-lift systems employed on conventional civil transport aircraft have, for the most part, remained largely unaltered since the mid-1900s. The rudiments of present day mechanical high-lift devices originated from early applications of trailing edge ailerons, where it was noted that the downward rotation of an aft hinged section on an aerofoil afforded an increase in camber, with an attendant increase in lift. Thus, the plain flap was conceptualised. Whilst plain flaps were employed on aircraft as early as 1914 and were standard on aircraft built by Fairey from 1916 onwards, they were rarely used. Wright's split flap proved more favourable, due to its simplicity. Developed in 1920 and widely employed on aircraft during the 1930s and 1940s, the split flap only rotated the lower surface over the aft section of the aerofoil. However, the increased camber of the split flap incurred a greater drag penalty than that of the plain flap.

Clearly, one of the most significant developments, in terms of mechanical high-lift design, was the evolution of the single slotted flap, which was developed independently by three different people around 1920. Separate investigations by Handley Page in England and both Lachmann and Mader in Germany showed that the single slotted flap was more favourable than the plain flap in terms of generating lift. However, despite experiments indicating that the single slotted flap increased aerofoil lift by over 60%, implementation of the device on aircraft was, similarly to the plain flap, initially slow.

The next significant development in high-lift devices was the Fowler flap, which originated from the independent studies of Fowler in the USA in 1924. Whilst increasing the effective wing camber, similarly to previous flap designs, the deployed Fowler flap extended beyond the trailing edge of the stowed wing, resulting in an increase in effective wing area and hence, an additional increment in the lift force generated. Despite the benefits, it was not until 1937 that the Fowler flap was implemented on a production aircraft.

Since the late 1930s, the only significant development in mechanical flap design was the combination of the slotted flap with the Fowler flap and the inclusion of additional slots. Whilst deploying a triple-slotted Fowler flap in conjunction with a leading-edge device

maximised the lift force achievable from a purely mechanical high-lift system, such complexity had a detrimental effect upon the design, production and maintenance costs, as well as increasing the weight penalty arising from the hydraulic actuation systems necessary for device deployment. Accordingly, more recent designs displayed a tendency to reduce the mechanical complexity of the high-lift system.

Lin et al (1992) noted that progression towards mechanically simpler high-lift systems was often impeded by the attendant degradation in aerodynamic performance. Furthermore, in reducing the number of flap elements from two or three to one, additional methods of boundary layer control were required to attenuate or prevent premature boundary layer separation evident over the upper surface of the flap, when extended to the higher flap deflection angles necessary to achieve a lift force comparable to a multi-element trailing-edge device.

Numerous methods of boundary layer control have been investigated over the years. For some methods, studies were brief, merely providing a first insight into the salient characteristics and determining the potential to influence boundary layer development. Serrated geometries were illustrative of this. Initially investigated as a means of noise attenuation, it was only in trying to understand the flow mechanisms by which this was achieved that the potential to influence the boundary layer development and favourably affect the aerodynamic characteristics became apparent. As such, the studies pertaining to boundary layer flow control over aerofoils, applicable to a potential high-lift configuration, were particularly limited. Consequently, the literature available is comprehensively outlined in Section 2.2 in order to justify its development and evaluation within the present high-lift context.

In contrast, other methods of boundary layer control have been developed to full maturity, optimised and implemented on production aircraft. One such method was tangential blowing, which was based upon the principle of supplying additional kinetic energy to the low energy fluid elements immediately adjacent to the surface in order to re-energise the boundary layer, preventing – or at the very least, delaying – separation. Research, development and optimisation of tangential blowing as a means of boundary layer and flow control has been comprehensively documented and as a result, it was necessary to limit the literature reviewed in Section 2.3 to those studies pertaining to blowing air tangentially from a slot over the upper surface of a trailing edge flap. However, with a multitude of literature available, rather than duplicate an exhaustive chronological account of the development of tangential blowing, references were

selected that highlighted the critical parameters influencing the effectiveness of the tangential blowing, together with those demonstrative of the effect of blowing boundary layer control upon the aerodynamic characteristics and performance attributes of a high-lift configuration. Of particular interest were the studies integrating wind-tunnel experiments with flight tests, as they verified the feasibility of practical implementation and confirmed whether or not the predicted benefits were indeed achievable during flight conditions. Whilst successful integration of tangential slot blowing on production aircraft justifies its subsequent evaluation within the context of the present high-lift configurations under consideration, the potential for further development and optimisation is also identified.

2.2 Passive Boundary Layer Control: Serrations

2.2.1 Introduction

Fascination with heavier-than-air flight has long since sought inspiration from birds. Whilst early attempts to fly focused on imitating the flapping motion of a bird's wings, with the foundation of fixed wing flight, attention turned to the geometry of the bird's wing.

As early as 1932, Graham's ornithological study of flight proposed that the slot(s) formed by the separation of individual outer flight feathers during flapping and gliding were aerodynamically comparable to a multi-slotted wing. Whilst Graham proposed that the slots were essentially nature's anti-stalling device, reducing the effective angle of incidence of the separated feathers and preventing trailing edge stall at high angles of incidence, Lachmann (1932) advocated that the primary purpose of the slotted wing-tip was to aid upward acceleration at takeoff, increasing the lift force generated at high angles of incidence with a bird advancing at a relatively low speed. However, it was Graham's (1934) studies of the flight of owls, in the capacity of noise attenuation, which highlighted the aerodynamic importance of the wing's geometry at the leading and trailing edge. Accordingly, it was proposed that the presence of a comb-like fringe or serration at the leading and trailing edge aided the owl's silent flight.

Subsequent experimental research on acoustic resonance confirmed that serrations reduced the noise generated by gas turbine engines, rotors and propellers, see for example Soderman (1973) or Smith and Sowers (1974). Extending this study to leading-edge serrations on stationary and rotating lifting surfaces, Hersh et al (1974)

noted that noise attenuation or elimination was particularly sensitive to the serration length and the location of the serrated geometry at the leading edge.

2.2.2 Effect of Leading-Edge Serrations

Instigated by the need to fully understand the flow mechanisms by which serrations reduced the noise generated by an aerofoil, Soderman's (1972) quasi-two-dimensional experiments, on a NACA 66_1-012 aerofoil section, duly extended the applicability of the results beyond noise attenuation to include, for example, delay of both boundary layer separation and aerofoil stall. Testing at a Mach number (M_∞) of 0.13 and a Reynolds number (Re) of 2.32×10^6, Soderman observed that the serration size, the spacing between serrations and the position of the serrations relative to the leading-edge were highly influential on the ensuing flow field.

A schematic of the Soderman's test model is shown in Figure 1. Defining the length of a serration (l) as the distance from the vertex to the base, Soderman's studies showed that serrations with a length-to-chord ratio (l/c) of 0.012 obstructed the flow field developing over the upper surface of the aerofoil and hence, had a detrimental effect upon the aerodynamic performance, decreasing the maximum lift coefficient (C_{lmax}), increasing the drag coefficient (C_d) and prompting the aerofoil to stall at a lower angle of incidence than the baseline model. In contrast, serrations with $0.0033\leq l/c\leq0.0067$ delayed separation to higher angles of incidence and increased C_{lmax}. Whilst the serrations appeared to have negligible effect upon C_d at low angles of incidence (α), the serrations reduced C_d at high α.

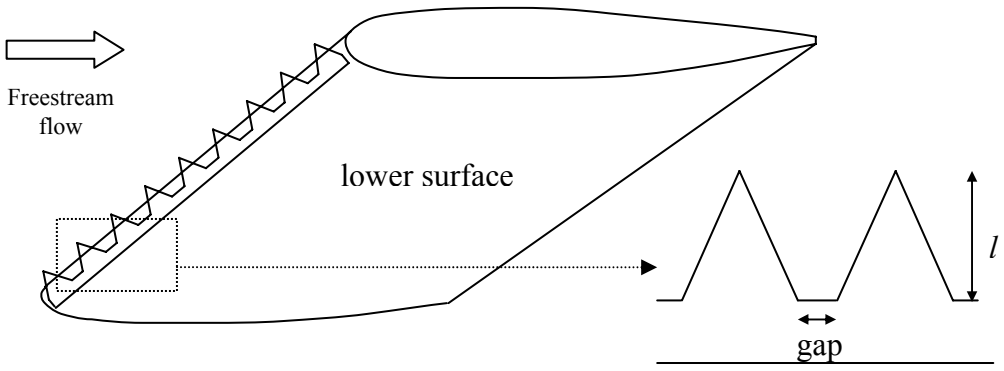

Figure 1: Schematic of leading-edge serrations on an aerofoil (Soderman, 1972)

Extending the gap between serrations from $0.5l$ to $1.5l$ increased both the lift-curve slope and C_{lmax}. However, C_{lmax} was relatively insensitive to further increments in the

gap between 3.5l to 7.5l, suggesting a limiting value, for which further increments in gap were no longer advantageous. Furthermore, inclination of the serrations, whether with or without gaps, had negligible effect upon the aerodynamic characteristics of the aerofoil.

The location of the leading edge serrations was critical. For an optimal serration geometry with l/c=0.0033, a gap equal to the serration length and a distance between serration vertices of 2l, the optimal location tested was 1.25%c from leading-edge centreline, resulting in an increment in the maximum lift coefficient (ΔC_{lmax}) of 0.27 and accounting for a 34% increment in comparison to the baseline configuration. Soderman noted that at the optimum location, the serrations were near the stagnation point at angles of incidence near stall. The sensitivity of the aerodynamic characteristics to the location of the serrated geometry was highlighted by positioning the serrations on the leading-edge centreline, 1.25%c upstream of the optimal location, which resulted in a decrease in C_l and an increase in C_d.

Oil flow visualisation identified "white and dark bands were etched in the oil behind each prong [extending] from the airfoil leading edge to the trailing edge". Soderman noted that magnification of the photographs showed a distinct three-dimensional circular pattern aft of each serration vertex, which was attributed to the development of counter-rotating vortices, rotating in the sense so as to "induce mutual upward movement from the surface". It was proposed that these streamwise vortices extended over the upper surface of the aerofoil, re-energising the boundary layer and delaying both leading and trailing edge separation to higher α.

Contrary to Soderman's experiments, Schwind and Allen's (1973) parametric study of 28° triangular serrated geometries implemented at the leading edge of the lower surface on a NACA 63-009 aerofoil section at Re=3.5×10^6 indicated that, irrespective of the gap between serrations and variations in l/c between 0.0007 and 0.0036, the leading edge serrations had no appreciable effect upon C_{lmax} and C_d. Although the serrations tended to decrease the severity or eliminate the sudden stall that was evident on the baseline aerofoil, no definite correlation with serration length or serration spacing was established. However, Schwind and Allen corroborated Soderman's analysis of the flow field visualisation, identifying that the shear layers, shed from the serration vertex, rolled up to form counter-rotating vortices.

Based upon a serration geometry that was comparable to Soderman's optimum test geometry, with the exception that the serration l/c was increased to 0.0057, Collins (1981) investigations of leading edge serrations on a symmetrical NACA 0015 aerofoil and a cambered NACA 2412 aerofoil at Re=3.6×10^5 showed that in comparison to the corresponding baseline configurations, the serrations modified the pressure distribution over the suction surface of the aerofoil, resulting in a 12% and 22% increase in the C_l-α gradient for the NACA 0015 and NACA 2412 aerofoil, respectively. For the cambered aerofoil, the increment in C_l due to the leading edge serrations decreased the zero-lift angle of incidence and increased C_{lmax}, although α_{stall} remained unchanged. However the favourable effect of the leading edge serrations upon C_l was negated at high α for the symmetrical aerofoil, rendering C_{lmax} and α_{stall} coincident with the baseline configuration, contradicting the increment in C_{lmax} and modification to α_{stall} evident in Soderman's experiments.

Thus, it was evident that the effectiveness of leading edge serrations in delaying boundary layer separation, and favourably influencing the resultant aerodynamic forces, was critically dependent upon the serration geometry and its leading edge location, the optimum for which was intrinsically dependent upon the configuration geometry under consideration.

2.2.3 Effect of Trailing-Edge Serrations on a Wing with a Blunt Trailing-Edge

Stemming from measurements on circular cylinders, which showed that fixing separation with a "broken" wire eliminated alternate shedding of vortices, the effects of serrated geometries at the trailing edge of a wing were initially investigated as a means of suppressing the periodic vortex shedding in the near wake generated by the blunt trailing edge of a wing at subsonic M_∞.

Early experiments by Tanner (1971) at high subsonic and transonic M_∞ proposed that for a rectangular wing with a blunt trailing edge, a favourable drag coefficient was dependent upon a moderate trailing-edge-thickness-to-maximum-profile-thickness ratio (d_{TE}/t) and maximising the base pressure, the latter of which correlated to a minimum base drag. Maintaining a d_{TE}/t of 0.75 and implementing the "broken" M-shaped geometry at the blunt trailing edge reduced the drag coefficient at zero lift (C_{D0}), comprising profile drag and base drag, by 16% and 26% at M_∞=0.5 and M_∞=0.9, respectively, in comparison to the corresponding configuration with a straight blunt

trailing edge. Note that C_{D0} for the M-shaped thick trailing edge geometry still exceeded that generated by a profile with a conventional sharp trailing edge by 74% and 14% at M_∞=0.5 and M_∞=1.2, respectively. Additional measurements at supersonic M_∞ showed that the drag of a straight blunt trailing edge configuration could be further reduced by decreasing d_{TE}/t to approximately 0.3, which suggested that further decrements in drag were achievable with the M-shaped blunt trailing edge geometry, subject to optimisation of d_{TE}/t.

The favourable effects of the M-shaped geometry at high subsonic and transonic regimes was extended to low-speed experiments at M_∞=0.1 (Tanner, 1972). Defining the geometry by $x_1/d_{TE}=x_2/d_{TE}$=3.8, h_1/d_{TE}=1.9 and h_2/d_{TE}=0.95 (see Figure 2), implementation of the M-shaped geometry at the blunt trailing edge of a rectangular wing with d_{TE}/t=0.58 reduced the base drag by 64% in comparison to the corresponding configuration with a blunt straight trailing edge and accordingly, increased the mean coefficient of base pressure (C_{PB}) from −0.48 with a blunt straight trailing edge to −0.173 with the M-shaped trailing edge geometry. Furthermore, C_{D0} for the straight thick trailing edge was 84% greater than that for the specified M-shaped geometry.

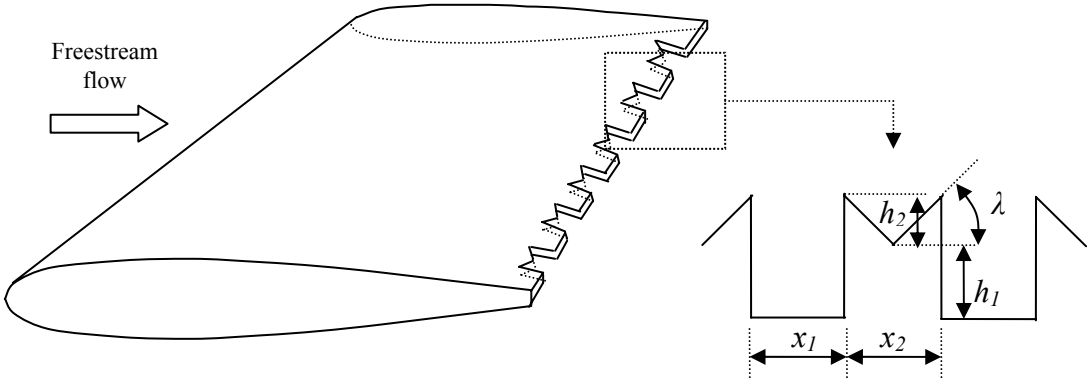

Figure 2: Schematic of "broken" M-shaped trailing-edge serrations on a wing with a blunt trailing edge (Tanner, 1972)

Again, it was suggested that d_{TE}/t be reduced for optimal aerodynamic gains. Additionally, it was noted that the M-shaped geometry increased the lift-curve gradient by 10% in comparison to the corresponding configuration with a sharp trailing edge.

Further experiments on a rectangular wing at M_∞=0.15 and Re=2×10^6 with d_{TE}/t=0.58 highlighted the importance of optimising the critical geometrical parameters defining the M-shaped trailing edge (Tanner, 1973). The near optimal h_1/d_{TE} of 1.9 previously

identified was maintained and further geometrical parameters of x_1/x_2=1 and tan λ=0.5 were specified, with x_1/d_{TE} the variable parameter. Accordingly, an optimal value for x_1/d_{TE} of 5.5 was determined, resulting in C_{PB}=−0.165 and accounting for a 66% reduction in base pressure in comparison to the corresponding blunt straight trailing edge. Thus, the base drag for the M-shaped trailing edge geometry was only approximately 35% of that for the blunt straight trailing edge. Extension of the parametric study highlighted the parameter λ, determining the included angle of the serration, as particularly influential on the base drag. Whilst an optimum value of λ was not determined, the greatest decrement in base drag was achieved with tan λ=0.66 and x_1/d_{TE}=5.0, increasing C_{PB} to −0.156, representing a 67% increase in base pressure in comparison to the blunt straight trailing edge. Thus, the base drag for the M-shaped trailing edge geometry was only approximately 32% of that for the blunt straight trailing edge. In comparison to the best M-shaped trailing edge geometry of previous experiments generating a C_{PB} of −0.173 (see Tanner, 1972), optimisation of the geometrical parameters to achieve a C_{PB}=−0.156 resulted in a further 13% reduction in base drag.

It was also noted that for a wing with a split flap, the wing with a blunt broken trailing edge increased the maximum lift coefficient for all flap deflection angles between 0° and 45°, in comparison to the corresponding configuration with a sharp trailing edge (Tanner, 1975). Whilst the increment was not quantified, this was the first indication that implementation of broken serrations at the trailing edge of a wing had a favourable effect upon the lift force generated by a wing with a simple mechanical high-lift device.

Gai and Sharma (1981) investigated the effect of an M-shaped trailing edge geometry on a two-dimensional aerofoil with an elliptic forebody and parallel upper and lower surfaces such that d_{TE}/t=1 and the trailing-edge-thickness-to-chord ratio (d_{TE}/c) was 0.1. Experimenting at a Re of 1.53×10^5 and with a trailing edge geometry defined by $x_1/d_{TE}=x_2/d_{TE}$=3, h_1/d_{TE}=2 and λ=32.5°, the base pressure was increased by 58%, corroborating Tanner's studies. Disparities in the magnitude of the increment were attributed to differences in Reynolds number and the finite span of the model in Tanner's experiments. Detailed pressure measurements within a single M-segment indicated a maximum pressure at the serration vertex, decreasing to a local minimum pressure at the midpoint between the vertex and the trough. Augmented by smoke flow visualisation, Gai and Sharma corroborated Tanner's studies, confirming the existence of two counter-rotating streamwise vortices developing from either side of the vertex of the M-shape.

Furthermore, recognising that the effect of triangular serrations as a means of reducing base drag had not previously been investigated, Gai and Sharma (1981) considered the effect of 60° and 120° triangular trailing edge serrations with l/d_{TE}=2 or l/c=0.2. The 60° triangular serrations increased the mean base pressure coefficient from −0.62 with a plain trailing edge to −0.33, accounting for a 47% increase in comparison to the baseline configuration, whereas the 120° triangular serrations increased the mean base pressure coefficient to −0.48, representing a 22% increment. This suggested that the effectiveness of the triangular serration in reducing the mean base pressure was dependent upon the included angle of the serration. Detailed measurements of a single 60° or 120° serration indicated a higher pressure at the serration vertex, decreasing in magnitude approximately linearly with distance either side of the vertex to a local minimum aligned with the trough. Similarly to the leading-edge serrations, the effectiveness of the triangular trailing edge serrations was attributed to the streamwise vortices generated, which for an aerofoil or wing with a blunt base, inhibited the two-dimensional vortex shedding.

2.2.4 Effect of Trailing-Edge Serrations on a Wing with a Sharp Trailing-Edge

Recognising that the studies thus far had not addressed the effect of serrated trailing-edge geometries on the aerodynamic characteristics of a wing with a sharp trailing edge, Vijgen et al (1989) extended Gai and Sharma's two-dimensional study of planar serrations at a blunt trailing edge to a wing-body combination with a full-span high aspect ratio high-mounted tapered wing. Based upon a NASA NLF(1)-0414F aerofoil section with a sharp finite trailing-edge thickness (d_{TE}) of 0.0038c, transition was fixed at 5%c on both the upper and lower surfaces of the full-span. A trailing-edge extension with a thickness of 0.0008c was attached to the lower surface of the baseline model across the outboard 78% semispan, accommodating the plain, scalloped or 60° triangular serrated geometries, a schematic for which is shown in Figure 3.

The planar extension accounted for a 3.2% increase in projected wing area, irrespective of the precise geometry. Accordingly, the scalloped and triangular serrations had an l/c of 0.038. Furthermore, Vijgen et al specified an additional parameter which defined the serrated geometry, namely that of the serration-length-to-total-trailing-edge-boundary-layer-thickness ratio (l/δ_{TE}). At a test Re of 1.1×10^6, based upon the mean aerodynamic chord, the length of the serrated and scalloped geometries correlated to $0.35\leq l/\delta_{TE}\leq0.65$ over $0°\leq\alpha\leq14°$ tested.

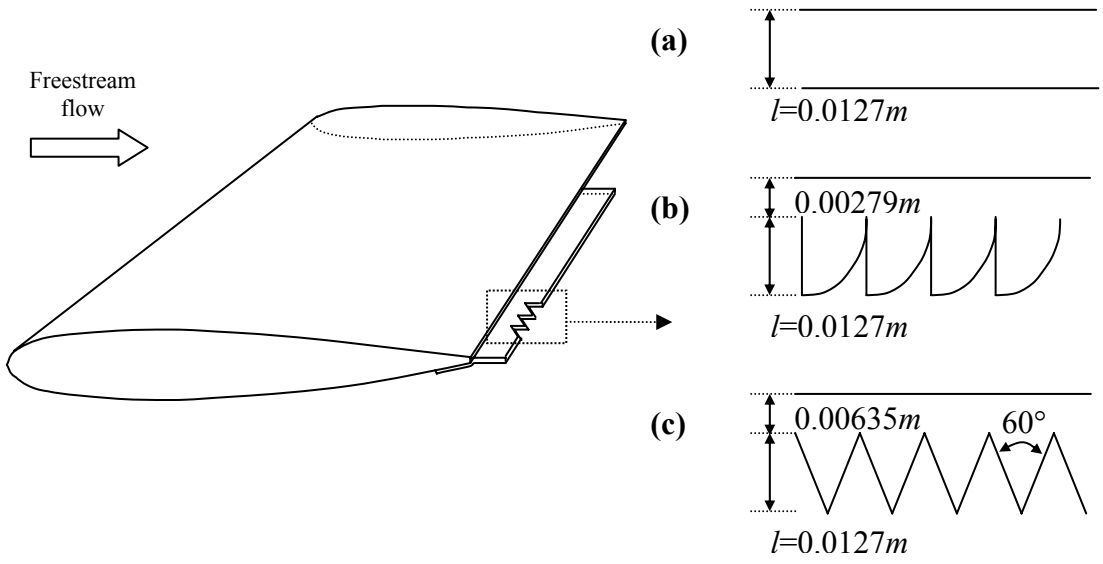

Figure 3: Planar extensions at Re=1.1×10^6: (a) solid, (b) scalloped serrations (c) triangular serrations (Vijgen et al, 1989)

The increased projected area afforded by the planar extensions, together with the modifications in the effective camber arising from variations in the boundary layer development, duly increased the C_L-α gradient in comparison to the baseline configuration, becoming non-linear for $\alpha \geq 4$ and increasing α_{stall}. Whilst the solid planar extension increased C_L by 0.1 at the upper test limit of α=14°, accounting for an 8% increment in comparison to the baseline configuration, the increment in the lift coefficient (ΔC_L) for the triangular serrated or scalloped planar extensions was 0.05, representing a 4% increment in comparison to the baseline configuration.

In comparison to the baseline configuration, the solid planar extension increased C_D for $C_L<0.5$. In contrast, the scalloped and triangular serrated geometries reduced C_D for $C_L<0.3$, with the most significant decrements arising from the triangular serrated configuration, accounting for a 3-6% (5-10 count) reduction in C_D. Accordingly, direct comparison of the solid and triangular serrated planar extensions indicated a 6-12% (10-20 count) reduction in C_D for low $C_L<0.3$ due to the triangular serrations. For $C_L>0.5$, all three planar extensions reduced C_D in comparison to the baseline configuration, with the magnitude of the decrement greatest for the triangular serrations.

Furthermore, in comparison to the baseline configuration, all three planar extensions increased the lift-to-drag ratio (L/D) for $C_L>0.5$, with the triangular serrated geometry generating the greatest increment in L/D for $0.5<C_L<1.0$. The planar extensions

increased the maximum lift-to-drag ratio $(L/D)_{max}$ from 21.0 for the baseline configuration to 21.5, 21.75 and 22.1 for the solid, scalloped and serrated geometries, respectively, correlating to a 2%, 3% and 5% increment in comparison to the baseline configuration, although the precise geometry of the planar extension had negligible effect upon the C_L at which $(L/D)_{max}$ occurred. Furthermore, the pitching moment characteristics were comparable for all three planar extensions.

With the upper surface turbulent boundary layer separating prematurely from the baseline model at $0.8c$ for $\alpha>1°$, Vijgen et al proposed that the streamwise vortices, generated immediately aft of the planar triangular serrations, entrained high-momentum flow to re-energise both the boundary layer immediately adjacent to the surface at the trailing edge of the aerofoil and the near wake, which accounted for the reduction in pressure drag and the corresponding increase in $(L/D)_{max}$.

Although no quantitative data was provided, Vijgen et al conducted additional experiments on a full-scale, semi-span, swept-wing-fuselage at a Re of 3.67×10^6, based upon the mean aerodynamic chord. Based upon a NASA HSNLF(1)-0213 aerofoil section with a sharp finite trailing edge thickness of $0.0017c$, transition was fixed at $5\%c$ and $10\%c$ on the upper and lower surface, respectively. A 60° triangular serrated planar extension was installed on the semi-span model, such that $0.4\leq l/\delta_{TE}\leq0.7$. The results indicated that $(L/D)_{max}$ was marginally increased, with C_D equal to or marginally reduced in comparison to the corresponding baseline and solid planar extension configurations. Vijgen et al proposed that the serrations were less influential on the flow field due to the trailing-edge flow remaining attached on the baseline configuration to greater angles of incidence and thus, the favourable effect of the serrations upon boundary layer separation was marginalised, if not negated.

2.2.5 Effect of Serrated Gurney Flaps on a Wing with a Sharp Trailing-Edge

Testing at $Re=1.1\times10^6$, Vijgen et al (1989) replaced the planar extension on the full-span high aspect ratio wing-body combination with full-span solid or 90° triangular serrated Gurney flaps attached to the upper surface of the wing, see Figure 4. Both Gurney flaps extended perpendicularly by $0.015c$ and remained submerged in the lower surface boundary layer at the trailing edge at low α, i.e. $d/\delta_{LS}<1$, where δ_{LS} was the boundary layer thickness at the lower surface trailing edge. Giguere et al (1997)

proposed that with the Gurney flap submerged within the boundary layer, a steady non-oscillatory wake was generated, affording a reduction in the drag force generated.

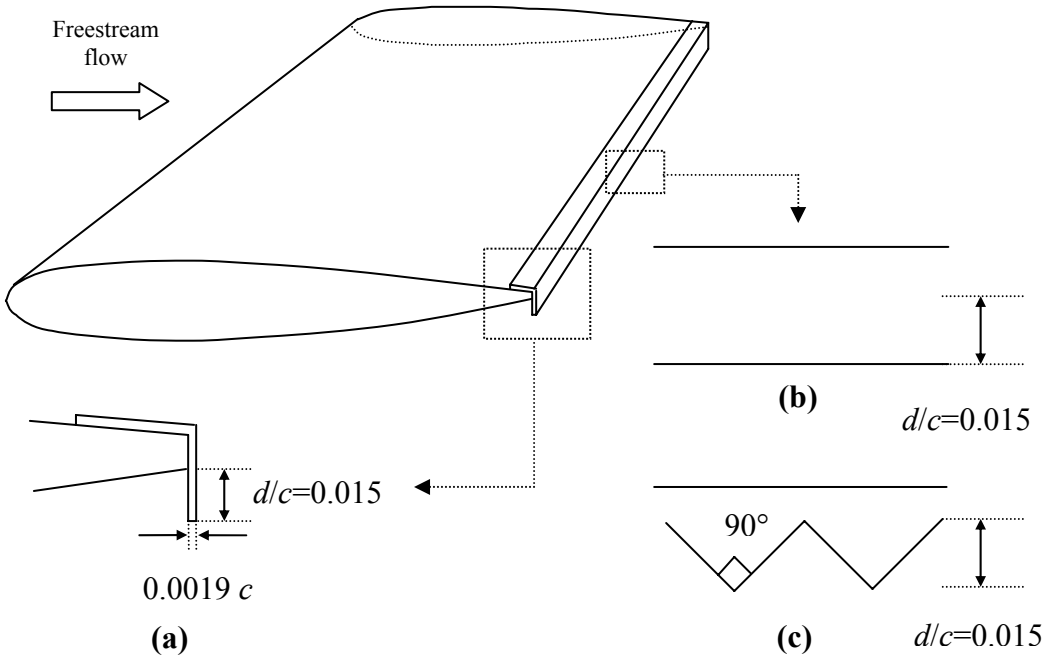

Figure 4: Non-planar extensions at Re=1.1×10^6: (a) configuration detail, (b) solid Gurney flap, (c) serrated Gurney flap (Vijgen et al, 1989)

The increased camber at the trailing edge of the aerofoil, afforded by the Gurney flap, increased C_L for all test α, with the solid Gurney flap heightening ΔC_L in comparison to the serrated Gurney flap for all α. Accordingly, the solid and serrated Gurney flaps increased C_{Lmax} by 0.25 and 0.15, respectively, corresponding to a 17% and 13% increment in comparison to the baseline configuration, although the Gurney flaps had negligible effect upon α_{stall}. Note that the projected frontal area of the solid Gurney flap was approximately twice that of the 90° serrated Gurney flap.

In comparison to the baseline configuration, the solid Gurney flap significantly increased C_D for C_L<0.5, accounting for an approximate 20% increment at a low C_L of 0.25. However, for C_L>0.6, the drag generated by the solid Gurney flap was less than that of the baseline configuration. In contrast, the serrated Gurney flap had negligible effect on C_D for C_L<0.4 but as C_L increased, C_D decreased in comparison to the baseline configuration. Accordingly, the serrated Gurney flap generated less drag than the solid Gurney flap for C_L<0.75, corroborating Gai and Palfrey (2003). The solid and serrated Gurney flaps increased $(L/D)_{max}$ from 21.0 to 22.25 and 22.75, respectively, correlating

to a 6-8% increment in comparison to the baseline configuration. The C_L at which $(L/D)_{max}$ occurred also increased with the implementation of the Gurney flaps.

Additional experiments were conducted on the full-scale, semi-span, swept-wing wing-fuselage combination at a *Re* of 3.67×10^6 (Vijgen et al, 1989). Solid or 60° triangular serrated Gurney flaps, 0.004*c* in thickness and extending across the full semi-span, were attached to the lower surface of the wing, see Figure 5 below.

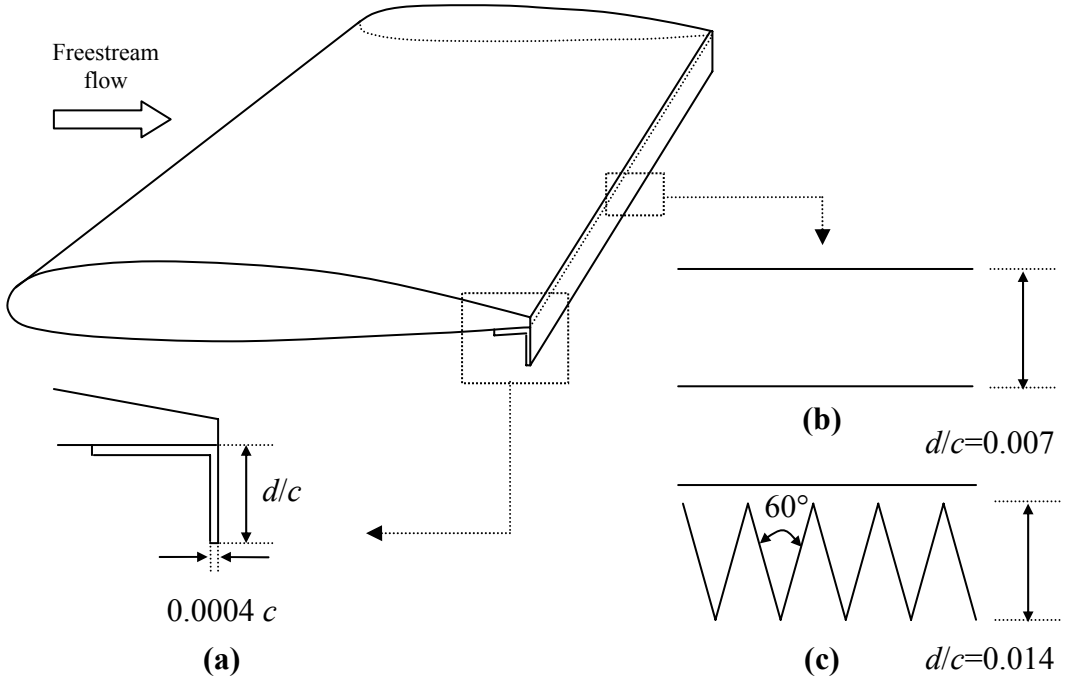

Figure 5: Non-planar extensions at *Re*=3.67×10^6 (a) configuration detail, (b) solid Gurney flap, (c) serrated Gurney flap (Vijgen et al, 1989)

In order to maintain an equivalent projected frontal area, the solid Gurney flap had a depth-to-chord ratio (d/c) of 0.007, whereas the serrated Gurney flap had a d/c of 0.014. Similarly to the experiments at $Re=1.1\times10^6$, the serrations remained submerged in the lower surface trailing-edge boundary layer at low α.

The presence of the Gurney flap at the trailing edge of the aerofoil increased C_L for all test α, with ΔC_L typically comparable irrespective of the precise Gurney flap geometry. However, a slight deviation was evident as α_{stall} was approached, with the solid and serrated Gurney flaps increasing C_{Lmax} by 0.2 and 0.1, respectively, corresponding to a 14% and 7% increment in comparison to the baseline configuration. Whilst the Gurney flap had no appreciable effect upon the nature of the stall, it did reduce α_{stall} from 20° to 18°. From the limited data, it was evident that the serrated Gurney flap typically

generated less drag than the solid Gurney flap at low C_L<0.25, although both exceeded the drag of the baseline configuration for C_L<0.65. Conversely, for high C_L>0.7, both the solid and serrated Gurney flap geometries generated less drag than the baseline configuration.

Additional water tunnel studies by Vijgen et al (1989) on a 74° triangular serrated Gurney flap at Re=1.0×10^4, substantiated the proposed vortex formation aft of the serrations on a Gurney flap, which was further corroborated by the water-tunnel studies of Neuhart and Pendergraft (1988) on a NACA 0012 aerofoil with a serrated Gurney flap. Most significantly, the latter study corroborated the postulation that the presence of serrations on the Gurney flap influenced the upstream boundary layer development and delayed boundary layer separation to a locale further downstream, accordingly allowing for a reduction in the pressure drag evident in Vijgen et al's wind-tunnel tests on the full-scale wing-body combination at Re=1.1×10^6.

Extending Neuhart and Pendergraft's (1988) qualitative study, Gai and Palfrey (2003) implemented a solid and 60° triangular serrated Gurney flap with l/c=0.025 and d/c=0.05 at the trailing edge of a two-dimensional NACA 0012 aerofoil. The Gurney flap generated a substantial increase in C_l for all 0°≤α≤12°, with ΔC_l due to the solid Gurney flap exceeding that of the serrated Gurney flap, which corroborated Vijgen et al's studies at Re=1.1×10^6. Accordingly, C_{lmax} was increased by 80% and 65% for the solid and serrated Gurney flaps, respectively. Both Gurney flaps also decreased α_{stall} from 10° for the baseline configuration to 8°. Similarly to Vijgen et al's studies at Re=3.67×10^6, whilst the serrated Gurney flap typically generated less drag than the solid Gurney flap, both incurred a notable drag penalty in comparison to the baseline configuration. Hence, both Gurney flaps had a detrimental effect upon L/D, decreasing $(L/D)_{max}$ by 7%. Flow visualisation corroborated the favourable influence of the Gurney flap on the point of boundary layer separation, although no distinction was made between the effects of the solid and serrated geometries.

2.2.6 Effect of Trailing Edge Serrations on a Deployed Single Slotted Flap

Finally, limited studies were conducted by Brennan (2002) on a two-dimensional model comprising a flat plate and a single-slotted trailing-edge flap, a schematic of which is shown in Figure 6. With a maximum thickness of 0.05m, the flat plate had a nominal chord of 1.5m. To prevent leading-edge separation, a 6:1 elliptical wooden leading-

edge formed the foremost 0.1*c*. Aft of this point, the upper surface was consistent with the geometry of the flat plate. On the lower surface, the maximum thickness was maintained between 0.1*c* and 0.62*c*, aft of which the geometry tapered to a 0.5*mm* finite trailing-edge, based upon a NACA 0012 aerofoil section aft of maximum thickness. A modular aluminium trailing-edge component extended across the aft 0.1*m* of the flat plate and facilitated the interchange of plain, 10mm and 20mm 60° triangular serrations. An aluminium single slotted flap, with a 0.15*m* chord, was positioned aft of the flat plate trailing edge.

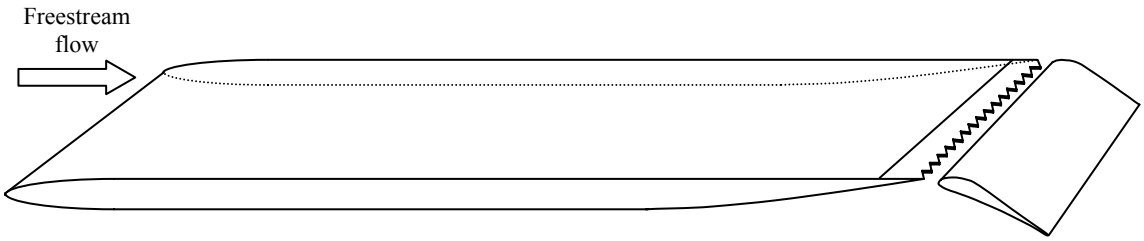

Figure 6: Schematic of two-dimensional modified flat plate and single slotted flap model (Brennan, 2002)

The analysis was predominantly qualitative, noting that the influence of the serrations on the flow field developing over the single slotted flap was dependent upon the position of the flap relative to the trailing edge serrations, although the effect of varying the flap lap/gap was not quantified. Furthermore, Brennan noted that when the vertical distance between flat plate trailing edge the flap exceeded 25*mm*, two distinct wakes were formed downstream of the flap, although this was not synonymous of an increase in the overall profile drag. Thus, whilst the tests suggested that serrations had the potential to favourably influence the flow field developing over the single slotted flap, no data was provided to quantify the effect of varying the flap lap/gap, deflection angle or serration length.

2.2.7 Conclusions for Passive Boundary Layer Control by Serrations

The preceding review of available literature highlighted that studies of serrated geometries thus far were predominantly conducted on a single component aerofoil or wing. In conclusion of the results, it was evident that for single component configurations:

- Optimising leading edge serrations, in terms of geometry and location, delayed boundary layer separation to higher α, increased C_{lmax} and reduced C_d at high α

- Optimising "M-shaped" geometry at a blunt trailing edge reduced base drag by nearly 70% in comparison to a straight blunt trailing edge configuration

- 60° triangular trailing edge serrations reduced C_D for any given C_L in comparison to the corresponding solid trailing edge configuration by a maximum of 6-12% at low C_L<0.3, increased L/D for C_L<1.0 and increased $(L/D)_{max}$ by 3%

- Counter-rotating streamwise vortices, generated aft of each trailing edge triangular serration vertex, re-energised both the boundary layer immediately adjacent to the surface at the trailing edge and the free shear layer in the near wake, accounting for the reduction in pressure drag and the corresponding increase in L/D

- Triangular serrations on a Gurney flap at the trailing edge of a single component wing typically delayed boundary layer separation to a locale further downstream, affording a reduction in pressure drag

Thus, research conducted on single component configurations clearly illustrated that serrated geometries could favourably influence boundary layer development, with subsequent benefits to the aerodynamic forces and performance characteristics.

However, studies pertaining to boundary layer flow control over multi-element configurations were particularly limited. Tanner's (1975) experiments provided the first indication that implementation of an M-shaped geometry at the blunt trailing edge of a wing with a simple mechanical split flap had a favourable effect upon the maximum lift force generated. Combined with Brennan's (2002) study, it was evident that implementation of triangular serrations at the trailing edge of a main element had the potential to favourably influence the boundary layer development over the upper surface of a single slotted trailing edge device, with subsequent benefits in aerodynamic performance. Hence, the effect of trailing edge triangular serrations within a high-lift configuration warranted further investigation.

2.3 Active Boundary Layer Control: Blowing

2.3.1 Introduction

Based upon the principle that the injection of high velocity air within the near surface boundary layer supplied additional kinetic energy to the low energy fluid elements immediately adjacent to the surface, it has long been shown that blowing air over the upper surface of a deployed trailing edge device was an effective means of delaying boundary layer separation and hence, favourably influenced the aerodynamic characteristics of the configuration.

As early as 1917, Föttinger proposed that by blowing a tangential jet of air over the upper surface of the leading-edge of a mechanical trailing-edge flap, shown schematically in Figure 7, trailing-edge boundary layer separation could be delayed or even eliminated (cited in Korbacher and Sridhar, 1960). However, it was not until 1931 that Bamber tested the concept and proved it was a beneficial means of boundary layer control. Based on Föttinger's principle, studies of tangential trailing-edge blowing expanded during the course of the next thirty years.

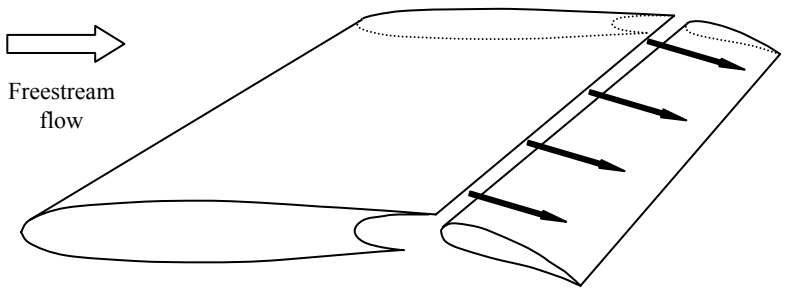

Figure 7: Schematic of tangential blowing over trailing-edge flap

However, it was the latter investigations of this period, particularly those of the early 1950s, which demonstrated a fundamental advance in the development of a practical boundary layer control system. With the advent of jet propulsion and the development of jet engines designed specifically for aircraft during the 1940s, a practical and accessible source of compressed air was available for use in a boundary layer control system. By 1952, Constant recognised that the propulsive jet of the modern aircraft could be integrated with the lifting system, expelling air from a slot nozzle along the trailing-edge of the main wing to achieve the required improvements in aerodynamic performance and hence, reduce the mechanical complexity of the high-lift devices prevalent at the time (cited in Korbacher and Sridhar, 1960).

Lachmann (1961) provides a highly comprehensive chronological review of these advances in blowing boundary layer control, specifically detailing the respective research developments in the United Kingdom, France, Germany and the United States of America. Rather than attempt to summarise such an extensive publication in the proceeding sections, references were selected that illustrated the effects of blowing air tangentially from a slot over the upper surface of a trailing edge flap within a high-lift configuration. Accordingly, the critical parameters influencing the effectiveness of tangential slot blowing are established, together with the salient trends in the resultant aerodynamic forces and performance characteristics of a multi-element configuration, when subject to tangential slot blowing.

2.3.2 Two-Dimensional Studies

In the first instance Dods and Watson's (1956) two-dimensional low-speed experiments are highlighted, as they illustrate the critical design parameters of a configuration, which influence the effectiveness of tangential slot blowing. For reference, the study was based upon a NACA 0006 thin aerofoil section, with 0.15c leading-edge slat and 0.30c trailing-edge flap, and conducted at M_∞=0.082, 0.117 and 0.143, corresponding to Re=2.3, 3.3 and 4.0×10^6, respectively. This is complemented by Turner's (1964) study on NACA 65$_5$-424 aerofoil section with a 0.35c flap at a Re=2.96×10^6, which illustrates the improvements in aerodynamic efficiency generated by blowing tangentially from a slot located at 0.65c.

(a) Influence of Flap Profile

Defining the critical momentum coefficient ($C_{\mu crit}$) as the point at which further increments in momentum coefficient (C_μ) resulted in only moderate increases in the lift coefficient at zero incidence ($C_{l\alpha=0°}$), Dods and Watson noted that the flap profile was critical to achieving a minimal $C_{\mu crit}$. For a given flap deflection angle (δ_f), profiles that gradually turned the flow from the blowing slot nozzle exit generated a lower $C_{\mu crit}$ than profiles which abruptly turned the flow. As expected, $C_{\mu crit}$ increased with successive increments in δ_f.

Whilst Dods and Watson noted that the incremental lift coefficient (ΔC_l) due to tangential slot blowing increased when the flap chord length was reduced from 0.30c to 0.15c, this was offset by the corresponding increase in C_μ required to maintain boundary layer attachment at the higher flap deflections necessary to generate comparable lift for

the configuration. However, it was proposed that the C_μ could be reduced by optimising the flap profile for the smaller flap chord.

(b) Influence of Flap Position

Dods and Watson noted that an optimum flap position necessitated that the upper surface of the flap leading-edge was positioned below the upper surface of the main element but located within the jet trajectory, ideally near the jet centreline. With these conditions satisfied, the optimal flap position was relatively insensitive to the precise vertical location of the flap. The optimal horizontal position of the flap, relative to the trailing-edge of the main element, was not determined. However $C_{\mu crit}$ increased as the horizontal distance between the trailing-edge flap and the blowing slot nozzle increased, such that with the flap deflected by 60°, moving the flap 0.5%c aft of the nozzle doubled $C_{\mu crit}$.

(c) Influence of Nozzle Height

In the experiments conducted by Dods and Watson, varying the nozzle-height-to-wing-chord ratio (h_n/c) between 0.00017 and 0.00065 had minimal effect upon ΔC_l for a given C_μ. This corroborated the two-dimensional wind-tunnel tests of Harkleroad and Murphy (cited by Dods and Watson, 1956) on a model F9F-5 wing section, whereby varying (h_n/c) between 0.00036 and 0.00072 had negligible effect upon ΔC_l. In contrast, Dods and Watson noted that ΔC_l was more sensitive to increments in (h_n/c) from 0.00065 to 0.00110, decreasing in magnitude for $C_\mu > C_{\mu crit}$. Although the degradation in ΔC_l was less prominent, similar trends were observed by Wallace and Stalter (also cited by Dods and Watson, 1956) in their two-dimensional experiments on a NACA 23015 aerofoil section for $0.00050 \leq (h_n/c) \leq 0.00150$. However, variations in flap configuration and nozzle design prevented such discrepancies to be resolved, suggesting that the optimum range of (h_n/c) was dependent upon the specified configuration geometry.

(d) Effect of Blowing on Aerodynamic Forces

Turner's experiments showed that for the two-element configuration, C_l-α and C_{lmax} increased with increasing C_μ. By deflecting the leading-edge slat in conjunction with the blown flap, Dods and Watson's study showed that ΔC_l was reduced at small C_μ. However, as C_μ increased, the adverse effect of the slat deflection upon ΔC_l became less prominent and for $C_\mu > 0.16$, extension of the leading-edge slat had a favourable effect upon ΔC_l. Significantly, Turner's studies indicated that tangential slot blowing reduced the section drag, with larger drag reductions evident at higher C_l. Furthermore,

increasing C_μ heightened the decrement in drag. Results suggested that at a C_μ of 0.01, tangential slot blowing increased $(L/D)_{max}$ by approximately 75%.

2.3.3 Three-Dimensional Studies: Straight-Wing Aircraft

Rolls and Innis (1956) provide a useful comparison of flight tests on an F9F-4 straight-wing aircraft at 5000*ft* with the three-dimensional wind-tunnel tests of Murphy et al, on a 1/5.5-scale model of the aircraft, cited therein. With a wing cross-section based on a NACA 64A010 aerofoil and the leading-edge slat deflected by 19°, air was ducted from the engine to the nozzle in the wing shroud and then expelled over the 45° flap, extending from 26% to 59% semispan. Lawford's (1968) wind-tunnel tests on a straight wing-fuselage model at $Re=0.9\times10^6$ are also included within the subsequent discussion, as the study highlighted the critical blowing quantities required to maintain boundary layer attachment on a full-span trailing-edge deflected flap.

(a) Effect of Blowing on Lift

At high C_μ, Rolls and Innis noted that the increment in C_L due to tangential slot blowing was approximately constant for any given $\alpha<\alpha_{stall}$. However, the flight test ΔC_L for the F9F-4 aircraft was greater than that of the corresponding small-scale wind-tunnel tests, with the differences attributed to variations in *Re* and increased global circulation.

(b) Effect of Blowing on Drag

For $C_L<1.7$, trailing-edge blowing on the F9F-4 aircraft increased the induced drag and consequently, the total C_D increased. However, for further increments in C_L, blowing air over the trailing-edge flap decreased the total C_D.

(c) Effect of Blowing on Stall Characteristics

Trailing-edge blowing on the F9F-4 aircraft delayed boundary layer separation to higher angles of incidence for the flight tests than for the small-scale wind-tunnel experiments, with the difference attributed to variations in *Re*. Although the pilots differed in their opinions of the precise stall characteristics, it was agreed that tangential slot blowing resulted in poor stall warning, occurring immediately prior to stall.

Lawford's tuft studies at 0.2*c* and 0.5*c* indicated that without blowing, the stall initiated at the trailing-edge for all full-span flap deflections. Tangential slot blowing modified the stall pattern: trailing-edge boundary layer attachment was maintained but the boundary layer tended to separate from the leading-edge, consistent with an abrupt and

severe stall and corroborating the pilots' observations on the F9F-4 aircraft. Increasing the angle of incidence and/or the flap deflection angle necessitated greater C_μ values to prevent trailing-edge boundary layer separation. Furthermore, spanwise variations in the minimum C_μ required for boundary layer attachment were attributed to either imperfections in the blowing slot or discontinuities on the configuration surface, resulting in a locally increased C_μ to prevent separation. This was confirmed by placing blockages into the blowing slot, whereby the resultant separation region downstream of the blockage and subsequent reduction in C_L increased the C_μ required for boundary layer attachment.

(d) Effect of Blowing on Takeoff Performance

The loss of thrust, arising from the installation of the blowing system on the F9F-4 aircraft, offset the potential benefits in takeoff performance, such that the ground run distance and the distance for clearing a 50*ft* obstacle were adversely affected by blowing over the trailing-edge flap. Whilst no quantitative data was obtained, the pilots noted that qualitatively, with blowing applied, it was more difficult to achieve nose-wheel lift off, which was associated with the nose-down pitching moment induced by blowing. Although the takeoff airspeed was reduced with blowing, this was offset by the decreased acceleration due to the increased drag.

(e) Effect of Blowing on Landing Performance

Blowing over the flap enabled an approach angle of incidence equal to or greater than that for the configuration without blowing, which corresponded to an approximate 10 knot reduction in approach speed. Typically, the thrust losses arising from the blowing system had a negligible effect upon the landing performance and hence, blowing favourably influenced the landing distances, reducing both the ground run and the total landing distance clearing a 50*ft* obstacle.

2.3.4 Three-Dimensional Studies: 35° Swept-Wing Configuration

A selection of studies on 35° sweptback wing configurations are detailed below, as these most succinctly typify the effect of tangential slot blowing on the resultant aerodynamic forces and performance characteristics of a high-lift configuration. Furthermore, the experimental studies are complemented by flight tests, which serve to identify potential disparities resulting from implementation of the boundary layer control system in free flight conditions.

Kelly and Tolhurst (1955) and Tolhurst and Kelly (1956) conducted full-scale three-dimensional wind-tunnel tests at Re=7.5×10^6 to determine the effects of blowing over the upper surface of the flap on an F-86D aircraft, both with and without the horizontal tail-plane installed. The wings were sweptback by 35° along the quarter-chord line and modified NACA 0012-64 and NACA 0011-64 aerofoil sections formed the wing root and tip, respectively. The standard single-slotted flap was replaced with a simple plain flap, deflected from 45° to a maximum of 85°. Air was bled from a modified J-34 engine to a slit, extending across the full-span of the flap upper surface.

Anderson et al (1956) documented the flight tests on an F-86F aircraft, conducted at sea level and 5000*ft*, with tangential slot blowing over the upper surface of the trailing-edge flap. The standard 38° slotted flap leading-edge was modified to accommodate a blowing system comparable to the aforesaid wind-tunnel investigations.

Kelly et al (1958) enhanced these investigations with more extensive full-scale wind-tunnel tests on the F-86D aircraft and flight tests on the F-86F aircraft. Additional tests were conducted with the nozzle located in the wing shroud, upstream of the simple plain deflected flap.

Kelly and Tucker (1956) extended the full-scale experimental studies of 35° sweptback wings to an F-93 aircraft at Re=7.6 and 10.7×10^6. The F-93 aircraft had a greater wing area than the F-86D aircraft but an equal flap area. The blowing system employed was comparable to that of Kelly and Tolhurst (1955). All experiments were conducted with the horizontal tail-plane removed and the leading-edge slats retracted.

Extending the investigations to carrier-type aircraft, Quigley et al (1957) reported on the flight characteristics of an FJ-3 aircraft at 5000*ft*. The wing shroud upstream of the flap was modified to accommodate the leading-edge of the flap, which itself was modified from the standard slotted flap to facilitate the blowing boundary layer control system. Air was bled from the J65 engine and ducted internally to the blowing slot extending across the span of the flap.

(a) Effect of Blowing on Lift

For a given α and δ_f, the initial rapid increase in C_L with increasing C_μ was attributed to the immediate effect of the blown air increasing the momentum in the near surface boundary layer and delaying, if not eliminating, separation. Furthermore, once the boundary layer was attached, considerable increases in C_μ were required to significantly

increase ΔC_L. The increased velocity of the blown air, beyond that necessary to maintain boundary layer attachment, essentially formed a "jet", which effectively extended the flap chord and duly increased global circulation, further augmenting the lift (Vlaenderen, 1959).

Both the full-scale wind-tunnel tests and the flight tests indicated that blowing over the upper surface of the flap increased the C_L-α gradient by approximately 10% and 35%, respectively.

Blowing tangentially over the upper surface of the flap deflected by 45°, 60° and 75° on the F-86D aircraft, increased $C_{L\alpha=0^\circ}$ by 0.32, 0.53 and 0.56, respectively, with no further increment in $C_{L\alpha=0^\circ}$ as the flap was deflected an additional 10° to the upper test limit of 85° (Kelly et al, 1958). Blowing over the trailing-edge flaps on the F-86F flight test aircraft increased $C_{L\alpha=0^\circ}$ by 0.19 and 0.33 at the flap deflection lower and upper test limits of 38° and 66°, respectively (Anderson et al, 1956). The decrement in $\Delta C_{L\alpha=0^\circ}$ for the flight tests, in comparison to the wind-tunnel tests, was attributed to variations in configuration detail, together with discrepancies between the corresponding C_μ, highlighting the sensitivity of the aerodynamic performance to variations in configuration geometry and blowing C_μ.

In comparison to the F-86D aircraft with a standard 38° single-slotted flap, blowing tangentially over flap deflections of 45°, 60° and 75° increased C_{Lmax} by 0.28, 0.4 and 0.46, respectively, with no further increment as the flap was deflected an additional 10° to the test upper limit of 85° (Kelly and Tolhurst, 1956). Thus the increment in C_{Lmax} was attributed firstly, to the increased flap deflection angle and secondly, to the application of blowing over the upper surface of the flap. Blowing over the upper surface of the standard 38° flap deflection for the flight tests on the F-86F aircraft increased C_{Lmax} by 0.17 in comparison to the corresponding configuration without blowing (Anderson et al, 1956). Accordingly, this increase in C_{Lmax} for the flight test was attributed entirely to the application of blowing over the flap. The combination of extending the flap to the upper test limit of 66° and applying blowing over the upper surface increased C_{Lmax} by 0.26 for the F-86F aircraft. Thus, for a given δ_f, the increment in C_{Lmax} for the flight tests was of a smaller magnitude than that for the corresponding wind-tunnel tests, due to variations in the configuration detail, together with discrepancies between the corresponding C_μ. Although the increments in C_{Lmax} were smaller, similar results were attained by Kelly and Tucker (1956) for their wind-

tunnel experiments on the F-93 aircraft, whereby blowing over flap deflections of 45° and 60° resulted in ΔC_{Lmax}=0.1 and 0.2, respectively.

Corroborating the two-dimensional experimental studies of Dods and Watson (1956), Kelly and Tolhurst's (1955) full-scale experimental investigations showed that for a given C_μ, ΔC_L was independent of variations in (h_n/c) between 0.00017 and 0.00067. This trend was corroborated by Kelly and Tucker's (1956) experiments on the F-93 aircraft, whereby blowing over a 45° or 60° flap and varying (h_n/c) between 0.00006 and 0.00042, had negligible effect upon C_L for a given C_μ and α. This was also consistent with the flight test observations of Quigley et al (1957) on the FJ-3 aircraft, although the range of test (h_n/c) varied between 0.00010 and 0.00021.

Quigley et al (1957) noted that whilst the increment in C_l due to blowing was relatively insensitive to the precise leading-edge device implemented on the FJ-3 aircraft, ΔC_{Lmax} was sensitive to the leading-edge device installed. Tolhurst and Kelly's (1956) experiments also suggested that with the application of blowing over the upper surface of the deflected flap, the aircraft's stability and control characteristics were intrinsically dependent upon the precise leading-edge device implemented.

The wind-tunnel experiments by Tolhurst and Kelly (1956) indicated that blowing tangentially over the flap modified the tail-plane incidence at which the maximum C_{Lmax} was achieved. It was also estimated that blowing over a 45° and 60° flap increased the downwash angle at the horizontal tail-plane by approximately 3.5° and 4.5°, respectively, modifying the global flow field surrounding the aircraft, with subsequent effects upon C_L.

Finally, Kelly and Tolhurst (1955) implemented a full-span step discontinuity on the upper surface of the flap, simulating imperfections arising from full-scale manufacture. For a given C_μ, the small reduction in C_L suggested that the flap was relatively insensitive to the upper surface discontinuity. However, the height of the discontinuity was a critical parameter, with C_L decreasing as the discontinuity extended into the flow field. It was also proposed that the distance between the discontinuity and the blowing slot nozzle was a critical factor: decreasing the distance amplified the adverse effect upon C_L.

(b) Effect of Blowing on Stall Angle

Increments in C_{Lmax} were firstly offset by a marginal decrease in α_{stall} arising from the increased flap deflections and secondly, by a more significant reduction in α_{stall} resulting from blowing over the upper surface of the trailing-edge flap. Accordingly, Kelly et al's (1958) wind-tunnel tests on the F-86D aircraft without a horizontal tail-plane showed that without blowing, deflecting the flap from 0° to a maximum of 85° resulted in a 3° decrease in α_{stall}. This doubled to a 6° reduction in α_{stall} when trailing-edge blowing was applied over the same flap deflection range. Similar trends were observed in the wind-tunnel tests on the F-93 aircraft (Kelly and Tucker, 1956) and the flight tests of the F-86F aircraft. Anderson et al (1956) noted that unfavourable stall characteristics were often exacerbated by the application of blowing and thus, installation of an appropriate leading-edge device could maintain leading-edge boundary layer attachment to higher angles of incidence, i.e. increase α_{stall}, and favourably influence the stall characteristics of the aircraft. Subsequent studies by Kelly and Tolhurst (1955) and later, Kelly et al (1958) confirmed that by deflecting the leading-edge slat in conjunction with 60° blown flap, α_{stall} was increased by 4° and the corresponding stall characteristics were favourably influenced, changing from an abrupt stall with leading-edge slat retracted, to a gradual stall with the slat deflected.

(c) Effects of Blowing on Drag

The full-scale wind-tunnel tests on the F-86D aircraft showed that for a given C_L, trailing-edge blowing increased C_D, see Kelly and Tolhurst (1955) or Kelly et al (1958). Although blowing over the upper surface of the trailing-edge flap eliminated or decreased the region of separation, the subsequent decrement in pressure drag was offset by an increase in the induced drag and hence, increased the total C_D. The increment in C_D was further heightened by the deployment of a leading-edge device, although the adverse effect of the leading-edge slat upon C_D was marginalised with increasing C_L, such that as C_{Lmax} was approached, deflection of a leading-edge device had negligible effect upon C_D. However, these trends were somewhat contradicted by the flight tests: whilst blowing over a given flap deflection sufficiently increased the induced drag at low and moderate C_L such that the total C_D increased, Anderson et al (1956) and Quigley et al (1957) noted that as C_{Lmax} was approached, tangential slot blowing over the upper surface of the flap decreased the total C_D.

Similarly to the two-dimensional experiments by Dods and Watson (1956), Kelly and Tolhurst (1955) noted that whilst smaller flap deflection angles minimised C_D, this optimisation was compromised by the larger C_μ required to generate comparable lift for

the configuration and the subsequent reduction in available thrust. Thus, they emphasised the need to consider the bleed air requirements and subsequent effects upon engine thrust, together with the drag characteristics, when optimising the blown flap.

(d) Influence of Blowing Nozzle Inclination and Position

At α=8° and 12°, applicable to takeoff and landing conditions, and with the trailing-edge flaps deflected by 60°, varying the angular position of the blowing nozzle had negligible affect upon the C_μ required to maintain boundary layer attachment, (Kelly and Tolhurst, 1955).

The position of the fixed nozzle with respect to the flap was more critical. With the flap deflected to the upper test limit of 85° and the nozzle positioned aft of the minimum pressure point, even the greatest C_μ achievable could not prevent boundary layer separation and the subsequent dramatic reduction in C_L. Accordingly, Kelly et al (1958) specified that for the flap effectiveness not to be degraded as the flap deflection was increased, the nozzle needed to be positioned such that at the greatest flap deflection, it was at the point of minimum pressure on the flap and hence, was upstream of this point for smaller flap deflections. If the slot was located at the trailing edge of the main element, then it may be inferred that the impingement of the jet of air on the upper surface of the flap must coincide with the point of minimum pressure on the flap at the greatest flap deflection and hence, be upstream of this point for smaller flap deflections. Furthermore, to ensure impingement of the jet of air on the flap surface, Wallace et al (cited in Lachmann, 1961) proposed that irrespective of the precise flap deflection angle implemented, the flap upper surface should be positioned tangentially to the slot centreline – corroborating the two-dimensional studies of Dods and Watson (1956). In addition, Wallace et al proposed that the flap upper surface be positioned at a radial distance from the slot upper lip equal to that of the slot width, to ensure a favourable trajectory of the jet of air.

(e) Effect of Blowing on Takeoff Performance

Blowing over a 45° flap with the maximum C_μ available only marginally reduced the takeoff distance over a 50*ft* obstacle when compared to the corresponding configuration without blowing, although the more favourable flap lift increments, resulting from the application of blowing, decreased the required takeoff angle of incidence (Anderson et al, 1956). However, by delaying blowing over the upper surface of the flap until the takeoff speed was reached, the thrust loss was decreased and the total takeoff distance was reduced by approximately 6%. Quigley et al's (1957) flight tests on the FJ-3

aircraft indicated that the effect of tangential slot blowing on the takeoff distance was dependent upon the leading-edge device implemented, reducing the total takeoff distance over a 50*ft* obstacle by a maximum of 12% when a cambered leading-edge was installed.

(f) Effect of Blowing on Landing Performance

Assuming an average gross landing weight and blowing over 55° and 66° flap on the F-86F aircraft with a leading edge device deployed, the total landing distance over a 50*ft* obstacle was reduced by approximately 20% (Anderson et al, 1956). Although the tangential slot blowing was less effective over a 55° flap on the FJ-3 aircraft, the total landing distance clearing a 50*ft* obstacle was reduced by approximately 13% in comparison to the corresponding configuration without blowing (Quigley et al, 1957).

2.3.5 Conclusions for Tangential Slot Blowing Literature

Subsequent studies on 45° and 49° sweptback wing configurations, such as Hickey and Aoyagi's (1958) large-scale three-dimensional wind-tunnel tests, Quigley et al's (1958) flight tests on a modified F-100A aircraft and Whittle and Lipson's (1954) full-scale experiments on a swept wing, illustrated that the salient attributes of tangential slot blowing on the resultant aerodynamic forces and performance characteristics of a high-lift configuration were consistent with those previously detailed in Section 2.3.4 for 35° swept-wing configurations. Accordingly, it can be concluded that:

- Blowing tangentially over the upper surface of the flap had the potential to delay or eliminate trailing edge boundary layer separation

- Increasing the angle of incidence and/or the flap deflection angle, together with imperfections in the blowing slot or discontinuities on the configuration surface, increased the C_μ required to prevent trailing-edge boundary layer separation

- Aerodynamic performance achievable with tangential slot blowing was sensitive to variations in configuration geometry and C_μ

- Typically, tangential slot blowing increased the C_L-α gradient and C_{Lmax} but decreased α_{stall} and heightened the severity of the stall characteristics, although installation of an appropriate leading-edge device favourably influenced both α_{stall} and the stall characteristics

- The decrement in pressure drag due to tangential slot blowing was typically offset by an increase in the corresponding induced drag at low and moderate C_L such that the total C_D increased but studies suggested that as C_{Lmax} was approached, tangential slot blowing decreased the total C_D

- Flap profiles which gradually turned the flow from the blowing slot nozzle exit reduced the C_μ required to maintain boundary layer attachment in comparison to profiles which abruptly turned the flow

- To maintain flap effectiveness over the δ_f range, the impingement of the jet of air upon the upper surface of the flap must coincide with the point of minimum pressure at the greatest δ_f and hence, be upstream of this point for smaller δ_f

- Evidence to suggest that with an appropriate leading-edge device implemented, tangential slot blowing reduced the takeoff distance, decreased the takeoff angle of incidence and decreased the takeoff airspeed, although the latter was offset by the decreased acceleration due to the increased drag

- Tangential slot blowing favourably influenced the landing distances, reducing both the ground run and the total landing distance clearing a 50*ft* obstacle, and with an appropriate leading-edge device implemented, reduced the average landing speed

Thus, the successful integration of tangential slot blowing on production aircraft justified its subsequent evaluation within the context of the present high-lift configurations under consideration.

However, both Kelly and Tolhurst (1955) and Dods and Watson (1956) noted that as the C_μ required to maintain boundary layer attachment over the upper surface of the flap increased, the available thrust decreased. Emphasising the need to consider the bleed air requirements and subsequent effects upon engine thrust when optimising the boundary layer control system, together with the drag characteristics of the high-lift configuration, it was evident that reducing the C_μ required to maintain boundary layer attachment would be advantageous in any boundary layer control optimisation.

With the configuration geometry of the present investigations fixed, modifications to the tangential blowing system were considered whereby the mass flow rate and hence, C_μ

could be reduced without any loss in boundary layer control or detriment to the aerodynamic performance. Accordingly, it was proposed to replace the blowing slot with discrete holes. Whilst it was understood that blowing through discrete holes as a means of boundary layer control over the upper surface of a trailing edge flap within a high-lift configuration had not previously been investigated, it was recognised that discrete holes were employed as a means of blade tip cooling in gas turbine engines. Szanca et al (1970) and Prust et al (1976) provide just two examples of ejecting coolant through discrete holes located at the tip of the turbine blade surface. Thus, a potential means of optimising the boundary layer control system was identified for further investigation.

3 Experimental Methodology

This chapter introduces the facilities in which the experimental programme was conducted. The models are described, together with the ancillary equipment and instrumentation. The test programme frameworks are outlined, as are the analysis methodologies.

3.1 Brough Wind-Tunnel

Small-scale two-dimensional experiments were conducted in the College of Aeronautics' open return, low-speed $0.61m \times 0.61m$ Brough wind-tunnel at Cranfield University.

Extending $10.7m$ in total length, the low turbulence facility consisted of a settling chamber with a $1.84m \times 1.84m$ cross-sectional area and a 9:1 contraction ratio. Four turbulence screens and a honeycomb were mounted in the intake to reduce variations in the freestream speed and promote uniform flow direction, resulting in a freestream turbulence intensity of approximately 0.25% (Bray, 1998; Powell, 2000).

The Brough wind-tunnel had a maximum speed of $45m/s$, dependent upon model size. The closed working-section extended $2.44m$ in length. Wooden and Perspex panels formed the fixed sidewalls in the steel framework. Access to the model was facilitated through an aperture within the central Perspex panel, with additional access to the working section provided by removable panels in the floor and ceiling.

A $0.05m$ rubber collar separated the working-section from the diffuser, reducing the adverse effect of vibrations – induced by the externally mounted $14.9kW$ motor – on the upstream flow field developing in the working-section. The diffuser terminated with a belt-driven fan, immediately aft of which the flow was deflected through 90° and ejected vertically upwards.

3.1.1 Model Description

The small-scale experiments focused on a two-dimensional model, comprising a flat plate and a single-slotted trailing-edge flap spanning the width of the closed working section.

With a maximum thickness of $0.05m$, the flat plate had a nominal chord (c) of $1.5m$. To prevent leading-edge separation, a 6:1 elliptical wooden leading-edge formed the

foremost 0.1c. Aft of this point, the upper surface was consistent with the geometry of the flat plate. On the lower surface, the maximum thickness was maintained between 0.1c and 0.62c, aft of which the geometry tapered to a 0.5mm trailing-edge, based upon a NACA 0012 aerofoil section aft of maximum thickness. A modular aluminium trailing-edge component extended across the aft 0.1m of the flat plate and facilitated the interchange of the trailing-edge geometries.

Previous experiments by Brennan (2002) defined three trailing-edge geometries:

- Plain trailing-edge
- 60° triangular serrated geometry, extending 10mm from vertex to base
- 60° triangular serrated geometry, extending 20mm from vertex to base

Note that the serration vertex was formed by a circular arc of 1mm radius.

As the fundamental impetus for the Brough experiments was to discern the effect of trailing edge serrations upon the aerodynamic characteristics of a single slotted flap, it was imperative that the flow field characteristics at the trailing edge of the flat plate simulated the salient features of the flow field at the trailing edge of a main element upstream of deflected flap within a multi-element configuration. That so being, it was deemed pertinent to be able to control the trailing-edge boundary layer thickness on the upper and lower surfaces of the flat plate, such that the upper-to-lower-surface-trailing-edge-boundary-layer-thickness ratio (δ_{us}/δ_{ls}) was representative of a high-lift configuration. Accordingly, a boundary layer control system was implemented, enabling the upper and lower surface boundary layers to be independently modified.

The boundary layer control system comprised two distinct aluminium porous surfaces, which were integrated flush with the flat plate surface to facilitate control of the trailing-edge boundary layer thickness. Extending 0.3m in length and 0.58m in width, each porous surface had a separate plenum chamber, the depth of which was defined by the local model thickness. The upper surface porous area extended from 0.39c to 0.59c and that on the lower surface extended from 0.64c to 0.84c. Hence, the plenum chamber corresponding to the upper surface porous area was located within the maximum thickness of the model and that corresponding to the lower surface was located within the aft tapered region.

Each orifice in the porous surface was 1*mm* in diameter, with 10*mm* between successive spanwise orifice centres. Thirty-one spanwise rows of orifices were drilled at 10*mm* intervals; each successive row offset by 2.5*mm* in the spanwise direction, creating a four row cyclical pattern. Based upon a porous plate area of $0.18m^2$, each porous plate initially had an open hole area of 0.80%. Following preliminary tests, the open hole area was increased to 2.34% and 3.09% on the upper and lower surface porous plates, respectively, with the disparity due to the manufacturing time available.

Five 0.015*m* diameter copper tubes, each with a slot across the central third, extended across the span of a given plenum chamber at equidistant intervals, normal to the freestream. Apertures in the central Perspex sections of the wind-tunnel sidewalls accommodated the external ducting from the plenum chamber to a $0.0144m^3$ box secured above the tunnel roof, to which a flow meter was affixed. Further ducting connected the flow meter to the power source for the boundary layer control system. Hence, the trailing-edge boundary layer thickness on the upper and lower surfaces of the flat plate could be individually regulated.

The test model pictured within the wind-tunnel facility is shown in Figure 8. (Note that the ducting for the boundary layer control – seen above the wind-tunnel – was removed for the photograph, so as not to conceal the model).

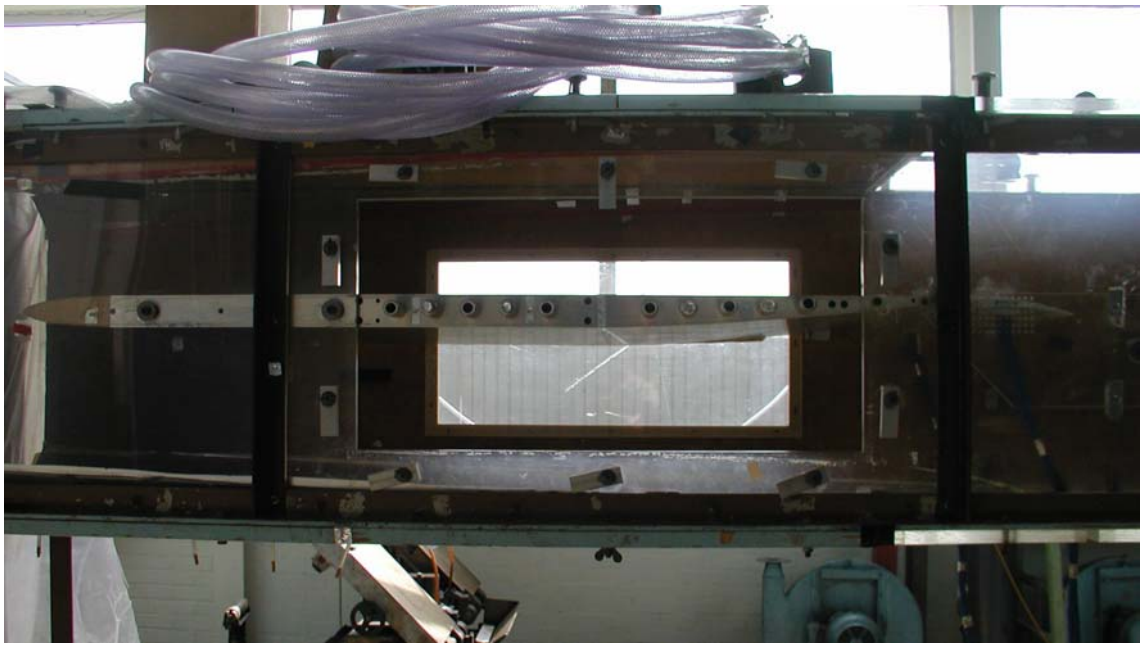

Figure 8: Photograph of flat plate and trailing edge flap model in the Brough wind-tunnel

An aluminium flap, with a 0.15*m* chord (c_{flap}), was positioned aft of the flat plate trailing edge. The geometry of the flap was defined by the HELIX project and the non-dimensional co-ordinates are given in Appendix A. So as to confirm the flow field dimensionality over the centre third of the span, surface static pressure orifices were located ±0.1*m* either side of the spanwise model centreline. Each comprised 23 orifices: 10 on the lower surface, 12 on the upper surface and one at the leading edge. The non-dimensional coordinates for the surface static pressure orifices are also given in Appendix A. A schematic of the model arrangement, comprising the modified flat plate and the single slotted trailing edge flap, is shown schematically in Figure 9 below.

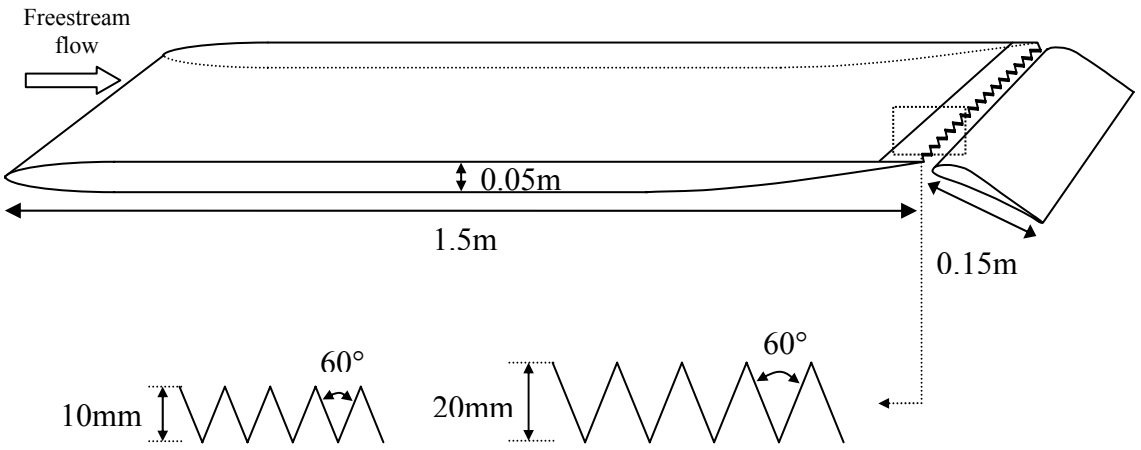

Figure 9: Schematic of two-dimensional flat plate and trailing edge flap model, Brough wind-tunnel

3.1.2 Variation of Flap Lap/Gap and Deflection Angle

A grid of holes, 0.01*m* between centres, on the internal tunnel sidewalls enabled the horizontal and vertical distances between the trailing-edge of the flat plate and the leading-edge of the flap to be varied over a range of flap deflection angles. For the parametric study under discussion, variation of the lap/gap was limited to a 10-point rectangular grid, incorporating a combination of five lap variations and two gap variations.

Whilst it was recognised that the gap was occasionally defined as the minimum distance between the trailing edge of the upstream element and the upper surface of the downstream element (see, for example, Foster et al (1970), Bertelrud and Ljungström (1974), Ljungström (1976) or van den Berg (1979)), the definition of lap and gap in the present investigation was consistent with that most prevalent in previous literature (see,

for example, Smith (1974) (1975), Moir et al (1972), Chin et al (1993) or ESDU data sheets). Accordingly, with the two reference points comprising (a) the midpoint of the flat plate trailing edge and (b) the leading edge of the flap, the lap and gap were defined as the horizontal and vertical distances, respectively, between the flat plate trailing edge and the flap leading edge. Accordingly, the non-dimensional lap and gap (normalised by the flap chord) corresponding to each position on the 10-point rectangular test grid is shown schematically in Figure 10.

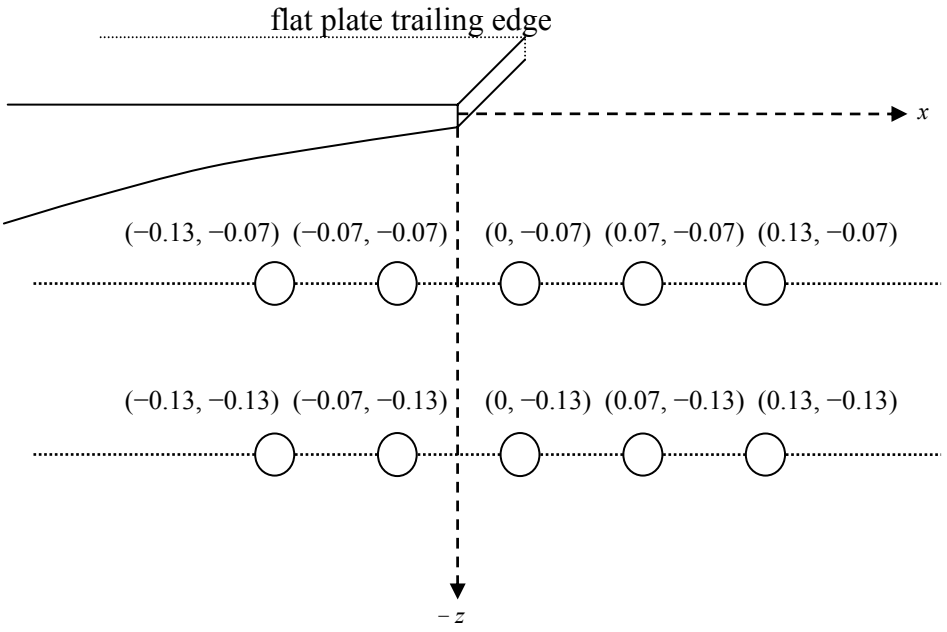

Figure 10: Schematic of non-dimensional flap lap/gap test grid, Brough wind-tunnel

The flap was rotated about a point located 4*mm* aft of the leading-edge along the chord line, i.e. at $0.03c_{flap}$. Two wires, positioned approximately $0.01m$ upstream of the flap trailing-edge and $0.095m$ inboard of the tunnel walls, extended vertically upwards to a pulley system mounted externally above the wind-tunnel, enabling the flap deflection angle to be manually incremented. Distribution of an externally mounted mass, on the corresponding wires extending vertically downwards through the wind-tunnel floor, prevented perturbation of the flap from its specified deflection angle when subject to freestream conditions. This was particularly necessary at large flap deflection angles, due to the buffeting induced by extensive boundary layer separation.

At each lap/gap grid position, the trailing-edge flap was deflected from 0° to a maximum of 25° (or the stall angle, if preceding this upper limit) in 5° increments.

Note that at a lap/gap of (−0.13, −0.07), the proximity of the upper surface flap leading-edge to the flat plate trailing edge rendered the lower deflection angle of 0° mechanically infeasible to implement.

3.1.3 Experimental Instrumentation

3.1.3.1 Freestream Dynamic Pressure Instrumentation

Control of the freestream tunnel speed was determined by monitoring the indicated dynamic pressure from the static rings located in the settling chamber and upstream of the working-section. The multiple static pressures at each reference ring yielded an average static pressure at that location. With the two sources connected across a digital manometer, the tunnel speed was set, either directly from the manometer display or from its output to a desktop computer. For the latter, in-house software addressed the analogue-to-digital converter to display the indicated freestream velocity.

3.1.3.2 Two-Dimensional Traverse Instrumentation

A flattened total pressure probe, 0.76*mm* in overall height and 2.9*mm* in overall width, was mounted on precision traverse gear, which in turn, was mounted on a two-dimensional traverse system. The precision traverse gear enabled highly accurate vertical motion along the z-axis over a finite range, with a resolution of 0.1*mm*. The infrastructure for the two-dimensional traverse system was mounted externally above the tunnel ceiling in the cross-stream direction. Two vertically mounted screw-thread linear slides enabled motion along the z-axis, whilst a horizontal linear slide, mounted between its carriages, provided spanwise movement along the y-axis, both with a typical resolution of 1*mm*. Driven by computer-based software, the two-dimensional traverse motion was controlled by a Compumotor AT6400 4-Axis Indexer and two Compumotor PDS-13 Stepper Drives. Whilst limited to motion along the y- and z-axes, additional access slots within the tunnel roof allowed the traverse system to be manually positioned at a nominated streamwise station along the x-axis. The total pressure probe was connected to a 0.5*psi* Setra 239 pressure transducer (s/n 640835), which was referenced to a surface static pressure on the wind-tunnel sidewall. In-house software addressed the analogue-to-digital converter and interacted with Parker Motion Architect software to control and co-ordinate both the movement of the traverse in the y- and z-planes and that of the precision traverse gear in the z-axis. The total pressure was sampled at specified position and the recorded data was output to a text file.

3.1.3.3 Surface Static Pressure Instrumentation

The 23 static pressure orifices at each spanwise flap location were connected sequentially to a 48-port mechanical pressure scanning valve, or Scanivalve, via pressure tubing of equal length. Control of the pressure scanner port selection was by means of a Solenoid Controller CTLR2/S2-S6 (s/n 2825), which in turn was connected to a three-channel control box, which synchronised the simultaneous progression through consecutive ports on up to three Scanivalves. The Scanivalve was, in turn, connected to a 0.5*psi* Setra 239 pressure transducer (s/n 633802), referenced to a static pressure on the wind-tunnel sidewall. The pressure transducer was then connected to the computer via a multi-channel control box, which synchronised the mechanical progression through sequential ports on the Scanivalve with the data acquisition at each port. In-house software allowed a sample rate and frequency to be defined and the recorded data was output to a text file.

3.1.3.4 Wake Survey Instrumentation

The wake rake was located at a nominal distance of 0.4*c* aft of the flat plate trailing-edge or three flap chord lengths aft of the flat plate and trailing edge flap combination. Positioned along the model spanwise centreline and aligned to the freestream, the wake rake consisted of 41 circular total pressure tubes, each 0.0015*m* in diameter. Although the spacing between port centres was non-uniform, particularly at the outer limits of the rake, the central portion displayed an average distance of 0.005*m* between successive centres. Instrumentation for the wake survey measurements was comparable to the surface static pressure instrumentation. Each total pressure tube from the wake rake was connected consecutively to a 48-port mechanical pressure scanning valve via tubing of equal length. Selection of consecutive ports on the Scanivalve was controlled by a Solenoid Controller CTLR2/S2-S6 (s/n 2839). The Scanivalve was, in turn, connected to a 0.5*psi* Setra 239 pressure transducer (s/n 640835), which was referenced to the surface static pressure on the tunnel sidewall. The pressure transducer was then connected to the computer via a multi-channel control box, which synchronised the mechanical progression through sequential ports on the Scanivalve with data acquisition at each port. In accordance with the instrumentation implemented, the measurements from the surface static pressure orifices and the wake rake surveys were recorded simultaneously for a given configuration.

3.1.4 Experimental Programme: Flat Plate

Unless otherwise stated, all tests were conducted at a nominal freestream velocity of $35m/s$ corresponding to a Reynolds number of 3.58×10^6, based on the flat plate chord. Initial experiments focused on the flow field analysis for the flat plate, in the absence of a trailing-edge device, and comprised:

- Shear layer analysis at the flat plate trailing edge
- Wake surveys aft of the flat plate trailing edge

3.1.4.1 Shear Layer Analysis at the Flat Plate Trailing Edge

The centre of the flattened total pressure probe was aligned with the midpoint of the flat plate trailing edge and traversed incrementally along the positive and negative z-axes, correlating to the flow field above and below the trailing edge, respectively.

It should be noted that at freestream conditions, the total pressure probe was deflected marginally aft, transposing the measurement plane $\approx2mm$ downstream of the flat plate trailing edge. Whilst essentially a free shear layer at this streamwise location, marking the onset of the developing wake, its proximity to the trailing edge rendered the total pressure measurements representative of the trailing edge boundary layer velocity gradients developing over the upper and lower surfaces of the flat plate. Although the absence of solid boundaries to enforce the no-slip condition at this streamwise position resulted in a non-zero velocity at z=0, i.e. when aligned with the trailing edge, the proximity of the measurements to the trailing edge meant that the effect of viscous diffusion on the velocity gradients were negligible and hence, the boundary layer thickness measured was representative of that at the trailing-edge of the flat plate.

(a) Plain Trailing Edge Component

With the plain geometry implemented at the trailing edge, the total pressure probe was initially positioned at the spanwise centreline and traversed incrementally along the positive and negative z-axis until there was no appreciable variation in the measurements, which was indicative of local freestream conditions. Additional traverses were conducted at $\pm0.05m$, $\pm0.1m$ and $\pm0.15m$ either side of the spanwise centreline in order to confirm the dimensionality of the flow field over the central 50% of the model span. Measurements were obtained initially with free transition and then with transition fixed on the upper surface of the flat plate.

(b) 10mm and 20mm Serrated Components

With transition fixed on the upper surface of the flat plate, either the 10mm or 20mm serrated geometry was implemented at the trailing edge. The total pressure probe was

initially aligned with the spanwise centreline, coinciding with the respective serration vertex, and traversed along the positive and negative z-axis until there was no appreciable variation in the measurements, pertaining to local freestream conditions being attained. Additional traverses were conducted at incremental spanwise locations, enabling the flow field between successive serration vertices to be surveyed symmetrically about the spanwise centreline. In close proximity to a serration vertex, the incremental distance was halved in order to provide a more detailed analysis of the flow field at this critical location. From the total pressure measurements immediately aft of the 10mm and 20mm serrations, the corresponding streamwise component of velocity (u-velocity component) was determined.

3.1.4.2 Wake Surveys Aft of the Flat Plate Trailing Edge

The wake rake surveys measured the total pressure in the developing wake downstream of the flat plate with either plain, 10mm or 20mm serrated geometries implemented at the trailing edge.

3.1.4.3 Summary of the Experimental Programme for the Flat Plate

Details of the flat plate experimental programme are summarised in Table 1 below:

Summary of Flat Plate Experimental Programme		
Trailing-Edge Geometry	U_∞ (***m/s***)	**Measurements**
Plain	35	Free Transition: Upper and lower surface trailing-edge boundary layer at y=0, ±0.05m, ±0.1m, ±0.15m Fixed Transition: Upper and lower surface trailing-edge boundary layer at y=0, ±0.05m, ±0.1m, ±0.15m
10mm Serrations	35	Fixed Transition: Upper and lower surface total pressure immediately aft of trailing edge at y=0mm, ±0.5mm, ±1.0mm, ±1.5mm, ±2.0mm, ±2.5mm, ±3.0mm, ±4.0mm, ±5.0mm, ±6.0mm, ±7.0mm, ±8.0mm, ±9.0mm, ±10.0mm, ±10.5mm, ±11.0mm, ±11.5mm, ±12.0mm, ±12.5mm, ±13.0mm, ±14.0mm, ±15.0mm, ±16.0mm, ±17.0mm
20mm Serrations	35	Fixed Transition: Upper and lower surface total pressure immediately aft of trailing edge at y=0mm, ±1.0mm, ±2.0mm, ±4.0mm, ±6.0mm, ±8.0mm, ±10.0mm, ±12.0mm, ±14.0mm, ±16.0mm, ±18.0mm, ±20.0mm, ±22.0mm, ±23.0mm
Plain 10mm Serrations 20mm Serrations	35	Fixed Transition: Wake rake survey

Table 1: Summary of the experimental programme for the flat plate model in the Brough wind-tunnel

3.1.5 Experimental Programme: Flat Plate and Trailing-Edge Flap

With the addition of a trailing-edge single slotted flap aft of the flat plate, the next phase of the small-scale experimental programme in the Brough wind tunnel focused upon the effect of serrated trailing edge geometries on the aerodynamic characteristics of the flap. Unless otherwise stated, all tests were conducted at a nominal freestream velocity of $35m/s$ corresponding to a Reynolds number of 3.58×10^5, based on flap chord.

With transition fixed on the upper surface of the flat plate, the parametric study comprised:

- Flat plate trailing edge geometry
  - Plain
  - 10mm 60° triangular serrations
  - 20mm 60° triangular serrations

- Lap/gap of the single slotted flap
  - 10-point rectangular grid

- Flap deflection angle (δ_f)
  - $0°\leq\delta_f\leq25°$, in 5° increments

Thus, for each of the flat plate trailing edge geometries at a given flap lap/gap and δ_f, the effect of the serrated trailing edge geometries on the developing flow field was determined by:

- Surface static pressure measurements over the trailing edge flap
- Wake rake surveys aft of the flat plate and trailing edge flap combination

Additional tests were conducted to establish the repeatability of the measurements and the effect of variations in Reynolds number.

3.1.6 Data Reduction

Each measurement was sampled at rate of $300Hz$ over a 5 second time period. In-house software determined the mean value of the sampled data, outputting the voltages to a text file. Programs were written in Matlab to process the data for subsequent analysis.

3.1.6.1 Freestream Velocity Measurements

A mean voltage, representative of the freestream dynamic pressure, was sampled simultaneously with each surface static pressure or total pressure measurement. Electrical offsets were subtracted from the mean voltages and the resultant values were multiplied by the appropriate calibration factors, both for the digital manometer and the wind tunnel (with regard to the latter, see Section 3.1.7). For the flat plate experiments, the calibration for the Digital Manometer FC016 (s/n FCB 4193) was $105.42 mmH_2O/V$. For the flat plate and single slotted flap combination, the calibration for the Digital Manometer FC016 (s/n FCB 6408) was $107.49 mmH_2O/V$. Finally, the measurements were converted into Pascals to give the dynamic pressure in the working section ($q_{w/s}$).

With the ambient pressure (p) and temperature (T) recorded simultaneously, the density was determined by the equation of state:

$$p = \rho RT \qquad [3.1]$$

where the universal gas constant for air, R, had the value of $287.26 Jkg^{-1}K^{-1}$. Assuming incompressible flow, subsequent application of Bernoulli's equation:

$$q = \frac{1}{2}\rho V^2 \qquad [3.2]$$

yielded the velocity in the working-section.

3.1.6.2 Boundary Layer Measurements Immediately Aft of the Flat Plate

Electrical offsets were subtracted from the mean voltages measured in the shear layer immediately aft of the flat plate. The resultant values were multiplied by the Setra transducer calibration of $156.11 mmH_2O/V$ (s/n 640835) and converted into standard units of Pascals. Application of Bernoulli's equation yielded the streamwise component of the local velocity (u-velocity component). The velocity at any given point in the shear layer was normalised by the velocity at the outer edge of the shear layer, representative of local freestream velocity.

For the plain trailing edge component, the non-dimensional velocity profiles were plotted against the z-axis at a given spanwise location. Following convention, the boundary layer thickness (δ) was arbitrarily defined as the distance from the surface where the local boundary layer velocity was 99% of the local freestream velocity. The non-dimensional streamwise component of velocity aft of the 10mm or 20mm serrated geometries was plotted against its relative position on the y- and z-axes.

3.1.6.3 Flap Surface Static Pressure Measurements

Electrical offsets were subtracted from the mean surface static pressures measurements, multiplied by the transducer calibration of $157.3 mmH_2O/V$ (s/n 633802) and converted into standard units of Pascals. Normalisation of the surface static pressures by the working section dynamic pressure determined the non-dimensional pressure coefficient (C_p):

$$C_p = \frac{p - p_{ref}}{q_{w/s}} \qquad [3.3]$$

The pressure distribution over the upper and lower surface of the flap was extrapolated to the trailing-edge by means of the one-dimensional cubic spline interpolation function within Matlab (Hanselman and Littlefield, 2001). Whilst the upper surface pressure distribution required two additional points to sufficiently define the distribution at the trailing-edge, the lower surface only required a single point. Thus, the pressure distributions over the upper and lower surfaces of the flap were plotted in coefficient form against the respective non-dimensional streamwise coordinates.

Integration of the measured pressure distributions determined the normal and axial forces acting perpendicular and parallel to the flap chord, respectively (see Appendix B for more details regarding the integration of the pressure distributions to obtain the aerodynamic forces). Based upon the normal (C_n) and axial (C_a) force coefficients, simple geometric relations established an expression for the force components of lift and drag acting perpendicular and parallel to freestream, respectively. Thus, with the flap aerofoil inclined at a specified angle to the freestream, which in this instance was represented by the flap deflection angle (δ_f), the non-dimensional lift (C_l) and drag (C_d) force coefficients per unit span were defined by:

$$C_l = C_n \cos\delta_f - C_a \sin\delta_f \qquad [3.4]$$

$$C_d = C_n \sin\delta_f + C_a \cos\delta_f \qquad [3.5]$$

It should be noted that for the present investigation, the above expressions for the lift and drag coefficients were purely dependent upon the pressure distributions over the flap and hence, did not include the effect of the shear stresses acting upon the surface. Accordingly, the drag coefficient only provided an estimate of the pressure drag and did not include the skin friction drag.

3.1.6.4 Wake Survey Measurements

Electrical offsets were subtracted from the mean total pressure measurements in the developing wake aft of the flap trailing edge and the values were multiplied by the transducer calibration of $156.11 mmH_2O/V$ (s/n 640835) before being converted to standard units. Application of Bernoulli's equation yielded the local velocity in the wake, which was normalised by the local freestream velocity and plotted against the relative position on the z-axis.

Based upon the principle that the rate of loss of momentum in the wake equated to the profile drag force acting upon the body (Houghton and Carpenter, 2003), Jones' (1936) wake traverse method was implemented. Thus, the profile drag coefficient per unit span (C_{dp}) was given by:

$$C_{dp_1} = 2\int_{w_1} \frac{\sqrt{(H_1 - p_1)}}{\sqrt{(H_\infty - p_\infty)}}\left(1 - \frac{\sqrt{(H_1 - p_\infty)}}{\sqrt{(H_\infty - p_\infty)}}\right) d\left(\frac{y_1}{c}\right) \qquad [3.6]$$

where H was the total pressure, p was the static pressure and the subscript 1 represented the measurement reference plane aft of the configuration trailing edge. In accordance with Jones (1936) and Barlow et al (1999), the freestream dynamic pressure ($H_\infty - p_\infty$) was the local freestream value determined from the measurements in the wake survey reference plane. Accordingly, the profile drag was evaluated by plotting

$$\frac{\sqrt{(H_1 - p_\infty)}}{\sqrt{(H_\infty - p_\infty)}}\left(1 - \frac{\sqrt{(H_1 - p_\infty)}}{\sqrt{(H_\infty - p_\infty)}}\right) \qquad [3.7]$$

against the relative position on the y-axis, which was normalised by the flap chord. The discrete data points were interpolated by means of a cubic spline routine in Matlab and the area of the polygon was calculated. Multiplication of this area by two yielded C_{dp}.

3.1.7 Assessment of Measurement Accuracy

The presence of solid boundaries, a finite distance from the model, produced both solid blockage and wake blockage, rendering the aerodynamic forces calculated experimentally unrepresentative of those arising in an unbounded flow field such as the free atmosphere. However, the flat plate and trailing edge flap configuration represented a substantial blockage within the working section and hence, invalidated the application of conventional two-dimensional blockage corrections (ESDU). Thus, in this instance, only a correction to the working section dynamic pressure was applied. Accordingly, with the model installed, the working section dynamic pressure was

correlated to the freestream dynamic pressure. Based upon flap lap, gap and deflection angle, a tunnel calibration factor was deduced and applied in the process of data reduction, see Table 2 below.

Summary of Brough Wind-Tunnel Calibration Factors										
	Gap: −0.07					Gap: −0.13				
δ_f	Lap −0.13	Lap −0.07	Lap 0	Lap 0.07	Lap 0.13	Lap −0.13	Lap −0.07	Lap 0	Lap 0.07	Lap 0.13
0°		1.12	1.13	1.10	1.12	1.14	1.13	1.13	1.12	1.11
5°	1.25	1.24	1.26	1.22	1.24	1.25	1.25	1.24	1.24	1.23
10°	1.35	1.36	1.40	1.35	1.36	1.38	1.37	1.37	1.36	1.35
15°	1.46	1.50	1.52	1.47	1.47	1.47	1.49	1.50	1.48	1.46
20°	1.56	1.61	1.64	1.60	1.56	1.55	1.60	1.62	1.56	1.31
25°	1.57	1.72	1.76	1.69	1.38	1.54	1.65	1.67	1.41	−

Table 2: Summary of Brough wind-tunnel calibration factors

Thus, in the absence of blockage corrections, the absolute values of the aerodynamic forces presented herein were in error. Nevertheless, the relative increments/decrements in the aerodynamic forces were assumed representative of the trends arising in the flow field development due to variations in configuration detail.

Clearly, the accuracy of aerodynamic forces determined from the static pressure measurements was influenced by the distribution of the static pressure orifices over the surface. A highly accurate and detailed surface pressure distribution was imperative to the precision of the drag force, as the required surface integration involved subtraction of a large force component in the thrust direction from a slightly larger force component in the drag direction (Chao and van Dam, 1999). However, whilst this potential source of error within the data was identified, it was not possible to quantify to what extent, if any, the distribution of the surface static pressure orifices affected the accuracy of the results.

A further source of error was incurred by virtue of assuming a constant static pressure across the wake in the designated measurement plane. Jones (1936) showed that by neglecting the static pressure variation across the wake at a measurement plane 0.05c aft of the trailing edge, there was a 22% error in the profile drag. However, assuming a constant static pressure at a measurement plane aft of 0.5c resulted in less than a 1% error in the profile drag. Locating the measurement plane one chord length aft of the trailing edge rendered the static pressure in the wake essentially indistinguishable from that of the freestream. Barlow et al (1999) corroborated this and recommended that for

the static pressure in the wake to be constant and to have returned to the tunnel static value, the measurement plane should be located at least 0.7*c* aft of the model trailing edge. Whilst not verified, it was reasonable to assume that at the location of the measurement plane in the present wake rake surveys, the streamlines across the entire plane were parallel to the freestream and that the static pressure across the wake was both constant and of a magnitude indistinguishable from the freestream static pressure. Accordingly, the necessary conditions associated with the momentum integral equation were satisfied and it was assumed that the error incurred by neglecting static pressure variations in the wake accounted for less than 1%.

3.2 8'×6' Wind-Tunnel

Large-scale experiments were conducted in the College of Aeronautics' subsonic, closed jet, closed single return low-speed 8'×6' (2.4*m*×1.8*m*) wind-tunnel at Cranfield University.

The wind-tunnel had a 7:1 contraction ratio upstream of the working section, which extended 5.18*m* in length. Powered by a 550*hp* motor and with a variable pitch fan, the tunnel had a maximum speed of 60*m*/*s*, dependent upon model geometry. Above the working-section was an electro-mechanical 6-component balance on a 360° turntable. Boundary layer control was employed on the wind-tunnel floor. The suction system consisted of a ram intake immediately upstream of the working-section, which effectively eliminated the boundary layer that had developed within the contraction cone, and a porous plate, which eliminated the boundary layer on the floor just prior to the model. The suction rate of the system was predefined and synchronised with the wind-tunnel speed.

3.2.1 General Model Description

The large-scale experiments were conducted on a two-dimensional three-element high-lift configuration, comprising a single slotted leading-edge slat, a main element and a single slotted trailing-edge flap, the geometry for which was defined by the HELIX project. The high-lift configuration is shown schematically in Figure 11.

Note that the cove geometry over the aft region of the main element lower surface facilitated the retraction of the trailing edge high-lift device and was hence, representative of a practical and mechanically feasible high-lift configuration.

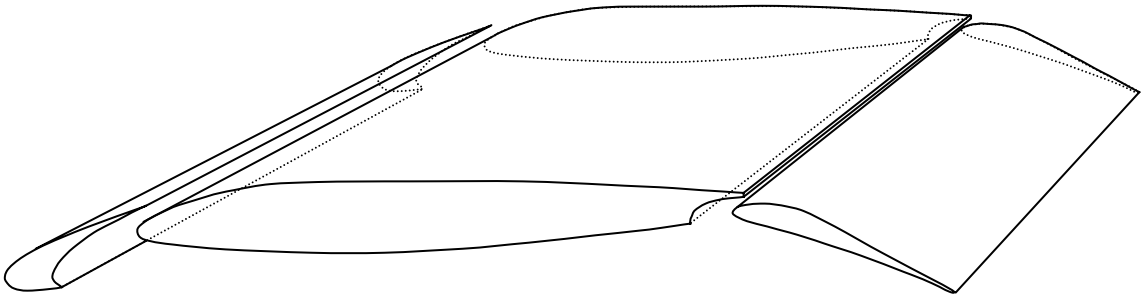

Figure 11: Schematic of two-dimensional high-lift configuration, 8'×6' wind-tunnel

With the leading edge slat and the trailing edge flap stowed, the high-lift configuration had a reference chord of 0.6*m*. Made of carbon fibre, the leading edge slat had a chord of 0.127*m*, with an aluminium insert accommodating the sharp trailing edge. The trailing edge flap was also made of carbon fibre and had a chord of 0.18*m*. The wooden main element had a modular trailing-edge component, facilitating the interchange of three distinct methods of high-lift boundary layer control: namely, serrated trailing edge geometries, tangential slot blowing and discrete blowing. Aluminium spars, contoured to the local geometry, were placed at approximately 0.14*m* intervals within the modular component at the trailing edge of the main element, together with the leading edge slat and trailing edge flap, in order to promote structural rigidity at freestream conditions.

The model spanned 1.4*m* between end plates, mounted either vertically or horizontally in the wind-tunnel, dependent upon the element of the experimental programme under consideration. Holes drilled in the end-plates provided a template for each configuration, ensuring accurate deflection angles for the leading-edge slat and trailing-edge flap were maintained throughout the tests.

The leading-edge slat, main element and trailing-edge flap were instrumented 19, 46 and 27 surface static pressure orifices, respectively. On each element, the static pressure orifices were inclined by 10° along the spanwise centreline to prevent interference. Normalised by the stowed reference chord, the non-dimensional co-ordinates for the surface static pressure orifices are given in Appendix A.

Three distinct test configurations were identified by the HELIX project:

- Takeoff configuration: 23° slat deflection and 38° flap deflection
- Landing configuration: 27° slat deflection and 48° flap deflection
- Extended flap configuration: 27° slat deflection and 58° flap deflection

Rotation point of the model – from which the model angle of incidence was determined – was located at the midpoint of the stowed reference chord. Relative to the rotation point of the model, the rotation points for the leading edge slat and trailing edge flap, normalised by the stowed reference chord, were given by (0.91, −0.99) and (−0.84, −0.28), respectively. Deflection of the leading-edge slat and/or trailing-edge flap to a specified angle correlated to a distinct lap/gap which, for comparative purposes, were normalised by the respective chords.

3.3 Large-Scale Wind-Tunnel Experiments: Serrations

This section details the necessary modifications to the aforesaid high-lift model, in order to investigate the effect of serrated trailing edge geometries on the flow field around a multi-element configuration. The experimental setup and instrumentation specific to the serrated trailing edge configuration are also described.

3.3.1 Model Description

In order to adapt the basic model to the specific requirements of this element of the experimental programme, a wooden component formed the modular trailing edge of the main element, within which a modular aluminium component extended across the aft $0.06m$, facilitating the interchange of the trailing-edge geometries. The main element trailing edge was truncated from its original design to accommodate the material thickness of the aluminium component, resulting in a trailing edge thickness of $0.5mm$ for any given trailing edge geometry. Modelling block on the lower surface of the aluminium trailing-edge component ensured that the contour of the original cove geometry was maintained over the aft region of the main element lower surface.

Prominent studies by Vijgen et al (1989) of serrated geometries at the trailing edge of a single element aerofoil proposed that the boundary layer thickness at the trailing edge of the aerofoil (δ_{TE}) was a critical parameter upon which the serration length was scaled. However, the complexities of the boundary layer at the trailing edge of a main element in a multi-element high-lift configuration, and its interaction with the wake from the upstream leading-edge device, rendered δ_{TE} an impractical scaling parameter in this instance. Accordingly, the three trailing edge geometries corresponded directly to those implemented in the Brough experiments, namely:

- Plain trailing-edge
- 60° triangular serrated geometry, extending 10mm from vertex to base
- 60° triangular serrated geometry, extending 20mm from vertex to base

Note that the serration vertex was once again formed by a circular arc of 1*mm* radius.

There were two distinct aspects to this element of the experimental programme, so defined by directional mounting of the model within the working section.

Mounted vertically in the wind-tunnel, the model extended between a 0.8*m* diameter circular end plate flush with the tunnel floor and a 1.2*m* diameter circular end-plate connected to a strut, which was in turn, mounted on the external balance above the tunnel roof, as pictured in Figure 12.

Figure 12: High-lift model mounted vertically in 8'×6' wind-tunnel

Note that the external balance was purely a mounting platform and hence, was locked during all experimentation. The turntable was flush with the tunnel roof and facilitated the increase in angle of incidence. A shroud, based on a symmetrical aerofoil section,

encased the strut between the end plate and the tunnel roof to reduce interference on the developing flow field.

When positioned horizontally in the wind-tunnel, the model was mounted between two 1.2*m* diameter circular end plates on twin struts extending from the six-component external balance above the tunnel roof. The model was mounted along the tunnel centreline in an inverted position and aligned to the freestream by means of the turntable, see Figure 13.

Figure 13: High-lift model mounted horizontally in 8'×6' wind-tunnel

Initially, the angle of incidence was determined by a digital inclinometer and the model was secured by means of a template of holes drilled in the end plates corresponding to each incremental angle. When implementation was feasible, the angle of incidence was incremented by means of a tail wire attached to a beam protruding from either end plate. The tail wire extended through the tunnel floor and the addition of a mass secured the model at a given angle of incidence, preventing deflection at freestream conditions.

3.3.2 Experimental Instrumentation

3.3.2.1 Freestream Dynamic Pressure Instrumentation

Similarly to the Brough experiments, the freestream dynamic pressure and tunnel speed were monitored either directly from the manometer display or from its output to a desktop computer (see Section 3.1.3 for more details).

3.3.2.2 Surface Static Pressure Instrumentation

The surface static pressure orifices on the main element were connected sequentially to a 48-port Scanivalve, via pressure tubing of equal length. Similarly, the surface static pressure orifices on the leading edge slat and the trailing edge flap were connected consecutively to a second 48-port Scanivalve. Control of the pressure scanner port selection for the main element, slat and flap was by means of Solenoid Controllers, which in turn were connected to a three-channel control box, synchronising the simultaneous progression through consecutive ports on both Scanivalves. Each Scanivalve was connected to a Setra 239 pressure transducer, referenced to the static pressure from the static rings and powered by 24V Isotech IPS 303D power supply. The pressure transducers were then connected to a computer via a multi-channel control box, which synchronised the mechanical progression through sequential ports on the Scanivalves with data acquisition at each pressure port. Details of the instrumentation associated with each element of the high-lift aerofoil are given in Table 3 below.

Surface Static Pressure Instrumentation and Pressure Transducer Calibrations for Serrated Trailing Edge High Lift Configuration			
Aerofoil Element	Solenoid Controller	Pressure Transducer	Transducer Calibration (mmH_2O/V)
Main	CTLR2/S2-S6 (s/n 2839)	0.5psi Setra 239 (s/n 633802)	151.18
Slat	CTLR2/S2-S6 (s/n 1788)	1psi Setra 239 (s/n 24847)	277.26
Flap	CTLR2/S2-S6 (s/n 1788)	1psi Setra 239 (s/n 24847)	277.26

Table 3: Surface static pressure instrumentation details and corresponding calibrations for the serrated trailing edge configuration, 8'×6' wind-tunnel

In-house software allowed a sample rate and frequency to be defined and the recorded data was output to a text file.

3.3.3 Experimental Programme

Unless otherwise stated, all tests were conducted at a freestream velocity of $40 m/s$ corresponding to a Reynolds number, based on stowed reference chord, of 1.64×10^6.

3.3.3.1 Surface Static Pressure Measurements

With the model mounted vertically, the experiments comprised:

- High-lift configuration
  - Takeoff configuration
  - Landing configuration

- Trailing edge geometry on the main element
  - Plain
  - 10mm 60° triangular serrations
  - 20mm 60° triangular serrations

- Angle of incidence (α)
  - $0°\leq\alpha\leq20°$ in 2° increments

For a given configuration, surface static pressure measurements were obtained over each of the three elements, from which the lift and drag forces were determined.

3.3.3.2 Balance Measurements

With the model mounted horizontally, the aerodynamic components of force acting on a given high-lift configuration were determined from measurements obtained by the external balance. The experimental programme displayed five distinct progressions of investigation, detailed below. Additional tests were conducted to establish the repeatability of the measurements and the effect of variations in Reynolds number.

(a) Two-Element High-Lift Configuration: Reduced Flap Deflection Angle

In the first instance, the leading edge slat was retracted to its stowed position, thus reducing the high-lift configuration to a two-element aerofoil. Based upon the previously defined flap rotation point, the deflection angle of the trailing edge flap was reduced, in order to establish whether the effectiveness of the serrations was negated by the large flap deflection angle of the takeoff and landing configurations. The study comprised:

- Trailing edge geometry on the main element
  - Plain
  - 10mm 60° triangular serrations
  - 20mm 60° triangular serrations

- Flap deflection angle (δ_f)
  - $0° \leq \delta_f \leq 15°$ in 5° increments

- Angle of incidence
  - $-2° \leq \alpha \leq \alpha_{stall} \leq 20°$ in 2° increments

(b) Three-Element High-Lift Configuration: Reduced Flap Deflection Angle

Due to time and facility constraints, the aerodynamic forces and moments acting on a three-element high-lift configuration were limited to a single configuration comprising a slat deflection angle of 23° and flap deflection angle of 15°. For each of the three trailing edge geometries, the angle of incidence was incremented over a reduced range between 12° and 20°, with the objective of establishing the salient variations in the aerodynamic forces arising from deployment of a leading edge high-lift device.

(c) Two-Element High-Lift Configuration: Effect of Varying Flap Lap/Gap on a Coarse Grid

Noting that thus far, each flap deflection angle corresponded to a specific flap lap/gap, the influence of flap lap/gap upon the effectiveness of the serrations was evaluated by means of a grid of holes, $10mm$ between centres, drilled in a $0.275m$ diameter circular insert on each end plate, which enabled the horizontal and vertical distances between the trailing-edge of the main element and the leading-edge of the flap to be varied. At each grid position, the trailing edge flap was deflected over a reduced range of angles.

Due to time constraints, the lap/gap grid was limited to a 5-point grid, incorporating a combination of three lap variations and two gap variations. Similarly to the Brough experiments, the lap and gap were referenced to the midpoint of the main element trailing edge and the leading edge of the trailing edge flap at a zero degree deflection angle. For comparative purposes the lap and gap were normalised by the flap chord and are shown schematically in Figure 14.

Note that three additional grid points nearest to the main element trailing edge, which would have completed an 8-point rectangular grid, were omitted as rotation of the flap

in these three points was rendered infeasible by the leading edge camber on the flap upper surface.

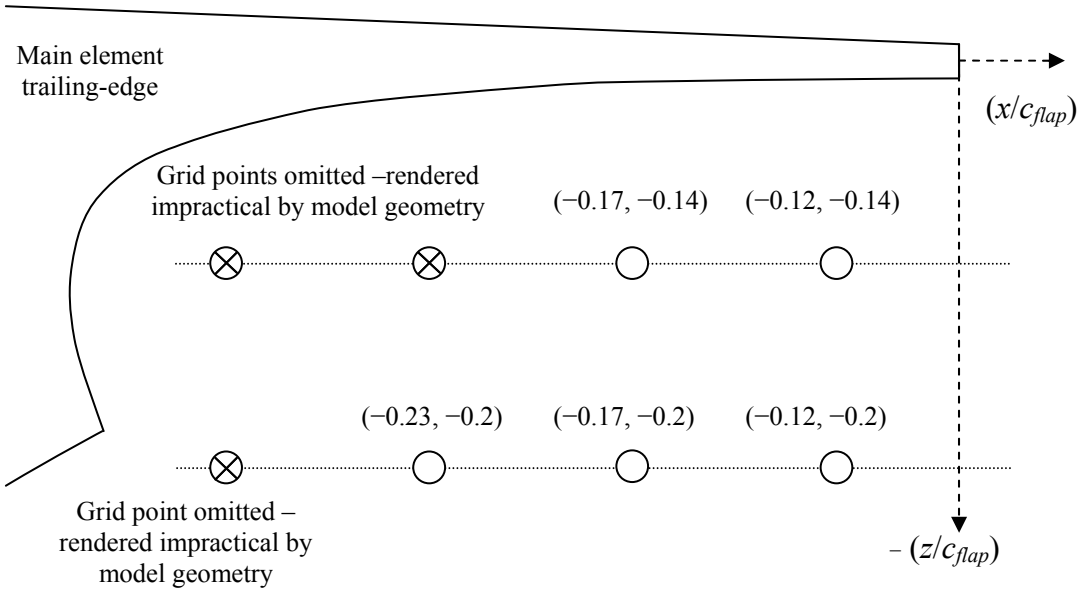

Figure 14: Schematic of coarse flap lap/gap grid for serrated trailing edge high-lift configuration

Initial investigations of the lap/gap variation focused on a two-element configuration, with the leading edge slat retracted to its stowed position. Accordingly, the variable parameters were:

- Trailing edge geometry on the main element
  - Plain
  - 10mm 60° triangular serrations
  - 20mm 60° triangular serrations

- Flap deflection angle
  - $0° \leq \delta_f \leq 15°$ in 5° increments

- Angle of incidence
  - $-2° \leq \alpha \leq 10°$ in 4° increments
  - $10° \leq \alpha \leq \alpha_{stall} \leq 20°$ in 2° increments

Smaller increments in incidence angle were implemented between 10° and 20° with the objective of capturing the stall angle more accurately. Note that only the flap lap/gap

position of (−0.12, −0.14) in the present study was comparable to the lap/gap of (−0.13, −0.13) in the Brough parametric study.

(d) Three-Element High-Lift Configuration: Single Coarse Grid Location

Based upon the limited coarse grid study, the effect of deflecting the leading-edge slat to 23° in combination with the trailing-edge flap was investigated for a single lap/gap position of (−0.23, −0.2). Accordingly, for each of the three trailing edge geometries, the flap deflection angle was increased from 0° to 15° and the angle of incidence was incremented between 4° and 20° in 2° increments.

(e) Two-Element High-Lift Configuration: Effect of Varying Flap Lap/Gap on a Fine Grid

Three additional points, 5*mm* between hole centres, were instrumented on the circular inserts within the model end plates, in order to determine whether the effectiveness of the serrations could be improved. Normalised by the flap chord, the resultant non-dimensional lap/gap distances, are shown schematically in Figure 15 relative to the coarse grid points.

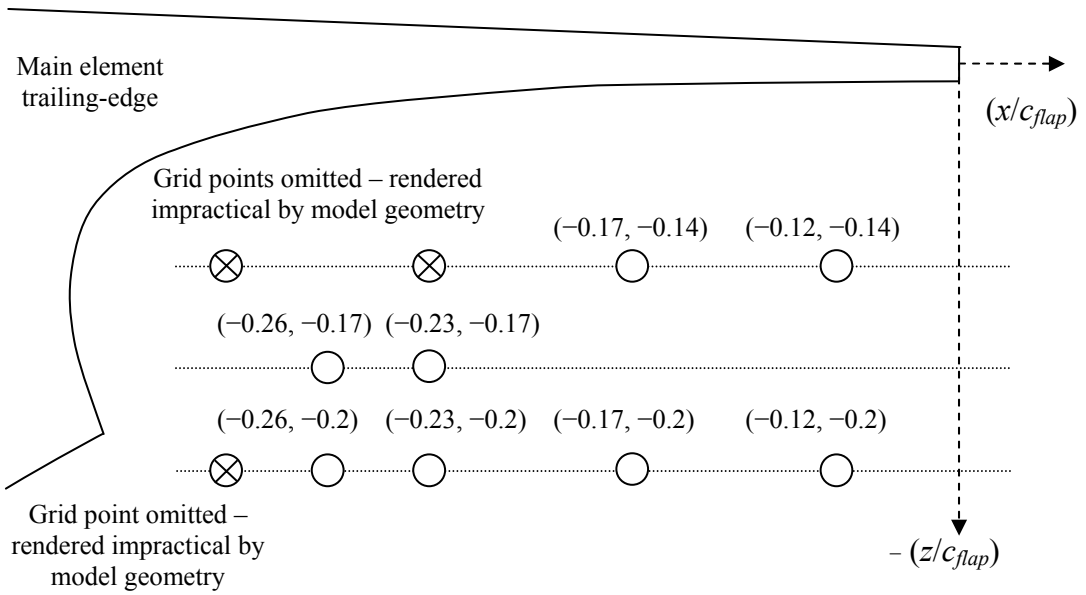

Figure 15: Schematic of fine flap lap/gap grid for serrated trailing edge high-lift configuration

With the leading edge slat retracted to its stowed position, the configuration variables comprised:

- Trailing edge geometry on the main element
  - Plain
  - 10mm 60° triangular serrations
  - 20mm 60° triangular serrations

- Flap deflection angle
  - $0° \leq \delta_f \leq 15°$ in 5° increments

- Angle of incidence
  - $4° \leq \alpha \leq \alpha_{stall}° \leq 20°$ in 2° increments

3.3.3.3 Surface Oil Flow Visualisation

The quantitative balance measurements were supplemented by surface oil flow visualisation over the upper surface of the trailing edge flap. The clarity of the surface flow patterns produced was particularly sensitive to the consistency of the flow visualisation mixture, comprising fluorescent powder, paraffin and oleic acid, the latter acting as a pigment dispersant. Recalling that the model was inverted within the working section, the viscosity of the mixture necessitated that it would not respond rapidly to the forces of gravity and yet would respond to the influence of surface shear stresses. That so being, the quantities of the mixture's components were determined by experimental verification. The resultant surface flow field was illuminated under ultraviolet light and photographed for subsequent analysis. Due to time constraints, only a single flap lap/gap position of (−0.26, −0.2) was supplemented by flow visualisation.

3.3.4 Data Reduction

3.3.4.1 Freestream Velocity Analysis

Similarly to the process described in Section 3.1.6, the mean freestream dynamic pressure from the static rings was recorded simultaneously with each surface static pressure measurement. The mean voltages were corrected for the electrical offsets, multiplied by both the Furness Controls Digital Manometer FC016 (s/n 9601307) calibration of $101.05 mmH_2O/V$ and the wind tunnel calibration of 1.11 and converted into standard units to give the working section dynamic pressure. Bernoulli's equation was then applied to determine in the working section velocity.

3.3.4.2 Surface Static Pressure Measurement Analysis

Each measurement was sampled at rate of 300*Hz* over a 5 second time period. In-house software determined the mean value of sampled data, outputting the voltages to a text file. Electrical offsets were subtracted and the mean voltages were multiplied by the relevant transducer calibration, detailed previously in Table 3. The static pressure gradient between the static rings and a local static pressure orifice on the tunnel sidewall, aligned with the model, was determined. Accordingly, the surface static pressure measurements were referenced to the local static pressure. The surface static pressures were duly converted into standard units of Pascals and normalised by the working section dynamic pressure to give the non-dimensional pressure coefficient.

By means of the one-dimensional cubic spline interpolation function within Matlab, the pressure distribution was extrapolated over the upper and lower surfaces of the leading edge slat to the trailing edge. The modular trailing edge component in the main element was not instrumented with surface static pressure orifices. Accordingly, the upper and lower surface pressure distributions were extrapolated by means of the data obtained from the modular trailing edge component used in baseline studies of the tangential slot blowing element of the experimental programme. In contrast, the trailing edge flap required no extrapolation of data.

Thus, the pressure distributions over the upper and lower surfaces of the leading edge slat, main element and trailing edge flap were plotted in coefficient form against the non-dimensional Cartesian co-ordinates, normalised by the stowed reference chord. Integration of the C_p distributions yielded the normal and axial forces acting upon the high-lift configuration, from which the lift and drag force coefficients per unit span were obtained

3.3.4.3 Aerodynamic Forces from Balance Analysis

For any given configuration, the normal (N_f), axial (A_f), side (S_f) and yaw (Y_f) forces exerted on the model were displayed on four dial encoders. Each force was manually balanced and the output was recorded manually. The ambient pressure, ambient temperature and the freestream dynamic pressure were also manually recorded for each configuration.

Prior to each test, with the wind off, the four aerodynamic forces were balanced and recorded, representing the offset conditions of the normal (N_{offset}), axial (D_{offset}), side

(S_{offset}) and yaw (Y_{offset}) forces, respectively. Based upon the pre-defined calibration matrix, the lift and drag forces were calculated from the equations:

$$L_f = 4.448\left\{\left(5.16\left(N_f - N_{offset}\right)\right) + \left(-0.004\left(A_f - A_{offset}\right)\right)\right\} \quad [3.8]$$

$$D_f = 4.448\left\{\left(0.416\left(A_f - A_{offset}\right)\right) + \left(0.0046\left(N_f - N_{offset}\right)\right)\right\} \quad [3.9]$$

Whilst the above equations appear independent of the side and yaw forces, it should be noted that the simultaneous balancing of all four forces highlighted the force interdependence. Accordingly, the non-dimensional lift and drag coefficients per unit span were determined by normalising the resultant lift and drag forces by the working section dynamic pressure.

3.3.5 Tare Corrections

The presence of the model's support structure in the freestream not only generated a component of drag or tare but also produced interference (Barlow et al, 1999). In this instance, only the tare corrections were evaluated. In the absence of the model, the aerodynamic forces were balanced and recorded over a range of freestream dynamic pressures. Plotting the normal force against the freestream dynamic pressure, the variation was deemed negligible for any given angle of incidence. In contrast, whilst independent of angle of incidence, the axial force varied with freestream dynamic pressure.

Accordingly, in the absence of a tail-wire, the resultant tare drag was evaluated by the equation:

$$D_{tare} = \left(0.0654 \times q_\infty\right) + 0.2848 \quad [3.10]$$

With the addition of a tail-wire, the resultant tare drag at any given freestream dynamic pressure was given by:

$$D_{tare} = \left(0.1086 \times q_\infty\right) - 0.6116 \quad [3.11]$$

3.3.6 Blockage Corrections

As a result of the constraints imposed on the flow field by the wind tunnel walls, the aerodynamic forces calculated experimentally were not representative of those arising in an unbounded flow field, such as the free atmosphere. Standard two-dimensional low-

speed corrections for solid blockage and wake blockage, as detailed by Barlow et al (1999), were applied to the freestream quantities, pressure coefficients and non-dimensional aerodynamic forces calculated from both the surface pressure distributions and the direct measurements from the overhead external balance. Further details of the corrections applied are given in Appendix C.

3.3.7 Assessment of Measurement Accuracy

With blockage corrections applied, the aerodynamic forces obtained from integration of the surface static pressure distributions were subject to the same potential inaccuracies identified in Section 3.1.7. A further source of error for the surface static pressure distributions involved the extrapolated data over the aft $0.2c_{main}$ of the main element. As the extrapolated data was based upon that obtained for the modular trailing edge component used in baseline studies of the tangential slot blowing element of the experimental programme, no provision was made for variations in trailing edge static pressure arising from implementation of the serrated geometries. It should also be noted that the drag data obtained from the balance was highly sensitive to local flow field anomalies and hence, included three-dimensional effects induced by the end plates (Ljungstrom, 1976). That so being, in the absence of significant regions of separation, the incremental changes identified in the drag force were deemed representative of the salient trends in flow field, although caution should be exercised at high angles of incidence.

3.4 Large-Scale Wind-Tunnel Experiments: Tangential Slot Blowing

This section details the modifications to the high-lift model necessary, in order to investigate the effect of tangential slot blowing on the flow field around a multi-element configuration. The experimental setup and instrumentation specific to the tangential slot blowing configuration are also described. Note that for all tangential slot blowing experiments, the model was mounted vertically in the wind tunnel, between two circular end plates, as described in Section 3.3.1.

3.4.1 Model Description

In order to adapt the basic model (detailed in Section 3.2) to the specific requirements of this element of the experimental programme, a carbon fibre component formed the modular trailing edge of the main element. Due to the limitations imposed by the

material thickness, the trailing edge was truncated to accommodate a 3:1 slot-height-to-material-thickness ratio (defined by the HELIX project), corresponding to a slot height of 1.95*mm* and a wall thickness either side of 0.65*mm*, shown schematically in Figure 16. An additional 16 surface static pressure orifices – 6 on the upper surface, 4 in the cove region and 6 on the lower surface – were instrumented on the modular trailing edge component.

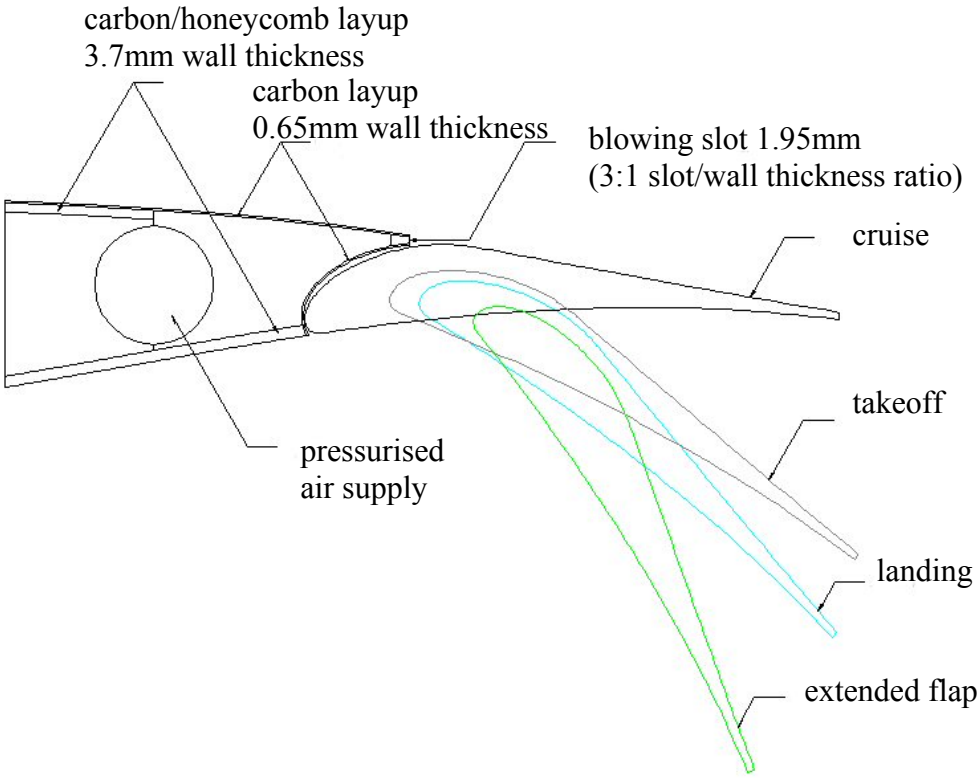

Figure 16: Schematic of tangential slot blowing modular trailing edge component

Compressed air was delivered to each end of a 38*mm* external diameter (31*mm* internal diameter) circular pipe, extending 1.5*m* in length across the model span and located immediately upstream of the modular trailing edge component, within the local thickness of the main element. Air was emitted into the internal cavity of the modular trailing edge component, by means of three spanwise lines of orifices in the pipe. The central line consisted of 60 circular holes, 8*mm* in diameter, with 22.1*mm* between successive hole centres. Aligned at ±30° to the central line, each additional spanwise line comprised 59 holes of circular diameter varying between 3.175*mm* and 6.35*mm*. By reducing the open hole area in the blowing pipe to 0.0008m^2 and restricting the compressed air supply to each flow meter to 3300 litres per minute, a nominal

momentum coefficient per unit span of 0.025 (defined by the HELIX project) was achieved with reasonable consistency over the central third of the span.

3.4.2 Experimental Instrumentation

3.4.2.1 Surface Static Pressure Instrumentation

The instrumentation for measuring and recording the surface static pressures on the main element, leading edge slat and trailing edge flap has already been described in Section 3.3.2. In addition, the surface static pressure orifices instrumented on the modular trailing edge component of the main element were connected sequentially to a third 48-port Scanivalve, which was similarly integrated into the instrumentation such that the mechanical progression through sequential ports on all three Scanivalves was synchronised with the data acquisition at each pressure port. For clarity, details of the instrumentation associated with each component of the high-lift aerofoil, together with the respective pressure transducer calibrations, are given in Table 4 below.

Surface Static Pressure Instrumentation and Pressure Transducer Calibrations for Tangential Slot Blowing High Lift Configuration			
Aerofoil Element	Solenoid Controller	Pressure Transducer	Calibration (mmH_2O/V)
Main	CTLR2/S2-S6 (s/n 2839)	0.5psi Setra 239 (s/n 633802)	151.18
Slat	CTLR2/S2-S6 (s/n 1788)	1psi Setra 239 (s/n 24847)	277.26
Flap	CTLR2/S2-S6 (s/n 1788)	1psi Setra 239 (s/n 24847)	277.26
Modular Trailing Edge	CTLR2/S2-S6 (s/n 2824)	0.5psi Setra 239 (s/n 47513)	139.02

Table 4: Surface static pressure instrumentation details and corresponding calibrations for the tangential slot blowing configuration

3.4.2.2 Thermocouple Instrumentation

A Type-K thermocouple was soldered to a piece of copper, contoured to the shape of the cove and secured with aluminium tape to the lower surface of the main element trailing edge. The copper element marginally protruded through the gap between the main element trailing edge and the leading edge of the flap upper surface, which enabled the thermocouple to be aligned with the slot along the spanwise centreline of

the model. In turn, the thermocouple was connected to an ATP TK 200 Type-K Thermometer (s/n 94086158), which digitally displayed the measured temperature.

3.4.3 Experimental Programme

Unless otherwise stated, all tests were conducted at a nominal freestream velocity of $40m/s$ corresponding to a Reynolds number of 1.64×10^6, based upon the stowed reference chord of $0.6m$. Furthermore, blowing was typically applied at a momentum coefficient (C_μ) of 0.025 (defined by the HELIX project).

3.4.3.1 Surface Static Pressure Measurements

Focusing on the effect of trailing edge tangential slot blowing on the surface static pressure distributions, the study comprised:

- High-lift configuration
  - Takeoff configuration: 23° slat deflection and 38° flap deflection
  - Landing configuration: 27° slat deflection and 48° flap deflection
  - Extended flap configuration: 27° slat deflection and 58° flap deflection

- Boundary layer control
  - None
  - Tangential slot blowing, C_μ=0.025

- Angle of incidence
  - $0°\leq\alpha\leq20°$ in 2° increments

Additional tests were conducted to establish the repeatability of the measurements and the effect of variations in Reynolds number. Furthermore, the effect of variations in the mass flow rate on the surface static pressure distribution over the takeoff configuration was also investigated. Due to time limitations, measurements were limited to a single configuration at α=8°, representative of takeoff conditions. Accordingly, the volume flow rate delivered to the blowing pipe was incremented between 4600 and 7200 litres per minute, in intervals of 400 litres per minute, and the corresponding surface static pressure measurements were duly sampled and recorded.

3.4.3.2 Surface Oil Flow Visualisation

The static pressure measurements were supplemented by surface oil flow visualisation over the upper surface of the trailing edge flap. As previously described in Section

3.3.3, the surface flow patterns were sensitive to the consistency of the flow visualisation mixture, necessitating continuous experimental verification of the component quantities to ensure flow pattern clarity. Again, the resultant surface flow field was illuminated under ultraviolet light and photographed for subsequent analysis.

3.4.4 Data Reduction

For clarity, the non-dimensional momentum coefficient per unit span (C_μ) was defined by:

$$C_\mu = \frac{\dot{m} V_{jet}}{\frac{1}{2}\rho U_\infty^2 c} \qquad [3.12]$$

where $\dot{m}$ and V_{jet} were the mass flow rate and the velocity of the jet of air, respectively.

Analysis of the surface static pressure measurements was analogous to that previously described in Section 3.3.4.

3.4.5 Assessment of Measurement Accuracy

With standard two-dimensional low-speed blockage corrections applied (see Appendix C for further details), the aerodynamic forces obtained from integration of the surface static pressure distributions were subject to the same potential inaccuracies identified in Section 3.1.7. Whilst it was also recognised that the blowing boundary layer control system was subject to total pressure losses, e.g. internal pressure losses due to ducting and frictional loses, it was not possible to quantify the magnitude of such losses incurred.

3.5 Large-Scale Wind-Tunnel Experiments: Discrete Blowing

This section details the modifications to the high-lift model necessary, in order to investigate the effect of discrete blowing upon the flow field around a multi-element configuration. The experimental setup and instrumentation specific to the discrete blowing configuration are also described. For all discrete blowing experiments, the model was mounted vertically in the wind tunnel, between two circular end plates, as described in Section 3.3.1.

3.5.1 Model Description

The modular trailing edge of the main element was formed by a carbon fibre component, instrumented with surface static pressure orifices, comparable to the tangential slot blowing model. Maintaining the truncated trailing edge thickness of 3.25*mm*, circular holes 2*mm* in diameter were drilled in the solid trailing edge across the span, with 4*mm* between hole centres. Restricting the compressed air supply to each flow meter to 3300 litres per minute and reducing the open hole area in the blowing pipe to $0.003m^2$, the required momentum coefficient of 0.025 was achieved with reasonable spanwise consistency. Subsequent modification to the spanwise distribution of the discrete orifices at the trailing edge of the main element was achieved by means of aluminium tape to conceal specific orifices.

3.5.2 Experimental Instrumentation

3.5.2.1 Surface Static Pressure Instrumentation

The instrumentation for measuring and recording the surface static pressures on the main element, leading edge slat, trailing edge flap and modular trailing edge component has already been described in Section 3.4.2. For clarity, details of the instrumentation associated with each component of the high-lift aerofoil, together with the respective pressure transducer calibrations, are given in Table 5 below.

Surface Static Pressure Instrumentation and Pressure Transducer Calibrations for Discrete Blowing High Lift Configuration			
Aerofoil Element	Pressure Transducer	Solenoid Controller	Calibration (mmH_2O/V)
Slat	0.5psi Setra 239 (s/n 47513)	CTLR2/S2-S6 (s/n 2839)	140.04
Modular Trailing Edge Component (Main Element)	0.5psi Setra 239 (s/n 47513)	CTLR2/S2-S6 (s/n 2839)	140.04
Main	0.5psi Setra 239 (s/n 633802)	CTLR2/S2-S6 (s/n 1788)	152.1
Flap	1psi Setra 239 (s/n 24847)	CTLR2/S2-S6 (s/n 1368)	284.56

Table 5: Surface static pressure instrumentation details and corresponding calibrations for discrete blowing configuration

3.5.3 Experimental Programme

Unless otherwise stated, all tests were conducted at a nominal freestream velocity of $40 m/s$ corresponding to a Reynolds number of 1.64×10^6, based on the stowed reference chord. Furthermore, blowing was typically applied at a momentum coefficient of 0.025.

3.5.3.1 Surface Static Pressure Measurements

Due to time and facility constraints, investigations regarding the effect of discrete blowing on the surface static pressure measurements were limited to the takeoff configuration. The configuration angle of incidence was increased from 0° to 20° in 2° increments. With all discrete trailing edge orifices open, air was blown over the upper surface of the deployed trailing edge flap at a C_μ of 0.025 and the resultant surface static pressure distributions were compared to the corresponding baseline configuration without any form of blowing boundary layer control.

Additional tests were conducted to establish the repeatability of the measurements and the effect of variations in Reynolds number. Furthermore, the effect of varying the mass flow rate was also investigated. Due to time limitations, measurements were limited to a single configuration at α=8°, representative of takeoff conditions. Accordingly, the volume flow rate delivered to the blowing pipe was incremented between 4600 and 6600 litres per minute, in intervals of 400 litres per minute, and the corresponding surface static pressure measurements were duly sampled and recorded.

3.5.3.2 Surface Oil Flow Visualisation

The quantitative surface pressure measurements were supplemented by surface oil flow visualisation over the upper surface of the trailing edge flap. In addition, the spanwise distribution of the discrete holes at the trailing edge was modified and the resultant surface flow characteristics over the upper surface of the flap were examined.

3.5.4 Data Reduction

Analysis of the surface static pressure measurements was analogous to that previously described in Section 3.3.4, with the exception that the relevant transducer calibrations were detailed in Table 5.

3.5.5 Assessment of Measurement Accuracy

With standard two-dimensional low-speed blockage corrections applied (see Appendix C for further details), the aerodynamic forces obtained from integration of the surface static pressure distributions were subject to the same potential inaccuracies identified in Section 3.1.7. Similarly to the tangential slot blowing configuration, it was recognised that the blowing boundary layer control system was subject to total pressure losses, although once again, it was not possible to quantify the magnitude of such losses incurred.

3.6 Chapter Summary

The experimental methodologies for each of the three high-lift technologies under consideration have been detailed within. The models for each element of the test programme were described, together with ancillary equipment and instrumentation. Finally, the test programmes were outlined and the subsequent analysis of data was explained.

4 Flat Plate Analysis

This chapter investigates the effect of plain, 10mm and 20mm 60° triangular serrated geometries on the developing flow field at the trailing edge of the flat plate, in the absence of an aft positioned single slotted flap.

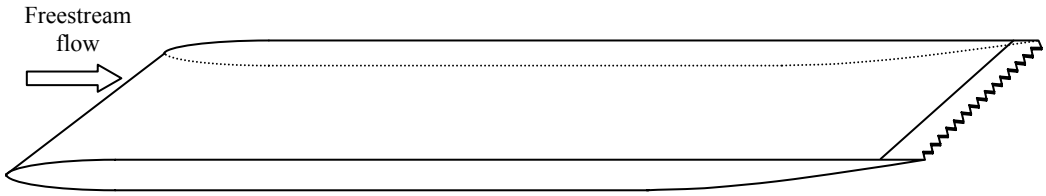

4.1 Plain Trailing Edge

With the plain geometry implemented at the trailing edge of the flat plate, the flow field was analysed immediately aft of the trailing edge to determine the effect of free and fixed transition on the flow field characteristics of the baseline flat plate model. Unless otherwise stated, all experiments were conducted at a nominal freestream velocity of $35m/s$ corresponding to a Reynolds number of 3.58×10^6, based upon the flat plate chord.

4.1.1 Flow Field Analysis at the Trailing Edge of the Flat Plate: Free Transition

The local velocity in the shear layer was initially evaluated immediately aft of the flat plate plain trailing edge at the spanwise centreline. Due to the proximity of the measurement plane to the flat plate trailing edge, it was assumed that the effects of viscous diffusion on the velocity gradients in the free shear layer had a negligible effect upon the overall shear layer thickness and was thus representative of the boundary layer thickness at the trailing edge of the flat plate.

The measurements indicated that with free transition on the upper and lower surfaces of the flat plate, the trailing edge boundary layer thickness was approximately $20mm$ and $28mm$, respectively, resulting in an upper-to-lower-surface-boundary-layer-thickness ratio (δ_{us}/δ_{ls}) of 1:1.3 at the trailing-edge of the flat plate.

Measurements at incremental spanwise locations displayed negligible variation in the non-dimensional velocity profiles, see Figure 17. Thus, the spanwise trailing edge measurements confirmed that any adverse effects induced by the presence of the tunnel

sidewalls on the flow field developing over the flat plate were restricted to the outer span. Accordingly, the flow field over the central 50% span, over which the subsequent measurements were attained, was two-dimensional.

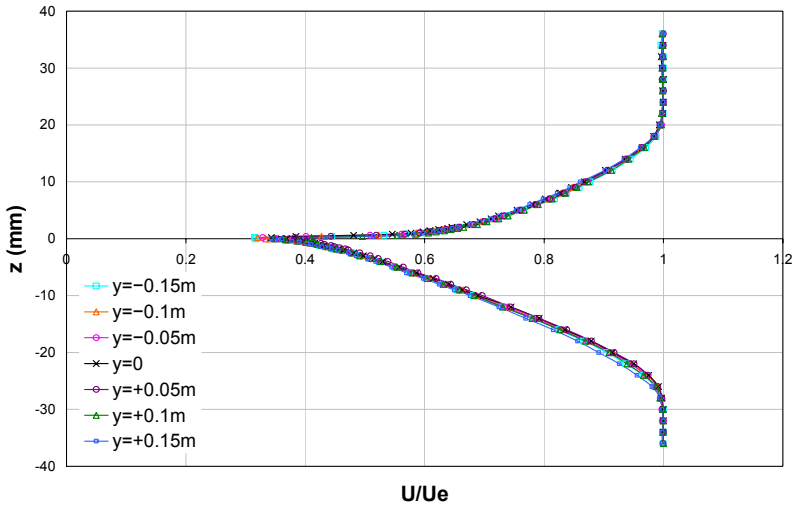

Figure 17: Non-dimensional velocity profiles across the span immediately aft of the flat plate plain trailing edge with free transition

4.1.2 Justification for the Application of Artificial Boundary Layer Control

As the fundamental impetus for the Brough experiments was to discern the effect of trailing edge serrations on the aerodynamic characteristics of a single slotted flap, it was imperative that the flow field characteristics at the trailing edge of the flat plate simulated the salient features of the flow field at the trailing edge of a main element upstream of deflected flap within a multi-element configuration. That so being, it was deemed pertinent to modify the trailing-edge boundary layer thickness on the upper and lower surfaces of the flat plate, such that (δ_{us}/δ_{ls}) was representative of a high-lift configuration.

A distinct value for (δ_{us}/δ_{ls}) at the trailing edge of the main element in a multi-element high-lift configuration proved difficult to ascertain. Not only was the boundary layer development dependent upon the Reynolds number but it was also notably influenced by the pressure gradients imposed by the aerofoil geometry, configuration angle of incidence and the external flow field. Furthermore, the highly complex flow field of wake and boundary layer interaction was particularly sensitive to variations in the specified lap/gap and deflection angle of the high-lift devices (Foster et al, 1970).

Whilst recognising that the formation of the boundary layer over a multi-element aerofoil was intrinsically dependent on several parameters, Van den Berg's (1979) extensive measurements on a two-dimensional aerofoil with a single slotted trailing edge flap provided a comprehensive analysis of the trailing edge boundary layer on the upper and lower surfaces of the main element at a Reynolds number of 2.51×10^6. Noting that the lower surface geometry of the main element was designed to ensure boundary layer attachment to the trailing edge, increasing α from 6° to 13.1°, increased (δ_{us}/δ_{ls}) from approximately 3.5:1 to 8:1, respectively.

Ratios of a comparable order of magnitude were inferred from other studies. These included Foster et al's (1970) two-dimensional measurements on a two-element configuration at α=0°, comprising a main element with a single slotted flap, which indicated $1<(\delta_{us}/\delta_{ls})\leq2$, depending upon the flap gap. This was further corroborated by Foster et al's (1972) analysis over a high-lift aerofoil at α=0°, whereby boundary layer velocity profiles over a main element and a single slotted flap indicated that (δ_{us}/δ_{ls}) was approximately 1.2:1 at the trailing edge of the main element. Extending this investigation to a three-element aerofoil by means of deploying a single slotted leading edge slat, suggested that (δ_{us}/δ_{ls}) was increased to approximately 8:1, which was duly attributed to the interaction of the shear layer from the slat with the upper surface boundary layer developing over the main element. However, studies by Stevens et al (1971) over a four-element aerofoil inferred a (δ_{us}/δ_{ls}) of approximately 5:1 at the trailing edge of the main element.

Clearly, the boundary layer thickness at the trailing edge of the main element in a multi-element high-lift configuration was highly sensitive to a number of interdependent parameters. Whilst attaining a distinct value for (δ_{us}/δ_{ls}) proved difficult, it was apparent that shear flows on the lower surface were typically negligibly thin compared to those on the upper surface (Nakayama, Kreplin, and Morgan, 1990) and thus, in the first instance, it was necessary to artificially increase the upper surface boundary layer thickness and/or decrease the lower surface boundary layer thickness over the flat plate.

4.1.3 Effect of Artificial Boundary Layer Control on the Trailing Edge Boundary Layer Velocity Profile and Thickness

Based upon the principle that removing the low energy fluid in the boundary layer immediately adjacent to the surface allowed a thinner boundary layer of high energy fluid to develop downstream, boundary layer suction was initially investigated as a

means of decreasing the lower surface boundary layer thickness. Accordingly, the lower surface boundary layer control system was connected to the $45m^3$ storage tank of the 2.5"×2.5" transonic wind-tunnel at Cranfield University, which was evacuated by an electrically driven $50kW$ vacuum pump to attain a near vacuum pressure. Subsequent suction through the 0.8% porous area on the lower surface, at a volume flow rate of 2200 litres per minute, reduced the lower surface trailing-edge boundary layer thickness from $28mm$ to $22mm$ at the spanwise centreline. Addressing the limitations imposed by the open hole area in the lower surface porous plate, boundary layer suction was applied through the lower surface porous plate with an increased open hole area of 3.1%. Suction at a volume flow rate of 4400 litres per minute through the lower surface porous plate reduced the trailing edge boundary layer thickness at the spanwise centreline to $20mm$, with a corresponding increase in the fullness of the velocity profile. No further reduction in the lower surface boundary layer thickness was achievable with the present boundary layer control system.

It was concluded that the most effective means of increasing the upper surface boundary layer thickness consisted of a $55mm$ strip of Lego board positioned across the model span, approximately $0.23c$ downstream of the leading edge. In addition, a $1.5mm$ diameter circular wire was glued above the Lego board perpendicular to the freestream direction, approximately $0.24c$ downstream of the model leading edge. Thus, the combined artificial surface roughness effectively fixed transition on the upper surface of the flat plate (White, 1991: pp 385-387) and resulted in an upper surface trailing edge boundary layer thickness of $40mm$.

Combination of this passive boundary layer control on the upper surface of the flat plate with the active boundary layer control on the lower surface resulted in an (δ_{us}/δ_{ls}) of 2:1 at the trailing edge of the flat plate. However, the relatively small improvement in (δ_{us}/δ_{ls}) failed to justify the implementation of active boundary layer control, particularly when considering the complexities in maintaining a constant suction flow rate for the duration of the data acquisition in a given measurement plane. For this reason, only the passive boundary layer control was implemented on the upper surface of the flat plate for the remainder of the experimental programme in the Brough wind tunnel, resulting in an (δ_{us}/δ_{ls}) of approximately 1.4:1.

Thus, with transition fixed, the velocity profile measurements indicated that the data was repeatable to within ±0.7%. Furthermore, measurements at incremental spanwise locations either side of the spanwise centreline indicated that the non-dimensional

velocity profiles were typically repeatable to within ±2%, with no appreciable variation to the estimated boundary layer thickness and hence, was demonstrative of a two-dimensional flow field over the central 50% span examined.

4.2 10mm Serrated Trailing Edge

With the 10mm 60° triangular serrated geometry implemented at the trailing edge of the flat plate, Figure 18 shows the contour plot for the non-dimensional streamwise component of velocity, calculated from the total pressure measurements in the shear layer immediately aft of the trailing edge, at incremental spanwise locations.

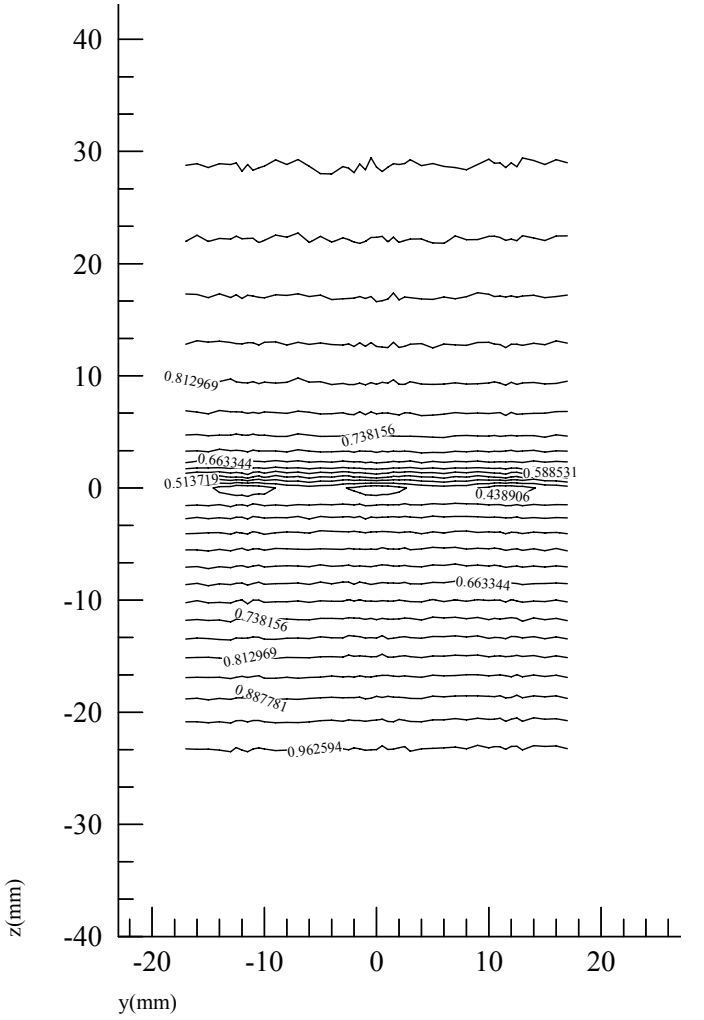

Figure 18: Non-dimensional velocity contour aft of 10mm 60° triangular serrations at the trailing edge of the flat plate

Distinct velocity deficits coincided with the serration vertices at y=0 and y=±11.5*mm*. With only the streamwise component of velocity determined from the measurements,

the velocity deficit was indicative of vorticity aft of the 10mm serrations. The measurements suggested that the flow field immediately aft of the 10mm trailing edge serrations was periodic, with a period of 11.5*mm*, i.e. equivalent to the distance between successive serration vertices. Furthermore, detailed measurements immediately aft of a singular 60° triangular serration indicated a higher pressure at the serration vertex, which decreased in magnitude approximately linearly with distance either side of the vertex to a local minimum aligned with the trough, corroborating the observations of Gai and Sharma (1981).

Measurements at a nominal distance of 0.4*c* aft of the flat plate trailing edge, where *c* was the flat plate chord, indicated that the 10mm serrated geometry had no appreciable effect upon the local velocity distribution within the developing wake and was typically repeatable to within ±1% of the measurements for the baseline configuration with the plain trailing edge geometry.

4.3 20mm Serrated Trailing Edge

The non-dimensional streamwise component of velocity at incremental spanwise locations, calculated from the total pressure measurements in the shear layer immediately aft of the 20mm 60° triangular serrated trailing edge geometry, is displayed in Figure 19.

Similarly to the 10mm serrated geometry, distinct velocity deficits were evident aft of the 20mm serrated trailing edge, coinciding with the serration vertices at y=0 and y=±23*mm*. Based only upon the streamwise component of velocity, the velocity deficit was indicative of vorticity aft of the 20mm triangular serrations. Once again, the measurements suggested that the flow field immediately aft of the 20mm 60° triangular trailing edge serrations was periodic, with a period of 23*mm*, i.e. equivalent to the distance between successive serration vertices. Similarly to the 10mm serrations, detailed measurements immediately aft of a singular 60° triangular serration indicated a higher pressure at the serration vertex, which decreased in magnitude approximately linearly with distance either side of the vertex to a local minimum aligned with the trough, once again corroborating the observations of Gai and Sharma (1981).

Wake surveys at a nominal distance of 0.4*c* aft of the flat plate trailing edge indicated that, similarly to the measurements for the 10mm serrated trailing edge, the 20mm serrated geometry had no appreciable effect upon the local velocity distribution within

the developing wake and was typically repeatable to within ±1% of the measurements for the baseline configuration with the plain trailing edge geometry.

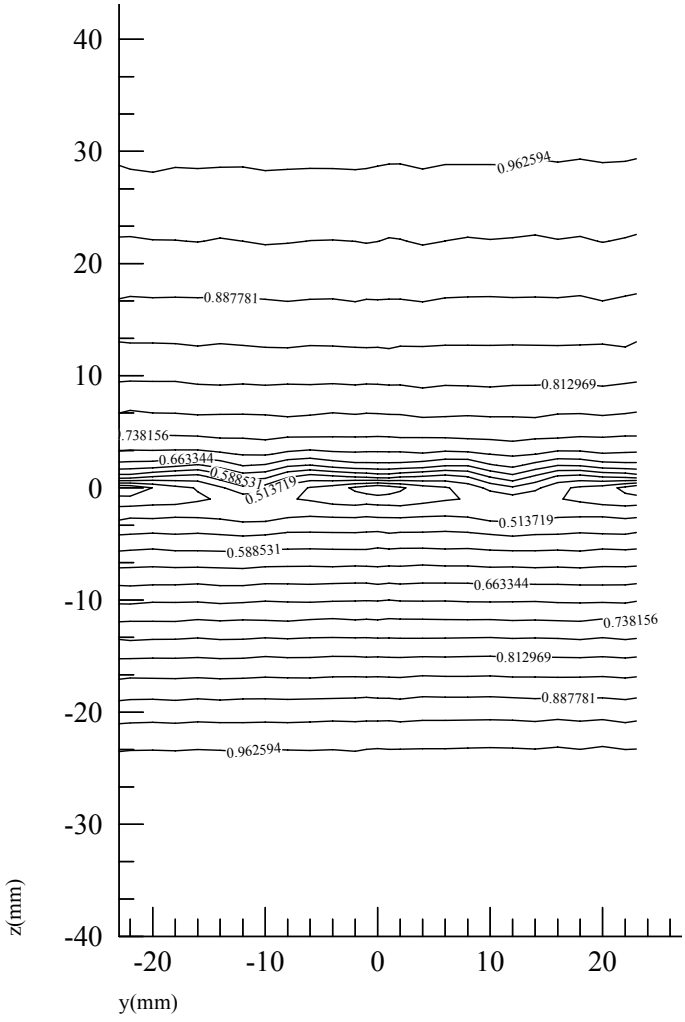

Figure 19: Non-dimensional velocity contour aft of 20mm 60° triangular serrations at the trailing edge of the flat plate

4.4 Chapter Summary

The local velocity in the shear layer was evaluated immediately aft of the flat plate plain trailing edge. Due to the proximity of the measurement plane to the trailing edge, it was assumed that the effects of viscous diffusion on the velocity gradients in the free shear layer had a negligible effect upon the overall shear layer thickness and was thus representative of the boundary layer thickness at the trailing edge of the flat plate.

Measurements at successive spanwise locations indicated a two-dimensional flow field over the central 50% span immediately aft of the flat plate trailing edge, irrespective of whether transition was free or fixed. Maintaining free transition, (δ_{us}/δ_{ls}) was 1:1.3. However, this was unrepresentative of the salient features of the flow field at the trailing edge of a main element in a multi-element high-lift configuration, necessitating artificial modification the boundary layer on the flat plate. Whilst the combination of passive and active boundary layer control resulted in an (δ_{us}/δ_{ls}) of 2:1, the impracticalities of maintaining constant suction within the experimental setup did not warrant its application. Accordingly, the experimental programme was conducted with only passive upper surface boundary layer control, generating an (δ_{us}/δ_{ls}) of 1.4:1.

Analysis of the streamwise component of velocity at incremental spanwise locations, immediately aft of the 10mm or 20mm 60° triangular serrations, displayed distinct velocity deficits coinciding with the respective serration vertices. This was indicative of vorticity immediately aft of the serrations. Furthermore, the measurements suggested that the flow field immediately aft of the serrated trailing edge geometries was periodic.

5 Flat Plate with Trailing-Edge Flap

This chapter considers a two-element configuration consisting of a single slotted flap aft of a flat plate. A parametric study was conducted, varying the flap lap/gap and deflection angle for each of the plain, 10mm and 20mm 60° triangular serrated trailing edge geometries. The serrated geometries were evaluated by means of key aerodynamic parameters identified.

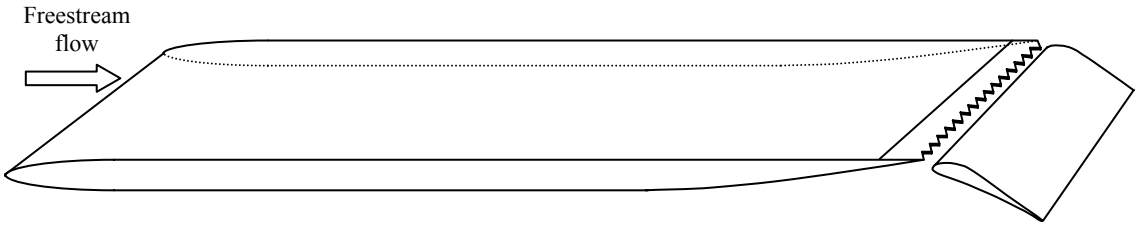

5.1 Plain Trailing Edge Configuration

With the plain geometry implemented at the trailing edge of the flat plate, the flow field developing over the single slotted flap was analysed to determine the aerodynamic characteristics of the baseline configuration. As established in the previous chapter, transition was fixed on the upper surface of the flat plate, generating an upper-to-lower-surface-boundary-layer-thickness ratio of 1.4:1 at the trailing edge of the flat plate. Free transition was maintained over the single slotted flap throughout. Unless otherwise stated, all experiments were conducted at a nominal freestream velocity of $35m/s$, corresponding to a Reynolds number of 3.58×10^5, based on flap chord.

Comparison of the surface static pressure distributions at $y=\pm0.1m$ either side of the spanwise centreline confirmed that any boundary layer separation induced by the presence of the tunnel sidewalls was restricted to the outer span regions of the flap. Although a slight anomaly was evident over the fore $0.05c_{flap}$ of the flap upper surface, the consistency with which these discrepancies arose across the parametric study suggested that such fluctuations were primarily attributed to marginal disparities in the geometric position of the respective spanwise static pressure orifices. Accordingly, it was concluded that the flow field, over which the subsequent measurements were attained, was two-dimensional.

The static pressure measurements over the trailing edge flap were typically repeatable to within ±3%, with the greatest fluctuations coinciding with the flow field development over the leading edge. That so being, both the lift and pressure drag force coefficients,

determined from integration of the surface static pressure distributions, were repeatable to within ±0.5%. The velocity profile measurements in the developing wake were typically repeatable to within ±1%, which rendered the profile drag coefficient repeatable to within approximately ±0.5%.

5.1.1 Characteristics of Baseline Configuration

The surface static pressure distributions measured over the single slotted flap aft of the modified flat plate are shown in Appendix D for each flap deflection angle and lap/gap tested. Note that the data denoted by the black line represents the baseline configuration with the plain trailing edge, discussed within the present section. Recall that at a lap/gap of (−0.13, −0.07), the proximity of the upper surface flap leading-edge to the flat plate trailing edge rendered the lower deflection angle of 0° mechanically infeasible to implement and thus, no data was presented for this configuration.

In the absence of significant regions of boundary layer separation over the upper surface of the single slotted flap, successive increments in the flap deflection angle (δ_f) from 0° to 25°, at a specified lap/gap, tended to progressively heighten the suction over the fore region of the flap upper surface, simultaneously transposing the point of minimum pressure marginally upstream and typically heightening the adverse pressure gradient developing immediately aft. Conversely, the lower surface static pressure was typically increased with successive increments in δ_f, simultaneously transposing the stagnation point marginally aft. Reduction in the upper surface trailing edge pressure coefficient was indicative of increased boundary layer thickness. The magnitude and extent of the reduction in the trailing edge static pressure was dependent upon the specified lap, gap and δ_f, with substantial decrements at high test δ_f suggesting a heightened susceptibility to separation (Chin et al, 1993).

Boundary layer separation was typified by an essentially uniform pressure coefficient (C_p) dominating an extensive region of the flap upper surface and was duly indicative of a dramatic loss in upper surface suction, consistent with aerofoil stall. The δ_f at which extensive boundary layer separation occurred was intrinsically dependent upon the lap/gap. For $\delta_f \leq 15°$, the C_p distributions suggested that boundary layer attachment was maintained to within close proximity of the trailing edge, irrespective of the lap/gap implemented. Increasing δ_f to 20° resulted in upper surface boundary layer separation aft of $0.05c_{flap}$ at the greatest lap/gap tested of (0.13, −0.13). A final increment in δ_f to 25° increased the lap/gap range over which extensive boundary layer separation

occurred. At the smaller test gap of −0.07, dramatic loss in suction over the aft $0.95c_{flap}$ was only evident at the maximum test lap of 0.13. However, by increasing the flap gap to −0.13, extensive separation was evident for all flap lap increments from 0 to 0.13, inclusive. Furthermore at δ_f=25°, the boundary layer separated over the aft $0.5c_{flap}$ of the flap upper surface when positioned at the lower flap lap test limit of −0.13, for both test flap gaps.

Comparison of the C_p distributions for a given δ_f highlighted the flow field sensitivity to variations in flap lap and gap. This was particularly evident over the fore region of the upper surface, with increments in lap and gap distinctly modifying the leading edge suction peak, both in magnitude and extent. At both test flap gaps, increments in flap lap from −0.13 to 0.13 progressively heightened the suction over the upper surface of the flap and increased the corresponding static pressure over the lower surface for $0° \leq \delta_f \leq 5°$. However, with subsequent increments in $\delta_f \geq 10°$, flap lap(s) were identified for which there was a distinct decrement in the leading edge suction in comparison to that at the lower flap lap test limit of −0.13. The range of flap laps over which a reduction in leading edge suction was evident, together with the magnitude of this decrement, was intrinsically dependent upon the specified flap lap and gap. Evidence of such flow field sensitivities to flap lap/gap and δ_f were manifested in the resultant aerodynamic forces. Accordingly, variations in the surface static pressure distributions due to increments in the flap lap, gap and δ_f were more tangibly evaluated in terms of the lift and drag forces acting on the two-dimensional aerofoil.

For a specified lap/gap, the non-dimensional lift coefficient per unit span (C_l) increased with δ_f until a maximum lift coefficient (C_{lmax}) was attained, coinciding with the stall angle for the flap (δ_{fstall}). Depending upon the extent of the upper surface boundary layer separation, C_l either decreased gradually for $\delta_f > \delta_{fstall}$, which corresponded to a mild stall, or precipitously, which was indicative of a severe stall.

Figure 20 shows the variation of C_l with δ_f at a flap gap of −0.07 over the flap lap range tested. Variations in C_l due to flap lap for a given δ_f were evaluated relative to the zero flap lap configuration, leading to the distinction between flap laps with the flap leading edge positioned upstream of the flat plate trailing edge, i.e. −0.13 and −0.07, and those with the flap leading edge positioned aft of the flat plate trailing edge, i.e. 0.07 and 0.13.

Quantifying ΔC_l accordingly, it was shown that positioning the flap leading edge upstream of the flat plate trailing edge at the lower lap test limit of −0.13 adversely

affected C_l for $\delta_f \leq 15°$. At $\delta_f = 5°$, ΔC_l accounted for a 30% reduction in comparison to the zero flap lap configuration, which was progressively reduced to an 8% decrement in C_l at $\delta_f = 15°$. However, with further increments in $\delta_f \geq 20°$, positioning the flap at a lap of −0.13 had a favourable effect upon C_l in comparison to the configurations positioned at either a flap lap of −0.07 or 0 and accounted for a 12% increment in C_l in comparison to the zero flap lap configuration.

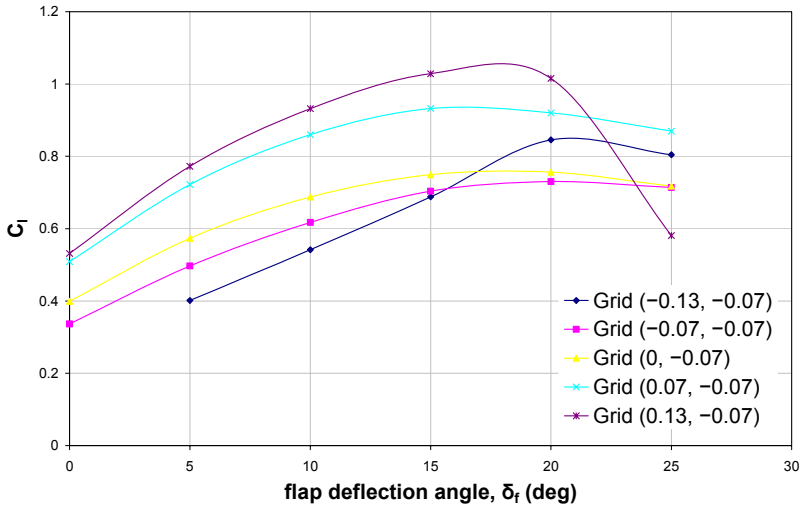

Figure 20: Variation of C_l with δ_f over test flap lap range at a flap gap of −0.07, plain trailing edge configuration

Positioning the flap leading edge immediately upstream of the flat plate trailing edge at a flap lap of −0.07 had a detrimental effect upon C_l for all test δ_f, although by incrementing the flap lap from −0.13 to −0.07, the decrement in C_l was reduced for $\delta_f \leq 15°$, accounting for a 16% and 6% reduction at $\delta_f = 0°$ and $\delta_f = 15°$, respectively. With further increments in $\delta_f \geq 20°$, the decrement in C_l was marginalised such that at $\delta_f = 25°$, there was no appreciable variation in C_l in comparison to the zero flap lap configuration.

Conversely, positioning the flap leading edge immediately aft of the flat plate trailing edge, at a lap of 0.07, increased C_l in comparison to the zero flap lap configuration for all test δ_f. The increment in C_l progressively decreased in magnitude with successive δ_f, from 28% at $\delta_f = 0°$ to a 21% increment in C_l at $\delta_f = 25°$.

Incrementing the flap lap from 0.07 to the upper test limit of 0.13 heightened ΔC_l for all $\delta_f \leq 20°$. The increment in C_l progressively increased in magnitude from a 33% increment in C_l at $\delta_f = 0°$ to a maximum 37% increment at $\delta_f = 15°$. A further increment in δ_f to 20° decreased ΔC_l to 34%. However, with a final increment in δ_f to 25°, ΔC_l correlated to a 19% decrement in C_l in comparison to the zero flap lap configuration,

which was indicative of severe stall and corroborated the extensive boundary layer separation aft of 0.05c, evident in the corresponding C_p distribution (see Appendix D, Figure 158(f)). In contrast, all other configurations at flap gap of −0.07 displayed a gradual loss in lift at δ_f=25°, indicative of the onset of mild stall.

Thus at a flap gap of −0.07, positioning the flap leading edge upstream of the flat plate trailing edge had a detrimental effect upon C_l for $\delta_f \leq 15°$, with only isolated increments in C_l evident at the lower lap test limit of −0.13 for $\delta_f \geq 20°$. In contrast, positioning the flap leading edge aft of the flat plate trailing edge typically had a favourable effect upon C_l. In particular, positioning the flap at a lap of 0.13 attained the maximum C_l for any given $\delta_f \leq 20°$ but with the onset of severe stall, the flap lap of 0.07 proved more favourable at the upper test limit of δ_f=25°.

Figure 21 shows the variation of C_l with δ_f at a flap gap of −0.13 over the flap lap range tested. Once again, quantifying variations in C_l relative to the zero flap lap configuration, it was shown that by positioning the flap leading edge upstream of the flat plate trailing edge at the lower lap test limit of −0.13, C_l was adversely affected for $\delta_f \leq 5°$. At δ_f=0°, ΔC_l accounted for a 19% reduction in comparison to the zero flap lap configuration, which was reduced to an 9% decrement in C_l at δ_f=5°. However, with further increments $\delta_f \geq 10°$, positioning the flap at a lap of −0.13 had a favourable effect upon C_l in comparison to the corresponding configurations positioned at either a flap lap of −0.07 or 0. Furthermore, in terms of increasing C_l, positioning the flap at a lap of −0.13 proved more favourable than all other flap laps tested for $\delta_f \geq 20°$. Specifically, positioning the flap at a lap of −0.13 increased C_l by 1% in comparison to the zero flap lap configuration at δ_f=10°, which was progressively increased to a 12% increment at δ_f=20°. Noting the substantial loss in lift for the zero flap lap configuration at δ_f=25°, which was characteristic of severe stall and corroborated the extensive upper surface boundary layer separation evident in the corresponding C_p distribution (see Appendix D, Figure 161(f)), it was apparent that positioning the flap at the lower lap test limit of −0.13 had a favourable effect upon the stall characteristics, generating an 81% increment in C_l in comparison to the zero flap lap configuration at δ_f=25°.

Positioning the flap leading edge immediately upstream of the flat plate trailing edge, at a flap lap of −0.07, had a detrimental effect upon C_l for $\delta_f \leq 10°$, with ΔC_l equating to a 16% reduction at δ_f=0°, which was progressively reduced in magnitude to a 4% decrement in C_l at δ_f=10°. With further increments in $15° \leq \delta_f < 20°$, any variation in C_l in comparison to the zero flap lap configuration was essentially negated but with a final

increment in δ_f to 25°, positioning the flap at a lap of −0.07 had a favourable effect upon the stall characteristics and hence, increased C_l by 76% in comparison to the zero flap lap configuration.

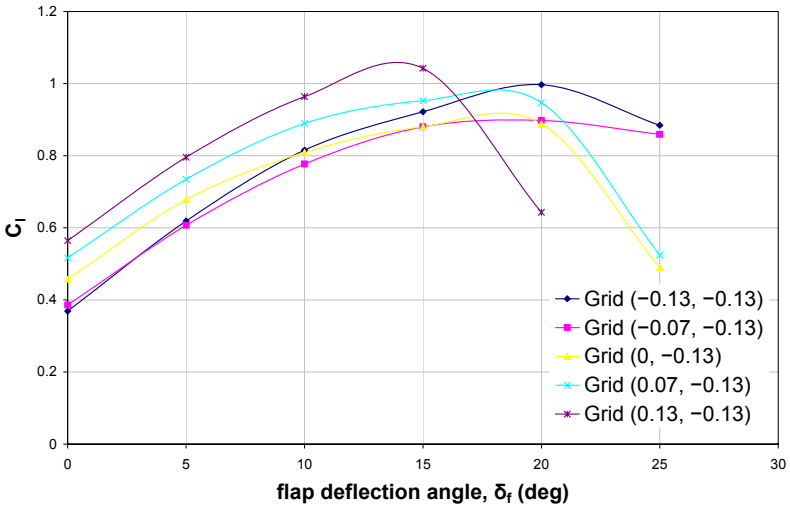

Figure 21: Variation of C_l with δ_f over test flap lap range at a flap gap of −0.13, plain trailing edge configuration

Conversely, positioning the flap leading edge immediately aft of the flat plate trailing edge, at a lap of 0.07, increased C_l in comparison to the zero flap lap configuration for all test δ_f. The increment in C_l tended to progressively decrease in magnitude with successive δ_f, from a 13% increment at δ_f=0° to a 7% increment in C_l at δ_f=25°. Similarly to the zero flap lap configuration, the flap stalled severely at δ_f=25°, characterised by the dramatic loss in lift and corroborated by the extensive boundary layer separation over the aft 0.95c evident in the corresponding C_p distribution (see Appendix D, Figure 161(f) and Figure 162(f)).

Incrementing the flap lap from 0.07 to the upper test limit of 0.13 heightened ΔC_l for all $\delta_f \leq 15°$. The increment in C_l tended to progressively decrease in magnitude with successive $\delta_f \leq 15°$, accounting for a 23% increment at δ_f=0° and reducing to an 18% increment in C_l at δ_f=15°. With a further increment in δ_f to 20°, ΔC_l correlated to a 28% decrement in C_l in comparison to the zero flap lap configuration, which was indicative of severe stall and corroborated the complete boundary layer separation aft of 0.05c evident in the corresponding C_p distribution (see Appendix D, Figure 163(e)).

Thus at a flap gap of −0.13, positioning the flap leading edge upstream of the flat plate trailing edge had a detrimental effect upon C_l for $\delta_f \leq 5°$, although anomalies arose at

higher δ_f, particularly when positioned at the lower lap test limit of −0.13. In contrast, positioning the flap leading edge aft of the flat plate trailing edge typically had a favourable effect upon C_l. In particular, positioning the flap at a lap of 0.13 attained the maximum C_l for any given $\delta_f \leq 15°$ but with the onset of severe stall, positioning the flap at a lap of −0.13 proved more favourable for $20° \leq \delta_f \leq 25°$.

Comparison of Figure 20 and Figure 21 indicated that in the absence of significant regions of boundary layer separation over the upper surface of the flap, increasing the flap gap from −0.07 to −0.13 increased C_l for a given flap lap and δ_f. Although, by positioning the flap leading edge upstream of the flat plate trailing edge, the sensitivity of C_l to variations in flap gap for a given δ_f was heightened.

Defining an optimum flap position by the maximum value of C_l attainable for a given δ_f (Foster et al, 1972), it was evident from Figure 20 and Figure 21 that the optimum lap/gap for $0° \leq \delta_f \leq 15°$ was (0.13, −0.13). However, each subsequent increment in δ_f corresponded to a particular optimum flap position. At δ_f=20°, the optimum flap position was defined by a lap/gap of (0.13, −0.07) and at δ_f=25°, the optimum flap position was defined by a lap/gap of (−0.13, −0.13).

Figure 20 and Figure 21 indicated that for a given flap lap, increasing the gap from −0.07 to −0.13 typically had negligible effect upon the measured δ_{fstall}. Thus, the angle at which the flap stalled appeared more sensitive to variations in the flap lap. However, the nature of the stall was sensitive to variations in both the flap lap and gap. At a flap gap of −0.07, the gradual loss in lift, characteristic of mild stall, was evident for all configurations tested at incremental flap laps between −0.13 and 0.07 but at the upper flap lap test limit of 0.13, the dramatic loss in lift was characteristic of severe stall. By increasing the flap gap to −0.13, mild stall was only characteristic of configurations with the flap leading edge located upstream of the flat plate trailing edge. For all other configurations tested at incremental flap laps between 0 and 0.13, the considerable loss in lift characterised the onset of abrupt stall. Thus, increasing the flap gap from −0.07 to −0.13 heightened the severity of flap stall for configurations with the leading edge either aligned with or located aft of the flat plate trailing edge.

Figure 22 shows the variation in C_{lmax} for a specified lap/gap. With the flap leading edge either aligned with or located upstream of the flat plate trailing edge, i.e. for a flap lap of 0, −0.07 or −0.13, increasing the flap gap from −0.07 to −0.13 notably increased C_{lmax}. In contrast, with the flap leading edge positioned aft of the flat plate trailing edge,

i.e. at a flap lap of either 0.07 or 0.13, increments in flap gap had marginal effect upon the magnitude of C_{lmax}.

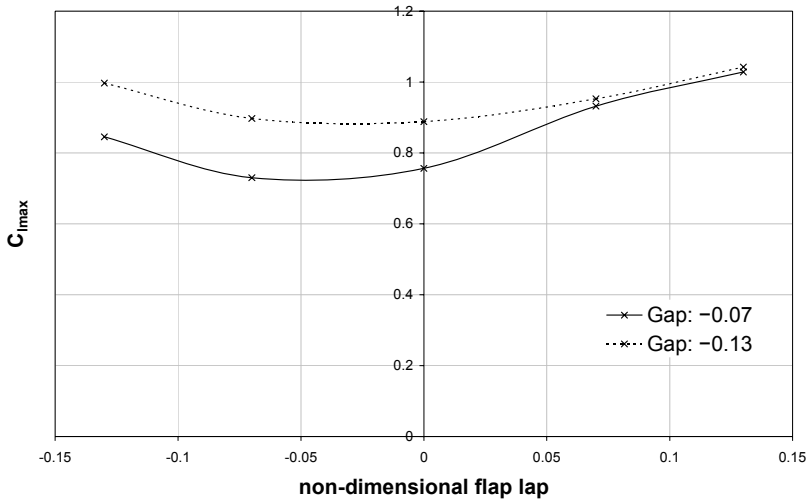

Figure 22: Effect of flap lap/gap upon C_{lmax} for plain trailing edge configuration

Specifically, incrementing the flap gap at a flap lap of −0.13 increased C_{lmax} by 0.15, equivalent to an 18% increment. A single increment in the flap lap to −0.07 heightened the sensitivity of C_{lmax} to variations in the flap gap, with a ΔC_{lmax} of 0.17 accounting for a 23% increment. With the flap leading edge aligned with the flat plate trailing edge, the deviation in C_{lmax} due to the flap gap was reduced to 0.13, representing a 17% increment. In contrast, ΔC_{lmax} was 0.02 at a flap lap of 0.07, decreasing to 0.01 at the upper flap lap test limit of 0.13, accounting for a 2% and 1% increment, respectively.

Furthermore, increasing the flap gap reduced the sensitivity of C_{lmax} to variations in flap lap. At the smaller flap gap of −0.07, C_{lmax} varied from a minimum value of 0.54 at a flap lap of −0.07 to a maximum of 0.86 at the upper flap lap of 0.13. In contrast at the larger flap gap of −0.13, C_{lmax} was less sensitive to variations in flap lap, deviating from a minimum of 0.71 at a flap lap of either −0.07 or 0 to a maximum of 0.88 at the upper flap lap of 0.13.

Appendix E shows the local velocity in the wake, measured aft of the flat plate and single slotted flap, normalised by the local freestream velocity and plotted against the relative position on the z-axis for each flap lap/gap and deflection angle tested. Note that the data denoted by the black line represents the baseline configuration with the plain trailing edge, discussed within the present section. In the absence of large regions of boundary layer separation over the upper surface of the trailing edge flap, incrementing δ_f at a specified lap/gap tended to deflect the wake cross-section

downwards in the measurement plane, i.e. transpose the wake centreline away from the flap lower surface. Whilst the wake velocity profile typically indicated that the wake from the flat plate was completely merged with that from the flap, there was evidence of a distinction between the wakes emanating from the flat plate and single slotted flap, particularly at the larger flap gap of −0.13. At a flap gap of −0.07, a distinction between the two wakes was only evident for $10° \leq \delta_f \leq 20°$ at a lap of 0.13 (see Figure 168(c)-(e)). However, at a flap gap of −0.13, a distinction between the wakes was evident for all flap laps. Specifically, for laps between −0.13 and 0, a distinction was evident for $15° \leq \delta_f \leq 20°$ (see (d) and (e) for Figure 169 through to Figure 171 in Appendix E), extending to $10° \leq \delta_f \leq 20°$ at a lap of 0.07 (see Appendix E, Figure 172(c)-(e)) and $5° \leq \delta_f \leq 15°$ at a lap 0.13 (see Appendix E, Figure 173(b)-(d)). For a given flap lap, the distinction between the two wakes became more prominent with increasing δ_f, suggesting a milder interaction between the developing wakes at high δ_f. This distinction was further enhanced when the flap leading edge was positioned aft of the flat plate trailing edge. Corroborating Foster et al (1972) and Bertelrud and Ljungström (1974), the milder interaction between the two wakes coincided with increased values of maximum C_l. Finally, significant regions of boundary layer separation over the trailing edge flap resulted in a considerable increase in the wake cross-section and a marked increase in the velocity defect (see Figure 168(f), Figure 171(f), Figure 172(f) and Figure 173(e) in Appendix E).

Distinct trends in the profile drag coefficient (C_{dp}), determined from the total pressure measurements in the wake, were difficult to ascertain. Figure 23 below shows the variation of C_{dp} with δ_f at a flap gap of −0.07 over the flap lap range tested.

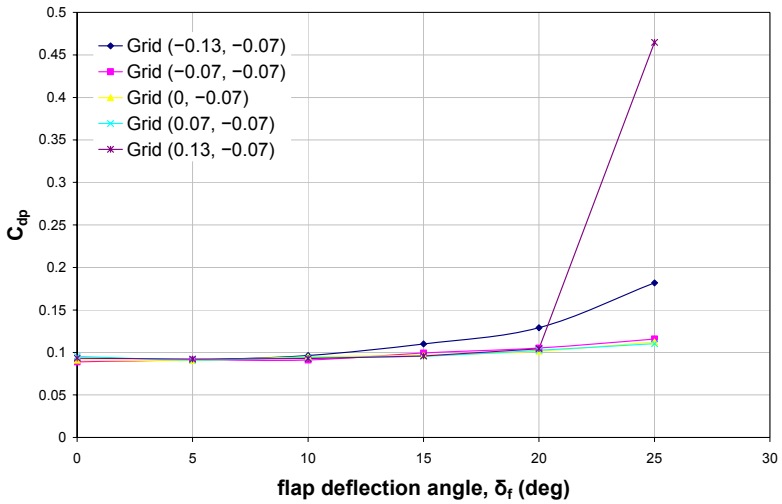

Figure 23: Variation of C_{dp} with δ_f over test flap lap range at a flap gap of −0.07, plain trailing edge configuration

Evaluating ΔC_{dp} relative to the zero flap lap configuration, it was noted that at a flap gap of −0.07, positioning the flap at the lower lap test limit of −0.13 increased C_{dp} in comparison to the zero flap lap configuration for all test δ_f. With successive increments in δ_f, the increment in C_{dp} progressively increased in magnitude from 2% at δ_f=10° to 27% at δ_f=20°. The marked increase in ΔC_{dp} to 62% at δ_f=25°, was consistent with the significant region of boundary layer separation aft of 0.5c evident over the flap upper surface in the corresponding C_p distribution (see Appendix D, Figure 154(e)). In contrast, positioning the flap at a lap of −0.07 had a favourable effect on C_{dp} for $\delta_f \leq 10°$, accounting for a maximum 4% decrement in comparison to the zero flap lap configuration. However, with subsequent increments in $15° \leq \delta_f \leq 25°$, C_{dp} was increased by approximately 3% in comparison to the zero flap lap configuration.

Positioning the flap leading edge aft of the flat plate trailing edge at a flap gap of −0.07 had a detrimental effect upon C_{dp}, in comparison to the zero flap lap configuration for $\delta_f \leq 5°$. At a lap of 0.07, C_{dp} was increased by 5% at δ_f=0°, reducing to a 1% increment at δ_f=5°. By incrementing the flap lap from 0.07 to 0.13, ΔC_{dp} represented a 2% increment for $\delta_f \leq 5°$. For $10° \leq \delta_f \leq 15°$, positioning the flap at a lap of 0.07 had a near negligible effect upon C_{dp} and incrementing the flap lap to 0.13 decreased C_{dp} by ≤2%. With a further increment in δ_f to 20°, C_{dp} was increased by 1% and 3% for a flap lap of 0.07 and 0.13, respectively. Whilst a final increment in δ_f to 25° resulted in a 2% decrement in C_{dp} at a flap lap of 0.07, positioning the flap at the upper lap test limit of 0.13 dramatically heightened the increment in C_{dp}, equating to over a 310% increase in comparison to the zero flap lap configuration. The magnitude of the increment was indicative of severe stall and corroborated the extensive boundary layer separation evident over the aft 0.95c_{flap} in the corresponding C_p distribution (see Appendix D, Figure 158(f)).

Figure 24 shows the variation of C_{dp} with δ_f at a flap gap of −0.13 over the flap lap range tested. At a flap gap of −0.13, positioning the flap leading edge upstream of the flat plate trailing edge decreased C_{dp} in comparison to the zero flap lap configuration at δ_f=0°, accounting for a 1% and 3% decrement at flap lap of −0.13 and −0.07, respectively. With further increments in $5° \leq \delta_f \leq 20°$, positioning the flap leading edge upstream of the flat plate trailing edge had a detrimental effect upon C_{dp}, in comparison to the zero flap lap configuration. ΔC_{dp} varied inconsistently with δ_f, attaining a maximum increment of 10% when positioned at a flap lap of −0.13, which was reduced to a maximum 5% increment at a flap lap of −0.07. With a final increment in δ_f to 25°, C_{dp} was once again reduced in magnitude in comparison to the zero flap lap

configuration, correlating to a 45% and 63% decrement in C_{dp} at a flap lap of −0.13 and −0.07, respectively. Recalling that extensive boundary layer separation was evident over the upper surface of the flap at δ_f=25° for the zero flap lap configuration (see Appendix D, Figure 161(f)), positioning the flap leading edge upstream of the flat plate trailing edge at a lap of −0.13 (see Appendix D, Figure 159(f)) delayed boundary layer separation to the aft $0.5c_{flap}$ of the flap upper surface, whereas at a lap of −0.07, boundary layer attachment was maintained to within close proximity of the trailing edge (see Appendix D, Figure 160(f)), both consequently reducing the resultant profile drag.

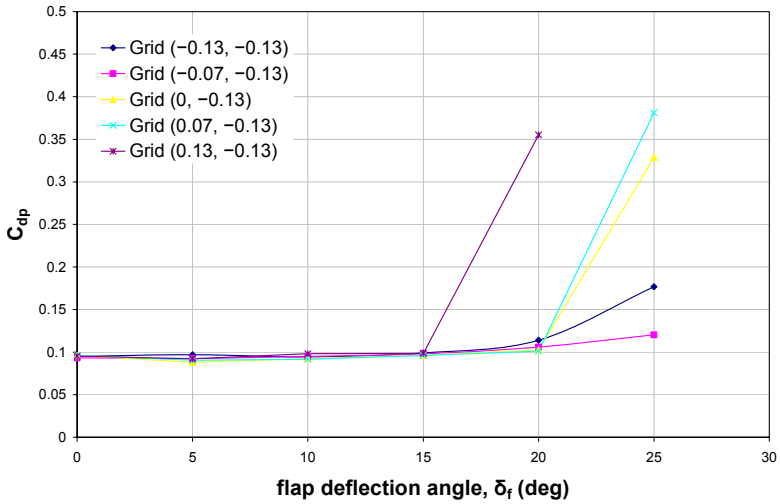

Figure 24: Variation of C_{dp} with δ_f over test flap lap range at a flap gap of −0.13, plain trailing edge configuration

At a flap gap of −0.13, positioning the flap leading edge immediately aft of the flap at a lap of 0.07 had negligible effect upon C_{dp} at δ_f=0° and for 10°≤δ_f≤20°. However, C_{dp} was increased by 3% and 16% at δ_f=5° and δ_f=25°, respectively. In contrast, whilst positioning the flap at the upper lap test limit of 0.13 had a near negligible effect upon C_{dp} at δ_f=0°, with further increments in δ_f, C_{dp} was increased, accounting for a 2-6% increment in comparison to the zero flap lap configuration for 5°≤δ_f≤15°. A final increment in δ_f to 20° substantially heightened the increment in C_{dp}, correlating to nearly a 250% increment in comparison to the zero flap lap configuration. The magnitude of the increment was indicative of severe stall and, once again, corroborated the extensive boundary layer separation evident in the corresponding C_p distribution (see Appendix D, Figure 163(e)).

Thus, the profile drag and hence, the developing wake were sensitive to variations in lap, gap and δ_f. Note that whilst both the pressure drag coefficient and the profile drag coefficient were calculated for each flap lap/gap and δ_f, only the results for the profile drag were discussed, as it was deemed to provide a more complete representation of

total drag force acting on the configuration. Additional analysis of the separate pressure drag data would not, in this instance, augment the evaluation of the baseline configuration.

Recognising that the ratio of lift-to-drag (L/D) was a critical parameter for phases in the flight envelope utilising high-lift devices, Figure 25 and Figure 26 display the variation in L/D with δ_f over the range of flap laps tested at a flap gap of −0.07 and −0.13, respectively. Note that L/D was based upon the profile drag calculations.

Once again, quantifying variations in L/D relative to the zero flap lap configuration, Figure 25 shows that positioning the flap leading edge upstream of the flat plate trailing edge at a flap gap of −0.07 had a detrimental effect upon L/D for all test δ_f. At a flap lap of −0.13, the decrement in L/D in comparison to the zero flap lap configuration tended to decrease in magnitude from a 30% decrement at δ_f=5° to 12% at δ_f=20°, although with a final increment in δ_f to 25°, the decrement was heightened to 31% due to the marked increment in C_{dp}, correlating to boundary layer separation aft of 0.5c. Incrementing the flap lap to −0.07 diminished the decrement in L/D for any given δ_f. Again, the decrement in L/D tended to progressively decrease in magnitude from 14% at δ_f=0° to a 4% decrement at δ_f=25°.

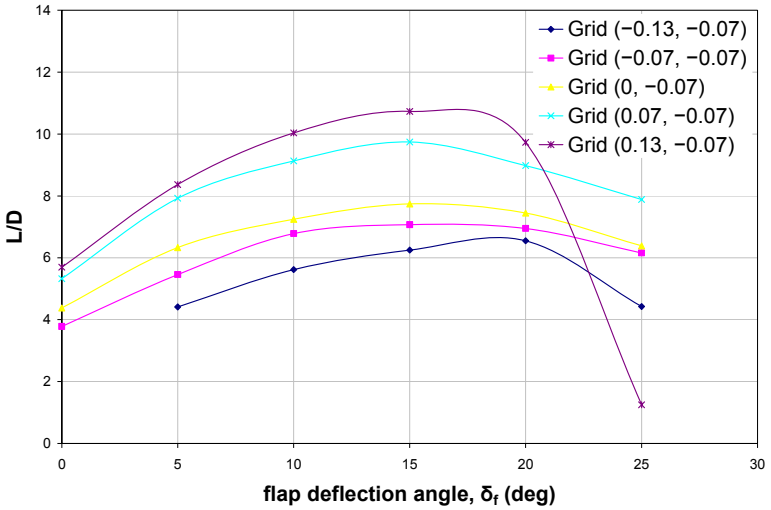

Figure 25: Variation of L/D with δ_f over test flap lap range at a flap gap of −0.07, plain trailing edge configuration

Positioning the flap leading edge aft of the flat plate trailing edge at a flap gap of −0.07 had a favourable effect upon L/D for all test δ_f, with only an isolated discrepancy arising at δ_f=25° at the upper flap lap test limit of 0.13 due to the onset of severe aerofoil stall. At a flap lap of 0.07, the increment in L/D progressively increased in magnitude from a 21% increment in L/D at δ_f=0° to a maximum 26% increment at δ_f=15°, although with

subsequent increments in $\delta_f \geq 20°$, the increment in L/D was reduced to 22% in comparison to the zero flap lap configuration. A final increment in flap lap to the upper test limit of 0.13 heightened the increment in L/D for $0° \leq \delta_f \leq 20°$, accounting for a 30% increment at $\delta_f = 0°$, which was progressively increased to a maximum 39% increment in comparison to the zero flap lap configuration for $10° \leq \delta_f \leq 15°$. By increasing δ_f to 20°, the increment in L/D was reduced to 31% but with severe stall evident at $\delta_f = 25°$, L/D dramatically decreased in magnitude, representing an 80% decrement in L/D when compared to the corresponding zero flap lap configuration.

Figure 26 shows that, at a flap gap of −0.13, positioning the flap at the lower lap test limit of −0.13 had a detrimental effect upon L/D for $0° \leq \delta_f \leq 10°$. For $\delta_f \leq 5°$, the decrement in L/D equated to an 18% reduction in comparison to the zero flap lap configuration, which was reduced to a 2% decrement at $\delta_f = 10°$. In contrast, positioning the flap at a lap of −0.13 increased L/D for $\delta_f \geq 15°$, accounting for a 2% increment for $15° \leq \delta_f \leq 20°$ and increasing to a 235% increment in L/D at $\delta_f = 25°$. The latter highlighted the favourable effect of the flap lap position upon the stall characteristics, in comparison to the corresponding zero flap lap configuration (compare baseline C_p distributions in Appendix D, Figure 159(f) and Figure 161(f)).

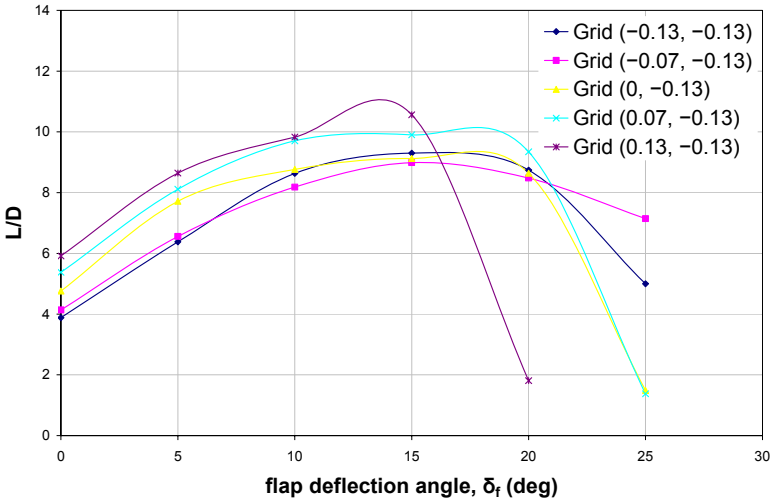

Figure 26: Variation of L/D with δ_f over test flap lap range at a flap gap of −0.13, plain trailing edge configuration

Similarly to the configuration at the smaller test flap gap of −0.07, positioning the flap at a lap of −0.07 and at a gap of −0.13 had a detrimental effect upon L/D for $\delta_f \leq 20°$. The magnitude of the decrement tended to progressively decrease in magnitude from 14% at $\delta_f = 0°$ to a 2% decrement at $\delta_f = 20°$. A final increment in δ_f to 25° once again highlighted the favourable effect of the flap position on the nature of the stall,

increasing L/D by 380% in comparison to the zero flap lap configuration (compare baseline C_p distributions in Appendix D, Figure 160(f) and Figure 161(f)).

At a flap gap of −0.13, positioning the flap at a lap of 0.07 had a favourable effect upon L/D in comparison to the zero flap lap configuration for $\delta_f \leq 20°$. The increment in L/D tended to progressively decrease in magnitude with successive δ_f, from 13% at $\delta_f=0°$ to an 8% increment in L/D at $\delta_f=20°$. Similarly to the zero flap lap configuration, the flap stalled severely at $\delta_f=25°$, characterised by the dramatic loss in lift and corroborated by the extensive boundary layer separation evident in the corresponding C_p distribution (see Appendix D, Figure 161(f) and Figure 162(f)). Accordingly, positioning the flap at a lap of 0.07 accounted for an 8% decrement in L/D at $\delta_f=25°$.

Incrementing the flap lap from 0.07 to the upper test limit of 0.13 heightened the increment in L/D for all $\delta_f \leq 15°$ at a flap gap of −0.13. The increment in L/D decreased in magnitude from a 24% increment at $\delta_f=0°$ to 12% for $5° \leq \delta_f \leq 10°$, although with a subsequent increment in δ_f to 15°, the increment in L/D was heightened to 16% in comparison to the zero flap lap configuration. A further increment in δ_f to 20° rendered the flap lap position detrimental, reducing L/D by 80% in comparison to the zero flap lap configuration. The magnitude of the decrement was indicative of severe stall and corroborated the complete boundary layer separation aft of $0.05c$ evident in the corresponding C_p distribution (compare baseline C_p distributions in Appendix D, Figure 161(e) and Figure 163(e)).

Comparison of Figure 25 and Figure 26 indicated that the optimum flap lap/gap position, in terms of attaining the maximum L/D, varied with δ_f. For $0° \leq \delta_f \leq 5°$, positioning the flap at a lap/gap of (0.13, −0.13) attained the maximum value of L/D. However, for $10° \leq \delta_f \leq 20°$, the maximum L/D was attained by positioning the flap at a lap/gap of (0.13, −0.07). A final increment in δ_f to 25° identified a lap/gap of (0.07, −0.07) as achieving the greatest L/D.

Finally, surface static pressure measurements over the trailing edge flap indicated that increments in nominal freestream velocity, correlating to Reynolds numbers based upon flap chord of 2.04, 2.55, 3.07, 3.58 and 3.88×10^5, tended to only marginally influence the flow field developing over the fore region of the flap upper surface, increasing the leading edge suction with increasing Reynolds number (see Appendix F, Figure 174). The corresponding mean velocity defect in the wake marginally decreased with increasing Reynolds number (see Appendix F, Figure 175). The measurements

suggested that the boundary layer at the flap trailing edge reduced in thickness with increasing Reynolds number, which was in accordance with theory. Thus, in terms of the resultant aerodynamic forces, increasing the Reynolds number increased C_l but decreased C_{dp}, corroborating the observations of Ljungström (1976). Quantifying the order of magnitude of these fluctuations in the aerodynamic forces, it was noted that at a flap lap/gap of (0, −0.07) and with δ_f=25°, incrementing the Reynolds number over the test range increased C_l by approximately 2% and decreased C_{dp} by approximately 4%. Sensitivity to variations in flap lap and gap was not expected to significantly affect the trends identified over the range of Reynolds numbers tested.

5.1.2 Summary of Baseline Configuration

With the plain geometry implemented at the trailing edge of the flat plate, the aerodynamic forces determined from the surface static pressure distributions and wake surveys indicated:

- For $\delta_f \leq 15°$, boundary layer attachment was maintained to within close proximity of the flap trailing edge, irrespective of the lap/gap tested
- Positioning the flap leading edge upstream of the flat plate trailing edge typically had a detrimental effect upon C_l and L/D at low δ_f, although the flap lap positions had a favourable effect upon the nature of stall at high test δ_f
- Positioning the flap leading edge aft of the flap plate trailing edge typically had a favourable effect upon C_l and L/D, although discrepancies arose at high δ_f due to the onset of severe stall
- In the absence of significant regions of boundary layer separation, increasing the flap gap from −0.07 to −0.13 typically increased C_l or L/D for a given flap lap and δ_f
- Increasing the flap gap from −0.07 to −0.13 heightened the severity of flap stall for configurations with the leading edge either aligned with or located aft of the flat plate trailing edge
- The profile drag measured in the developing wake was highly sensitive to variations in flap lap, gap and δ_f
- Based upon the maximum C_l attainable for a given δ_f, the optimum lap/gap was (0.13, −0.13) for $0° \leq \delta_f \leq 15°$, (0.13, −0.07) at δ_f=20° and (−0.13, −0.13) at δ_f=25°
- In terms of attaining the maximum L/D, the optimum lap/gap differed from that at which the maximum C_l was achieved for δ_f=10°, 15° and 25°, instead corresponding to (0.13, −0.07) for $10° \leq \delta_f \leq 15°$ and (0.07, −0.07) at δ_f=25°

5.2 10mm Serrated Trailing Edge

With the 10mm 60° triangular serrated geometry implemented at the trailing edge of the flat plate, a parametric study of the flap lap, gap and deflection angle was conducted and the flow field developing over the single slotted flap was examined by means of surface static pressure measurements and wake surveys. For a given flap lap/gap and δ_f, the resultant aerodynamic forces were compared to the corresponding baseline configuration with the plain trailing edge geometry and accordingly, the effect of the 10mm serrations upon the flow field development was evaluated.

Transition was fixed on the upper surface of the flat plate, generating an upper-to-lower-surface-boundary-layer-thickness ratio of 1.4:1 at the trailing edge of the flat plate. Free transition was maintained on the single slotted flap throughout. Unless otherwise stated, all experiments were conducted at a nominal freestream velocity of $35m/s$ corresponding to a Reynolds number of 3.58×10^5, based on flap chord.

Similarly to the baseline configuration, comparison of the surface static pressure distributions at $y=\pm0.1m$ confirmed that implementation of the 10mm serrations at the trailing edge of the flat plate did not adversely affect the dimensionality of the flow field developing over the single slotted flap. Thus, the flow field, over which the subsequent measurements were attained, was two-dimensional in nature. Furthermore, implementation of the 10mm serrated geometry had no appreciable effect upon the repeatability of the measurements, as previously stated in Section 5.1.

5.2.1 Effect of 10mm Serrations on the Pressure Distribution

The C_p distributions for the 10mm serrated configuration are shown in Appendix D for all test lap/gap and deflection angles. Recall that at a lap/gap of (−0.13, −0.07), the proximity of the upper surface flap leading-edge to the flat plate trailing edge rendered the lower deflection angle of 0° mechanically infeasible to implement and thus, no data was presented for this configuration.

(a) Flap Lap/Gap: (−0.13, −0.07)

By positioning the flap at a lap/gap of (−0.13, −0.07), the 10mm serrations only had a favourable effect upon the leading edge flow field at δ_f=5°, marginally increasing the suction over the fore $0.15c_{flap}$ of the flap upper surface, in comparison to the corresponding plain trailing edge configuration. With subsequent increments in δ_f, the 10mm serrations adversely affected the leading edge suction. For $10°\leq\delta_f\leq15°$, the

10mm serrations reduced the suction over the fore $0.2c_{flap}$ of the flap upper surface, with the magnitude of the decrement notably heightened at δ_f=15°. Increasing the δ_f to 20° further heightened the decrement in leading edge suction, both in magnitude and extent, although the increment in static pressure was marginalised aft of $0.2c_{flap}$ with distance downstream. Whilst variation in the upper surface C_p distribution was negated aft of $0.4c_{flap}$, there was a notable increase in static pressure over the aft $0.2c_{flap}$ due to the presence of the 10mm serrations, which suggested that the 10mm serrations reduced the trailing edge boundary layer thickness at δ_f=20°. A final increment in δ_f to 25° displayed the most significant variation in the flow field development arising from the implementation of the 10mm serrations: whilst the 10mm serrations notably reduced the leading edge suction over the fore $0.15c_{flap}$, the ensuing adverse pressure gradient aft of the point of minimum pressure was milder than that for the plain trailing edge configuration and, as a result, boundary layer separation was delayed from $0.5c_{flap}$ to within close proximity of the trailing edge. Furthermore, the 10mm serrations typically had no appreciable effect upon the lower surface C_p distribution for $\delta_f \leq 20°$. However at δ_f=25°, the 10mm serrations increased the lower surface static pressure aft of $0.15c_{flap}$, with the increment increasing in magnitude with distance downstream, indicative of a reduced trailing edge boundary layer thickness in comparison to the corresponding plain trailing edge configuration.

(b) Flap Lap/Gap: (−0.07, −0.07)

At a flap lap/gap of (−0.07, −0.07), the 10mm serrations increased the suction over the fore $0.2c_{flap}$ of the flap upper surface for $\delta_f \leq 15°$, although the increment was marginalised with successive δ_f. Aft of $0.2c_{flap}$, the upper surface C_p distribution was essentially coincident with that for the corresponding baseline configuration. Incrementing δ_f to 20° negated the favourable effect of the 10mm serrations upon the leading edge flow field development, rendering the upper surface C_p distribution indiscernible from that of the corresponding baseline configuration. With a final increment in δ_f to 25°, the 10mm serrations had an adverse effect upon the flow field developing over the leading edge, reducing the suction between $0.05c_{flap}$ and $0.2c_{flap}$, in comparison to the baseline configuration. Aft of this point, any adverse effect of the 10mm serrations was marginalised and the upper surface static pressure measurements were indistinguishable from those corresponding to the plain trailing edge geometry. Furthermore, the 10mm serrations typically had no appreciable effect upon the lower surface C_p distribution for all test δ_f when compared to the corresponding plain trailing edge configurations.

(c) Flap Lap/Gap: (0, −0.07)

Aligning the leading edge of the flap with the trailing edge of the flat plate, at the smaller test flap gap of −0.07, extended the favourable effect of the 10mm serrations on the developing flow field over the entire range of δ_f tested. The 10mm serrations increased the suction over the fore $0.3c_{flap}$ of the flap upper surface. The magnitude of this increment was greatest at the leading edge and decreased with distance downstream, such that any variation in the pressure coefficient aft of $0.3c_{flap}$ was essentially negated and the upper surface C_p distribution was coincident with that for the corresponding baseline configuration. In contrast to the trend observed in the measurements at a flap lap/gap of (−0.07, −0.07), the increment in the leading edge suction was heightened with successive increments in δ_f. Despite marginal variations in the lower surface static pressure over the fore $0.05c_{flap}$ for $5° \leq \delta_f \leq 15°$, the magnitude of the increment was not indicative of a significant feature in the flow field and thus, it was concluded that the 10mm serrated geometry typically had no appreciable effect upon the lower surface pressure distribution when compared to the corresponding plain trailing edge configurations.

(d) Flap Lap/Gap: (0.07, −0.07)

With the flap leading edge positioned immediately aft of the flat plate trailing edge at a lap/gap of (0.07, −0.07), the range of δ_f over which the 10mm serrations had a favourable effect upon the leading edge flow field was limited to $5° \leq \delta_f \leq 20°$. At $\delta_f = 0°$, the 10mm serrations had negligible effect upon the flow field developing over the upper surface of the single slotted flap. However, incrementing δ_f to 5° prompted the 10mm serrations to increase the suction over the fore $0.2c_{flap}$ of the flap upper surface. The increment in leading edge suction was progressively heightened with successive increments in $\delta_f \leq 20°$. A final increment in δ_f to 25° rendered the 10mm serrations detrimental to the developing flow field, prompting boundary layer separation aft of $0.15c_{flap}$. By comparison, the C_p distribution for the plain trailing edge configuration indicated that the boundary layer remained attached to within close proximity of the trailing edge, although the trailing edge boundary layer thickness was markedly increased, heightening its susceptibility to separation. Furthermore, the 10mm serrations marginally decreased the static pressure over the lower surface of the flap for $\delta_f \leq 20°$, which suggested a marginal increase in the boundary layer thickness in comparison to the baseline configuration. Coinciding with the extensive upper surface boundary layer separation was a considerable decrease in lower surface static pressure at $\delta_f = 25°$, suggesting that the 10mm serrations substantially increased the lower surface boundary layer thickness in comparison to the plain trailing edge configuration.

(e) Flap Lap/Gap: (0.13, −0.07)

Increasing the flap lap from 0.07 to 0.13 had negligible effect upon the range of δ_f over which the 10mm serrations heightened the leading edge suction. Once again, the 10mm serrations had negligible effect upon the flow field developing over the upper surface of the single slotted flap at δ_f=0°. With further increments in 5°≤δ_f≤20°, the 10mm serrations increased the suction over fore 0.15c_{flap} of the flap upper surface. Increasing δ_f from 5° to 10°, heightened the decrement in leading edge static pressure but with subsequent increments in 15°≤δ_f≤20°, the increment in leading edge suction was marginalised. All increments in leading edge suction were of a smaller magnitude than those observed with the flap positioned at a lap/gap of (0.07, −0.07). Furthermore, the 10mm serrations notably decreased the static pressure over the aft 0.2c_{flap} of the flap upper surface at δ_f=20°, with the decrement increasing in magnitude with distance downstream. This decrement was indicative of an increased upper surface trailing edge boundary layer thickness, suggesting heightened susceptibility to trailing edge boundary layer separation when the 10mm serrated geometry was implemented. Analogous to the baseline configuration, increasing δ_f to 25° prompted extensive boundary layer separation over the upper surface of the flap aft of 0.05c_{flap}. Over the lower surface of the flap, the 10mm serrations decreased the static pressure for δ_f≤20° when compared to the plain trailing edge configuration. The magnitude of the decrement was progressively heightened with successive increments in δ_f, suggesting a progressive increment in the boundary layer thickness.

(f) Flap Lap/Gap: (−0.13, −0.13)

By increasing the flap gap from −0.07 to −0.13 at a flap lap of −0.13, the range of δ_f over which the 10mm serrations heightened the leading edge suction was restricted to δ_f=0°. Accordingly, the 10mm serrations marginally increased the leading edge suction over the fore 0.2c of the flap upper surface at δ_f=0°, aft of which the C_p distribution was essentially coincident with that of the plain trailing edge configuration. However, with subsequent increments in δ_f, the 10mm serrations adversely affected the leading edge suction, with the decrement in leading edge suction progressively heightened in magnitude with successive increments in 5°≤δ_f≤20°. The decrement was greatest over the fore 0.2c_{flap} of the upper surface, decreasing in magnitude with distance downstream such that aft of 0.4c_{flap}, the C_p distribution was comparable to the baseline configuration. A slight anomaly to this trend arose at δ_f=20°, with the 10mm serrations additionally increasing the static pressure over the aft 0.15c_{flap}, suggesting that the 10mm serrations reduced the trailing edge boundary layer thickness in comparison to the baseline configuration. Similarly to the configuration at the smaller test flap gap of −0.07, a

final increment in δ_f to 25° displayed the most significant variation in the flow field development arising from the implementation of the 10mm serrations: whilst the 10mm serrations notably reduced the leading edge suction over the fore $0.15c_{flap}$, the ensuing adverse pressure gradient aft of the point of minimum pressure was milder than that for the baseline configuration and as a result, the point of boundary layer separation was delayed from $0.5c_{flap}$ to within close proximity of the trailing edge. Whilst the 10mm serrations had no appreciable effect upon the lower surface C_p distribution at δ_f=0° and δ_f=15°, the serrated geometry marginally reduced the lower surface static pressure for 5°≤δ_f≤10°, suggesting a slight increase in the boundary layer thickness. At δ_f=20°, the 10mm serrations marginally increased the lower surface static pressure over the aft $0.15c$ and at δ_f=25°, this increment extended over the entire lower surface, increasing in magnitude with distance downstream, suggesting a reduction in the boundary layer thickness in comparison to the corresponding baseline configurations at high test δ_f.

(g) Flap Lap/Gap: (−0.07, −0.13)

Incrementing the flap lap from −0.13 to −0.07 at a flap gap of −0.13 extended the range of δ_f over which the 10mm serrations increased the leading edge suction from δ_f=0° to δ_f≤10°, whereas increasing the flap gap from −0.07 to −0.13 at a flap lap of −0.07 reduced the range of δ_f over which the 10mm serrations increased the leading edge suction from δ_f≤15° to δ_f≤10°. For δ_f≤5°, the increment in leading edge suction was most significant over the fore $0.3c_{flap}$, decreasing in magnitude with distance downstream such that, aft of $0.4c_{flap}$, the upper surface C_p distribution was coincident with that for the plain trailing edge configuration. Increasing δ_f to 10° marginalised the increment in leading edge suction, both in magnitude and extent, such that aft of $0.15c_{flap}$ there was negligible variation between the upper surface C_p distributions for the plain and 10mm serrated configurations. With further increments in δ_f≥15°, the 10mm serrations reduced the suction over the fore $0.2c_{flap}$ of the flap upper surface, aft of which the upper surface C_p distribution was essentially coincident with the baseline configuration. In addition, the 10mm serrations marginally increased the static pressure over the aft $0.15c_{flap}$ of the flap upper surface at δ_f=25°, suggesting a slight reduction in the trailing edge boundary layer thickness in comparison to the corresponding baseline configuration. The 10mm serrations had no appreciable effect upon the lower surface C_p distribution.

(h) Flap Lap/Gap: (0, −0.13)

With the leading edge of the flap aligned with the trailing edge of the flat plate, increasing the flap gap from −0.07 to −0.13 reduced the range of δ_f over which the

10mm serrations increased the leading edge suction from $\delta_f \leq 25°$ to $\delta_f \leq 20°$. In contrast, maintaining the flap gap of −0.13 and increasing the flap lap from −0.07 to 0 had a favourable effect, extending the range of δ_f over which the 10mm serrations decreased the leading edge static pressure from $\delta_f \leq 10°$ to $\delta_f \leq 20°$. For successive increments in $0° \leq \delta_f \leq 20°$, the 10mm serrations progressively heightened the leading edge suction over the fore $0.3c_{flap}$ of the flap upper surface when compared to the corresponding baseline configurations. The increment in suction was greatest over the fore $0.2c_{flap}$ and decreased in magnitude with distance downstream, such that aft of $0.3c$ the upper surface C_p distribution was comparable to the baseline configuration. Analogous to the baseline configuration, increasing δ_f to 25° prompted extensive boundary layer separation over the upper surface of the flap aft of $0.05c_{flap}$. Whilst the 10mm serrations had no appreciable effect upon the lower surface C_p distribution for $\delta_f \leq 5°$, the serrated geometry marginally reduced the lower surface static pressure for $10° \leq \delta_f \leq 25°$, suggesting a slight increase in the boundary layer thickness in comparison to the baseline configuration.

(i) Flap Lap/Gap: (0.07, −0.13)

Increasing the flap gap from −0.07 to −0.13 at a flap lap of 0.07 reduced the range of δ_f over which the 10mm serrations increased the leading edge suction from $\delta_f \leq 20°$ to $\delta_f \leq 15°$, simultaneously decreasing the δ_f at which the 10mm serrations prompted extensive boundary layer separation over the upper surface of the flap. Similarly, by maintaining a flap gap of −0.13 and increasing the flap lap from 0 to 0.07, the range of δ_f over which the 10mm serrations increased the leading edge suction was reduced from $\delta_f \leq 20°$ to $\delta_f \leq 15°$, again decreasing the δ_f at which the 10mm serrations prompted extensive boundary layer separation over the upper surface of the flap. For $0° \leq \delta_f \leq 15°$, the 10mm serrations heightened the leading edge suction over the fore $0.2c_{flap}$ of the flap upper surface, aft of which, the upper surface C_p distribution was essentially coincident with that of the plain trailing edge configuration. The magnitude of the increment in leading edge suction was typically heightened with successive increments δ_f. Incrementing δ_f to 20° highlighted the detrimental effect of the 10mm serrated geometry upon the developing flow field over the deflected flap: whilst the C_p distribution for the baseline configuration indicated that the boundary layer remained attached to within close proximity of the trailing edge, the 10mm serrations provoked extensive boundary layer separation over the upper surface of the flap extending aft of $0.05c_{flap}$. In the absence of significant regions of boundary layer separation, the 10mm serrations had no appreciable effect upon the lower surface C_p distribution. However at $\delta_f = 20°$, the 10mm serrations markedly reduced the static pressure over the lower surface

of the flap in comparison to the corresponding baseline configuration, suggesting an increase in the boundary layer thickness.

(j) Flap Lap/Gap: (0.13, −0.13)

With a flap lap of 0.13, increasing the flap gap from −0.07 to −0.13 modified the range of δ_f over which the 10mm serrations increased the leading edge suction from $5° \leq \delta_f \leq 20°$ to $0° \leq \delta_f \leq 15°$, simultaneously decreasing the δ_f at which the 10mm serrations prompted extensive boundary layer separation over the upper surface of the flap from $\delta_f = 25°$ to $\delta_f = 20°$. In contrast, maintaining a flap gap of −0.13 and increasing the flap lap from 0.07 to 0.13 had no effect upon the range of δ_f over which the 10mm serrations increased the leading edge suction or promoted extensive boundary layer separation. For $0° \leq \delta_f \leq 5°$, the 10mm serrations heightened the leading edge suction over the fore $0.2c_{flap}$ of the flap upper surface, aft of which, the upper surface C_p distribution was essentially coincident with that of the plain trailing edge configuration. Whilst the leading edge suction was similarly heightened by the 10mm serrations for $10° \leq \delta_f \leq 15°$, the region influenced was reduced to the fore $0.15c_{flap}$ of the flap upper surface, aft of which, the upper surface C_p distribution was comparable to the baseline configuration. Analogous to the plain trailing edge configuration, by incrementing δ_f to 20°, extensive boundary layer separation occurred over the upper surface of the flap aft of $0.05c_{flap}$. Whilst the 10mm serrations had no appreciable effect upon the lower surface C_p distribution for $\delta_f \leq 10°$, the serrated geometry marginally reduced the lower surface static pressure for $15° \leq \delta_f \leq 20°$, suggesting a slight increase in the boundary layer thickness, in comparison to the corresponding plain trailing edge configuration.

5.2.2 Effect of 10mm Trailing Edge Serrations on the Lift Coefficient

Variations in the surface static pressure distributions over the trailing edge flap due to the 10mm serrations were more tangibly evaluated in terms of the salient trends in the aerodynamic forces acting upon the two-dimensional flap. Direct comparison of the lift coefficient for the 10mm serrated configuration at a specified flap lap/gap and δ_f with the corresponding baseline configuration with the plain trailing edge resulted in the incremental lift coefficient (ΔC_l) due to the 10mm serrations. Accordingly, Figure 27 and Figure 28 show ΔC_l due to the 10mm serrations and its variation with δ_f for each test flap lap at a flap gap of −0.07 and −0.13, respectively.

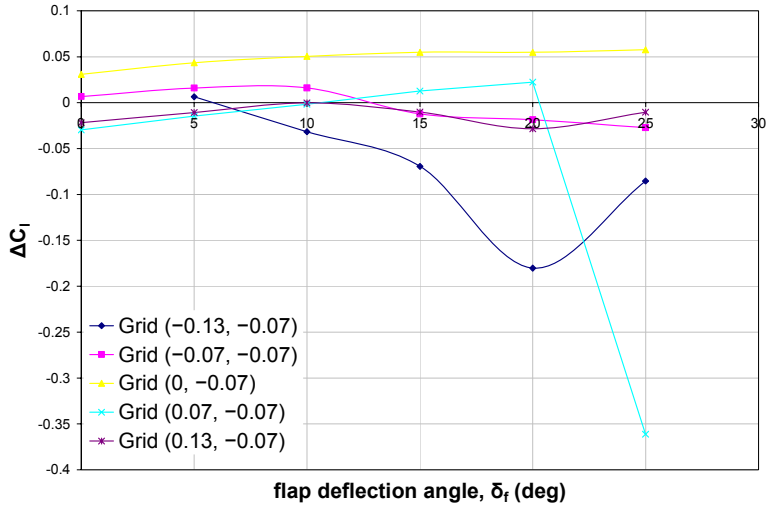

Figure 27: ΔC_l due to 10mm serrations at a flap gap of −0.07, $0°\leq\delta_f\leq25°$

(a) Flap Lap/Gap: (−0.13, −0.07)

At a flap lap/gap of (−0.13, −0.07), the 10mm serrations had detrimental effect upon C_l for all but δ_f=5° when compared to the plain trailing edge configuration. At δ_f=5°, the 10mm serrations increased C_l by 0.01, accounting for 2% increment in comparison to the baseline configuration. However, with subsequent increments in δ_f, the 10mm serrations had a detrimental effect upon C_l. The decrement in C_l due to the 10mm serrations was progressively heightened in magnitude with successive increments in $10°\leq\delta_f\leq20°$, from −0.03 at δ_f=10° to a maximum of −0.18 at δ_f=20°, accounting for a 6% and 21% decrement, respectively. However, with a final increment in δ_f to 25°, ΔC_l was reduced to −0.09, representing an 11% decrement in comparison to the baseline configuration. This reduction in ΔC_l was attributed to the favourable effect of the 10mm serrations upon the point of boundary layer separation at δ_f=25°, preventing separation aft of $0.5c_{flap}$ and maintaining boundary layer attachment to within close proximity of the flap trailing edge (see C_p distribution in Appendix D, Figure 154(e)).

(b) Flap Lap/Gap: (−0.07, −0.07)

A single increment in the flap lap from −0.13 to −0.07, at a flap gap of −0.07, extended the range of δ_f over which the 10mm serrations had a favourable effect upon C_l to include $0°\leq\delta_f\leq10°$. The increment in C_l progressively increased in magnitude from 0.01 at δ_f=0° to 0.02 for $5°\leq\delta_f\leq10°$, accounting for a 2% and 3% increment, respectively. With subsequent increments in δ_f, the 10mm serrations had a detrimental effect upon C_l in comparison to the baseline configuration, which was progressively heightened with successive δ_f. Accordingly, at δ_f=15°, the 10mm serrations reduced C_l by −0.01,

increasing to −0.03 at δ_f=25° and representing a 2% and 4% reduction in C_l, respectively.

(c) Flap Lap/Gap: (0, −0.07)

Aligning the flap leading edge with the trailing edge of the flat plate, at a flap gap of −0.07, significantly improved the lift force generated over the trailing edge flap when the 10mm serrations were implemented. In comparison to the baseline configuration, the 10mm serrations increased C_l by a minimum of 0.03 and a maximum of 0.06, correlating to a consistent 7-8% increment in C_l across the entire range of δ_f tested.

(d) Flap Lap/Gap: (0.07, −0.07)

Incrementing the flap lap from 0 to 0.07 reduced the range of δ_f over which the 10mm serrations had a favourable effect upon C_l. Despite evidence of the 10mm serrations distinctly heightening the leading edge suction in comparison to the plain trailing edge configuration, the 10mm serrated geometry had a detrimental effect upon the lift force generated both for 0°≤δ_f≤5° and at the upper test limit of δ_f=25°. At δ_f=0°, the 10mm serrations decreased C_l by −0.03, accounting for a 6% reduction in C_l when compared to the baseline configuration but with successive increments in δ_f, this decrement in lift was marginalised such that at δ_f=10°, there was no appreciable variation in C_l due to the 10mm serrated geometry. For 15°≤δ_f≤20°, the 10mm serrations marginally increased C_l, accounting for 1-2% increment in comparison to the baseline configuration. Although with a final increment in δ_f to 25°, the 10mm serrations reduced C_l by −0.36, equating to an approximate 40% decrement in comparison to the plain trailing edge configuration. The dramatic loss in lift was characteristic of severe aerofoil stall and corroborated the C_p distributions (see Appendix D, Figure 157(f)), which indicated that, whilst the upper surface boundary layer remained attached to within close proximity of the trailing edge for the plain trailing edge configuration, the 10mm serrations prompted extensive boundary layer separation aft of $0.15c_{flap}$ of the flap upper surface.

(e) Flap Lap/Gap: (0.13, −0.07)

Incrementing the flap lap to the upper test limit of 0.13 extended the range of δ_f over which the 10mm serrations had a detrimental effect upon C_l to include all test δ_f, although ΔC_l varied inconsistently throughout. The decrement in C_l due to the 10mm serrations was initially reduced in magnitude from 4% at δ_f=0° to a near negligible variation in C_l at δ_f=10°. With further increments in 15°≤δ_f≤20°, the decrement in C_l was progressively heightened in magnitude, attaining a maximum ΔC_l of −0.03 at δ_f=20° and accounting for a 3% decrement, although with a final increment in δ_f to 25°,

ΔC_l was once again reduced in magnitude to −0.01, equating to a 2% decrement in C_l, in comparison to the corresponding plain trailing edge configuration.

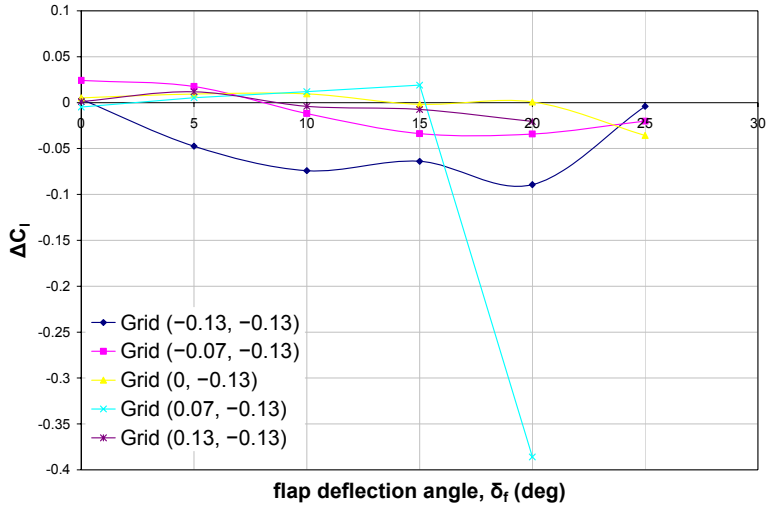

Figure 28: ΔC_l due to 10mm serrations at a flap gap of −0.13, 0°≤δ_f≤25°

(f) Flap Lap/Gap: (−0.13, −0.13)

By increasing the flap gap from −0.07 to −0.13 at a flap lap of −0.13, the range of δ_f over which the 10mm serrations had a favourable effect upon C_l was restricted to δ_f=0°. Whilst the 10mm serrations increased C_l by 1% at δ_f=0°, with subsequent increments in δ_f, the 10mm serrations had a detrimental effect upon C_l. There was a tendency for ΔC_l to progressively increase in magnitude with successive 5°≤δ_f≤20°, from a ΔC_l of −0.05 at δ_f=5° to −0.09 at δ_f=20°, correlating to an 8-9% reduction in C_l. However, increasing δ_f to 25° essentially negated any variation in C_l due to the 10mm serrations. Similarly to the configuration at the smaller flap gap of −0.07, the reduction in the magnitude of ΔC_l at δ_f=25° was attributed to the 10mm serrations delaying separation aft of 0.5c_{flap} and promoting boundary layer attachment to within close proximity of the flap trailing edge (see C_p distribution in Appendix D, Figure 159(f)).

(g) Flap Lap/Gap: (−0.07, −0.13)

Incrementing the flap lap from −0.13 to −0.07 at a flap gap of −0.13 increased the range of δ_f over which the 10mm serrations had a favourable effect upon C_l from δ_f=0° to 0°≤δ_f≤5°. In contrast, increasing the flap gap from −0.07 to −0.13 at a flap lap of −0.07 reduced the range of δ_f over which the 10mm serrations were beneficial to C_l from δ_f≤10° to δ_f≤5°. At δ_f=0°, the 10mm serrations increased C_l by 0.02, equating to a 6% increment but with a single increment in δ_f to 5°, ΔC_l due to the 10mm serrations was reduced, accounting for a 3% increment in comparison to the corresponding baseline

configuration. With subsequent increments in $\delta_f \geq 10°$, the 10mm serrations had a detrimental effect upon C_l, which was progressively heightened with successive $10° \leq \delta_f \leq 20°$, from −0.01 at $\delta_f = 10°$ to −0.03 at $\delta_f = 20°$, correlating to a 2% and 4% reduction in lift, respectively. A final increment in δ_f to the upper test limit of 25° reduced the decrement in C_l to −0.02, equating to a 2% reduction in lift due to the 10mm serrations when compared to the corresponding baseline configuration.

(h) Flap Lap/Gap: (0, −0.13)

With the leading edge of the flap aligned with the trailing edge of the flat plate, increasing the flap gap from −0.07 to −0.13 reduced the range of δ_f over which the 10mm serrations had a favourable effect upon C_l from all test δ_f to $0° \leq \delta_f \leq 10°$, simultaneously reducing the magnitude of the increment in C_l. Conversely, by maintaining a flap gap of −0.13 and increasing the flap lap from −0.07 to 0, the range of δ_f over which the 10mm serrations were beneficial to C_l was increased from $\delta_f \leq 5°$ to $\delta_f \leq 10°$. However, the increment in C_l due to the 10mm serrations only accounted for a maximum of 0.01 for $0° \leq \delta_f \leq 10°$, correlating to a 1% increment in comparison to the baseline configuration. Incrementing δ_f to 15° and 20° negated any variation in C_l due to implementation of the 10mm serrated trailing edge geometry. Even though the C_p distributions for both the plain and 10mm serrated configurations demonstrated extensive boundary layer separation over the upper surface of the flap at $\delta_f = 25°$ (see Appendix D, Figure 161(f)), variations in the magnitude of the measured static pressure resulted in the 10mm serrations reducing C_l by −0.04, equating to a 7% decrement in C_l when compared to the corresponding plain trailing edge configuration.

(i) Flap Lap/Gap: (0.07, −0.13)

Increasing the flap gap from −0.07 to −0.13 at a flap lap of 0.07 modified the range of δ_f over which the 10mm serrations had a favourable effect upon C_l from $15° \leq \delta_f \leq 20°$ to $5° \leq \delta_f \leq 15°$, simultaneously reducing the δ_f at which there was a dramatic loss in lift from $\delta_f = 25°$ to $\delta_f = 20°$. Similarly, maintaining a flap gap of −0.13 and increasing the flap lap from 0 to 0.07 also modified the range of δ_f over which the 10mm serrations had a favourable effect upon C_l from $0° \leq \delta_f \leq 10°$ to $5° \leq \delta_f \leq 15°$, simultaneously reducing the δ_f at which there was a substantial loss in lift from $\delta_f = 25°$ to $\delta_f = 20°$. Accordingly, at a lap/gap of (0.07, −0.13), the 10mm serrations accounted for a 1% reduction in C_l when compared to the baseline configuration at $\delta_f = 0°$ but incrementing δ_f to 5° resulted in the 10mm serrations increasing C_l by 1%. With subsequent increments in $10° \leq \delta_f \leq 15°$, the increment in C_l was increased to a maximum of 0.02 at $\delta_f = 15°$, representing a 2% increment in C_l in comparison to the baseline configuration. A further increment in δ_f to

20°, rendered the 10mm serrations detrimental, reducing C_l by −0.39 and corresponding to a 40% decrement in comparison to the plain trailing edge configuration. The dramatic loss in lift was characteristic of severe aerofoil stall and corroborated the C_p distributions (see Appendix D, Figure 162(e)), which indicated that whilst the upper surface boundary layer remained attached to within close proximity of the trailing edge for the plain trailing edge configuration, the 10mm serrations prompted extensive boundary layer separation aft of $0.05c_{flap}$ over the upper surface of the flap.

(j) Flap Lap/Gap: (0.13, −0.13)

Maintaining a flap gap of −0.13 and increasing the flap lap from 0.07 to 0.13 reduced the range of δ_f over which the 10mm serrations had a favourable effect upon C_l from $5° \leq \delta_f \leq 15°$ to $\delta_f = 5°$. In contrast, increasing the flap gap from −0.07 to −0.13 at a flap lap of 0.13 defined a single δ_f for which the 10mm serrations were beneficial to C_l. At $\delta_f = 0°$, the 10mm serrations had no appreciable effect upon the C_l generated over the single slotted flap but with a single increment in δ_f to 5°, the 10mm serrations increased C_l by 0.01, equating to a 2% increment in comparison to the baseline configuration. For $10° \leq \delta_f \leq 15°$, the 10mm serrations decreased C_l, although accounting for <1% reduction in comparison to the baseline configuration. At $\delta_f = 20°$, ΔC_l was heightened to −0.02, correlating to 3% reduction in comparison to the plain trailing edge configuration, even though the C_p distributions for both the plain and 10mm serrated configurations demonstrated extensive boundary layer separation over the upper surface of the flap (see Appendix D, Figure 163(e)).

5.2.3 Effect of 10mm Trailing Edge Serrations on the Maximum Lift Coefficient

For a complete aircraft, the maximum lift coefficient (C_{lmax}) determined the stalling speed of the aircraft, which was critical in defining the takeoff and landing velocities – the phases of the flight envelope requiring high-lift devices. Thus, it was important to determine whether the 10mm serrations had a favourable or detrimental effect upon C_{lmax} in comparison to the baseline configuration.

Figure 29 and Figure 30 show the effect of the 10mm serrations upon C_{lmax} in comparison to the plain trailing edge configuration at a flap gap of −0.07 and −0.13, respectively.

Figure 29 showed that by positioning the flap leading edge upstream of the flat plate trailing edge at a flap gap of −0.07, the 10mm serrations had a detrimental effect upon C_{lmax}. This was particularly evident at the lower flap lap limit of −0.13, whereby the 10mm serrations reduced C_{lmax} by −0.13, correlating to a 15% decrement. Incrementing the flap lap to −0.07 reduced the magnitude of the decrement such that the 10mm serrations reduced C_{lmax} by −0.02 and accounted for a 3% reduction in comparison to the corresponding baseline configuration. In contrast, with the flap leading edge aligned with trailing edge of the flat plate, the 10mm serrations increased C_{lmax} by 0.05, equating to a 7% increment. The favourable effect of the 10mm serrations on C_{lmax} was maintained at a flap lap of 0.07, although the increment was marginalised to 0.01 or a 1% increment. However, by incrementing the flap lap to the upper test limit of 0.13, the 10mm serrations marginally reduced C_{lmax} by −0.01, accounting for a 1% decrement in comparison to the baseline configuration. Thus, the data suggested that at a flap gap of −0.07, the 10mm serrations had a detrimental effect upon C_{lmax} when the flap leading edge was positioned upstream of the flap plate trailing edge, particularly at the lower flap lap test limit of −0.13 but in contrast, was particularly favourable when aligned with the flat plate trailing edge.

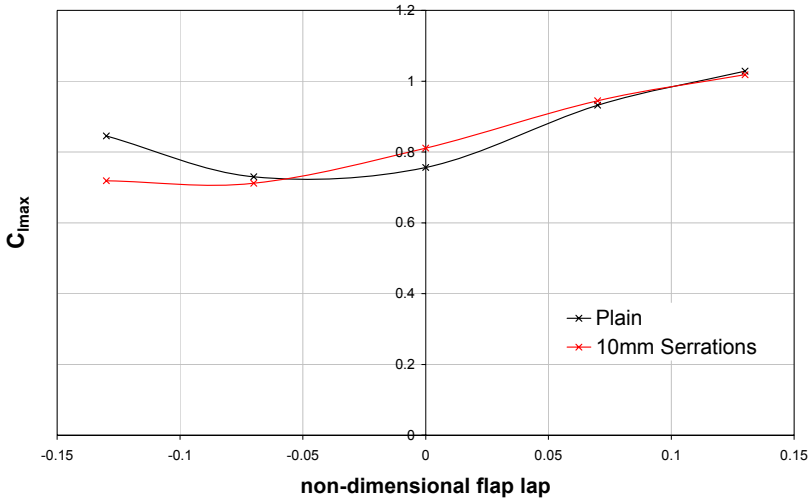

Figure 29: Effect of 10mm serrations upon C_{lmax} at a flap gap of −0.07

Figure 30 shows that increasing the flap gap from −0.07 to −0.13 marginalised the sensitivity of C_{lmax} to variations in the flat plate trailing edge geometry. This was particularly notable at the lower flap lap test limit of −0.13, whereby increasing the flap gap reduced the degradation in C_{lmax}, arising from the presence of the 10mm serrations, to −0.09 or a 9% reduction in comparison to the baseline configuration. At a flap lap of −0.07, the 10mm serrations accounted for a 4% reduction in C_{lmax} but with a further increment in flap lap to 0, any variation in C_{lmax} due to the 10mm serrations was

negated. Similarly to the configuration at the smaller test flap gap of −0.07, positioning the flap leading edge immediately aft of the flat plate trailing edge at a flap lap of 0.07 had a favourable effect, increasing C_{lmax} by 0.02 and correlating to a 2% increment in comparison to the baseline configuration. However, by incrementing the flap lap to the upper test limit of 0.13, the 10mm serrations once again decreased C_{lmax} by −0.01, equating to a 1% decrement. Note that at a flap gap of −0.13, the 10mm serrations still had a detrimental effect upon C_{lmax} when the flap leading edge was positioned upstream of the flat plate trailing edge, although the favourable effect of the 10mm serrations upon C_{lmax} at a flap lap of zero was negated.

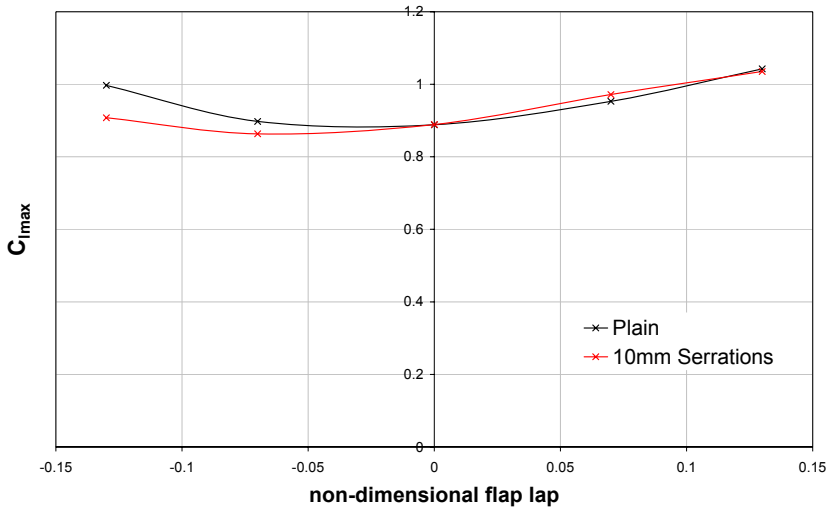

Figure 30: Effect of 10mm serrations upon C_{lmax} at a flap gap of −0.13

Figure 31 highlights the effect of increasing the flap gap from −0.07 to −0.13 for the 10mm serrated configuration. Most significantly, increasing the flap gap from −0.07 to −0.13 minimised the sensitivity of C_{lmax} to variations in flap lap over the designated test range.

Similarly to the plain trailing edge configuration, incrementing the flap gap for the 10mm serrated configuration increased the C_{lmax} for any given flap lap tested. Again, this deviation in C_{lmax} due to the flap gap was most notable with the flap leading edge positioned either upstream of or in alignment with the flat plate trailing edge. At the lower flap lap test limit of −0.13, incrementing the flap gap from −0.07 to −0.13 with the 10mm serrated geometry implemented at the trailing edge of the flat plate, increased C_{lmax} by 0.19, accounting for a 26% increment, which exceeded the magnitude of ΔC_{lmax} for the corresponding baseline configuration. At a flap lap of −0.07, ΔC_{lmax} decreased to 0.15, representing a 21% increment due to the increase in flap gap. By aligning the flap

leading edge with the flat plate trailing edge, ΔC_{lmax} was approximately halved to 0.08, equating to a 10% increment.

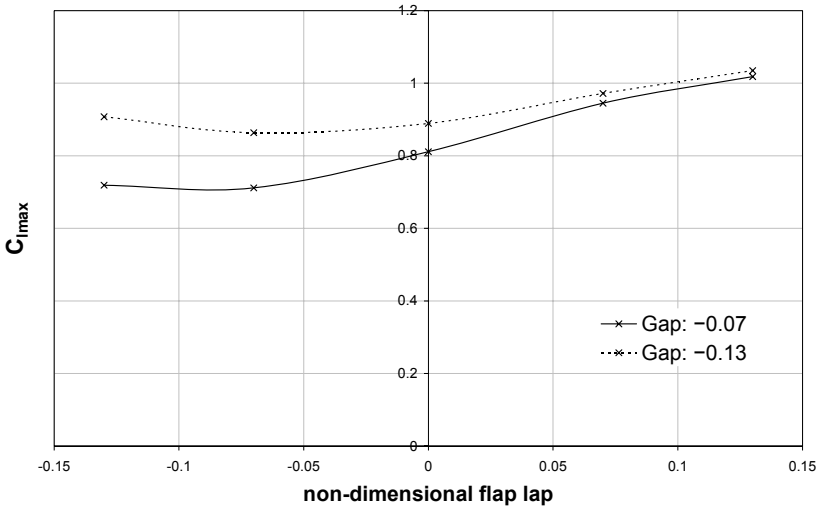

Figure 31: Effect of flap lap/gap upon C_{lmax} for 10mm serrated configuration

With further increments in flap lap, the sensitivity of C_{lmax} to variations in the flap gap was marginalised such that at a flap lap of 0.07 and 0.13, ΔC_{lmax} accounted for a 3% and 2% increment, respectively. This suggested that, similarly to the plain trailing edge configuration, C_{lmax} for the 10mm serrated trailing edge configuration was less sensitive to variations in flap gap when the flap leading edge was positioned aft of the flat plate trailing edge, i.e. at a flap lap of 0.07 or 0.13.

5.2.4 Effect of 10mm Trailing Edge Serrations on the Stall Angle

Due to the uniform increments in δ_f at which the measurements were obtained, the precise stall angle of the flap (δ_{fstall}) was difficult to ascertain for any given configuration. Typically, the 10mm serrations had no appreciable effect upon the indicated stall angle. However, two exceptions to this trend arose: firstly, at a flap lap/gap of (−0.13, −0.07), δ_{fstall} was extended from 20° for the baseline configuration to 25° for the 10mm serrated geometry; and secondly, at a flap lap/gap of (0.07, −0.13), δ_{fstall} was decreased from 20° for the baseline configuration to 15° with the 10mm serrated geometry. Note that in comparison to the plain trailing edge configuration, the 10mm serrations significantly heightened the severity of the stall when positioned at a flap lap of 0.07 at either flap gap.

5.2.5 Effect of 10mm Trailing Edge Serrations on the Drag Coefficient

Similarly to the baseline configuration, analysis of the profile drag measurements was deemed to provide a more complete representation of the effect of the 10mm serrations upon the overall configuration drag and hence, in this instance, further analysis of the pressure drag individually did not augment the evaluation of the 10mm serrated geometry. Direct comparison of the profile drag for the 10mm serrated configuration at a specified flap lap/gap and δ_f with the corresponding baseline configuration with the plain trailing edge resulted in the incremental profile drag coefficient (ΔC_{dp}) due to the 10mm serrations. Accordingly, Figure 32 and Figure 33 show the incremental variation in C_{dp} with δ_f for all test flap laps at a flap gap of −0.07 and −0.13, respectively.

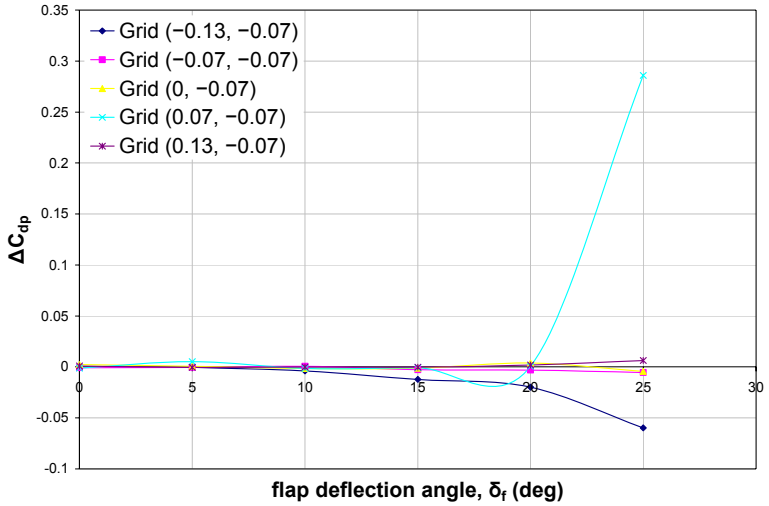

Figure 32: ΔC_{dp} due to 10mm serrations at a flap gap of −0.07, $0°\leq\delta_f\leq25°$

(a) Flap Lap/Gap: (−0.13, −0.07)

At a flap lap/gap of (−0.13, −0.07), the 10mm serrations had favourable effect upon C_{dp} for $5°\leq\delta_f\leq25°$, progressively heightening ΔC_{dp} from near negligible at δ_f=5° to −0.02 at δ_f=20°, the latter correlating to a 15% decrement in C_{dp}. A final increment in δ_f to the upper test limit of 25° substantially heightened ΔC_{dp} to −0.06, accounting for a 33% reduction in comparison to the baseline configuration. This corroborated the considerable reduction in the wake cross-section for the 10mm serrated configuration in comparison to the plain trailing edge configuration (see Appendix E, Figure 164(e)), which was attributed to 10mm serrations preventing boundary layer separation aft of $0.5c_{flap}$ on the flap upper surface and promoting boundary layer attachment to within close proximity of the flap trailing edge.

(b) Flap Lap/Gap: (−0.07, −0.07)

Incrementing the flap lap from −0.13 to −0.07 at a flap gap of −0.07 tended to diminish the decrement in C_{dp} due to the 10mm serrations for a given δ_f. For $0° \leq \delta_f \leq 10°$, the 10mm serrations had a near negligible effect upon C_{dp}, accounting for less than a 1% decrement in comparison to the baseline configuration. With further increments in δ_f, ΔC_{dp} was progressively heightened in magnitude from −0.003 at δ_f=15° to a maximum of −0.005 at δ_f=25°, equating to a 3% and 5% decrement, respectively, in comparison to the baseline configuration.

(c) Flap Lap/Gap: (0, −0.07)

By incrementing the flap lap from −0.07 to 0 at a flap gap of −0.07, ΔC_{dp} due to the 10mm serrations varied inconsistently for all test δ_f. At δ_f=0°, the 10mm serrations had a detrimental effect upon C_{dp}, accounting for a 3% increment, although incrementing δ_f to 5° essentially negated any variation in C_{dp} due to the 10mm serrations. By incrementing δ_f to 10°, the 10mm serrations reduced C_{dp} by −0.002, representative of a 2% decrement in comparison to the baseline configuration. Whilst the decrement was marginalised to 1% at δ_f=15°, there was an isolated increase in C_{dp} to 0.004 at δ_f=20°, with the 10mm serrations accounting for a 4% increment in comparison to the baseline configuration. However, with a final increment in δ_f to 25°, the 10mm serrations once again favourably influenced C_{dp}, reducing the profile drag by −0.004 or 4% in comparison to the plain trailing edge configuration.

(d) Flap Lap/Gap: (0.07, −0.07)

Similarly to the configuration at a flap lap/gap of (0, −0.07), ΔC_{dp} due to the 10mm serrations varied inconsistently with δ_f when positioned at a lap/gap of (0.07, −0.07). For $\delta_f \leq 15°$, the 10mm serrations typically decreased C_{dp} by less than −0.002 or 2% in comparison to the corresponding baseline configuration. However, an isolated discrepancy arose at δ_f=5°, whereby the 10mm serrations increased C_{dp} by 0.005, representative of a 6% increment. Whilst at δ_f=20°, the increment in C_{dp} due to the 10mm serrations was near negligible in magnitude, with a final increment in δ_f to 25°, the 10mm serrations dramatically increased ΔC_{dp} to 0.29, which accounted for a 260% increment in comparison to the corresponding plain trailing edge configuration. The considerable magnitude of this increment in C_{dp} corroborated the marked increase in the wake cross-section in the measurement plane for the 10mm serrated configuration (see Appendix E, Figure 167(f)) and was attributed to the 10mm serrations promoting extensive boundary layer separation over the upper surface of the flap.

(e) Flap Lap/Gap: (0.13, −0.07)

Whilst ΔC_{dp} varied inconsistently with δ_f, the 10mm serrations appeared to have a relatively minimal influence upon C_{dp} at a lap/gap of (0.13, −0.07). At δ_f=0°, the 10mm serrations increased C_{dp} by 1% but with further increments in 5°≤δ_f≤15°, ΔC_{dp} was near negligible, accounting for less than a 1% decrement in comparison to the baseline configuration. By incrementing δ_f≥20°, the 10mm serrations had a detrimental effect upon C_{dp}, increasing C_{dp} by 0.002 at δ_f=20°, which was heightened to 0.006 at δ_f=25°, although both increments correlated to less than a 2% increment in C_{dp} in comparison to the baseline configuration.

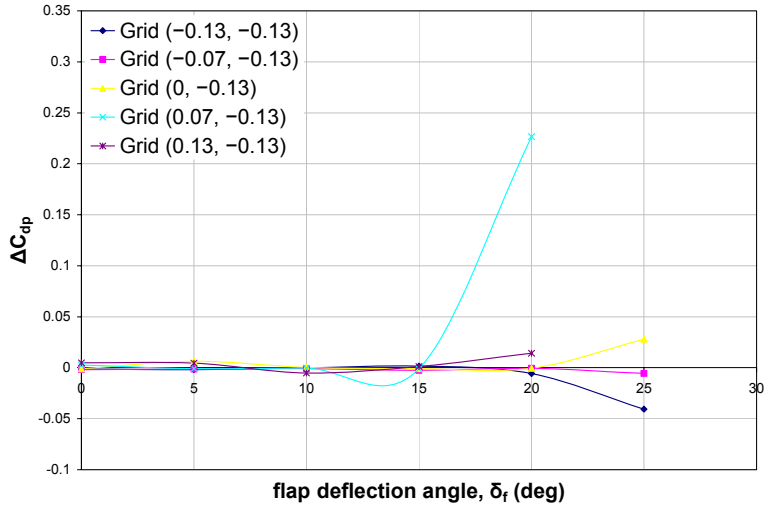

Figure 33: ΔC_{dp} due to 10mm serrations at a flap gap of −0.13, 0°≤δ_f≤25°

(f) Flap Lap/Gap: (−0.13, −0.13)

The variation of ΔC_{dp} with δ_f due to the 10mm serrations at a lap/gap of (−0.13, −0.13) was less consistent than that observed at the smaller flap test gap of −0.07, where the 10mm serrations decreased C_{dp} for all test δ_f. For 0°≤δ_f≤5°, the decrement in C_{dp} due to the 10mm serrations accounted for less than a 2% reduction in comparison to the baseline configuration. By increasing δ_f to 10°, any variation in C_{dp} due to the 10mm serrations was essentially negated, although at δ_f=15°, the 10mm serrations increased C_{dp} by 0.002, equating to 2% increment in comparison to the baseline configuration. With subsequent increments in δ_f≥20°, the 10mm serrations had a favourable effect upon C_{dp}. The decrement in C_{dp} was heightened from −0.006 at δ_f=20° to a maximum of −0.04 at δ_f=25°, representative of a 1% and 23% decrement, respectively, in comparison to the plain trailing edge configuration. The notable increase in the magnitude of this decrement at δ_f=25° corroborated the reduction in the wake cross-section for the 10mm serrated configuration in comparison to the baseline configuration

(see Appendix E, Figure 169(f)). Similarly to the configuration at the smaller test gap of −0.07, this was attributed to 10mm serrations preventing boundary layer separation aft of $0.5c_{flap}$ on the flap upper surface and promoting boundary layer attachment to within close proximity of the flap trailing edge.

(g) Flap Lap/Gap: (−0.07, −0.13)

At a lap/gap of (−0.07, −0.13), the magnitude of the decrement in C_{dp} due to the 10mm serrations varied inconsistently with δ_f. Whether increasing the flap gap from −0.07 to −0.13 at a flap lap of −0.07 or increasing the flap lap from −0.13 to −0.07 at a flap gap of −0.13, the range of δ_f over which the 10mm serrations had a favourable effect upon C_{dp} was extended to include all test δ_f. For $0° \leq \delta_f \leq 5°$, ΔC_{dp} due to the 10mm serrations progressively decreased in magnitude, accounting for a 2% reduction at δ_f=0° and a 1% decrement at δ_f=10°. At δ_f=15°, ΔC_{dp} was heightened to −0.003, accounting for a 3% decrement in comparison to the baseline configuration but with a further increment in δ_f to 20°, ΔC_{dp} was essentially negated. With a final increment in δ_f to 25°, ΔC_{dp} due to the 10mm serrations attained a maximum value of −0.006, representative of a 5% decrement in comparison to the plain trailing edge configuration.

(h) Flap Lap/Gap: (0, −0.13)

At a lap/gap of (0, −0.13), ΔC_{dp} due to the 10mm serrations varied inconsistently with δ_f. Similarly to the configuration at the smaller test flap gap of −0.07, the 10mm serrations decreased C_{dp} for the majority of δ_f tested but isolated discrepancies were once again evident. In contrast, maintaining a flap gap of −0.13 and increasing the flap lap from −0.07 to 0 heightened the inconsistency of ΔC_{dp} with δ_f. Specifically, the 10mm serrations decreased C_{dp} by 1% in comparison to the baseline configuration at δ_f=0° but with a single increment in δ_f to 5°, the 10mm serrations had a detrimental effect upon C_{dp}, increasing the profile drag by 0.006 and accounting for a 7% increment. Any variation in C_{dp} due to the 10mm serrated trailing edge geometry was essentially negated for $10° \leq \delta_f \leq 20°$, although by increasing δ_f to 25°, the 10mm serrations notably increased C_{dp} by 0.03, accounting for a 9% increment in comparison to the plain trailing edge configuration. This marked increment in C_{dp} at δ_f=25° corroborated the distinct increase in the wake velocity defect due to the 10mm serrations (see Appendix E, Figure 171(f)).

(i) Flap Lap/Gap: (0.07, −0.13)

At a flap lap/gap of (0.07, −0.13), ΔC_{dp} due to the 10mm serrations varied inconsistently with δ_f and was thus similar to the configuration either at a lap/gap of (0, −0.13) or

(0.07, −0.07). At δ_f=0°, the 10mm serrations increased C_{dp} by 0.003, corresponding to a 3% increment in comparison to the baseline configuration but with subsequent increments in 5°≤δ_f≤15°, ΔC_{dp} due to the 10mm serrations was essentially negated. A final increment in δ_f to 20° resulted in the 10mm serrations dramatically increasing ΔC_{dp} to 0.23, which accounted for over a 220% increase in profile drag in comparison to the corresponding plain trailing edge configuration. The considerable magnitude of this increment corroborated the marked increase in the wake cross-section for the 10mm serrated configuration (see Appendix E, Figure 172(e)) and was attributed to the extensive boundary layer separation evident over the upper surface of the flap, whilst the corresponding baseline configuration maintained boundary layer attachment to within close proximity of the trailing edge.

(j) Flap Lap/Gap: (0.13, −0.13)

At a lap/gap of (0.13, −0.13), ΔC_{dp} due to the 10mm serrations varied inconsistently with δ_f and was thus similar to the configuration either at a lap/gap of (0.07, −0.13) or (0.13, −0.07). For 0°≤δ_f≤5°, a ΔC_{dp} of 0.005 accounted for a 5% increase in profile drag in comparison to the baseline configuration. A single increment in δ_f to 10° resulted in the 10mm serrations decreasing C_{dp} by −0.005, equating to a 5% decrement. However with further increments δ_f≥15°, the 10mm serrations once again had a detrimental effect upon C_{dp}, which was progressively heightened such that at δ_f=20°, a ΔC_{dp} of 0.014 was representative of a 4% increment in comparison to the baseline configuration.

5.2.6 Effect of 10mm Trailing Edge Serrations on the Lift-to-Drag Ratio

As L/D was an important parameter to consider for high-lift configurations, Figure 34 shows the variation of L/D with δ_f for each of the plain, 10mm and 20mm serrated trailing edge configurations at a specified test flap lap/gap. Direct comparison of L/D for the 10mm serrated configuration at a specified flap lap/gap and δ_f with the corresponding baseline configuration with the plain trailing edge resulted in the increment/decrement in L/D due to the 10mm serrations. Note that all calculations for L/D were based upon the profile drag.

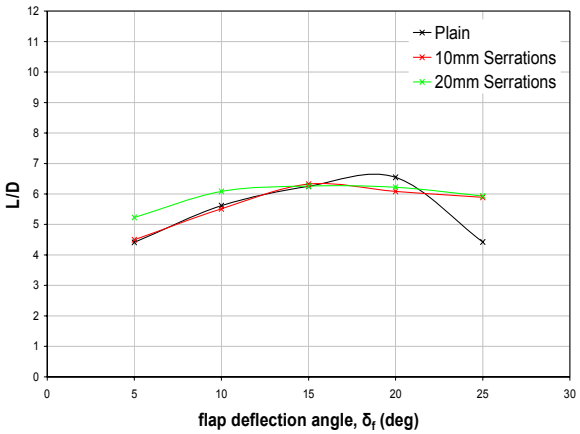

(a) Lap/Gap: (−0.13, −0.07)

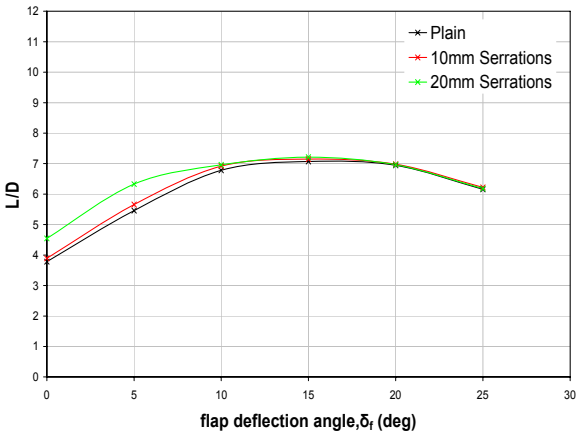

(b) Lap/Gap: (−0.07, −0.07)

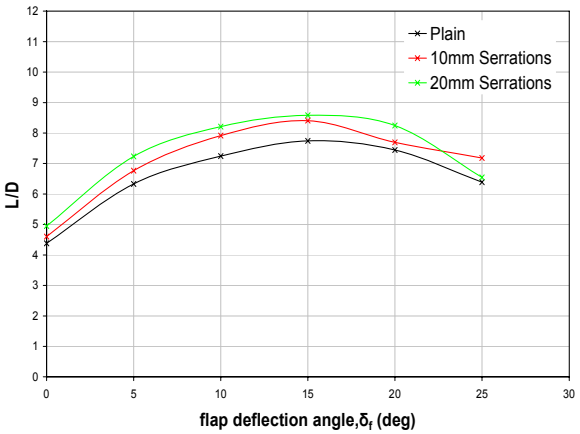

(c) Lap/Gap: (0, −0.07)

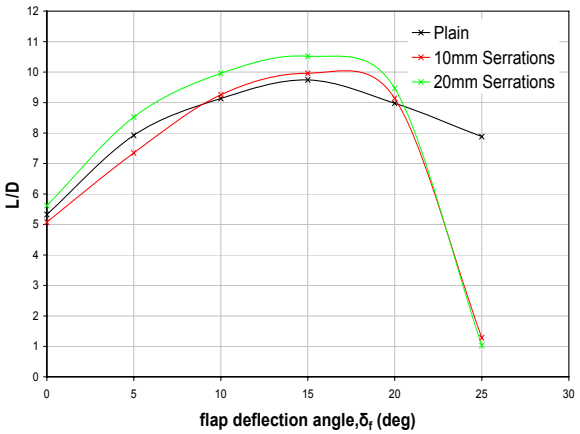

(d) Lap/Gap: (0.07, −0.07)

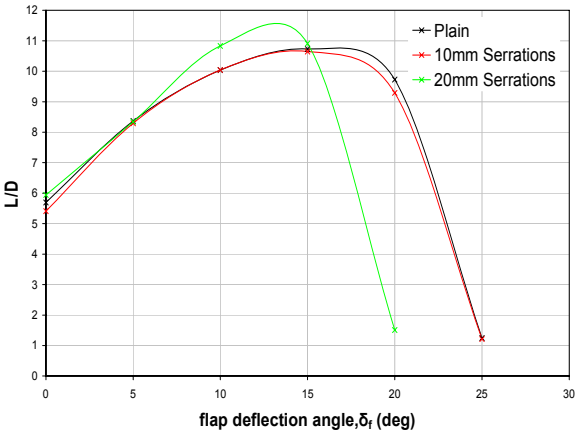

(e) Lap/Gap: (0.13, −0.07)

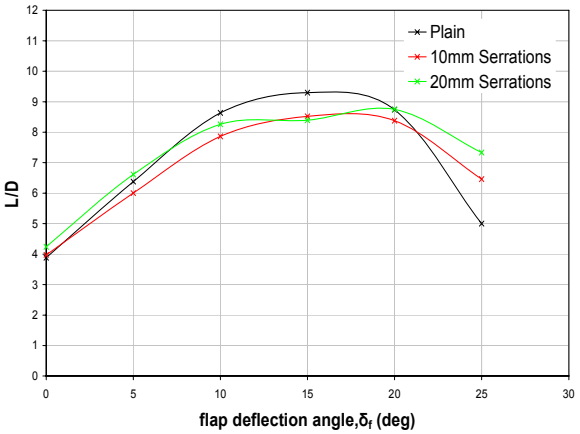

(f) Lap/Gap: (−0.13, −0.13)

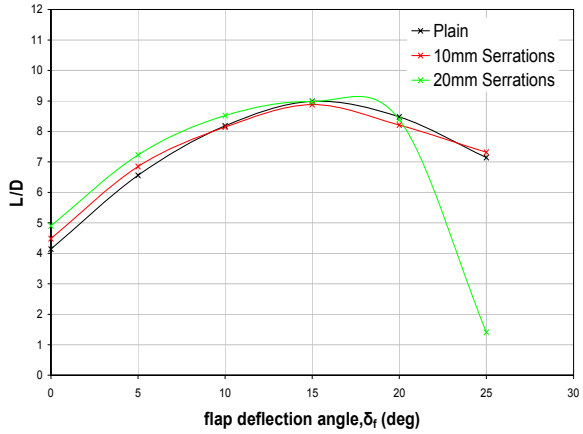

(g) Lap/Gap: (−0.07, −0.13)

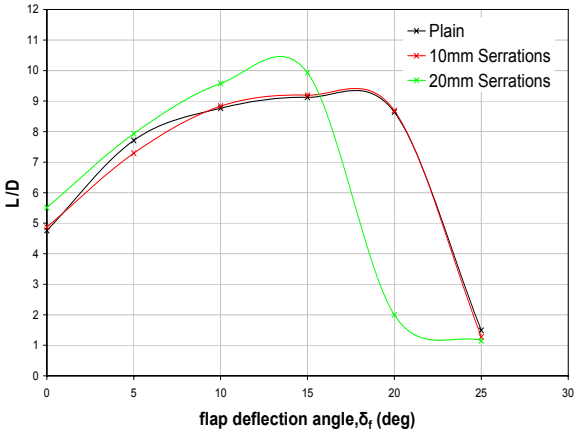

(h) Lap/Gap: (0, −0.13)

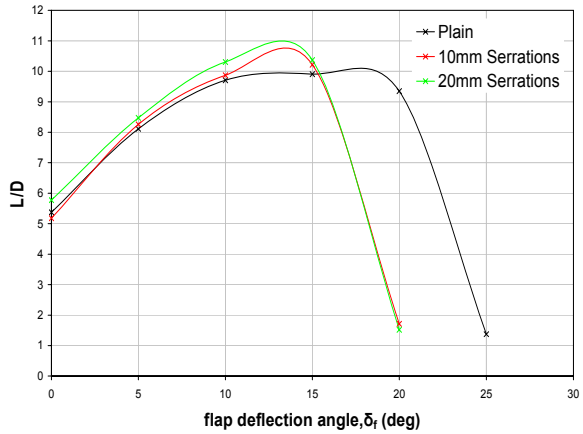

(i) Lap/Gap: (0.07, −0.13)

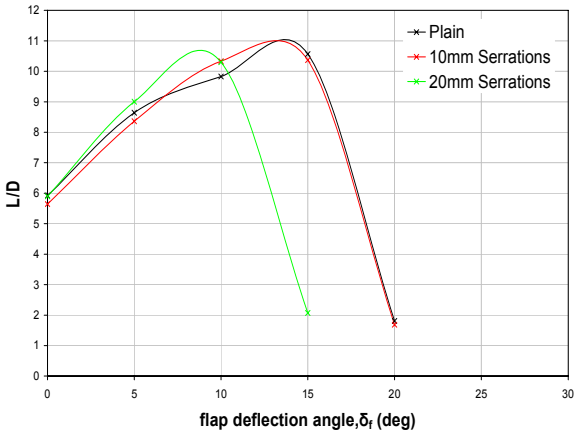

(j) Lap/Gap: (0.13, −0.13)

Figure 34: Variation of *L*/*D* with δ_f for plain, 10mm and 20mm serrated trailing edge configurations

(a) Flap Lap/Gap: (−0.13, −0.07)

At a flap lap/gap of (−0.07, −0.07), the effect of the 10mm serrations upon *L*/*D* was inconsistent, increasing *L*/*D* for δ_f=5°, 15° and 25° in comparison to the baseline configuration. The favourable effect of the 10mm serrations upon C_{dp} and C_l at δ_f=5° resulted in a 2% increase in *L*/*D* in comparison to the baseline configuration. At δ_f=10°, the favourable effect of the 10mm serrations upon C_{dp} was insufficient to offset the degradation in C_l, resulting in a 2% reduction in *L*/*D* in comparison to the plain trailing edge configuration. Conversely, with a further increment in δ_f to 15°, the decrement in C_{dp} was sufficient to offset the decrement in C_l and the 10mm serrations increased *L*/*D* by 1%. Although the reduction in C_{dp} due to the 10mm serrations was heightened at δ_f=20°, it was insufficient to offset the marked decrement in the corresponding C_l and

hence, the 10mm serrations reduced L/D by 7%. In contrast, combining the marked decrement in C_{dp} at δ_f=25° with the increment in C_l rendered the 10mm serrations highly favourable, increasing L/D by 33% in comparison to the baseline configuration. This marked increment in L/D at δ_f=25° corroborated the favourable effect of the 10mm serrations upon boundary layer development over the upper surface of the flap, preventing boundary layer separation at $0.5c_{flap}$ and promoting boundary layer attachment to within close proximity of the trailing edge.

(b) Flap Lap/Gap: (−0.07, −0.07)

At a flap lap/gap of (−0.07, −0.07), the 10mm serrations increased L/D for $\delta_f \leq 10°$ in comparison to the baseline configuration. For low δ_f, the favourable effect of the 10mm serrations upon C_l, combined with the decrement in C_{dp}, resulted in a 3% and 4% increment in L/D at δ_f=0° and δ_f=5°, respectively. Despite the slight increment in C_{dp} at δ_f=10°, the corresponding increment in C_l maintained a 2% increment in L/D in comparison to the baseline configuration. For $15° \leq \delta_f \leq 25°$, the degradation in C_l due to the 10mm serrations was negated by the corresponding decrement in C_{dp}, resulting in a near negligible deviation in L/D in comparison to the plain trailing edge configuration.

(c) Flap Lap/Gap: (0, −0.07)

Whilst the effect of the 10mm serrations upon C_{dp} varied inconsistently, due to the significant increment in C_l, L/D was not adversely affected, although the increment in L/D due to the 10mm serrations did vary inconsistently with δ_f. Accordingly, the 10mm serrations increased L/D by 5% at δ_f=0° when compared to the plain trailing edge configuration. With further increments in δ_f, the increment in L/D was heightened to 9% for $10° \leq \delta_f \leq 15°$. The isolated increment in C_{dp} at δ_f=20° reduced the corresponding increment in L/D to 3% but with a final increment in δ_f to 25°, the 10mm serrations increased L/D by 12% in comparison to the baseline configuration.

(d) Flap Lap/Gap: (0.07, −0.07)

At a lap/gap of (0.07, −0.07), the favourable effect of the 10mm serrations upon L/D was limited to $10° \leq \delta_f \leq 20°$ when compared to the plain trailing edge configuration. At δ_f=0°, the decrement in C_{dp} was insufficient to offset the corresponding decrement in C_l, decreasing L/D by 5%. Combination of the degradation in both C_l and C_{dp} due to the 10mm serrations at δ_f=5° heightened the decrement in L/D to 7%. However at δ_f=10°, the decrement in C_{dp} was sufficient to offset the decrement in C_l, increasing L/D by 1% in comparison to the baseline configuration. With the 10mm serrations favourably influencing both C_l and C_{dp} at δ_f=15°, the increment in L/D was heightened to 2%.

Despite the increase in C_{dp} at δ_f=20° due to the 10mm serrations, the corresponding increase in C_l was sufficient to maintain a 2% increment in L/D. With a final increment in δ_f to 25°, the dramatic increment in C_{dp}, combined with the decrement in C_l, to decrease L/D by 84% in comparison to the baseline configuration.

(e) Flap Lap/Gap: (0.13, −0.07)

At a flap lap/gap of (0.13, −0.07), the 10mm serrations tended to decrease L/D for all test δ_f in comparison to the baseline configuration. Typically, the degradation of the 10mm serrations on both C_l and C_{dp} combined to reduce L/D by 3-5% at low and high δ_f. Discrepancies arose for 5°≤δ_f≤15°: despite an isolated decrement in C_{dp} at δ_f=5° and δ_f=15°, when combined with the decrement in C_l, the net effect on L/D was merely to marginalise the decrement in L/D due to the 10mm serrations to 1%. Furthermore, the negligible effect of the 10mm serrations on the aerodynamic forces at δ_f=10° resulted in no discernible decrement in L/D, when compared to the plain trailing edge configuration.

(f) Flap Lap/Gap: (−0.13, −0.13)

By increasing the flap gap from −0.07 to −0.13 at a flap lap of −0.13, the effect of the 10mm serrations upon L/D was more consistent, only increasing L/D at the upper and lower test limits of δ_f=0° and δ_f=25°. The favourable effect of the 10mm serrations upon C_{dp} and C_l at δ_f=0° resulted in a 2% increase in L/D in comparison to the baseline configuration. However, despite the decrement in C_{dp} for 5°≤δ_f≤10°, the corresponding decrement in C_l resulted in a 6% reduction in L/D at δ_f=5°, which was heightened to a 9% reduction at δ_f=10°. With the 10mm serrations degrading both C_l and C_{dp} at δ_f=15°, the decrement in L/D due to the 10mm serrations was maintained at an 8% reduction in comparison to the plain trailing edge configuration. At δ_f=20°, the decrement in C_{dp} was insufficient to offset the decrement in C_l, decreasing L/D by 4% in comparison to the baseline configuration. However, with a final increment in δ_f to 25°, the marked reduction in C_{dp} offset the decrement in C_l to increase L/D by 29% in comparison to the plain trailing edge configuration. This marked increment in L/D at δ_f=25° corroborated the favourable effect of the 10mm serrations upon boundary layer development over the upper surface of the flap, preventing boundary layer separation at $0.5c_{flap}$ and promoting boundary layer attachment to within close proximity of the trailing edge.

(g) Flap Lap/Gap: (−0.07, −0.13)

Incrementing the flap gap from −0.07 to −0.13 at a flap lap of −0.07 limited the range of δ_f over which the 10mm serrations were beneficial to L/D to δ_f≤5° and δ_f=25° when

compared to the baseline configuration. The decrement in C_{dp} due to the 10mm serrations combined with the increment in C_l at δ_f=0° and δ_f=5° to increase L/D by 8% and 4%, respectively. However, with further increments in 10°≤δ_f≤20°, the decrement in C_{dp} due to the 10mm serrations was insufficient to offset the corresponding decrement in C_l, reducing L/D by a maximum of 3% at δ_f=20°. However, with a final increment in δ_f to 25°, the reduction in C_{dp} offset the decrement in C_l, increasing L/D by 3% in comparison to the plain trailing edge configuration.

(h) Flap Lap/Gap: (0, −0.13)

With the flap leading edge aligned with the flat plate trailing edge, increasing the flap gap from −0.07 to −0.13 limited the range of δ_f over which the 10mm serrations were beneficial to L/D. The favourable effect of the 10mm serrations upon C_{dp} and C_l at δ_f=0° resulted in a 2% increase in L/D in comparison to the baseline configuration. However, the increment in C_{dp} due to the 10mm serrations at δ_f=5° offset the increment in C_l, decreasing L/D by 5% in comparison to the baseline configuration. For 10°≤δ_f≤20°, the 10mm serrations accounted for a ±1% deviation in L/D when compared to the baseline configuration but with a final increment in δ_f to 25°, the marked increment in C_{dp} combined with the decrement in C_l to decrease L/D by 14%.

(i) Flap Lap/Gap: (0.07, −0.13)

Incrementing the flap gap from −0.07 to −0.13 at a flap lap of 0.07 modified the upper and lower limits of the range of δ_f over which the 10mm serrations increased L/D from 10°≤δ_f≤20° to 5°≤δ_f≤15°. At δ_f=0°, the increment in C_{dp} combined with the decrement in C_l to decrease L/D by 4% in comparison to the baseline configuration. However, for 5°≤δ_f≤15°, the decrement in C_{dp} due to the 10mm serrations complemented the corresponding increase in C_l and accordingly, increased L/D by 2-3%. In contrast, the dramatic increment in C_{dp} due to the 10mm serrations at δ_f=20°, combined with the decrement in C_l, to reduce L/D by 82% in comparison to the baseline configuration.

(j) Flap Lap/Gap: (0.13, −0.13)

By increasing the flap gap from −0.07 to −0.13 at a flap lap of −0.13, a single δ_f was identified for which the 10mm serrations increased L/D when compared to the baseline configuration. Although the 10mm serrations had a near negligible effect upon C_l at δ_f=0°, the corresponding increase in C_{dp} resulted in a 5% reduction in L/D in comparison to the baseline configuration. Whilst the 10mm serrations increased C_{dp} at δ_f=5°, the corresponding C_l was also increased, reducing the decrement in L/D due to the 10mm serrations to 3%. In contrast, the decrement in C_{dp} at δ_f=10° offset the

decrement in C_l and increased L/D by 5% in comparison to the baseline configuration. However, with further increments in δ_f, the increment in C_{dp} combined with the decrement in C_l to progressively reduce L/D in comparison to the baseline configuration, accounting for a 2% reduction at δ_f=15°, which was heightened to a 7% reduction at δ_f=20°.

5.2.7 Final Evaluation of 10mm Serrated Trailing Edge Configuration

10mm 60° triangular serrations were implemented at the trailing edge of the flat plate upstream of a single slotted flap. A parametric study of the flap lap, gap and δ_f was conducted and the subsequent analysis indicated that:

In terms of increasing C_l and L/D for a given flap lap/gap configuration, the 10mm serrations were most effective at a flap lap/gap of (0, −0.07). In comparison to the corresponding baseline configuration, the 10mm serrations increased C_l by 7-8% across the entire range of δ_f tested. The effect of the 10mm serrations on C_{dp} was less favourable, only decreasing C_{dp} for δ_f=10°, 15° and 25°. However, the corresponding increment in C_l due to the 10mm serrations was sufficient to offset any increment in C_{dp}. Accordingly, the 10mm serrations increased L/D for all test δ_f, with the increment varying between 3% and 12%, dependent upon δ_f.

Whilst it was recognised that the 10mm serrations also increased L/D for all test δ_f at a flap lap/gap of (−0.07, −0.07), the increment in L/D only accounted for a 1-4% increase in comparison to the corresponding baseline configuration. This was attributed to the 10mm serrations only favourably influencing C_l for $0° \leq \delta_f \leq 10°$ and hence, the increment in L/D was achieved by the favourable effect of the 10mm serrations upon C_{dp}.

It should be noted that the flap lap/gap for which the 10mm serrations most effectively increased C_l and L/D did not correlate to the optimum flap lap/gap in terms of maximising the overall C_l or L/D for the 10mm serrated configuration.

In terms of attaining the maximum value of C_l for the 10mm serrated configuration, the optimum lap/gap varied in accordance with the specified δ_f, see Figure 35. Accordingly, Figure 35 shows that for $0° \leq \delta_f \leq 15°$, positioning the flap at a lap/gap of (0.13, −0.13) achieved the maximum value of C_l. At δ_f=20°, the optimum flap position was defined by a lap/gap of (0.13, −0.07) and with a final increment in δ_f to 25°, the maximum C_l was attained at a flap lap/gap of (−0.13, −0.13). Thus, in comparison to

the baseline configuration, implementing the 10mm serrations at the trailing edge of the flat plate had no appreciable effect upon the optimum flap lap/gap at a given δ_f, for which a maximum value of C_l was attained.

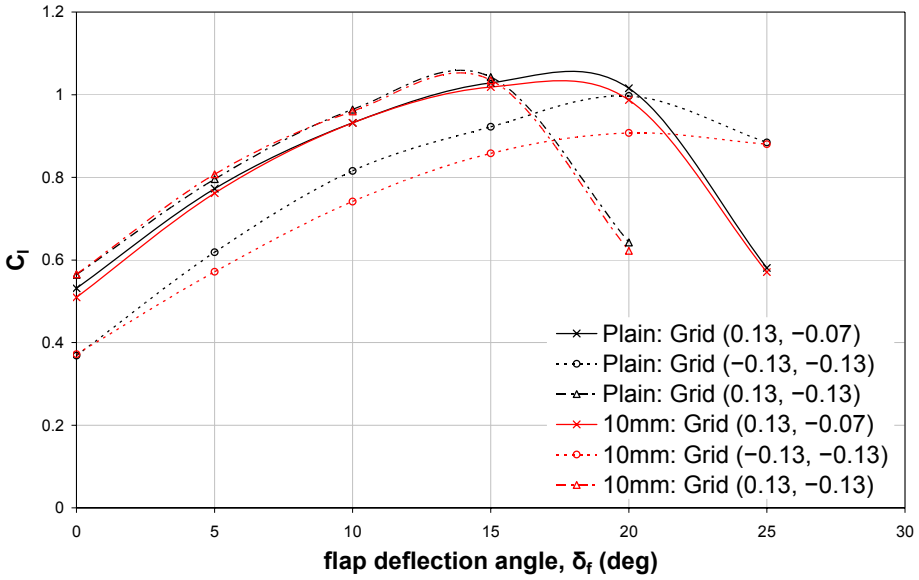

Figure 35: Comparison of optimum lap/gap in terms of maximising overall C_l for plain and 10mm serrated configurations

In terms of attaining the maximum value of L/D, the optimum lap/gap for the 10mm serrated configuration also varied in accordance with the specified δ_f (see Figure 36), although by taking the profile drag into consideration, differed from the optimum lap/gap positions identified for achieving the maximum C_l at a given δ_f.

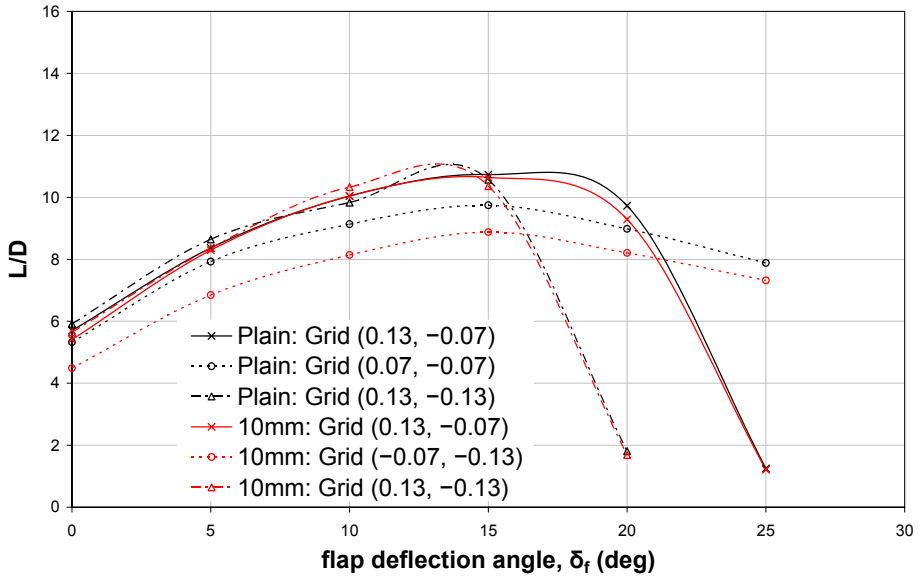

Figure 36: Comparison of optimum lap/gap in terms of maximising overall L/D for plain and 10mm serrated configurations

Accordingly, Figure 36 shows that positioning the flap at a lap/gap of (0.13, −0.13) achieved the maximum value of L/D for $0° \leq \delta_f \leq 10°$. For $15° \leq \delta_f \leq 20°$, the optimum flap position was defined by a lap/gap of (0.13, −0.07) and with a final increment in δ_f to 25°, the maximum L/D was attained at a flap lap/gap of (−0.07, −0.13). Thus, implementing the 10mm serrations at the trailing edge of the flat plate modified the optimum flap lap/gap for which a maximum value of L/D was attained when compared to the baseline configuration. Anomalies arose at δ_f=10° and δ_f=25°, with the baseline configuration identifying the optimum lap/gap as (0.13, −0.07) and (0.07, −0.07), respectively.

Based upon the optimum lap/gap identified above, Figure 35 and Figure 36 show that the plain geometry was typically more favourable than the 10mm serrations for a given δ_f, generating a maximum C_l or L/D of greater magnitude than the corresponding 10mm serrated configuration. However, the variation in C_l between the plain and 10mm serrated configurations for $0° \leq \delta_f \leq 15°$ was near negligible, with an isolated 2% increment for the 10mm serrated configuration at δ_f=5°. With regard to L/D, an isolated discrepancy arose at δ_f=10°, with the 10mm serrations proving more favourable than the plain configuration.

In terms of C_{lmax}, the 10mm serrations were detrimental when the flap leading edge was positioned upstream of the flat plate trailing edge, irrespective of the flap gap employed. In contrast, with the flap leading edge either aligned with or positioned immediately aft of the flat plate trailing edge at a lap of 0.07, the 10mm serrations increased C_{lmax} in comparison to the corresponding plain trailing edge configuration. However, at the upper flap lap test limit of 0.13, a marginal decrement in C_{lmax} was once again evident due to the presence of the 10mm serrations.

Establishing the effect of the 10mm serrations on C_{dp} was difficult to ascertain as there was a tendency for ΔC_{dp} to vary inconsistently with δ_f at a specified lap/gap. Nevertheless, the 10mm serrations typically had a favourable effect upon C_{dp} when the flap leading edge was positioned upstream of the flat plate trailing edge, i.e. at a flap lap of −0.13 or −0.07, at either test flap gap. With the flap leading edge either aligned with the flat plate trailing edge or positioned aft, the favourable effect of the 10mm serrations was typically limited to $\delta_f \leq 15°$, although isolated discrepancies were evident.

Most significantly, it was by positioning the flap at the lower lap test limit of −0.13, at either a flap gap of −0.07 or −0.13, that clear evidence was provided of the favourable

effect of the 10mm serrations on the boundary layer development at high δ_f. At δ_f=25°, the C_p distribution for the baseline configuration indicated that the upper surface boundary layer separated aft of $0.5c_{flap}$ (see Appendix D, Figure 154(e) and Figure 159(f)). However, the C_p distribution for the corresponding 10mm serrated configuration indicated that, whilst reducing the leading edge suction, the boundary layer remained attached to within close proximity of the flap trailing edge, although the decrement in trailing edge pressure was indicative of a thickening boundary layer and thus, a heightened susceptibility to separation. The result was an approximate 30% increase in L/D due to the 10mm serrations when compared to the corresponding plain trailing edge configuration.

In the absence of flow visualisation for the present experiments, it was postulated that vortical structures emanated from each serration vertex, similarly to the flow visualisation of, for example, Soderman (1972) and Gai and Sharma (1981). Accordingly, the favourable influence of the 10mm serrations upon C_{dp} may be attributed to the development of the streamwise vortices. With the flap leading edge positioned upstream of the flat plate trailing edge, it was hypothesised that, the streamwise vortices remained near to the surface across the chordwise extent of the flap, enabling streamwise momentum to be transferred to the near surface boundary layer, favourably influencing its development and hence, subsequently reducing the profile drag. This was particularly evident for the configuration positioned at the lower flap lap test limit of −0.13, whereby it was proposed that the streamwise vortices transferred momentum to the near surface boundary layer, preventing separation at $0.5c_{flap}$ and promoting boundary layer attachment to within close proximity of the trailing edge. In contrast, with the flap leading edge aligned with or positioned aft of the flat plate trailing edge, it was proposed that the streamwise vortices were transposed away from the surface of the flap as they developed downstream, thus becoming less capable of transferring streamwise momentum to the near surface boundary layer and subsequently reducing or negating the favourable influence upon the profile drag. This would suggest that the streamwise development of the vortices – and hence, their effectiveness in delaying/eliminating boundary layer separation – was highly sensitive to the configuration detail, particularly the flap lap/gap and deflection angle. Further studies are required to determine the precise flow field mechanisms by which the 10mm serrations delayed boundary layer separation at a flap lap of −0.13 and favourably influenced the profile drag.

5.3 20mm Serrated Trailing Edge

With the 20mm 60° triangular serrated geometry implemented at the trailing edge of the flat plate, a parametric study of the flap lap, gap and deflection angle was conducted and the flow field developing over the flap was examined by means of surface static pressure measurements and wake surveys. For a given flap lap/gap and δ_f, the resultant aerodynamic forces were compared to the corresponding baseline configuration and accordingly, the effectiveness of the 20mm serrations was evaluated.

Transition was fixed on the upper surface of the flat plate, generating an upper-to-lower-surface-boundary-layer-thickness ratio of 1.4:1 at the trailing edge of the flat plate. Free transition was maintained on the single slotted flap throughout. Unless otherwise stated, all experiments were conducted at a nominal freestream velocity of $35m/s$ corresponding to a Reynolds number of 3.58×10^5, based on flap chord.

Similarly to the baseline and 10mm serrated configurations, comparison of the surface static pressure distributions at $y=\pm0.1m$ confirmed that implementation of the 20mm serrations at the trailing edge of the flat plate did not adversely effect the dimensionality of the flow field developing over the single slotted flap. Thus, the flow field over which the subsequent measurements were attained was two-dimensional in nature. Furthermore, implementation of the 20mm serrated geometry had no appreciable effect upon the repeatability of the measurements previously stated in Section 5.1.

5.3.1 Effect of 20mm Trailing Edge Serrations on the Pressure Distribution

The C_p distributions for the 20mm serrated configuration are shown in Appendix D for all test lap/gap and deflection angles. Recall that at a lap/gap of (−0.13, −0.07), the proximity of the upper surface flap leading-edge to the flat plate trailing edge rendered the lower deflection angle of 0° mechanically infeasible to implement and thus no data was presented for this configuration.

(a) Flap Lap/Gap: (−0.13, −0.07)

In comparison to both the baseline and 10mm serrated configurations at a lap/gap of (−0.13, −0.07), the 20mm serrations increased the suction over the upper surface of the flap for $5°\leq\delta_f\leq10°$. The increment was most prominent over the fore $0.2c_{flap}$ and was marginalised with distance downstream such that any variation in the upper C_p distribution was essentially negated over the aft $0.15c_{flap}$. A slight discrepancy to this

trend arose at δ_f=10°, where despite heightening the leading edge suction, the 20mm serrations reduced the minimum pressure coefficient of the suction peak. For 15°≤δ_f≤20°, the 20mm serrations reduced the suction over the fore 0.2c_{flap} of the flap upper surface, aft of which, the upper surface C_p distribution was analogous to the baseline configuration. A discrepancy arose over the aft 0.2c_{flap} at δ_f=20°, whereby the 20mm serrations increased in trailing edge static pressure, suggesting that, similarly to the 10mm serrations, the 20mm serrations reduced the trailing edge boundary layer thickness. Note that the 20mm serrations tended to reduce the leading edge suction more significantly than the 10mm serrations for 15°≤δ_f≤25°. Similarly to the 10mm serrated configuration, a final increment in δ_f to 25° displayed the most significant variation in the flow field development arising from the implementation of the 20mm serrations: whilst the 20mm serrations notably reduced the leading edge suction over the fore 0.15c_{flap}, the ensuing adverse pressure gradient aft of the point of minimum pressure was milder than that for the baseline configuration and as a result, the point of boundary layer separation was delayed from 0.5c_{flap} to within close proximity of the trailing edge. Furthermore, the 20mm serrations typically had no appreciable effect upon the lower surface C_p distribution for δ_f≤20°. However at δ_f=25°, the 20mm serrations increased the lower surface static pressure aft of 0.15c_{flap}. The increment increased in magnitude with distance downstream, exceeding the magnitude of the corresponding increment for 10mm serrated configuration and hence, suggested that the 20mm serrations further reduced the boundary layer thickness in comparison to both the plain and 10mm serrated configurations.

(b) Flap Lap/Gap: (−0.07, −0.07)

In comparison to both the plain and 10mm serrated configurations, the 20mm serrations heightened the suction over the upper surface of the flap for all test δ_f when positioned at a flap lap/gap of (−0.07, −0.07). The increment in leading edge suction was most prominent over the fore 0.2c_{flap} of the flap upper surface, aft of which, the magnitude of the increment was marginalised with distance downstream, such that the C_p distributions were essentially coincident over the aft 0.3c_{flap} of the flap upper surface. The increment in leading edge suction, due to the 20mm serrations, was progressively heightened with successive increments in δ_f≤20° but was marginalised with a final increment in δ_f to 25°. Furthermore, the 20mm serrations typically had no appreciable effect upon the lower surface C_p distribution for all test δ_f when compared to the corresponding plain trailing edge configurations.

(c) Flap Lap/Gap: (0, −0.07)

With the flap leading edge aligned with the trailing edge of the flat plate at the smaller test flap gap of −0.07, the 20mm serrations had a favourable effect upon the developing flow field for all test δ_f. In comparison to both the plain and 10mm serrated configurations, the 20mm serrations increased the suction over the fore $0.3c_{flap}$ of the flap upper surface. For any given δ_f, the magnitude of this increment was greatest at the leading edge and decreased in magnitude with distance downstream, such that any variation aft of $0.3c_{flap}$ was essentially negated and the upper surface C_p distribution was comparable with that for the corresponding baseline and 10mm serrated configurations. However, a discrepancy arose at δ_f=25°, whereby the 20mm serrations decreased the static pressure over the aft $0.2c_{flap}$ of the flap upper surface. This indicated that the presence of the 20mm serrations increased the trailing edge boundary layer thickness in comparison to both the plain and 10mm serrated configurations. Furthermore, the increment in the leading edge suction was progressively heightened with successive increments in δ_f. Despite isolated discrepancies in lower surface static pressure over the fore $0.05c_{flap}$ for $5° \leq \delta_f \leq 15°$, the 20mm serrations typically had no appreciable effect upon the lower surface pressure distribution. However, the 20mm serrations decreased the static pressure over the aft $0.5c_{flap}$ of the lower surface at δ_f=25°. The decrement increased in magnitude with distance downstream and suggested an increase in the boundary layer thickness in comparison to both the baseline and 10mm serrated configurations

(d) Flap Lap/Gap: (0.07, −0.07)

Increasing the flap lap from 0 to 0.07 at a flap gap of −0.07 reduced the upper limit for the range of δ_f over which the 20mm serrations had a favourable effect upon the developing flow field from 25° to 20°. For $\delta_f \leq 20°$, the 20mm serrations heightened the suction most significantly over fore $0.2c_{flap}$ of the flap upper surface, both in comparison to the plain and 10mm serrated configurations. Aft of $0.2c_{flap}$, the increment in suction due to the 20mm serrations was marginalised with distance downstream, rendering the C_p distributions comparable over the aft $0.4c_{flap}$, irrespective of the precise trailing edge geometry implemented. Furthermore, the increment in leading edge suction was progressively heightened with successive increments in $\delta_f \leq 20°$. Similarly to the 10mm serrations, a final increment in δ_f to 25° rendered the 20mm serrations detrimental to the developing flow field, prompting boundary layer separation aft of $0.05c_{flap}$. By comparison, the C_p distribution for the baseline configuration indicated that the boundary layer remained attached to within close proximity of the trailing edge, although the trailing edge boundary layer thickness was

markedly increased, heightening its susceptibility to separation. Whilst the 20mm serrations typically had no appreciable effect upon the lower surface C_p distribution for $\delta_f \leq 15°$, the 20mm serrations marginally decreased the static pressure over the aft $0.5c_{flap}$ of the flap lower surface at $\delta_f = 20°$, which suggested a marginal increase in the boundary layer thickness. The considerable decrease in lower surface static pressure at $\delta_f = 25°$ was attributed to the extensive upper surface boundary layer separation induced by the 20mm serrations and suggested a considerable increase in the lower surface boundary layer thickness in comparison to the baseline configuration.

(e) Flap Lap/Gap: (0.13, −0.07)

Increasing the flap lap from 0.07 to 0.13 further reduced the range of δ_f over which the 20mm serrations heightened the leading edge suction from $\delta_f \leq 20°$ to $\delta_f \leq 15°$. For $\delta_f \leq 15°$, the 20mm serrations markedly increased the suction over fore $0.2c_{flap}$ of the flap upper surface in comparison to both the plain and 10mm serrated configurations. The increment in suction due to the 20mm serrations was marginalised with distance downstream, such that aft of $0.7c_{flap}$, there was no appreciable variation in the upper surface C_p distribution. A final increment in δ_f to 20° rendered the 20mm serrations detrimental to the developing flow field, prompting boundary layer separation aft of $0.05c_{flap}$. By comparison, the C_p distribution for the baseline and 10mm serrated configurations indicated that the boundary layer remained attached to within close proximity of the trailing edge at $\delta_f = 20°$, although the trailing edge boundary layer thickness was markedly increased, particularly for the 10mm serrated configuration, heightening its susceptibility to separation. With the exception of a marginal increment in static pressure over the fore $0.1c_{flap}$ of the flap lower surface, the 20mm serrations typically had no appreciable effect upon the C_p distribution for $\delta_f \leq 10°$. However, a decrement in the trailing edge static pressure was evident at $\delta_f = 15°$, which was comparable to the 10mm serrated configuration and hence, also indicative of a marginal increase in the boundary layer thickness. At $\delta_f = 20°$, the substantial decrement in static pressure due to the 20mm serrations extended over the entire lower surface and was attributed to the extensive upper surface boundary layer separation induced by the 20mm serrations.

(f) Flap Lap/Gap: (−0.13, −0.13)

By increasing the flap gap from −0.07 to −0.13 at a flap lap of −0.13, the upper limit for the range of δ_f over which the 20mm serrations increased the leading edge suction was reduced from 10° to 5°. For $0° \leq \delta_f \leq 5°$, the 20mm serrations increased the suction in comparison to both the plain and 10mm serrated configurations. At $\delta_f = 0°$, the

increment in leading edge suction was most prominent over the fore $0.2c_{flap}$, aft of which, the increment was marginalised with distance downstream such that there was no appreciable variation in the C_p distribution due to the 20mm serrations over the aft $0.3c_{flap}$. A single increment in δ_f to 5° diminished the increment in leading edge suction due to the 20mm serrations, both in magnitude and extent. Accordingly, the increment in suction extended over the fore $0.15c_{flap}$, aft of which, the increment was marginalised such that there was no appreciable fluctuation in the upper surface C_p distribution aft of $0.4c_{flap}$, irrespective of the precise trailing edge geometry implemented. For subsequent increments in $\delta_f \geq 10°$, the 20mm serrations adversely affected the leading edge suction, with the decrement progressively heightened in magnitude with successive increments in δ_f. The decrement was most prominent over the fore $0.2c_{flap}$ of the upper surface and was marginalised with distance downstream such that aft of $0.4c_{flap}$, the C_p distribution was comparable to the baseline configuration. A slight anomaly to this trend arose at $\delta_f=20°$, with the 20mm serrations increasing the static pressure over the aft $0.15c_{flap}$, suggesting that similarly to the 10mm serrations, the 20mm serrations reduced the trailing edge boundary layer thickness in comparison to the baseline configuration. Direct comparison of the 10mm and 20mm serrated configurations for $10° \leq \delta_f \leq 20°$ indicated that whilst the 20mm serrations had a more favourable effect upon the leading edge suction at $\delta_f=10°$, the effect of the 10mm and 20mm serrated geometries were analogous at $\delta_f=15°$. However, for $20° \leq \delta_f \leq 25°$, the 10mm serrations heightened the leading edge suction in comparison to the 20mm serrated configuration. Similarly to the configuration at the smaller test flap gap of −0.07, a final increment in δ_f to 25° displayed the most significant variation in the flow field development arising from the implementation of the 20mm serrations: whilst the 20mm serrations notably reduced the leading edge suction over the fore $0.15c_{flap}$ in comparison to both the plain and 10mm serrated configurations, the point of boundary layer separation was – similarly to the 10mm serrated configuration – delayed from $0.5c_{flap}$ to within close proximity of the trailing edge. Regarding the lower surface of the flap, the 20mm serrations typically had no appreciable effect upon C_p distribution for $\delta_f \leq 15°$. However, similarly to the 10mm serrated configuration, the 20mm serrations marginally increased the lower surface static pressure over the aft $0.15c_{flap}$ at $\delta_f=20°$, extending this increment over the entire lower surface at $\delta_f=25°$. The increment in static pressure increased in magnitude with distance downstream and exceeded that for the corresponding 10mm serrated configuration, which suggested that the 20mm serrations decreased the lower surface trailing edge boundary layer thickness in comparison to both the baseline and 10mm serrated configurations.

(g) Flap Lap/Gap: (−0.07, −0.13)

Incrementing the flap lap from −0.13 to −0.07 at a flap gap of −0.13 extended the range of δ_f over which the 10mm serrations increased the leading edge suction from $\delta_f \leq 5°$ to $\delta_f \leq 20°$. In contrast, increasing the flap gap from −0.07 to −0.13 at a flap lap of −0.07 reduced the upper limit for the range of δ_f over which the 10mm serrations increased the leading edge suction. For $\delta_f \leq 10°$, the increment in leading edge suction due to the 20mm serrations was most significant over the fore $0.2c_{flap}$, decreasing in magnitude with distance downstream such that aft of $0.7c_{flap}$, the upper surface C_p distribution was coincident with that for the baseline configuration. With further increments in $15° \leq \delta_f \leq 20°$, the increment in leading edge suction was progressively marginalised, both in magnitude and extent, such that aft of $0.15c_{flap}$ there was no appreciable variation between the upper surface C_p distributions, irrespective of the trailing edge geometry implemented. A final increment in δ_f to 25° rendered the 20mm serrations detrimental to the developing flow field, prompting boundary layer separation aft of $0.05c_{flap}$. By comparison, the C_p distribution for the baseline and 10mm serrated configurations indicated that the boundary layer remained attached to within close proximity of the trailing edge at $\delta_f = 25°$, although the decrement in trailing edge static pressure suggested an increased boundary layer thickness, which was more susceptible to separation. The 20mm serrations typically had no appreciable effect upon the lower surface C_p distribution for $\delta_f \leq 20°$, although with extensive upper surface boundary layer separation induced by the 20mm serrations at $\delta_f = 25°$, the corresponding lower surface exhibited a substantial reduction in static pressure, suggesting a considerable increase in the lower surface boundary layer thickness in comparison to the corresponding plain and 10mm serrated configurations.

(h) Flap Lap/Gap: (0, −0.13)

With the leading edge of the flap aligned with the trailing edge of the flat plate, increasing the flap gap from −0.07 to −0.13 reduced the upper limit of the range of δ_f over which the 10mm serrations increased the leading edge suction from 25° to 15°. Whilst maintaining the flap gap of −0.13 and increasing the flap lap from −0.07 to 0 had a favourable effect upon the magnitude of the increment in leading edge suction, it too reduced the upper limit for the range of δ_f over which the 20mm serrations increased the leading edge suction from $\delta_f \leq 20°$ to $\delta_f \leq 15°$, simultaneously lowering the δ_f at which the 20mm serrations promoted extensive upper surface boundary layer separation. Specifically for $0° \leq \delta_f \leq 15°$, the 20mm serrations heightened the leading edge suction most significantly over the fore $0.3c_{flap}$ of the flap upper surface, aft of which, the increment in suction decreased in magnitude with distance downstream, such that over

the aft $0.2c_{flap}$, the upper surface C_p distribution was comparable to the baseline and 10mm serrated configurations. Whilst the C_p distributions for the baseline and 10mm serrated configurations indicated that the boundary layer remained attached to within close proximity of the trailing edge at δ_f=20°, the 20mm serrations prompted extensive boundary layer separation over the upper surface of the flap aft of $0.05c_{flap}$. With the exception of slight discrepancies in the C_p distribution over the fore $0.1c_{flap}$ of the flap lower surface for $5° \leq \delta_f \leq 10°$, the 20mm serrations typically had no appreciable effect upon the lower surface C_p distribution for $0° \leq \delta_f \leq 15°$ when compared to the baseline configuration. However, a marked decrease in the lower surface static pressure due to the 20mm serrations was evident at δ_f=20°, which suggested an increase in the lower surface boundary layer thickness in comparison to both the corresponding plain and 10mm serrated configurations.

(i) Flap Lap/Gap: (0.07, −0.13)

Maintaining a flap gap of −0.13 and increasing the flap lap from 0 to 0.07 had negligible effect upon the range of δ_f over which the 20mm serrations increased the leading edge suction. In contrast, increasing the flap gap from −0.07 to −0.13 at a flap lap of 0.07 reduced the upper limit of the range of δ_f over which the 20mm serrations increased the leading edge suction from 20° to 15°, simultaneously decreasing the δ_f at which the 20mm serrations prompted extensive boundary layer separation over the upper surface of the flap. For $0° \leq \delta_f \leq 15°$, the 20mm serrations heightened the leading edge suction in comparison to both the plain and 10mm serrated configurations. The increment in suction was most significant over the fore $0.2c_{flap}$ of the flap upper surface, aft of which, the magnitude of the increment was marginalised such that aft of $0.6c_{flap}$ the precise trailing edge geometry implemented had no appreciable effect upon the upper surface C_p distribution. The magnitude of the increment in leading edge suction was typically heightened with successive increments δ_f. Incrementing δ_f to 20° highlighted the detrimental effect of the 20mm serrated geometry upon the flow field developing over the deflected flap: whilst the C_p distribution for the baseline configuration indicated that the boundary layer remained attached to within close proximity of the trailing edge, the 20mm serrations – similarly to the 10mm serrations – generated extensive boundary layer separation over the upper surface of the flap aft of $0.05c_{flap}$. With regard to the lower surface, the 20mm serrations typically had no appreciable effect upon the C_p distribution for $\delta_f \leq 15°$. However at δ_f=20°, the 20mm serrations markedly reduced the static pressure over the lower surface of the flap in comparison to the corresponding baseline configuration. This trend was comparable to

that observed for the corresponding 10mm serrated configuration and again, suggested a considerable increase in the lower surface boundary layer thickness.

(j) Flap Lap/Gap: (0.13, −0.13)

Whether increasing the flap gap from −0.07 to −0.13 at a flap lap of 0.13 or increasing the flap lap from 0.07 to 0.13 at a flap gap of −0.13, the upper limit of the range of δ_f over which the 20mm serrations increased the leading edge suction was reduced from 15° to 10°, simultaneously decreasing the δ_f at which the 20mm serrations prompted extensive boundary layer separation over the upper surface of the flap from 20° to 15°. For $0° \leq \delta_f \leq 10°$, the 20mm serrations heightened the leading edge suction most significantly over the fore $0.2c_{flap}$ of the flap upper surface, aft of which, the magnitude of the increment was marginalised with distance downstream such that aft of $0.6c_{flap}$, the upper surface C_p distribution was essentially coincident with that of the baseline or 10mm serrated configuration. Incrementing δ_f to 15° rendered the 20mm serrations detrimental to the developing flow field, prompting extensive boundary layer separation aft of $0.05c_{flap}$. By comparison, the C_p distribution for the baseline and 10mm serrated configurations indicated that the boundary layer remained attached to within close proximity of the trailing edge at δ_f=15°. In the absence of significant regions of boundary layer separation, the 20mm serrations typically had no appreciable effect upon the lower surface C_p distribution. However, at δ_f=15°, the 20mm serrations markedly reduced the static pressure over the lower surface of the flap in comparison to both the corresponding baseline and 10mm serrated configurations, suggesting a notable increase in the lower surface boundary layer thickness.

5.3.2 Effect of 20mm Trailing Edge Serrations on the Lift Coefficient

Variations in the surface static pressure distributions over the trailing edge flap due to the 20mm serrations were more tangibly evaluated in terms of the salient trends in the aerodynamic forces acting upon the single slotted flap. Direct comparison of the lift coefficient for the 20mm serrated configuration at a specified flap lap/gap and δ_f with the corresponding baseline configuration with the plain trailing edge resulted in the incremental lift coefficient (ΔC_l) due to the 20mm serrations. Accordingly, Figure 37 and Figure 38 show ΔC_l due to the 20mm serrations and its variation with δ_f for each test flap lap at a flap gap of −0.07 and −0.13, respectively.

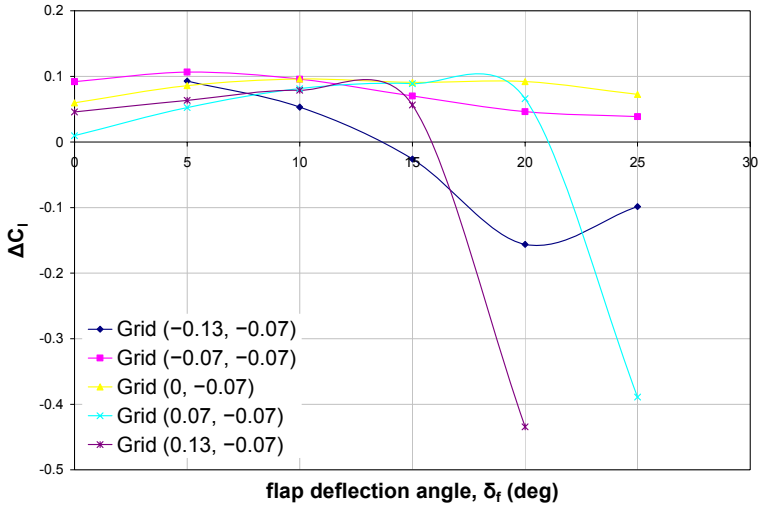

Figure 37: ΔC_l due to 20mm serrations at a flap gap of −0.07, $0° \leq \delta_f \leq 25°$

(a) Flap Lap/Gap: (−0.13, −0.07)

At a flap lap/gap of (−0.13, −0.07), the 20mm serrations only had favourable effect upon C_l for $5° \leq \delta_f \leq 10°$ when compared to the plain trailing edge configuration. At δ_f=5°, the 20mm serrations increased C_l by 0.09, accounting for a 23% increment. A single increment in δ_f to 10° decreased the increment in C_l due to the 20mm serrations to 0.05, accounting for a 10% increment in comparison to the baseline configuration. With subsequent increments in δ_f, the 20mm serrations had a detrimental effect upon C_l. At δ_f=15°, the 20mm serrations reduced C_l by 4%, which was increased to a maximum ΔC_l of −0.16, equating to a 19% decrement at δ_f=20°. A final increment in δ_f to 25° reduced the decrement in C_l to −0.1, representative of a 12% reduction in C_l when compared to the plain trailing edge configuration. Whilst the significant loss in leading edge suction due to the 20mm serrations had a detrimental effect upon C_l at δ_f=25°, ΔC_l was reduced in magnitude as the 20mm serrations delayed separation aft of $0.5c_{flap}$ and promoted boundary layer attachment to within close proximity of the flap trailing edge (see Appendix D, Figure 154(e)).

(b) Flap Lap/Gap: (−0.07, −0.07)

A single increment in the flap lap from −0.13 to −0.07, at a flap gap of −0.07, extended the range of δ_f over which the 20mm serrations had a favourable effect upon C_l to include all test δ_f. At δ_f=0°, the 20mm serrations increased C_l by 0.09, accounting for a 27% increment in comparison to the baseline configuration. A single increment in δ_f to 5° maximised ΔC_l to 0.11, equating to a 22% increase in the lift force generated over the trailing edge flap. With subsequent increments in δ_f, ΔC_l progressively decreased in

magnitude from ΔC_l=0.09 at δ_f=10° to ΔC_l=0.04 at δ_f=25°, correlating to a 16% and 5% increment in C_l, respectively, in comparison to the baseline configuration.

(c) Flap Lap/Gap: (0, −0.07)

Similarly to the configuration at a lap/gap of (−0.07, −0.07), the 20mm serrations increased C_l for all test δ_f at a lap/gap of (0, −0.07). Accounting for a 14-15% increment in C_l in comparison to the baseline configuration for $0° \leq \delta_f \leq 10°$, ΔC_l progressively increased from 0.06 at δ_f=0° to a maximum of 0.1 at δ_f=10°. With further increments in δ_f, ΔC_l decreased in magnitude, equating to a 12% increment for $15° \leq \delta_f \leq 20°$ and reducing to a minimum ΔC_l of 0.07 at δ_f=25°, correlating to a 10% increment in comparison to the baseline configuration.

(d) Flap Lap/Gap: (0.07, −0.07)

Incrementing the lap from 0 to 0.07 at a gap of −0.07 reduced the upper limit for the range of δ_f over which the 20mm serrations had a favourable effect upon C_l from $0° \leq \delta_f \leq 25°$ to $0° \leq \delta_f \leq 20°$, simultaneously introducing a δ_f for which there was a dramatic loss in lift, consistent with severe aerofoil stall. For $0° \leq \delta_f \leq 15°$, the increment in C_l due to the 20mm serrations progressively increased in magnitude from 0.01 at δ_f=0° to 0.09 at δ_f=15°, correlating to a 2% and 10% increment in C_l, respectively. Incrementing δ_f to 20° reduced ΔC_l to 0.07, representative of a 7% increment in comparison to the baseline configuration. However, a final increment in δ_f to 25° rendered the 20mm serrations detrimental to C_l, decreasing C_l by −0.39 and equating to a 45% decrement in lift when compared to the plain trailing edge configuration. The dramatic loss in lift was characteristic of severe aerofoil stall and corroborated the C_p distributions, which indicated that whilst the upper surface boundary layer remained attached to within close proximity of the trailing edge for the plain trailing edge configuration, both the 10mm and 20mm serrations prompted extensive boundary layer separation over the upper surface of the flap (see Appendix D, Figure 157(f)).

(e) Flap Lap/Gap: (0.13, −0.07)

A final increment in flap lap from 0.07 to the upper test limit of 0.13 at a flap gap of −0.07 further reduced the range of δ_f over which the 20mm serrations had a favourable effect upon C_l from $0° \leq \delta_f \leq 20°$ to $0° \leq \delta_f \leq 15°$, simultaneously reducing the δ_f at which there was a dramatic loss in lift. For $0° \leq \delta_f \leq 10°$, the increment in C_l due to the 20mm serrations progressively increased in magnitude from 0.05 at δ_f=0° to 0.08 at δ_f=10°, correlating to a 9% increment in C_l throughout. Incrementing δ_f to 15° reduced ΔC_l to 0.06, representative of a 6% increment in comparison to the plain trailing edge

configuration. However, a further increment in δ_f to 20° rendered the 20mm serrations detrimental to the flow field development, decreasing C_l by −0.43, which accounted for a 43% decrement in C_l in comparison to the baseline configuration. Once again, the dramatic loss in lift was characteristic of severe aerofoil stall and corroborated the C_p distributions, which indicated that the 20mm serrations prompted extensive boundary layer separation over the upper surface of the flap, whilst the plain and 10mm serrated trailing edge configurations maintained upper surface boundary layer attachment to within close proximity of the trailing edge (see Appendix D, Figure 158(e)).

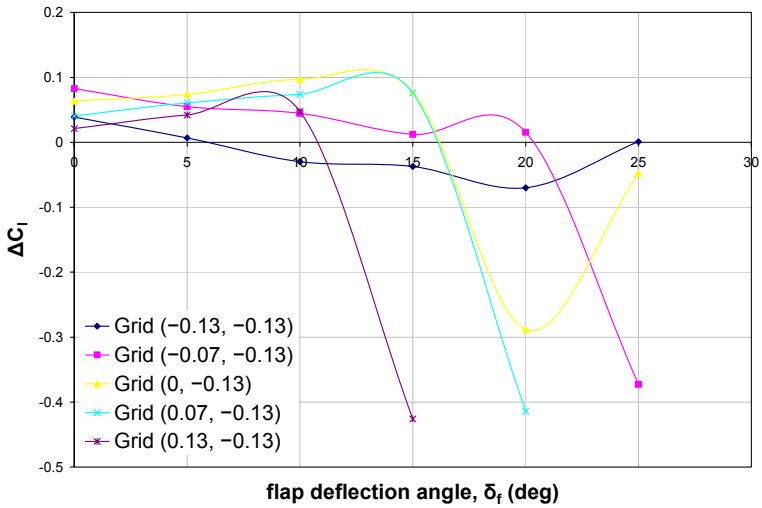

Figure 38: ΔC_l due to 20mm serrations at a flap gap of −0.13, 0°≤δ_f≤25°

(f) Flap Lap/Gap: (−0.13, −0.13)

By increasing the flap gap from −0.07 to −0.13 at a flap lap of −0.13, the range of δ_f over which the 20mm serrations had a favourable effect upon C_l was reduced from 5°≤δ_f≤10° to 0°≤δ_f≤5°. Whilst the 20mm serrations increased C_l by 0.04 at δ_f=0°, accounting for an 11% increment in comparison to the baseline configuration, the increment in C_l due to the 20mm serrations was marginalised to 0.01 at δ_f=5°, correlating to a 1% increment. With subsequent increments in 10°≤δ_f≤20°, the 20mm serrations had a detrimental effect upon the lift force generated. ΔC_l was progressively heightened in magnitude from −0.03 at δ_f=10° to −0.07 at δ_f=20°, correlating to a 4% and 7% decrement in C_l, respectively, when compared to the baseline configuration. However, as a result of the 20mm serrations preventing boundary layer separation at 0.5c_{flap} and promoting boundary layer attachment to within close proximity of the flap trailing edge at δ_f=25° (see Appendix D, Figure 159(f)), the decrement in C_l due to the 20mm serrations was negated and was hence, comparable to the plain trailing edge configuration.

(g) Flap Lap/Gap: (−0.07, −0.13)

Incrementing the flap lap from −0.13 to −0.07 at a flap gap of −0.13 significantly increased the range of δ_f over which the 20mm serrations had a favourable effect upon C_l from $0°\leq\delta_f\leq5°$ to $0°\leq\delta_f\leq20°$. In contrast, increasing the flap gap from −0.07 to −0.13 at a flap lap of −0.07 reduced the range of δ_f over which the 20mm serrations were beneficial to C_l from $0°\leq\delta_f\leq25°$ to $0°\leq\delta_f\leq20°$, simultaneously introducing a δ_f for which there was a dramatic loss in lift, consistent with severe aerofoil stall. At δ_f=0°, the 20mm serrations increased C_l by 0.08, accounting for a 21% increment in comparison to the baseline configuration. With further increments in $5°\leq\delta_f\leq20°$, ΔC_l progressively decreased in magnitude from 0.05 at δ_f=5° to 0.01 at δ_f=20°, correlating to a 9% and 2% increment, respectively. A final increment in δ_f to the upper test limit of 25° dramatically reduced C_l by −0.37, equating to a 43% decrement in comparison to the baseline configuration. The dramatic loss in lift once again corroborated the corresponding C_p distributions, which indicated that the 20mm serrations promoted extensive boundary layer separation over the upper surface of the flap, whilst the plain and 10mm serrated trailing edge configurations maintained upper surface boundary layer attachment to within close proximity of the trailing edge (see Appendix D, Figure 160(f)).

(h) Flap Lap/Gap: (0, −0.13)

Incrementing the flap lap from −0.07 to 0 at a flap gap of −0.13 reduced the range of δ_f over which the 20mm serrations increased C_l from $0°\leq\delta_f\leq20°$ to $0°\leq\delta_f\leq15°$, simultaneously decreasing the δ_f for which there was a significant loss in lift. Similarly, increasing the flap gap from −0.07 to −0.13 at a flap lap of 0 reduced the range of δ_f over which the 20mm serrations were beneficial to C_l from $0°\leq\delta_f\leq25°$ to $0°\leq\delta_f\leq15°$, simultaneously introducing a δ_f for which there was a dramatic loss in lift, characteristic of aerofoil stall. For $0°\leq\delta_f\leq10°$, the 20mm serrations increased C_l by 11-14%, with ΔC_l progressively increasing in magnitude from 0.06 at δ_f=0° to 0.1 at δ_f=10°. A further increment in δ_f to 15° reduced ΔC_l to 0.08, correlating to a 9% increment in comparison to the baseline configuration. However, with subsequent increments in δ_f, the 20mm serrations had a detrimental effect upon C_l. The dramatic 33% loss in lift at δ_f=20° was consistent with extensive upper surface boundary layer separation evident in the C_p distribution for the 20mm serrated configuration, contrasting the baseline and 10mm serrated configurations, for which boundary layer attachment was maintained to within close proximity of the flap trailing edge (see Appendix D, Figure 161(e)). As extensive boundary layer separation had developed over the upper surface of all three configurations at δ_f=25°, the decrement in C_l due to the 20mm serrations was reduced to

10% in comparison to the baseline configuration and was attributed to variations in the static pressure measurements (see Appendix D, Figure 161(f)).

(i) Flap Lap/Gap: (0.07, −0.13)

Increasing the flap gap from −0.07 to −0.13 at a flap lap of 0.07 had a detrimental effect upon the range of δ_f over which the 20mm serrations increased C_l, simultaneously decreasing the δ_f for which there was a significant loss in lift from δ_f=25° to δ_f=20°. In contrast, maintaining a flap gap of −0.13 and increasing the flap lap from 0 to 0.07 had negligible effect upon the range of δ_f over which the 20mm serrations had a favourable effect upon C_l. For $0° \leq \delta_f \leq 15°$, the increment in C_l due to the 20mm serrations progressively increased in magnitude from 0.04 at δ_f=0° to 0.08 at δ_f=15°, correlating to an approximate 8% increment throughout, in comparison to the baseline configuration. However, by increasing δ_f to 20°, the 20mm serrations reduced C_l by 44% in comparison to the plain trailing edge configuration. The dramatic loss in lift was characteristic of severe aerofoil stall and corroborated the C_p distributions, which indicated that whilst the upper surface boundary layer remained attached to within close proximity of the trailing edge for the plain trailing edge configuration, the 20mm serrations – similarly to the 10mm serrations – prompted extensive boundary layer separation over the upper surface of the flap (see Appendix D, Figure 162(e)).

(j) Flap Lap/Gap: (0.13, −0.13)

Maintaining a flap gap of −0.13 and increasing the flap lap from 0.07 to 0.13, or by increasing the flap gap from −0.07 to −0.13 at a flap lap of 0.13, the range of δ_f over which the 20mm serrations had a favourable effect upon C_l was further reduced from $0° \leq \delta_f \leq 15°$ to $0° \leq \delta_f \leq 10°$, simultaneously reducing the δ_f for which there was a significant loss in lift from 20° to 15°. For $0° \leq \delta_f \leq 10°$, the increment in C_l due to the 20mm serrations progressively increased in magnitude from 0.02 at δ_f=0° to 0.05 at δ_f=10°, correlating to 4-5% increment in C_l in comparison to the baseline configuration. However, with a further increment in δ_f to 15°, the 20mm serrations substantially decreased C_l by −0.43, representative of a 41% in decrement in C_l. The magnitude of this decrement was once again characteristic of severe aerofoil stall and corroborated the C_p distributions, which indicated that whilst the upper surface boundary layer remained attached to within close proximity of the trailing edge for the plain and 10mm serrated trailing edge configurations, the 20mm serrations prompted extensive boundary layer separation over the upper surface of the flap (see Appendix D, Figure 163(d)).

5.3.3 Effect of 20mm Trailing Edge Serrations on the Maximum Lift Coefficient

Recalling that for a complete aircraft, the maximum lift coefficient (C_{lmax}) determined the stalling speed of the aircraft, which was critical in defining the takeoff and landing velocities, it was important to determine whether the 20mm serrations had a favourable or detrimental effect upon C_{lmax} in comparison to the baseline configuration.

Figure 39 and Figure 40 show the effect of the 20mm serrations on C_{lmax} in comparison to the plain trailing edge configuration at a flap gap of −0.07 and −0.13, respectively.

Figure 39 shows that at a flap gap of −0.07 and a flap lap of −0.13, the 20mm serrations reduced C_{lmax} by −0.14, representing a 17% decrement in comparison to the corresponding plain trailing edge configuration. However, with subsequent increments in flap lap over the test range, the 20mm serrations had a favourable effect upon C_{lmax}. With the flap leading edge positioned immediately upstream of the flat plate trailing edge at a lap of −0.07, the 20mm serrations increased C_{lmax} by 0.05 in comparison to the baseline configuration, equating to a 6% increment. Aligning the flap leading edge with the flat plate trailing edge heightened the increment in C_{lmax} due to the 20mm serrations to 0.09, attaining a maximum 12% increment in comparison to the baseline configuration.

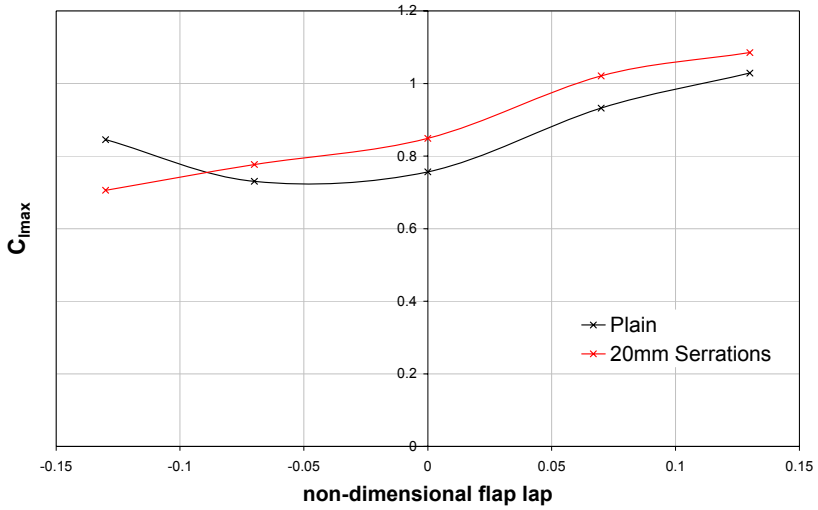

Figure 39: Effect of 20mm serrations on C_{lmax} at a flap gap of −0.07

By positioning the flap leading edge immediately aft of the flat plate trailing edge at a lap of 0.07, a ΔC_{lmax} of 0.09 was maintained, which correlated to a 10% increment due to the 20mm serrations in comparison to the baseline configuration. However, with a further increment in flap lap to the upper test limit of 0.13, the increment in C_{lmax} was

reduced to 0.06, corresponding to a 5% increment in comparison to the plain trailing edge configuration. Thus, the data indicated that at a flap gap of −0.07, the 20mm serrations had a favourable effect upon C_{lmax} for test flap laps between −0.07 and 0.13, inclusive.

Figure 40 shows that increasing the flap gap from −0.07 to −0.13 marginalised the sensitivity of C_{lmax} to the variations in the flat plate trailing edge geometry. This was particularly notable at the lower flap lap test limit of −0.13, whereby increasing the flap gap reduced the decrement in C_{lmax} to −0.07 in comparison to the baseline configuration, accounting for a 7% decrement. However at a flap lap of −0.07, the increment in C_{lmax} due to the 20mm serrations was also reduced at the larger test flap gap, with a ΔC_{lmax} of 0.02 accounting for a 2% increment in comparison to the baseline configuration. With further increments in flap lap to either 0 or 0.07, the 20mm serrations increased C_{lmax} by 0.07 and 0.08, respectively, equating to an 8% increment in comparison to the plain trailing edge configuration. However, incrementing the flap lap to the upper test limit of 0.13 at the larger flap gap −0.13 rendered the 20mm serrations detrimental, decreasing C_{lmax} by −0.03 or 3% in comparison to the plain trailing edge configuration. Thus, increasing the flap gap from −0.07 to −0.13 reduced the range of flap laps over which the 20mm serrations had a favourable effect upon C_{lmax}.

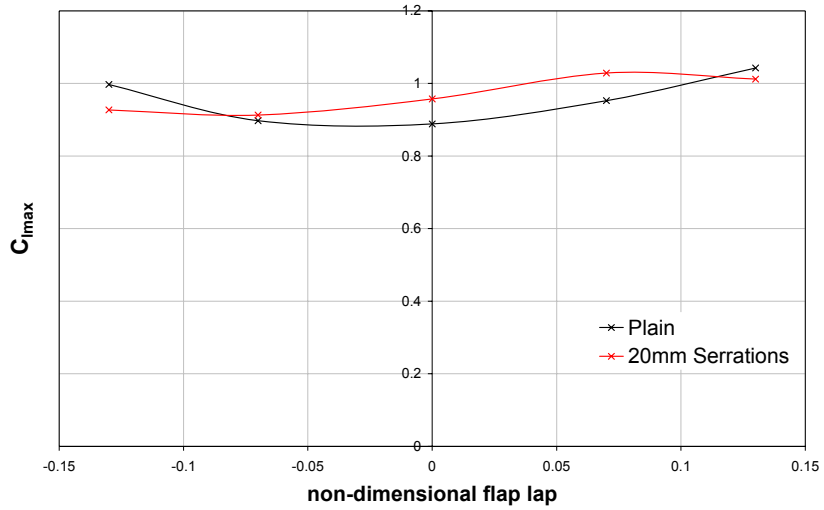

Figure 40: Effect of 20mm serrations on C_{lmax} at a flap gap of −0.13

Figure 41 highlights the effect of increasing the flap gap from −0.07 to −0.13 for the 20mm serrated configuration. Most significantly, increasing the flap gap from −0.07 to −0.13 minimised the sensitivity of C_{lmax} to variations in flap lap over the designated test range. Similarly to the plain and 10mm serrated trailing edge configurations, incrementing the flap gap increased the C_{lmax} for any given flap test lap between −0.13

and 0.07. Again, this deviation in C_{lmax} due to the flap gap was most notable with the flap leading edge positioned either upstream of or in alignment with the flat plate trailing edge. At the lower flap lap test limit of −0.13, incrementing the flap gap from −0.07 to −0.13 with the 20mm serrated geometry implemented at the trailing edge of the flat plate, increased C_{lmax} by 0.22, accounting for a 31% increment, which exceeded the magnitude of ΔC_{lmax} for the corresponding baseline and 10mm serrated configurations. Incrementing the flap lap to −0.07 decreased ΔC_{lmax} to 0.14, representing an 18% increment in C_{lmax} due to the increment in flap gap.

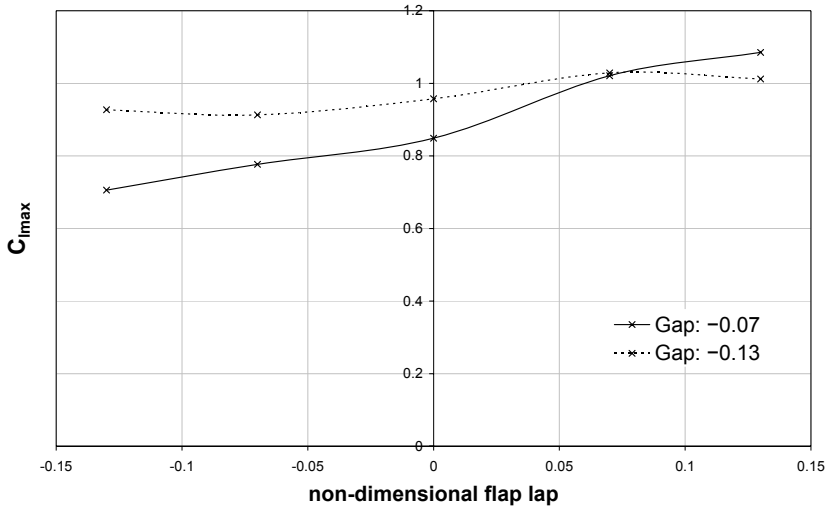

Figure 41: Effect of flap lap/gap on C_{lmax} for 20mm serrated configuration

By aligning the flap leading edge with the flat plate trailing edge, ΔC_{lmax} was further reduced to 0.11, equating to a 13% increment. With a further increment to a flap lap of 0.07, the sensitivity of C_{lmax} to variations in the flap gap was essentially negated. However, unlike the plain and 10mm serrated trailing edge configurations, incrementing the flap gap from −0.07 to −0.13 at the upper lap test limit of 0.13 had a detrimental effect upon C_{lmax} for the 20mm serrated configuration, with a ΔC_{lmax} of −0.07 equating to a 7% decrement. Thus, for the 20mm serrated configuration, C_{lmax} at a given flap lap was typically sensitive to variations in flap gap.

5.3.4 Effect of 20mm Trailing Edge Serrations on the Stall Angle

At a flap gap of −0.07, the 20mm serrations typically had no appreciable effect upon the indicated stall angle for flap laps between −0.07 and 0.13. However, at a flap lap/gap of (−0.13, −0.07), the 20mm serrations extended the stall angle from 20° to 25°. More significantly, the 20mm serrations notably heightened the severity of the stall when the leading edge of the flap was positioned aft of the flat plate trailing edge. At a flap gap of −0.13, the 20mm serrations typically had no appreciable affect upon the indicated

stall angle for flap laps between −0.13 and 0.07. However, at a flap lap/gap of (0.13, −0.13), the 20mm serrations reduced the stall angle from 15° to 10°. More significantly, the 20mm serrations notably heightened the severity of the stall for all flap laps between −0.07 and 0.13, inclusive.

5.3.5 Effect of 20mm Trailing Edge Serrations on the Drag Coefficient

Similarly to the baseline and 10mm serrated trailing edge configurations, analysis of the profile drag measurements was deemed to provide a more complete representation of the effect of the 20mm serrations on the overall configuration drag. In this instance, further analysis of the pressure drag individually did not augment the evaluation of the 20mm serrated geometry. Direct comparison of the profile drag for the 20mm serrated configuration at a specified flap lap/gap and δ_f with the corresponding baseline configuration with the plain trailing edge resulted in the incremental profile drag coefficient (ΔC_{dp}) due to the 20mm serrations.

Figure 42 and Figure 43 show the incremental variation in C_{dp} with δ_f for all test flap laps at a flap gap of −0.07 and −0.13, respectively.

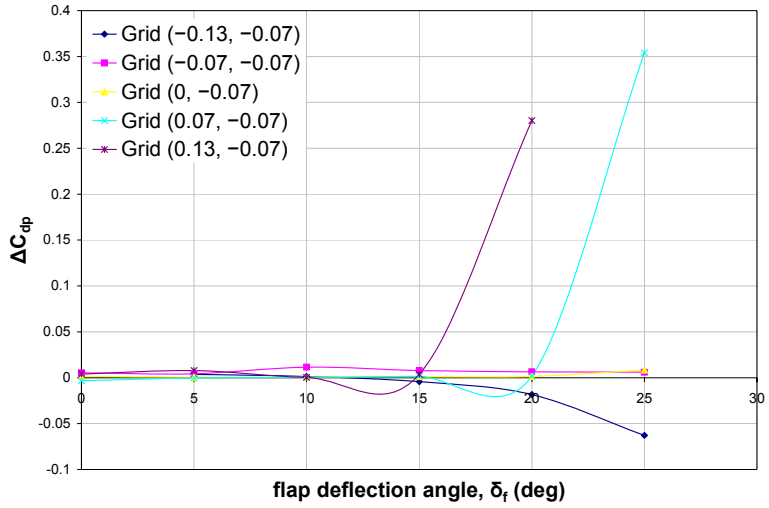

Figure 42: ΔC_{dp} due to 20mm serrations at a flap gap of −0.07, $0° \leq \delta_f \leq 25°$

(a) Flap Lap/Gap: (−0.13, −0.07)

At a flap lap/gap of (−0.13, −0.07), the 20mm serrations adversely affected C_{dp} for $5° \leq \delta_f \leq 10°$ and favourably influenced C_{dp} for $15° \leq \delta_f \leq 25°$. The increment in C_{dp} reduced in magnitude from 0.004 at δ_f=5° to 0.001 at δ_f=10°, accounting for a 4% and 1% increment, respectively, in comparison to the baseline configuration. With a single

increment in δ_f to 15°, the 20mm serrations reduced C_{dp} by −0.004, representing a 4% decrement. By incrementing δ_f to 20°, ΔC_{dp} was heightened to −0.018, accounting for a 14% decrement in comparison to the baseline configuration. A final increment in δ_f to 25° substantially heightened ΔC_{dp} to −0.06, accounting for a 35% reduction in comparison to the baseline configuration, corroborating the notable reduction in the wake cross-section for the 20mm serrated configuration (see Appendix E, Figure 164(e)). The magnitude of the reduction was attributed to 20mm serrations preventing boundary layer separation at $0.5c_{flap}$ and promoting boundary layer attachment to within close proximity of the flap trailing edge (see Appendix D, Figure 154(e)).

(b) Flap Lap/Gap: (−0.07, −0.07)

Increasing the flap lap from −0.13 to −0.07, at a flap gap of −0.07, extended the range of δ_f over which the 20mm serrations had a detrimental effect upon C_{dp} from $5° \leq \delta_f \leq 10°$ to all test δ_f. For $0° \leq \delta_f \leq 10°$, the increment in C_{dp} due to the 20mm serrations progressively increased in magnitude from 0.005 at δ_f=0° to 0.01 at δ_f=10°, accounting for a 6% and 13% increment in C_{dp}, respectively. With subsequent increments in $\delta_f \geq 15°$, ΔC_{dp} progressively decreased in magnitude, attaining a value of 0.006 at δ_f=25° and equating to a 5% increment in comparison to the baseline configuration.

(c) Flap Lap/Gap: (0, −0.07)

Incrementing the flap lap from −0.07 to 0, at a flap gap of −0.07, tended to reduce the magnitude of ΔC_{dp} for any given test δ_f. Specifically, the increment in C_{dp} due to the 20mm serrations progressively decreased in magnitude from a 2% increment at δ_f=0° to a near negligible variation for $5° \leq \delta_f \leq 20°$. A final increment in δ_f to 25°, heightened ΔC_{dp} to a maximum of 0.008, equating to a 7% increment in comparison to the baseline configuration. Thus, with the flap leading edge aligned with the flat plate trailing edge, the 20mm serrations appeared to have minimal influence upon C_{dp}.

(d) Flap Lap/Gap: (0.07, −0.07)

Increasing the flap lap from 0 to 0.07, at a flap gap of −0.07, reduced the range of δ_f over which the 20mm serrations were detrimental to C_{dp}. At δ_f=0°, the 20mm serrations had a favourable effect upon C_{dp}, with ΔC_{dp} of −0.003 representing a 3% reduction in comparison to the baseline configuration. Increments in δ_f to 5° and 10° essentially negated any variation in C_{dp} due to the 20mm serrations. With subsequent increments $15° \leq \delta_f \leq 25°$, the 20mm serrations had a detrimental effect upon C_{dp}. For $15° \leq \delta_f \leq 20°$, the 20mm serrations accounted for a 2% increment in C_{dp} in comparison to the baseline configuration. With a final increment in δ_f to 25°, the 20mm serrations dramatically increased ΔC_{dp} to 0.35, which accounted for a 320% increase in profile drag in

comparison to the corresponding plain trailing edge configuration. The considerable magnitude of this increment in C_{dp} corroborated the marked increase in the wake cross-section in the measurement plane for the 20mm serrated configuration (see Appendix E, Figure 167(f)), attributed to the extensive boundary layer separation evident over the upper surface of the single slotted flap (see Appendix D, Figure 157(f)). In contrast, the corresponding plain trailing edge configuration maintained boundary layer attachment to within close proximity of the trailing edge, with an attendant smaller wake cross-section.

(e) Flap Lap/Gap: (0.13, −0.07)

Increasing the flap lap from 0.07 to 0.13, at a flap gap of −0.07, once again extended the range of δ_f over which the 20mm serrations were detrimental to C_{dp} to include all test δ_f, simultaneously reducing the δ_f for which there was a dramatic increase in drag. ΔC_{dp} increased in magnitude from 0.004 at δ_f=0° to 0.008 at δ_f=5°, correlating to a 4% and 9% increment, respectively, in comparison to the baseline configuration. A subsequent increment in δ_f to 10°, marginalised any variation in C_{dp} due to the 20mm serrations but with further increments $\delta_f \geq 15°$, ΔC_{dp} was heightened in magnitude. This was particularly evident at δ_f=20°, whereby a ΔC_{dp} of 0.28 accounted for nearly a 270% increase in profile drag in comparison to the baseline configuration. The considerable magnitude of this increment in C_{dp} corroborated the marked increase in the wake cross-section in the measurement plane (see Appendix E, Figure 168(e)), attributed to the extensive boundary layer separation over the upper surface of the single slotted flap aft of the 20mm serrated trailing edge (see Appendix D, Figure 158(e)). Again, this contrasted the plain trailing edge configuration, which maintained boundary layer attachment to within close proximity of the trailing edge.

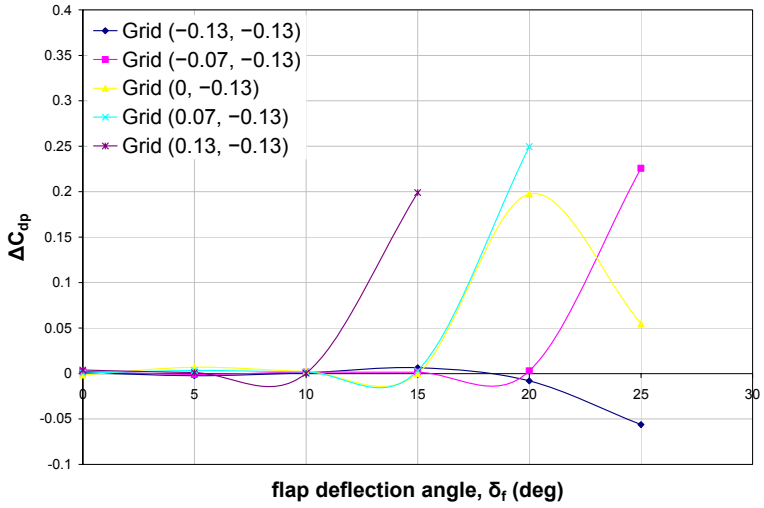

Figure 43: ΔC_{dp} due to 20mm serrations at a flap gap of −0.13, $0° \leq \delta_f \leq 25°$

(f) Flap Lap/Gap: (−0.13, −0.13)

The variation of C_{dp} with δ_f for the 20mm serrated configuration at a lap/gap of (−0.13, −0.13) was less consistent than that observed at the smaller flap test gap of −0.07. At δ_f=0°, the 20mm serrations increased C_{dp} by 1% but with a single increment in δ_f to 5°, the 20mm serrations decreased C_{dp} by −0.002, equating to a 3% reduction in comparison to the baseline configuration. With further increments in δ_f to 10° and 15°, the 20mm serrations once again increased C_{dp}, accounting for a maximum ΔC_{dp} of 0.006 at δ_f=15°, correlating to a 6% increment. By incrementing δ_f to 20° and 25°, the 20mm serrations were once again advantageous, decreasing C_{dp}, by −0.008 at δ_f=20°, equating to a 7% reduction, which was markedly heightened to −0.056 at δ_f=25°, representative of a 32% reduction in C_{dp} in comparison to the baseline configuration. The magnitude of the reduction at δ_f=25° was attributed to 20mm serrations preventing boundary layer separation at 0.5c_{flap} and promoting boundary layer attachment to within close proximity of the flap trailing edge (see Appendix D, Figure 159(f)).

(g) Flap Lap/Gap: (−0.07, −0.13)

Incrementing the flap lap from −0.13 to −0.07 at a flap gap of −0.13 increased the range of δ_f over which the 20mm serrations had a detrimental effect upon C_{dp}. In contrast, increasing the flap gap from −0.07 to −0.13 at a flap lap of −0.07 reduced the range of δ_f over which the 20mm serrations had a detrimental effect upon C_{dp}. At δ_f=0°, the 20mm serrations increased C_{dp} by 3% in comparison to the baseline configuration. Whilst a single increment in δ_f to 5° reduced ΔC_{dp} to 1%, with further increments in δ_f, the 20mm serrations had a detrimental effect upon C_{dp}. ΔC_{dp} was progressively heightened in magnitude from 0.001 at δ_f=10° to 0.003 at δ_f=20°, correlating to a 1-3% increment in comparison to the baseline configuration. A final increment in δ_f to 25° dramatically increased ΔC_{dp} to 0.23, which accounted for nearly a 190% increase in profile drag in comparison to the corresponding plain trailing edge configuration. The considerable magnitude of this increment in C_{dp} corroborated the marked increase in the wake cross-section in the measurement plane at δ_f=25° (see Appendix E, Figure 170(f)), attributed to the extensive boundary layer separation evident over the upper surface of the single slotted flap aft of the 20mm serrated trailing edge (see Appendix D, Figure 160(f)). In contrast, the corresponding plain trailing edge configuration maintained boundary layer attachment to within close proximity of the trailing edge.

(h) Flap Lap/Gap: (0, −0.13)

Increasing the flap gap from −0.07 to −0.13 at zero flap lap introduced isolated δ_f for which the 20mm serrations proved beneficial to C_{dp}. Conversely, maintaining a flap gap

of −0.13 and increasing the flap lap from −0.07 to 0 heightened the inconsistency of ΔC_{dp} with δ_f. At δ_f=0°, the 20mm serrations decreased C_{dp} by 2% in comparison to the baseline configuration. However, a single increment in δ_f to 5° rendered the 20mm serrations detrimental to C_{dp}, increasing C_{dp} by 0.007 in comparison to the baseline configuration and corresponding to an 8% increment. At δ_f=10°, ΔC_{dp} was reduced to 0.002, accounting for a 3% increment and with a further increment in δ_f to 15°, any variation in C_{dp} due to the 20mm serrations was essentially negated. By increasing δ_f to 20°, the 20mm serrations markedly increased C_{dp} by 0.2, accounting for over a 190% increment in comparison to the plain trailing edge configuration. The substantial magnitude of this increment in C_{dp} corroborated the marked increase in the wake cross-section in the measurement plane for the 20mm serrated configuration (see Appendix E, Figure 171(e)), which was attributed to the extensive boundary layer separation evident over the upper surface of the single slotted flap (see Appendix D, Figure 161(e)). In contrast, the corresponding plain trailing edge configuration once again maintained boundary layer attachment to within close proximity of the trailing edge (see Appendix D, Figure 161(e)). Although extensive boundary layer separation was evident over the upper surface of the flap, irrespective of the trailing edge geometry at δ_f=25°, variations in the measured static pressure and wake cross-section still resulted in the 20mm serrations increasing C_{dp} by 17% in comparison to the baseline configuration (see Appendix D, Figure 161(f) and Appendix E, Figure 171(f)).

(i) Flap Lap/Gap: (0.07, −0.13)

Whether increasing the flap lap from 0 to 0.07 at a flap gap of −0.13 or increasing the flap gap from −0.07 to −0.13 at a flap lap of 0.07, the range of δ_f over which the 20mm serrations had a detrimental effect upon C_{dp} was extended to include all test δ_f. At a lap/gap of (0.07, −0.13), ΔC_{dp} due to the 20mm serrations varied inconsistently with δ_f. Whilst the 20mm serrations had near negligible effect upon C_{dp} at δ_f=0°, variations in ΔC_{dp} for $5° \leq \delta_f \leq 15°$ correlated to a 2-4% increment in comparison to the baseline configuration. By increasing δ_f to 20°, the 20mm serrations dramatically increased C_{dp} by 0.25, accounting for nearly a 250% increment in comparison to the plain trailing edge configuration. The considerable magnitude of this increment in C_{dp} once again corroborated the marked increase in the wake cross-section in the measurement plane (see Appendix E, Figure 172(e)), attributed to the extensive upper surface boundary layer separation for the 20mm serrated trailing edge configuration (see Appendix D, Figure 162(e)). Similarly to previous configurations, the corresponding plain trailing edge configuration maintained boundary layer attachment to within close proximity of the trailing edge at δ_f=20°.

(j) Flap Lap/Gap: (0.13, −0.13)

Whether increasing the flap lap from 0.07 to 0.13 at a flap gap of −0.13 or increasing the flap gap from −0.07 to −0.13 at a flap lap of 0.13, the 20mm serrations had a detrimental effect upon C_{dp} for all test δ_f. For $0° \leq \delta_f \leq 10°$, the increment in C_{dp} due to the 20mm serrations progressively decreased in magnitude from 0.004 at δ_f=0°, corresponding to a 4% increment, to a near negligible increment at δ_f=10°. However, with a final increment in δ_f to 15°, ΔC_{dp} was substantially increased to 0.2, accounting for over a 200% increment in C_{dp} when compared to the corresponding baseline configuration. The considerable magnitude of this increment in C_{dp} at δ_f=15° corroborated the marked increase in the wake cross-section in the measurement plane for the 20mm serrated configuration (see Appendix E, Figure 173(d)), which was attributed to the extensive boundary layer separation over the upper surface of the single slotted flap (see Appendix D, Figure 163(d)). As noted for previous configurations, the corresponding plain trailing edge configuration once again maintained boundary layer attachment to within close proximity of the trailing edge at δ_f=15°.

5.3.6 Effect of 20mm Trailing Edge Serrations on *L*/*D*

Similarly to the 10mm serrated configuration, the effect of the 20mm serrations on L/D for a given flap lap, gap and δ_f was evaluated by direct comparison with the corresponding plain trailing edge configuration (see Figure 34).

(a) Flap Lap/Gap: (−0.13, −0.07)

At a flap lap/gap of (−0.13, −0.07), the 20mm serrations increased L/D for $\delta_f \leq 10°$ and δ_f=25°. For $\delta_f \leq 10°$, the detrimental effect of the 20mm serrations upon C_{dp} was offset by the increment in C_l, resulting in a 19% and 8% increase in L/D at δ_f=5° and δ_f=10°, respectively. Conversely, the favourable effect of the 20mm serrations upon C_{dp} was just sufficient to offset the corresponding degradation in C_l at δ_f=15°, with the net result of no appreciable variation in L/D in comparison to the plain trailing edge configuration. In contrast, the decrement in C_{dp} at δ_f=20° was insufficient to offset the corresponding decrement in C_l and hence, the 20mm serrations reduced L/D by 5% in comparison to the baseline configuration. However, with a final increment in δ_f to 25°, the degradation in C_l due to the 20mm serrations was offset by the more marked reduction in C_{dp}, increasing L/D by 34% in comparison to the plain trailing edge configuration. This marked increment in L/D at δ_f=25° corroborated the favourable effect of the 20mm serrations upon boundary layer development over the upper surface of the flap,

preventing boundary layer separation at $0.5c_{flap}$ and promoting boundary layer attachment to within close proximity of the trailing edge.

(b) Flap Lap/Gap: (−0.07, −0.07)

Despite the increase in C_{dp} for all test δ_f at a flap lap/gap of (−0.07, −0.07), the favourable effect of the 20mm serrations on the corresponding C_l was sufficient to increase the resultant L/D for all $\delta_f \leq 15°$. The increment in L/D due to the 20mm serrations was greatest at $\delta_f = 0°$, accounting for a 20% increment in comparison to the corresponding baseline configuration. This reduced to a 16% increment in L/D at $\delta_f = 5°$. With further increments in $10° \leq \delta_f \leq 15°$, the increment in L/D was significantly reduced, equating to a 2-3% increment in comparison to the plain trailing edge configuration. However, with further increments in $\delta_f \geq 20°$, any variation in L/D due to the 20mm serrations was essentially negated and L/D was comparable to the baseline configuration.

(c) Flap Lap/Gap: (0, −0.07)

At a flap lap/gap of (0, −0.07), the 20mm serrations increased L/D for all test δ_f. For $0° \leq \delta_f \leq 20°$, the <2% increment in C_{dp} due to the 20mm serrations was offset by a 12-15% increment in C_l, resulting in an 11-14% increase in L/D in comparison to the baseline configuration. However, with a notable 7% increase in C_{dp} at $\delta_f = 25°$, the favourable effect of the 20mm serrations on C_l was marginalised, resulting in a 3% increase in L/D in comparison to the baseline configuration.

(d) Flap Lap/Gap: (0.07, −0.07)

At a lap/gap of (0.07, −0.07), the 20mm serrations increased L/D for all $0° \leq \delta_f \leq 20°$. For $\delta_f \leq 5°$, the favourable effect of the 20mm serrations upon both C_l and C_{dp} increased L/D by 6% and 8% at $\delta_f = 0°$ and $\delta_f = 5°$, respectively. Furthermore, the increment in C_{dp} due to the 20mm serrations for $10° \leq \delta_f \leq 20°$ was insufficient to offset the corresponding increment in C_l and as a result, the 20mm serrations increased L/D by 9% and 5% at $\delta_f = 10°$ and $\delta_f = 20°$, respectively, when compared to the baseline configuration. However, the dramatic increase in C_{dp} at $\delta_f = 25°$ combined with the marked decrement in C_l to decrease L/D by 87% in comparison to the baseline configuration. Similarly to the 10mm serrated configuration, this considerable decrement in L/D at $\delta_f = 25°$ was attributed to the extensive boundary layer separation evident over the upper surface of the flap for the 20mm serrated configuration. In contrast, the corresponding plain trailing edge configuration promoted boundary layer attachment to within close proximity of the trailing edge at $\delta_f = 25°$.

(e) Flap Lap/Gap: (0.13, −0.07)

At a flap lap/gap of (0.13, −0.07), the 20mm serrations tended to increase L/D, although discrepancies arose at δ_f=5° and δ_f=20°. At δ_f=0°, the increment in C_{dp} due to the 20mm serrations was insufficient to offset the increment in C_l, increasing L/D by 4% in comparison to the baseline configuration. However, with the increment in C_{dp} heightened at δ_f=5°, the favourable effect of the 20mm serrations upon C_l was negated, rendering L/D comparable to the plain trailing edge configuration. With the increment in C_{dp} marginalised at δ_f=10°, the favourable effect of the 20mm serrations upon C_l maximised the increment in L/D, accounting for an 8% increase in comparison to the baseline configuration, although with a further increment in δ_f to 15°, the increment in L/D due to the 20mm serrations was reduced to 2%. With a final increment in δ_f to 20°, the substantial increase in C_{dp} combined with the considerable decrement in C_l to decrease L/D by 85% in comparison to the baseline configuration. This considerable decrement in L/D at δ_f=20° was attributed to the extensive boundary layer separation evident over the upper surface of the flap for the 20mm serrated configuration. In contrast, both the corresponding plain and 10mm serrated trailing edge geometries promoted boundary layer attachment to within close proximity of the trailing edge at δ_f=20°.

(f) Flap Lap/Gap: (−0.13, −0.13)

Increasing the flap gap from −0.07 to −0.13 at a flap lap of −0.13 decreased the range of δ_f over which the 20mm serrations had a favourable effect upon L/D. The increment in C_{dp} at δ_f=0° was insufficient to offset the corresponding increment in C_l, resulting in a 9% increase in L/D in comparison to the baseline configuration. At δ_f=5°, the increment in C_l combined with the decrement in C_{dp} to increase L/D by 4% in comparison to the baseline configuration. In contrast, the degradation in both C_l and C_{dp} for $10° \leq \delta_f \leq 15°$ resulted in the 20mm serrations decreasing L/D in comparison to the baseline configuration by 4% and 10% at δ_f=10° and δ_f=15°, respectively. However, the decrement in C_{dp} at δ_f=20° was just sufficient to offset the corresponding decrement in C_l, rendering L/D comparable to the plain trailing edge configuration. However, with a final increment in δ_f to 25°, the 20mm serrations had negligible effect upon C_l, which when combined with the marked reduction in C_{dp}, increased L/D by 47% in comparison to the plain trailing edge configuration. Similarly to the configuration at the smaller test flap gap of −0.07, this marked increment in L/D corroborated the favourable effect of the 20mm serrations upon boundary layer development over the upper surface of the flap, preventing boundary layer separation at $0.5c_{flap}$ and promoting boundary layer attachment to within close proximity of the trailing edge.

(g) Flap Lap/Gap: (−0.07, −0.13)

Incrementing the flap gap from −0.07 to −0.13 at a flap lap of −0.07 limited the range of δ_f over which the 20mm serrations were beneficial to L/D from $\delta_f \leq 15°$ to $\delta_f \leq 10°$. At $\delta_f = 0°$, the increment in C_{dp} was insufficient to offset the corresponding marked increment in C_l, resulting in an 18% increase in L/D in comparison to the baseline configuration. The favourable effect of the 20mm serrations upon both C_{dp} and C_l at $\delta_f = 5°$ increased L/D, although the magnitude of the increment was reduced and accounted for a 10% increment in comparison to the baseline configuration. With a further increment in δ_f to 10°, the increment in C_l offset the adverse effect of the 20mm serrations upon C_{dp}, increasing L/D by 4%. Whilst the 20mm serrations had no appreciable effect upon L/D at $\delta_f = 15°$, the increment in C_l at $\delta_f = 20°$ was insufficient to offset the corresponding increment in C_{dp}, reducing L/D by 1% in comparison to the baseline configuration. With a final increment in δ_f to 25°, the substantial increase in C_{dp} combined with the considerable decrement in C_l to decrease L/D by 80% in comparison to the baseline configuration. This considerable decrement in L/D at $\delta_f = 25°$ was attributed to the extensive boundary layer separation evident over the upper surface of the flap. In contrast, both the corresponding plain and 10mm serrated trailing edge geometries promoted boundary layer attachment to within close proximity of the trailing edge at $\delta_f = 25°$.

(h) Flap Lap/Gap: (0, −0.13)

With the flap leading edge aligned with the flat plate trailing edge, increasing the flap gap from −0.07 to −0.13 limited the range of δ_f over which the 20mm serrations were beneficial to L/D from $\delta_f \leq 25°$ to $\delta_f \leq 15°$. The favourable effect of the 20mm serrations upon C_{dp} and C_l at $\delta_f = 0°$ resulted in a 16% increase in L/D in comparison to the baseline configuration. For $5° \leq \delta_f \leq 15°$ the increment in C_l due to the 20mm serrations offset the corresponding increment in C_{dp}, accounting for a 3% increment in L/D at $\delta_f = 5°$ and a 9% increment for $10° \leq \delta_f \leq 15°$. With a further increment in δ_f to 20°, the substantial increase in C_{dp} combined with the considerable decrement in C_l to decrease L/D by 77% in comparison to the baseline configuration. Once again, the substantial magnitude of this decrement at $\delta_f = 20°$ was attributed to the extensive boundary layer separation evident over the upper surface of the flap. In contrast, both the corresponding plain and 10mm serrated trailing edge geometries promoted boundary layer attachment to within close proximity of the trailing edge at $\delta_f = 20°$. A final increment in δ_f to the upper test limit of 25° reduced the decrement in L/D to 23%. As all three trailing edge geometries generated extensive regions of boundary layer separation over the upper surface of the

flap at δ_f=25°, the decrement in L/D was attributed to variations in the corresponding C_p distributions and wake cross-sections.

(i) Flap Lap/Gap: (0.07, −0.13)

Incrementing the flap gap from −0.07 to −0.13 at a flap lap of 0.07 reduced the range of δ_f over which the 20mm serrations increased L/D from $\delta_f \leq 20°$ to $\delta_f \leq 15°$, simultaneously lowering the δ_f for which there was a dramatic reduction in L/D from 25° to 20°. For $0° \leq \delta_f \leq 15°$, the increment in C_l due to the 20mm serrations was sufficient to offset the corresponding increment in C_{dp}, resulting in a 4-7% increment in L/D, depending upon the given δ_f. With a further increment in δ_f to 20°, the dramatic increase in C_{dp} combined with the considerable decrement in C_l to decrease L/D by 84% in comparison to the baseline configuration. As with previous configurations, the considerable magnitude of this decrement at δ_f=20° was attributed to the extensive boundary layer separation evident over the upper surface of the flap for the 20mm serrated configuration, which was comparable to the corresponding 10mm serrated configuration. In contrast, the C_p distribution for the corresponding plain trailing edge configuration at δ_f=20° indicated that boundary layer remained attachment to within close proximity of the trailing edge.

(j) Flap Lap/Gap: (0.13, −0.13)

By increasing the flap gap from −0.07 to −0.13 at a flap lap of 0.13, the range of δ_f over which the 20mm serrations had a favourable effect upon L/D was reduced. At δ_f=0°, the 20mm serrations had a near negligible effect of upon L/D, which was attributed to the increment in C_{dp} negating the corresponding increment in C_l due to the 20mm serrations. However, with further increments in $5° \leq \delta_f \leq 10°$, the increment in C_l due to the 20mm serrations was sufficient to offset any corresponding increment in C_{dp}, increasing L/D by 4-5% in comparison to the baseline configuration. Once again, with a further increment in δ_f to 15°, the dramatic increase in C_{dp} combined with the considerable decrement in C_l to decrease L/D by 80% in comparison to the baseline configuration. In contrast to the corresponding plain and 10mm serrated trailing edge configurations at δ_f=15°, which maintained boundary layer attachment to within close proximity of the trailing edge, the 20mm serrations promoted extensive boundary layer separation over the upper surface of the single slotted flap, which accounted for the considerable decrement in L/D.

5.3.7 Final Evaluation of 20mm Serrated Trailing Edge Configuration

20mm 60° triangular serrations were implemented at the trailing edge of the flat plate upstream of a single slotted flap. A parametric study of the flap lap, gap and δ_f was conducted and the subsequent analysis indicated that:

In terms of increasing C_l and L/D for a given flap lap/gap configuration, increasing the serration length from 10mm to 20mm heightened the effectiveness of the serrated trailing edge geometry on the single slotted flap. Whilst there were other lap/gap configurations for which the 20mm serrations generated greater increments in C_l and/or L/D at a single δ_f or for a specific range of δ_f, it was at a flap lap/gap of (0, −0.07) that the 20mm serrations increased both C_l and L/D most consistently across the entire range of test δ_f.

In comparison to the corresponding baseline configuration, the 20mm serrations increased C_l by 12-15% for $0° \leq \delta_f \leq 20°$ at a lap/gap of (0, −0.07). Whilst the 20mm serrations had a detrimental effect upon C_{dp} for $0° \leq \delta_f \leq 20°$, the magnitude of the increment accounted for <2% and was hence, offset by the corresponding increase in C_l. Accordingly, the 20mm serrations increased L/D by 11-14% in comparison to the baseline configuration for $0° \leq \delta_f \leq 20°$. At $\delta_f = 25°$, the increment in C_l was decreased to 10%, whereas the increment in C_{dp} was increased to 7%, resulting in a diminished increment in L/D of 3% in comparison to the corresponding plain trailing edge configuration.

Thus, in terms of increasing C_l and L/D, both the 10mm and 20mm serrations were most effective at a flap lap/gap of (0, −0.07). Compared to the plain trailing edge configuration, the increment in L/D due to the 20mm serrations exceeded the corresponding increment for the 10mm serrated configuration for $0° \leq \delta_f \leq 20°$. However, the 10mm serrations had a more favourable effect upon L/D at $\delta_f = 25°$ than the 20mm serrations. Specifically, with the 10mm serrations favourably affecting both C_l and C_{dp} at $\delta_f = 25°$, the resultant 12% increment in L/D due to the 10mm serrations was fourfold that of the corresponding increment in L/D due to 20mm serrations.

Similarly to the 10mm serrated configuration, the flap lap/gap for which the 20mm serrations most effectively increased C_l and L/D in comparison to the plain trailing edge configuration did not correlate to the optimum flap lap/gap in terms of maximising the overall C_l or L/D for the 20mm serrated configuration.

In terms of attaining the maximum value of C_l for the 20mm serrated configuration, Figure 44 shows that the optimum lap/gap coincided with (0.13, −0.13) for $0° \leq \delta_f \leq 10°$. At δ_f=15° and δ_f=20°, positioning the flap at a lap/gap of (0.13, −0.07) and (0.07, −0.07), respectively, achieved the maximum C_l. With a final increment in δ_f to 25°, the maximum C_l was attained at a flap lap/gap of (−0.13, −0.13). Thus, implementing the 20mm serrations at the trailing edge of the flat plate modified the optimum flap lap/gap for which a maximum value of C_l was attained, both with respect to the baseline and 10mm serrated configurations, with discrepancies arising at δ_f=15° and δ_f=20°.

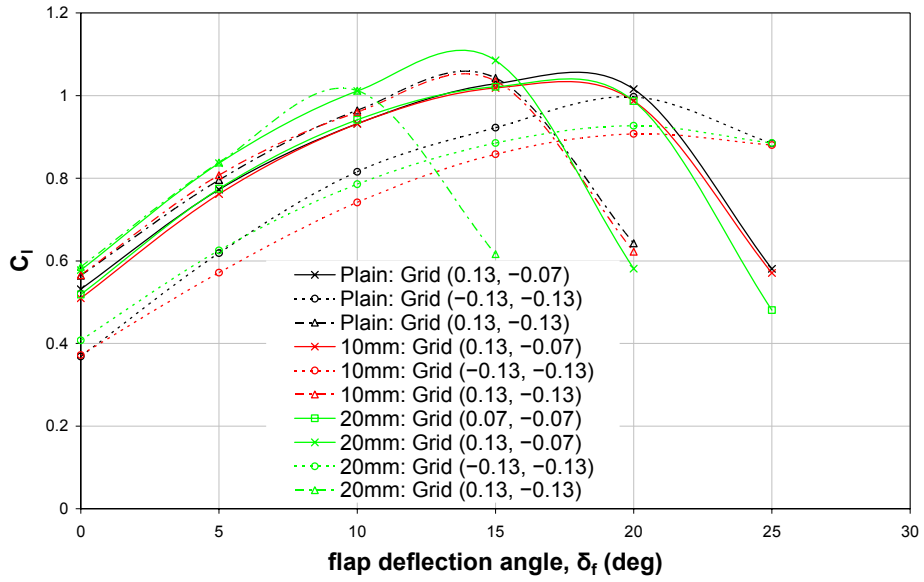

Figure 44: Comparison of optimum lap/gap in terms of maximising overall C_l for plain, 10mm and 20mm serrated configurations

In terms of attaining the maximum value of L/D, the optimum lap/gap for the 20mm serrated configuration also varied in accordance with the specified δ_f. Note that for the 20mm serrated configuration, the optimum lap/gap in terms of maximising the overall L/D at a given δ_f differed from the optimum lap/gap identified for achieving the maximum C_l at a given δ_f.

Accordingly, Figure 45 shows that positioning the flap at a lap/gap of (0.13, −0.13) achieved the maximum value of L/D for $0° \leq \delta_f \leq 5°$. For $10° \leq \delta_f \leq 15°$, the optimum flap position was defined by a lap/gap of (0.13, −0.07). At δ_f=20°, the optimum lap/gap was (0.07, −0.07) and with a final increment in δ_f to 25°, the maximum L/D was attained at a flap lap/gap of (−0.13, −0.13). Thus, implementing the 20mm serrations at the trailing edge of the flat plate modified the optimum flap lap/gap for which a maximum value of L/D was attained in comparison to both the baseline and 10mm serrated configurations.

Anomalies arose at δ_f=20° and δ_f=25° when compared to the baseline configuration and at δ_f=10°, δ_f=20° and δ_f=25°, when compared to the 10mm serrated configuration.

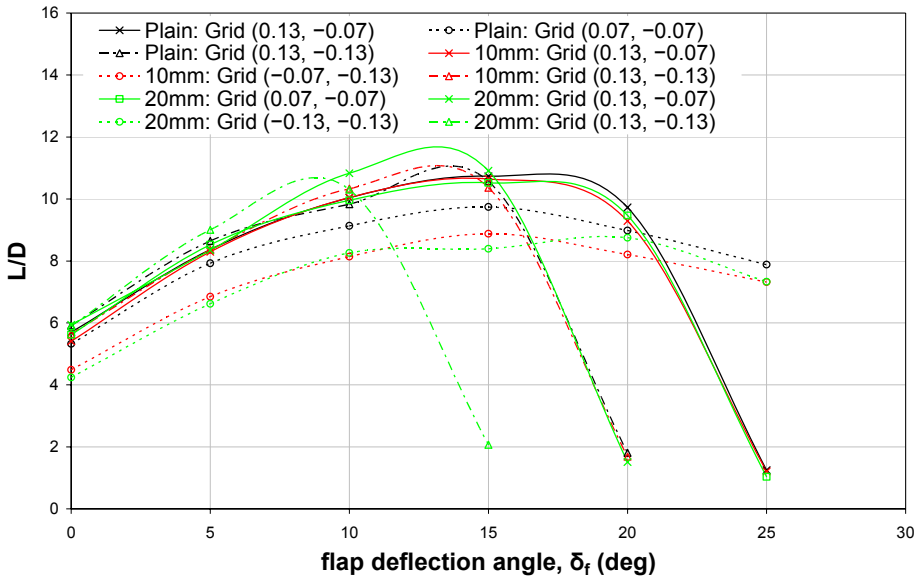

Figure 45: Comparison of optimum lap/gap in terms of maximising overall *L*/*D* for plain, 10mm and 20mm serrated configurations

Based upon the aforesaid optimum lap/gap identified, Figure 44 and Figure 45 showed that the 20mm serrations were more favourable than the both the plain and 10mm serrated configurations for $\delta_f \leq 15°$, generating a C_l or L/D of greater magnitude than the corresponding plain or 10mm serrated configurations. However, the plain geometry was more favourable for $20° \leq \delta_f \leq 25°$, generating a C_l or L/D of greater magnitude than the corresponding 10mm or 20mm serrated configurations.

In terms of C_{lmax}, the 20mm serrations were detrimental when the flap leading edge was positioned upstream of the flat plate trailing edge at the lower lap test limit of −0.13. However, with subsequent increments in flap lap between −0.07 and 0.13, the 20mm serrations tended to increase C_{lmax}.

Establishing the effect of the 20mm serrations on C_{dp} was difficult to ascertain as there was a tendency for ΔC_{dp} to vary inconsistently with δ_f at a specified flap lap/gap. Nevertheless, the 20mm serrations typically only had a favourable effect upon C_{dp} over a limited range of δ_f when the flap leading edge was positioned at the lower lap test limit of −0.13, at either test flap gap. Otherwise, the 20mm serrations were typically detrimental to C_{dp}.

Similarly to the 10mm serrated configuration, positioning the flap at the lower lap test limit of −0.13, at either a flap gap of −0.07 or −0.13, provided clear evidence of the favourable effect of the 20mm serrations on the boundary layer development at high δ_f. At δ_f=25°, the C_p distribution for the baseline configuration indicated that the upper surface boundary layer separated aft of $0.5c_{flap}$. However, the C_p distribution for the corresponding 20mm serrated configuration indicated that, whilst reducing the leading edge suction, the boundary layer remained attached to within close proximity of flap the trailing edge, although the decrement in trailing edge pressure was indicative of a thickening boundary layer and thus, a heightened susceptibility to separation. Whilst the 10mm serrations similarly prevented boundary layer separation and also displayed a marked increase in the trailing edge static pressure, the precise C_p distribution over the aft region of the upper surface was sensitive to the serration length implemented. When compared to the corresponding plain trailing edge configuration, the result was a 34% increase in L/D due to the 20mm serrations at a flap gap of −0.07, increasing to a 47% increase in L/D at a flap gap of −0.13.

Similarly to the 10mm serrations, it was postulated that vortical structures emanated from each vertex of the 20mm serrations, analogous to the flow field visualised by Soderman (1972) and Gai and Sharma (1981). Accordingly, it was hypothesised that with the flap positioned at the lower flap lap test limit of −0.13, the streamwise vortices remained near to the surface across the chordwise extent of the flap, enabling streamwise momentum to be transferred to the near surface boundary layer, preventing separation at $0.5c_{flap}$ and promoting boundary layer attachment to within close proximity of the trailing edge. Further studies are required to determine the precise flow field mechanisms by which the 20mm serrations delayed boundary layer separation and also, to discern the flow field mechanisms by which the 20mm serrations degraded the flow field development at high test δ_f, most notably when the flap leading edge was positioned aft of the flat plate trailing edge.

5.4 Chapter Summary

10mm and 20mm 60° triangular serrations were implemented at the trailing edge of a flat plate upstream of a single slotted flap. A parametric study was conducted, varying the flap lap, gap and deflection angle. The resultant aerodynamic forces, obtained from the surface static pressure distributions and wake surveys, were compared to the corresponding plain trailing edge configuration. Evaluation of the data indicated:

- Influence of serrated geometries on the flow field developing over the single slotted flap was critically dependent upon flap lap/gap and δ_f
- In terms of increasing C_l and L/D, 20mm serrations were more favourable than the 10mm serrations, suggesting that the serration length was a critical parameter
- Both the 10mm and 20mm serrations were most effective in terms of increasing C_l and L/D at a flap lap/gap of (0, −0.07), although this did not correlate to the optimum flap lap/gap in terms of maximising the overall C_l or L/D
- At a lap/gap of (0, −0.07), the 10mm serrations increased C_l by 7-8% and L/D by 3-12% for all test δ_f, whereas the 20mm serrations increased C_l by 12-15% and increased L/D by 11-14% for $0° \leq \delta_f \leq 20°$
- For $\delta_f \leq 15°$, 20mm serrations typically increased C_l and L/D for any given test lap/gap
- 20mm serrations significantly heightened the severity of stall, particularly with the flap leading edge positioned aft of the flat plate trailing edge
- In terms of decreasing the profile drag, the 10mm serrations were more favourable than the 20mm serrations
- With the flap positioned at the lower lap test limit of −0.13, there was clear evidence of the favourable effect of serrated geometries upon boundary layer development at $\delta_f = 25°$, with both the 10mm and 20mm serrations preventing boundary layer separation over the upper surface of the single slotted flap aft of $0.5c_{flap}$ and promoting boundary layer attachment to within close proximity of the flap trailing edge
- Further studies are required to gain an understanding of the flow field mechanisms by which the serrations improve/degrade the boundary layer development

6 High-Lift Configuration: Trailing-Edge Serrations

This chapter considers the effect of implementing serrated geometries at the trailing edge of a main element on the resultant aerodynamic forces acting on a multi-element high lift configuration. Following preliminary investigations on two predefined configurations, a parametric study was conducted varying the flap lap, gap and deflection angle for each of the plain, 10mm and 20mm 60° triangular serrated trailing edge geometries. The serrated geometries were then evaluated by means of key aerodynamic parameters identified.

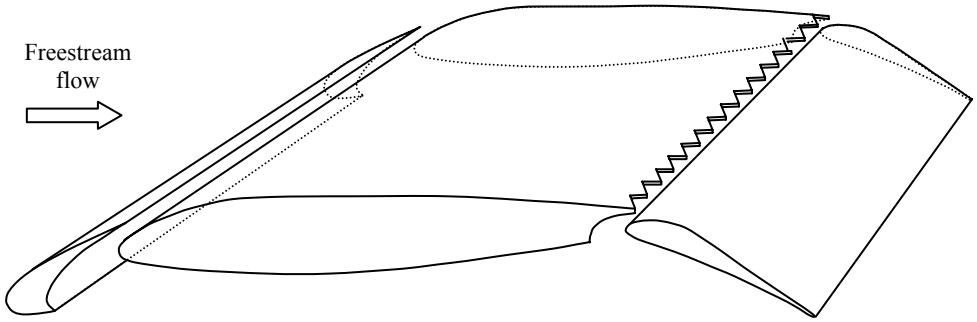

6.1 Takeoff Configuration

In the first instance, plain, 10mm or 20mm 60° triangular serrated geometries were implemented at the trailing edge of the main element of the takeoff configuration (see inset in schematic on page xiv for further details of serrated geometries).

By virtue of the predefined geometry, the 23° deflection angle of the leading edge slat and 38° deflection angle of the trailing edge flap determined the position of the fore and aft high-lift devices relative to the main element, such that the non-dimensional lap/gap was (−0.06, −0.23) and (−0.06, −0.11), respectively. With the lap, gap and deflection angle of the leading edge slat and trailing edge flap fixed, the angle of incidence of the high lift configuration was varied for each of the plain, 10mm and 20mm serrated trailing edge geometries. The flow field developing over the high lift configuration was subsequently analysed by means of the surface static pressure distributions and the resultant aerodynamic forces. Note that in this instance, only the pressure drag was determined. As a result, whilst the salient trends in L/D were noted, deviations in L/D due to the serrated geometries were not discussed in detail, as it was recognised that consideration of the pressure drag alone, obtained purely from the integration of the surface static pressure distribution, was insufficient to accurately evaluate the aerodynamic performance of the configuration in terms of L/D.

Basic oil flow visualisation, complemented by a small number of tufts, indicated that whilst boundary layer separation was induced by the end plates over the outboard span, the central third of the span was typically unaffected and thus, the flow field over which the subsequent measurements were attained was essentially two-dimensional. Free transition was maintained throughout on each of the three elements and unless otherwise stated, all experiments on the specified high-lift configuration were conducted at a nominal freestream velocity of 40m/s, corresponding to a Reynolds number of 1.64×10^6, based upon stowed reference chord.

6.1.1 Plain Trailing Edge

In the first instance, it was necessary to ascertain the effect of varying the configuration angle of incidence (α) on the surface static pressure distributions when the plain geometry was implemented at the trailing edge of the main element.

Figure 46 shows the non-dimensional static pressure coefficient (C_p) for the takeoff configuration at α=4°, 12° and 20°, with the plain trailing edge geometry implemented at the trailing edge of the main element. The C_p distributions indicated that increasing α from 0° to 20° had a marked effect upon the static pressure over the leading edge slat and the main element, although in contrast, the C_p distribution over the trailing edge flap appeared relatively insensitive to increments in α.

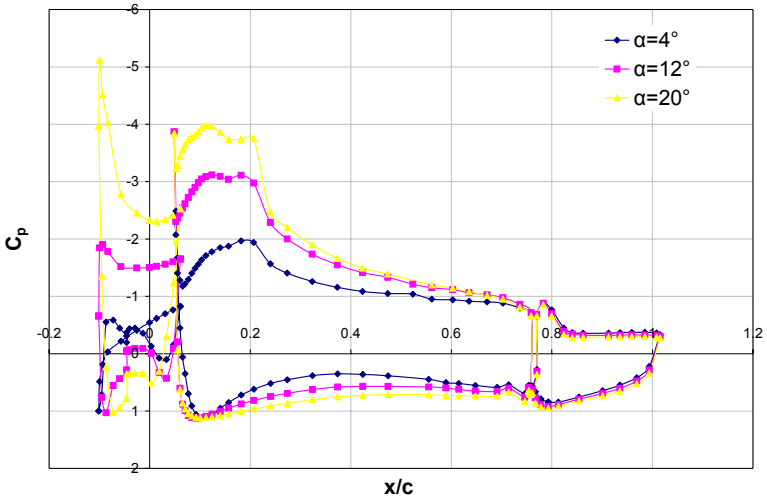

Figure 46: Effect of angle of incidence on C_p distribution for baseline takeoff configuration with plain trailing edge

Increasing α from 0° to 20° typically heightened the suction over the upper surface of the slat. This increment in suction was most prominent over the fore region of the upper surface and tended to decrease in magnitude with distance downstream. Over the lower

surface of the slat, increasing α transposed the stagnation point marginally aft. Upstream of the stagnation point and over the aft $0.25c_{slat}$ of the lower surface, the static pressure tended to progressively decrease in magnitude with successive increments in α between 0° to 20°. Conversely, for the lower surface region extending aft of the stagnation point to $0.75c_{slat}$, there was a tendency for the static pressure to increase in magnitude with successive increments in α. In particular, the flow field over the deployed leading edge slat significantly improved for $\alpha \geq 8°$.

With regard to the main element, the increment in suction over the upper surface was most evident over the fore $0.25c_{main}$, decreasing in magnitude with distance downstream such that any deviation in C_p due to α was essentially negated at the trailing edge. Over the lower surface of the main element, increasing α increased the C_p, both immediately upstream and aft of the stagnation point. Downstream of the stagnation point, the increment in C_p initially increased in magnitude, although aft of $0.4c_{main}$ the deviation in C_p due to α progressively decreased in magnitude, such that any deviation in C_p was essentially marginalised at the trailing edge.

Furthermore, for any given α, two distinct suction peaks were evident over the fore region of the upper surface C_p distribution for the main element. The first suction peak was located at the foremost point of the upper surface leading edge for all test α. The magnitude of the first suction peak was progressively heightened with increments in $\alpha \leq 8°$, although with subsequent increments in $8° \leq \alpha \leq 20°$, there was minimal variation in the magnitude. Despite the severity of the adverse pressure gradient immediately aft of the first suction peak, boundary layer attachment was maintained and the developing flow field gave rise to a second suction peak, which was progressively heightened in magnitude with successive increments in α. The location of the minimum pressure coefficient (C_{pmin}) for the second suction peak was sensitive to variations in α. At $\alpha = 8°$, a localised increase in static pressure was recorded at $0.15c_{main}$, which was heightened with successive increments in α, such that the location of C_{pmin} for the second suction peak was transposed upstream from approximately $0.2c_{main}$ to $0.1c_{main}$ for $14° \leq \alpha \leq 20°$. The first suction peak was attributed to the effect of the wake from the slat on the flow field developing over the fore region of the main element, whereas the second suction peak was primarily attributed to the geometry of the main element (Foster et al, 1970).

In contrast, Figure 46 indicated that increasing α had no appreciable effect upon the C_p distribution over the trailing edge flap, with marginal increments in the upper and lower surface static pressures hardly discernible between successive angles of incidence. The

C_p distributions indicated that boundary layer separation over the upper surface of the flap was independent of α, with the boundary layer separating at approximately $0.35c_{flap}$ for $0° \leq \alpha \leq 20°$.

Integration of the C_p distributions over the three-element aerofoil yielded the resultant aerodynamic forces acting upon the baseline takeoff configuration. From Figure 47 it was evident that the lift coefficient (C_l) increased approximately linearly with α for $2° \leq \alpha \leq 16°$. The non-linearity of the lift curve at $\alpha=0°$ was attributed to the substantial degradation of the flow field over the leading edge slat and main element, whereas the reduced lift-curve gradient for $\alpha>16°$ was characteristic of the onset of stall.

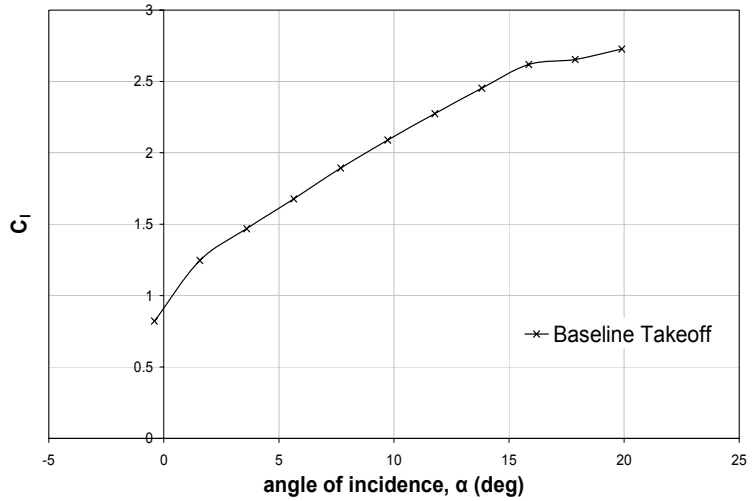

Figure 47: C_l-α curve for the baseline takeoff configuration

Figure 48 shows that for $0.8 \leq C_l \leq 1.8$, the drag coefficient (C_d) varied between 0.09 and 0.12 but for $C_l>1.8$, C_d increased substantially, attaining a value of 0.29 at a maximum lift coefficient of 2.7, coinciding with the maximum test α of 20°.

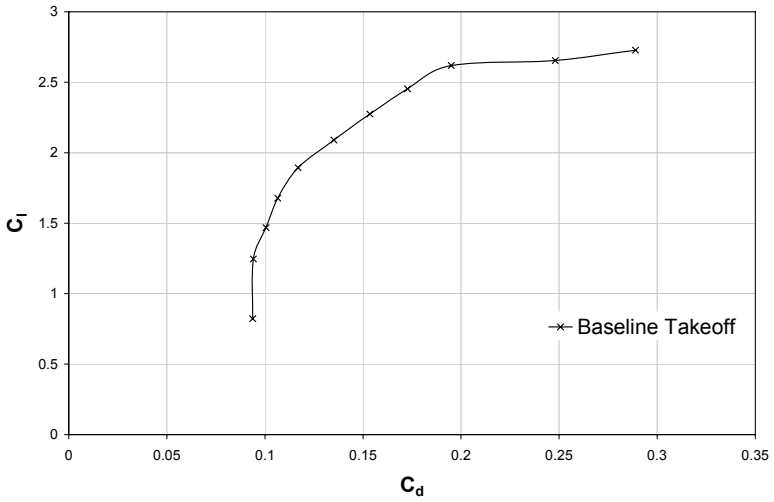

Figure 48: Drag polar for baseline takeoff configuration

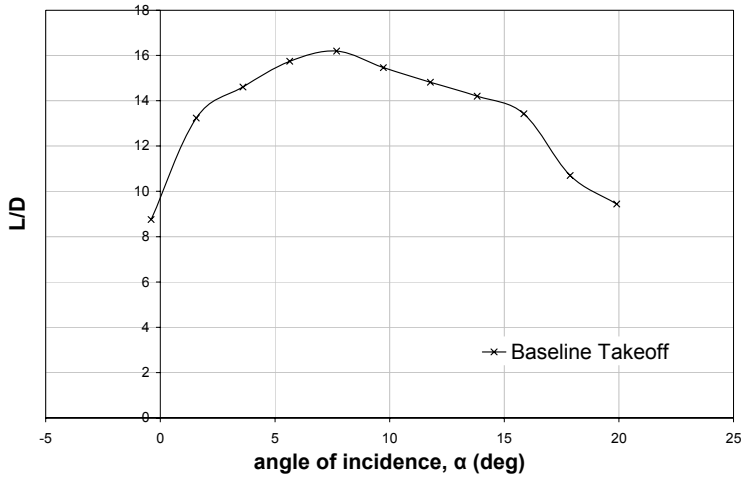

Figure 49: Variation of *L*/*D* with angle of incidence for baseline takeoff configuration

Accordingly, the lift-to-drag ratio (*L*/*D*) increased with successive angles of incidence, from 8.8 at α=0° to a maximum value of 16.2 at α=8°, see Figure 49. With subsequent increments in α, *L*/*D* progressively decreased in magnitude to 9.4 at α=20°, coinciding with the marked increase in C_d.

6.1.2 10mm Serrated Trailing Edge

The C_p distributions for the 10mm serrated takeoff configuration are shown in Appendix G for all angles of incidence tested. The corresponding C_p distributions for the plain and 20mm serrated takeoff configurations are also shown for comparative purposes at each angle of incidence.

Accordingly, Figure 176 in Appendix G showed that implementation of the 10mm serrations at the trailing edge of the main element modified the surface static pressure distributions developing over all three elements of the takeoff configuration when compared to the corresponding baseline configuration with the plain trailing edge. Specifically, whilst the 10mm serrations had no appreciable effect upon the C_p distribution over the leading edge slat for $\alpha \leq 4°$, the 10mm serrated geometry reduced the suction over the upper surface of the slat for $6° \leq \alpha \leq 16°$, with the decrement in suction progressively heightened with successive increments in $6° \leq \alpha \leq 14°$. At α=14°, the decrement in suction due to the 10mm serrations was notably heightened over the aft $0.4c_{slat}$, indicative of a marked decrease in trailing edge boundary layer thickness in comparison to the baseline configuration. With a further increment in α to 16°, the decrement in suction was marginalised and for $\alpha \geq 18°$, the 10mm serrations had negligible effect upon the C_p distribution over the leading edge slat.

At α=0°, the 10mm serrations reduced the suction over the upper surface of the main element and decreased the corresponding pressure over the lower surface in comparison to the baseline takeoff configuration. By increasing α to 2°, the decrement in suction over the upper surface was maintained, although the reduction in the lower surface pressure was limited to the fore $0.15c_{main}$. With further increments in $4° \leq \alpha \leq 16°$, the 10mm serrations continued to reduce the suction over the upper surface of the main element but had no appreciable effect upon the lower surface C_p distribution. For $\alpha \geq 18°$, the 10mm serrated geometry had negligible effect upon the C_p distribution over the main element and was coincident with that of the corresponding baseline takeoff configuration.

With regard to the trailing edge flap, the 10mm serrations tended to marginally heighten the suction over the fore $0.1c_{flap}$ and increase the lower surface C_p over the fore $0.2c_{flap}$, aft of which the pressure distribution was in agreement with the corresponding plain trailing edge configuration for all test α. The 10mm serrations had no appreciable effect upon the adverse pressure gradient immediately aft of the upper surface C_{pmin} at the flap leading edge and similarly to the plain trailing edge configuration, the boundary layer separated at $0.35c_{flap}$, irrespective of the specified α.

Similarly to the plain trailing edge configuration, Figure 50 below shows that the resultant lift coefficient for the 10mm serrated configuration increased approximately linearly with α for $2° \leq \alpha \leq 16°$, only becoming non-linear at low and high test α.

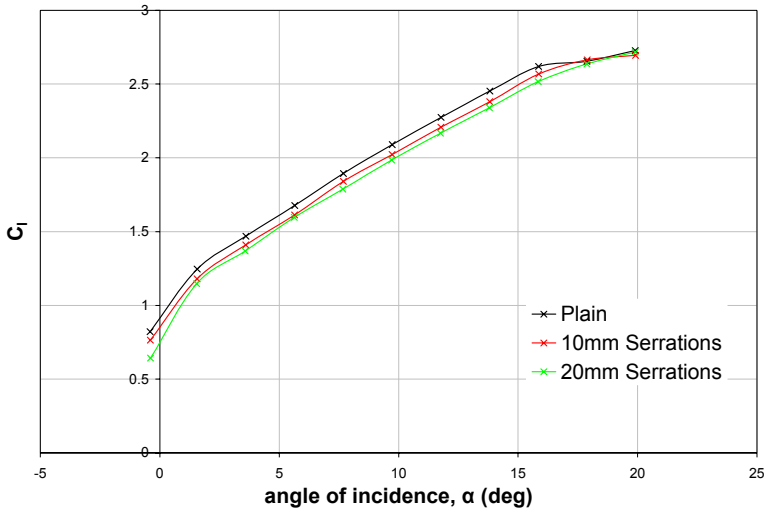

Figure 50: C_l-α curve for takeoff configuration with plain, 10mm and 20mm serrated trailing edges

In comparison to the baseline takeoff configuration, the 10mm serrations had a detrimental effect upon C_l for all test α, with the exception of α=18°. Clarified in Figure

51, it can be seen that for $0° \leq \alpha \leq 16°$, the decrement in C_l due to the 10mm serrations varied inconsistently between −0.05 and −0.07, although the corresponding percentage decrement tended to progressively decrease in magnitude from a maximum 7% decrement at α=0° to a 2% reduction in C_l at α=16°. Whilst the 10mm serrations increased C_l by 0.01 at α=18°, with a final increment in α to 20°, C_l was reduced by −0.03, correlating to a 1% decrement in comparison to the baseline takeoff configuration.

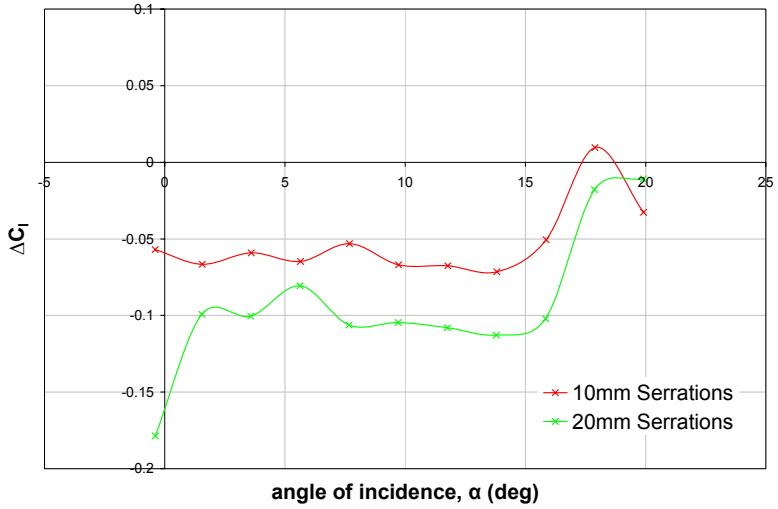

Figure 51: Variation of ΔC_l with angle of incidence due to 10mm and 20mm serrations, takeoff configuration

Similarly, direct comparison of the pressure drag for the 10mm serrated configuration at a specified α with the corresponding plain trailing edge configuration resulted in the incremental pressure drag coefficient (ΔC_d) due to the 10mm serrations, shown in Figure 52 below.

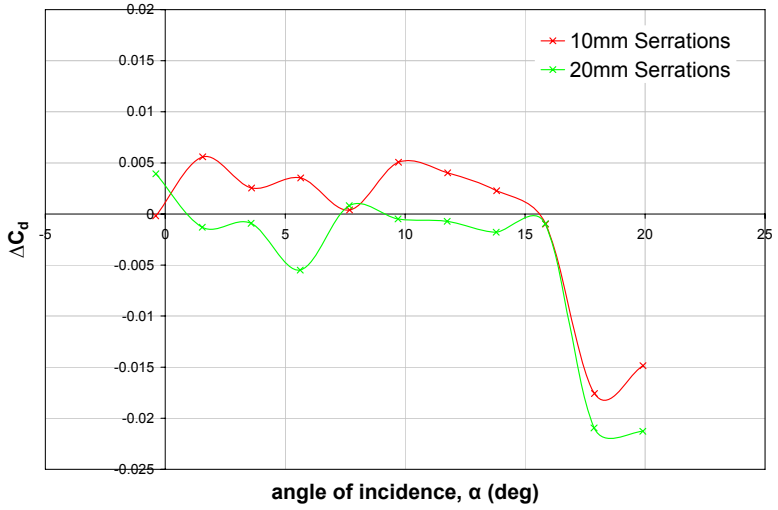

Figure 52: Variation of ΔC_d with angle of incidence due to 10mm and 20mm serrations, takeoff configuration

From Figure 52 it was evident that whilst the 10mm serrations had a near negligible effect upon the pressure drag at α=0°, with subsequent increments in 2°≤α≤14°, the 10mm serrated geometry had a detrimental effect upon C_d in comparison to the corresponding baseline takeoff configuration. The increment in C_d due to the 10mm serrations varied inconsistently between 0.002 and 0.005 for 2°≤α≤14°, with the corresponding percentage increment attaining a maximum value of 6% at α=2° and then varying between 1% and 3% for 4°≤α≤14°. Note that a discrepancy arose at α=8°, with ΔC_d near negligible in magnitude. Conversely, increments in 16°≤α≤20° indicated that the 10mm serrations were favourable. Although the decrement in C_d was less than 1% at α=16°, with a further increment in α to 18°, ΔC_d was heightened to −0.018, accounting for a 7% reduction in C_d in comparison to the corresponding baseline takeoff configuration. A final increment in α to 20° reduced ΔC_d to −0.015, representing a 5% reduction in C_d due to the 10mm serrations when compared to the baseline configuration.

The resultant drag polar indicated that the 10mm serrations typically increased the pressure drag in comparison to the plain trailing edge takeoff configuration for any given C_l≤2.6, see Figure 53.

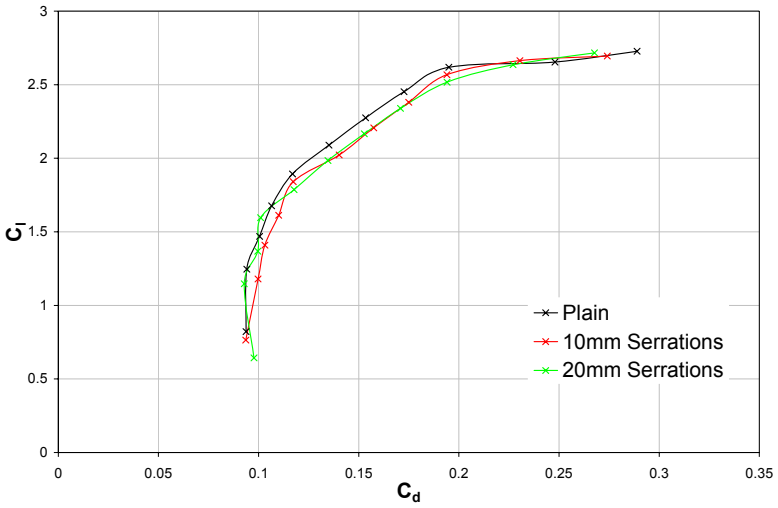

Figure 53: Drag polar for takeoff configuration with plain, 10mm and 20mm serrated trailing edges

Finally, Figure 54 shows the variation of L/D with α for the 10mm serrated configuration in comparison to the corresponding baseline configuration. From Figure 54 it was evident that similarly to the baseline configuration, L/D increased with successive increments in α from 8.2 at α=0° to a maximum value of 15.7 at α=8°. With subsequent increments in α≥10°, L/D progressively decreased in magnitude, attaining a value of 9.8 at α=20°. Direct comparison of the 10mm serrated takeoff configuration

with the plain trailing edge takeoff configuration indicated that the decrement in C_l due to the 10mm serrations, together with the corresponding increment in C_d, typically rendered the 10mm serrations detrimental to L/D in comparison to the baseline takeoff configuration for $0° \leq \alpha \leq 16°$. However, isolated discrepancies arose for $\alpha \geq 18°$, with the decrement in pressure drag offsetting the corresponding decrement in C_l due to the 10mm serrations and increasing L/D in comparison to the baseline takeoff configuration.

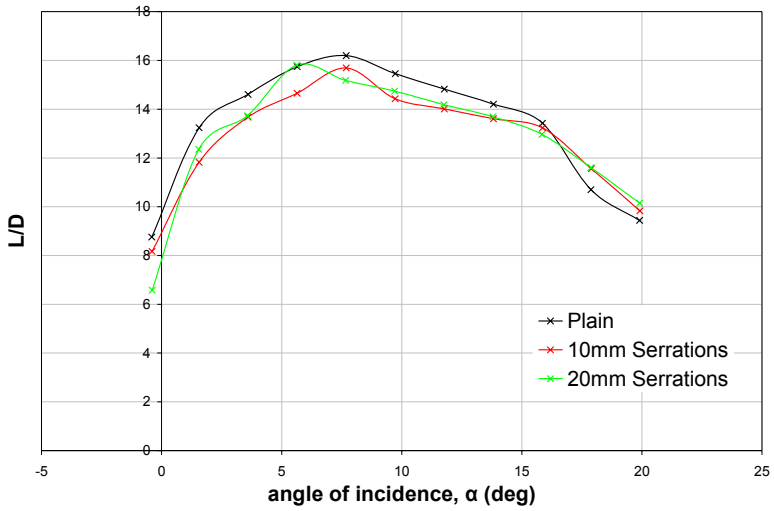

Figure 54: Variation of *L*/*D* with angle of incidence for takeoff configuration with plain, 10mm and 20mm serrated trailing edges

6.1.3 20mm Serrated Trailing Edge

Appendix G displays the C_p distributions for the 20mm serrated takeoff configuration for all angles of incidence tested. Accordingly, Figure 176 in Appendix G showed that similarly to the 10mm serrations, implementation of the 20mm serrations at the trailing edge of the main element modified the surface static pressure distributions developing over all three elements of the takeoff configuration when compared to the corresponding baseline configuration with the plain trailing edge.

Specifically, the effect of the 20mm serrations upon the C_p distribution over the leading edge slat was analogous to that of the 10mm serrations. Hence, the 20mm serrations had negligible effect upon the C_p distribution over the leading edge slat for $\alpha \leq 4°$. However, the 20mm serrated geometry reduced the suction over the upper surface of the slat in comparison to the plain trailing edge takeoff configuration for $6° \leq \alpha \leq 16°$. For any given α, the magnitude of the decrement in suction due to the 20mm serrations

exceeded that due to the 10mm serrations. The decrement in suction due to the 20mm serrations was progressively heightened with successive increments in $6° \leq \alpha \leq 14°$, with the most prominent reduction in upper surface suction occurring over the aft $0.4c_{slat}$ at $\alpha=14°$. With a further increment in α to 16°, the decrement in suction was marginalised and for $\alpha \geq 18°$, the 20mm serrations had no appreciable effect upon the C_p distribution over the leading edge slat.

Similarly, the effect of the 20mm serrations upon the C_p distribution over the main element was comparable to that observed for the 10mm serrations, although the increment in serration length from 10mm to 20mm heightened the decrement in suction for any given α. At $\alpha=0°$, the 20mm serrations notably reduced the suction over the upper surface of the main element and decreased the corresponding pressure over the lower surface in comparison to the baseline takeoff configuration. By increasing α to 2°, the decrement in suction over the upper surface was maintained, although the decrement in the lower surface static pressure was limited to the fore $0.15c_{main}$. With further increments in α, the 20mm serrations continued to reduce the suction over the upper surface of the main element but had no appreciable effect upon the lower surface C_p distribution. Furthermore, the range of α over which the 20mm serrations reduced the upper surface suction was extended to 18° and hence, only at the upper test limit of $\alpha=20°$ was the C_p distribution over the main element of the 20mm serrated configuration coincident with that of the corresponding baseline and 10mm serrated takeoff configurations.

With regard to the trailing edge flap, the 20mm serrations tended to decrease the upper surface C_p over the fore $0.1c_{flap}$ and increase the lower surface C_p over the fore $0.2c_{flap}$, aft of which the pressure distribution was in agreement with both the corresponding plain and 10mm serrated trailing edge takeoff configurations for $2° \leq \alpha \leq 20°$. Once again, ΔC_p due to the 20mm serrations exceeded that for the 10mm serrated configuration. In addition, two distinct leading edge suction peaks were evident for $2° \leq \alpha \leq 10°$, the second smaller in magnitude than the first. The first suction peak was attributed to the wake from the main element influencing the flow field developing over the fore region of the flap, whereas the second suction peak was primarily attributed to the flap geometry (Foster et al, 1970). With successive increments in $\alpha \geq 12°$, the distinction between the two leading edge suction peaks over the upper surface of the flap was diminished, forming a single suction peak at the upper surface leading edge. Aft of $0.1c_{flap}$, the 20mm serrations had no appreciable effect upon the adverse pressure gradient and similarly to the plain and 10mm serrated trailing edge configurations, the boundary

layer over the upper surface of the flap separated at $0.35c_{flap}$ for $2° \leq \alpha \leq 20°$. The exception to these trends arose at $\alpha=0°$, whereby the 20mm serrations markedly heightened the upper surface suction over the fore $0.6c_{flap}$ and delayed separation to the aft $0.4c_{flap}$ in comparison to both the plain and 10mm serrated configurations. Note that the magnitude of C_{pmin} was marginally diminished. On the lower surface of the flap, the 20mm serrations substantially decreased the pressure at $\alpha=0°$, with the magnitude of the decrement marginalised with distance downstream, such that any deviation in C_p due to the 20mm serrations was negated at the trailing edge.

Figure 50 shows that similarly to the plain and 10mm serrated trailing edge takeoff configurations, the resultant lift coefficient for the 20mm serrated takeoff configuration increased approximately linearly with α for $2° \leq \alpha \leq 16°$, only becoming non-linear at low and high test α. From Figure 51, it was evident that the 20mm serrations had a detrimental effect upon C_l for all test α when compared to the baseline takeoff configuration. Furthermore, it was noted that the magnitude of the decrement due to the 20mm serrations exceeded the corresponding decrement in C_l due to the 10mm serrations for all $\alpha \leq 18°$. The decrement in C_l due to the 20mm serrations was greatest at $\alpha=0°$, decreasing C_l by -0.18 and accounting for a 22% reduction in comparison to the corresponding baseline takeoff configuration. With subsequent increments in $2° \leq \alpha \leq 16°$, ΔC_l varied inconsistently between -0.08 and -0.11, although the corresponding percentage decrement tended to decrease in magnitude from an 8% decrement at $\alpha=2°$ to a 4% reduction in C_l at $\alpha=16°$. At $\alpha=18°$ and 20°, ΔC_l was minimised to -0.02 and -0.01, respectively, representing less than a 1% reduction in C_l in comparison to the corresponding baseline takeoff configuration.

Direct comparison of the pressure drag for the 20mm serrated takeoff configuration with the corresponding baseline configuration showed that whilst the 20mm serrations increased C_d by 0.004 at $\alpha=0°$, equating to a 4% increment in comparison to the baseline configuration, with further increments in $\alpha \geq 2°$, the 20mm serrations tended to reduce C_d, see Figure 52. For $2° \leq \alpha \leq 16°$, the decrement in C_d due to the 20mm serrations varied inconsistently between -0.001 and -0.002 but as this accounted for less than a 1% reduction in C_d in comparison to the baseline configuration and the measurements were repeatable to within ±1%, the deviation in pressure drag due to the 20mm serrations was deemed near negligible. Two isolated discrepancies arose: at $\alpha=6°$, the decrement was heightened to -0.006, correlating to a 5% reduction in C_d and at $\alpha=8°$, the decrement in C_d was negated. It was not known whether this heightened decrement was due to a feature in the flow field or experimental error. With subsequent

increments in $\alpha \geq 18°$, the 20mm serrations decreased C_d by −0.021, which equated to a 7-8% reduction in C_d in comparison to the baseline takeoff configuration. Accordingly, the drag polar in Figure 53 showed that in comparison to the baseline takeoff configuration, the 20mm serrations increased the pressure drag for any given $C_l \leq 2.6$. However, an isolated discrepancy arose at a C_l of 1.6, coinciding with the marked decrement in C_d at $\alpha=6°$.

From Figure 54 it was evident that L/D increased with successive increments in α from 6.6 at $\alpha=0°$ to a maximum of 15.8 at $\alpha=6°$. Note that in comparison to both the plain and 10mm serrated trailing edge takeoff configurations, the 20mm serrations reduced the α at which the maximum L/D occurred from $\alpha=8°$ to $\alpha=6°$. With subsequent increments in $\alpha \geq 8°$, L/D progressively decreased in magnitude to a value of 10.1 at $\alpha=20°$. Despite the decrement in C_d due to the 20mm serrations, it was insufficient to offset the corresponding decrement in C_l for $0° \leq \alpha \leq 16°$, typically rendering the 20mm serrations detrimental to L/D in comparison to the baseline takeoff configuration. Similarly to the 10mm serrated takeoff configuration, isolated discrepancies arose for $\alpha \geq 18°$, with the heightened decrement in pressure drag offsetting the corresponding decrement in C_l due to the 20mm serrations, increasing L/D in comparison to the baseline takeoff configuration.

6.1.4 Summary for Takeoff Configuration

As a result of implementing 10mm or 20mm 60° triangular serrated geometries at the trailing edge of the main element upstream of a single slotted flap in a three-element high-lift takeoff configuration, it was concluded that:

- Serrated geometries had negligible effect upon the point of boundary layer separation on the upper surface of the flap, with only an isolated exception for the 20mm serrations at $\alpha=0°$
- Both 10mm and 20mm serrations typically had a detrimental effect upon C_l
- Increasing serration length from 10mm to 20mm heightened the decrement in C_l
- 10mm serrations increased the pressure drag for $2° \leq \alpha \leq 14°$ by up to 6%
- 20mm typically had a near negligible effect upon the pressure drag for $2° \leq \alpha \leq 16°$

6.2 Landing Configuration

Evaluation of the surface static pressure distribution developing over a high-lift configuration, as a result of implementing 10mm or 20mm serrations at the trailing edge of the main element, was extended to include analysis of the landing configuration.

The predefined geometry for the landing configuration, comprising a 27° leading edge slat and a 48° trailing edge flap, determined the position of the fore and aft elements relative to the main element such that the non-dimensional lap/gap was (0.04, −0.17) and (0, −0.13), respectively. Thus with the lap, gap and deflection angle of the leading edge slat and trailing edge flap fixed, the angle of incidence of the high lift configuration was varied for each of the plain, 10mm and 20mm serrated trailing edge geometries. The flow field developing over the landing configuration was subsequently analysed by means of the surface static pressure distributions and the resultant aerodynamic forces. Note that once again, only the pressure drag was determined. As a result, whilst the salient trends in L/D were noted, deviations in L/D due to the serrated geometries were not discussed in detail as it was recognised that consideration of the pressure drag alone, obtained purely from the integration of the surface static pressure distribution, was insufficient to accurately evaluate the aerodynamic performance of the configuration in terms of L/D.

Similarly to the takeoff configuration, basic oil flow visualisation, complemented by a small number of tufts, indicated that whilst boundary layer separation was induced by the end plates over the outboard span, the central third of the span was typically unaffected. Thus, the flow field over which the subsequent measurements were attained was essentially two-dimensional. Free transition was maintained throughout on each of the three elements and unless otherwise stated, all experiments on the specified high-lift configuration were conducted at a nominal freestream velocity of $40m/s$, corresponding to a Reynolds number of 1.64×10^6, based upon stowed reference chord.

6.2.1 Plain Trailing Edge

In the first instance, it was necessary to ascertain the effect of varying the configuration angle of incidence on the surface static pressure distributions, when the plain geometry was implemented at the trailing edge of the main element.

Figure 55 shows the C_p distribution for the landing configuration at α=4°, 12° and 20°, with the plain trailing edge geometry implemented at the trailing edge of the main

element. The effect of incrementing α from 0° to 20° on the C_p distribution over the baseline landing configuration was analogous to that identified for the baseline takeoff configuration.

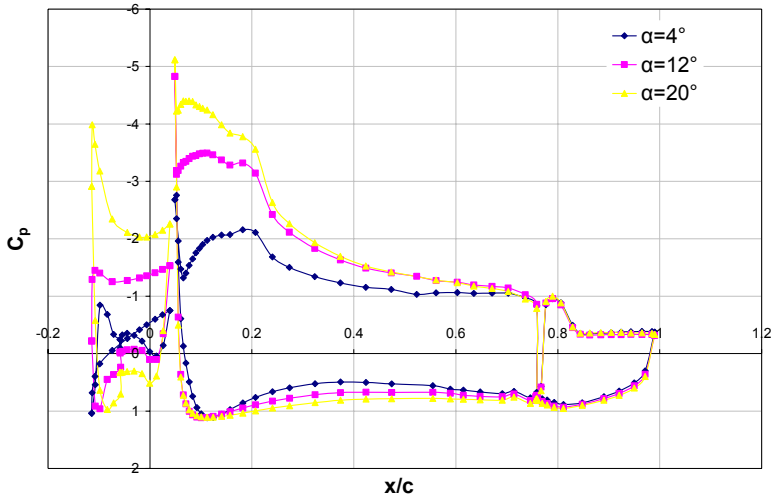

Figure 55: Effect of angle of incidence on C_p distribution for baseline landing configuration with plain trailing edge

However, two exceptions were noted. Firstly, the second suction peak developing over the upper surface of the main element, whilst progressively heightened in magnitude with successive increments in α, was more sensitive to variations in α than that previously identified for the baseline takeoff configuration. In particular, it was noted that due to the localised increase in static pressure at $0.15c_{main}$ for $\alpha \geq 8°$, the location of the measured C_{pmin} was transposed upstream from $0.2c_{main}$ for $\alpha \leq 8°$ to $0.1c_{main}$ for $10° \leq \alpha \leq 14°$. With subsequent increments in $\alpha \geq 16°$, C_{pmin} was transposed progressively further upstream such that at $\alpha=20°$, the measured C_{pmin} for the second suction peak was located at $0.05c_{main}$. Thus, whilst Foster et al (1970) noted that the second suction peak was primarily attributed to the geometry of the main element, comparison of the takeoff and landing configurations suggested that the slat lap/gap and/or developing wake from the leading edge slat also influenced the second suction peak, particularly the location of the local C_{pmin}. Secondly, the point of boundary layer separation over the upper surface of the trailing edge flap was delayed to approximately $0.4c_{flap}$ for the landing configuration, although similarly to the takeoff configuration, this appeared to be relatively insensitive to variations in α.

Figure 56 shows that the resultant lift coefficient increased approximately linearly with α for $2° \leq \alpha \leq 16°$. The non-linearity of the lift curve at $\alpha=0°$ was attributed to the

substantial degradation of the flow field over the leading edge slat and main element, whereas the reduced lift-curve gradient for $\alpha \geq 18°$ was characteristic of the onset of stall.

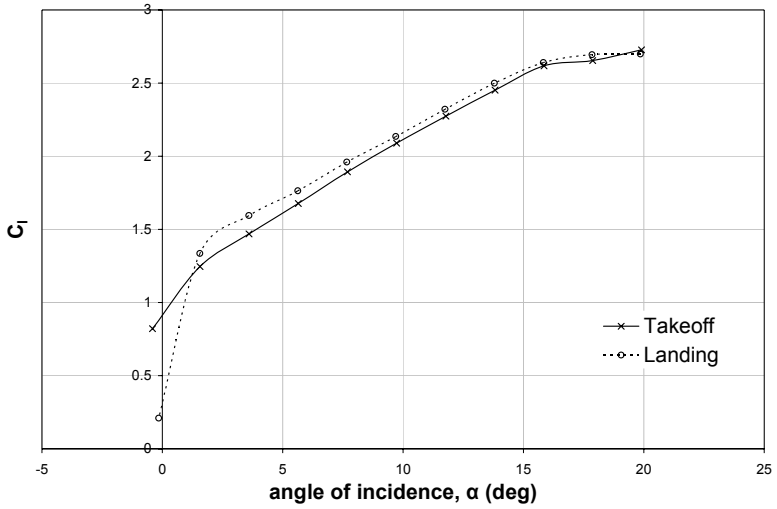

Figure 56: Comparison of C_l-α curves for baseline takeoff and baseline landing configurations

Furthermore, Figure 56 showed that in comparison to the baseline takeoff configuration, the degradation in the flow field at $\alpha=0°$ was substantially heightened for the baseline landing configuration, resulting in a significant loss in lift by comparison. For $2° \leq \alpha \leq 18°$, the magnitude of C_l for the baseline landing configuration exceeded that of the corresponding baseline takeoff configuration. Although for $\alpha \geq 10°$, the increment in C_l due to the increased leading-edge slat and trailing-edge flap deflection angles of the landing configuration accounted for less than a 2% increment in lift in comparison to the corresponding baseline takeoff configuration. At the upper test limit of $\alpha=20°$, the resultant C_l for the baseline landing configuration was comparable to that of the corresponding baseline takeoff configuration.

Figure 57 shows that whilst C_d for the baseline landing configuration varied between 0.15 and 0.16 for $1.3 \leq C_l \leq 2$, C_d markedly increased for increments in $C_l > 2$, attaining a value of 0.33 at a maximum lift coefficient of 2.7, coinciding with the maximum test α of 20°. Furthermore, for any given C_l over a comparable range, the landing configuration notably heightened the corresponding pressure drag in comparison to the takeoff configuration, although the disparity between the two configurations was reduced at high C_l for $2.6 \leq C_l \leq 2.9$.

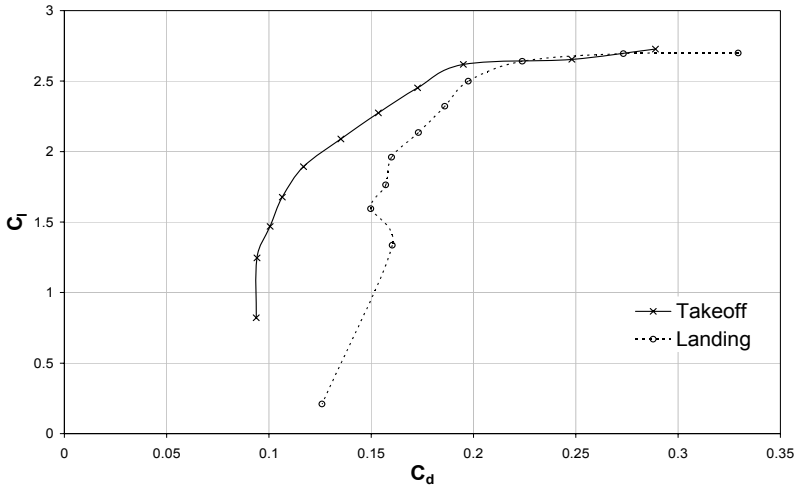

Figure 57: Drag polar for baseline takeoff and baseline landing configurations

Figure 58 shows that for the baseline landing configuration, L/D increased in magnitude with successive increments in $\alpha \leq 14°$, from 1.7 at $\alpha=0°$ to a maximum value of 12.7 at $\alpha=14°$. With subsequent increments in $\alpha \geq 16°$, L/D decreased in magnitude to 8.2 at $\alpha=20°$.

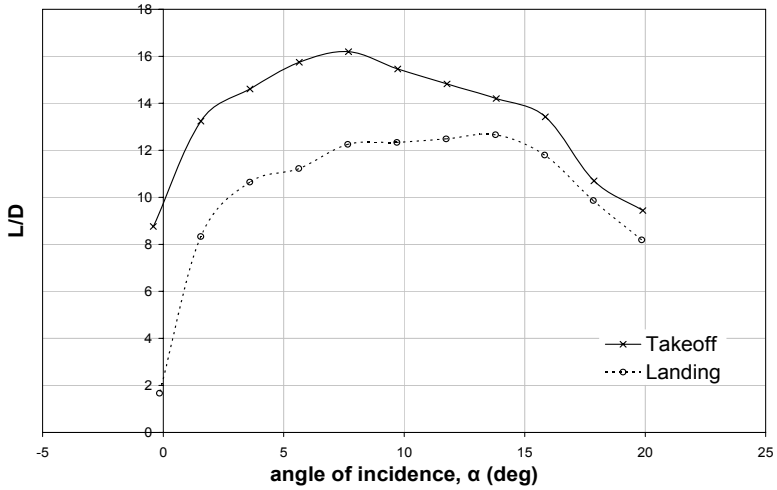

Figure 58: Variation of L/D with angle of incidence for baseline takeoff and baseline landing configurations

Furthermore, Figure 58 showed that the L/D for the baseline takeoff configuration exceeded that of the corresponding baseline landing configuration for all test α.

6.2.2 10mm Serrated Trailing Edge

The C_p distributions for the 10mm serrated landing configuration are shown in Appendix H for all angles of incidence tested. The corresponding C_p distributions for

the plain and 20mm serrated takeoff configurations at a given angle of incidence are also shown for comparative purposes.

Accordingly, Figure 177 in Appendix H showed that implementation of the 10mm serrations at the trailing edge of the main element modified the surface static pressure distributions developing over all three elements of the landing configuration.

Whilst the 10mm serrations had no appreciable effect upon the C_p distribution over the leading edge slat for $\alpha \leq 6°$, the 10mm serrated geometry reduced the suction over the upper surface of the slat for $8° \leq \alpha \leq 14°$, although increments in α appeared to have no appreciable effect upon the magnitude of the decrement. At $\alpha=16°$, the decrement in suction due to the 10mm serrations was limited to the aft $0.4c_{slat}$. With further increments in $\alpha \geq 18°$, the 10mm serrations had negligible effect upon the C_p distribution over the leading edge slat. The 10mm serrations had no appreciable effect upon the lower surface C_p distribution for all test α.

At $\alpha=0°$, the 10mm serrations had no appreciable effect upon the C_p distribution over the main element. Incrementing α to 2° reduced the suction over the upper surface of the main element and decreased the lower surface pressure over the fore $0.3c_{main}$. With further increments in $4° \leq \alpha \leq 16°$, the 10mm serrations continued to reduce the suction over the upper surface of the main element in comparison to the baseline configuration but any influence of the 10mm serrations upon the lower surface C_p distribution was negated. At $\alpha=18°$, the 10mm serrated geometry had negligible effect upon the C_p distribution over the main element and was coincident with that of the corresponding baseline landing configuration. However, a final increment in α to 20° resulted in the 10mm serrations heightening the suction over the fore $0.2c_{main}$ of the main element upper surface, aft of which, the C_p distribution was comparable to baseline configuration. Similarly to the configurations for $4° \leq \alpha \leq 16°$, the 10mm serrations had negligible effect upon the C_p distribution over the lower surface of the main element for $18° \leq \alpha \leq 20°$.

With regard to the trailing edge flap, the 10mm serrations tended to marginally heighten the suction over the fore $0.2c_{flap}$ of the upper surface and increase the pressure over the fore $0.25c_{flap}$ of the lower surface, aft of which the C_p distribution was essentially in agreement with the corresponding baseline landing configuration. The magnitude of ΔC_p appeared relatively insensitive to variations in α. The 10mm serrations had no appreciable effect upon the adverse pressure gradient immediately aft of the minimum

pressure at the leading edge of flap upper surface and similarly to the plain trailing edge configuration, the boundary layer separated at $0.4c_{flap}$, irrespective of the specified α.

Similarly to the plain trailing edge configuration, Figure 59 shows that the resultant lift coefficient for the 10mm serrated configuration increased approximately linearly with α for $2° \leq \alpha \leq 16°$, only becoming non-linear at low and high test α.

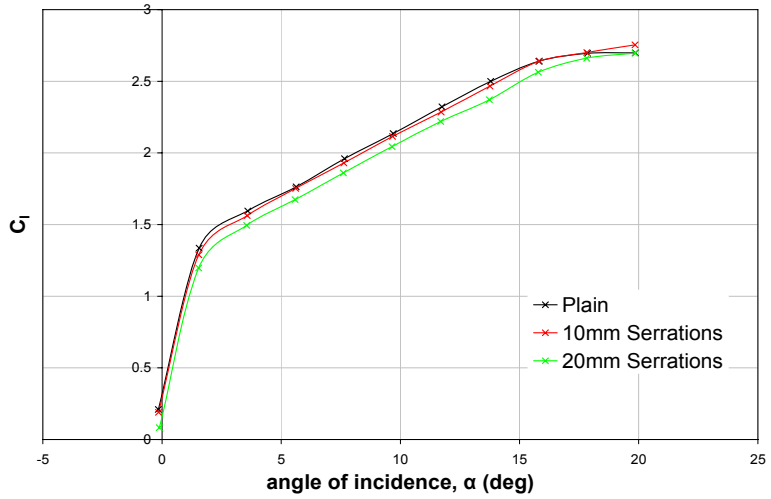

Figure 59: C_l-α curve for landing configuration with plain, 10mm and 20mm serrated trailing edges

In comparison to the baseline landing configuration, the 10mm serrations had a detrimental effect upon C_l for all test $\alpha \leq 16°$.

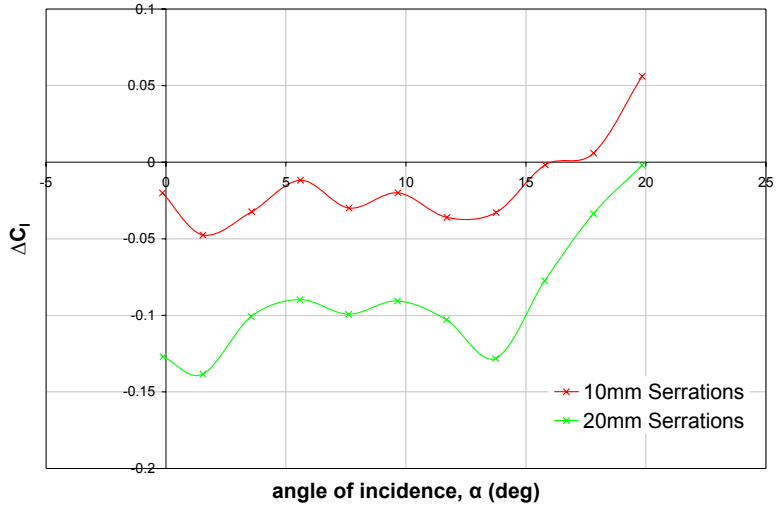

Figure 60: Variation of ΔC_l with angle of incidence due to 10mm and 20mm serrations, landing configuration

Clarified in Figure 60 above, it can be seen that for $0° \leq \alpha \leq 14°$, the decrement in C_l due to the 10mm serrations varied inconsistently between −0.01 and −0.05. The

corresponding percentage decrement decreased from a maximum of 10% at α=0° to a 4% decrement at α=2° and with further increments in 4°≤α≤14°, ΔC_l accounted for ≤2% reduction in comparison to the baseline landing configuration. Whilst the 10mm serrations had no appreciable effect upon C_l at α=16°, a marginal increment in C_l was evident at α=18°, which was heightened to a ΔC_l of 0.06 at α=20°, representing a 2% increment in comparison to the baseline landing configuration.

Similarly, direct comparison of the pressure drag for the 10mm serrated configuration at a specified α, with the corresponding plain trailing edge configuration, resulted in the incremental pressure drag coefficient (ΔC_d) due to the 10mm serrations, shown in Figure 61 below.

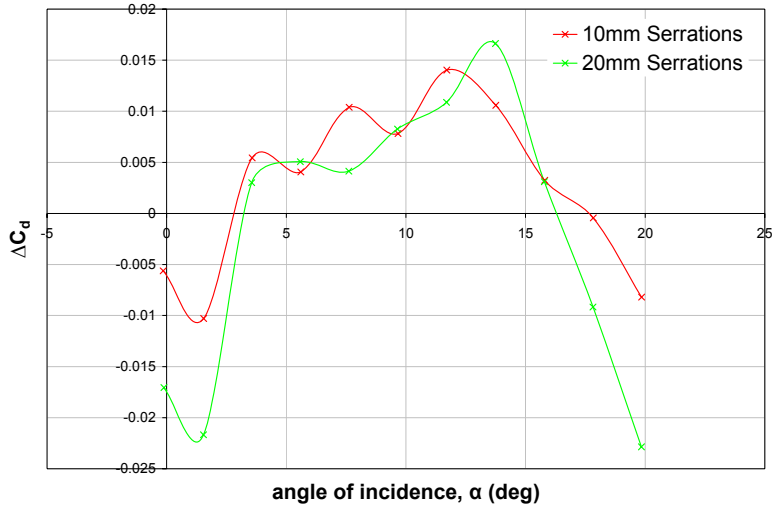

Figure 61: Variation of ΔC_d with angle of incidence due to 10mm and 20mm serrations, landing configuration

From Figure 61 it was evident that whilst the 10mm serrations had a favourable effect upon C_d for α≤2° and α≥18°, the 10mm serrated geometry increased C_d in comparison to the baseline landing configuration for 4°≤α≤16°. Specifically, the 10mm serrations reduced C_d by −0.006 at α=0°, which was heightened to −0.01 at α=2°, corresponding to a 4% and 6% reduction, respectively, in comparison to the baseline landing configuration. With further increments in α≤12°, ΔC_d varied inconsistently between 0.004 and a maximum of 0.014, accounting for a 3-8% increment in C_d due to the 10mm serrations. Although with further increments in 14°≤α≤16°, ΔC_d progressively decreased in magnitude to 0.003 at α=16°, equating to a 1% increment in comparison to the baseline landing configuration. With subsequent increments in α≥18°, the 10mm serrations progressively heightened the decrement in C_d due to the 10mm serrations from a near negligible effect at α=18° to −0.008 at α=20°, correlating to a 2% decrement in C_d in comparison to the corresponding baseline landing configuration.

The drag polar in Figure 62 indicated that, whilst the 10mm serrations reduced C_d in comparison to the baseline configuration for a given $C_l \leq 1.5$, with subsequent increments in C_l, the 10mm serrations increased C_d in comparison to the corresponding plain trailing edge configuration, although a marginal decrement in C_d due to the 10mm serrations was evident near C_{lmax}.

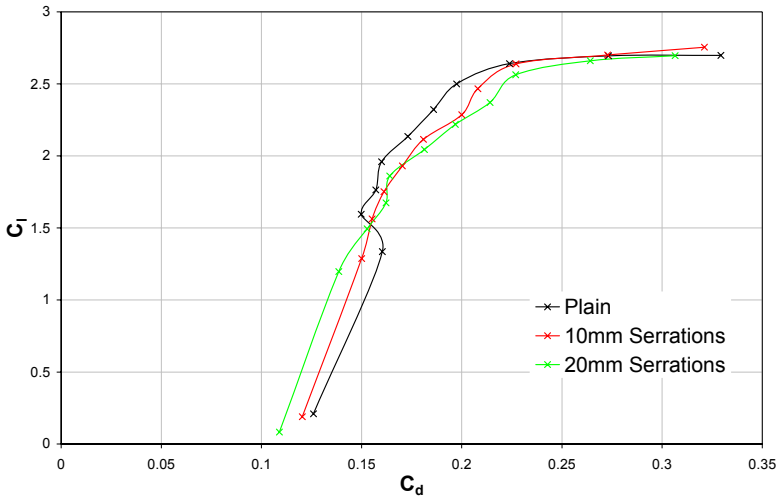

Figure 62: Drag polar for landing configuration with plain, 10mm and 20mm serrated trailing edges

Finally, Figure 63 shows the variation of L/D with α for the 10mm serrated configuration in comparison to the corresponding baseline landing configuration.

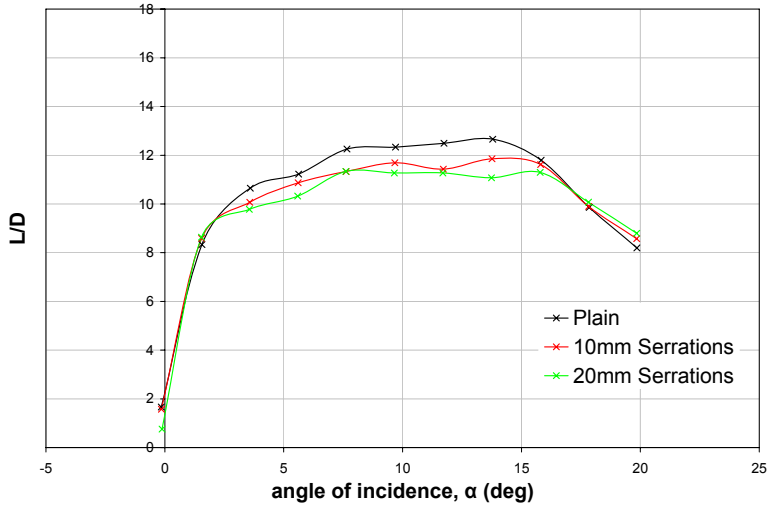

Figure 63: Variation of L/D with angle of incidence for landing configuration with plain, 10mm and 20mm serrated trailing edges

From Figure 63 it was evident that similarly to the baseline configuration, L/D tended to increase with successive increments in α, from 1.6 at α=0° to a maximum value of 11.9 at α=14°. With subsequent increments in α, L/D progressively decreased in magnitude,

attaining a value of 8.6 at α=20°. Note that the decrement in C_l due to the 10mm serrations, together with the corresponding increment in C_d, rendered the 10mm serrations detrimental to L/D in comparison to the baseline landing configuration for 4°≤α≤16°. For α≤2°, the decrement in C_d due to the 10mm serrations offset the corresponding decrement in C_l to increase L/D in comparison to the baseline configuration and for α≥18°, the favourable effect of the 10mm serrations upon both C_l and C_d also resulted in an increment in L/D in comparison to the baseline landing configuration.

6.2.3 20mm Serrated Trailing Edge

Appendix H displays the C_p distributions for the 20mm serrated landing configuration for all angles of incidence tested. Accordingly, Figure 177 in Appendix H shows that similarly to the 10mm serrations, implementation of the 20mm serrations at the trailing edge of the main element modified the surface static pressure distributions developing over all three elements of the landing configuration.

Similarly to the 10mm serrated configuration, the 20mm serrations had no appreciable effect upon the C_p distribution over the leading edge slat for α≤4° but increasing the serration length extended the range of α over which a decrement in the upper surface suction was evident. Accordingly, the 20mm serrated geometry reduced the suction over the upper surface of the slat for 6°≤α≤16°. Although increments in α appeared to have no appreciable effect upon the magnitude of the decrement in suction, increasing the serration length from 10mm to 20mm heightened the magnitude of the decrement for any given α. At α=18°, the decrement in suction due to the 20mm serrations was limited to the aft 0.4c_{slat} and with a final increment in α to 20°, the 20mm serrations had negligible effect upon the C_p distribution over the leading edge slat when compared to the baseline landing configuration.

For the main element of the landing configuration, the 20mm serrations reduced the suction over the upper surface for all 0°≤α≤18° in comparison to the baseline configuration, with the increment in serration length from 10mm to 20mm heightening the decrement in suction for any given α. A final increment in α to 20° essentially negated any deviation in the upper surface C_p distribution arising from the presence of the 20mm serrations, although a marginal decrement in suction was still evident over the mid-chord region. Over the lower surface of the main element, the 20mm serrations reduced the pressure in comparison to the baseline landing configuration at α=0°,

although with further increments in α to 2° and 4°, the decrement in lower surface pressure was limited to the fore $0.4c_{main}$ and $0.15c_{main}$, respectively. Further increments in $6° \leq \alpha \leq 20°$ negated any effect of the 20mm serrations on the lower surface C_p distribution, which was thus comparable to baseline configuration.

However, it was over the trailing edge flap that the influence of the 20mm serrations on the C_p distribution was most notable. For all test α, the 20mm serrations tended to heighten the suction over the fore $0.1c_{flap}$ of the flap upper surface in comparison to the baseline landing configuration, yet reduce the suction between $0.1c_{flap}$ and $0.3c_{flap}$. For $\alpha \leq 12°$, the upper surface C_p distribution for the 20mm serrated landing configuration was essentially coincident with the corresponding baseline configuration aft of $0.4c_{flap}$, indicating the 20mm had no appreciable effect upon the point of upper surface boundary layer separation. However for $\alpha \geq 14°$, the upper surface C_p distributions suggested that the 20mm serrations marginally delayed the point of separation from $0.4c_{flap}$ to $0.5c_{flap}$ in comparison to the baseline configuration, although it was unclear why the 20mm serrations proved favourable with regard to the point of boundary layer separation for $\alpha \geq 14°$. Over the lower surface of the flap, the 20mm serrations typically increased the pressure over the fore $0.25c_{flap}$ for all test α, aft of which, the C_p distribution was in agreement with the corresponding plain trailing edge configuration.

Similarly to the plain and 10mm serrated configurations, Figure 59 showed that the resultant lift coefficient for the 20mm serrated configuration increased approximately linearly with α for $2° \leq \alpha \leq 16°$, only becoming non-linear at low and high test α. From Figure 60 it was evident that in comparison to the baseline landing configuration, the 20mm serrations had a detrimental effect upon C_l for all test α. Furthermore, increasing the serration length from 10mm to 20mm heightened the decrement in C_l. At α=0°, the 20mm serrations decreased C_l by −0.13, accounting for a 60% decrement in comparison to the baseline landing configuration. Increasing α to 2° heightened the decrement in C_l to a maximum −0.14, corresponding to a 10% reduction. With further increments in $4° \leq \alpha \leq 14°$, the decrement in C_l varied inconsistently between −0.09 and −0.13, equating to a 4-6% reduction in C_l in comparison to the baseline configuration. However, ΔC_l progressively decreased in magnitude for $\alpha \geq 16°$, such that at α=20°, any variation in C_l due to the 20mm serrations was essentially negated.

Figure 61 indicated that the influence of the 20mm serrations upon C_d was comparable to the 10mm serrated geometry, decreasing C_d for $\alpha \leq 2°$ and $\alpha \geq 18°$ but increasing C_d for $4° \leq \alpha \leq 16°$ when compared to the plain trailing edge landing configuration. The

decrement in C_d due to the 20mm serrations was heightened from −0.017 at α=0° to −0.022 at α=2°, accounting for a 14% reduction in comparison to the baseline landing configuration. With further increments in 4°≤α≤14°, the increment C_d due to the 20mm serrations tended to progressively increase in magnitude from 0.003 at α=4° to 0.017 at α=14°, correlating to a 2% and 8% increment, respectively. At α=16°, ΔC_d was marginalised to a 1% increment and with further increments in α≥18°, the decrement in C_d due to the 20mm serrations was progressively heightened from −0.009 at α=18° to a maximum −0.023 at α=20°, accounting for a 3% and 7% reduction, respectively, in comparison to the baseline landing configuration.

Recalling that the surface static pressure distributions indicated that the 20mm serrations delayed separation from $0.4c_{flap}$ to $0.5c_{flap}$ for α≥14°, it was evident that this did not necessarily coincide with a reduction in pressure drag. This was attributed to the influence of the 20mm serrations upon the flow field development over the entire configuration. Similarly to the experiments in the Brough wind-tunnel, it was postulated that vortical structures emanated from each vertex of the 20mm serrations, in accordance with the flow visualisation of Soderman (1972) and Gai and Sharma (1981). Accordingly, it was hypothesised that the development of the streamwise vortices transferred streamwise momentum to the near surface boundary layer and hence, delayed separation further aft for α≥14°. However, the flow field development over the landing configuration in the presence of a serrated trailing edge was not understood and thus, the reason for which the 20mm serrations favourably influenced the boundary layer development at high α, and yet had negligible effect upon the separation at low α, was unclear. Further studies are required to gain an in-depth understanding of the flow field mechanisms by which the serrations favourably influenced boundary layer development.

The drag polar in Figure 62 indicated that whilst the 20mm serrations reduced C_d in comparison to both the baseline and 10mm serrated configurations for C_l≤1.5, with subsequent increments in C_l, the 20mm serrations increased C_d in comparison to the plain trailing edge landing configuration, although a marginal decrement in C_d due to the 20mm serrations was evident near maximum lift. Note that the increment in C_d due to the 20mm serrations typically exceeded the corresponding increment due to the 10mm serrations for 1.5<C_l<2.7.

The variation in L/D with α was less consistent for the 20mm serrated configuration than for the plain and 10mm serrated configurations, see Figure 63. For the 20mm

serrated landing configuration, L/D increased from 0.8 at α=0° to a maximum value of 11.3 at α=8° and whilst L/D fluctuated inconsistently between 11.1 and 11.3 for 10°≤α≤16°, there was a gradual decrease in the magnitude of L/D for α≥18° to a value of 8.8 at α=20°. From Figure 63 it was evident that the detrimental effect of the 20mm serrations upon both C_l and C_d for 4°≤α≤16° decreased L/D in comparison to the baseline takeoff configuration. At α=0°, the decrement in C_d due to the 20mm serrations was insufficient to offset the corresponding decrement in C_l, once again reducing L/D. In contrast, for α=2° and for α≥18°, the decrement in C_d due to the 20mm serrations was sufficient to offset the corresponding decrement in C_l, increasing L/D in comparison to the baseline landing configuration.

6.2.4 Summary for Landing Configuration

As a result of implementing 10mm or 20mm 60° triangular serrated geometries at the trailing edge of the main element upstream of a single slotted flap in a three-element high-lift landing configuration, it was concluded that:

- 10mm serrations had negligible effect upon point of boundary layer separation on the upper surface of the flap
- 20mm serrations delayed boundary layer separation on the upper surface of the flap from $0.4c_{flap}$ to $0.5c_{flap}$ for α≥14°
- Both 10mm and 20mm serrations typically had a detrimental effect upon C_l
- Increasing serration length heightened decrement in C_l
- Both 10mm and 20mm serrations increased pressure drag for 4°≤α≤16° by 2-8%
- Decrements in pressure drag due to serrated geometries limited to α≤2° and α≥18°
- Further studies are required to investigate the flow field mechanisms by which the 20mm serrations delayed the point of boundary layer separation for α≥14°

6.3 Two-Element High-Lift Configuration: δ_s=0°, δ_f=5°

In order to establish whether the effectiveness of the serrations was thwarted by the large flap deflection angles of the takeoff and landing configurations, the deflection angle of the trailing edge flap was markedly reduced to incorporate angles between 5° and 15°. In the first instance, the leading edge slat was retracted for simplicity.

The resultant aerodynamic forces were obtained from the balance measurements. Note that over the range of flap deflection angles tested, the lift and drag coefficients were typically repeatable to within ±0.02 and ±0.002, respectively. Implementation of the 10mm or 20mm serrated geometries had no appreciable effect upon the repeatability of the measurements.

6.3.1 Plain Trailing Edge

With the plain geometry implemented at the trailing edge of the main element and the leading edge slat retracted to the stowed position, the trailing edge flap was deflected to 5°, correlating to a flap lap/gap of (−0.23, −0.13). Balance data for the baseline configuration indicated that C_l increased approximately linearly with α for $-2° \leq \alpha \leq 12°$, from 0.3 at $\alpha=-2°$ to a C_{lmax} of 2.0, corresponding to a stall angle (α_{stall}) of 12°. Typically, C_d increased gradually with C_l, although a considerable increase in C_d was evident for $C_l > C_{lmax}$. Hence, the resultant L/D increased from 10.8 at $\alpha=-2°$ to a maximum of 17.9 at $\alpha=2°$, see Figure 66. With further increments in $\alpha \leq \alpha_{stall}$, L/D decreased approximately linearly to 12.9 at $\alpha=12°$, although a substantial reduction in L/D was evident for $\alpha > \alpha_{stall}$, attaining a minimum value of 4.5 at $\alpha=14°$.

6.3.2 10mm Serrated Trailing Edge

Figure 64 shows that in comparison to the baseline plain trailing edge configuration, implementation of the 10mm serrations at the trailing edge of the main element tended to favourably influence C_l for all test α.

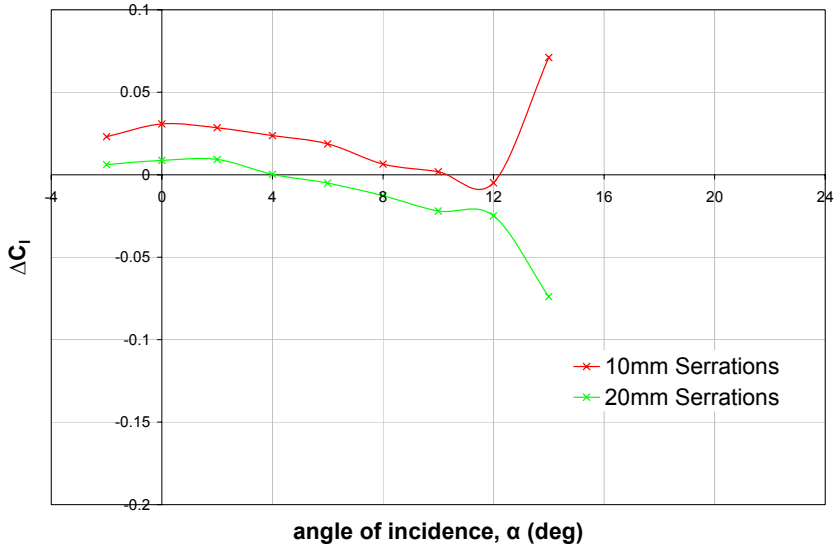

Figure 64: Variation of ΔC_l with angle of incidence due to 10mm and 20mm serrations, $\delta_s=0°$, $\delta_f=5°$

The increment in C_l initially increased in magnitude from 0.02 at α=−2° to a maximum value of 0.03 at α=0°, accounting for an 8% and 5% increase in C_l, respectively. With subsequent increments in $\alpha<\alpha_{stall}$, ΔC_l progressively decreased in magnitude such that any benefit in C_l due to the 10mm serrations was essentially negated for α=10°. An isolated discrepancy to this trend arose at α=12°, coinciding with the stall angle, whereby the 10mm serrations reduced C_l in comparison to the plain trailing edge configuration, although the magnitude of the decrement was near negligible. However, the 10mm serrations once again increased C_l by 0.07 for $\alpha>\alpha_{stall}$, representing a 5% increment in comparison to the baseline configuration.

In comparison to the plain trailing edge configuration, the 10mm serrations increased C_d for $\alpha<\alpha_{stall}$, see Figure 65. ΔC_d progressively increased in magnitude with successive increments in $-2° \leq \alpha \leq 6°$ between 0.001 and 0.002, accounting for a 3-4% increment in comparison to the corresponding baseline configuration. For subsequent increments in $8° \leq \alpha \leq 10°$, ΔC_d progressively decreased in magnitude to approximately 0.001, representing ≤1% increment in C_d. A further increment in α to the stall angle of 12° resulted in a marginal decrement in C_d which was heightened to a maximum decrement of −0.003 at α=14°, corresponding to less than a 1% reduction in C_d in comparison to the baseline configuration. Note that the 10mm serrations had no appreciable effect upon the drag polar for $C_l \leq C_{lmax}$.

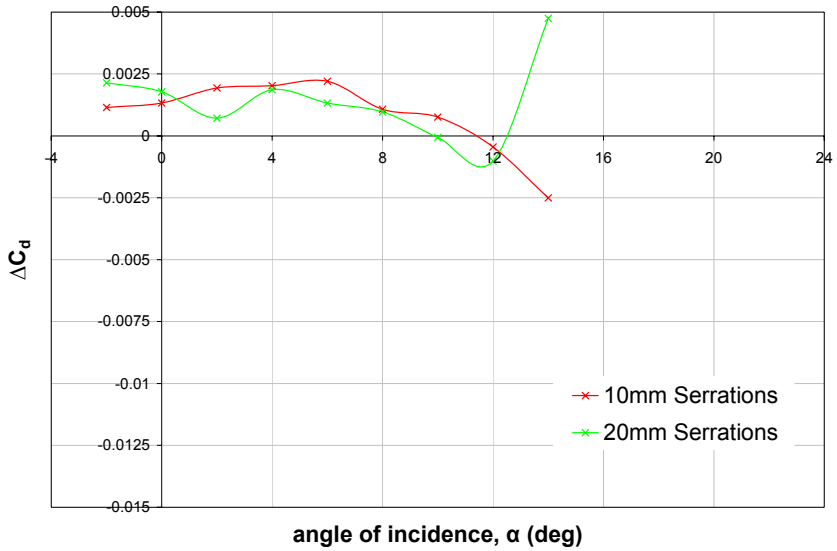

Figure 65: Variation of ΔC_d with angle of incidence due to 10mm and 20mm serrations, δ_s=0°, δ_f=5°

Accordingly, Figure 66 showed that at low test $\alpha \leq 0°$, the increment in C_l was sufficient to offset the corresponding increment in C_d, increasing L/D by 3% and 2% at α=−2° and

α=0°, respectively, in comparison to the plain trailing edge configuration. However, with further increments in 2°≤α≤10°, the increment in C_l was negated by the corresponding increment in C_d and hence, the 10mm serrations had no appreciable effect upon L/D in comparison to the corresponding baseline configuration. At the stall angle of 12°, the 10mm serrations had negligible effect upon L/D but with a final increment in α to 14°, the 10mm serrations favourably influenced both C_l and C_d with a resultant 6% increment in L/D in comparison to the baseline configuration at post-stall conditions.

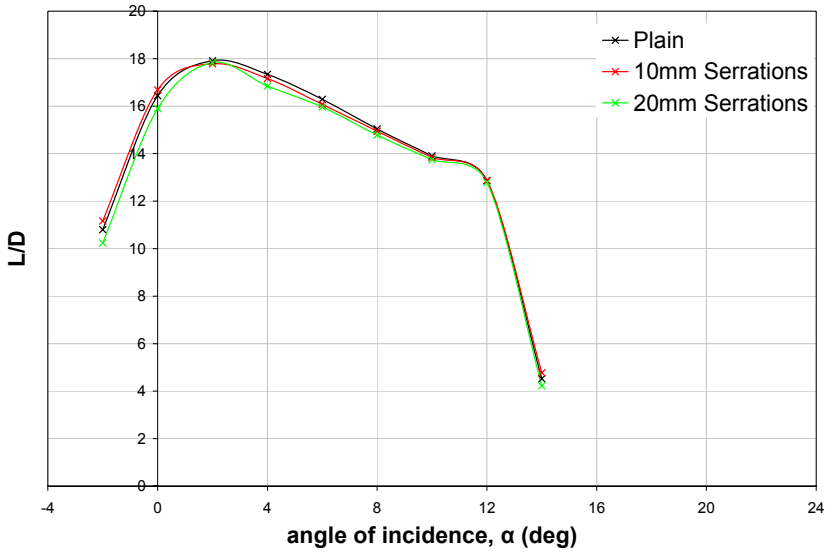

Figure 66: Variation of L/D with angle of incidence for high-lift configuration with plain, 10mm and 20mm serrated trailing edges, δ_s=0°, δ_f=5°

6.3.3 20mm Serrated Trailing Edge

By increasing the serration length from 10mm to 20mm, the range of α over which the serrated geometry had a favourable effect upon C_l was reduced to −2°≤α≤2°. Furthermore, it was evident from Figure 64 that increasing the serration length had a detrimental effect upon the magnitude of ΔC_l. The increment in C_l increased in magnitude from 0.006 at α=−2° to a maximum value of 0.009 at α=2°, although the corresponding percentage increments reduced in magnitude from 2% to 1%, respectively. However, any benefit in C_l due to the 20mm serrations was negated at α=4° and with subsequent increments in α, the decrement in C_l due to the 20mm serrations tended to progressively increase in magnitude. For 6°≤α≤12°, ΔC_l accounted for ≤1% decrement in comparison to the baseline configuration but a final increment in α to 14° heightened the decrement in C_l to −0.07, equating to a 5% reduction, which contrasted the effect of the smaller 10mm serrations at post-stall conditions.

Similarly to the 10mm serrated configuration, the 20mm serrations increased C_d for $\alpha \leq 8°$ in comparison to the plain trailing edge configuration, see Figure 65. ΔC_d varied inconsistently with α between 0.001 and 0.002, accounting for a maximum 8% increment at $\alpha = -2°$ and a 5% increment at $\alpha = 0°$, reducing to a 1-3% increment for $4° \leq \alpha \leq 8°$. With a further increment in α to 10°, any effect upon C_d due to the 20mm serrations was essentially negated. A further increment in α to the stall angle of 12° resulted in a marginal decrement in C_d, which was heightened to a maximum decrement of −0.005 at $\alpha = 14°$, corresponding to a 2% reduction in C_d due to the 20mm serrations when compared to the corresponding baseline configuration. Accordingly, the drag polar indicated that the 20mm serrations marginally increased C_d for any given $C_l \leq C_{lmax}$.

Thus, increasing the serration length from 10mm to 20mm extended the range of α over which the serrated geometry had detrimental effect upon L/D to include all test α, see Figure 66. Accordingly, for $-2° \leq \alpha \leq 4°$, the favourable effect of the 20mm serrations upon C_l was insufficient to offset the corresponding increment in C_d, reducing L/D by a maximum of 5% at $\alpha = -2°$. Subsequent increments in $\alpha \leq 4°$ indicated that the decrement in L/D varied inconsistently, accounting for up to a 3% decrement in comparison to the baseline configuration. With further increments in $6° \leq \alpha \leq 10°$, the decrement in C_l combined with the corresponding increment in C_d, resulting in a 1-2% decrement in L/D in comparison to the corresponding baseline configuration. At the stall angle of 12°, the isolated decrement in C_d due to the 20mm serrations was negated by the corresponding decrement in C_l and with a final increment in α to 14°, L/D was reduced by 7% due to the adverse effect of the 20mm serrations upon both C_l and C_d at post-stall conditions. Hence, increasing the serration length from 10mm to 20mm typically heightened the magnitude of the decrement in L/D.

6.3.4 Summary for Two-Element Configuration: $\delta_s = 0°$, $\delta_f = 5°$

As a result of implementing 10mm or 20mm 60° triangular serrated geometries at the trailing edge of the main element upstream of a single slotted flap in a two-element high-lift configuration with $\delta_s = 0°$ and $\delta_f = 5°$, it was concluded that:

- 10mm serrations typically increased C_l, with the greatest increments at low α
- 20mm serrations reduced the magnitude of the increment in C_l to ≤2% for $\alpha \leq 4°$ and had a detrimental effect upon C_l for $\alpha \geq 6°$
- Both 10mm and 20mm serrations increased C_d for $\alpha < \alpha_{stall}$, although ΔC_d was typically reduced by the larger serration length

- 10mm serrations increased L/D by 2-3% for $\alpha \leq 0°$ but decreased L/D for $\alpha \geq 2°$
- 20mm serrations decreased L/D for all test α, heightening the magnitude of the decrement in comparison to the 10mm serrations

6.4 Two-Element High-Lift Configuration: δ_s=0°, δ_f=10°

Maintaining the leading edge slat in its stowed position, the trailing edge flap was deflected to 10°, generating a flap lap/gap of (−0.21, −0.12).

6.4.1 Plain Trailing Edge

Similarly to the configuration with δ_f=5°, C_l increased approximately linearly with α for $-2° < \alpha < 12°$, from a C_l of 0.6 at α=−2° to a C_{lmax} of 2.3, corresponding to a stall angle of 12°. Typically, C_d increased gradually with C_l, although a considerable increase in C_d was evident for $C_l > C_{lmax}$. Accordingly, L/D increased from 15.3 at α=−2° to a maximum value of 16.9 at α=0°, see Figure 69. With further increments in $\alpha \geq 2°$, L/D decreased approximately linearly for $\alpha \leq \alpha_{stall}$ to 11.6 at α=12°, although with a final increment in α to 14°, L/D was markedly reduced to a minimum value of 4.5.

6.4.2 10mm Serrated Trailing Edge

Figure 67 shows that implementation of the 10mm serrations at the trailing edge of the main element only had a favourable effect upon C_l at α=−2°, increasing C_l by 0.01 and accounting for a 2% increment in comparison to the plain trailing edge configuration. At α=0°, the 10mm serrations had no appreciable effect upon C_l but with further increments in $\alpha \geq 2°$, the 10mm serrations reduced C_l in comparison to the baseline configuration. The decrement in C_l tended to increase in magnitude with successive increments in α, from −0.01 at α=2° to −0.05 at α=14°, correlating to a 1% and 3% increment, respectively, in comparison to the plain trailing edge configuration. Hence, increasing the δ_f from 5° to 10° significantly reduced the range of α over which the 10mm serrations had a favourable effect upon C_l.

In contrast, increasing δ_f from 5° to 10° increased the range of α over which the 10mm serrations had a favourable effect upon C_d to $4° \leq \alpha \leq 14°$, see Figure 68. ΔC_d due the 10mm serrations varied inconsistently for $-2° \leq \alpha \leq 2°$, having no appreciable effect upon C_d at α=0° and increasing C_d by 3% and 1% at α=−2° and 2°, respectively. With successive increments in $4° \leq \alpha \leq 12°$, the decrement in C_d due to the 10mm serrations was

progressively heightened in magnitude, attaining a maximum ΔC_d of −0.004 at α=12° and accounting for ≤2% reduction in C_d throughout. A final increment in α to 14° reduced the decrement in C_d to −0.003, equating to a less than 1% reduction in C_d in comparison to the plain trailing edge configuration. The corresponding drag polar indicated that the 10mm serrations increased C_d for any given C_l>1.0.

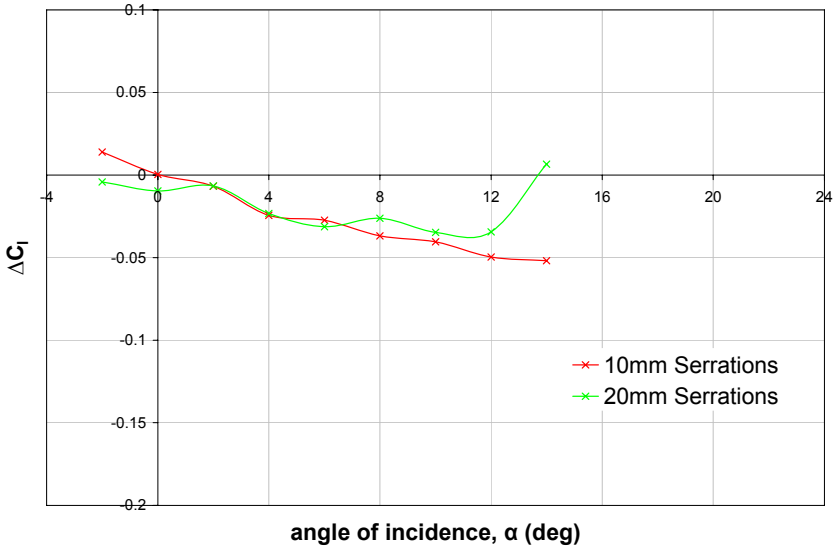

Figure 67: Variation of ΔC_l with angle of incidence due to 10mm and 20mm serrations, δ_s=0°, δ_f=10°

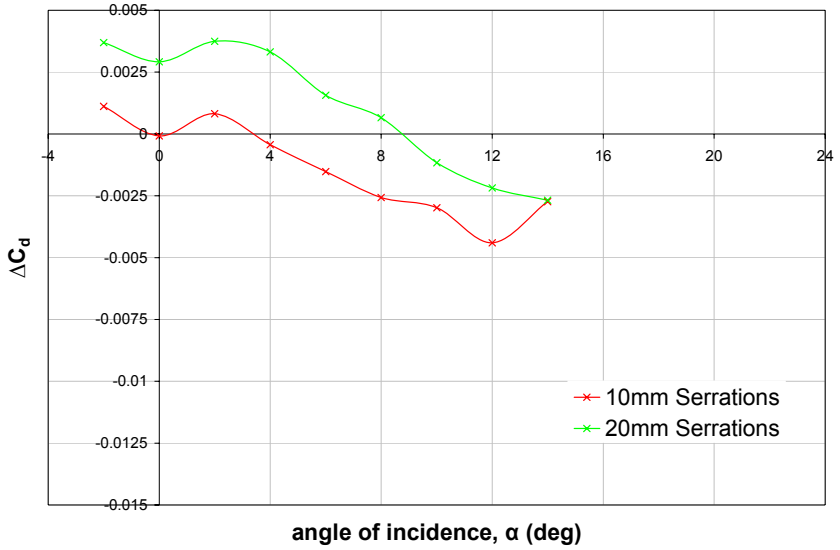

Figure 68: Variation of ΔC_d with angle of incidence due to 10mm and 20mm serrations, δ_s=0°, δ_f=10°

Accordingly at α=−2°, the increment in C_l was sufficient to offset the corresponding increment in C_d, with the net result of no appreciable effect upon L/D in comparison to the baseline configuration, see Figure 69. With the 10mm serrations having a near

negligible effect upon both C_l and C_d at α=0°, L/D for the 10mm serrated configuration was coincident with the plain trailing edge configuration. In contrast, the adverse effect of the 10mm serrations on both C_l and C_d at α=2° resulted in a 2% decrement in L/D, which was marginalised to a 1% decrement at α=4°.

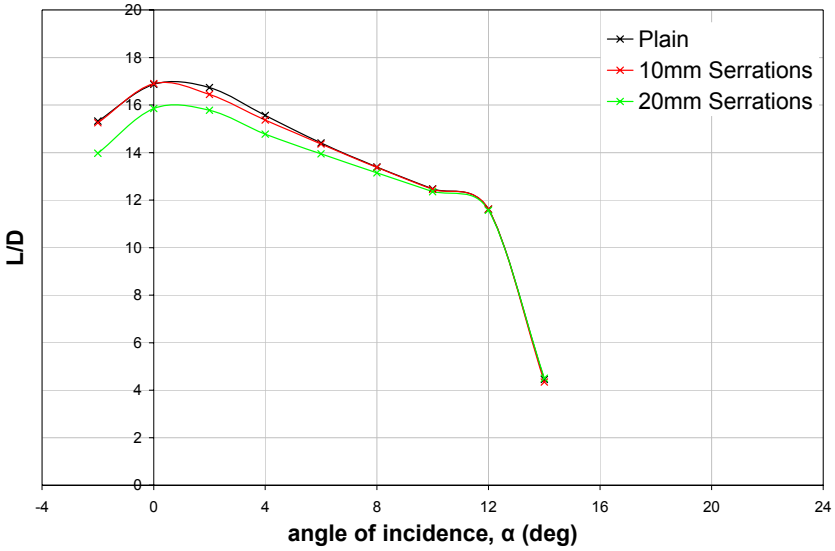

Figure 69: Variation of L/D with angle of incidence for high-lift configuration with plain, 10mm and 20mm serrated trailing edges, δ_s=0°, δ_f=10°

With subsequent increments in 6°≤α≤12°, the decrement in C_l negated the corresponding decrement in C_d, with the net effect of the 10mm serrations having no appreciable effect upon L/D when compared to the baseline configuration. Although with a final increment in α to 14°, L/D was reduced by 3% in comparison to the plain trailing edge configuration, as the decrement in C_d due to the 10mm serrations was insufficient to offset the corresponding decrement in C_l.

6.4.3 20mm Serrated Trailing Edge

Figure 67 showed that by increasing the serration length from 10mm to 20mm, the range of α over which the serrated geometry had a favourable effect upon C_l was reduced to α=14°, i.e. post-stall conditions. For $\alpha \leq \alpha_{stall}$, the decrement in C_l due to the 20mm serrations varied inconsistently, from −0.004 at α=−2° to −0.035 at α=10° and α=12°, correlating to a less than 2% reduction in C_l throughout. At α=14°, the 20mm serrations marginally increased C_l by 0.007, accounting for a less than 1% increment in comparison to the baseline configuration and contrasting the effect of the smaller 10mm serrations at post-stall conditions. Hence, increasing the δ_f from 5° to 10° reduced the range of α over which the 20mm serrations were beneficial to C_l in comparison to the baseline plain trailing edge configuration.

Increasing the serration length from 10mm to 20mm reduced the range of α over which the serrated geometry had a favourable effect upon C_d to $10° \leq \alpha \leq 14°$. Figure 68 showed that the 20mm serrations increased C_d for all $-2° \leq \alpha \leq 8°$. ΔC_d varied inconsistently for $-2° \leq \alpha \leq 2°$, accounting for a 9% increment at $\alpha = -2°$ and reducing to a 5% increment for $0° \leq \alpha \leq 2°$. Subsequent increments in $4° \leq \alpha \leq 8°$ progressively decreased ΔC_d such that at $\alpha = 8°$, ΔC_d was reduced to 0.001, equating to <1% increment in comparison to the baseline configuration. With further increments in $\alpha \geq 10°$, the decrement in C_d due to the 20mm serrations was progressively heightened in magnitude from −0.001 at $\alpha = 10°$ to −0.003 at $\alpha = 14°$, representative of ≤1% decrement in C_d throughout. Accordingly, the drag polar indicated that the 20mm serrations increased C_d for any given $C_l \leq C_{lmax}$.

Thus, the 20mm serrations had a detrimental effect upon L/D for all test $\alpha \leq \alpha_{stall}$, see Figure 69. Accordingly, for $-2° \leq \alpha \leq 8°$, the adverse effect of the 20mm serrations upon both C_l and C_d resulted in a marked decrement in L/D. At $\alpha = -2°$, the 20mm serrations reduced L/D by a maximum of 9%. With subsequent increments in α, the decrement in L/D progressively decreased in magnitude, accounting for a 2% reduction at $\alpha = 8°$. For $10° \leq \alpha \leq 12°$, the decrement in C_l offset the corresponding decrement in C_d and as a result, the 20mm serrations had no appreciable effect upon L/D in comparison to the corresponding baseline configuration. The negligible effect of the 20mm serrations upon L/D, when compared to the baseline configuration, extended to post-stall conditions of $\alpha = 14°$.

6.4.4 Summary for Two-Element Configuration: $\delta_s = 0°$, $\delta_f = 10°$

As a result of implementing 10mm or 20mm 60° triangular serrated geometries at the trailing edge of the main element upstream of a single slotted flap in a two-element high-lift configuration with $\delta_s = 0°$ and $\delta_f = 10°$, it was concluded that:

- Increasing δ_f from 5° to 10° essentially negated the favourable effect of the serrated geometries upon C_l but extended the range of α over which the serrated geometries had a favourable effect upon C_d
- ΔC_l due to 10mm and 20mm serrations was of comparable magnitude for $\alpha \leq 6°$
- Increasing serration length to 20mm reduced the decrement in C_l for $\alpha \geq 8°$
- 10mm serrations had a favourable effect upon C_d for $\alpha \geq 4°$
- 20mm serrations had a favourable effect upon C_d for $\alpha \geq 10°$
- 10mm serrations typically had no appreciable effect upon L/D
- 20mm serrations reduced L/D for $\alpha \leq 8°$, with no appreciable effect thereafter

6.5 Two-Element High-Lift Configuration: δ_s=0°, δ_f=15°

With the leading edge slat retracted, the trailing edge flap deflection angle was increased to 15°, generating a flap lap/gap of (−0.18, −0.12).

6.5.1 Plain Trailing Edge

Similarly to the configuration with δ_f=5° and 10°, C_l increased approximately linearly with α for $-2° < \alpha < 12°$, from 1.0 at α=−2° to a C_{lmax} of 2.6 corresponding to a stall angle of 12°. Increasing δ_f from 5° to 15° had negligible effect upon the measured α_{stall} but the corresponding C_{lmax} increased with δ_f. Typically, C_d increased gradually with C_l, although a considerable increase in C_d was evident for $C_l > C_{lmax}$. A maximum L/D of 16.1 coincided with the minimum test α of −2°, see Figure 72. With further increments in $0° \le \alpha \le \alpha_{stall}$, L/D decreased approximately linearly to a value of 10.6 at α=12°, although with a final increment in α to 14°, L/D was markedly reduced to a minimum value of 4.1.

6.5.2 10mm Serrated Trailing Edge

Figure 70 shows that implementation of the 10mm serrations at the trailing edge of the main element had a detrimental effect upon C_l for $-2° \le \alpha \le 12°$.

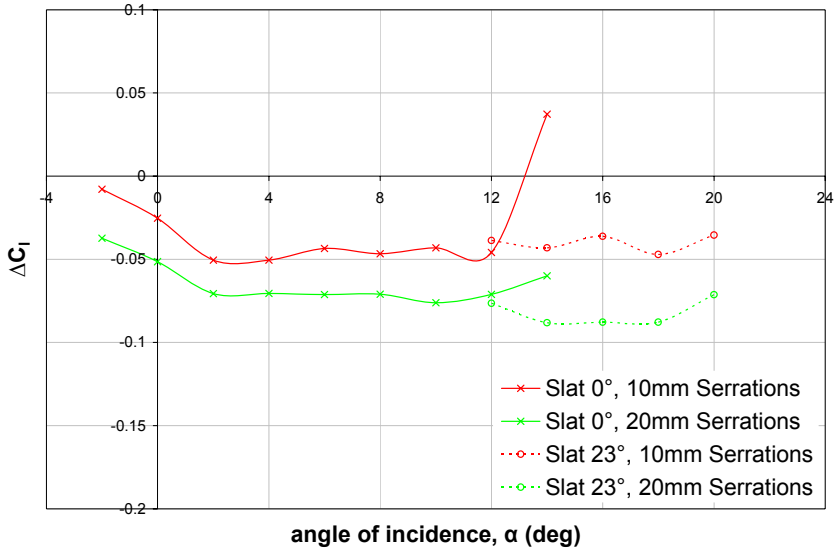

Figure 70: Variation of ΔC_l with angle of incidence due to 10mm and 20mm serrations, δ_s=0°, δ_f=15° and δ_s=23°, δ_f=15°

Initially, the decrement in C_l due to the 10mm serrations was heightened with successive increments in α from −0.01 at α=−2° to −0.05 at α=2°, correlating to a 1% and 3% decrement, respectively, in comparison to the baseline configuration. With

subsequent increments $4° \leq \alpha \leq 12°$, ΔC_l varied inconsistently between −0.04 and −0.05, accounting for a 2-3% reduction in C_l in comparison to the plain trailing edge configuration. In contrast, a final increment in α beyond stall to 14° had a favourable effect and increased C_l by 0.04, equating to a 2% increment in comparison to the baseline configuration.

With regard to C_d, the 10mm serrations had a detrimental effect for $-2° \leq \alpha \leq 0°$ and increased C_d by a maximum of 0.001 at α=0°, accounting for a 1% increment in comparison to the baseline configuration, see Figure 71. Successive increments in $\alpha \geq 2°$ indicated that the 10mm serrations had a favourable effect upon C_d in comparison to the plain configuration. Whilst anomalies arose, the decrement in C_d was progressively heightened in magnitude from a ΔC_d of −0.001 at α=2° to −0.006 at α=12° and 14°, correlating to a 1-2% decrement throughout. Accordingly, the drag polar indicated that the 10mm serrations increased C_d for any given $C_l \leq C_{lmax}$ when compared to the baseline configuration.

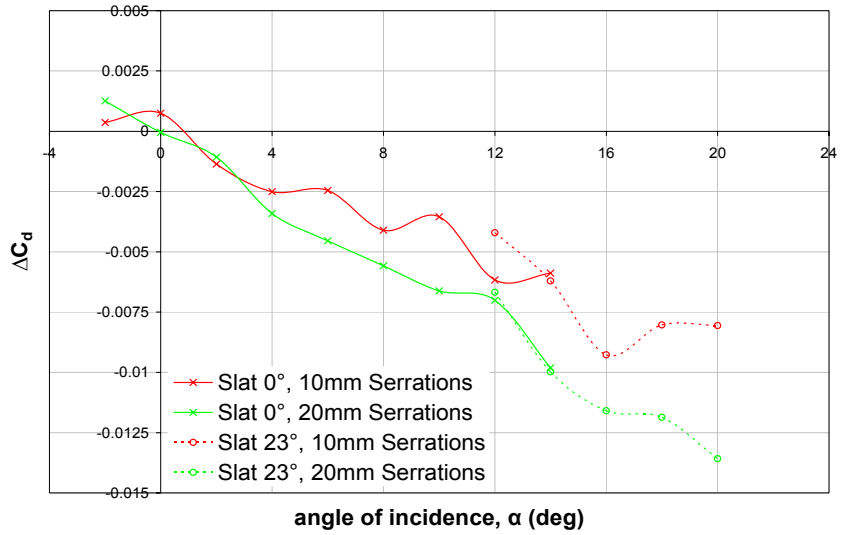

Figure 71: Variation of ΔC_d with angle of incidence due to 10mm and 20mm serrations, δ_s=0°, δ_f=15° and δ_s=23°, δ_f=15°

Thus, the adverse effect of the 10mm serrations on both C_l and C_d for $-2° \leq \alpha \leq 0°$ resulted in 1% decrement in L/D at α=−2° in comparison to the baseline configuration, increasing to a 3% decrement at α=0°, see Figure 72. For $2° \leq \alpha \leq 12°$, the decrement in C_d due to the 10mm serrations was insufficient to offset the corresponding decrement in C_l. Accordingly, the 10mm serrations accounted for a 2% decrement in L/D at α=2°, although with subsequent increments in α, the decrement in L/D was marginalised such that, any variation in L/D due to the 10mm serrations was essentially negated for

8°≤α≤12°. However, due to the favourable effect of the 10mm serrations upon both C_l and C_d at post-stall conditions, L/D was increased by 4% at α=14° in comparison to the plain trailing edge configuration.

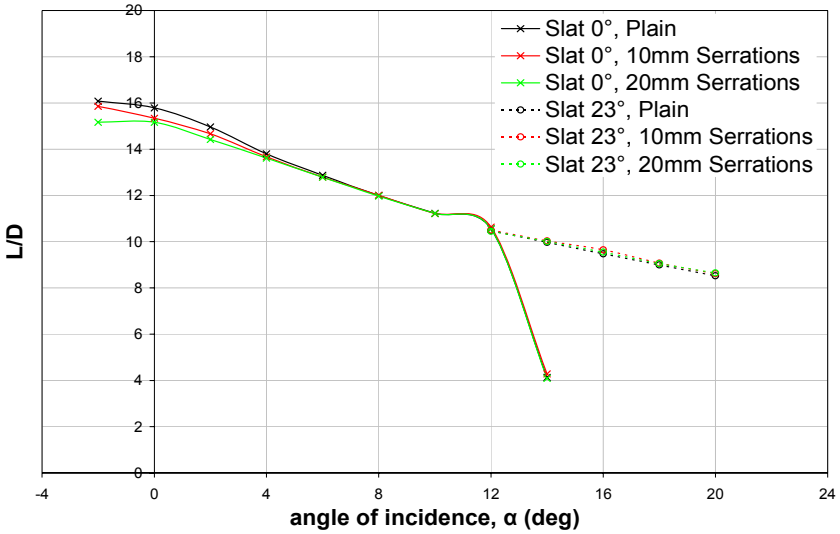

Figure 72: Variation of L/D with angle of incidence for high-lift configuration with plain, 10mm and 20mm serrated trailing edges, δ_s=0°, δ_f=15° and δ_s=23°, δ_f=15°

6.5.3 20mm Serrated Trailing Edge

Increasing the serration length from 10mm to 20mm rendered the serrated geometry detrimental to C_l for all test α, simultaneously heightening the decrement for any given α, see Figure 70. ΔC_l was progressively heightened in magnitude at low α from −0.04 at α=−2° to −0.07 at α=2°, accounting for a 4% and 5% reduction in comparison to the baseline configuration, respectively. However, with subsequent increments in 2°≤α≤12°, ΔC_l appeared relatively insensitive to α, although the corresponding percentage decrement tended to progressively decrease in magnitude, equating to a 3% reduction in C_l at α=12°. A final increment in α to 14° marginally reduced ΔC_l to −0.06, correlating to a 4% reduction in C_l when compared to the corresponding plain trailing edge configuration. Thus, increasing δ_f from 10° to 15° heightened the decrement in C_l due to the 20mm serrations.

Increasing the serration length from 10mm to 20mm heightened the decrement in C_d for 4°≤α≤14°, see Figure 71. Similarly to the 10mm serrated configuration, the 20mm serrations had a detrimental effect upon C_d at α=−2°, increasing C_d by 0.001 or 2% in comparison to the baseline configuration. However, by increasing α to 0°, any variation in C_d due to the 20mm serrations was essentially negated. For 2°≤α≤14°, the decrement

in C_d was progressively heightened in magnitude from of −0.001 at α=2° to −0.01 at α=14°, correlating to a 1-3% reduction in C_d throughout when compared to the baseline configuration. Based upon the drag polar, the 20mm serrations increased C_d for any given $C_l \leq C_{lmax}$, with the increment in C_d heightened in comparison to that for the 10mm serrated configuration. Similarly to the 10mm serrated configuration, increasing δ_f from 10° to 15° heightened the favourable effect of the 20mm serrations upon C_d.

Thus, the 20mm serrations had detrimental effect upon L/D for all $\alpha \leq 6°$, see Figure 72. For $-2° \leq \alpha \leq 0°$, the adverse effect of the 20mm serrations upon both C_l and C_d resulted in a 6% reduction in L/D at α=−2°, reducing to a 4% decrement at α=0° in comparison to the baseline configuration. Although the 20mm serrations had a favourable effect upon C_d for $2° \leq \alpha \leq 6°$, the heightened decrement in the corresponding C_l resulted in a reduction in L/D in comparison to the plain trailing edge configuration. The decrement in L/D progressively decreased in magnitude from 4% at α=2° to 1% reduction at α=6°. With further increments in $\alpha \geq 8°$, the decrement in L/D due to the 20mm serrations was essentially negated in comparison to the baseline configuration.

6.5.4 Summary for Two-Element Configuration: δ_s=0°, δ_f=15°

As a result of implementing 10mm or 20mm 60° triangular serrated geometries at the trailing edge of the main element upstream of a single slotted flap in a two-element high-lift configuration with δ_s=0° and δ_f=15°, it was concluded that:

- Both 10mm and 20mm serrations had a detrimental effect upon C_l for all test α
- Both 10mm and 20mm serrations typically had a favourable effect upon C_d
- Increasing δ_f from 10° to 15° heightened the favourable effect of the serrated geometries upon C_d
- Increasing the serration length from 10mm to 20mm heightened the decrement in both C_l and C_d for any given α
- Both 10mm and 20mm serrations reduced L/D for $\alpha \leq 6°$, with no appreciable effect thereafter

6.6 Three-Element High-Lift Configuration: δ_s=23°, δ_f=15°

In order to determine whether the effectiveness of the 10mm and 20mm trailing edge serrated geometries could be improved by deflection of a leading edge high lift device, a single slotted slat was deployed in conjunction with the trailing edge flap. Deflecting

the leading edge slat by 23° and the trailing edge flap by 15° generated a slat and flap lap/gap of (−0.06, −0.23) and (−0.18, −0.12), respectively. The resultant aerodynamic forces were obtained from the balance measurements.

6.6.1 Plain Trailing Edge

With the plain geometry implemented at the trailing edge of the main element, C_l progressively increased with α to a maximum C_l of 3.3 at α=20°, although the lift curve no longer displayed the linearity of that previously observed, when the leading edge slat was retracted. Recalling that, with the slat retracted, the configuration stalled at α=12°, deflection of the leading edge device increased α_{stall} beyond the test range. However, the limited range of measurements indicated that deflection of the leading edge slat reduced C_l for any comparable α, which was consistent with the theory that deflection of a leading edge device in conjunction with a trailing edge device reduced the lift coefficient at zero angle of incidence due to the negative camber near the leading edge (McCormick, 1995). Furthermore, with the leading edge slat deflected, C_d increased with C_l, attaining a maximum C_d of 0.38 at α=20°. The resultant L/D progressively decreased with successive α from 10.5 at α=12° to 8.5 at α=20° (see Figure 72).

6.6.2 10mm Serrated Trailing Edge

Implementation of the 10mm serrations at the trailing edge of the main element had a detrimental effect upon C_l when compared to the corresponding plain trailing edge configuration, see Figure 70. For 12°≤α≤20°, the decrement in C_l due to the 10mm serrations fluctuated between −0.04 and −0.05, correlating to a 1-2% reduction in comparison to the corresponding plain trailing edge configuration. Furthermore, deflection of the leading edge slat in conjunction with the 10mm serrated trailing edge geometry maintained the favourable effect upon C_d to higher test α, see Figure 71. The decrement in C_d due to the 10mm serrations was progressively heightened from −0.004 at α=12° to a maximum of −0.009 at α=16°, correlating to a 2-3% decrement in comparison to the baseline plain trailing edge configuration. With further increments in 18°≤α≤20°, ΔC_d was reduced to −0.008, equating to a 2% reduction in C_d in comparison to the plain trailing edge three-element configuration. Accordingly, the decrement in C_d was sufficient to offset the corresponding decrement in C_l, increasing L/D in comparison to the baseline configuration, see Figure 72. The increment in L/D due to

the 10mm serrations varied inconsistently for $12° \leq \alpha \leq 20°$ but accounted for a less than 2% deviation throughout in comparison to the baseline configuration.

6.6.3 20mm Serrated Trailing Edge

Increasing the serration length from 10mm to 20mm with the leading edge slat deflected heightened the decrement in C_l for all $12° \leq \alpha \leq 20°$, see Figure 70. The decrement in C_l was heightened from −0.08 at α=12° to −0.09 for $14° \leq \alpha \leq 18°$, only decreasing in magnitude to −0.07 at α=20°. The corresponding percentage decrement fluctuated between 2% and 3% in comparison to the baseline three-element configuration. Similarly to the 10mm serrations, deflection of the leading edge slat in conjunction with the 20mm serrated trailing edge geometry maintained the favourable effect upon C_d to higher test α, see Figure 71. The decrement in C_d due to the 20mm serrations progressively increased in magnitude with successive increments in α from −0.007 at α=12° to a maximum of −0.014 at α=20°, accounting for a 3-4% reduction in C_d in comparison to the corresponding plain trailing edge configuration. The decrement in C_d due to the 20mm serrations was essentially negated by the corresponding decrement in C_l, resulting in near negligible variation in L/D in comparison to the baseline configuration for $12° \leq \alpha \leq 18°$, with only an isolated 1% increment in L/D at α=20°, see Figure 72.

6.6.4 Summary for Three-Element Configuration: δ_s=23°, δ_f=15°

As a result of implementing 10mm or 20mm 60° triangular serrated geometries at the trailing edge of the main element upstream of a single slotted flap in a three-element high-lift configuration with δ_s=23° and δ_f=15°, it was concluded that:

- Deflection of a leading edge slat increased C_{lmax} and α_{stall}, for all trailing edge geometries
- Deflection of a leading edge slat merely extended the detrimental effect of the serrations upon C_l and the favourable effect of the serrations upon C_d to higher test α
- Increasing the serration length from 10mm to 20mm heightened the decrement in both C_l and C_d for all test α
- 10mm serrations increased L/D by a maximum of 2% for $12° \leq \alpha \leq 20°$
- 20mm serrations had no appreciable effect upon L/D for $12° \leq \alpha \leq 20°$

In conclusion, whilst it was evident that increasing δ_f from 5° to 15°, within a two-element configuration, heightened the favourable effect of the serrated geometries upon C_d, this was typically accompanied by a corresponding decrement in C_l. Deployment of a leading edge slat merely extended these trends in C_l and C_d to higher α. Based upon the balance measurements alone, the reason for this degradation in C_l was unclear and a simple hypothetical model of the development of streamwise vortices, aft of each serration vertex, failed to provide insight into the flow mechanisms by which the serrations decreased C_d but degraded C_l. Thus, further studies are required to gain an in-depth understanding of the flow field development over the high-lift configuration when serrated trailing edge geometries are implemented.

6.7 Two-Element High-Lift Configuration: Coarse Flap Lap/Gap Grid

Noting that for each configuration tested thus far, the flap lap and gap were distinct for each flap deflection angle, a parametric study was conducted by which the flap deflection angle was incremented between 0° and 15° at each position on a 5-point coarse lap/gap grid (see Section 3.3.3 for coarse grid details). In the first instance, the leading edge slat was retracted for simplicity. Note that due to the severity of stall, α_{stall} itself was undefined and thus, the final measurement for a given configuration inferred that the configuration stalled violently within the next 2° increment in incidence angle.

The resultant aerodynamic forces were obtained from the balance measurements. Similarly to the previous tests, the lift and drag coefficients were typically repeatable to within ±0.02 and ±0.002, respectively. Implementation of the 10mm or 20mm serrated geometries had no appreciable effect upon the repeatability of the measurements.

6.7.1 Plain Trailing Edge

With leading edge slat retracted and the plain geometry implemented at the trailing edge of the main element, it was necessary to ascertain the baseline aerodynamic characteristics of a configuration at a specified flap lap/gap when subject to increments in α and δ_f.

The C_l-α curve for the baseline plain trailing edge configuration at a given flap lap/gap is shown in Figure 178 in Appendix I for all test δ_f. Further comparisons of the C_l-α

curve for the baseline configuration at a specified test δ_f are displayed in Figure 179 in Appendix I for all coarse flap lap/gap grid positions tested.

At a flap lap/gap of (−0.17, −0.14), successive increments in δ_f between 0° and 15° increased C_l for any given $\alpha<\alpha_{stall}$, with α_{stall} occurring in the 2° increment beyond 16° for all δ_f tested (see Appendix I, Figure 178(a)).

Similarly, successive increments in δ_f between 0° and 15° increased C_l for any given $\alpha<\alpha_{stall}$, at a flap lap/gap of (−0.12, −0.14), see Appendix I, Figure 178(b). Maintaining the flap gap of −0.14 and incrementing the flap lap from −0.17 to −0.12 had a detrimental effect upon C_l for $\alpha<12°$ at $\delta_f=0°$ (see Appendix I, Figure 179(a)). The decrement in C_l decreased in magnitude with successive increments in α such that any variation in C_l was negated for $12°\leq\alpha<\alpha_{stall}$. Although the decrement in C_l due to the increment in lap was essentially negated at $\delta_f=5°$ across the range of α tested, with further increments in $10°\leq\delta_f\leq15°$, incrementing the flap lap from −0.17 to −0.12 tended to have a detrimental effect upon C_l (see Appendix I, Figure 179(b)-(d)). At $\delta_f=10°$, the increment in the flap lap reduced C_l for $\alpha<12°$ but with the final increment in δ_f to 15°, the increment in the flap lap notably reduced C_l for all $\alpha<\alpha_{stall}$. Furthermore, the decrement in C_l was heightened with successive increments in δ_f. However, the increment in flap lap extended the range of α over which measurements were obtained for $0°\leq\delta_f\leq5°$, inferring an increase in α_{stall} to beyond 18°, simultaneously increasing C_{lmax} for the given δ_f.

Increasing the flap gap to −0.2 and positioning the flap incrementally upstream at a lap of −0.23 at $\delta_f=0°$ increased C_l for $\alpha\leq6°$ in comparison to the corresponding configuration at a lap/gap of (−0.17, −0.14), although the increment decreased in magnitude with successive increments in α (see Appendix I, Figure 179(a)). In contrast, C_l was reduced for $10°\leq\alpha<\alpha_{stall}$ at $\delta_f=0°$, with the magnitude of the decrement progressively heightened with increasing α. At $\delta_f=5°$, the increment in C_l was only evident for $\alpha\leq2°$ and with successive increments in α, C_l was adversely affected by the lap/gap variation, with the decrement in C_l increasing in magnitude with α (see Appendix I, Figure 179(b)). With successive increments in $10°\leq\delta_f\leq15°$, the decrement in C_l, due to the lap/gap variation, was magnified for any given α (see Appendix I, Figure 179(c) and (d)). Similarly to the flap lap/gap of (−0.17, −0.14), α_{stall} occurred in the increment beyond 16° for all δ_f tested and again, successive increments in δ_f between 0° and 15° increased C_l for any given $\alpha<\alpha_{stall}$ (see Appendix I, Figure 178(e))

Increasing the flap gap to −0.2 whilst at a flap lap −0.17 had a favourable effect upon C_l at δ_f=0° for $\alpha<\alpha_{stall}$ (see Appendix I, Figure 179(a)). However by increasing δ_f to 5°, the increment in C_l was only evident at α=−2° and with successive increments in α, increasing the flap gap had a detrimental effect upon C_l (see Appendix I, Figure 179(b)). The decrement in C_l arising when the flap gap was increased from −0.14 to −0.2 was heightened with successive increments in 10°≤δ_f≤15° for all test α (see Appendix I, Figure 179(c) and (d)). Similarly to the flap lap/gap of (−0.17, −0.14), α_{stall} occurred in the increment beyond 16° for all δ_f tested and successive increments in δ_f between 0° and 15° increased C_l for any given $\alpha<\alpha_{stall}$ (see Appendix I, Figure 178(c)).

Positioning the flap at a lap/gap of (−0.12, −0.2) increased C_l at δ_f=0° for $\alpha<\alpha_{stall}$ when compared to the corresponding configuration at the smaller flap gap of −0.14, with the resultant C_l comparable in magnitude to the corresponding configuration at a lap/gap of (−0.17, −0.2), see Appendix I, Figure 179(a). However, by increasing δ_f to 5°, the increment in flap gap at a flap lap of −0.17 had a detrimental effect upon C_l for all test α (see Appendix I, Figure 179(b)). This adverse effect upon C_l was maintained at δ_f=10° for all test α and with a final increment in δ_f to 15°, the decrement in C_l due to the increment in flap gap at a flap lap of −0.17 was substantially magnified, notably increasing in magnitude with successive increments in α (see Appendix I, Figure 179(c) and (d)). Again, α_{stall} occurred in the increment beyond 16° for all δ_f tested. Note that whilst C_l increased with successive increments in δ_f between 0° and 10° for any given $\alpha<\alpha_{stall}$, the increment in C_l was limited to α≤10° at δ_f=15°. For 12°≤α≤14°, any increment in C_l due to the increment in δ_f from 10° to 15° was essentially negated and at the upper test limit of α=16°, the C_l attained with δ_f=15° was marginally degraded in comparison to that attained with δ_f=10° (see Appendix I, Figure 178(d)).

Thus, in terms of attaining the maximum C_l for a given α, positioning the flap at a lap/gap of either (−0.17, −0.2) or (−0.12, −0.2) was most favourable at δ_f=0° but with successive increments in 5°≤δ_f≤15°, a lap/gap of (−0.17, −0.14) was optimal (see Appendix I, Figure 179(a)-(d)).

The drag polar for each baseline configuration at a given flap lap/gap is shown in Figure 180 in Appendix I, with further comparisons for a specified test δ_f displayed in Figure 181 in Appendix I. For clarity, the resultant L/D for each baseline configuration at a given flap lap/gap is shown in Figure 182 in Appendix I, with additional graphs comparing L/D for the baseline configuration at a specified test δ_f displayed in Figure 183 in Appendix I.

Evaluating C_l and C_d in terms of L/D, it was evident that at δ_f=0°, locating the flap at a lap/gap of (−0.17, −0.14) generated the maximum L/D for $\alpha \leq 10°$, although for $\alpha \geq 12°$, L/D appeared relatively insensitive to variations in lap/gap (see Appendix I, Figure 183(a)). At δ_f=5°, positioning flap at a lap/gap of (−0.12, −0.14) was most beneficial in terms of L/D for $\alpha < 10°$, whilst L/D appeared relatively insensitive to the precise flap lap/gap position for $10° \leq \alpha \leq 16°$ (see Appendix I, Figure 183(b)). With further increments in $10° \leq \delta_f \leq 15°$, positioning the flap at a gap of −0.14 had the most favourable effect upon L/D for $\alpha \leq 12°$, irrespective of the precise test flap lap implemented (see Appendix I, Figure 183(c) and (d)). Again, L/D appeared relatively insensitive to variations in lap/gap for $14° \leq \alpha \leq 16°$ at both δ_f=10° and δ_f=15°. Thus, for the baseline configuration, it was evident that for angles of incidence where L/D was sensitive to variations in lap/gap, positioning the flap at the smaller test gap of −0.14 was most beneficial in terms of L/D, with the precise lap dependent upon δ_f.

6.7.2 10mm Serrated Trailing Edge

(a) Flap Lap/Gap: (−0.17, −0.14)

Figure 73 shows that in comparison to the corresponding plain trailing edge configuration, the 10mm serrations decreased C_l for all α and δ_f tested at a flap lap/gap of (−0.17, −0.14).

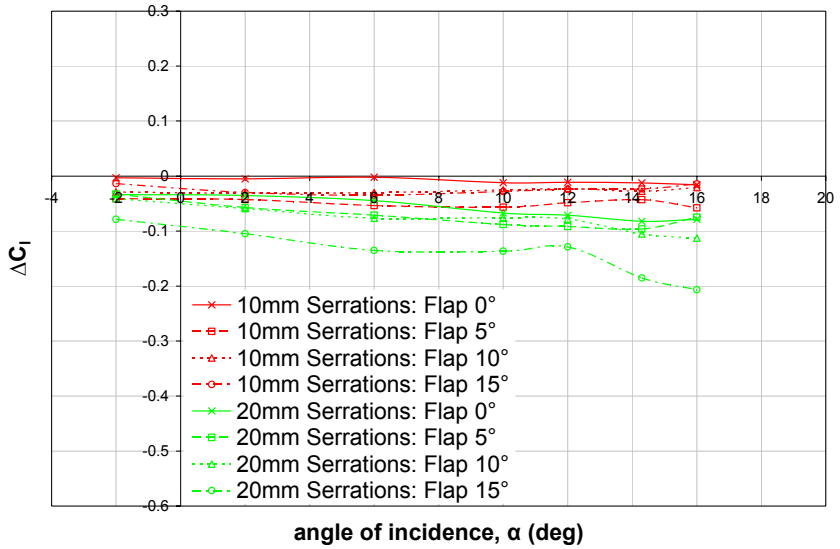

Figure 73: Variation of ΔC_l with angle of incidence due to 10mm and 20mm serrations at a flap lap/gap of (−0.17, −0.14), δ_s=0°, $0° \leq \delta_f \leq 15°$

At δ_f=0°, the decrement in C_l due to the 10mm serrations tended to increase in magnitude with successive α, although accounting for <1.5% reduction in C_l in

comparison to the plain trailing edge configuration. With subsequent increments in δ_f, the decrement in C_l varied inconsistently with α. Increasing δ_f to 5° maximised ΔC_l, representing an average 3% reduction in C_l. However, with subsequent increments in $10° \leq \delta_f \leq 15°$, ΔC_l decreased in magnitude, typically accounting for <2% reduction in C_l in comparison to the plain trailing edge configuration, i.e. ΔC_l was relatively insensitive both to variations in test δ_f between 10° and 15° for any given α and also relatively insensitive to variations in α.

Although ΔC_d varied inconsistently with α for all δ_f, there was a tendency for the 10mm serrations to decrease C_d, see Figure 184(a) in Appendix J. A notable exception to this trend arose at δ_f=0°, whereby the 10mm serrations increased C_d for $0° \leq \alpha \leq 10°$. The 10mm serrations had negligible effect upon the drag polar, although it was evident that for all δ_f tested, the 10mm serrations extended the upper limit of α over which measurements were obtained from 16° to 18°, inferring an increase in α_{stall}.

Evaluation of the effects of the 10mm serrations on C_l and C_d in terms of L/D indicated that typically, the 10mm serrations had either no appreciable effect upon L/D or decreased L/D in comparison to the corresponding plain trailing edge configuration, see Figure 74.

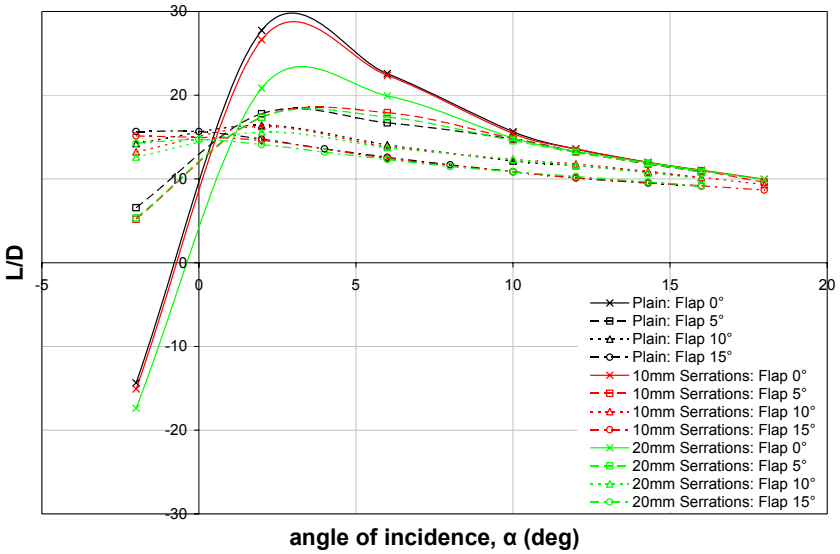

Figure 74: Variation of L/D with angle of incidence for plain, 10mm and 20mm serrated configurations at a flap lap/gap of (−0.17, −0.14), δ_s=0°, $0° \leq \delta_f \leq 15°$

At δ_f=0°, the 10mm serrations reduced L/D by a maximum of 4% for $-2° \leq \alpha \leq 10°$, although with subsequent increments in α, any variation in L/D due to the 10mm serrations was negated. Whilst at δ_f =5°, the 10mm serrations adversely affected L/D for $\alpha \leq 2°$ and there was an isolated increment of 7% at α=6°, L/D was comparable to the

plain trailing edge configuration for $\alpha \geq 10°$. With further increments in $10° \leq \delta_f \leq 15°$, the 10mm serrations typically had negligible effect upon L/D, with only isolated decrements at $\alpha = -2°$.

(b) Flap Lap/Gap: (−0.12, −0.14)

Similarly to the configuration at a flap lap/gap of (−0.17, −0.14), the 10mm serrations decreased C_l for all α and δ_f tested at a flap lap/gap of (−0.12, −0.14), see Figure 75. For any given α, the decrement in C_l was heightened in magnitude with successive increments in $0° \leq \delta_f \leq 10°$. However, with a further increment in δ_f to 15°, ΔC_l decreased in magnitude such that for a given α, the decrement in C_l was less than that for the 10mm serrated configuration with $\delta_f = 5°$.

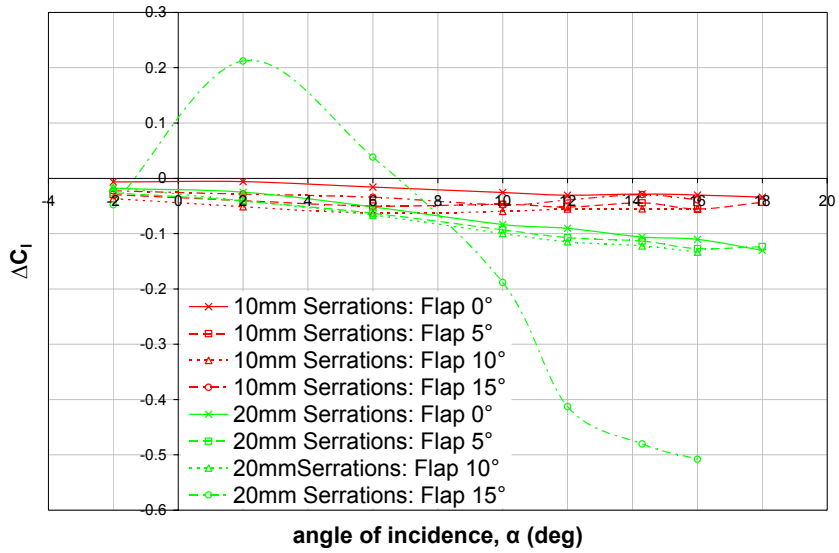

Figure 75: Variation of ΔC_l with angle of incidence due to 10mm and 20mm serrations at a flap lap/gap of (−0.12, −0.14), $\delta_s = 0°$, $0° \leq \delta_f \leq 15°$

At $\delta_f = 0°$, ΔC_l due to the 10mm serrations was progressively heightened with successive α, attaining a maximum decrement of −0.03 and accounting for an approximate 2% reduction in C_l for all α. However for $5° \leq \delta_f \leq 15°$, ΔC_l was progressively heightened with successive increments in $\alpha \leq 6°$, although with subsequent increments in $\alpha \geq 10°$, the decrement in C_l varied inconsistently. At $\delta_f = 5°$ and $\delta_f = 10°$, the maximum decrements in C_l were −0.05 and −0.06, respectively, typically correlating to less than a 4% reduction in C_l for all α.

Again, ΔC_d varied inconsistently with α for all δ_f but there was a tendency for the 10mm serrations to decrease C_d for any given δ_f, see Figure 184(b) in Appendix J. Notable discrepancies to this trend arose at $\delta_f = 0°$, whereby the 10mm serrations increased C_d for

$\alpha \leq 6°$. The 10mm serrations had negligible effect upon the drag polar, although it was evident that at $\delta_f = 10°$, the serrated geometry extended the upper limit of α over which measurements were obtained from 16° to 18°, inferring an increase in α_{stall}. Accordingly, in terms of L/D, the 10mm serrations had a detrimental effect at $\delta_f = 0°$ for $-2° < \alpha < 10°$, see Figure 76. The magnitude of the decrement was greatest at $\alpha = 2°$, accounting for a 13% reduction in L/D in comparison to the baseline configuration, and decreased in magnitude thereafter such that for $\alpha \geq 10°$, the 10mm serrations had negligible effect upon L/D. At $\delta_f = 5°$, the decrement in L/D due to the 10mm serrations was limited to $\alpha \leq 2°$ and whilst an isolated increment in L/D was evident at $\alpha = 6°$, any variation in L/D due to the 10mm serrations was negated for $\alpha \geq 10°$. With further increments in $10° \leq \delta_f \leq 15°$, the 10mm serrations typically had negligible effect upon L/D when compared to the corresponding baseline configuration.

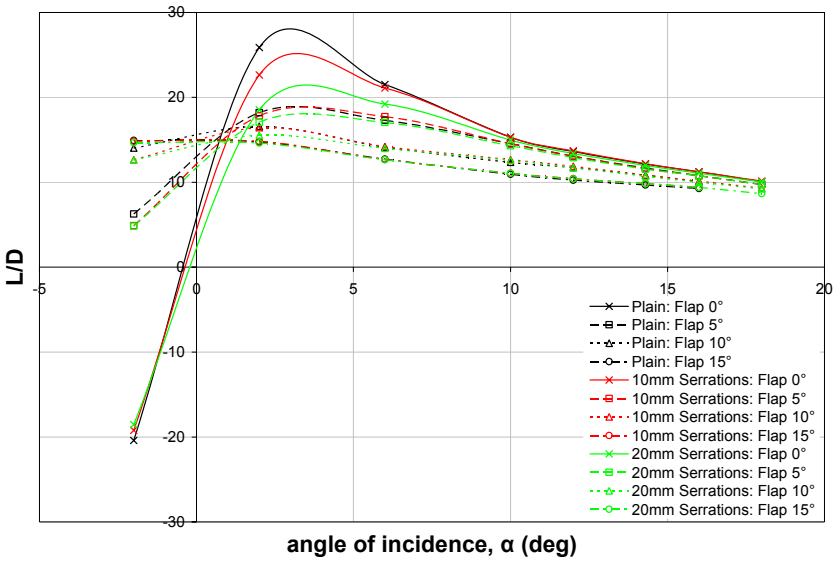

Figure 76: Variation of L/D with angle of incidence for plain, 10mm and 20mm serrated configurations at a flap lap/gap of (−0.12, −0.14), $\delta_s = 0°$, $0° \leq \delta_f \leq 15°$

(c) Flap Lap/Gap: (−0.23, −0.2)

In contrast to the previous grid positions, the 10mm serrations increased C_l for all α at $\delta_f = 0°$ at a flap lap/gap of (−0.23, −0.2), see Figure 77. The maximum ΔC_l of 0.01 was attained at low α, accounting for 2% increment. As α was increased, ΔC_l was minimised, rendering any variations due to the 10mm serrated geometry negligible for $\alpha \geq 12°$. Increasing δ_f to 5° essentially negated the deviation in C_l due to the 10mm serrations for $\alpha \leq 2°$ and with subsequent increments in $\alpha > 2°$, the 10mm serrations had a detrimental effect upon C_l, equating to ≤1% reduction throughout, irrespective of the variation in ΔC_l. At $\delta_f = 10°$, the 10mm serrations had a marginally favourable effect

upon C_l for $\alpha \leq 2°$ but conversely, the 10mm serrations adversely affected C_l for $\alpha > 2°$, with the decrement increasing in magnitude with successive increments in α, attaining a maximum ΔC_l of −0.02 at $\alpha = 16°$. Note that whilst the above trends were identified for $0° \leq \delta_f \leq 10°$, the magnitude of ΔC_l was such that based upon measurement repeatability, ΔC_l was not necessarily indicative of the 10mm serrations varying the flow field development. A final increment in δ_f to 15° heightened the detrimental effect of the 10mm serrations upon C_l for $\alpha \geq 2°$, attaining a maximum decrement of −0.1 at $\alpha = 16°$, which equated to a 3% reduction in comparison to the plain trailing edge configuration.

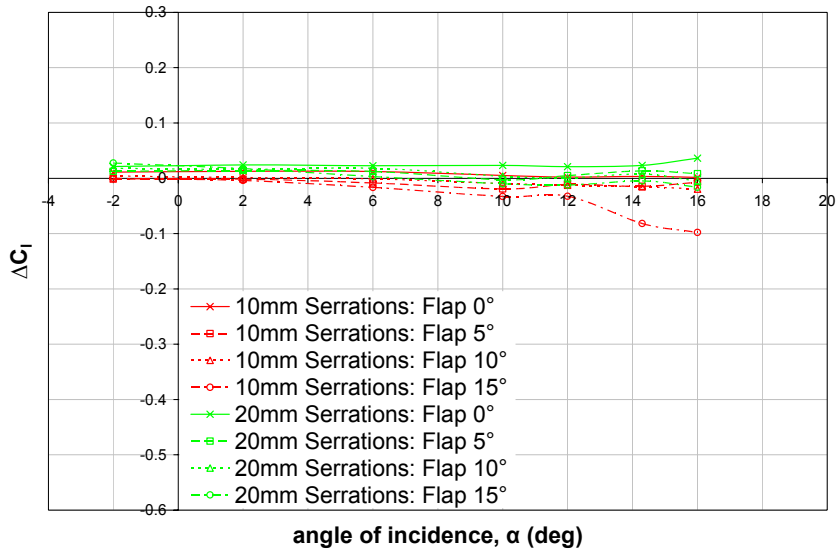

Figure 77: Variation of ΔC_l with angle of incidence due to 10mm and 20mm serrations at a flap lap/gap of (−0.23, −0.2), δ_s=0°, $0° \leq \delta_f \leq 15°$

Whether the 10mm serrations increased or decreased C_d, there was a tendency for ΔC_d to vary inconsistently with α for all δ_f, see Figure 184(c) in Appendix J. At $\delta_f = 0°$, the 10mm serrations increased C_d for all α, whereas for $5° \leq \delta_f \leq 15°$, the 10mm serrations decreased C_d for all α. Despite the fluctuations in C_d, the 10mm serrations had negligible effect upon the corresponding drag polar when compared to the corresponding plain trailing edge configuration.

In terms of L/D, the 10mm serrations had a detrimental effect at $\delta_f = 0°$ for $0° < \alpha < 12°$, with the magnitude of the decrement increasing to a maximum of 4% at $\alpha = 2°$ and decreasing in magnitude thereafter such that for $\alpha \geq 12°$, the 10mm serrations had negligible effect upon L/D, see Figure 78. In contrast, a single increment in δ_f to 5° notably increased L/D for $-2° < \alpha < 8°$. The greatest increment in L/D of 5% occurred at $\alpha = 2°$ and the increment in L/D decreased in magnitude thereafter. The increment in L/D was maintained at $\delta_f = 10°$, although it was limited to $-2° \leq \alpha \leq 3°$ with the greatest

increment of 2% once again evident at α=2° and any variation negated for α>3°. With a final increment in δ_f to 15°, the 10mm serrations typically had no discernible effect upon L/D in comparison to the baseline configuration.

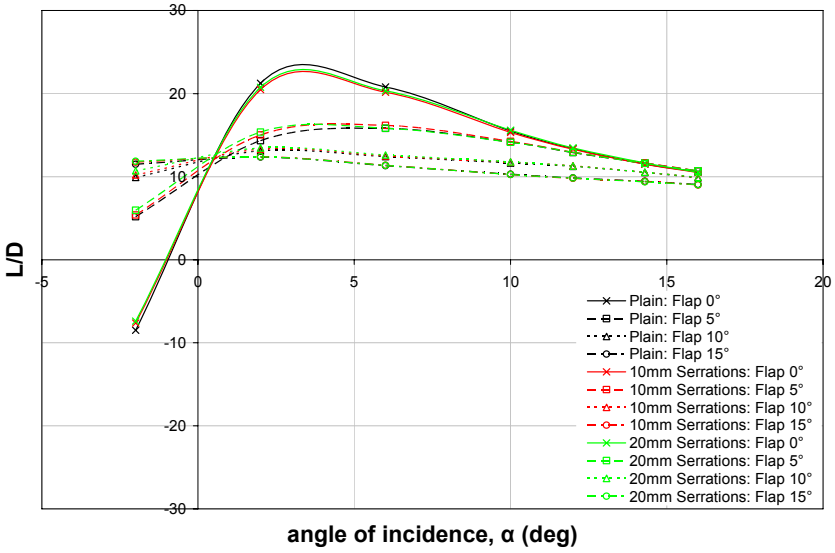

Figure 78: Variation of L/D with angle of incidence for plain, 10mm and 20mm serrated configurations at a flap lap/gap of (−0.23, −0.2), δ_s=0°, 0°≤δ_f≤15°

(d) Flap Lap/Gap: (−0.17, −0.2)

Maintaining the flap gap of −0.2 and positioning the flap incrementally downstream at a lap of −0.17, degraded the effectiveness of the 10mm serrations, and once again decreased C_l in comparison to the plain trailing edge configuration for all α and δ_f tested, see Figure 79.

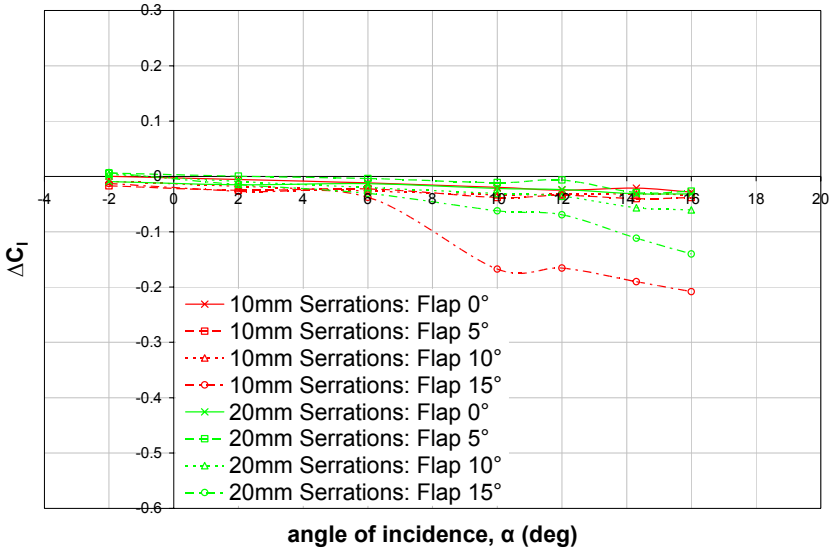

Figure 79: Variation of ΔC_l with angle of incidence due to 10mm and 20mm serrations at a flap lap/gap of (−0.17, −0.2), δ_s=0°, 0°≤δ_f≤15°

At δ_f=0°, the decrement in C_l tended to increase in magnitude with successive α, attaining a maximum decrement of −0.03 and accounting for <1.5% reduction in lift for all α. With successive increments in 5°≤δ_f≤15°, the decrement in C_l for any given α was progressively heightened, although ΔC_l varied inconsistently with α for any given δ_f. For 5°≤δ_f≤10°, ΔC_l typically accounted for ≤2% reduction in lift in comparison to the baseline configuration but the substantial decrements evident at δ_f=15° corresponded to a 7% decrement in C_l for 10°≤α≤16°.

The 10mm serrations decreased C_d in comparison to the plain trailing edge configuration, although ΔC_d varied inconsistently with α for all δ_f, see Figure 184(d) in Appendix J. Whilst the 10mm serrations had negligible effect upon the drag polar for δ_f≤10°, the similarity was limited to low C_l at δ_f=15°, as the 10mm serrations increased C_d for any given C_l>1.9. In addition, the 10mm serrated geometry extended the upper limit of α, over which measurements were obtained, from 16° to 18°, inferring an increase in α_{stall} in comparison to the baseline configuration.

Evaluation of the effects of the 10mm serrations on C_l and C_d in terms of L/D indicated that the 10mm serrations had a detrimental effect upon L/D for α≤6° at δ_f=0°, see Figure 80. The decrement was heightened to a maximum 3% reduction at α=2° and decreased in magnitude thereafter, such that deviations in L/D due to the 10mm serrations were marginalised at high test α.

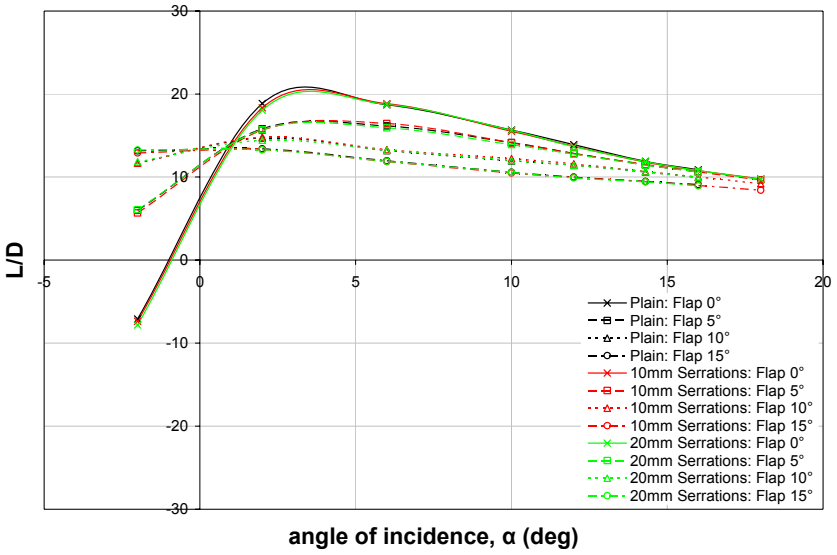

Figure 80: Variation of L/D with angle of incidence for plain, 10mm and 20mm serrated configurations at a flap lap/gap of (−0.17, −0.2), δ_s=0°, 0°≤δ_f≤15°

Similarly to the corresponding configuration at a smaller flap gap of −0.14, the decrement in L/D due to the 10mm serrations was maintained at δ_f=5° for α≤2°.

However, there was an isolated increment in L/D accounting for a 2% increase at α=6° prior to any variation being negated for $\alpha \geq 10°$. Determining a distinct range of α over which the 10mm serrations increased L/D at δ_f=5° was limited by the large incremental values in $\alpha \leq 10°$ at which measurements were obtained. At δ_f=10°, the detrimental effect of the 10mm serrations upon L/D was limited to α=−2° and with subsequent increments in α, the 10mm serrations increased α, accounting for ≤2% increment in comparison to the baseline configuration. A final increment in δ_f to 15° rendered the 10mm serrations detrimental to L/D at low α in comparison to the baseline configuration. The 2% decrement in L/D was greatest at α=−2° and reduced in magnitude thereafter, such that deviations in L/D due to the 10mm serrations were essentially negated for $\alpha \geq 10°$.

(e) Flap Lap/Gap: (−0.12, −0.2)

A final increment in the flap lap from −0.17 to −0.12, whilst maintaining the flap gap of −0.2, heightened the decrement in C_l due to the 10mm serrations at δ_f=0°, attaining a maximum decrement of −0.05 and typically reducing the lift by 2-3% for all α, see Figure 81.

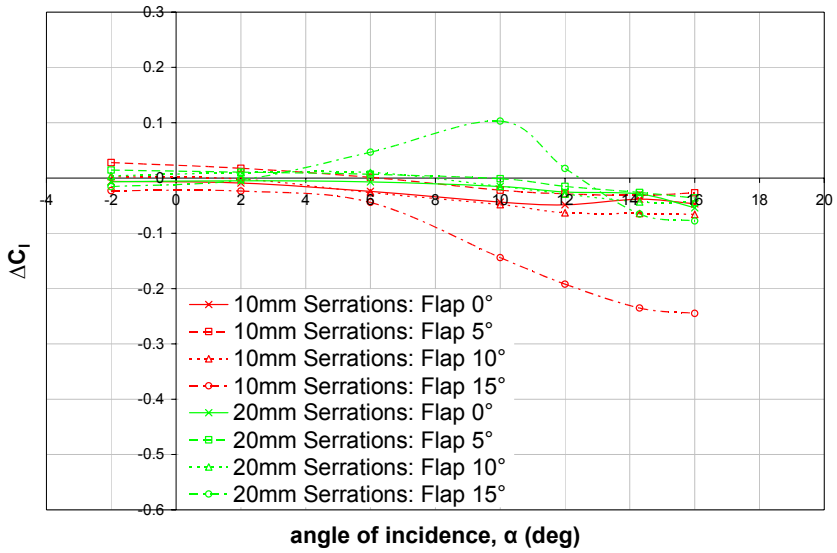

Figure 81: Variation of ΔC_l with angle of incidence due to 10mm and 20mm serrations at a flap lap/gap of (−0.12, −0.2), δ_s=0°, 0°≤δ_f≤15°

In contrast, Figure 81 showed that the 10mm serrations increased C_l in comparison to the baseline configuration for $\alpha \leq 6°$ at δ_f=5°, attaining a maximum increment of 0.03 at α=−2° and decreasing in magnitude thereafter. For α>6°, the 10mm serrations adversely affected C_l, with the decrement progressively heightened in magnitude with successive α and accounting for <1.5% reduction in C_l in comparison to the baseline configuration. Increasing δ_f to 10° essentially negated the deviation in C_l due to the

10mm serrations at α=−2° and had a detrimental effect upon C_l with subsequent increments in α≥2°, equating to ≤2.5% reduction in C_l when compared to the plain trailing edge configuration. A final increment in δ_f to 15° heightened the detrimental effect of the 10mm serrations upon C_l for all α, with substantial reductions in lift evident for α≥8°, accounting for up to a 9% decrement in C_l in comparison to the plain trailing edge configuration.

Whilst ΔC_d varied inconsistently with α for all δ_f, there was a tendency for the 10mm serrations to decrease C_d, although isolated discrepancies were evident, see Figure 184(e) in Appendix J. Similarly to the configuration at a flap lap/gap of (−0.17, −0.2), the 10mm serrations had negligible effect upon the drag polar for δ_f≤10°, although the 10mm serrated geometry extended the upper limit of α, over which measurements were obtained, from 16° to 18°, inferring an increase in α_{stall} in comparison to the corresponding plain trailing edge configuration. Whilst the drag polar for the plain and 10mm serrated configurations were comparable for low C_l at δ_f=15°, the 10mm serrations increased C_d for any given C_l>1.8, in comparison to the corresponding plain trailing edge configuration.

In terms of L/D, the 10mm serrations typically reduced L/D by <2% for −2°≤α<12° at δ_f=0°, with any deviation in L/D negated for α≥12°, although an isolated 1% increment in L/D was evident at α=6° when compared to the baseline configuration, see Figure 82.

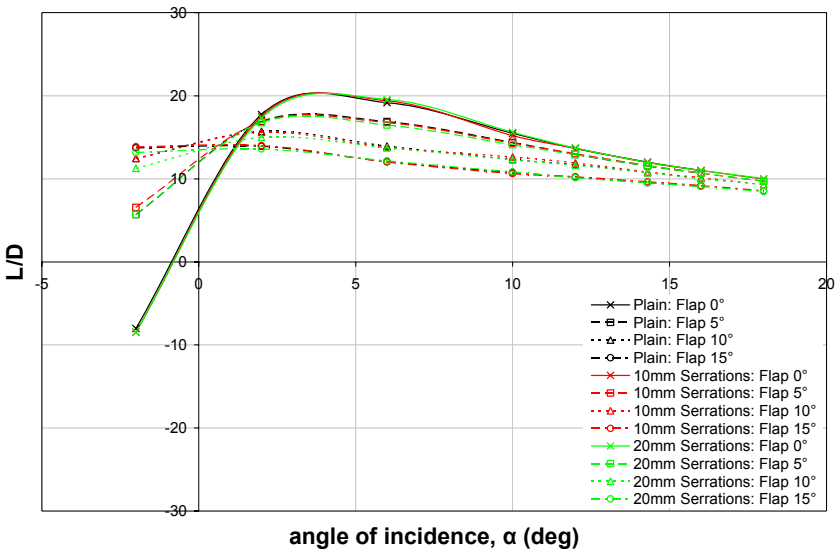

Figure 82: Variation of L/D with angle of incidence for plain, 10mm and 20mm serrated configurations at a flap lap/gap of (−0.12, −0.2), δ_s=0°, 0°≤δ_f≤15°

At δ_f=5°, the 10mm serrations typically had no discernible effect upon L/D in comparison to the baseline configuration. At δ_f=10°, the 10mm serrations reduced L/D by <1% for 2°≤α≤6°, although with subsequent increments in α, the 10mm serrations increased L/D by up to 3% at α=10°. With a final increment in δ_f to 15°, the 10mm serrations had no appreciable effect upon L/D, when compared to the corresponding plain trailing edge configuration.

6.7.3 20mm Serrated Trailing Edge

(a) Flap Lap/Gap: (−0.17, −0.14)

Similarly to the 10mm serrations, the 20mm serrations adversely affected C_l at a flap lap/gap of (−0.17, −0.14) for all α and δ_f tested, see Figure 73. For any given δ_f, the decrement in C_l due to the 20mm serrations tended to progressively heighten in magnitude with successive increments in α. At δ_f=0°, ΔC_l due to the 20mm serrations typically accounted for 3-4% reduction in comparison to the plain trailing edge configuration. Successive increments in 5°≤δ_f≤10° tended to progressively heighten the magnitude of decrement in C_l for any given α, although isolated discrepancies arose at each δ_f. At δ_f=15°, the decrement in C_l due to the 20mm serrations substantially increased in magnitude for all α, attaining a maximum decrement of −0.21 and accounting for 5-8% reduction in C_l throughout. Thus, increasing the serration length from 10mm to 20mm tended to increase the magnitude of the decrement in C_l for any given α and δ_f tested.

The trends in C_d due to the 20mm serrations were comparable to those observed for the 10mm serrated geometry, although the magnitude of ΔC_d typically exceeded that for the corresponding 10mm serrated configuration, see Figure 184(a) in Appendix J. Thus, ΔC_d varied inconsistently with α for all δ_f, with the 20mm serrations typically decreasing C_d in comparison to the plain trailing edge configuration. Once again, a notable discrepancy to this trend arose at δ_f=0°, whereby the 20mm serrations increased C_d for 0°≤α≤10°, with the increment heightened by the increased serration length. Although the 20mm serrations had negligible effect upon the drag polar at δ_f=5° and 10°, the 20mm serrations marginally increased C_d for any given C_l at both δ_f=0° and δ_f=15°. The 20mm serrations only extended the upper limit of α over which measurements were obtained from 16° to 18° at δ_f=0°, from which it was inferred that α_{stall} was increased.

Evaluation of the effects of the 20mm serrations upon C_l and C_d in terms of L/D indicated that the 20mm serrations had a detrimental effect upon L/D for $-2° \leq \alpha < 14°$ at $\delta_f = 0°$, see Figure 74. The magnitude of the decrement was greatest at $\alpha = 2°$, accounting for a 25% reduction in L/D in comparison to the plain trailing edge configuration, and decreased in magnitude with subsequent increments in α, such that any variation in L/D due to the 20mm serrations was essentially negated for $\alpha \geq 14°$. The trend at $\delta_f = 5°$ was comparable to the 10mm serrated configuration, with the 20mm serrations adversely affecting L/D for $\alpha \leq 2°$ in comparison to the baseline configuration and having negligible effect upon L/D for $\alpha \geq 10°$. Once again, there was an isolated increment in L/D at $\alpha = 6°$ equating to a 4% increase due to the 20mm serrations, which was smaller than the corresponding increment identified for the 10mm serrated configuration at $\delta_f = 5°$. However, with further increments in $10° \leq \delta_f \leq 15°$, the 20mm serrations reduced L/D for $\alpha \leq 6°$. For both $\delta_f = 10°$ and $\delta_f = 15°$, the decrement in L/D was greatest at $\alpha = -2°$ and decreased in magnitude with successive increments in α such that the 20mm serrations had no appreciable affect upon L/D for $\alpha \geq 10°$ when compared to the baseline configuration.

(b) Flap Lap/Gap: (−0.12, −0.14)

The 20mm serrations, like the 10mm serrations, had a detrimental affect upon C_l for $\delta_f \leq 10°$ at a flap lap/gap of (−0.12, −0.14), see Figure 75. At $\delta_f = 0°$, the decrement in C_l was heightened with successive increments in α, attaining a maximum ΔC_l of −0.13 at $\alpha = 18°$ and corresponding to a 5-8% reduction in C_l in comparison to the plain trailing edge configuration for all test α. Typically, successive increments in $\delta_f \leq 10°$ progressively heightened the magnitude of ΔC_l for a given α. At $\delta_f = 5°$, ΔC_l typically accounted for a 5% reduction in C_l in comparison to the plain trailing edge configuration. By incrementing δ_f from 5° to 10°, the magnitude of the decrement in C_l due to the 20mm serrations was heightened for $\alpha \geq 6°$, attaining a maximum of −0.14 at $\alpha = 16°$ and representing a 3-5% reduction in lift throughout. However for $\alpha \leq 2°$, ΔC_l decreased such that it was comparable in magnitude to that at $\delta_f = 0°$ for $\alpha = -2°$ and analogous to ΔC_l at $\delta_f = 5°$ for $\alpha = 2°$. With a final increment in δ_f to 15°, ΔC_l varied irregularly. Whilst the decrement in C_l was notably heightened for $\alpha = -2°$ and $\alpha \geq 10°$, there existed a finite range of α for which the 20mm serrations increased C_l in comparison to the plain trailing edge configuration. Specifically, a maximum ΔC_l of 0.2 was attained at $\alpha = 2°$, accounting for a 15% increase in C_l, although by $\alpha = 6°$, ΔC_l had diminished to 0.04, equating to a 2% increment in comparison to the baseline configuration. Note that these fluctuations from the trends were defined by only two data points. For $\alpha \geq 10°$, the adverse effect of the 20mm serrations upon C_l was

substantially magnified at δ_f=15° when compared to all other δ_f, progressively decreasing C_l to a maximum decrement of −0.5 at α=16° and representing a 17% reduction in the lift force generated. Direct comparison of the 10mm and 20mm serrated trailing edge configurations indicated that for any given δ_f, increasing the serration length typically heightened the decrement in C_l, particularly at high test α.

Whilst ΔC_d varied inconsistently with α for all δ_f, there was a tendency for the 20mm serrations to decrease C_d, although isolated discrepancies were evident, see Figure 184(b) in Appendix J. The most substantial deviation to the trend occurred at δ_f=15°, with ΔC_d oscillating erratically with α between favourable decrements and adverse increments. However, without additional balance measurements, it could not be ascertained as to whether these variations in the trends were attributed to features in the flow field or due to isolated experimental errors incurred. With regard to the drag polar, the 20mm serrations marginally increased C_d for any given C_l at δ_f=0°. Although no appreciable effect was discerned for $C_l \leq 2$ at δ_f=5° and 10°, with further increments in C_l, the 20mm serrations once again marginally increased C_d in comparison to the baseline configuration. At δ_f=15°, the 20mm serrations had negligible effect upon the drag polar for $C_l \leq 1.8$ but notably increased C_d for any given $C_l > 1.8$. The 20mm serrations only extended the upper limit of α over which measurements were obtained from 16° to 18° at δ_f=10° and δ_f=15°, inferring an increment in α_{stall}.

In terms of L/D, the 20mm serrations had a detrimental effect at δ_f=0° for $-2° < \alpha < 12°$, with the magnitude of the decrement attaining a maximum 28% reduction in L/D at α=2° and decreasing in magnitude thereafter such that for $\alpha \geq 12°$, the 20mm serrations had negligible effect upon L/D, see Figure 76. At δ_f=5° and 10°, the 20mm serrations reduced L/D in comparison to the baseline configuration for $\alpha \leq 6°$, with any variation essentially negated for thereafter. Despite the marked variations in C_l and C_d, with a final increment in δ_f to 15°, the 20mm serrations had negligible effect upon L/D in comparison to the plain trailing edge configuration.

As an additional note, (−0.12, −0.14) represented the only flap lap/gap comparable to the test flap lap/gap of (−0.13, −0.13) in the Brough wind-tunnel experiments. For the latter experiments conducted at α=0°, the favourable effect of the 10mm and 20mm serrations upon C_l was limited to δ_f=0° and $0° \leq \delta_f \leq 5°$, respectively. However, whilst the Brough experiments considered the effect of the serrated geometries upon the aerodynamic characteristics of an aft positioned single slotted flap, the high-lift configuration, detailed within the present section, considered the effect of the serrated

geometries upon the resultant aerodynamic forces acting upon a two-element configuration. This, when combined with the significant disparities between the test configuration geometries, rendered comparisons ineffective.

(c) Flap Lap/Gap: (−0.23, −0.2)

At a flap lap/gap of (−0.23, −0.2), the 20mm serrations had a distinctly favourable effect upon C_l for all δ_f, although the range of α over which C_l was increased was reduced with successive increments in δ_f, see Figure 77. The 20mm serrations increased C_l for all α at δ_f=0°. With ΔC_l varying between 0.02 and 0.025 for $-2° \leq \alpha \leq 14°$, the increment in C_l due to the 20mm serrations appeared relatively insensitive to α at δ_f=0°, only increasing to 0.035 at α=16° and accounting for a 2% increment for $\alpha \geq 6°$ when compared to the baseline configuration. At δ_f=5°, the increment in C_l due to the 20mm serrations was reduced to approximately 0.013 for $-2° \leq \alpha \leq 6°$, although ΔC_l was more sensitive to variations in $\alpha \geq 10°$. Measurements indicated an anomaly at α=10°, with the 20mm serrations adversely affecting C_l, albeit on a marginal scale. Incrementing δ_f to 10° increased ΔC_l to approximately 0.017 for $-2° \leq \alpha \leq 6°$ when compared to the baseline configuration, the consistency of which again suggested the relative insensitivity of ΔC_l to increments in low α. However, ΔC_l varied inconsistently for $\alpha > 6°$ corresponding to a maximum ±1% variation in C_l due to the 20mm serrations throughout in comparison to the baseline configuration. A final increment in δ_f to 15° indicated that whilst the 20mm serrations increased C_l for $-2° \leq \alpha \leq 6°$, ΔC_l decreased in magnitude with successive increments in $\alpha \leq 6°$. Comparatively, ΔC_l notably exceeded that for $\delta_f \leq 10°$ at $\alpha = -2°$ and was marginally greater than that for $5° \leq \delta_f \leq 10°$ at α=2°. With further increments in $\alpha \geq 10°$, the 20mm serrations adversely affected C_l in comparison to the baseline configuration, with the decrement varying inconsistently with increments in α but accounting for <1% reduction in lift throughout. Direct comparison of the 10mm and 20mm serrated configurations indicated that increasing the serration length was highly beneficial to the lift generated, increasing the range of α and δ_f over which the serrated geometry was favourable.

Figure 184(c) in Appendix J showed that ΔC_d due to the 20mm serrations varied inconsistently with α for all δ_f, typically increasing C_d at δ_f=0°, 5° and 15°, with only isolated decrements in C_d at δ_f=5° and 15°. In contrast, the 20mm serrations decreased C_d at δ_f=10°, the decrement varying irregularly with α and accounting for <1.5% reduction in C_d with only an isolated increment at α=14°. Despite the variation in C_l and C_d, the 20mm serrations had no appreciable effect upon the drag polar when compared to the corresponding plain trailing edge configuration.

In terms of L/D, the 20mm serrations had a detrimental effect at δ_f=0° for 0°<α<10°, with the magnitude of the decrement increasing to a maximum of 3% at α=2° and decreasing in magnitude thereafter such that for α≥10°, the 20mm serrations had negligible effect upon L/D in comparison to the baseline configuration, see Figure 78. In contrast, a single increment in δ_f to 5° notably increased L/D for −2°≤α<6° in comparison to the baseline configuration, with the greatest increment of 15% occurring at α=−2° and decreasing in magnitude thereafter such that the increment was reduced to 7% at α=2° and essentially negated for α≥6°. The increment in L/D was maintained for −2°≤α≤10° at δ_f=10°, with the greatest increment of 8% once again evident at α=−2° and decreasing thereafter, such that L/D was essentially coincident with the plain trailing edge data for α≥12°. With a final increment in δ_f to 15°, the 20mm serrations had no appreciable effect upon L/D when compared to the baseline plain trailing edge configuration, with only an isolated 3% increment at α=−2°.

(d) Flap Lap/Gap: (−0.17, −0.2)

Maintaining the flap gap of −0.2 and positioning the flap incrementally downstream at a lap of −0.17, degraded the effectiveness of the 20mm serrations, typically decreasing C_l in comparison to the plain trailing edge configuration for all α and δ_f tested, with only isolated increments evident at α=−2° for 5°≤δ_f≤15°, see Figure 79. Whilst there was a tendency for the decrement in C_l to be progressively heightened in magnitude with successive α for any given δ_f, isolated anomalies were evident. At δ_f=0°, the decrement in C_l due to the 20mm serrations was progressively heightened in magnitude with α, attaining a maximum of −0.03 at α=16°, typically accounting for a 1% reduction in C_l for 6°≤α≤16° when compared to the plain trailing edge configuration. Incrementing δ_f from 0° to 5° typically reduced the magnitude of the decrement in C_l due to the 20mm serrations for any given α, representing ≤1% reduction in comparison to the baseline configuration. In contrast, increasing δ_f to 10° heightened the decrement in C_l to 2% for α≥6°, although a marginal reduction in ΔC_l was evident for α≤2° in comparison to the configurations with δ_f≤5°. With a final increment in δ_f to 15°, ΔC_l was comparable in magnitude to the corresponding configuration with δ_f=0° at α=2° but with subsequent increments in α≥6°, the decrement in C_l exceeded that of the corresponding configurations with δ_f≤10°, markedly reducing C_l for α≥14° and equating to a maximum 5% reduction in C_l in comparison to the baseline configuration. Direct comparison of the 10mm and 20mm serrated configurations indicated that increasing the serration length tended to heighten the decrement in C_l for δ_f=0°. In contrast, with further increments in 5°≤δ_f≤15°, increasing the serration length tended to diminish the adverse effect upon C_l, with the exception of α≥12° at δ_f=10° where once again, ΔC_l was

heightened by the 20mm serrations. Thus, whilst both serrated geometries had an adverse effect upon C_l, increasing the serration length from 10mm to 20mm was typically less detrimental to the lift force generated for $5° \leq \delta_f \leq 15°$.

ΔC_d due to the 20mm serrations varied inconsistently with α for all δ_f, typically decreasing C_d for all α at δ_f=0°, 10° and 15°, although isolated increments were evident, see Figure 184(d) in Appendix J. At δ_f=5°, the 20mm serrations increased C_d for $\alpha \leq 12°$ and only decreased C_d for $\alpha \geq 14°$. The 20mm serrations had negligible effect upon the drag polar for $0° \leq \delta_f \leq 10°$. Whilst at δ_f=15°, the drag polar for the 20mm serrated configuration was comparable to both the plain and 10mm serrated configurations for $C_l \leq 1.9$, the 20mm serrations increased C_d for any given $C_l > 1.9$. Furthermore, the 20mm serrations extended the upper limit of α, over which measurements were obtained, from 16° to 18° at δ_f=0°, inferring an increase in α_{stall} in comparison to the corresponding plain trailing edge configuration.

Evaluation of the effects of the 20mm serrations on C_l and C_d in terms of L/D indicated that similarly to the 10mm serrated geometry, the 20mm serrations had a detrimental effect upon L/D for $-2° \leq \alpha \leq 6°$ at δ_f=0°, see Figure 80. The magnitude of the decrement was greatest at α=2°, accounting for a 4% reduction in comparison to the baseline configuration and exceeding that of the corresponding 10mm serrated configuration. With further increments in α, deviations in L/D due to the 20mm serrations were marginalised and negated as α_{stall} was approached. In contrast to the 10mm serrations, the 20mm serrated geometry decreased L/D by <2% at δ_f=5° for $2° \leq \alpha \leq 12°$ and was comparable to the plain trailing edge configuration for $\alpha < 2°$ and $\alpha > 12°$. With further increments in $10° \leq \delta_f \leq 15°$, the 20mm serrations had no appreciable effect upon L/D in comparison to the plain trailing edge configuration, with only an isolated 2% decrement at α=2° for δ_f=10°.

(e) Flap Lap/Gap: (−0.12, −0.2)

A final increment in the flap lap from −0.17 to −0.12 at a flap gap of −0.2, typically improved the effectiveness of the 20mm serrations, reducing the decrement in C_l and introducing ranges of α for which the 20mm serrations increased C_l, see Figure 81. Whilst there was a tendency for the decrement in C_l to be progressively heightened in magnitude with successive α for any given δ_f, isolated anomalies were evident. At δ_f=0°, the decrement in C_l due to the 20mm serrations was progressively heightened with α, attaining a maximum ΔC_l of −0.06 at α=16° and typically accounting for a 1-2% reduction in C_l in comparison to the plain trailing edge configuration for $2° \leq \alpha \leq 16°$. By

incrementing δ_f from 0° to 5°, the 20mm serrations not only increased C_l for $-2° \leq \alpha \leq 6°$ but also reduced the decrement in C_l for $\alpha \geq 10°$, representing ≤1% reduction in comparison to the baseline configuration. A similar trend was noted at δ_f=10°, with the 20mm serrations marginally increasing C_l for $-2° \leq \alpha \leq 6°$ but adversely affecting C_l for $\alpha \geq 10°$. The decrement in C_l due to the 20mm serrations at δ_f=10° exceeded that of configurations at smaller test δ_f, reducing C_l by 1-2% in comparison to the plain trailing edge configuration. With a final increment in δ_f to 15°, ΔC_l varied irregularly: whilst the 20mm serrations had a detrimental effect upon C_l for $\alpha \leq 2°$ and $\alpha \geq 14°$, the 20mm serrations increased C_l for $6° \leq \alpha \leq 12°$, attaining a maximum ΔC_l of 0.1 at α=10° and accounting for a 5% increment in comparison to the baseline configuration. Evidence of a finite range of α at δ_f=15° over which the 20mm serrations increased C_l corroborated the corresponding 20mm serrated configuration when positioned at the smaller flap gap of −0.14, suggesting that the increment in C_l was attributable to a flow field feature as opposed to experimental error. Increasing the serration length from 10mm to 20mm typically diminished the decrement in C_l. Whilst the 20mm serrations reduced the increment in C_l at δ_f=5° in comparison to the 10mm serrations, the 20mm serrations were generally more favourable at both δ_f=10° and δ_f=15°, extending the range of α over which the serrated geometry increased C_l and heightening the magnitude of the increment.

Similarly to the 10mm serrated configuration, ΔC_d due to the 20mm serrations varied inconsistently with α for all δ_f, see Figure 184(e) in Appendix J. At δ_f=0°, the 20mm serrations decreased C_d but with subsequent increments in δ_f, there was a tendency for the 20mm serrations to increase C_d at low to mid α and decrease C_d at high test α. Similarly to the 10mm serrated configuration, the 20mm serrations had negligible effect upon the drag polar for $\delta_f \leq 10°$, although likewise, the 20mm serrated geometry extended the upper limit of α, over which measurements were obtained, from 16° to 18°, inferring that the serrations duly increased α_{stall} in comparison to the corresponding plain trailing edge configuration. At δ_f=15°, the drag polar for the plain and 20mm serrated configurations were comparable.

At δ_f=0°, the 20mm serrations typically reduced L/D by less than 3% for $-2° \leq \alpha \leq 2°$ and although there was an isolated 2% increment at α=6°, with further increments in $\alpha \geq 10°$, any variation in L/D due to the 20mm serrations was essentially negated, see Figure 82. At δ_f=5°, the 20mm serrations decreased L/D by a maximum of 2% for $2° \leq \alpha \leq 10°$ but was comparable to the plain trailing edge configuration for $\alpha \geq 12°$. The 20mm serrations notably reduced L/D for $-2° \leq \alpha \leq 6°$ at δ_f=10°, with a maximum 10%

decrement coinciding with α=−2°, although the decrement was marginalised with successive increments in α, such that any variation was essentially negated for α≥10°. With a final increment in δ_f to 15°, the decrement in L/D due to the 20mm serrations was limited to −2°≤α≤2°, attaining a maximum 4% reduction in L/D at α=−2° and decreasing in magnitude thereafter such that for α≥6°, the 20mm serrations had no appreciable effect upon L/D when compared to the corresponding plain trailing edge configuration.

6.7.4 Summary for the Two-Element Configuration: Coarse Lap/Gap Grid

Based upon the coarse lap/gap parametric study of a two-element high-lift configuration comprising a main element with either a plain, 10mm or 20mm 60° triangular serrated trailing edge and a single slotted flap deflected between 0° and 15°, the resultant aerodynamic forces, determined from balance measurements, indicated that:

- 10mm serrations were typically highly ineffective and although increasing the serration length to 20mm proved more beneficial to C_l and L/D, the favourable effects were limited
- 10mm serrations tended to reduce C_l in comparison to the plain trailing edge configuration
- In terms of increasing C_l, both 10mm and 20mm serrations were most effective at a flap lap/gap of (−0.23, −0.2), although the favourable effect of the 10mm serrations was limited to δ_f=0°
- Increasing the serration length to 20mm at a lap/gap of (−0.23, −0.2) increased the range of α and δ_f over which the serrated geometry was favourable: ΔC_l due to the 20mm serrations was relatively consistent at δ_f=0° for all test α but with successive increments in δ_f, the range of α over which the 20mm serrations increased C_l was reduced, as was the magnitude of the increment
- The flap lap/gap for which the 20mm serrations most effectively increased C_l did, for the most part, correlate to the optimum flap lap/gap in terms of maximising the overall C_l for the 20mm serrated configuration, although discrepancies arose at δ_f=5° and δ_f=10° for α≥10° and at δ_f=15° for all test α, with the flap lap/gap of (−0.12, −0.2) proving optimal
- With serrations implemented and δ_f=15°, C_l was highly sensitive to variations in flap lap/gap at mid to high test α

- Tendency for the serrated geometries to reduce C_d, although the magnitude of decrement was typically insufficient to offset the corresponding decrement in C_l
- 10mm and 20mm serrations typically had no appreciable effect upon L/D or reduced L/D in comparison to the baseline configuration, although exceptions were evident, particularly at a lap/gap of (−0.23, −0.2)
- The optimum lap/gap, in terms of attaining a maximum L/D, was highly sensitive to variations in both α and δ_f, rendering distinct trends difficult to ascertain

6.8 Three-Element High-Lift Configuration: Single Flap Lap/Gap

In order to determine whether the effectiveness of the 10mm and 20mm trailing edge serrated geometries could be improved by deflection of a leading edge high-lift device, a single slotted slat was deployed in conjunction with the trailing edge flap at a single flap lap/gap position. The resultant aerodynamic forces were obtained from the balance measurements.

6.8.1 Plain Trailing Edge

With the trailing edge flap positioned at a lap/gap of (−0.23, −0.2) and the leading edge slat retracted in its stowed position, C_l increased approximately linearly with α for all δ_f, stalling abruptly between α=16° and 18°. Deployment of the leading edge slat by 23° extended the range of α over which measurements were obtained from 16° to 20° for all δ_f tested. Comparison of the two- and three-element configurations in Figure 83 showed that, in accordance with theory, deflection of the leading edge slat degraded the C_l achievable for any given α over a comparable test range.

The decrement in C_l due to the deflection of the leading edge slat was greatest at α=4°, decreasing in magnitude with successive increments in $\alpha \leq 16°$ and with successive increments in δ_f. Accordingly, any variation in C_l due to deflection of the leading edge slat was essentially negated at α=16° for the configuration with δ_f=15°. Despite the degradation in C_l for $4° \leq \alpha \leq 16°$, the increase in the lift-curve gradient for the three-element configuration not only extended α_{stall} but also significantly increased C_{lmax} for all δ_f tested.

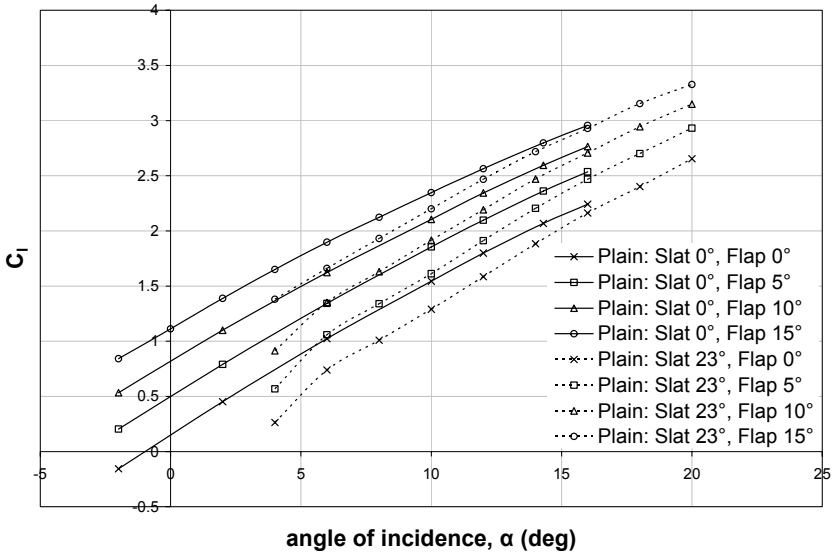

Figure 83: Variation of C_l with angle of incidence for a three-element plain trailing edge high lift configuration at a flap lap/gap of (−0.23, −0.2)

6.8.2 10mm Serrated Trailing Edge

At a flap lap/gap of (−0.23, −0.2), implementation of the 10mm serrations at the trailing edge of the main element in a three-element configuration, had a detrimental effect upon C_l for all α and δ_f, with only isolated exceptions arising at δ_f=10° and 15°, see Figure 84.

With the leading edge slat deployed, ΔC_l appeared highly sensitive to increments in α, varying inconsistently with α for all δ_f. Recalling that for the two-element configuration, the 10mm serrations increased C_l for all α at δ_f=0°, deflection of the leading edge slat rendered the 10mm serrations detrimental, decreasing C_l for all $4° \leq \alpha \leq 20°$. A maximum decrement of −0.03 was attained at α=6°, accounting for a 5% reduction in C_l, but with subsequent increments in $\alpha \geq 6°$, ΔC_l decreased in magnitude equating to <1% reduction in C_l in comparison to the plain trailing edge configuration. Increasing δ_f from 0° to 5° for the three-element configuration tended to heighten the decrement in C_l due to the 10mm serrations, although due to the fluctuation of ΔC_l, isolated discrepancies were evident over the test range of α. In comparison to the two-element configuration, deflection of the leading edge slat at δ_f=5° heightened the decrement in C_l for $4° \leq \alpha \leq 8°$ but was of a comparable magnitude for $\alpha \geq 10°$. Comparison of the two- and three-element configurations for $0° \leq \delta_f \leq 5°$ suggested that the effectiveness of the serrations was sensitive to local boundary layer development, duly modified by the deployment of the leading-edge device, from which it may be

inferred that optimisation of the serration geometry was dependent upon the specified configuration geometry.

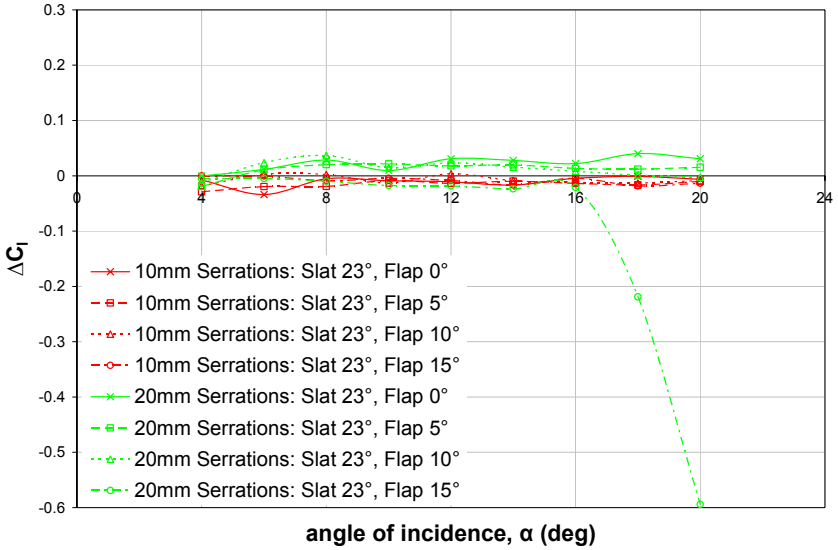

Figure 84: Variation of ΔC_l with angle of incidence due to 10mm and 20mm serrations at a flap lap/gap of (−0.23, −0.2), δ_s=23°, 0°≤δ_f≤15°

For the three-element configuration at δ_f=10°, ΔC_l oscillated irregularly between favourable increments and adverse decrements over the range of α tested. Note that the magnitude of ΔC_l was marginal, accounting for ≤0.5% deviation from the plain trailing edge configuration, irrespective of the polarity of ΔC_l, with the exception of a 2% decrement at α=4°. In comparison to the two-element configuration, the measurements suggested that deflection of the leading edge slat at δ_f=10° typically diminished or negated the decrement in C_l, only heightening the decrement at α=4° and 16°. A final increment in δ_f to 15° for the three-element configuration negated any effect of the 10mm serrations upon C_l for 4°≤α≤6° but with subsequent increments in α≥8°, the 10mm serrations adversely affected C_l, although only accounting for ≤0.5% reduction in comparison to the corresponding plain trailing edge configuration. Similarly to the configuration with δ_f=10°, the measurements suggested that deflecting the leading edge slat at δ_f=15° tended to diminish the decrement in C_l due to the 10mm serrations, when compared to the corresponding two-element configuration. Whilst the above deviations in C_l due to the 10mm serrations have been identified, it should be noted that the magnitude of ΔC_l was such that, with the exception of isolated points, there was essentially negligible variation in the lift generated by the three-element plain and 10mm serrated configurations for a given α and δ_f.

With ΔC_d varying inconsistently with α for all δ_f (see Figure 85), identifying the effect of the 10mm serrations on the drag of the three-element configuration was difficult to

ascertain. Although there was a tendency for the 10mm serrations to decrease C_d for $0°\leq\delta_f\leq10°$, discrepancies to this trend arose at each δ_f, with the 10mm serrated geometry either negating the deviation in C_d or increasing C_d for isolated α within the test range. In contrast, the 10mm serrations tended to increase C_d at $\delta_f=15°$, only decreasing C_d for $\alpha=14°$ and $18°\leq\alpha\leq20°$. That so being, the 10mm serrations typically had no appreciable effect upon the drag polar, with only an isolated marginal increase in C_d for $0.5<C_l<1.0$ at $\delta_f=0°$ when compared to the corresponding baseline configuration.

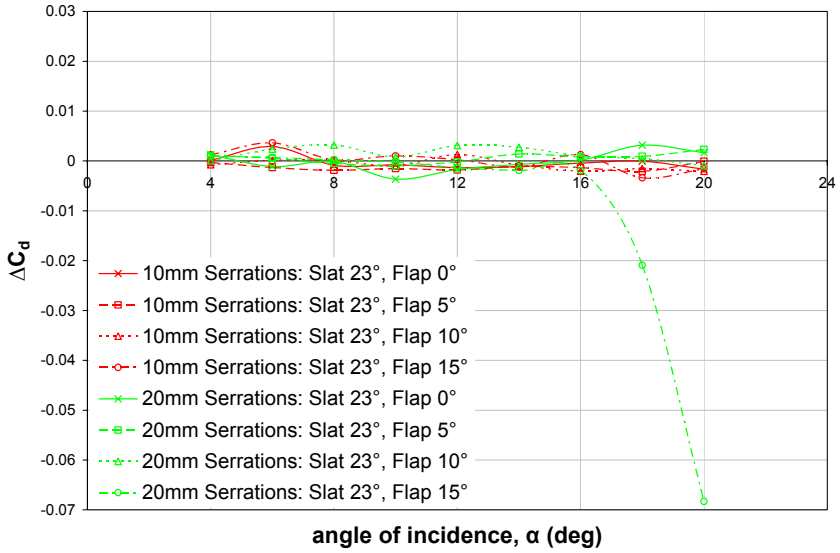

Figure 85: Variation of ΔC_d with angle of incidence due to 10mm and 20mm serrations at a flap lap/gap of (−0.23, −0.2), $\delta_s=23°$, $0°\leq\delta_f\leq15°$

In terms of L/D, Figure 86 shows that in comparison to the plain trailing edge configuration, the 10mm serrations had a detrimental effect at $\delta_f=0°$ for $4°\leq\alpha\leq6°$, with the decrement heightened from 3% at $\alpha=4°$ to a maximum of 9% at $\alpha=6°$. With further increments in α, the decrement in L/D decreased in magnitude such that for $\alpha\geq8°$, the 10mm serrations had negligible effect upon L/D at $\delta_f=0°$ when compared to the baseline configuration. At $\delta_f=5°$, the 10mm serrations reduced L/D by a maximum of 5% at $\alpha=4°$ but with further increments in α, any variation in L/D due to the 10mm serrations was essentially negated. By increasing δ_f to 10°, the 10mm serrations had no discernible effect upon L/D in comparison to the baseline configuration, with only an isolated 1% decrement at $\alpha=4°$. With a final increment in δ_f to 15°, the detrimental effect of the 10mm serrations upon L/D was limited to $4°\leq\alpha\leq10°$, with the greatest decrement of 2% occurring at $\alpha=6°$ and marginalised with increments in α thereafter, rendering any variation in L/D essentially negligible for $\alpha\geq10°$.

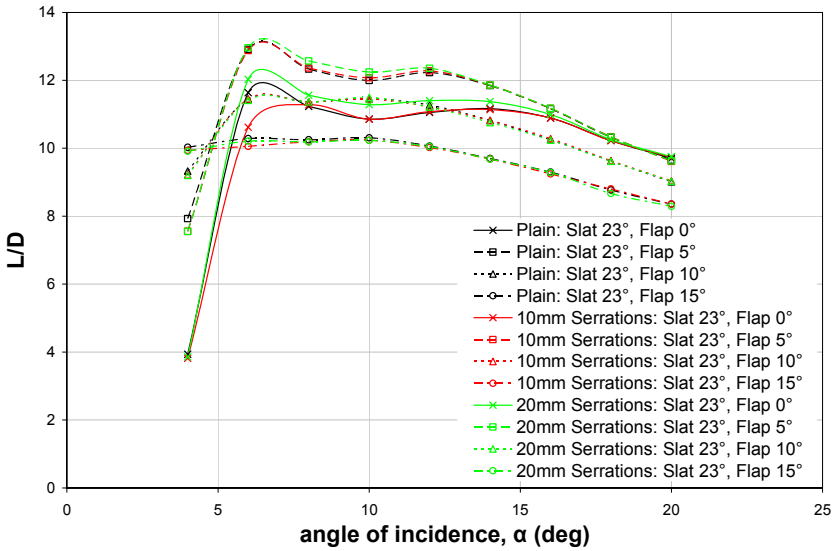

Figure 86: Variation of L/D with angle of incidence for plain, 10mm and 20mm serrated configurations at a flap lap/gap of (−0.23, −0.2), δ_s=23°, 0°≤δ_f≤15°

6.8.3 20mm Serrated Trailing Edge

Figure 84 also showed the incremental lift coefficient for the 20mm serrated three-element configuration at a flap lap/gap of (−0.23, −0.2) when compared to the corresponding baseline configuration. From Figure 84, it was evident that in contrast to the 10mm serrations, implementation of 20mm serrations at the trailing edge of the main element in a three-element configuration tended to increase C_l for all α for δ_f≤10° when compared to the corresponding baseline configuration. Note that isolated discrepancies arose at α=4° for 0°≤δ_f≤10° and at α=20° for δ_f=10°, for which the 20mm serrations diminished the decrement in C_l in comparison to that of the 10mm serrated configuration. Furthermore, Figure 84 showed that similarly to the 10mm serrated configuration, ΔC_l due to the 20mm serrations appeared highly sensitive to α, varying inconsistently for all δ_f. In comparison to the corresponding two-element configuration at δ_f=0°, deflection of the leading edge slat had a detrimental effect upon C_l for 4°≤α≤6°, negating the benefits of the serrations evident for the two-element configuration at α=4° and approximately halving the increment in C_l at α=6°. However, with further increments in α, there was tendency for the deflection of the leading edge slat to heighten the increment in C_l, accounting for a 1-3% increment in comparison to the plain trailing edge configuration for 8°≤α≤20°. Isolated exceptions occurred at α=10° and α=16°, for which the 20mm serrations had a more favourable effect upon C_l, when the slat was stowed. Comparison of the two- and three-element 20mm serrated configurations at δ_f=0° highlighted the increased sensitivity of ΔC_l to α when the

leading edge slat was deflected, as opposed to the relative consistency of ΔC_l with increments in α when the slat was retracted.

From Figure 84 it was evident that increasing δ_f from 0° to 5° tended to diminish the increment in C_l for the three-element 20mm serrated configuration. The increment in C_l due to the 20mm serrations was relatively consistent for $6° \leq \alpha \leq 20°$, equating to an approximate 1% increment in C_l in comparison to the corresponding three-element baseline configuration. Note that deflection of the leading edge slat at δ_f=5° had an adverse effect upon the C_l generated by 20mm serrated configuration at α=4° and whilst ΔC_l was of comparable magnitude to the two-element configuration at α=6°, deflection of the leading edge slat had a favourable effect upon C_l with subsequent increments in $8° \leq \alpha \leq 20°$.

Whilst a single increment in δ_f from 5° to 10° reduced the decrement in C_l due to the 20mm serrations at α=4°, with further increments in $6° \leq \alpha \leq 12°$, incrementing δ_f from 5° to 10° tended to heighten the increment in C_l, accounting for a 1-2% increase in comparison to the corresponding three-element plain trailing edge configuration (see Figure 84). For $14° \leq \alpha \leq 16°$, incrementing δ_f from 5° to 10° diminished the increment in C_l due to the 20mm serrations and with further increments in $\alpha \geq 18°$, any variation in C_l due to the 20mm serrations was essentially negated in comparison to the corresponding three-element plain trailing edge configuration. Direct comparison of the two- and three-element 20mm serrated configurations at δ_f=10° indicated that whilst deflection of the leading edge slat had an adverse effect upon C_l at α=4°, with further increments in α, deflection of the leading edge slat heightened the increment in C_l for all comparative α.
In contrast, with a final increment in δ_f from 10° to 15°, Figure 84 showed that the 20mm serrations had a detrimental effect upon C_l for all test α. At δ_f=15°, the decrement in C_l due to the 20mm serrations tended to progressively increase in magnitude with successive α. Whilst accounting for <1% reduction in C_l for $4° \leq \alpha \leq 16°$, ΔC_l significantly increased with further increments in α, equating to a 7% and 18% reduction in C_l in comparison to the corresponding three-element plain trailing edge configuration at α=18° and α=20°, respectively. Thus, increasing the serration length from 10mm to 20mm for the three-element configuration at δ_f=15° reduced the decrement in C_l for $4° \leq \alpha \leq 6°$ but heightened the decrement, with increasing magnitude, as α was incremented from 8° to 20°. Furthermore, direct comparison of the two- and three-element 20mm serrated configurations at δ_f=15° indicated that deflection of the leading edge slat heightened the decrement in C_l for all comparative $4° \leq \alpha \leq 16°$.

Whilst the above deviations in C_l due to the 20mm serrations were identified, it should be noted that the magnitude of ΔC_l was such that the variation in the lift generated by the three-element 20mm serrated configuration in comparison to the baseline configuration was essentially negligible for any given α and δ_f. The notable exception to this trend was the distinct degradation in lift generated by the 20mm serrated configuration for $18° \leq \alpha \leq 20°$ at $\delta_f = 15°$, which resulted in a definite value of C_{lmax} and α_{stall} at 18°.

From Figure 85 it was evident that the 20mm serrations tended to decrease C_d for $\delta_f = 0°$ and 15° but increase C_d for $\delta_f = 5°$ and 10°, with ΔC_d varying inconsistently with α for any given δ_f. Note that discrepancies were evident at each δ_f, with the 20mm serrated geometry either having negligible effect upon C_d in comparison to the baseline configuration or increasing/decreasing C_d for finite ranges of α within the test range. Whilst the 20mm serrations typically had no appreciable effect upon the drag polar for $5° \leq \delta_f \leq 15°$, a marginal reduction in C_d was evident for all C_l at $\delta_f = 0°$ when compared to the baseline configuration.

Finally, Figure 86 indicated that whilst at $\delta_f = 0°$, the 20mm serrations reduced L/D by 2% in comparison to the corresponding three-element baseline configuration at $\alpha = 4°$, the 20mm serrations increased L/D by 3-4% for $6° \leq \alpha \leq 12°$. With further increments in $\alpha \geq 14°$, the increment in L/D was progressively reduced in magnitude such that any variation in comparison to the baseline configuration was negligible for $\alpha \geq 18°$. At $\delta_f = 5°$, the 20mm serrations reduced L/D by 5% at $\alpha = 4°$ when compared to the corresponding baseline configuration. With subsequent increments in $\alpha \geq 6°$, the 20mm serrations increased L/D, attaining a maximum increment of 2% at $\alpha = 10°$ and decreasing in magnitude thereafter such that the 20mm serrations had no appreciable effect upon L/D for $\alpha \geq 14°$. By increasing δ_f to 10°, the 20mm serrations had no discernible effect upon L/D in comparison to the corresponding three-element baseline configuration, with only an isolated 1% decrement at $\alpha = 4°$. With a final increment in δ_f to 15°, the detrimental effect of the 20mm serrations upon L/D was limited to $4° \leq \alpha \leq 10°$, with the greatest decrement of 1% occurring at $\alpha = 4°$. Whilst any deviation in L/D was negated for $12° \leq \alpha \leq 16°$, a 1% reduction in L/D arose for $\alpha \geq 18°$, with the latter attributed to the heightened drag coinciding with the onset of stall. Thus, increasing the serration length from 10mm to 20mm had a favourable effect upon L/D at $\delta_f = 0°$ and 5°, heightening the increment in L/D for significant ranges of α, although the benefits of increasing the serration length were less evident for $\delta_f \geq 10°$.

6.8.4 Summary for the Three-Element Configuration: Single Lap/Gap

As a result of implementing 10mm or 20mm 60° triangular serrated geometries at the trailing edge of the main element upstream of a single slotted flap in a three-element high-lift configuration at a lap/gap of (−0.23, −0.2), it was concluded that:

- Deployment of the leading edge slat, rendered the 10mm serrations unfavourable at δ_f=0° and heightened the decrement in C_l at δ_f=5° but diminished the decrement in C_l for 10°≤δ_f≤15°
- Deployment of the leading edge slat typically heightened the increment in C_l due to the 20mm serrations, such that C_l was increased for all α and δ_f≤10°
- With the leading edge slat deployed, ΔC_l due to the serrated geometries appeared highly sensitive to variations in α for any given δ_f
- 10mm serrations tended to either reduce L/D or had a near negligible effect
- 20mm serrations increased L/D over a finite range of α at δ_f=0° and δ_f=5° but otherwise had a detrimental or near negligible effect
- Data highlighted that the effectiveness of the serrations was sensitive to deployment of a leading edge high-lift device

6.9 Two-Element High-Lift Configuration: Fine Flap Lap/Gap Grid

Recognising that the serrated geometries were typically most effective within the two-element configuration when the flap was positioned at lap/gap of (−0.23, −0.2), a finer lap/gap grid of three points was implemented in the immediate vicinity (see Section 3.3.3 for details of fine grid), with the intention of establishing whether the effectiveness of the serrations could be further improved. The resultant aerodynamic forces were obtained from the balance measurements.

6.9.1 Plain Trailing Edge

The C_l-α curve for each baseline plain trailing edge configuration at a given flap lap/gap in the fine grid is shown in Figure 185 in Appendix K for all test δ_f. Further comparisons of the fine flap lap/gap grid for the baseline C_l-α curve configuration at a specified test δ_f are displayed in Figure 186 in Appendix K. Note that with regard to Figure 186, data for the corresponding plain trailing edge configuration at the coarse lap/gap grid position of (−0.23, −0.2) was also included for comparative purposes.

As rotation of the flap at a lap/gap of (−0.23, −0.14) was rendered infeasible by the geometry of the model, locating the trailing edge flap at a gap of −0.17 represented the smallest flap gap viable at a lap of −0.23. Figure 185(a) in Appendix K shows the C_l-α curve for the baseline configuration for all test δ_f at a lap/gap of (−0.23, −0.17). From Figure 185(a) it was evident that successive increments in δ_f from 0° to 15° increased C_l for any given test α. Furthermore, Figure 186(a) showed that in comparison to the coarse flap lap/gap grid position of (−0.23, −0.2), positioning the trailing edge flap at a lap/gap of (−0.23, −0.17) had a negligible effect upon C_l at δ_f=0° for $\alpha \leq 12°$. However, decreasing the flap gap from −0.2 to −0.17 at a flap lap of −0.23 marginally decreased C_l for $12° < \alpha \leq 16°$ at δ_f=0° such that the C_l was reduced in magnitude in comparison to all of the coarse grid lap/gap positions previously tested. However, reducing the flap gap from −0.2 to −0.17 did extend the upper range of α over which measurements were obtained from 16° at to 18°, inferring an increase in both C_{lmax} and the corresponding α_{stall} at δ_f=0°. Reducing the flap gap from −0.2 to −0.17 at δ_f=5° had no appreciable effect upon C_l for $-2° \leq \alpha \leq 16°$ (see Figure 186(b)), although the range of α over which measurements were obtained was extended from 16° to 20°, with a corresponding increase in both C_{lmax} and α_{stall}. With further increments in $\delta_f \geq 10°$, positioning the flap at a lap/gap of (−0.23, −0.17) had a favourable effect upon C_l for all α in comparison to the configuration at a flap lap/gap of (−0.23, −0.2), as well as extending the range of α over which measurements were obtained from 16° to 20°, corresponding to an increase in both C_{lmax} and α_{stall} (see Figure 186(c) and (d)).

Maintaining a flap gap of −0.17 and positioning the trailing edge flap incrementally upstream at a flap lap of −0.26, represented the most upstream lap location feasible at the specified gap. Similarly to the configuration at a lap/gap of (−0.23, −0.17), it was evident from the C_l-α curve in Figure 185(b) in Appendix K that by positioning the baseline configuration at a lap/gap of (−0.26, −0.17), C_l increased with successive increments in δ_f from 0° to 15° for any given test α. Furthermore, Figure 186(a) showed that in comparison to both the coarse flap lap/gap grid position of (−0.23, −0.2) and the fine flap lap/gap grid position of (−0.23, −0.17), positioning the trailing edge flap at a lap/gap of (−0.26, −0.17) had negligible effect upon C_l at δ_f=0° for $\alpha \leq 2°$. However, positioning the flap at a lap/gap of (−0.26, −0.17) had a detrimental effect upon C_l for $\alpha \geq 6°$ at δ_f=0° when compared to both the coarse lap/gap grid position of (−0.23, −0.2) and the fine lap/gap grid position of (−0.23, −0.17). Note that whilst the decrement in C_l was heightened with successive increments in α, the range of α over which measurements were obtained was extended from 16° to 18° when compared to the baseline configuration at the coarse lap/gap grid position of (−0.23, −0.2), with an

increase in both C_{lmax} and α_{stall} at δ_f=0°. For 5°≤δ_f≤10°, positioning the trailing edge flap at a lap/gap of (−0.26, −0.17) was detrimental to C_l for all test α when compared to both the coarse flap lap/gap grid position of (−0.23, −0.2) and the fine flap lap/gap grid position of (−0.23, −0.17). Again, the decrement in C_l was heightened with successive increments in α. Note that in comparison to the baseline configuration at a lap/gap of (−0.23, −0.2), positioning the flap at a lap/gap of (−0.26, −0.17) extended the range of α over which measurements were obtained from 16° to 18° and 20° at δ_f=5° and δ_f=10°, respectively, with a corresponding increase in both C_{lmax} and α_{stall} (see Figure 186(b) and (c)). With a final increment in δ_f to 15°, positioning the flap at a lap/gap of (−0.26, −0.17) had negligible effect upon C_l in comparison to the corresponding configuration at the coarse lap/gap grid of (−0.23, −0.2) but once again extended the range of α over which measurements were obtained from 16° to 20°, with a corresponding increase in both C_{lmax} and α_{stall} (see Figure 186(d)). However, positioning the flap at a lap/gap of (−0.26, −0.17) still degraded C_l in comparison to the fine lap/gap grid position of (−0.23, −0.17) for all test α at δ_f=15°.

Finally, by positioning the baseline configuration at a flap lap/gap of (−0.26, −0.2), it was once again noted that C_l increased with successive increments in δ_f from 0° to 15° for any given test α, see Figure 185(c) in Appendix K. However, it was evident from Figure 186 in Appendix K that positioning the baseline configuration at a flap lap/gap of (−0.26, −0.2) typically had a detrimental effect upon C_l in comparison to the other fine lap/gap grid positions tested. Figure 186(a) showed that whilst positioning the flap at a lap/gap of (−0.26, −0.2) was the most favourable grid position tested for α=−2° at δ_f=0°, any benefits were marginalised at α=2° and with further increments in α≥6°, C_l was progressively reduced in magnitude in comparison to both the coarse lap/gap grid position of (−0.23, −0.2) and the fine lap/gap grid position of (−0.23, −0.17). However, the C_l-α curve at δ_f=0° was analogous to that for the baseline configuration positioned at a fine grid flap lap/gap of (−0.26, −0.17), similarly extending the range of α over which measurements were obtained from 16° to 18° when compared to the baseline configuration at the coarse lap/gap grid position of (−0.23, −0.2), with a corresponding increase in both C_{lmax} and α_{stall}. At δ_f=5°, Figure 186(b) showed that the C_l attained for the baseline configuration at a lap/gap of (−0.26, −0.2) was comparable to that at a lap/gap of (−0.26, −0.17) for α≤6°. However, with subsequent increments in α≥6°, positioning the flap at a lap/gap of (−0.26, −0.2) had a detrimental effect upon C_l in comparison to the configuration at the smaller flap gap of −0.17. The decrement in C_l was heightened with successive increments in α, although the range of α over which measurements were obtained was still extended from 16° to 18° when compared to the

baseline configuration at a coarse lap/gap grid position of (−0.23, −0.2), with a corresponding increase in α_{stall} but negligible variation in C_{lmax}. Note that at δ_f=5°, the C_l attained for the baseline configuration at a lap/gap of (−0.26, −0.2) was degraded in comparison to the corresponding configurations at a fine flap lap/gap grid position of (−0.23, −0.17) or a coarse flap lap/gap grid position of (−0.23, −0.2) for all comparable test α. Whilst positioning the flap at a lap/gap of (−0.26, −0.2) attained a C_l comparable to other grid locations for α=−2° at δ_f=10°, with subsequent increments in $\alpha\geq$2°, C_l was progressively reduced in magnitude in comparison to both of the coarse grid lap/gap and the fine grid lap/gap positions previously tested, see Figure 186(c). Again, the range of α over which the measurements were obtained was extended to 20°, increasing α_{stall} and C_{lmax} in comparison to the baseline configuration at the coarse lap/gap grid position of (−0.23, −0.2). With a final increment in δ_f to 15°, it was evident from Figure 186(d) that positioning the flap at a lap/gap of (−0.26, −0.2) had a detrimental effect upon C_l for all test α in comparison to all fine grid lap/gap positions previously tested and the coarse grid lap/gap position. Note that once again, the upper range of α over which measurements were obtained was extended from 16° to 20° in comparison to the coarse grid lap/gap of (−0.23, −0.2), with a subsequent increase in α_{stall} and C_{lmax}.

Thus, based upon the fine lap/gap grid, positioning the flap at a lap/gap of (−0.23, −0.17) was most favourable in terms of attaining the maximum C_l for any given α at a specified δ_f between 0° and 15° (see Figure 186(a)-(d)).

Recalling the coarse grid lap/gap studies for the two-element plain trailing edge configuration, positioning the flap at a lap/gap of either (−0.17, −0.2) or (−0.12, −0.2) was most favourable in terms of attaining the maximum C_l for a given α at δ_f=0° but with successive increments in 5°$\leq\delta_f\leq$15° a lap/gap of (−0.17, −0.14) typically achieved the maximum C_l for a given α. Accordingly, the optimum lap/gap, in terms of attaining the maximum C_l for a given α and δ_f, are compared for the coarse and fine lap/gap grids in Figure 87. From Figure 87 it was evident that whilst positioning the flap at the optimum fine lap/gap grid location of (−0.23, −0.17) typically decreased C_l in comparison to the corresponding optimum coarse lap/gap identified for all comparable α at a given δ_f, the optimum fine lap/gap grid increased α_{stall} for all test δ_f and increased C_{lmax} for δ_f=0° and 10°$\leq\delta_f\leq$15°, with the C_{lmax} of a comparable magnitude at δ_f=5°.

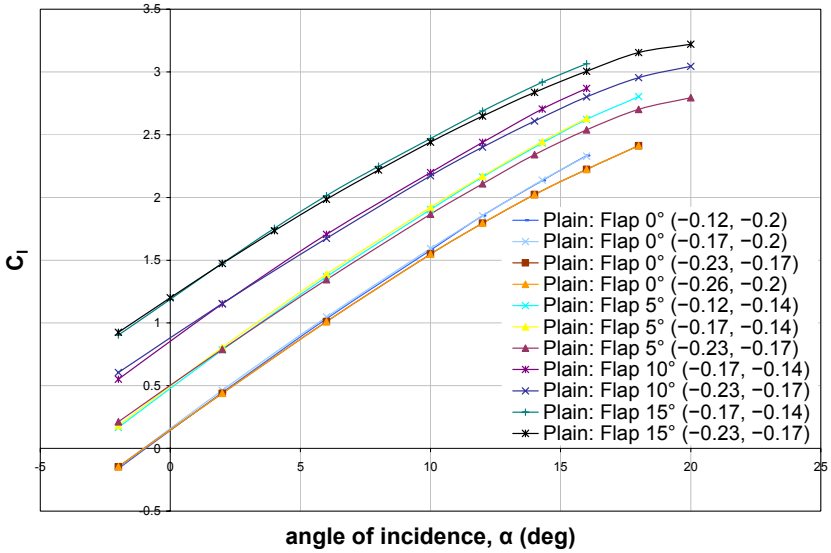

Figure 87: Comparison of optimum coarse and fine lap/gap locations in terms of attaining the maximum C_l for a given α and specified δ_f for the baseline configuration

The drag polar for each baseline configuration at a given flap lap/gap is shown in Figure 187, with further comparisons for a specified test δ_f displayed in Figure 188, both shown in Appendix K. Figure 188 highlighted that positioning the flap at the fine grid lap/gap of (−0.23, −0.17) proved most favourable in terms of reducing C_d at a given C_l for all test δ_f, i.e. decreasing the flap gap from −0.2 to −0.17 at a flap lap of −0.23 notably reduced C_d at a given C_l. Maintaining the flap gap of −0.17 and incrementing the flap lap from −0.23 to −0.26 tended to increase C_d for a given C_l at all test δ_f. Note that the C_d generated by the baseline configuration at a flap lap/gap of (−0.26, −0.17) was typically less than that for the corresponding baseline configurations positioned at a flap gap of −0.2 and at a flap lap of either −0.23 or −0.26. Conversely, incrementing the flap lap from −0.23 to −0.26 at a flap gap of −0.2 tended to increase C_d at a given C_l for all test δ_f, with a marked increment in C_d evident in comparison to the corresponding baseline configurations at a flap lap/gap of (−0.26, −0.17), particularly at high test δ_f.

The resultant L/D for each baseline configuration at a given flap lap/gap is shown in Figure 189, with additional graphs comparing L/D for the baseline configuration at a specified test δ_f displayed Figure 190, both of which are in Appendix K.

From Figure 190(a)-(d) it was evident that by decreasing the flap gap from −0.2 to −0.17 at a flap lap of −0.23, L/D was significantly improved for all $\alpha \geq 0°$ and δ_f. At δ_f=0°, reduction in the flap gap from −0.2 to −0.17 at the specified flap lap of −0.23 increased L/D by a maximum of 27% at α=2°, with the increment reducing to 10% at

α=6° and varying between a 4-7% increment thereafter. By increasing δ_f from 0° to 5°, the percentage increment in L/D due to the reduction in flap gap at a flap lap of −0.23 was more than halved at α=2° to a 12% increase, decreasing to a 7% increment at α=6°, although varying between a 6-7% increment thereafter. With further increments in $\delta_f \geq$10°, the increment in L/D due to the reduction in flap gap from −0.2 to −0.17 at a flap lap of −0.23 was greatest at α=−2°, decreasing in magnitude with subsequent increments in α. At δ_f=10°, the increment in L/D due to the reduction in flap gap from −0.2 to −0.17 accounted for an 18% increment at α=2°, 12% at α=6° and varying irregularly between a 3-5% increment for 10°≤α≤16°. The increments were of a similar magnitude at δ_f=15°, accounting for a 15% increment at α=2° and 10% at α=6° and progressively decreasing from a 5% to 3% increment with successive increments in 10°≤α≤16°.

Incrementally transposing the flap upstream from −0.23 to −0.26 at a flap gap of −0.17 typically reduced L/D for all $\alpha \geq$0° and δ_f, see Figure 190(a)-(d). At δ_f=0°, incrementing the flap lap upstream from −0.23 to −0.26 at the specified flap gap of −0.17 decreased L/D by a maximum of 14% at α=2°, with the magnitude of the decrement progressively decreasing, such that any reduction in L/D due to the flap lap variation was negated for $\alpha \geq$12°. A discrepancy to this trend arose at δ_f=5° whereby L/D was relatively insensitive to the variation in flap lap from −0.23 to −0.26 for all α, with only an isolated 6% increment in L/D occurring at α=6°. With further increments in $\delta_f \geq$10°, the decrement in L/D due to the increment in flap lap from −0.23 to −0.26 at a flap gap of −0.17 was restricted to $\alpha \leq$6°. At δ_f=10°, this decrement accounted for a 17% reduction in L/D at α=−2°, decreasing to an 8% reduction in L/D at α=2° and progressively reducing in magnitude thereafter. At δ_f=15°, this decrement in L/D was reduced to 7% at α=−2°, with the decrement progressively decreasing in magnitude with successive increment in $\alpha \leq$6°. Whilst for $\alpha \geq$10°, incrementing the flap lap from −0.23 to −0.26 at a flap gap of −0.17 increased L/D by ≤3% at δ_f=10°, any variation in L/D was essentially negated for the configuration with δ_f=15°.

Finally, Figure 190(a)-(d) showed that in terms of L/D, incrementing the flap lap from −0.23 to −0.26 at a flap gap of −0.2 was detrimental for 0°≤α≤10° at δ_f=0°, decreasing L/D by 10% at α=2°, with the deviation diminishing with subsequent increments in α such that L/D was relatively insensitive to the aforesaid increment in flap lap for 12°≤α≤16°. In contrast, incrementing the flap lap from −0.23 to −0.26 at a flap gap of −0.2 increased L/D at δ_f=5° for 0°≤α≤16°. The magnitude of the increment initially increased with α, attaining a maximum increment of 6% at α=6° before decreasing in

magnitude to a 2% increment at α=16°. Whilst incrementing the flap lap from −0.23 to −0.26 at a flap gap of −0.2 at δ_f=10°, had a detrimental effect upon L/D at low α, accounting for a 5% decrement at α=2°, with further increments in 6°≤α≤16°, L/D was increased by 3-6%. The detrimental effect of incrementing the flap lap from −0.23 to −0.26 at a flap gap of −0.2 was heightened at δ_f=15°, both in magnitude and extent, with increments in L/D of 2-3% limited to 8°≤α≤16°.

Thus, from Figure 190 it was evident that positioning the flap at a lap/gap of (−0.23, −0.17) was typically the most favourable of the fine lap/gap grid positions in terms of attaining the maximum L/D for any given α at a specified δ_f between 0° and 15°.

6.9.2 10mm Serrated Trailing Edge

(a) Flap Lap/Gap: (−0.23, −0.17)

In comparison to the corresponding plain trailing edge configuration at a flap lap/gap of (−0.23, −0.17), the 10mm serrations decreased C_l for all α and δ_f tested, with ΔC_l varying inconsistently with α for any given δ_f, see Figure 88.

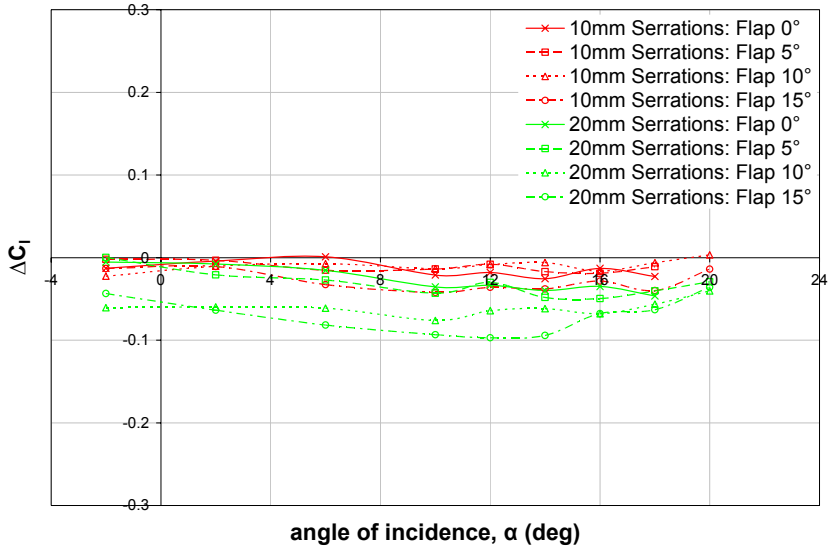

Figure 88: Variation of ΔC_l with angle of incidence due to 10mm and 20mm serrations at a flap lap/gap of (−0.23, −0.17), δ_s=0°, 0°≤δ_f≤15°,

At δ_f=0°, the decrement in C_l due to the 10mm serrations typically accounted for ≤1% reduction in C_l, although an isolated discrepancy arose at α=6°, whereby any variation in C_l due to the 10mm serrations was negated. Increasing δ_f from 0° to 5° only heightened the decrement in C_l at α=6° and α=16°, with ΔC_l due to the 10mm serrations typically comparable to or less than that of the configuration with δ_f=0°. Whilst the

decrement in C_l continued to vary inconsistently at δ_f=10°, ΔC_l was typically comparable to or less than that of the δ_f=5° configuration, with ΔC_l only heightened in magnitude for $\alpha \leq 2°$ and again, accounting for ≤1% reduction in C_l in comparison to the corresponding baseline configuration. However, incrementing δ_f from 10° to 15° heightened the decrement in C_l for all $\alpha \geq 6°$, typically equating to a 1-2% reduction in comparison to the plain trailing edge configuration. This suggested that with the 10mm serrations implemented at the trailing edge of the main element, the resultant lift for the two-element configuration was relatively insensitive to variations in $0° \leq \delta_f \leq 10°$ for $-2° \leq \alpha \leq \alpha_{stall}$.

Although ΔC_d varied inconsistently with α for all δ_f, there was a tendency for the 10mm serrations to decrease C_d, see Figure 191(a) in Appendix L. Notable exceptions to this trend arose at δ_f=0°, whereby the 10mm serrations increased C_d for $-2° \leq \alpha \leq 12°$ in comparison to the corresponding baseline configuration. Further increments in C_d were evident for $2° \leq \alpha \leq 6°$ and $\alpha \geq 16°$ at δ_f=10° and $-2° \leq \alpha \leq 2°$ at δ_f=15°.

Whilst the 10mm serrations had negligible effect upon the drag polar, evaluation of the effects of the 10mm serrations on C_l and C_d in terms of L/D indicated that the 10mm serrations had a detrimental effect upon L/D for $-2° \leq \alpha \leq 12°$ at δ_f=0°, see Figure 89.

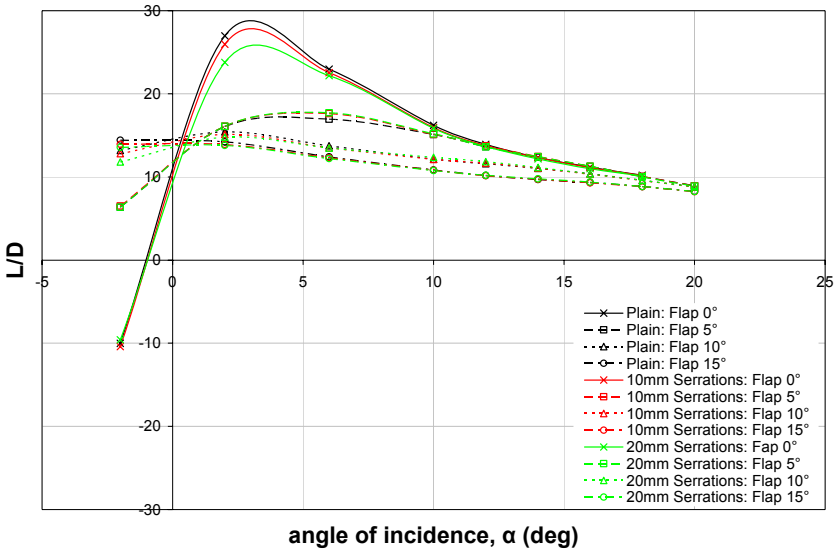

Figure 89: Variation of L/D with angle of incidence for plain, 10mm and 20mm serrated configurations at a flap lap/gap of (−0.23, −0.17), δ_s=0°, $0° \leq \delta_f \leq 15°$

Specifically, the maximum decrement of 4% coincided with α=2° at δ_f=0° and decreased in magnitude with subsequent increments in α to a 1% decrement at α=12°. For $\alpha \geq 14°$, any variation in L/D due to the 10mm serrations was essentially negated in

comparison to the corresponding baseline configuration at δ_f=0°. At δ_f =5°, the 10mm serrations typically had no appreciable effect upon L/D, with only an isolated increment of 4% at α=6°. However, with further increments in $\delta_f \geq$10°, the 10mm serrations adversely affected L/D, correlating to a 2% decrement in comparison to the baseline configuration for $\alpha \leq$6°. The decrement in L/D progressively decreased in magnitude with successive increments in α such that any deviation in L/D due to the 10mm serrations was essentially negated for $\alpha \geq$10°, rendering L/D comparable to the plain trailing edge configuration.

(b) Flap Lap/Gap: (−0.26, −0.17)

At a flap lap/gap of (−0.26, −0.17), the 10mm serrations typically decreased C_l for all α and δ_f when compared the corresponding plain trailing edge configuration, see Figure 90, although discrepancies arose for $\alpha \leq$2° for the configurations with δ_f=0° or δ_f=10°.

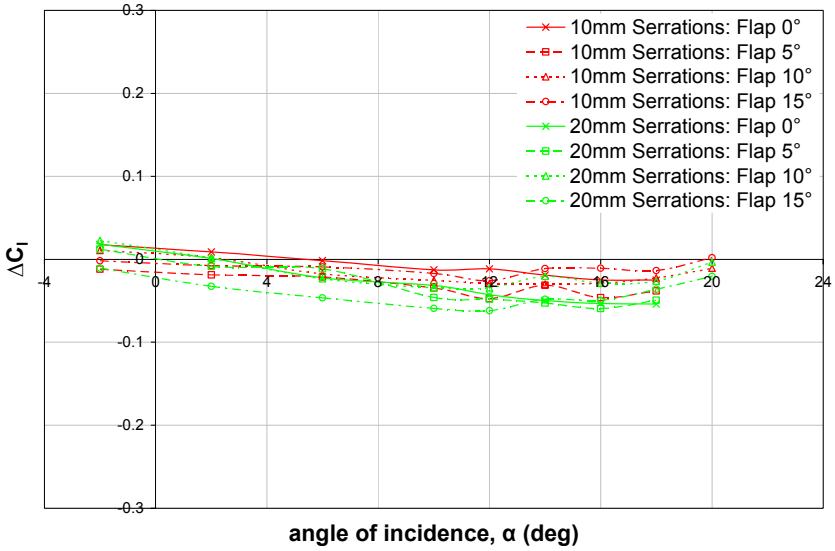

Figure 90: Variation of ΔC_l with angle of incidence due to 10mm and 20mm serrations at a flap lap/gap of (−0.26, −0.17), δ_s=0°, 0°≤δ_f≤15°

At δ_f=0°, the decrement in C_l due to the 10mm serrations was typically heightened in magnitude with successive increments in 6°≤α≤18°, although accounting for less than a 1% reduction in C_l in comparison to the corresponding plain trailing edge configuration. With subsequent increments in δ_f, the decrement in C_l was typically heightened in magnitude with successive increments in $\alpha \leq$12° but varied inconsistently with further increments in $\alpha \geq$14°. Increasing δ_f to 5° maximised ΔC_l for all α, typically representing a 2-3% reduction in C_l, but with subsequent increments in 10°≤δ_f≤15°, ΔC_l decreased in magnitude, typically accounting for ≤1% reduction in C_l in comparison to the plain trailing edge configuration.

Figure 191(b) in Appendix L showed that the 10mm serrations increased C_d for $-2° \leq \alpha \leq 12°$ at $\delta_f=0°$ and for $\alpha \leq 2°$ at both $\delta_f=10°$ and $\delta_f=15°$ when compared to the corresponding plain trailing edge configuration. In contrast, the 10mm serrations decreased C_d, to a greater or lesser extent, for all α at $\delta_f=5°$ and for $6° \leq \alpha \leq 18°$ at both $\delta_f=10°$ and $\delta_f=15°$. Irrespective of whether the 10mm serration increased or decreased C_d, ΔC_d varied inconsistently with α for all δ_f. Typically, the 10mm serrations had negligible effect upon the drag polar, although a marginal increase in C_d was evident for $C_l>1$ at $\delta_f=0°$ and for $C_l>1.8$ at $\delta_f=5°$.

Evaluation of the effects of the 10mm serrations upon C_l and C_d in terms of L/D indicated that the 10mm serrations adversely affected L/D for $0° \leq \alpha \leq 12°$ at $\delta_f=0°$, attaining a maximum decrement of 7% at $\alpha=2°$ and decreasing in magnitude thereafter, such that any variation was essentially negated for $14° \leq \alpha \leq 18°$, see Figure 91.

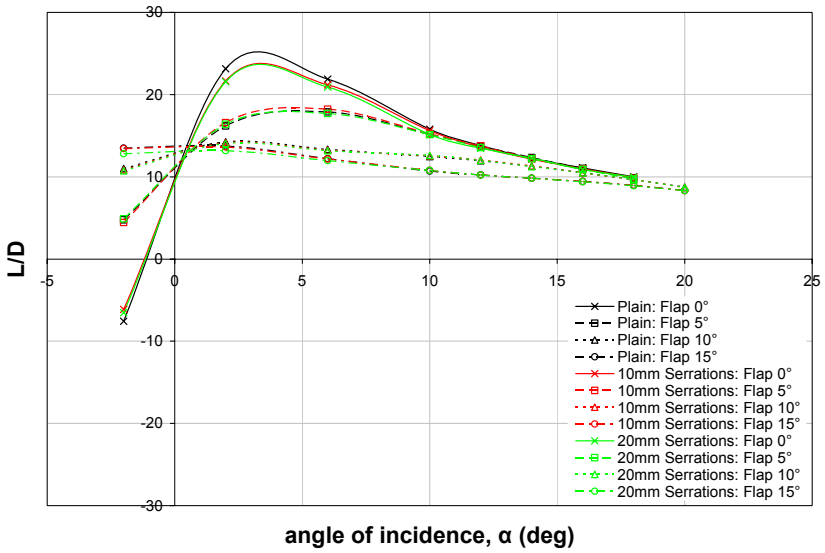

Figure 91: Variation of L/D with angle of incidence for plain, 10mm and 20mm serrated configurations at a flap lap/gap of (−0.26, −0.17), $\delta_s=0°$, $0° \leq \delta_f \leq 15°$

In contrast, the 10mm serrations increased L/D for $0° \leq \alpha \leq 10°$ at $\delta_f=5°$, with the maximum increment of 3% occurring at $\alpha=2°$ and progressively decreasing in magnitude with successive α, rendering L/D essentially comparable to the plain trailing edge configuration for $\alpha \geq 12°$. However, with further increments in $\delta_f \geq 10°$, the 10mm serrations had no appreciable effect upon L/D.

(c) Flap Lap/Gap: (−0.26, −0.2)

In contrast to the two grid positions previously discussed, the 10mm serrations increased C_l at a flap lap/gap of (−0.26, −0.2) for all α and $\delta_f \leq 10°$, with only a single

isolated discrepancy for α=−2° at δ_f=5°, see Figure 92. Whilst ΔC_l due to the 10mm serrations varied inconsistently with α between 0.02 and 0.03 at δ_f=0°, the corresponding percentage increment in C_l progressively decreased in magnitude with successive increments in α from 5% at α=2° to 1% at α=18°. Increasing δ_f to 5° reduced the magnitude of the increment in C_l for 0°≤α≤18°, typically varying between 0.01 and 0.02 and accounting for a 2-3% increment in comparison to the corresponding plain trailing edge configuration. With a further increment in δ_f to 10°, ΔC_l due to the 10mm serrations typically exceeded that of both the δ_f=0° and δ_f=5° configurations for all α. At δ_f=10°, the ΔC_l of 0.055 due to the 10mm serrations was relatively insensitive to increments in −2°≤α≤6°, although the corresponding percentage increments decreased from 11% at α=−2° to 4% increment at α=6°. With further increments in α, ΔC_l tended to decrease in magnitude from 0.04 to 0.01, correlating to a 1-2% increment for 10°≤α≤16°. A final increment in δ_f to 15° restricted the increment in C_l due to the 10mm serrations to −2°≤α≤6°. Whilst at α=−2°, ΔC_l was comparable to the corresponding 10mm serrated configuration with δ_f=0° and accounted for a 2% increment, ΔC_l diminished in magnitude with successive increments in α such that ΔC_l was of a smaller magnitude than that of the corresponding configurations with 0°≤δ_f≤10° for 2°≤α≤6°. With subsequent increments in α≥10° at δ_f=15°, the variation in C_l was marginalised such that the 10mm serrations typically had no appreciable effect upon C_l in comparison to the corresponding plain trailing edge configuration.

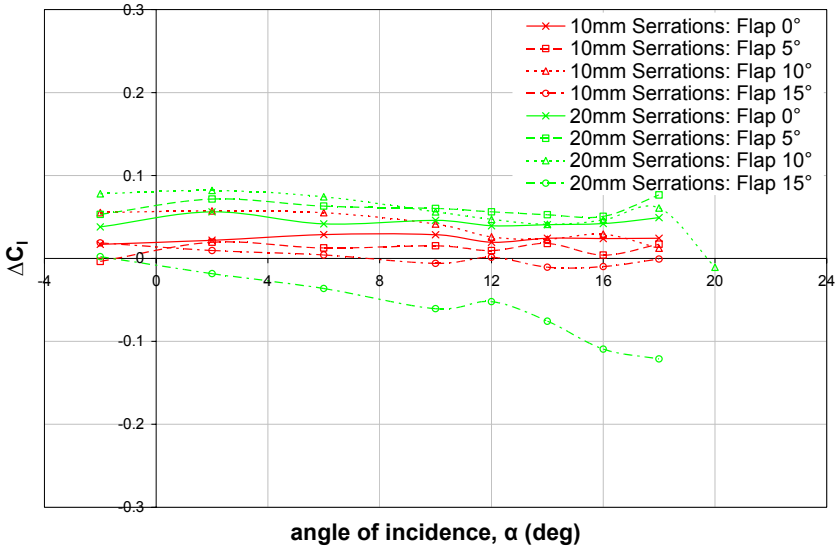

Figure 92: Variation of ΔC_l with angle of incidence due to 10mm and 20mm serrations at a flap lap/gap of (−0.26, −0.2), δ_s=0°, 0°≤δ_f≤15°

From Figure 191(c) in Appendix L it was evident that the effect of the 10mm serrations upon C_d was difficult to ascertain. ΔC_d due to the 10mm serrations varied inconsistently

with α for any given δ_f, although there was a tendency for the 10mm serrations to increase C_d at δ_f=0° and δ_f=10° and decrease C_d at δ_f=5° and δ_f=15°. The 10mm serrations had no appreciable effect upon the drag polar in comparison to the corresponding plain trailing edge configuration for all δ_f tested. In contrast to previous lap/gap positions tested, the 10mm serrations decreased the range of α over which measurements were obtained from 20° at δ_f=10° and δ_f=15° with the plain trailing edge geometry to 18° with the 10mm serrated trailing edge, corresponding to an attendant decrement in both α_{stall} and C_{lmax}.

Amalgamation of the effect of the 10mm serrations upon C_l and C_d in terms of L/D indicated that the 10mm serrations reduced L/D for $-2° \leq \alpha \leq 2°$ at δ_f=0°, accounting for a 13% and 5% decrement at α=−2° and α=2°, respectively. With subsequent increments in $\alpha \geq 6°$ at δ_f=0°, the 10mm serrations typically had no appreciable effect upon L/D in comparison to the plain trailing edge configuration, see Figure 93.

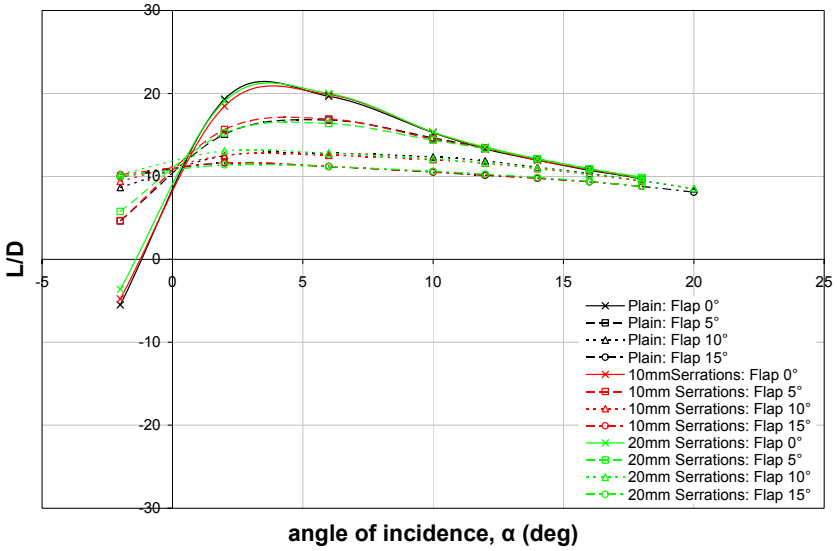

Figure 93: Variation of L/D with angle of incidence for plain, 10mm and 20mm serrated configurations at a flap lap/gap of (−0.26, −0.2), δ_s=0°, $0° \leq \delta_f \leq 15°$

At δ_f=5°, the 10mm serrations typically had no appreciable effect upon L/D in comparison to the plain trailing edge configuration, although an isolated 4% increment was evident at α=2°. However, a further increment in δ_f to 10° rendered the 10mm serrations detrimental to L/D for $6° \leq \alpha \leq 18°$, accounting for a 1-2% reduction in comparison to the plain trailing edge configuration. Finally, at δ_f=15°, the 10mm serrations typically had no appreciable effect upon L/D with only an isolated 3% increment at α=−2°.

6.9.3 20mm Serrated Trailing Edge

(a) Flap Lap/Gap: (−0.23, −0.17)

Similarly to the 10mm serrations, the 20mm serrations had a detrimental effect upon C_l for all α and δ_f at a flap lap/gap of (−0.23, −0.17), see Figure 88. At δ_f=0°, the decrement in C_l due to the 20mm serrations tended to heighten in magnitude with successive increments in α, accounting for a 2% reduction in comparison to the plain trailing edge configuration. A single increment in δ_f to 5° typically heightened the decrement in C_l due to the 20mm serrations for any given 0°≤α≤14°, although decrements in ΔC_l were evident at the upper and lower test limits of α. Increasing δ_f to 10° notably heightened the magnitude of the decrement in C_l due to the 20mm serrations for all α, equating to a 2-5% reduction throughout. A final increment in δ_f to 15° heightened ΔC_l for all 2°≤α≤14°, correlating to a 3-4% decrement in comparison to the plain trailing edge configuration, with isolated discrepancies arising at low and high test α. Direct comparison of the 10mm and 20mm serrated trailing edge configurations indicated that typically, by increasing the serration length, the decrement in C_l was heightened for all α at any given δ_f, with the increment becoming more prominent at high test δ_f.

Figure 191(a) in Appendix L showed that there was a tendency for the 20mm serrations to decrease C_d, although ΔC_d often varied inconsistently with α for any given δ_f. Notable discrepancies arose for −2°≤α≤10° at δ_f=0°, with the 20mm serrations increasing C_d in comparison to the plain trailing edge configuration.

Whilst the 20mm serrations had negligible effect upon the drag polar, evaluation of the effects of the 20mm serrations upon C_l and C_d in terms of L/D indicated that the 20mm serrations had a detrimental effect upon L/D for all test α at δ_f=0°, see Figure 89. A maximum decrement of 12% coincided with α=2° and with subsequent increments in α, the decrement in L/D was marginalised, equating to a 1% decrement in comparison to the baseline configuration at α=18°. Thus, increasing the serration length from 10mm to 20mm at δ_f=0° heightened the decrement in L/D. At δ_f=5°, the 20mm serrations typically had no appreciable effect upon L/D, with only an isolated 5% increment at α=6°, which marginally exceeded the corresponding increment for the 10mm serrated configuration. Similarly to the 10mm serrated configuration, the 20mm serrations had a detrimental effect upon L/D at δ_f=10° for −2°≤α≤6°. A maximum decrement of 10% coincided with α=−2°, decreasing to a 4% and 1% decrement at α=2° and α=6°, respectively. However, for 10°≤α≤14°, the 20mm serrations increased L/D by 1-2%, although with subsequent increments in α≥16° any variation in L/D was essentially

negated in comparison to the corresponding plain trailing edge configuration at δ_f=10°. Similarly, the 20mm serrations reduced L/D at δ_f=15° for −2°≤α≤6°, accounting for a 6% decrement at α=−2° which was marginalised to a 2% decrement at α=6°. With further increments in α, the 20mm serrations typically had no appreciable effect upon L/D in comparison to the plain trailing edge configuration. Thus, increasing the serration length from 10mm to 20mm typically heightened the decrement in L/D, when compared to the plain trailing edge configuration.

(b) Flap Lap/Gap: (−0.26, −0.17)

Figure 90 showed that, at a flap lap/gap of (−0.26, −0.17), the 20mm serrations typically decreased C_l for all α and δ_f when compared the corresponding plain trailing edge configuration. An exception to this trend arose at δ_f=0°, with the 20mm serrations increasing C_l for α≤2°. With subsequent increments in 6°≤α≤18°, the decrement in C_l progressively increased in magnitude to a maximum of −0.05 at α=18° and accounting for a 2-3% reduction in C_l in comparison to the baseline configuration for all 6°≤α≤18°. Whilst at δ_f=5°, the 20mm serrations increased C_l for α=−2°, with further increments in α≥2°, C_l was adversely affected, correlating to a 1-3% decrement in comparison to the baseline configuration. Although the 20mm serrations increased C_l for α≤2° at δ_f=10°, with subsequent increments in α≥6°, the 20mm serrations had a detrimental effect upon C_l, accounting for 1-2% reduction in comparison to the plain trailing edge configuration. Accordingly, the magnitude of the decrement was comparable to the configuration with δ_f=0° for 6°≤α≤10° but with subsequent increments in α≥12°, ΔC_l was of a smaller magnitude than that of the corresponding 20mm serrated configurations with δ_f≤5°. With a final increment in δ_f to 15°, the decrement in C_l due to the 20mm serrations was progressively heightened in magnitude with successive increments in α≤12°, representing a 2% reduction in C_l and exceeding the decrements in C_l for the corresponding configurations with δ_f≤10°. However, with successive increments in α≥14°, the magnitude of the decrement in C_l was less than that for the corresponding configuration with δ_f≤5°, equating to a 1-2% reduction in C_l in comparison to the baseline configuration. Hence, increasing the serration length from 10mm to 20mm clearly heightened the magnitude of the decrement in C_l at δ_f=0° and δ_f=15°. At δ_f=5°, increasing the serration length reduced the decrement in C_l for 0°≤α≤6° but in contrast, heightened the decrement in C_l for α≥10°. At δ_f=10°, the 20mm serrations heightened the increment in C_l at α=−2° in comparison to the 10mm serrations but also tended to heighten the decrement in C_l for α≥2°.

Irrespective of whether the 20mm serration increased or decreased C_d, Figure 191(b) in Appendix L indicated that ΔC_d varied inconsistently with α for all δ_f. There was a tendency for the 20mm serrations to reduce C_d in comparison to the plain trailing edge configuration, although exceptions were evident for each test δ_f, particularly at δ_f=0°, whereby the 20mm serrations increased C_d for 2°≤α≤10°. Typically, the 20mm serrations had negligible effect upon the drag polar, although a marginal increase in C_d was evident for C_l>1 at δ_f=0° and for C_l>1.7 at δ_f=5° when compared to the plain trailing edge configuration.

Evaluation of the effects of the 20mm serrations upon C_l and C_d in terms of L/D indicated that the 20mm serrations had a detrimental effect upon L/D for all α≥2° at δ_f=0°, see Figure 91. The magnitude of the decrement was decreased from 7% at α=2° to less than a 2% decrement for all α≥12°. Whilst the 20mm serrations had a favourable effect upon L/D at δ_f=5° for α≤2°, the increment was reduced from 3% at α=−2° to 1% at α=2°, which was less favourable than the effect of the 10mm serrations. Furthermore, for α≥6°, the 20mm serrations had a near negligible effect upon L/D at δ_f=5° in comparison to the baseline configuration. For both δ_f=10° and δ_f=15°, the 20mm serrations had a detrimental effect upon L/D for −2°≤α≤6°. At δ_f=10°, the maximum decrement of 2% coincided with α=−2° and was reduced to 1% with subsequent increments in α, whereas increasing δ_f to 15° heightened the decrement to 5% α=−2°, reducing to a 2% decrement at α=6°. Whilst both δ_f of 10° and 15° demonstrated a 1% increment in L/D at α=10°, with subsequent increments in α≥12°, the 20mm serrations had no appreciable effect upon L/D in comparison to the plain trailing edge configuration. Thus, increasing the serration length from 10mm to 20mm typically heightened the decrement in L/D or marginalised an increment.

(c) Flap Lap/Gap: (−0.26, −0.2)

Similarly to the 10mm serrations, the 20mm serrations notably increased C_l at a flap lap/gap of (−0.26, −0.2) for all α at δ_f≤10, exceeding the magnitude of the increment for the corresponding 10mm serrated configuration, with only an isolated discrepancy arising for α=20° at δ_f=10°, see Figure 92. The increment in C_l due to the 20mm serrations varied inconsistently with α for all δ_f, although ΔC_l tended to increase in magnitude with successive increments in δ_f≤10° for any given α≤6°. With further increments in α≥10°, the 20mm serrations were most effective for the configuration with δ_f=5°, generating the maximum increment in C_l. At δ_f=0°, ΔC_l due to the 20mm serrations appeared relatively insensitive to increments in α, varying between 0.04 and 0.05 However, the corresponding percentage increment in C_l progressively decreased

with α from a 13% increment at α=2° to 2% for 12°≤α≤18°. Increasing δ_f to 5° heightened the magnitude of the increment in C_l for all α, equating to a 10% increment at α=2° and decreasing to a 2-3% increment for 10°≤α≤18°. With a further increment in δ_f to 10°, ΔC_l due to the 20mm serrations exceeded that of both the δ_f=0° and δ_f=5° configurations for −2°≤α≤6°, progressively decreasing from an 8% increment at α=2° to a 5% increment at α=6°. For 10°≤α≤18°, the increment in C_l due to the 20mm serrations corresponded to a 2-3% increase in comparison to the plain trailing edge configuration, with any deviation in C_l essentially negated at α=20°. A final increment in δ_f to 15° rendered the 20mm serrations detrimental to C_l. With successive increments in α, the adverse effect of the 20mm serrations upon C_l was heightened in magnitude, corresponding to a 2-4% reduction in C_l in comparison to the plain trailing edge configuration for 2°≤α≤18° and thus, exceeding the decrement in C_l for the corresponding 10mm serrated configuration.

From Figure 191(c) in Appendix L, it was evident that the 20mm serrations tended to increase C_d for all α and δ_f≤10°, with ΔC_d varying inconsistently with α. However, at δ_f=15°, the 20mm serrations decreased C_d for 6°≤α≤20°, with the magnitude of the decrement typically heightened with successive α. Whilst the 20mm serrations had no appreciable effect upon the drag polar at low C_l, a marginal reduction in C_d was evident for C_l>1.5 at δ_f=0°, for C_l>2 at δ_f=5° and for C_l>2.7 at δ_f=10°. Conversely, the 20mm serrations marginally increased C_d for C_l>2.8 at δ_f=15°. Additionally, the 20mm serrations decreased the range of α over which measurements were obtained at δ_f=15° from 20° with a plain trailing edge to 18°, corresponding to a decrease in both C_{lmax} and α_{stall}.

Amalgamation of the effect of the 20mm serrations upon C_l and C_d in terms of L/D indicated that the increment in C_d tended to offset the corresponding increment in C_l, see Figure 93. At δ_f=0°, the effect of the 20mm serrations upon L/D was inconsistent at low test α, with a marked increment at α=−2° and a 2% decrement at α=2°. However, with subsequent increments in α≥6°, the favourable effect of the 20mm serrations upon C_l was marginalised by the increment in C_d, corresponding to a 1-2% increment in L/D in comparison to the plain trailing edge configuration. Hence, increasing the serration length from 10mm to 20mm at δ_f=0° typically heightened the increment in L/D and diminished the isolated decrement at α=2°. At δ_f=5°, the 20mm serrations increased L/D for α≤2°, accounting for a 24% increment at α=−2°, which was marginalised to a 1% increment at α=2°. However, in contrast to the 10mm serrations, the 20mm serrations marginally decreased L/D by 2-3% for 6°≤α≤10°, although similarly to the

10mm serrations, any variation in L/D was essentially negated for $\alpha \geq 12°$. Increasing the serration length to 20mm at $\delta_f = 10°$ heightened the increment in L/D to 18% at $\alpha = -2°$ and extended the range of α over which the 20mm serrations were beneficial to L/D such that the 20mm serrations increased L/D by 5% in comparison to the baseline configuration at $\alpha = 2°$ prior to any variation in L/D being negated for $\alpha \geq 6°$. Note that an exception arose for $10° \leq \alpha \leq 12°$ at $\delta_f = 10°$, with the 20mm serrations reducing L/D by 2% in comparison to the plain trailing edge configuration. Similarly to the 10mm serrations, the 20mm serrations had negligible effect upon L/D at $\delta_f = 15°$, with only an isolated 2% decrement at $\alpha = 2°$ and a 1% increment for $12° \leq \alpha \leq 14°$.

6.9.4 Oil Flow Visualisation at a Flap Lap/Gap of (−0.26, −0.2)

Recognising the heightened effectiveness of the serrated geometries at a lap/gap of (−0.26, −0.2), surface oil flow visualisation was used to identify salient features in the flow field topography over the upper surface of the single slotted flap as a result of the implementing either 10mm or 20mm 60° triangular serrations at the trailing-edge of the main element.

Recall that at a flap lap/gap of (−0.26, −0.2), the 10mm serrations increased C_l for all α and $\delta_f \leq 10°$ and with a final increment in δ_f to 15°, the favourable effect of the 10mm serrations upon C_l was limited to $\alpha \leq 6°$. Similarly, the 20mm serrations notably increased C_l at a flap lap/gap of (−0.26, −0.2) for all α and $\delta_f \leq 10°$, exceeding the magnitude of the increment for the corresponding 10mm serrated configuration, although a final increment in δ_f to 15° rendered the 20mm serrations detrimental to C_l.

For each test δ_f between 5° and 15°, oil flow visualisation was obtained over the upper surface of the flap for $\alpha = 4°$, 8° and 12° for each of the three trailing edge geometries. Note that the flow direction (denoted by U_∞) in each photograph is from top to bottom.

Figure 94 and Figure 95 show the oil flow visualisation over the upper surface of the single slotted flap deflected to 5°, with the leading edge slat retracted and the configuration inclined to a 4° and 8° angle of incidence, respectively.

The surface oil flow visualisation in Figure 94 and Figure 95 show that with $\delta_f = 5°$, the upper surface boundary layer remained attached to the flap trailing edge for both $\alpha = 4°$ and $\alpha = 8°$, irrespective of the precise geometry employed at the trailing edge of the main element. For configurations at $\alpha = 4°$ or $\alpha = 8°$, the flow field generated over the upper

surface of the flap, downstream of the 10mm serrations, was comparable to that for the baseline configuration with the plain trailing edge geometry.

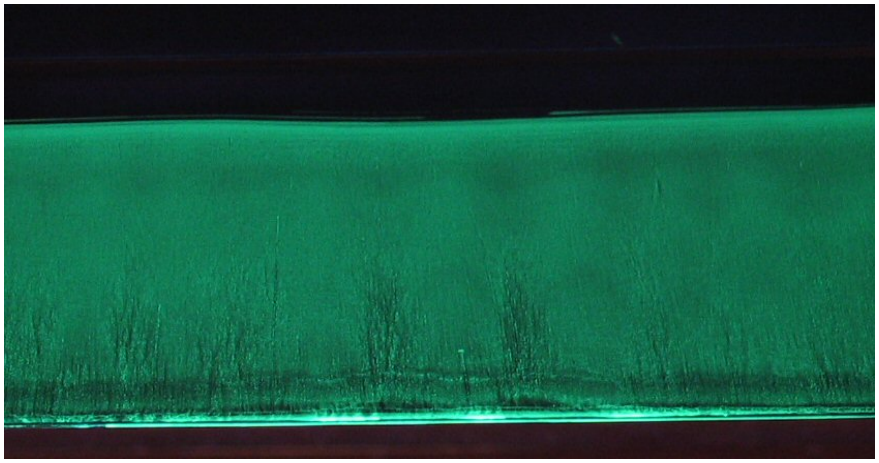

(a) Plain

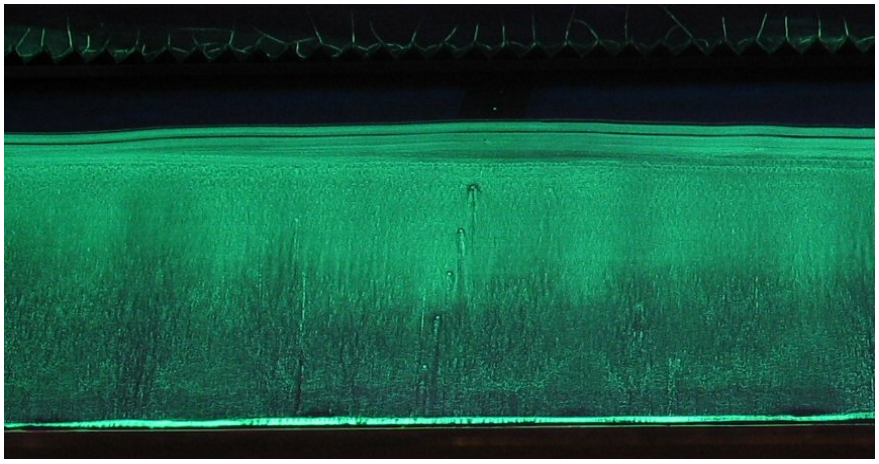

(b) 10mm 60° Triangular Serrations

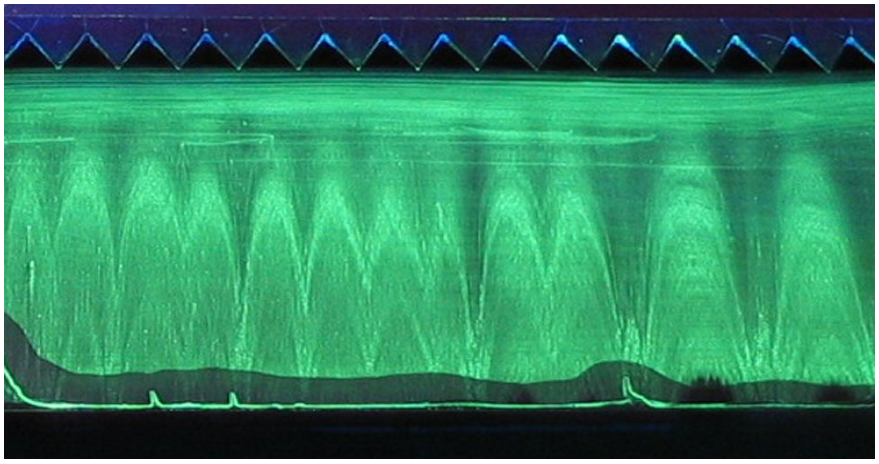

(c) 20mm 60° Triangular Serrations

Figure 94: Surface oil flow visualisation for δ_f=5°, α=4°

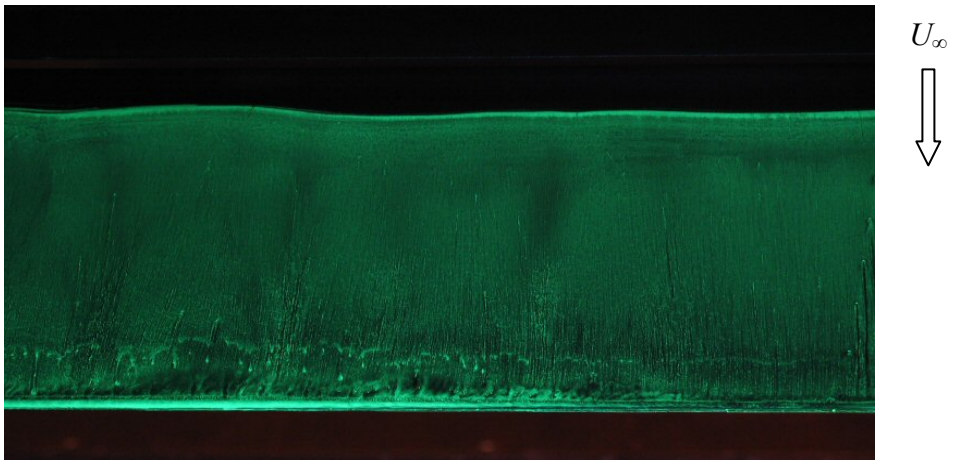

(a) Plain

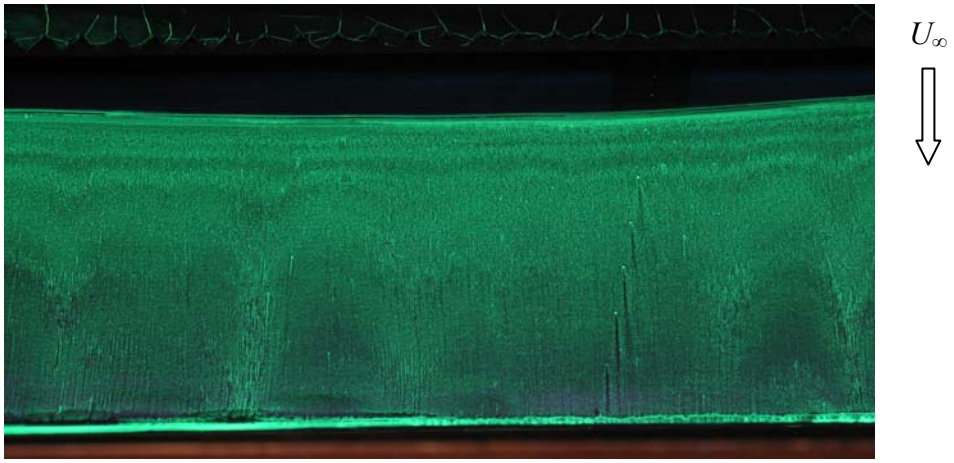

(b) 10mm 60° Triangular Serrations

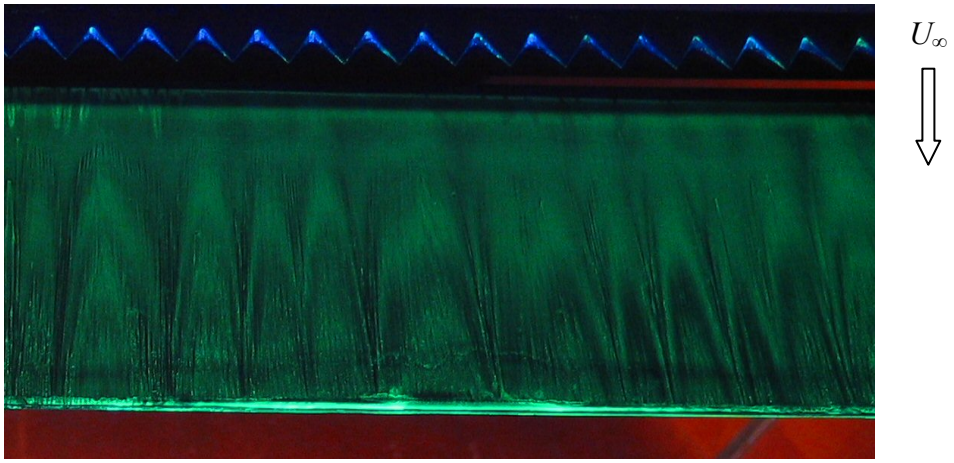

(c) 20mm 60° Triangular Serrations

Figure 95: Surface oil flow visualisation for δ_f=5°, α=8°

In contrast, with the 20mm serrations implemented, Figure 94(c) and Figure 95(c) show that the flow field developing over the upper surface of the flap was highly three-

dimensional and displayed distinct evidence of wake structure emanating from each individual 60° triangular vertex. The dark bands indicative of a developing wake structure aft of each serration vertex, interspersed with the dark green bands of oil flow visualisation mixture corroborated the flow field visualisation of Soderman (1972), namely, "white and dark bands were etched in the oil behind each prong [extending] from the airfoil leading edge to the trailing edge".

Recalling that Soderman (1972) attributed the distinct three-dimensional circular pattern aft of each serration vertex to the development of counter-rotating vortices, which were corroborated by the flow visualisation of Schwind and Allen (1973) and Gai and Sharma (1981), it was proposed that similarly, the oil flow visualisation for the present experiment on a two-element high-lift configuration with δ_f=5° at either α=4° or α=8° provided evidence for the existence of longitudinal vortices emanating from the serration vertices. Whether the configuration was inclined to α=4° or α=8°, the width of each wake structure progressively diminished with increasing distance downstream. At α=4°, this wake structure typically dissipated between $0.5c_{flap}$ and $0.7c_{flap}$, although by increasing α to 8°, the distinct wake structure emanating from each individual vertex typically extended over the entire upper surface to within close proximity of the flap trailing edge. This suggested that these vortical structures emanating from each individual vertex were stronger in terms of their impact upon the surface flow characteristics on the flap when the configuration was at α=8° than at α=4°. Note that the absence of such wake structures emanating from the vertices of the 10mm serrations did not counter their existence; moreover, it suggested that for the given configuration, the assumed vortical structures were weak in terms of their impact upon the surface flow characteristics of the flap upper surface.

A possible schematic for the development of the vortical structures is proposed in Figure 96. Figure 96 is illustrative of the generation of counter-rotating upflow vortices from the serrated trailing edge. Specifically, when viewed in the freestream direction, it is postulated that the shear layer developing over a single serration rolls up to form a clockwise rotating vortex from the right-hand edge and conversely, a counter-clockwise rotating vortex from the left-hand edge, thus inducing upflow in the central region between the vortices. However, the precise rotational direction of the longitudinal vortices emanating from a serration vertex was unclear. Thus dependent upon the pressure difference, a pair of counter-rotating downflow vortices may alternatively be generated aft of the serration vertex.

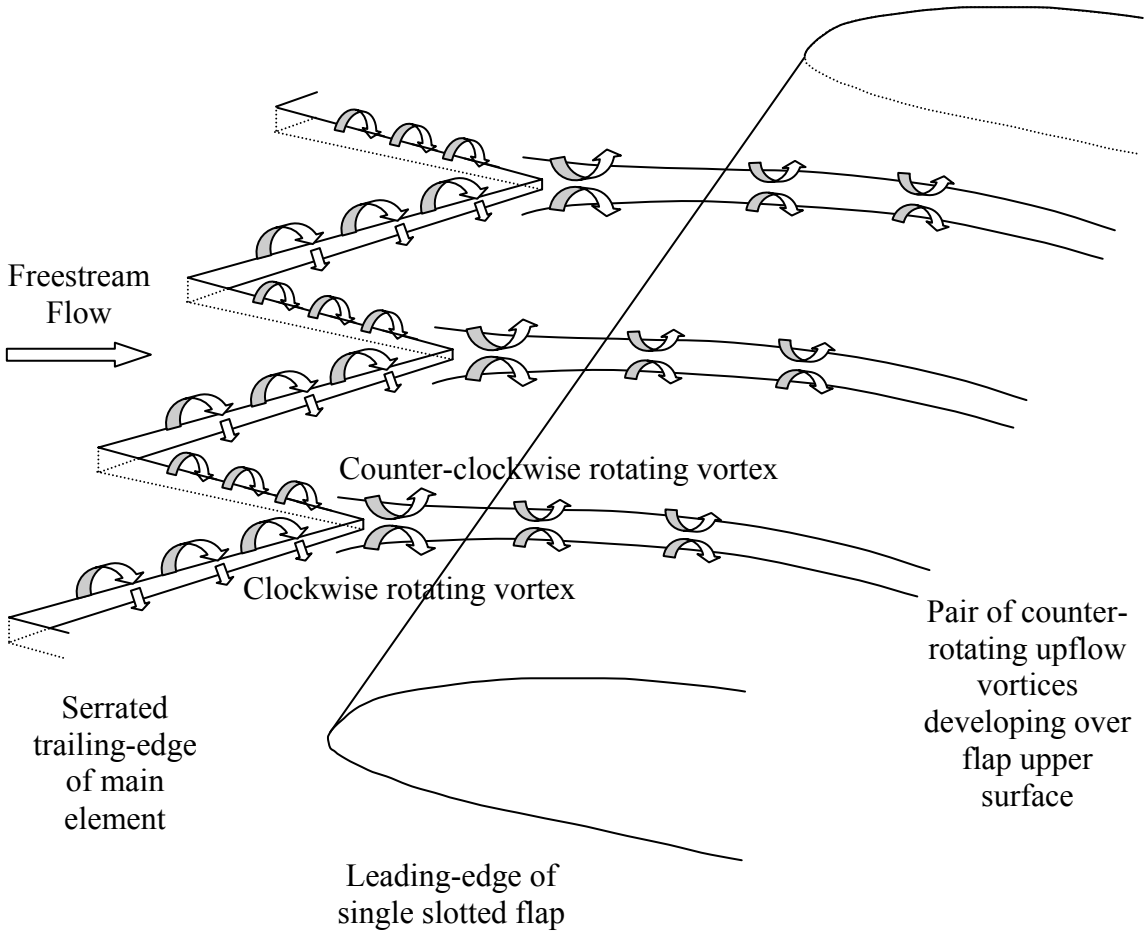

Figure 96: Schematic of counter-rotating upflow vortices emanating from serrations

With regard to the development of the counter-rotating vortices aft of the trailing edge serrations, Ashill et al's (2001) studies of sub-boundary layer vortex generators are of particular interest. Accordingly, the flow field analysis for a forward-facing wedge and joined vanes, both of which are geometrically similar to a serration, suggest that the counter-rotating vortices generated aft of a serration are in close proximity, which may result in adverse interference between the vortices, consequently reducing the vorticity and promoting streamwise decay.

Increasing α to 12°, Figure 97 showed that for the configuration with δ_f=5° and the plain geometry implemented at the trailing edge of the main element, the boundary layer over the upper surface of the single slotted flap typically remained attached to within $0.05c_{flap}$ of the trailing edge.

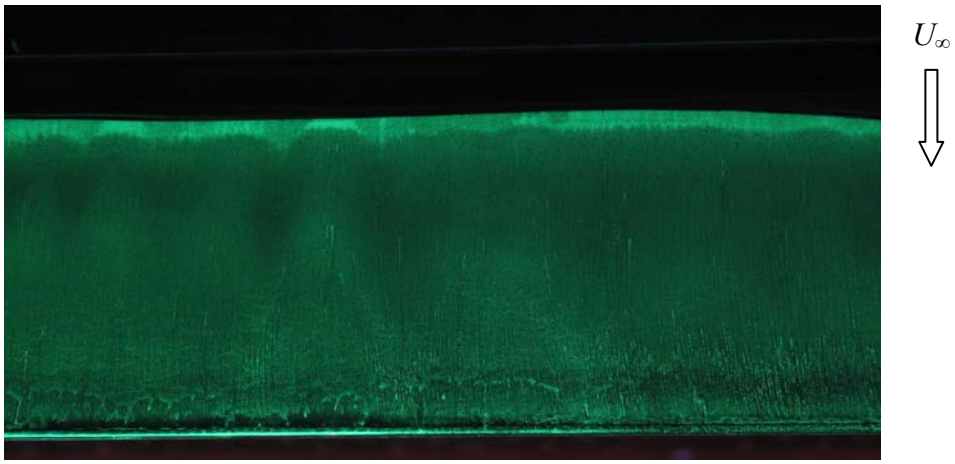

(a) Plain

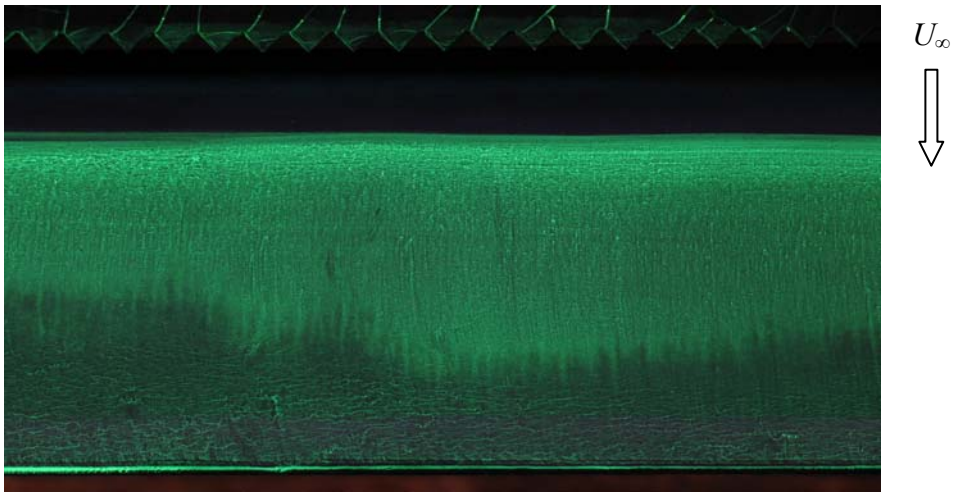

(b) 10mm 60° Triangular Serrations

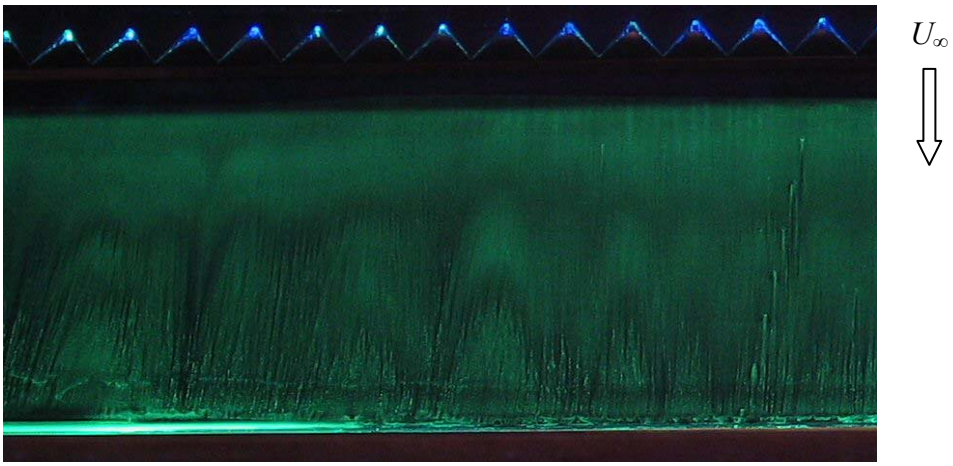

(c) 20mm 60° Triangular Serrations

Figure 97: Surface oil flow visualisation for δ_f=5°, α=12°

Implementing the 10mm serrations at the trailing edge of the main element promoted boundary layer attachment to the flap trailing edge, although the surface flow field did

not exhibit any identifiable characteristics to provide evidence of the flow field mechanisms by which the 10mm serrations delayed boundary layer separation.

With the 20mm serrations implemented at the trailing edge of the main element, the boundary layer remained attached to within close proximity of the trailing edge. In contrast to the 10mm serrated configuration, the 20mm serrations generated a highly three-dimensional flow field over the upper surface of the flap.

Whilst the oil flow visualisation for the 20mm serrated configuration displayed evidence of a wake structure emanating from each individual 60° triangular vertex (see Figure 97(c)), which was indicative of the existence of vortical structures generated aft of each serration, each wake structure was far less distinct than that observed at either α=4° or 8°. This suggested that the impact of the vortical structures upon the surface flow characteristics was distinctly weakened by increasing α to 12°. The lack of clarity with which the wake structures were manifested in the flow field over the upper surface of the flap meant that, whilst it was evident that the individual wake structures dissipated with distance downstream, it was difficult to ascertain the chordwise extent over which the vortical structures influenced the upper surface flow field.

Figure 98 shows that with the plain geometry implemented at the trailing edge of the main element, increasing δ_f from 5° to 10° at α=4° typically provoked boundary layer separation over the aft $0.15c_{flap}$, although the separation line was three-dimensional and fluctuated across the span.

In contrast, implementing the 10mm serrations at the trailing edge of the main element promoted boundary layer attachment to the flap trailing edge. Similarly to the configurations with δ_f=5°, the surface flow field did not exhibit any identifiable characteristics to provide evidence of the flow field mechanisms by which the 10mm serrations prevented boundary layer separation. This did not refute the existence of such vortical structures emanating from the serration vertices, observed in previous studies but once again, did indicate that the assumed wake structures generated aft of the serration vertices had negligible impact upon the surface flow characteristics over the upper surface of the flap.

With the 20mm serrations implemented at the trailing edge of the main element, boundary layer attachment was promoted to the flap trailing edge. Note that the distinct line in Figure 98(c), marked by the differentiation in colour over the aft approximate

$0.15c_{flap}$, was attributed to inconsistencies within the flow visualisation mixture and was not representative of a flow field attribute.

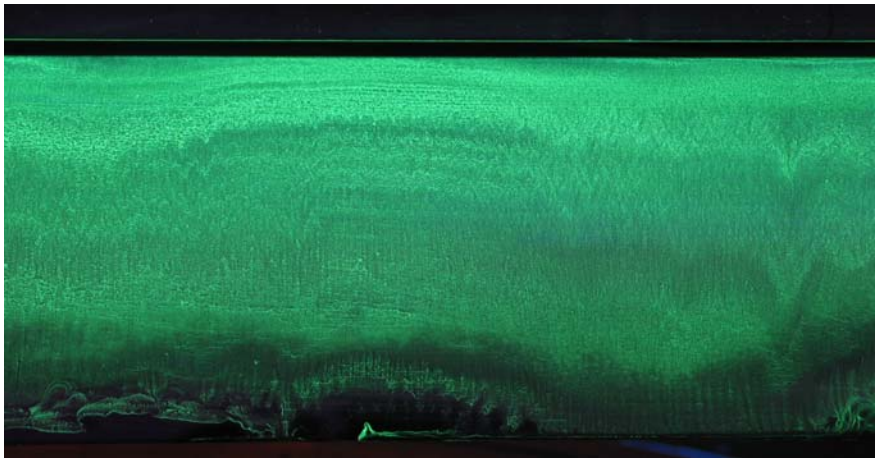

(a) Plain

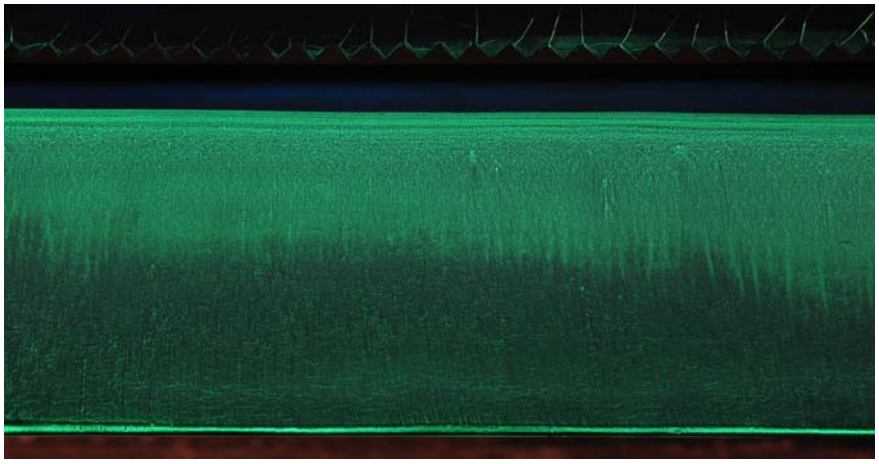

(b) 10mm 60° Triangular Serrations

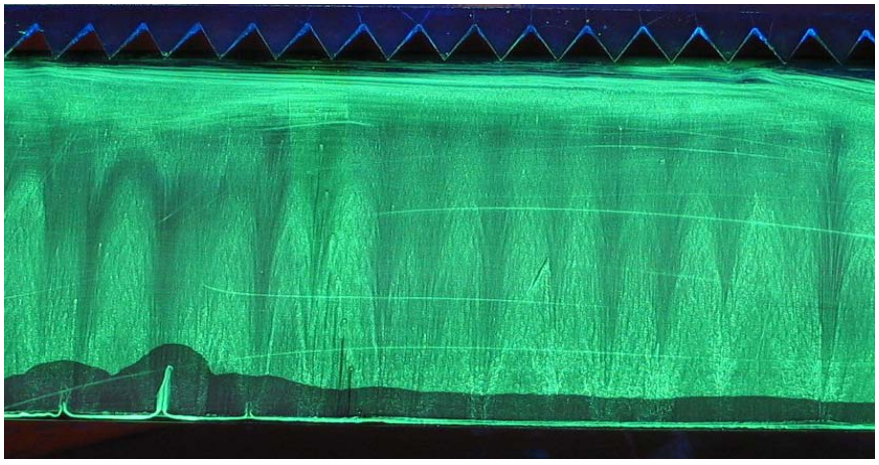

(c) 20mm 60° Triangular Serrations

Figure 98: Surface oil flow visualisation for δ_f=10°, α=4°

The flow field developing over the upper surface of the flap aft of the 20mm serrations was highly three-dimensional and displayed distinct evidence of wake structures emanating from each individual 60° triangular vertex (see Figure 98(c)).

Once again, based upon the observations of earlier studies, the oil flow visualisation for the present experiment on a two-element high-lift configuration with δ_f=10° at α=4° suggested that longitudinal vortices emanated from the serration vertices. The distinct wake structure emanating from each individual vertex typically extended over the entire upper surface to within close proximity of the flap trailing edge, with the width of each wake structure progressively diminishing with increasing distance downstream (see Figure 98(c)). This suggested that these vortical structures emanating from each individual vertex had a relatively strong impact upon surface flow characteristics of the flap for the specified configuration.

By increasing α to 8°, Figure 99 shows that the flow field developing over the upper surface of the flap aft of the plain trailing edge geometry was more favourable than that at α=4°, with the boundary layer typically remaining attached to within $0.1c_{flap}$ of the trailing edge.

Similarly to the configuration with δ_f=10° at α=4°, the 10mm serrations promoted boundary layer attachment to the flap trailing edge, although the surface flow field did not exhibit any evidence of the existence of wake structures emanating from the serration vertices. Once again, this did not counter the existence of such vortical structures but instead suggested that the wake structures simply had negligible impact upon the surface flow characteristics for the given configuration.

The 20mm serrations typically maintained boundary layer attachment to within $0.1c_{flap}$ of the trailing edge but unlike previous configurations, the surface flow visualisation did not exhibit any evidence of the wake structures emanating from each serration vertex. This suggested that increasing α from 4° to 8° with δ_f=10° distinctly weakened the vortical structures in terms of their impact upon the surface flow characteristics of the flap.

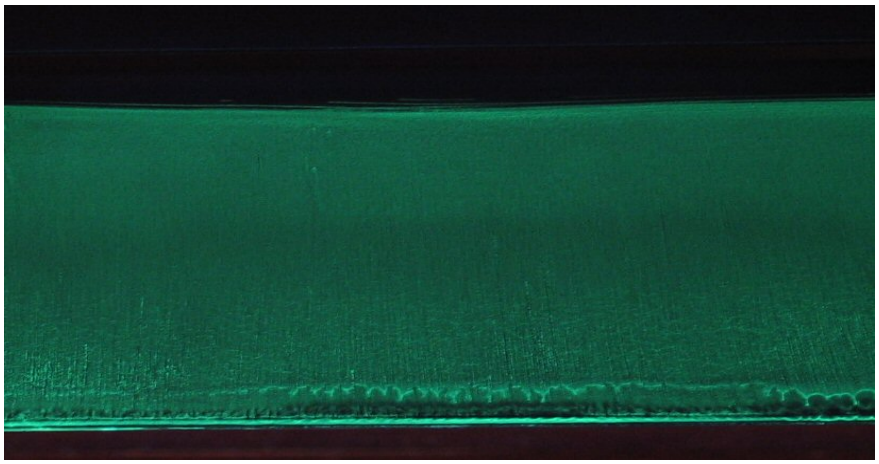

(a) Plain

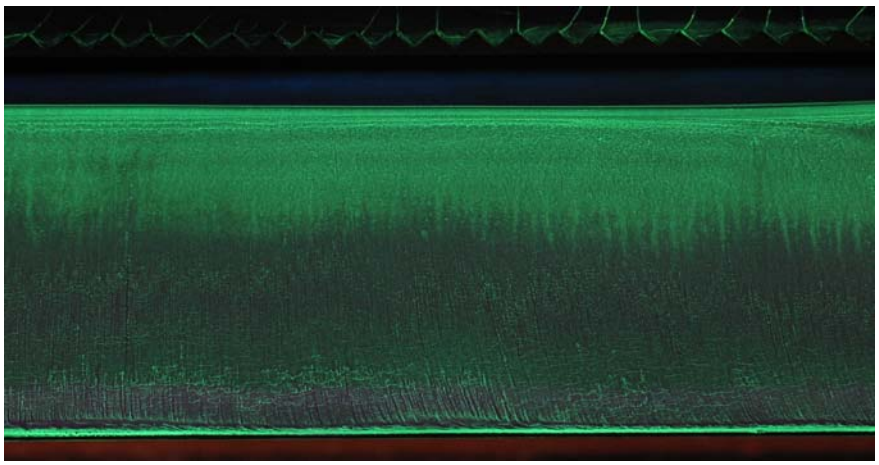

(b) 10mm 60° Triangular Serrations

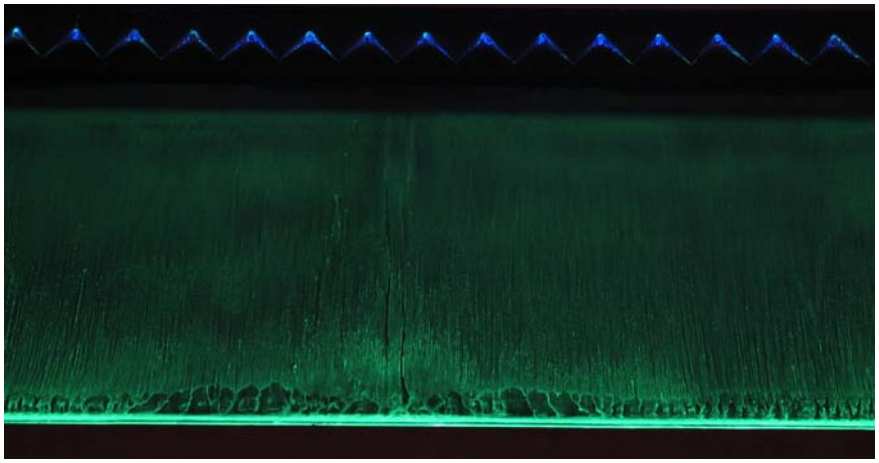

(c) 20mm 60° Triangular Serrations

Figure 99: Surface oil flow visualisation for δ_f=10°, α=8°

By increasing α from 8° to 12° with δ_f=10°, Figure 100 shows that with the plain trailing edge geometry implemented, trailing edge boundary layer separation was

extended upstream. Whilst the point of separation varied across the span, boundary layer separation was typically evident over the aft $0.15c_{flap}$ to $0.25c_{flap}$.

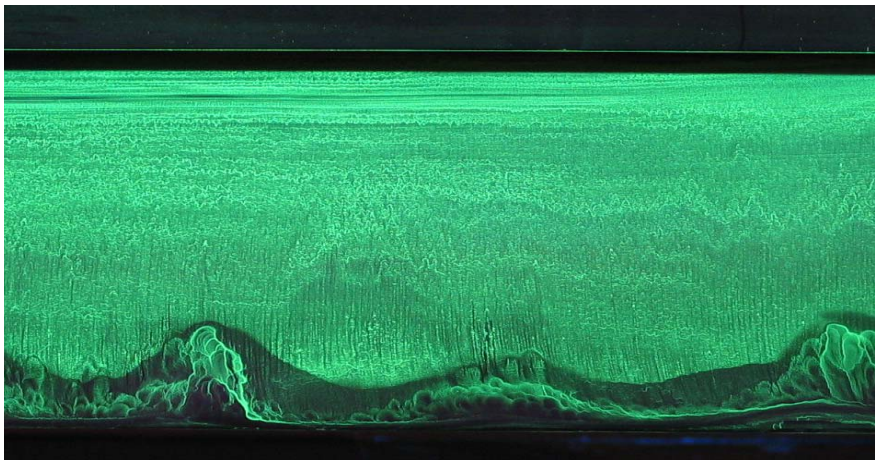

(a) Plain

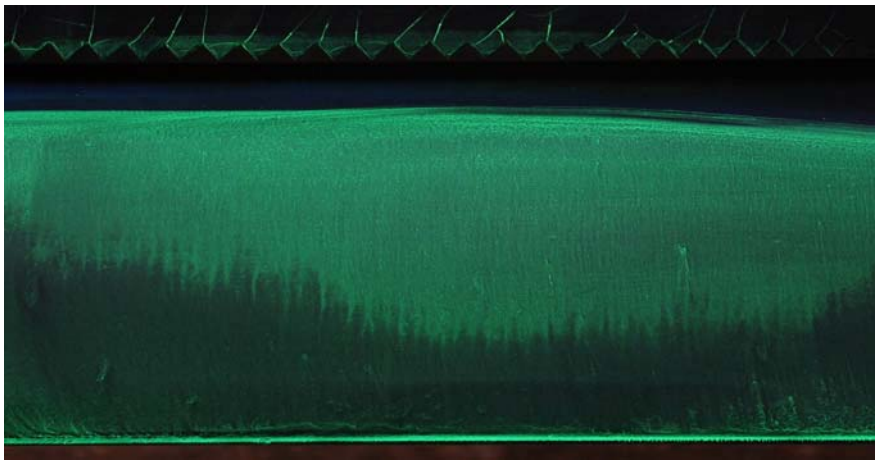

(b) 10mm 60° Triangular Serrations

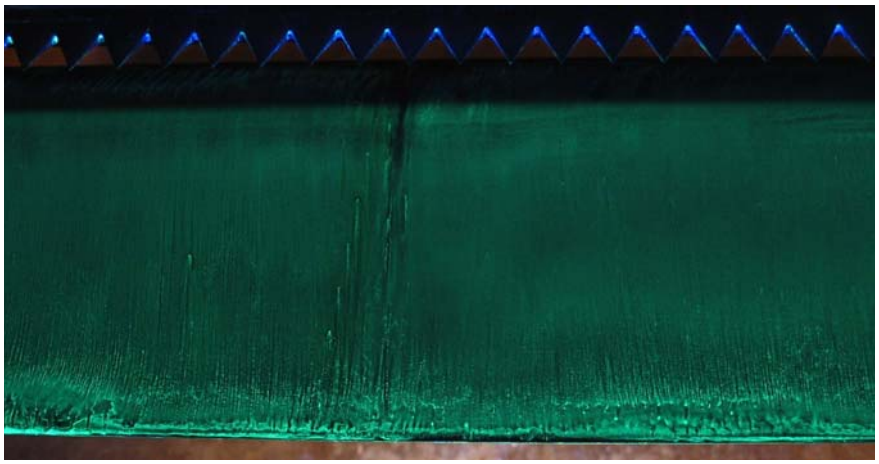

(c) 20mm 60° Triangular Serrations

Figure 100: Surface oil flow visualisation for δ_f=10°, α=12°

In contrast, the 10mm serrations prevented boundary layer separation over the upper surface of the flap. Once again, the surface flow field displayed no evidence of the flow mechanisms by which boundary layer attachment was achieved, suggesting that the wake structures and hence the vortices, emanating from the serration vertices, had no impact upon the upper surface flow characteristics.

The 20mm serrations typically maintained boundary layer attachment to within $0.05c_{flap}$ of the trailing edge. Similarly to both the corresponding 10mm serrated configuration at α=12° and the 20mm serrated configuration at α=8°, the surface flow visualisation did not exhibit any evidence of the wake structures emanating from each serration vertex, suggesting that the assumed vortical structures were weak in terms of their impact upon the surface flow characteristics over the upper surface of the deflected flap.

By increasing δ_f from 10° to 15° at α=4°, Figure 101 shows that the flow field generated over the upper surface of the single slotted flap aft of the plain geometry was slightly more favourable than that at δ_f=10°, with boundary layer separation typically limited to the aft $0.1c_{flap}$.

The 10mm serrations proved favourable to the flow field development over the upper surface of the flap for the configuration with δ_f=15° and α=4°, typically delaying boundary layer separation to within close proximity of the trailing edge, although local fluctuations to this trend were evident over the span.

With the 20mm serrations implemented at the trailing edge of the main element, the flow field developing over the upper surface of the flap was comparable to that with the plain trailing edge: boundary layer separation was typically limited to the aft $0.1c_{flap}$, although notable fluctuations in the point of boundary layer separation were evident across the span. Note that flow field generated over the upper surface of the flap aft of both the 10mm and 20mm serrated geometries exhibited no evidence of the wake structures emanating from the respective serration vertices, suggesting that the assumed vortical structures had negligible impact upon the upper surface flow characteristics of the trailing edge flap at α=4°.

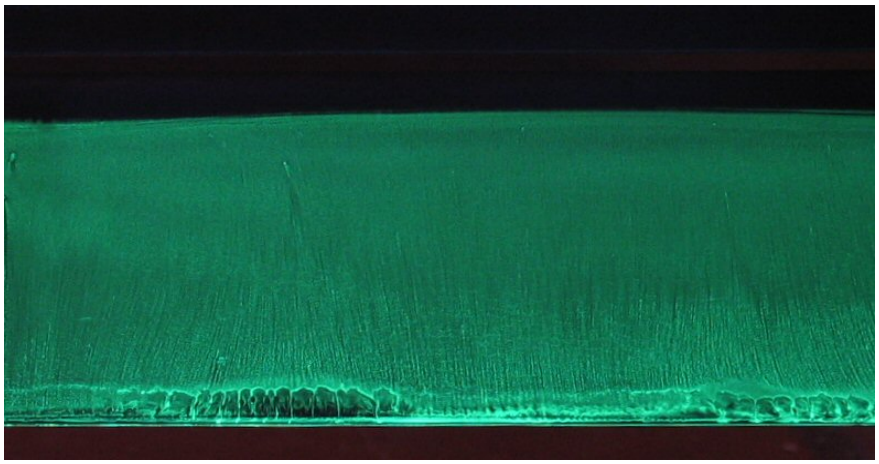

(a) Plain

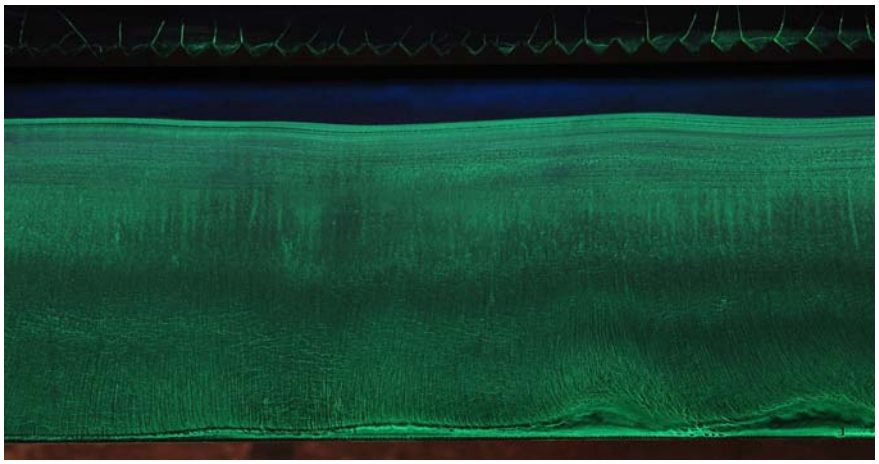

(b) 10mm 60° Triangular Serrations

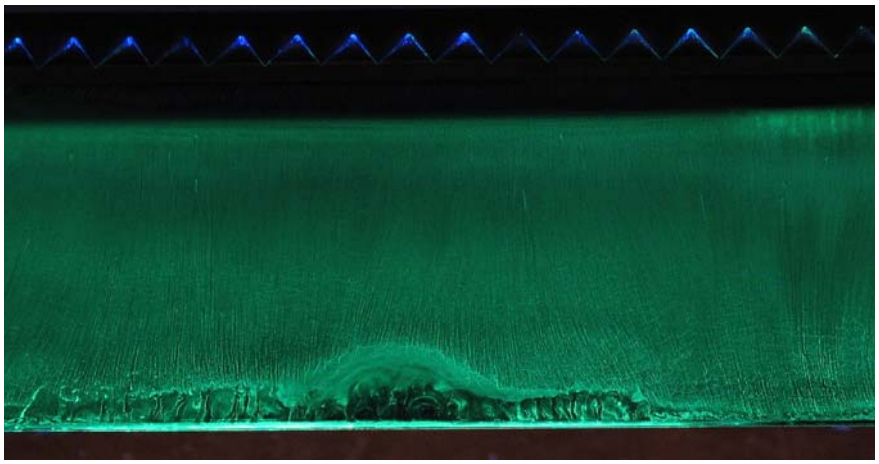

(c) 20mm 60° Triangular Serrations

Figure 101: Surface oil flow visualisation for δ_f=15°, α=4°

Maintaining a δ_f of 15° and increasing α from 4° to 8° had no appreciable effect upon the extent of boundary layer separation over the upper surface of the flap when the plain

geometry was implemented at the trailing edge of the main element, with separation limited to the aft $0.1c_{flap}$, see Figure 102.

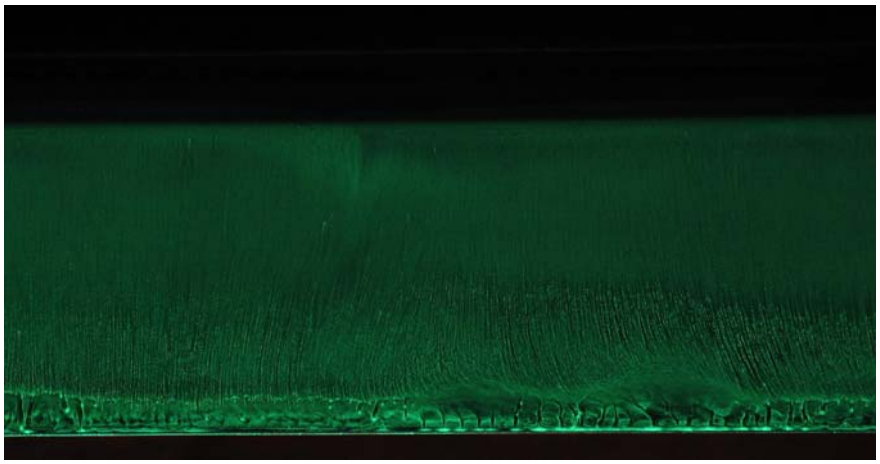

(a) Plain

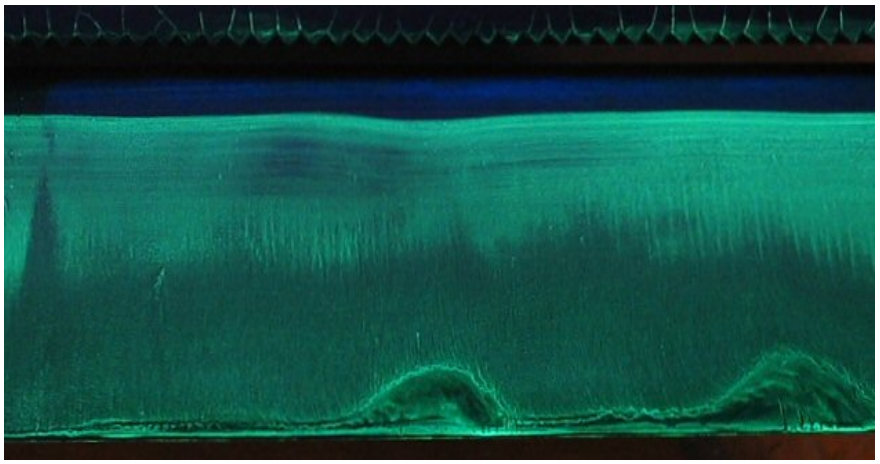

(b) 10mm 60° Triangular Serrations

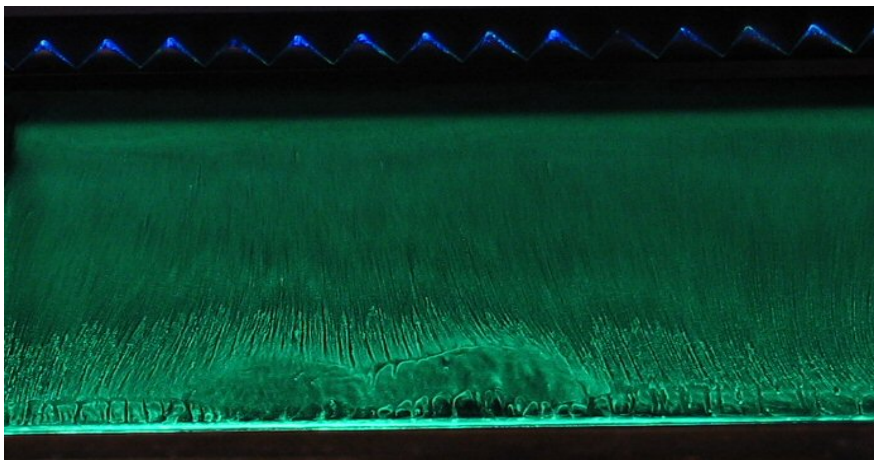

(c) 20mm 60° Triangular Serrations

Figure 102: Surface oil flow visualisation for δ_f=15°, α=8°

With the 10mm serrations implemented at the trailing edge of the main element, the point of boundary layer separation displayed a greater degree of variation across the span than the plain trailing edge configuration. Whilst boundary layer attachment was maintained to within close proximity of the trailing edge at some spanwise locations, localised separation extended further upstream, extending over the aft $0.25c_{flap}$.

The boundary layer over the upper surface of the single slotted flap, aft of the 20mm serrations, typically remained attached to between $0.8c_{flap}$ and $0.9c_{flap}$, although similarly to the 10mm serrated configuration, localised separation extended over the aft $0.25c_{flap}$. Thus, in terms of preventing boundary layer separation at α=8°, the serrated geometries were not advantageous when δ_f was deflected to 15°. Once again, the surface flow field developing aft of the 10mm or 20mm serrations did not exhibit any evidence of the wake structures emanating from the respective serration vertices. Accordingly, this suggested that the vortices developing from the serrations were weak in terms of their impact upon the surface flow characteristics for the given configuration.

By increasing α from 8° to 12° with δ_f=15°, Figure 103 showed that with the plain trailing edge geometry implemented, trailing edge boundary layer separation extended upstream over the upper surface of the single slotted flap. Whilst the point of boundary layer separation fluctuated across the span, separation was typically evident over the aft $0.3c_{flap}$ of the flap upper surface.

However, implementation of either the 10mm or 20mm serrations at the trailing edge of the main element had a detrimental effect in terms of promoting boundary layer attachment over the upper surface of the flap. Marked deviations in the point of boundary layer separation were evident across the span with both the 10mm ad 20mm serrated geometries displaying substantial regions of boundary layer separation extending over the aft $0.8c_{flap}$. However, there were isolated regions where boundary layer attachment was maintained to within close proximity of the trailing edge. The reason for such dramatic disparity was not understood and could only be attributed to the highly three-dimensional nature of the developing flow field. Thus, at α=12° and with the flap deflected by 15° at a lap/gap of (−0.26, −0.2), the 10mm and 20mm serrated geometries were distinctly detrimental to the flow field development over the upper surface of the single slotted flap.

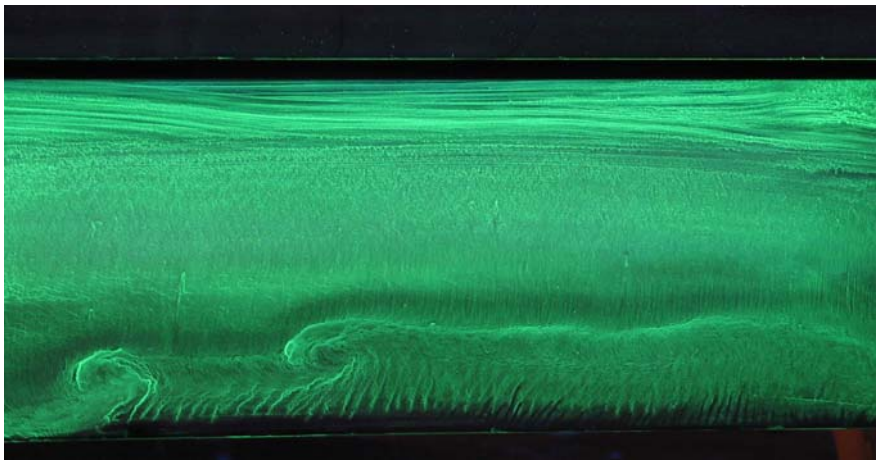

(a) Plain

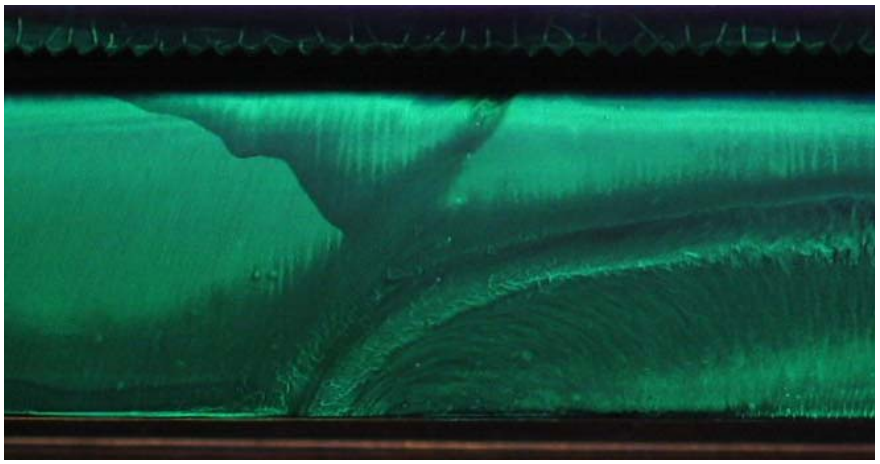

(b) 10mm 60° Triangular Serrations

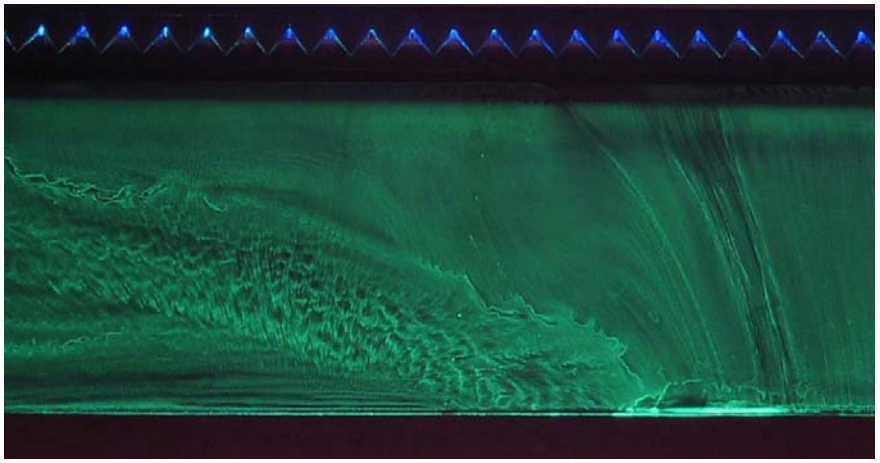

(c) 20mm 60° Triangular Serrations

Figure 103: Surface oil flow visualisation for δ_f=15°, α=12°

Thus in conclusion, for the configuration with δ_f=5°, boundary layer attachment over the upper surface of the single slotted flap was typically maintained to within close proximity of the trailing edge for α=4°, 8° and 12°, irrespective of the precise geometry

implemented at the trailing edge of the main element. Furthermore, the surface flow visualisation displayed evidence of wake structures emanating from the vertices of the 20mm serrations, corroborating the observations of Soderman, and hence suggesting the existence of vortical structures generated from the serration vertices. As α was increased to 12°, these vortical structures were distinctly weakened in terms of their impact upon the surface flow characteristics on the flap. By increasing δ_f to 10°, both the 10mm and 20mm serrations had a favourable effect upon the boundary layer development over the upper surface of the flap, typically delaying separation in comparison to the plain trailing edge configuration at α=4°, 8° and 12°. However, wake structures emanating from the vertices of the 20mm serrations were only evident at α=4°. The absence of wake structures evident over the upper surface of the flap did not counter their existence but instead, suggested that such flow field attributes were weak in terms of their impact upon the surface characteristics of the developing flow field. Note that the weak impact of these wake structures upon the surface flow field characteristics did not necessarily infer diminished capability to prevent boundary layer separation, as evident from the flow visualisation at δ_f=10°. Thus, in terms of the hypothesis that the development of streamwise vortices, aft of the serration vertices, transferred momentum to the near surface boundary layer and hence, delayed separation, the oil flow visualisation suggested that such vortices did not necessarily have to strongly impact the surface in order to promote sufficient mixing to prevent/delay boundary layer separation. A final increment in δ_f to 15° rendered both the 10mm and 20mm serrations unfavourable, typically increasing the extent of trailing edge boundary layer separation in comparison to the plain configuration, particularly at α=12°.

6.9.5 Reynolds Number Run

Figure 104 shows the effect of Reynolds number on the aerodynamic forces obtained from the balance data for the two-element configuration comprising a main element with 20mm serrated trailing edge and a single slotted flap deflected to 5° at a lap/gap of (−0.26, −0.2). Measurements were obtained for α=8° and α=12°, which were applicable to takeoff and landing incidence angles. Based upon the stowed reference chord, the Reynolds numbers (Re) of 8.4×10^5, 1.06×10^6, 1.26×10^6, 1.47×10^6, 1.68×10^6 and 1.87×10^6 correlated to increments in freestream velocity from 25m/s to 45m/s in 5m/s increments.

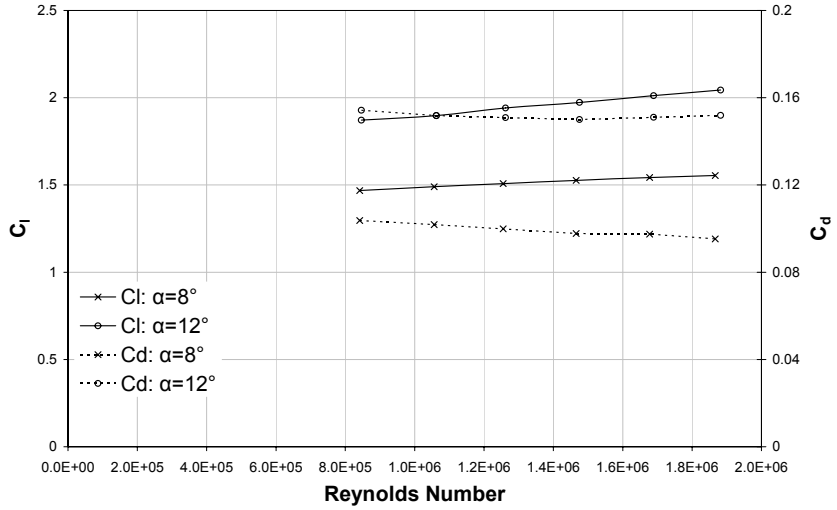

Figure 104: Effect of Reynolds number on C_l and C_d for 20mm serrated configuration at a flap lap/gap of (−0.26, −0.2), δ_s=0°, δ_f=5°, α=8° and 12°

Increments in Reynolds number from 8.41×10^5 to 1.87×10^6 tended to increase C_l for both configurations at α=8° and α=12°, corroborating the observations of Ljungström (1976). Specifically, C_l increased from 1.47 at Re=8.41×10^5 to 1.55 at Re=1.87×10^6 at α=8°, accounting for a 5% increment. The variation in C_l due to Re was marginally increased to 9% at α=12°, increasing from 1.87 at Re=8.41×10^5 to 2.04 at Re=1.87×10^6. At α=8°, increasing the Re from 8.41×10^5 to 1.87×10^6 decreased C_d by 0.008, accounting for an 8% decrement and corroborating the trends in profile drag observed by Ljungström. By increasing α to 12°, the variation in C_d was marginalised to 0.004, correlating to a 3% decrement. However, C_d initially decreased by 0.004 with increments in Re from 8.41×10^5 to 1.47×10^6, prior to increasing by 0.002 with further increments in Re to 1.87×10^6.

6.9.6 Summary for Two-Element Configuration: Fine Lap/Gap Grid

Based upon the fine lap/gap parametric study of a two-element high-lift configuration comprising a main element with either a plain, 10mm or 20mm 60° triangular serrated trailing edge and a single slotted flap deflected between 0° and 15°, the resultant aerodynamic forces, determined from balance measurements, indicated that:

- In terms of increasing C_l, the serrated geometries were only beneficial at a lap/gap of (−0.26, −0.2)
- 10mm serrations increased C_l at a flap lap/gap of (−0.26, −0.2) for all α and $\delta_f\leq10°$ with the increment in C_l greatest for δ_f=10°. A final increment in δ_f to 15° restricted the favourable influence of the 10mm serrations upon C_l to $-2°\leq\alpha\leq6°$

and marginalised the magnitude of ΔC_l in comparison to the corresponding configurations with $0° \leq \delta_f \leq 10°$

- With the exception of $-2° \leq \alpha \leq 2°$ at $\delta_f = 0°$, the flap lap/gap for which the 10mm serrations most effectively increased C_l did not correlate to the optimum flap lap/gap in terms of maximising the overall C_l for the 10mm serrated configuration, which typically coincided with (−0.23, −0.17) for $0° \leq \delta_f \leq 15°$ over the range of α tested
- 20mm serrations notably increased C_l at a flap lap/gap of (−0.26, −0.2) for all α and $\delta_f \leq 10°$, although in contrast to the 10mm serrations, a final increment in δ_f to 15° rendered the 20mm serrations detrimental to C_l for all test α
- With the exception of $-2° \leq \alpha \leq 12°$ at $\delta_f = 0°$ and $-2° \leq \alpha \leq 2°$ at $\delta_f = 5°$, the flap lap/gap for which the 20mm serrations most effectively increased C_l did not correlate to the optimum flap lap/gap in terms of maximising the overall C_l for the 20mm serrated configuration, which coincided with a flap lap/gap of (−0.26, −0.17) for $\alpha \geq 14°$ at $\delta_f = 0°$ and (−0.23, −0.17) for $\alpha \geq 6°$ at $\delta_f = 5°$ and for all test α at $10° \leq \delta_f \leq 15°$
- Increasing the serration length from 10mm to 20mm typically heightened the magnitude of the increment in C_l for any test α and $\delta_f \leq 10°$
- Distinct trends ΔC_d due to the serrated geometries were difficult to ascertain as ΔC_d tended to vary inconsistently
- Although isolated exceptions arose, the serrated geometries typically had an adverse effect upon L/D or at the very least, no appreciable effect upon L/D, rendering distinct trends difficult to ascertain
- Oil flow visualisation over the upper surface of the flap at lap/gap of (−0.26, −0.2) displayed evidence of wake structures emanating from the vertices of the 20mm serrations for $\alpha = 4°$, 8° and 12° at $\delta_f = 5°$ and for $\alpha = 4°$ at $\delta_f = 10°$ and hence, suggested the existence of vortical structures generated from the each serration
- Oil flow visualisation at lap/gap of (−0.26, −0.2) indicated that both the 10mm and 20mm serrations delayed boundary layer separation over the upper surface of the flap for $\alpha = 4°$, 8° and 12° at $\delta_f = 10°$
- By increasing δ_f to 15°, oil flow visualisation at lap/gap of (−0.26, −0.2) indicated that both the 10mm and 20mm serrations increased the region of trailing edge boundary layer separation in comparison to the plain configuration, particularly at $\alpha = 12°$
- Further flow visualisation studies are required to gain an in-depth understanding of the flow field mechanisms by which the serrations favourably influenced boundary layer development

6.10 Chapter Summary

10mm or 20mm 60° triangular serrations were implemented at the trailing edge of main element upstream of a single slotted flap, both with and without a leading-edge high-lift device. Characteristic of the high-lift configuration was the cove geometry over the aft lower surface of the main element, facilitating the retraction of the trailing-edge high-lift device in cruise conditions.

Initial studies on the three-element takeoff and landing configurations indicated that:

- Serrated geometries had no appreciable effect upon point of boundary layer separation on the upper surface of the flap, with the exception that the 20mm serrations delayed boundary layer separation from $0.4c_{flap}$ to $0.5c_{flap}$ for $\alpha \geq 14°$ in the landing configuration
- Both 10mm and 20mm serrations typically had a detrimental effect upon C_l for the takeoff and landing configurations with the decrement in C_l heightened by increasing the serration length

Further studies on a two-element configuration showed that:

- A parametric study of the flap lap/gap and δ_f indicated that implementing serrations at the trailing edge of the main element upstream of a single slotted flap was typically unfavourable in terms of C_l, suggesting that the effectiveness of the serrations was highly sensitive to the precise configuration geometry
- A single lap/gap of (−0.26, −0.2) was identified for which both the 10mm and 20mm serrations were most effective, increasing C_l for all test α and $\delta_f \leq 10°$ with the 20mm serrations, corresponding to $11\%c_{flap}$, proving more effective than the 10mm serrations, corresponding to $6\%c_{flap}$
- Increment in C_l due to the 20mm serrations was also relatively consistent at $\delta_f = 0°$ for all test α at a lap/gap of (−0.23, −0.2) but with successive increments in δ_f, the range of α over which the 20mm serrations increased C_l was reduced, as was the magnitude of the increment
- The serrated geometries tended to reduce C_d, although ΔC_d varied inconsistently with α and the magnitude of decrement was typically insufficient to offset a corresponding decrement in C_l
- Distinct trends regarding the effect of the serrated geometries upon L/D were difficult to ascertain

- Oil flow visualisation over the upper surface of the flap at lap/gap of (−0.26, −0.2) exhibited wake structures emanating from individual vertices of the 20mm serrations for α=4°, 8° and 12° at δ_f=5° and for α=4° at δ_f=10°, suggesting evidence of vortical structures generated from the serrated geometry and corroborating previous studies
- Further flow visualisation studies are required in order to gain an in-depth understanding of the flow field mechanisms by which the serrations favourably influence boundary layer development

Finally, limited data for the deployment of a leading-edge device in conjunction with the trailing-edge device suggested that:

- The effects of the serrated geometries on the aerodynamic characteristics of a representative high-lift configuration were highly sensitive to the deployment of a leading-edge high-lift device, indicating the need to optimise the serration geometry for the complete configuration under consideration

7 High-Lift Configuration: Tangential Slot Blowing

This chapter considers the effect of blowing air tangentially from a slot at the trailing edge of the main element over the upper surface of a single slotted trailing edge flap within a three-element high-lift configuration.

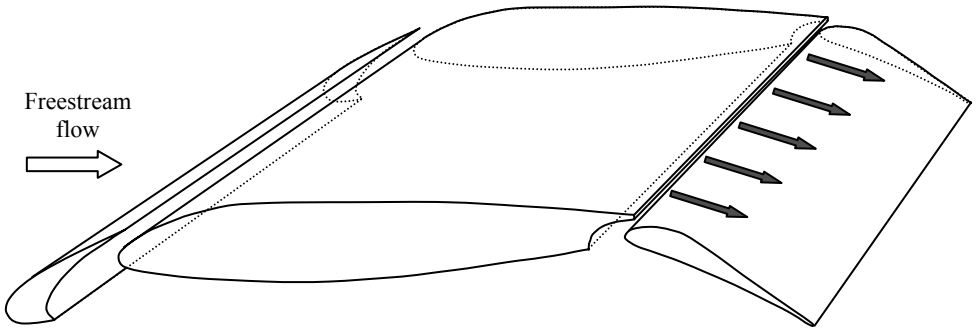

7.1 Introduction

Investigations of conventional blowing boundary layer control comprised blowing a jet of air tangentially from a slot at the trailing edge of the main element over the upper surface of a single slotted flap within a three-element high-lift configuration (see inset in schematic on page xv or Figure 16 for further details of blowing slot). With the lap, gap and deflection angle of the high-lift devices fixed, the configuration angle of incidence was incremented, both with and without tangential slot blowing. The flow field developing over the high-lift configuration was duly analysed and the effectiveness of tangential slot blowing as a means of delaying boundary layer separation was evaluated accordingly. Free transition was maintained throughout on each of the three elements and unless otherwise stated, all experiments were conducted at a nominal freestream velocity of $40m/s$, corresponding to a Reynolds number of 1.64×10^6, based upon stowed reference chord.

In the absence of tangential slot blowing over the trailing edge flap of the high-lift configuration, measurements indicated that the corrected C_p values were typically repeatable to within ±0.06, with greater deviations occurring at the trailing edge of the flap and diminishing the repeatability of the measurements to within ±0.15.

The implementation of tangential slot blowing marginally reduced the repeatability of the measurements, such that the corrected C_p values were typically repeatable to within ±0.2. However, it should be noted that a greater deviation in repeated measurements occurred over the leading edge of the flap upper surface and was hence, directly

attributed to the errors incurred by inherent fluctuations in the volume flow rate for the jet of blown air.

In terms of the resultant aerodynamic forces generated over the three-element configuration, calculations indicated that C_l was typically repeatable to within ±1% and C_d was typically repeatable to within ±2%. Note that in this instance, only the pressure drag was determined from the integration of the surface static pressure measurements.

7.2 Baseline Takeoff Configuration

By virtue of the predefined configuration geometry, the 23° deflection angle of the leading edge slat and 38° deflection angle of the trailing edge flap determined the a non-dimensional slat and flap lap/gap of (−0.06, −0.23) and (0.01, −0.12), respectively.

Figure 105 shows the C_p distribution for the takeoff configuration at α=4°, 12° and 20°, in the absence of tangential slot blowing. Similarly to the takeoff configuration with the plain geometry implemented at the trailing edge of the main element, the C_p distributions for the baseline takeoff configuration without tangential slot blowing indicated that increasing α from 0° to 20° had a marked effect upon the static pressure distribution over the leading edge slat and the main element, although the C_p distribution over the trailing edge flap appeared relatively insensitive to increments in α.

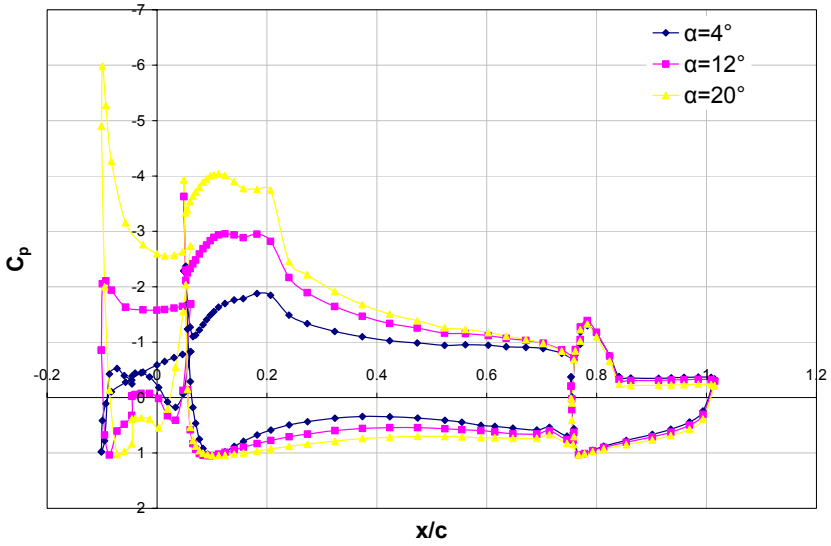

Figure 105: Effect of angle of incidence on C_p distribution for baseline takeoff configuration without tangential slot blowing

Whilst the salient attributes of the C_p distributions across the incremental range of α were analogous to those previously identified for the baseline takeoff configuration with

the plain geometry implemented at the trailing edge of the main element (see Section 6.1.1 for more details), the variation in the flap lap between the two configurations rendered the precise magnitude of the static pressure distributions distinct. This was particularly evident with respect to the magnitude of the suction peak at the leading edge of the flap upper surface, highlighting the sensitivity of the flap static pressure distribution to variations in flap lap. Specifically, incrementing the flap lap from −0.11 (defined by the baseline takeoff configuration with plain trailing edge) to 0.01 (defined by the baseline takeoff configuration without tangential slot blowing) notably heightened the magnitude of the leading edge suction over the flap upper surface.

Accordingly, the resultant aerodynamic forces determined from integration of the C_p distributions over the three-element baseline takeoff configuration without tangential slot blowing deviated from those of the baseline takeoff configuration with the plain trailing edge geometry, typically yielding larger values of C_l and smaller values of C_d.

For the baseline takeoff configuration without tangential slot blowing, Figure 106 shows that C_l increased from 0.83 at α=0° to 1.23 at α=2°. With further increments in $\alpha \leq 16°$, C_l increased approximately linearly with α attaining a C_l of 2.65 at α=16°. Further increments in α to the upper test limit of 20° exhibited a reduction in the lift-curve gradient, characteristic of the onset of stall.

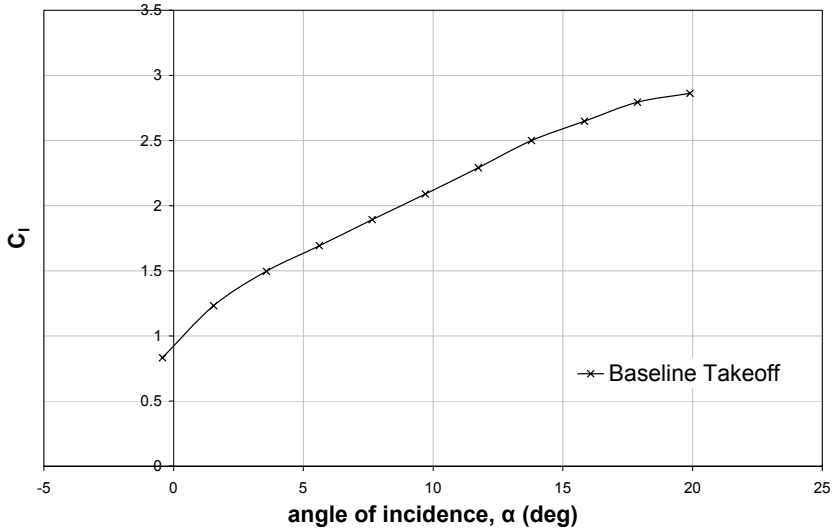

Figure 106: C_l-α curve for baseline takeoff configuration without tangential slot blowing

From Figure 107 it was evident that for increments in $0.8 \leq C_l \leq 1.5$, the C_d calculated directly from integration of the C_p distributions initially decreased in magnitude from 0.1 to a minimum of 0.09. With further increments in $1.5 < C_l \leq 2.1$, C_d progressively

increased in magnitude to 0.13 and with further increments in C_l>2.1, the increment in C_d was heightened, attaining a maximum value of 0.23 at the measured maximum lift coefficient (C_{lmax}) of 2.86, coinciding with the upper test limit of α=20°.

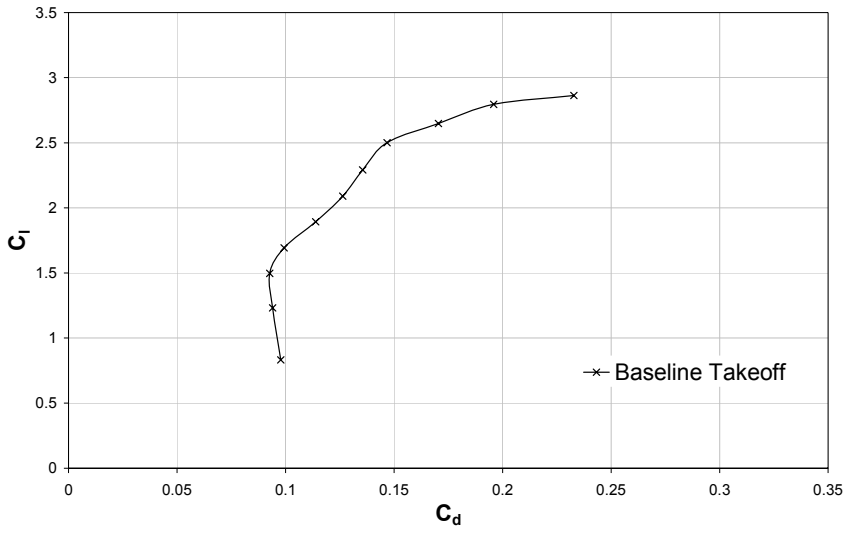

Figure 107: Drag polar for baseline takeoff configuration without tangential slot blowing

Amalgamation of C_l and C_d in terms of L/D indicated that by incrementing α from 0° to 6°, L/D increased from 8.5 to 17.1, see Figure 108. A slight decline in L/D was evident for 6°<α≤10°, decreasing to a local minimum of 16.5 at α=10°, before once again increasing to a local maximum of 17 at α=14°. With successive increments in α>14°, L/D progressively decreased in magnitude to 12.3 at α=20°.

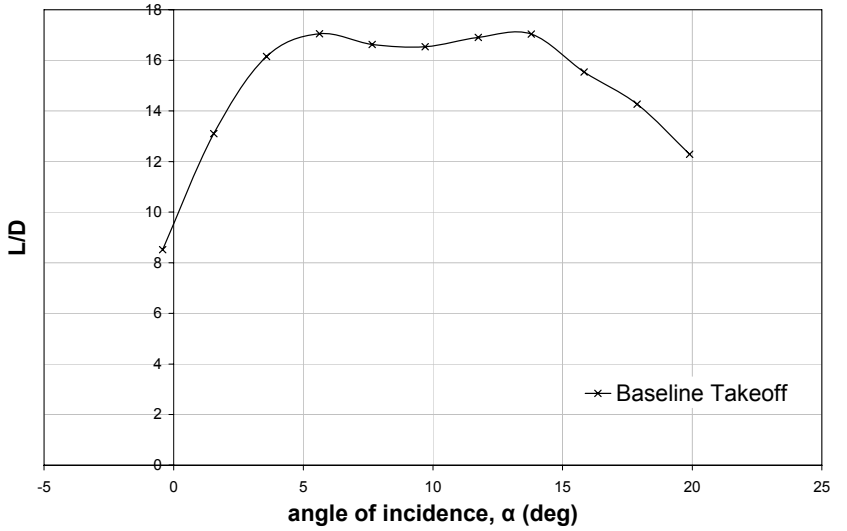

Figure 108: Variation of *L*/*D* with angle of incidence for baseline takeoff configuration without tangential slot blowing

7.3 Takeoff Configuration with Tangential Slot Blowing

Although measurements confirmed that the temperature of jet of air at the slot was approximately ambient, attempts to establish the velocity of the jet of air were thwarted by the sensitivity of the measurement to the precise position of the total pressure probe relative to the trailing edge slot. Thus, assuming no appreciable variation in density, the velocity of the jet of air was determined theoretically by means of the equation of continuity, based upon the known volume flow rate. Accordingly, a reference momentum coefficient (C_μ) of 0.025 was defined for tests at a freestream velocity of $40m/s$. However, this failed to account for the losses incurred within the system and variations in the jet velocity across the span of the model.

7.3.1 Effect of Tangential Slot Blowing on C_p Distribution

Figure 109(a)-(k) shows the effect of blowing tangentially from a slot at the trailing edge of the main element over a deflected single slotted flap in the three-element takeoff configuration. The influence of tangential slot blowing on the developing flow field was not limited to the trailing edge flap and also extended upstream, modifying the surface pressure distribution over the main element, although the extent to which the tangential slot blowing affected the flow field developing over the main element was notably reduced with increasing angle of incidence. However, tangential slot blowing had no appreciable effect upon the flow field developing over the leading edge slat, irrespective of the angle of incidence.

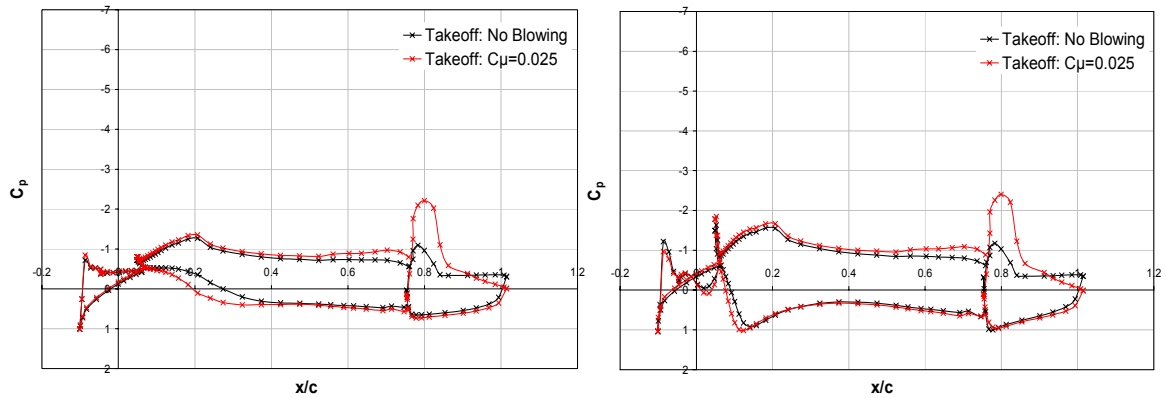

(a) α=0° **(b) α=2°**

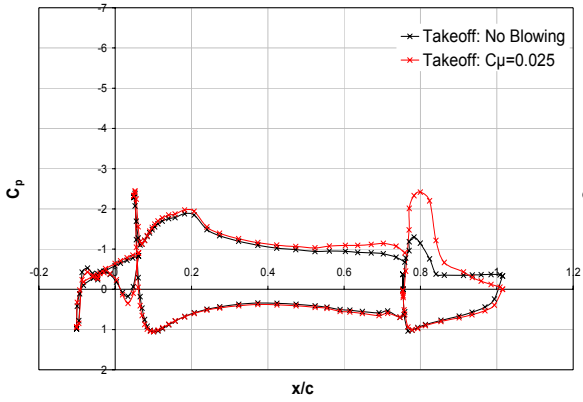

(c) α=4°

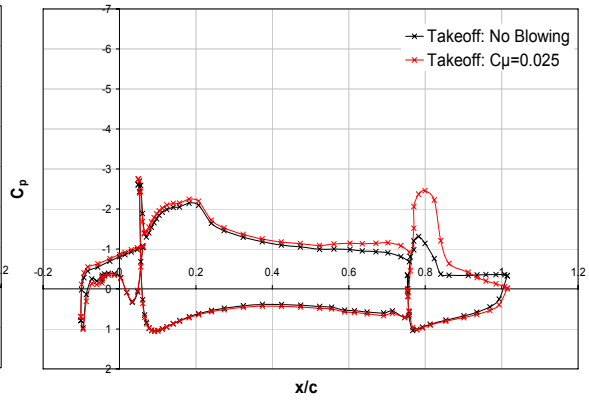

(d) α=6°

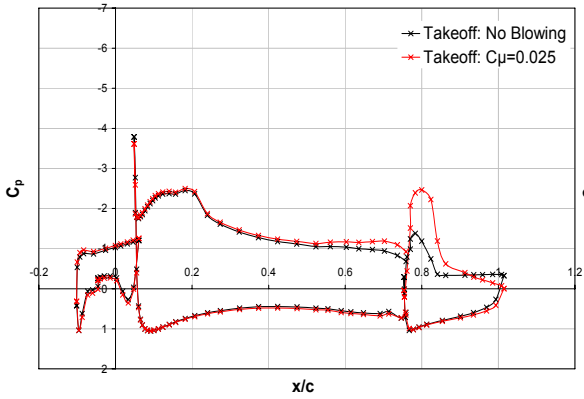

(e) α=8°

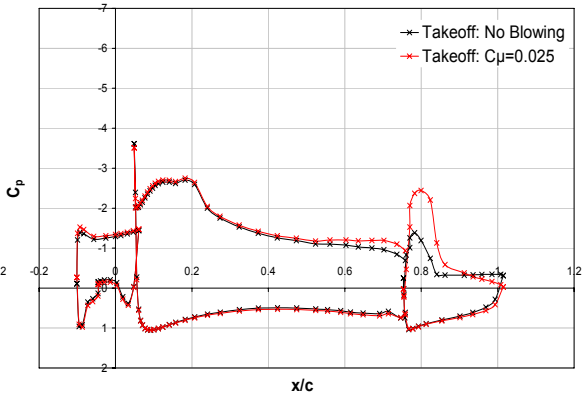

(f) α=10°

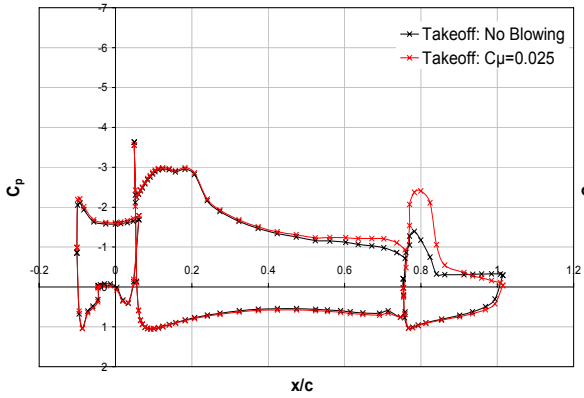

(g) α=12°

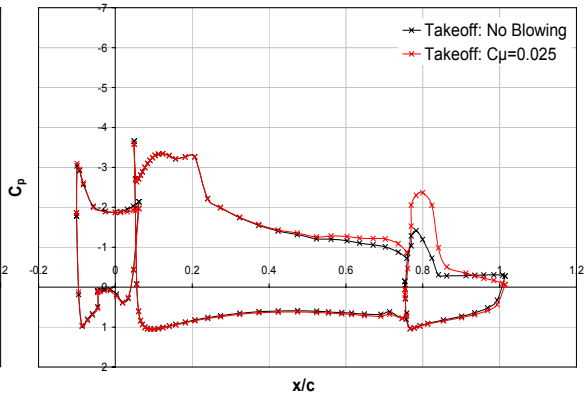

(h) α=14°

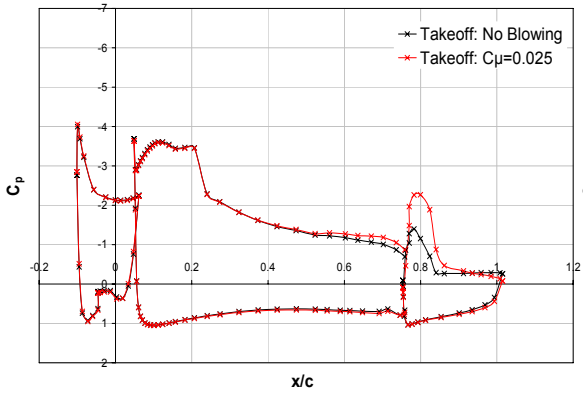

(i) α=16°

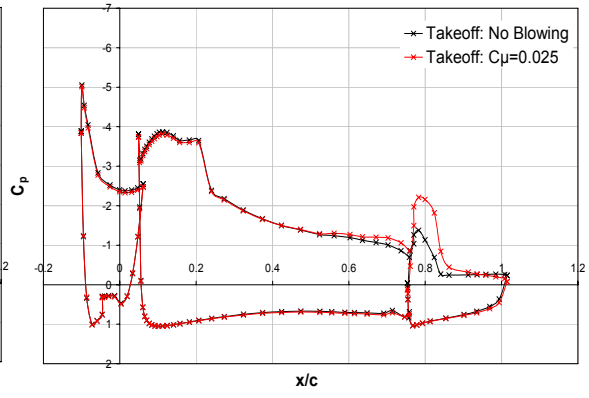

(j) α=18°

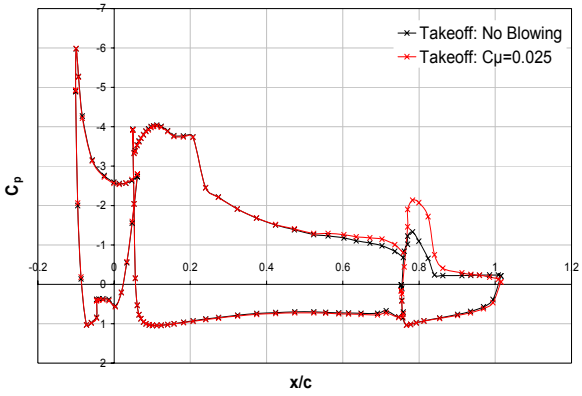

(k) α=20°

Figure 109(a)-(k): Effect of tangential slot blowing on the C_p distribution for the takeoff configuration

Figure 109(a) shows the extent to which the tangential slot blowing influenced the flow field developing upstream at low angles of incidence. Specifically, tangential slot blowing increased the static pressure over the lower surface of the main element at α=0°. The increment was greatest over the fore $0.4c_{main}$ and was marginalised with distance downstream. On the upper surface of the main element, tangential slot blowing heightened the suction, with the increment in suction increasing in magnitude with distance downstream towards the trailing edge. The decrement in static pressure at the trailing edge of the main element suggested that blowing tangentially heightened the thickness of the upper surface boundary layer at the trailing edge of the main element in comparison to the corresponding baseline configuration. Similarly to the main element, tangential slot blowing increased the static pressure over the lower surface of the trailing edge flap, with the increment increasing in magnitude with distance downstream. As expected, the effect of tangential slot blowing was most prominent over the upper surface of the trailing edge flap, considerably heightening the leading edge suction over the fore $0.4c_{flap}$. Quantifying the increment in suction by means of the variation in the magnitude of the minimum pressure coefficient (C_{pmin}), indicated that tangential slot blowing magnified the suction peak from −1.09 to −2.21, transposing the location of the measured C_{pmin} marginally aft from $0.11c_{flap}$ to $0.18c_{flap}$. Most significantly, blowing tangentially from a slot, at a C_μ of 0.025, prevented boundary layer separation at $0.35c_{flap}$ on the upper surface of the trailing edge flap, maintaining boundary layer attachment to within close proximity of the trailing edge.

The favourable effect of tangential slot blowing on the boundary layer development was corroborated by the corresponding surface oil flow visualisation over the upper surface of the flap for the takeoff configuration at α=0°, see Figure 110.

Figure 110(a) and (b): Oil flow visualisation over the flap upper surface for the takeoff configuration at α=0°, (a) without and (b) with tangential slot blowing

Note that the direction of the flow (denoted by U_∞) was from right to left in all photographs. As indicated in the C_p distribution, the boundary layer separated at approximately $0.3c_{flap}$ in the absence of tangential slot blowing, with a highly three-dimensional recirculating flow evident over the aft $0.7c_{flap}$, see Figure 110(a). In contrast, Figure 110(b) shows that tangential slot blowing maintained boundary layer attachment to within close proximity of the trailing edge. Note that the slight anomaly evident over the lower region of the photograph in Figure 110(b) was attributed to fluctuations in the jet velocity over the span due to a local inconsistency in the jet slot.

Similarly to the baseline configuration, Figure 109(b) showed that by increasing α from 0° to 2°, a distinct stagnation point was generated at the leading edge of the main element although the application of tangential slot blowing transposed the stagnation point marginally upstream from $0.15c_{main}$ to $0.1c_{main}$. Upstream of the stagnation point, tangential slot blowing increased the leading edge static pressure and whilst immediately downstream of the stagnation point, the pressure distribution was coincident with the corresponding baseline configuration, a marginal increase in static pressure due to the active boundary layer control was evident over the aft $0.5c_{main}$ of the lower surface. The upper surface C_p distribution over the main element was analogous to that of the baseline takeoff configuration, with two suction peaks occurring over the

leading edge region at α=2°. Similarly to the configuration at α=0°, tangential slot blowing heightened the suction over the upper surface of the main element, with the decrement in static pressure increasing in magnitude with distance downstream towards the main element trailing edge. Figure 109(c) through to Figure 109(g) showed that for 4°≤α≤12°, blowing tangentially from a slot at the trailing edge of the main element had no appreciable effect upon the lower surface pressure distribution over the fore region of the main element, although a marginal increment in static pressure was evident over the aft $0.5c_{main}$, suggesting a slight decrement in the lower surface trailing edge boundary layer thickness. Over the upper surface of the main element, Figure 109(c) through to Figure 109(g) showed that tangential slot blowing heightened the suction. Although the decrement in static pressure over the fore $0.5c_{main}$ was marginal, the suction was progressively heightened in magnitude with distance downstream towards the main element trailing edge, indicating an increased trailing edge boundary layer thickness due to the active boundary layer control. Figure 109(h) through to Figure 109(k) showed that with further increments in α≥14°, the influence of tangential slot blowing on lower surface pressure distribution of the main element was reduced both in extent and magnitude, with only a minimal increase in static pressure discernible over the aft $0.15c_{main}$. Furthermore, any variation in static pressure due to the tangential slot blowing was negated over the fore region of the main element upper surface, with the suction only heightened over the aft $0.4c_{main}$. Once again, the increment in suction due to the active boundary layer control increased in magnitude with distance downstream.

With regard to the trailing edge flap, Figure 109(b) through to Figure 109(e) showed that incrementing α between 2° to 8° essentially negated any variation in static pressure due to the tangential slot blowing over the fore $0.4c_{flap}$ of the flap lower surface, although the influence of the active boundary layer control was evident over the aft $0.6c_{flap}$, incrementing the static pressure with increasing magnitude with distance downstream towards the trailing edge. This increment in static pressure suggested that tangential slot blowing decreased the lower surface boundary layer thickness at the trailing edge of the flap when compared to the corresponding baseline configuration. With further increments in α≥10°, the region over which tangential slot blowing influenced the lower surface static pressure was limited to the aft $0.3c_{flap}$ and although the increment in C_p continued to increase in magnitude with distance downstream, the increment was marginalised with successive increments in α, see Figure 109(f) through to Figure 109(k). Similarly to configuration with α=0°, Figure 109(b) through to Figure 109(k) showed that the effect of tangential slot blowing over the upper surface of the trailing edge flap was most prominent over the fore $0.4c_{flap}$, considerably heightening

the leading edge suction in comparison to the corresponding baseline configuration for $2°\leq\alpha\leq20°$. Quantifying the increment in leading edge suction by means of C_{pmin}, it was evident that tangential slot blowing had maximum effect at α=2°, heightening C_{pmin} from −1.17 for the baseline configuration to −2.40 with blowing boundary layer control, see Figure 109(b). With further increments in $\alpha\geq4°$, Figure 109(c) through to Figure 109(k) showed that the decrement in leading edge static pressure due to tangential slot blowing progressively reduced in magnitude such that at α=20°, blowing tangentially from the slot at the trailing edge of the main element only accounted for a ΔC_{pmin} of −0.8. Similarly to the configuration at α=0°, tangential slot blowing transposed the location of the measured C_{pmin} marginally aft from $0.11c_{flap}$ to $0.18c_{flap}$ for $\alpha\leq14°$, although with subsequent increments in $\alpha\geq16°$, the location of the measured C_{pmin} was unaffected by tangential slot blowing. Aft of $0.4c_{flap}$, the increment in suction due to the tangential slot blowing was marginalised and over the aft region of the flap upper surface, tangential slot blowing increased the static pressure in comparison to the corresponding baseline configuration. For any given $2°\leq\alpha\leq16°$, the increment in static pressure extended over the aft $0.3c_{flap}$, with the increment increasing in magnitude with distance downstream. This increment in trailing edge static pressure was indicative of a thinner upper surface trailing edge boundary layer with the application of tangential slot blowing, associated with the delay of boundary layer separation to within close proximity of the trailing edge. With successive increments in α between 2° and 16°, the increment in trailing edge static pressure due to tangential slot blowing was marginally reduced in magnitude, indicating that for the takeoff configuration with tangential slot blowing, the trailing edge boundary layer increased in thickness with successive increments in α. Further increments in $\alpha\geq18°$ reduced both the magnitude and extent of the increment in trailing edge static pressure arising from the application of tangential slot blowing, suggesting a further increment in the trailing edge boundary layer thickness, although the C_p distributions were still indicative of the boundary layer remaining attached to within close proximity of the trailing edge of the flap upper surface when tangential slot blowing was applied.

The salient features of the oil flow visualisation over the upper surface of the flap for the takeoff configuration for $2°\leq\alpha\leq20°$ were consistent with those previously identified at α=0°. In the absence of tangential slot blowing, a distinct separation line was evident at approximately $0.3c_{flap}$, corroborating the respective C_p distributions shown in Figure 109. Aft of this point, the oil flow visualisation demonstrated a highly three-dimensional region of recirculating flow, consistent with boundary layer separation. Conversely, blowing tangentially from a slot at the trailing edge of the main element

over the upper surface of the flap maintained boundary layer attachment to within close proximity of the trailing edge, as indicated by the corresponding C_p distributions shown in Figure 109. Based upon the observations of Kelly et al (1958), this suggested that the impingement of the jet of air upon the flap upper surface was either upstream of or coincident with the point of minimum pressure for all test α. Oil flow visualisation over the upper surface of the flap for the takeoff configuration at α=6° is shown in Figure 111 below. Figure 111(a) and (b) are representative of the aforesaid salient features of the flow field, with and without tangential slot blowing, respectively.

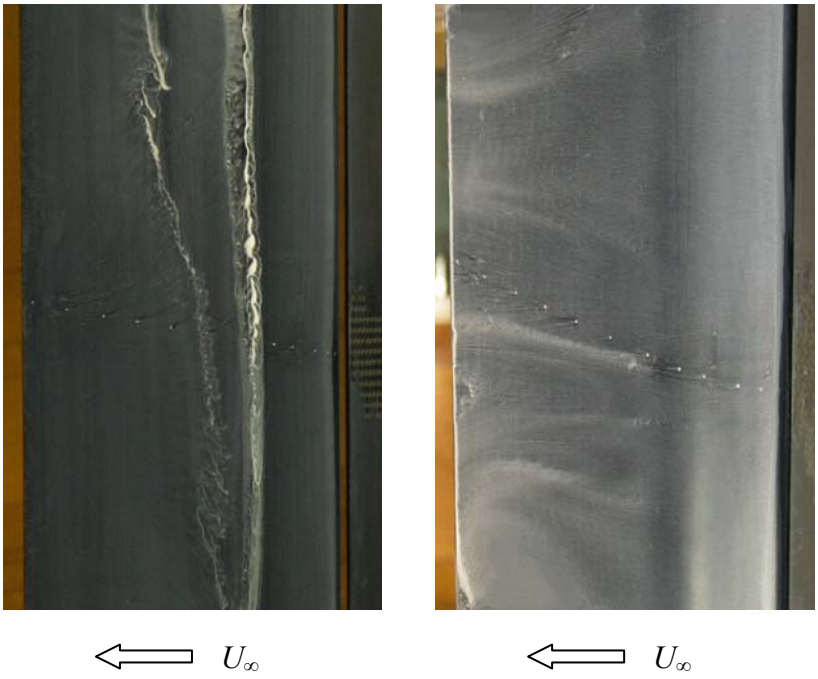

Figure 111(a) and (b): Oil flow visualisation over the flap upper surface for the takeoff configuration at α=6°, (a) without and (b) with tangential slot blowing

It should be noted that for any given α, the flow field development over the upper surface of the flap, when subject to tangential slot blowing, was highly sensitive to variations in the jet velocity, inconsistencies in the slot geometry and defects in model surface finish, resulting in localised regions of premature boundary layer separation across the span. This sensitivity was heightened with successive increments in test α and exacerbated at locations coincident with the internal spars, the latter of which obstructed the jet of air. Furthermore, three-dimensional anomalies, induced by separation over the outer span regions, were also heightened at high test α, entraining fluid into localised regions of recirculating flow. However, within the immediate vicinity of the surface static pressure orifices, the oil surface flow visualisation demonstrated that boundary layer attachment was maintained to within close proximity of the trailing edge, for all test α. This suggested that by addressing the defects within

the boundary layer control system to ensure uniform jet velocity and eliminating slot/surface irregularities, boundary layer attachment could be maintained to within close proximity of the trailing edge over a significant proportion of the span, reducing the extent of localised regions of boundary layer separation.

7.3.2 Effect of Tangential Slot Blowing on the Aerodynamic Forces

Figure 112 shows that blowing tangentially over the flap upper surface from a slot at the trailing edge of the main element with a C_μ of 0.025 had a favourable effect upon the lift force generated over the three-element configuration, increasing C_l for all test α.

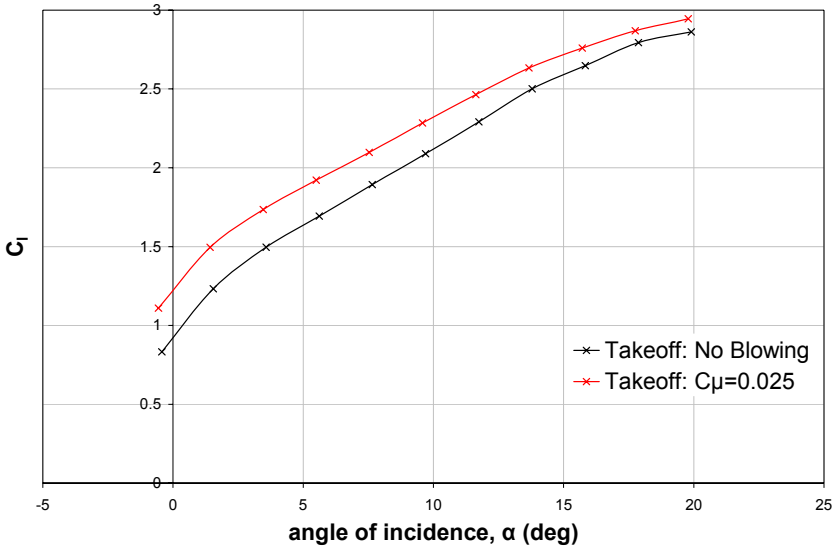

Figure 112: C_l-α curve for takeoff configuration, with and without tangential slot blowing

The increment in C_l due to tangential slot blowing is clarified in Figure 113 for the takeoff configuration. Note that the corresponding increments in C_l for the landing and extended flap configurations are shown for comparative purposes. Figure 113 shows that for the takeoff configuration, the increment in C_l was greatest at α=0°, with ΔC_l=0.28 accounting for a 33% increase in lift force generated. With successive increments in α, ΔC_l due to tangential slot blowing steadily decreased in magnitude. At α=2°, ΔC_l was 0.26, decreasing to a ΔC_l of 0.19 at α=10°, corresponding to a 21% and 9% increment in C_l, respectively, in comparison to the corresponding baseline takeoff configuration. At α=18°, the increment in C_l due to tangential slot blowing was reduced to a minimum of 0.07 and although there was a marginal increase in ΔC_l to 0.08 at the upper test limit of α=20°, both accounted for a 3% increase in C_l in comparison to the corresponding baseline takeoff configuration without tangential slot blowing.

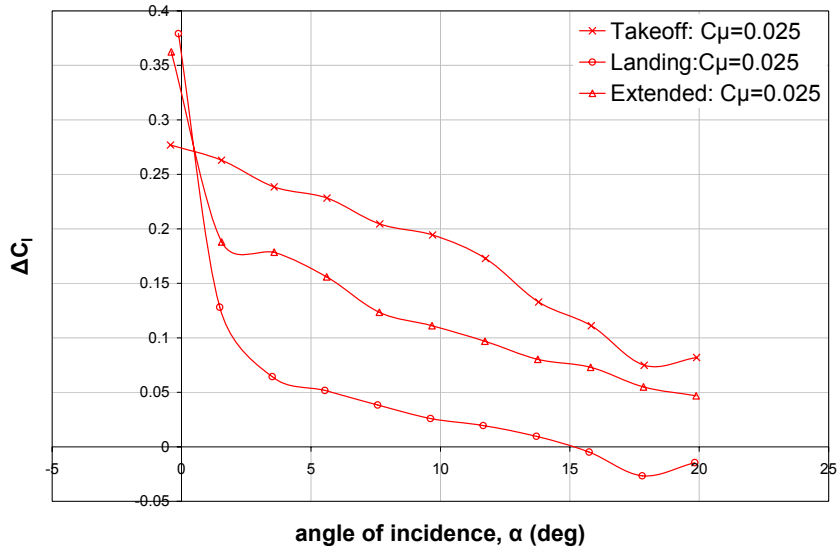

Figure 113: Variation of ΔC_l with angle of incidence due to tangential slot blowing for takeoff, landing and extended flap configurations

Blowing tangentially from a slot at the trailing edge of the main element increased the C_d for any given C_l. Whilst it was recognised that the elimination of boundary layer separation would typically be associated with a corresponding reduction in pressure drag, the increment in pressure drag observed was attributed to the influence of tangential slot blowing on the flow field developing over the entire configuration.

Figure 114 shows how the increment in C_d due to tangential slot blowing varied with α for the takeoff configuration. Note that the corresponding increments in C_d for the landing and extended flap configurations are shown in Figure 114 for comparative purposes.

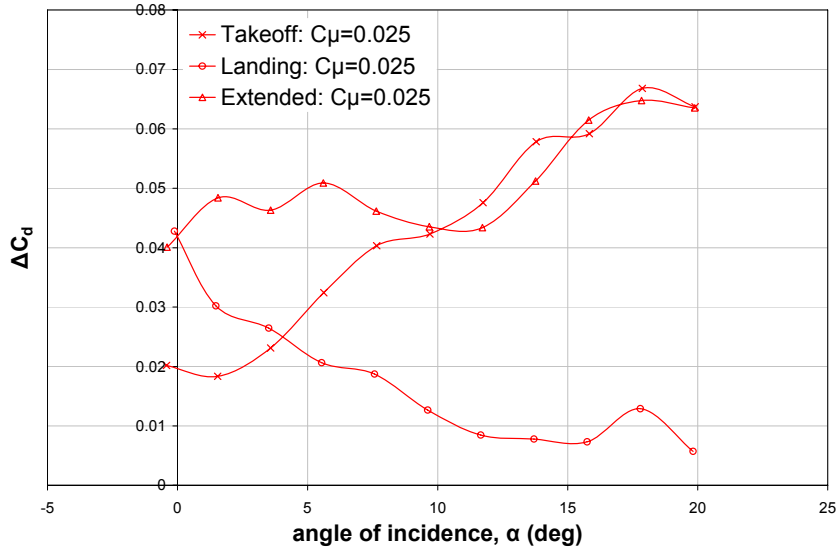

Figure 114 Variation of ΔC_d with angle of incidence due to tangential slot blowing for takeoff, landing and extended flap configurations

Accordingly, Figure 114 shows that there was a tendency for the increment in pressure drag to progressively increase with successive increments in α, from 0.02 at α=0° to a maximum of 0.067 at high test α.

Based upon the pressure drag calculations alone, Figure 115 shows that tangential slot blowing decreased L/D for 4°≤α≤20° in comparison to the corresponding baseline takeoff configuration. At α=4°, the decrement correlated to a 7% reduction in L/D, which was progressively heightened to a maximum 24% decrement at α=14°. With further increments in α≥16°, the decrement in L/D was reduced in magnitude, correlating to a 19% reduction in comparison to the baseline configuration at the upper test limit of α=20°.

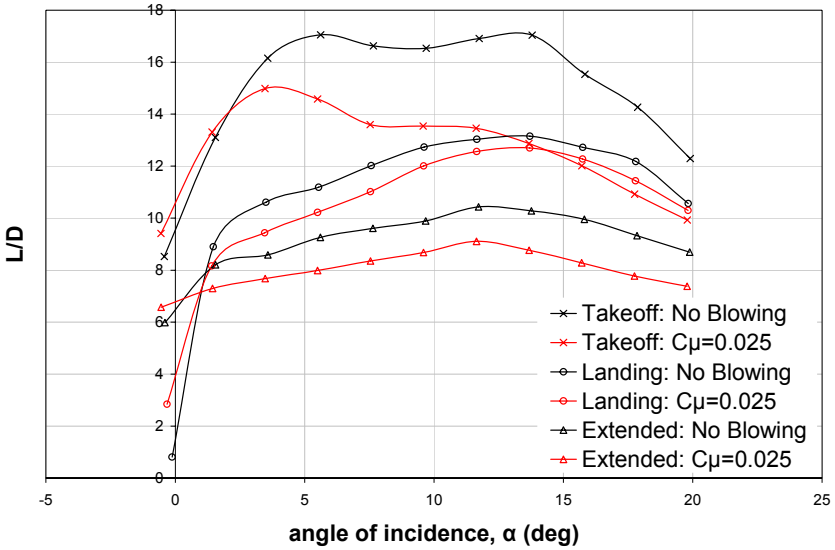

Figure 115: Variation of *L*/*D* with angle of incidence for takeoff, landing and extended flap configurations, with and without tangential slot blowing

In contrast, the increment in C_l was sufficient to offset the corresponding increment in pressure drag at low test α, increasing L/D by 10% and 2% at α=0° and α=2°, respectively. Whilst these trends in L/D were identified, it was recognised that consideration of the pressure drag alone, obtained purely from the integration of the surface static pressure distribution, was insufficient to accurately evaluate the aerodynamic performance of the configuration in terms of L/D.

7.4 Baseline Landing Configuration

By virtue of the predefined geometry of the landing configuration, the 27° deflection angle of the leading edge slat and 48° deflection angle of the trailing edge flap determined the a non-dimensional slat and flap lap/gap of (0.04, −0.17) and (0.06, −0.13), respectively.

Figure 116 shows the C_p distribution for the landing configuration at α=4°, 12° and 20°, in the absence of tangential slot blowing. Similarly to the landing configuration with the plain geometry implemented at the trailing edge of the main element, the C_p distributions for the baseline landing configuration without tangential slot blowing indicated that increasing α from 0° to 20° had a marked affect upon the static pressure distribution over the leading edge slat and the main element, although the C_p distribution over the trailing edge flap appeared relatively insensitive to increments in α.

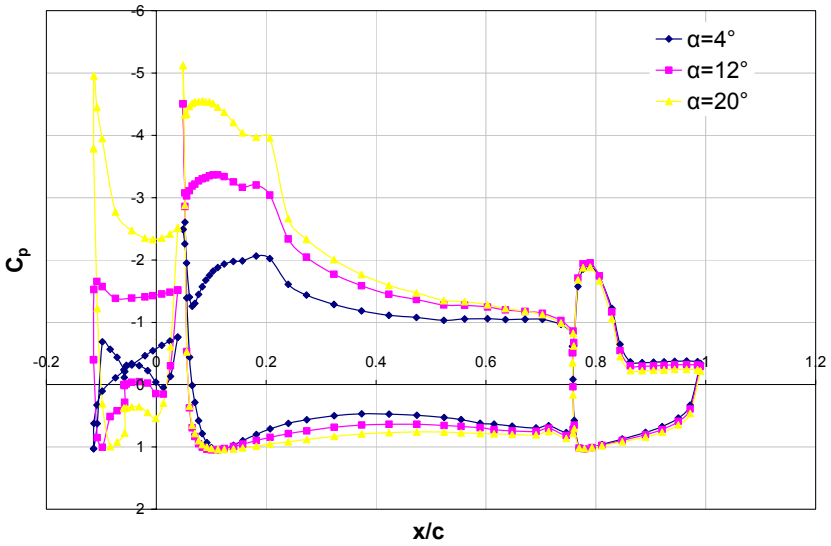

Figure 116: Effect of angle of incidence on C_p distribution for landing configuration without tangential slot blowing

Whilst the salient attributes of the C_p distributions across the incremental range of α were analogous to those previously identified for the baseline landing configuration with the plain geometry implemented at the trailing edge of the main element (see Section 6.2.1 for more details), the variation in the flap lap between the two configurations rendered the precise magnitude of the static pressure distributions distinct. This was particularly evident with respect to the magnitude of the suction peak at the leading edge of the flap upper surface, highlighting the sensitivity of the flap static pressure distribution to variations in flap lap. Specifically, incrementing the flap lap from 0 (defined by the baseline landing configuration with plain trailing edge) to

0.06 (defined by the baseline landing configuration without tangential slot blowing) substantially heightened the magnitude of the leading edge suction over the flap upper surface. Accordingly, the resultant aerodynamic forces, determined from integration of the C_p distributions over the three-element baseline landing configuration without tangential slot blowing, deviated from those of the landing configuration with the plain trailing edge geometry, typically yielding larger values of C_l and smaller values of C_d. .

Figure 117 shows the C_l-α curve for the baseline landing configuration in the absence of tangential slot blowing. The degradation of the flow field over the landing configuration at α=0° was corroborated by the resultant near negligible lift force of 0.1. A single increment in α from 0° to 2° significantly increased C_l to 1.43, attesting to the improved flow field evident in the surface static pressure distributions (see Figure 120 for C_p distributions).

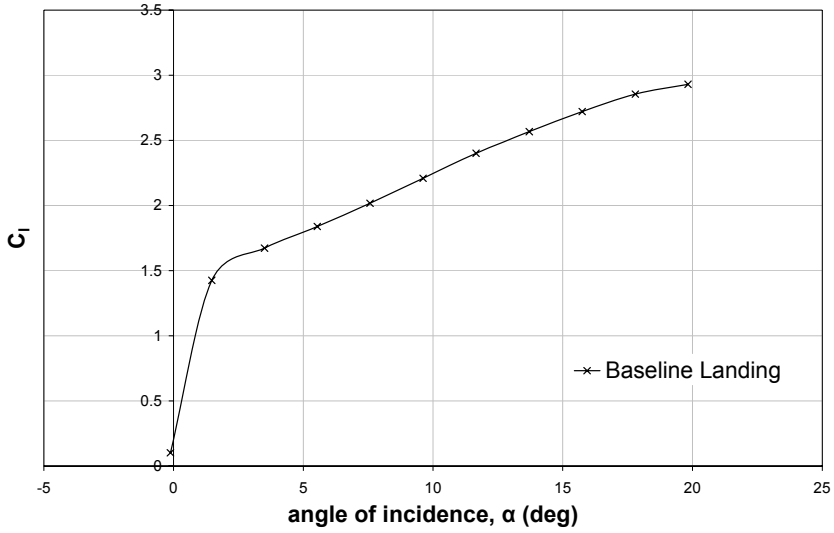

Figure 117: C_l-α curve for baseline landing configuration without tangential slot blowing

With further increments in $\alpha \leq 16°$, C_l increased approximately linearly with α, attaining a C_l of 2.72 at α=16°, although the reduction in the lift-curve gradient as the upper test limit of α=20° was approached was characteristic of the onset of stall.

From Figure 118 it was evident that whilst C_d tended to increase with C_l, there was a marginal decrement in C_d for $1.43 \leq C_l \leq 1.67$, corresponding to the increment in α from 2° to 4°. At high C_l, the corresponding increment in C_d was markedly heightened, attaining a maximum C_d of 0.28 at the measured C_{lmax} of 2.93 occurring at the upper test limit of α=20°.

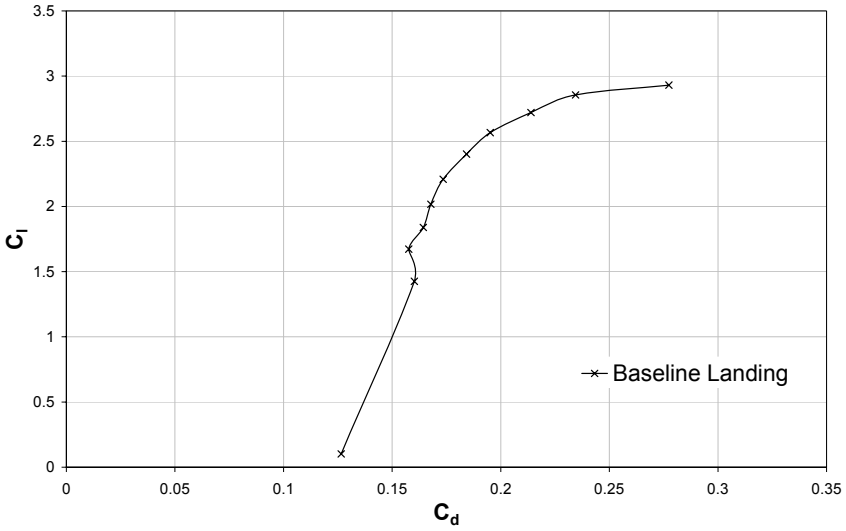

Figure 118: Drag polar for baseline landing configuration without tangential slot blowing

Consideration of both C_l and C_d indicated that by incrementing α from 0° to 14°, L/D increased from 0.8 to a maximum of 13.2, respectively (see Figure 119). Again, the most significant increment in L/D coincided with the increment in α from 0° to 2°, increasing L/D from 0.8 to 8.9. With successive increments in α>14°, L/D progressively decreased in magnitude to 10.6 at α=20°.

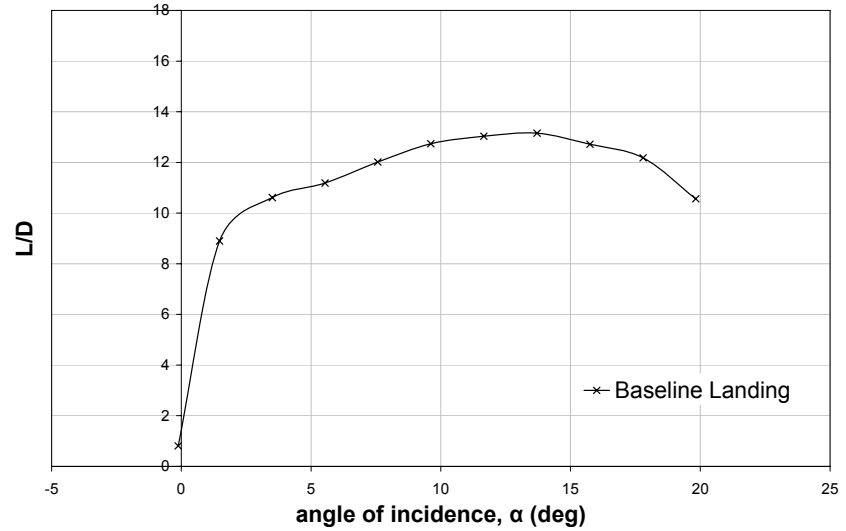

Figure 119: Variation of *L*/*D* with angle of incidence for baseline landing configuration in the absence of tangential slot blowing

7.5 Landing Configuration with Tangential Slot Blowing

Based upon a nominal momentum coefficient of 0.025, air was blown tangentially from a slot at the trailing edge of the main element over the upper surface of the deflected flap within the landing configuration.

7.5.1 Effect of Tangential Slot Blowing on C_p Distributions

Figure 120(a)-(k) show the effect of tangential slot blowing on the measured C_p distributions in comparison to the baseline configuration at a given α.

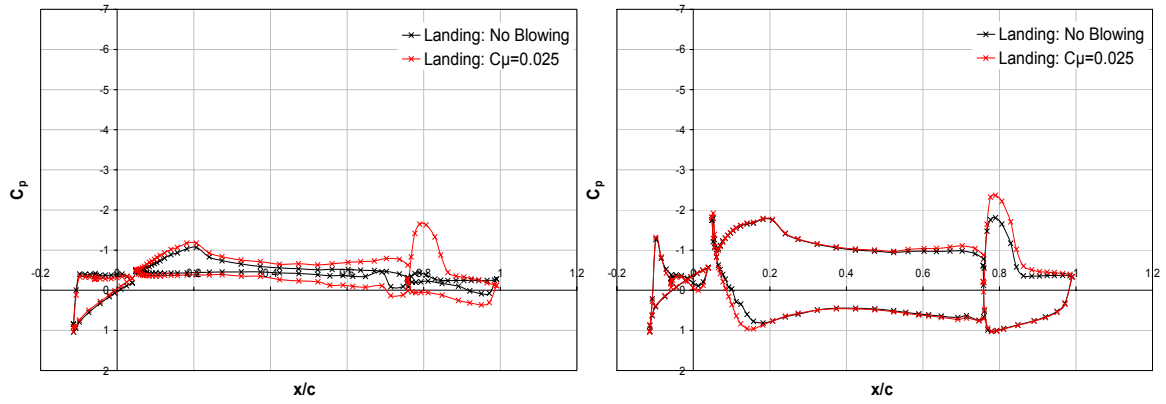

(a) α=0° **(b) α=2°**

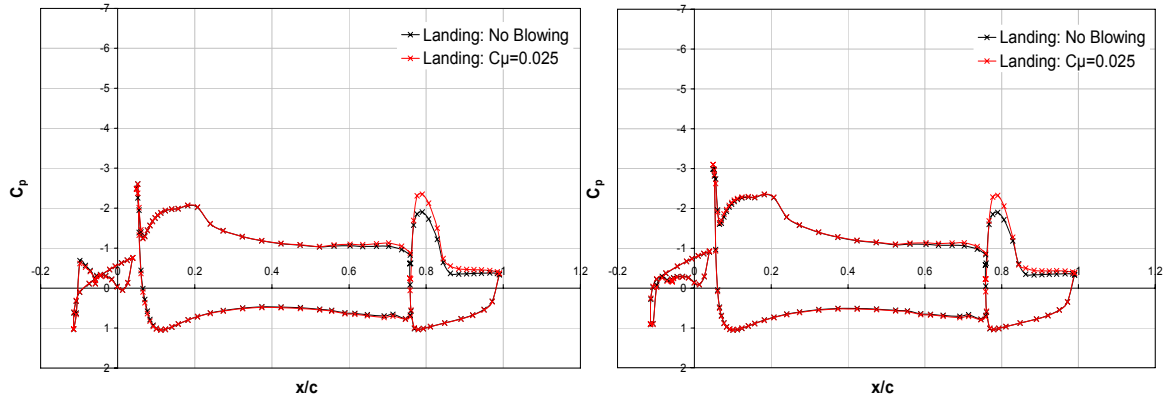

(c) α=4° **(d) α=6°**

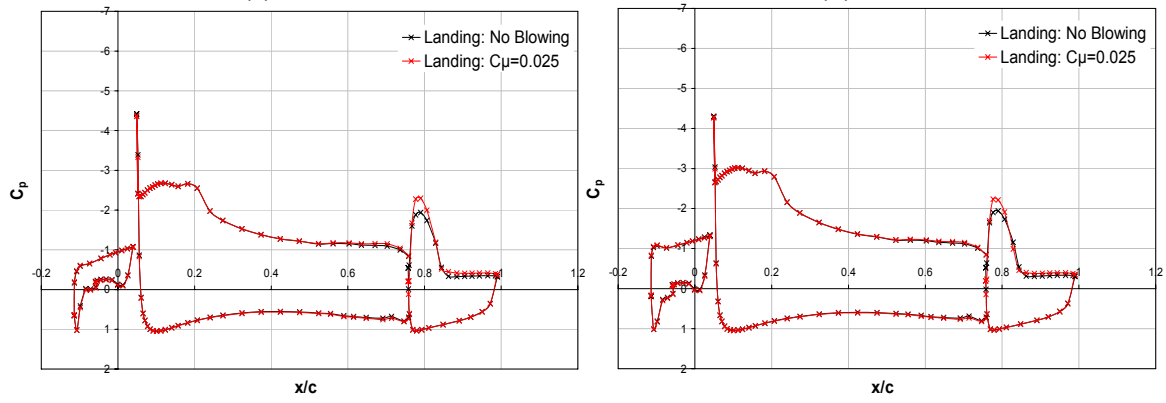

(e) α=8° **(f) α=10°**

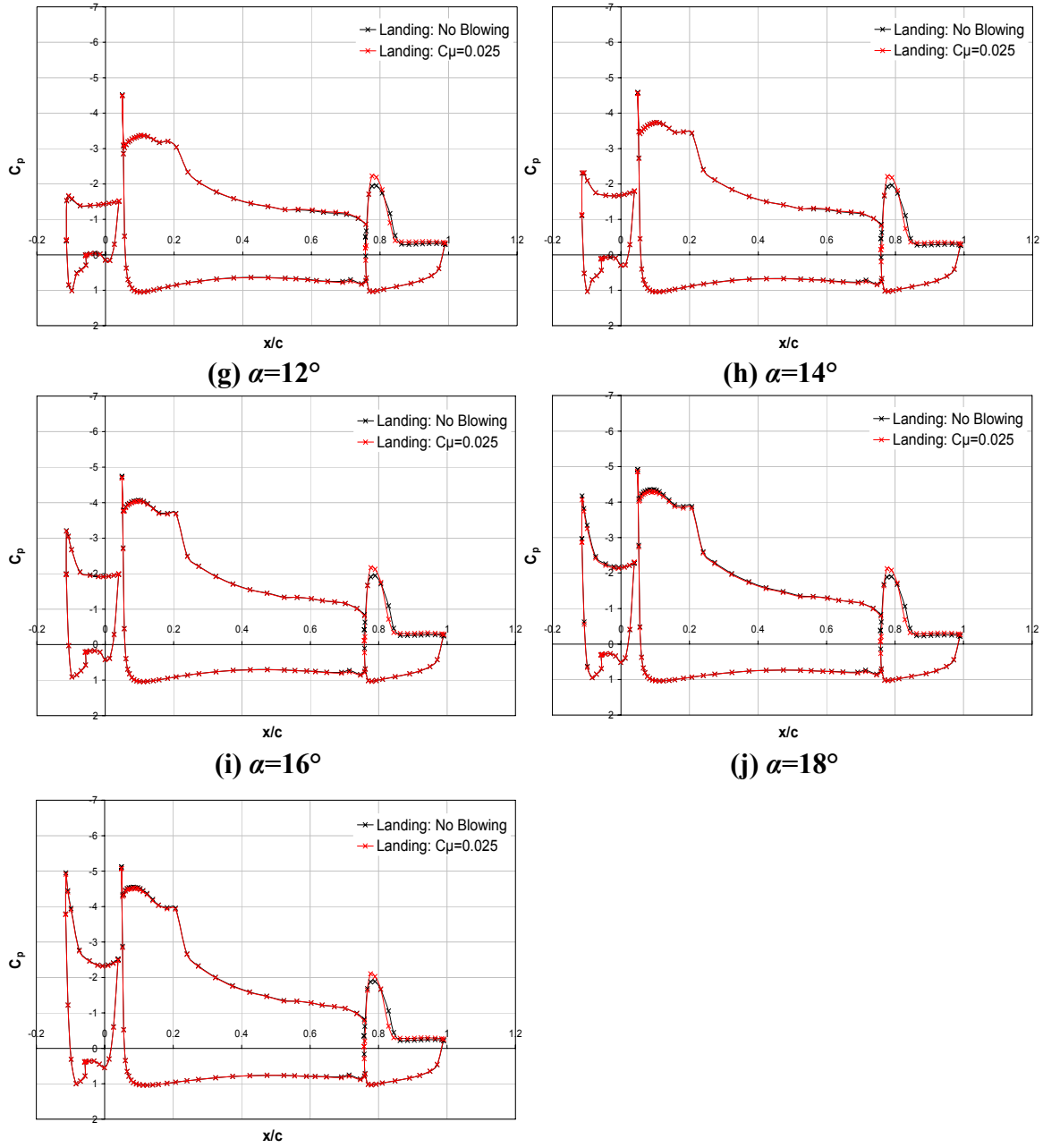

(g) α=12°

(h) α=14°

(i) α=16°

(j) α=18°

(k) α=20°

Figure 120(a)-(k): Effect of tangential slot blowing on the C_p distribution for the landing configuration

From Figure 120 it was evident that the influence of tangential slot blowing on the flow field developing over the landing configuration was not limited to the trailing edge flap and instead, extended upstream, modifying the surface pressure distribution over the main element, although the extent to which the tangential slot blowing affected the flow field developing over the main element was notably reduced with increasing angle of incidence. Irrespective of the angle of incidence, the measurements indicated that

tangential slot blowing at C_μ=0.025 had no appreciable effect upon the flow field developing over the leading edge slat in comparison to the baseline configuration.

Figure 120(a) showed that whilst tangential slot blowing favourably influenced the flow field developing over the trailing edge flap and main element, the active boundary layer control was insufficient to notably improve the flow field around the landing configuration at α=0°.

Increasing α from 0° to 2°, Figure 120(b) showed that tangential slot blowing increased the static pressure over the fore $0.2c_{main}$ of the main element lower surface, generating a distinct stagnation point at $0.15c_{main}$. Aft of $0.2c_{main}$, the tangential slot blowing had no appreciable effect upon the lower surface static pressure distribution. The static pressure distribution over the upper surface of the main element was analogous to the baseline configuration, with two suction peaks occurring over the leading edge region. However, an increment in suction was evident over the aft $0.3c_{main}$, which increased in magnitude with distance downstream towards the main element trailing edge and was indicative of an increased boundary layer thickness in comparison to the baseline configuration. Figure 120(c) through to Figure 120(e) showed that for $4° \leq \alpha \leq 8°$, blowing tangentially from a slot had no appreciable effect upon the lower surface pressure distribution over the main element and whilst an increment in suction due to tangential slot blowing was still evident over the aft $0.2c_{main}$ of the main element upper surface, the magnitude of the deviation in C_p was marginalised with successive increments in α. Figure 120(f) through to Figure 120(k) showed that with further increments in $\alpha \geq 10°$, tangential slot blowing still had negligible influence on lower surface pressure distribution of the main element and furthermore, any variation in static pressure due to the tangential slot blowing was essentially negated over the upper surface of the main element.

With regard to the trailing edge flap, tangential slot blowing had no appreciable effect upon the lower surface static pressure distribution for $2° \leq \alpha \leq 20°$. Figure 120(b) and Figure 120(c) showed that at α=2° and α=4°, blowing tangentially from a slot at the trailing edge of the main element heightened the suction over the upper surface of the flap. The decrement in static pressure due to tangential slot blowing was greatest over the fore $0.4c_{flap}$ and decreased in magnitude thereafter. Quantifying the increment in leading edge suction due to tangential slot blowing by the magnitude of the measured C_{pmin}, it was evident that the decrement in static pressure was maximised at α=2°, decreasing C_{pmin} from −1.81 for the baseline configuration to −2.36 with tangential slot

blowing, see Figure 120(b). Further increments in $\alpha \geq 4°$ showed that the increment in leading edge suction due to tangential slot blowing was progressively minimised such that at $\alpha=20°$, blowing tangentially from the slot at the trailing edge of the main element merely heightened the measured C_{pmin} from −1.89 to −2.11. Although particularly mild, the adverse pressure gradient over the aft $0.45c_{flap}$ of the flap upper surface for $2° \leq \alpha \leq 4°$ suggested that the tangential slot blowing delayed boundary layer separation to within close proximity of the trailing edge. Unfortunately, due to time and facility constraints, it was not possible to investigate the surface flow field characteristics by means of oil flow visualisation in order to augment the quantitative measurements from the C_p distributions and confirm whether or not boundary layer attachment was maintained. Figure 120(d) and Figure 120(e) showed that increasing α to 6° or 8° reduced the extent over which tangential slot blowing heightened the leading edge suction over the flap upper surface such that the increment in suction was most notable over the fore $0.3c_{flap}$, immediately aft of which, the C_p distributions were essentially coincident with the corresponding baseline configuration. The uniformity of the static pressure measurements over the aft $0.45c_{flap}$ of the blown flap configuration was consistent with boundary layer separation, suggesting that tangential slot blowing merely delayed the point of separation from $0.45c_{flap}$ to $0.55c_{flap}$ for $6° \leq \alpha \leq 8°$. Figure 120(f) through to Figure 120(k) showed that with further increments in $\alpha \geq 10°$, the region over which tangential slot blowing heightened the leading edge suction over the flap upper surface was reduced to the fore $0.2c_{flap}$, aft of which there was a small region of increased static pressure, coinciding with heightened severity of the adverse pressure gradient. Whilst tangential slot blowing did not influence the location of the measured C_{pmin} for $0° \leq \alpha \leq 8°$, with subsequent increments in $\alpha \geq 10°$, tangential slot blowing transposed the location of the measured C_{pmin} marginally upstream from $0.14c_{flap}$ to $0.08c_{flap}$, with the subsequent adverse pressure gradient prompting earlier separation. Consequently, boundary layer separation occurred at approximately $0.4c_{flap}$ for $\alpha \geq 10°$, $0.05c_{flap}$ upstream of that for the corresponding baseline configurations. Hence, the C_p distributions indicated that tangential slot blowing promoted premature separation for $10° \leq \alpha \leq 20°$. Based upon Kelly et al's (1958) observations, this suggested that the landing configuration was not optimised with regard to the impingement of the jet of air upon the flap upper surface relative to the point of minimum pressure over the range of test α and hence, the effectiveness of tangential slot blowing as a means of maintaining boundary layer attachment was diminished.

7.5.2 Effect of Tangential Slot Blowing on the Aerodynamic Forces

Blowing tangentially over the single slotted trailing edge flap of the landing configuration at a nominal C_μ of 0.025 had a favourable effect upon the resultant aerodynamic lift force generated for $\alpha \leq 12°$, see Figure 121.

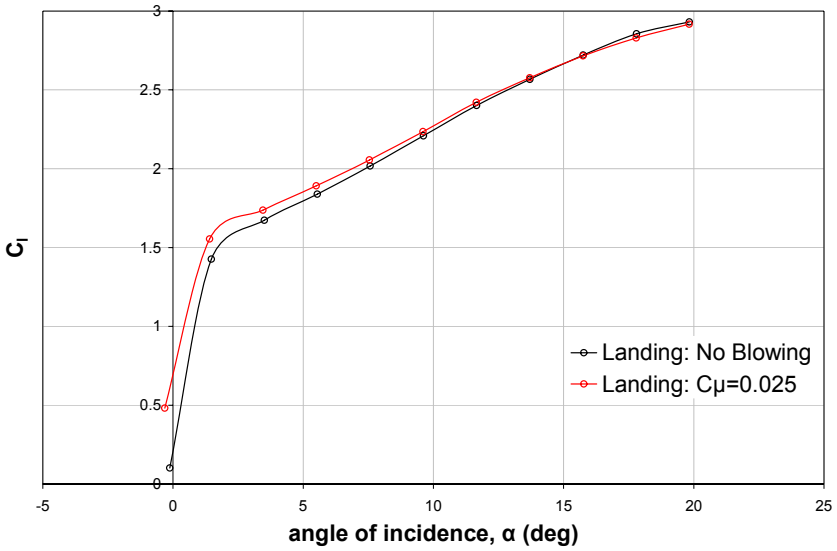

Figure 121: C_l-α curve for landing configuration, with and without tangential slot blowing

This increment in C_l was greatest at α=0°, with ΔC_l=0.38 indicative of the favourable effect of active boundary layer control on the inferior flow field developing over the configuration at zero incidence. With the C_p distributions in Figure 120 demonstrative of an improved flow field over the baseline configuration for $\alpha \geq 2°$, the increment in C_l due to tangential slot blowing was less prominent, reducing ΔC_l to 0.13 at α=2°, accounting for a 9% increase in the lift force generated over the landing configuration. At α=4°, ΔC_l was approximately halved to 0.06, representing a 4% increase in C_l due to tangential slot blowing. The increment in C_l due to tangential slot blowing steadily decreased in magnitude with subsequent increments in $\alpha \geq 6°$, such that at α=12°, ΔC_l was a mere 0.02, equating to <1% increment in C_l when compared to the corresponding baseline configuration without tangential slot blowing. Any favourable effect of tangential slot blowing upon C_l was essentially negated at α=14° and with further increments in $\alpha \geq 16°$, a marginal degradation in C_l of <1% was evident. Figure 113 clearly illustrates this variation of ΔC_l with α.

Again it was noted that blowing tangentially over the single slotted trailing edge flap at a C_μ of 0.025 increased the pressure drag for any given C_l. In contrast to the takeoff configuration, Figure 114 showed that there was a tendency for the increment in C_d to

progressively decrease in magnitude with successive increments in α, from a maximum of 0.042 at α=0° to a minimum of 0.006 at α=20°. Similarly to the takeoff configuration, the delay of boundary layer separation would typically be associated with a corresponding reduction in pressure drag and accordingly, the increment in pressure drag was attributed to the influence of tangential slot blowing on the developing flow field over the entire configuration. Thus, with the C_p distributions in Figure 120 indicating that tangential slot blowing had minimal effect upon the developing flow field over the landing configuration at high test α, the increment in C_d was duly marginalised and the corresponding increment in C_l was negated.

Based upon the pressure drag alone, Figure 115 showed that tangential slot blowing decreased L/D for 2°≤α≤20° in comparison to the corresponding baseline landing configuration. Consequently, it was evident that the increment in C_l for α≤14° was typically insufficient to offset the corresponding increment in C_d. For 2°≤α≤8°, the decrement in L/D correlated to an 8-11% reduction in comparison to the baseline landing configuration, reducing to a 3-6% decrement for α≥10°, with only an isolated increment in L/D at α=0°. Whilst these basic trends in L/D were identified it was recognised that, similarly to the takeoff configuration, consideration of the pressure drag alone, obtained purely from the integration of the surface static pressure distribution, was insufficient to accurately evaluate the aerodynamic performance of the landing configuration in terms of L/D.

7.6 Baseline Extended Flap Configuration

Similarly to the takeoff and landing configurations, the lap, gap and deflection angle of the leading-edge slat and trailing-edge flap were fixed by virtue of the predefined geometry of the extended flap configuration, with the 27° leading edge slat and 58° trailing edge flap defining a non-dimensional slat and flap lap/gap of (0.04, −0.17) and (0.11, −0.15), respectively.

Figure 122 shows the C_p distribution for the extended flap configuration at α=4°, 12° and 20°, in the absence of tangential slot blowing. The C_p distributions indicated that increasing α from 0° to 20° had a marked effect upon the static pressure over the leading edge slat and the main element, although in contrast, the C_p distribution over the trailing edge flap appeared relatively insensitive to increments in α.

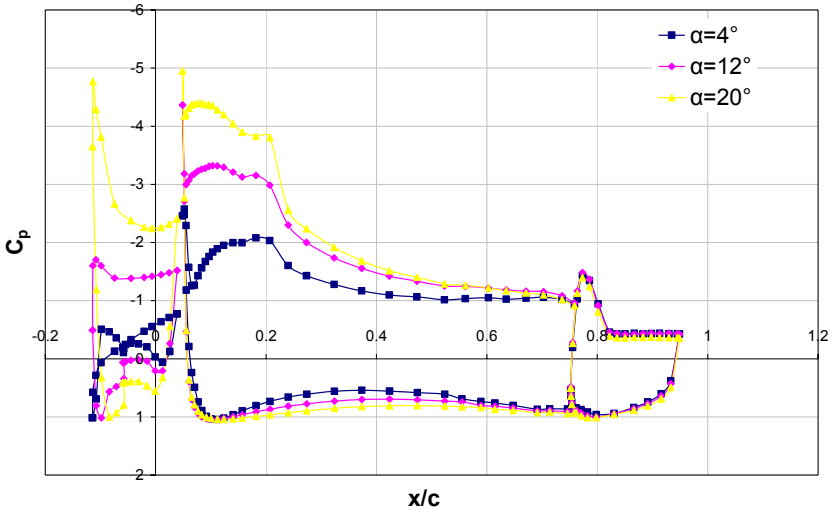

Figure 122: Effect of angle of incidence on C_p distribution for extended flap configuration without tangential slot blowing

Increasing α from 0° to 20° typically heightened the suction over the upper surface of the slat. This increment in suction was most prominent over the fore region of the upper surface and tended to decrease in magnitude with distance downstream. Over the lower surface of the slat, increasing α transposed the stagnation point marginally aft. Upstream of the stagnation point and over the aft $0.25c_{slat}$ of the lower surface, the static pressure tended to progressively decrease in magnitude with successive increments in α between 0° to 20°. Conversely, for the lower surface region extending aft of the stagnation point to $0.75c_{slat}$, there was a tendency for the static pressure to increase in magnitude with successive increments in α. In particular, the flow field over the deployed leading edge slat significantly improved for $\alpha \geq 8°$.

Similarly to the landing configuration, increasing α from 0° to 2° significantly improved the flow field developing over the extended flap configuration. This was particularly evident over the main element, with the increment in α notably heightening the suction over the upper surface and generating two distinct suction peaks over the leading edge. With successive increments in $\alpha \geq 4°$, the suction over the upper surface of the main element was progressively heightened in magnitude. The increment in suction was most prominent over the fore $0.25c_{main}$ of the upper surface and was marginalised with distance downstream. Analogous to the takeoff and landing high-lift configurations discussed previously, the first suction peak occurred at the foremost location of the upper surface leading edge and was attributed to the developing wake aft of the leading edge device, whereas the second suction peak was attributed primarily the geometry of

the main element (Foster et al, 1970). Whilst the location of the first suction peak was independent of α and the local C_{pmin} was heightened with successive increments in α, the location of C_{pmin} for the second suction peak was sensitive to variations in α. At α=6°, a localised increase in static pressure was recorded at $0.15c_{main}$, which was heightened with successive increments in α, such that the location of C_{pmin} for the second suction peak was transposed upstream from approximately $0.2c_{main}$ for $2° \leq \alpha \leq 8°$ to $0.1c_{main}$ at α=10°. With further increments in $\alpha \geq 12°$, C_{pmin} was transposed progressively further upstream such that at α=20°, the measured C_{pmin} for the second suction peak was located at approximately $0.05c_{main}$. Furthermore, the adverse pressure gradient aft of the second suction peak, whilst heightened with successive increments in α, did not appear to have a detrimental effect upon the developing flow field, with the C_p distributions indicative of upper surface boundary layer attachment maintained to the trailing edge of the main element for all α. On the lower surface of the main element, incrementing α from 0° to 2° significantly increased the static pressure over the lower surface of the main element and generated a distinct stagnation point at $0.1c_{main}$. For $4° \leq \alpha \leq 20°$, the stagnation point was transposed upstream to $0.07c_{main}$. Accordingly, incrementing α from 2° to 4° increased the static pressure upstream of the stagnation point. However, further increments in $\alpha \geq 6°$ had no appreciable effect upon the C_p distribution upstream of the stagnation point. Downstream of the stagnation point, the static pressure increased with successive increments in α, with the increment most notable over the mid chord region and marginalised in magnitude with distance downstream towards the main element trailing edge.

With regard to the trailing edge flap, increasing α from 0° to 2° heightened the leading edge suction over the fore $0.2c_{flap}$ of the upper surface and significantly increased the static pressure over the lower surface, generating a distinct stagnation point at approximately $0.15c_{flap}$. Subsequent increments in α had no appreciable effect upon the C_p distribution over the trailing edge flap, with marginal deviations in the upper and lower surface static pressures hardly discernible between successive angles of incidence.

In terms of the resultant aerodynamic forces acting on the three-element extended flap configuration, Figure 123 shows that a single increment in α from 0° to 2° markedly increased C_l from 1.01 to 1.49, attesting to the improved flow field evident in the surface static pressure distributions (see Figure 126 for C_p distributions). With further increments in $\alpha \leq 14°$, C_l increased approximately linearly with α, attaining a C_l of 2.50

at α=14°, although the reduced magnitude of the increment between successive α as the upper test limit of α=20° was approached was characteristic of the onset of stall.

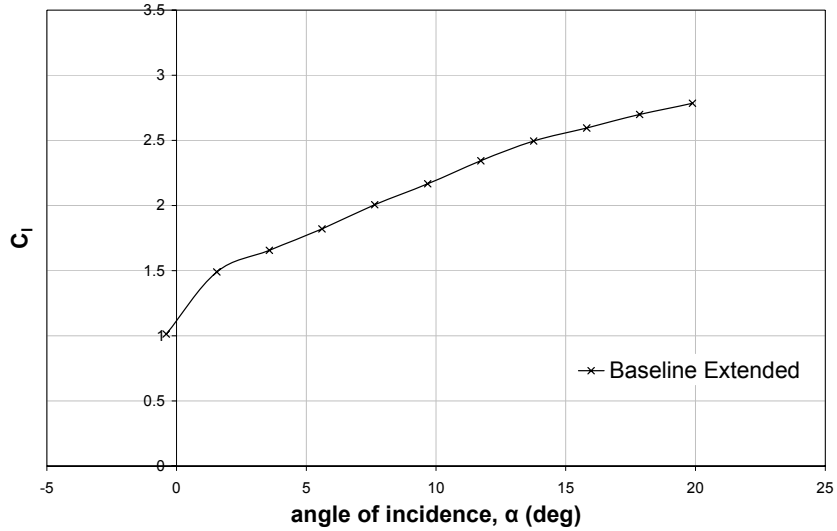

Figure 123: C_l-α curve for baseline extended flap configuration without tangential slot blowing

From Figure 124 it was evident that C_d progressively increased with increments in C_l. Although, the increment in C_d was notably heightened at high C_l>2.3, attaining a maximum of 0.32 at the measured C_{lmax} of 2.78, occurring at the upper test limit of α=20°.

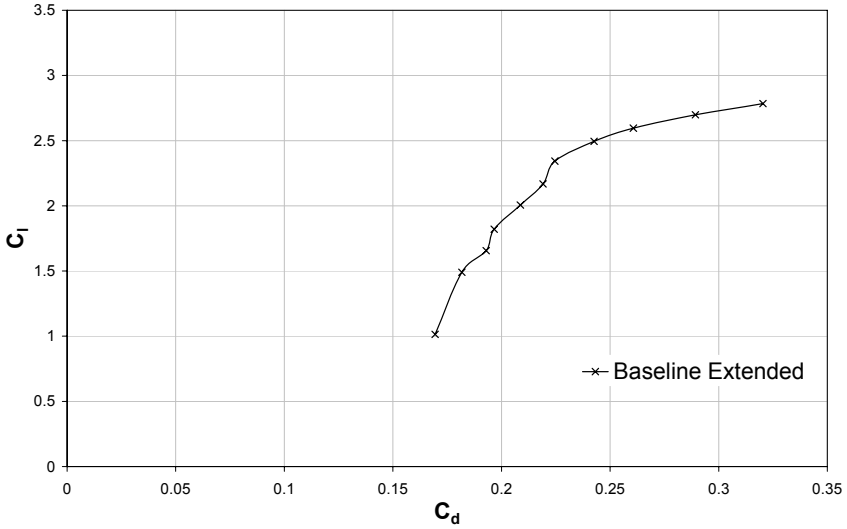

Figure 124: Drag polar for baseline extended flap configuration without tangential slot blowing

Amalgamation of C_l and C_d in terms of L/D indicated that by incrementing α from 0° to 12°, L/D increased from 6.0 to a maximum of 10.4, respectively, for the baseline extended flap configuration in the absence of tangential slot blowing, see Figure 125.

With successive increments in α>12°, L/D progressively decreased in magnitude to 8.7 at α=20°.

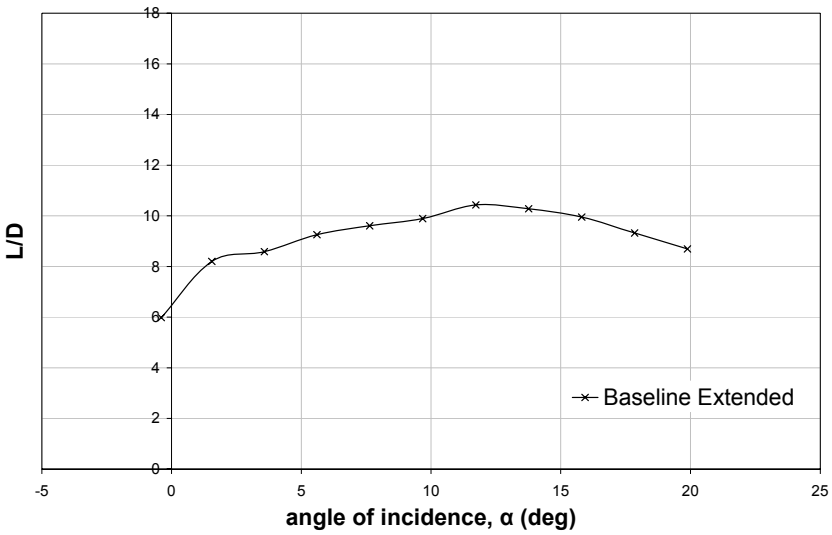

Figure 125: Variation of L/D with angle of incidence for baseline extended flap configuration without tangential slot blowing

7.7 Extended Flap Configuration with Tangential Slot Blowing

Similarly to the takeoff and landing configurations, air was blown tangentially at a nominal C_μ of 0.025 from a slot at the trailing edge of the main element over the upper surface of a deflected single slotted flap within the three-element extended flap configuration.

7.7.1 Effect of Tangential Slot Blowing on C_p Distribution

Figure 126(a)-(k) show the effect of tangential slot blowing on the measured C_p distributions in comparison to the corresponding baseline configuration at a given α. The influence of tangential slot blowing on the developing flow field was not limited to the trailing edge flap and also extended upstream, modifying the surface pressure distribution over the main element, although the extent to which the tangential slot blowing affected the flow field developing over the main element was notably reduced with increasing angle of incidence. However, implementation of tangential slot blowing had no appreciable effect upon the flow field developing over the leading edge slat for all angles of incidence tested.

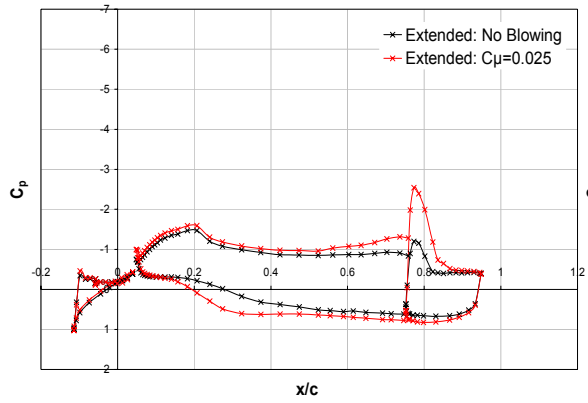

(a) α=0°

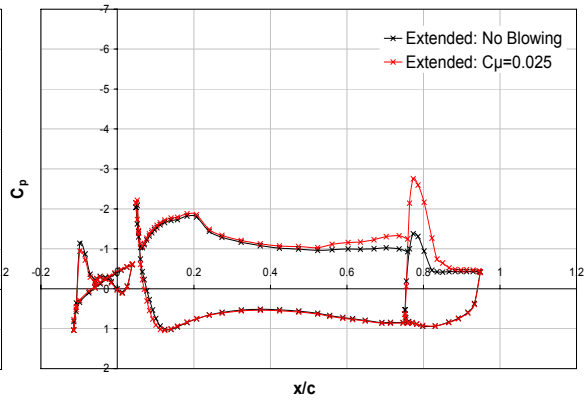

(b) α=2°

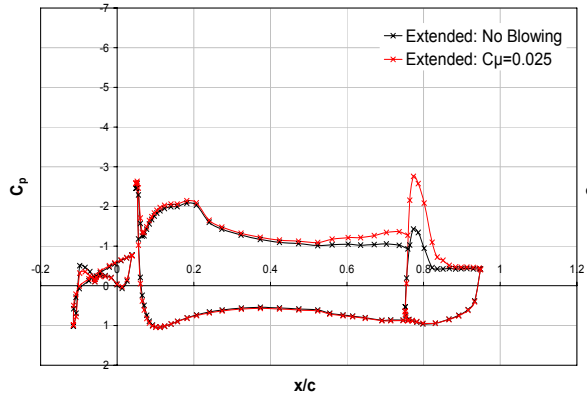

(c) α=4°

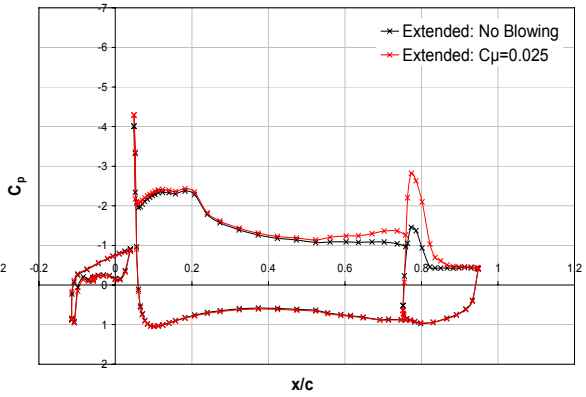

(d) α=6°

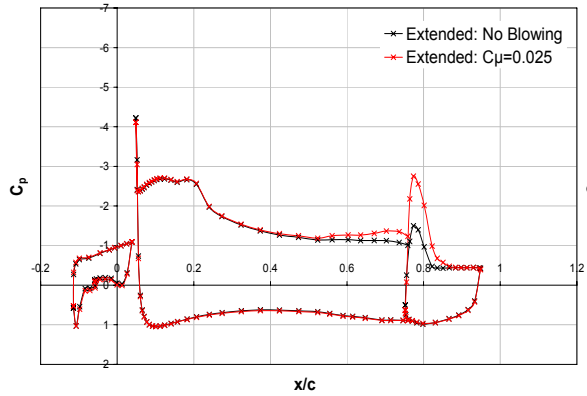

(e) α=8°

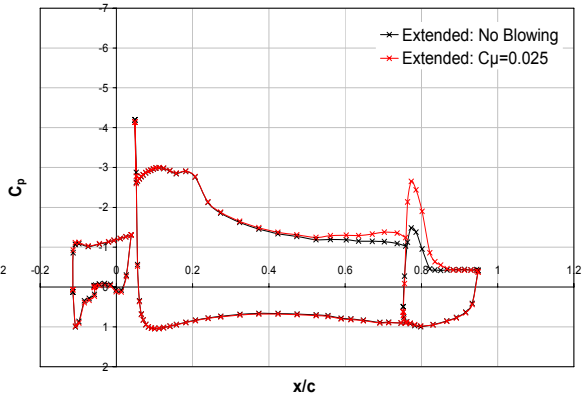

(f) α=10°

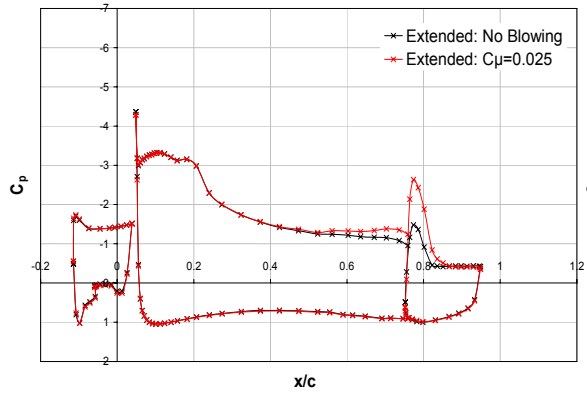

(g) α=12°

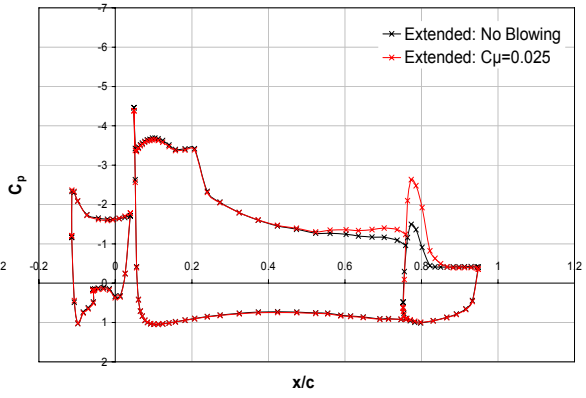

(h) α=14°

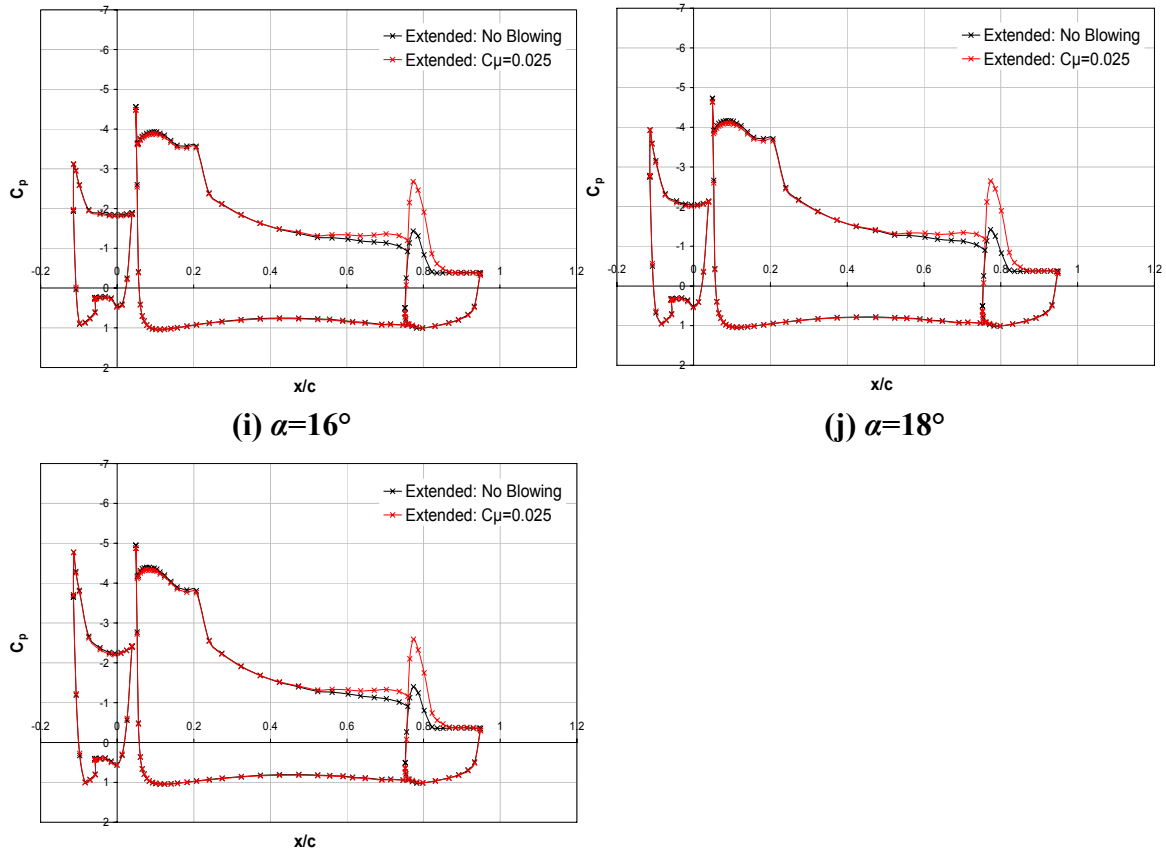

(i) α=16° **(j) α=18°**

(k) α=20°

Figure 126(a)-(k): Effect of tangential slot blowing on C_p distribution for extended flap configuration

Figure 126(a) shows the extent to which the tangential slot blowing influenced the upstream flow field at low angles of incidence. At α=0°, tangential slot blowing increased the static pressure over the lower surface of the main element for all but the fore $0.1c_{main}$. The increment was greatest between $0.1c_{main}$ and $0.6c_{main}$, decreasing in magnitude with subsequent distance downstream towards the trailing edge. On the upper surface of the main element, tangential slot blowing increased the suction at α=0°, with the corresponding decrement in static pressure heightened in magnitude with distance downstream, particularly over the aft $0.3c_{main}$. Furthermore, blowing boundary layer control modified the flow field such that a distinct suction peak was generated at the foremost point on the upper surface leading edge at α=0° – an attribute which only became apparent on the baseline configuration at α=2°. As the foremost suction peak was attributed to the influence of the wake developing aft of the leading-edge slat, its existence at α=0° suggested that the blowing boundary layer control modified the flow field over the entire configuration, even though there was no appreciable variation in the C_p distribution over the leading-edge slat. As expected, the effect of tangential slot blowing was most prominent over the upper surface of the trailing edge flap at α=0°,

notably heightening the suction over the upper surface. The increment in leading edge suction was most significant over the fore $0.4c_{flap}$, decreasing in magnitude thereafter with distance downstream. Most significantly, the mild adverse pressure gradient over the aft $0.35c_{flap}$ of the upper surface suggested that by blowing tangentially from a slot at a C_μ of 0.025, boundary layer separation was delayed from $0.4c_{flap}$ to within close proximity of the trailing edge. Unfortunately, due to time and facility constraints, it was not possible to investigate the surface flow field characteristics by means of oil flow visualisation in order to augment the quantitative measurements from the C_p distribution and verify whether tangential slot blowing prevented boundary layer separation. On the lower surface of the flap, tangential slot blowing increased the static pressure at α=0°, although the increment decreased in magnitude with distance downstream such that any deviation in C_p was essentially negated at the trailing edge.

By increasing α from 0° to 2°, a distinct stagnation point was generated at $0.1c_{main}$ over the leading edge of the main element, coincident with that of the baseline configuration, see Figure 126(b). Upstream of the stagnation point, tangential slot blowing increased the static pressure in comparison to the baseline configuration, whereas aft of the stagnation point, the blowing boundary layer control had no appreciable effect upon the lower surface C_p distribution. The upper surface C_p distribution over the main element was analogous to the baseline configuration, with two suction peaks occurring over the leading edge region at α=2°. Tangential slot blowing increased the suction over the upper surface of the main element and whilst the increment in suction was marginal over the fore $0.4c_{main}$, ΔC_p increased in magnitude with distance downstream, most distinctly over the aft $0.3c_{main}$. Whilst tangential slot blowing had no appreciable effect upon the lower surface C_p distribution over the main element for $\alpha \geq 4°$, its influence on the corresponding upper surface C_p distribution appeared more sensitive to variations in α. Figure 126(c) and Figure 126(d) showed that similarly to the configuration at α=2°, blowing air tangentially over the extended flap configuration at α=4° or α=6° tended to only marginally heighten the suction over the upper surface of the main element, although the decrement in static pressure markedly increased in magnitude over the aft $0.3c_{main}$. For $8° \leq \alpha \leq 20°$, Figure 126(e) through to Figure 126(k) showed that the influence of tangential slot blowing over the upper surface C_p distribution of the main element was limited to the aft $0.3c_{main}$, with the suction progressively heightened in magnitude with distance downstream towards the trailing edge. This decrement in static pressure over the aft region of the main element suggested that tangential slot blowing increased the upper surface boundary layer thickness at the trailing edge of the main element in comparison to the corresponding baseline configuration.

With regard to the trailing edge flap, increments in $\alpha \geq 2°$ negated any variation in static pressure over the lower surface due to the tangential slot blowing. On the upper surface of the flap, tangential slot blowing heightened the suction. Figure 126(b) through to Figure 126(k) showed that the decrement in static pressure was most prominent over the fore $0.4c_{flap}$ and decreased in magnitude thereafter such that the C_p distribution was essentially coincident with the baseline configuration over the aft $0.35c_{flap}$. Quantifying the increment in leading edge suction due to tangential slot blowing by the magnitude of the measured C_{pmin}, it was evident that the decrement in static pressure was relatively consistent for $2° \leq \alpha \leq 6°$, with a ΔC_{pmin} of approximately 1.4. With further increments in $\alpha \geq 8°$, the increment in leading edge suction due to tangential slot blowing was progressively reduced such that at $\alpha = 20°$, blowing tangentially from the slot at the trailing edge of the main element heightened the measured C_{pmin} from −1.40 for the baseline configuration to −2.59, accounting for a ΔC_{pmin} of approximately 1.2. Note that tangential slot blowing had negligible effect upon the location of the measured C_{pmin} for any given α, occurring at $0.1c_{flap}$ throughout. Most significantly, by blowing tangentially from a slot at the trailing edge of the main element over the upper surface of the deflected flap, boundary layer separation was delayed from $0.4c_{flap}$ to $0.65c_{flap}$ for all $2° \leq \alpha \leq 20°$. Based upon Kelly et al's (1958) observations, this suggested that similarly to the landing configuration, the extended flap configuration was not optimised with regard to the impingement of the jet of air upon the flap upper surface relative to the point of minimum pressure for the range of test α and hence, the effectiveness of tangential slot blowing, as a means of maintaining boundary layer attachment, was diminished. Furthermore, it was recognised that due to the magnitude of the flap deflection angle, a higher momentum coefficient may be required to maintain boundary layer attachment to within close proximity of the trailing edge.

7.7.2 Effect of Tangential Slot Blowing on the Aerodynamic Forces

Blowing tangentially over the upper surface of the deflected single slotted flap at a C_μ of 0.025 had a favourable effect upon the resultant aerodynamic lift force generated over the extended flap configuration for all test α, see Figure 127.

This increment in C_l was greatest at $\alpha = 0°$, with $\Delta C_l = 0.36$ accounting for a 36% increase in the lift force generated in comparison to the corresponding baseline configuration without tangential slot blowing. The measurements suggested that tangential slot blowing was particularly advantageous at $\alpha = 0°$ as blowing air over the upper surface of the flap dramatically improved the flow field development and unlike the baseline

configuration, maintained boundary layer attachment to within close proximity of the trailing edge, with an attendant increase in the resultant C_l.

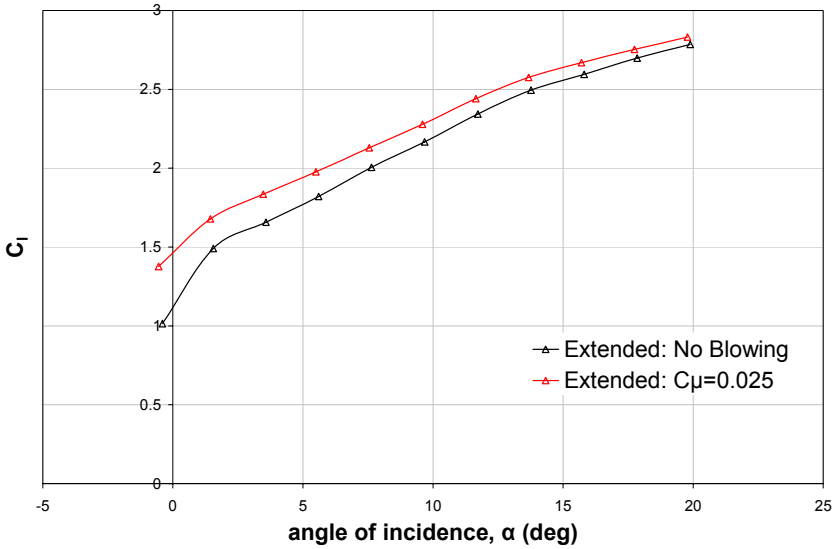

Figure 127: C_l-α curve for extended flap configuration, with and without tangential slot blowing

A single increment in α to 2° markedly reduced the increment in C_l due to tangential slot blowing, approximately halving ΔC_l to 0.19 and significantly reducing the percentage increment to 13%. With further increments in α, ΔC_l steadily decreased in magnitude. Specifically, ΔC_l decreased to 0.11 at α=10°, representing a 5% increase in C_l, and at the upper test limit of α=20°, ΔC_l was minimised to 0.05, equating to a 2% increase in C_l in comparison to the corresponding baseline configuration without tangential slot blowing. Figure 113 clearly illustrates this variation of ΔC_l with α.

Similarly to the takeoff and landing configurations, tangential slot blowing increased the pressure drag for any given C_l. As previously noted, the delay of boundary layer separation would typically be associated with a corresponding reduction in pressure drag and accordingly, the increment in pressure drag was attributed to the influence of tangential slot blowing on the developing flow field over the entire extended flap configuration. Figure 114 showed that the increment in pressure drag varied inconsistently between 0.04 and 0.05 for $0° \leq \alpha \leq 14°$, although with subsequent increments in $\alpha \geq 16°$ the increment was progressively heightened in magnitude, attaining a maximum value of 0.064 at α=20°.

Accordingly, based upon pressure drag alone, tangential slot blowing reduced L/D by between 11-17% for $2° \leq \alpha \leq 20°$ in comparison to the corresponding baseline extended

flap configuration, with only an isolated 10% increment at α=0°, see Figure 115. However, it was recognised that consideration of the pressure drag alone, obtained purely from the integration of the surface static pressure distribution, was insufficient to accurately evaluate the aerodynamic performance of the extended flap configuration in terms of L/D.

7.8 Effect of C_μ on C_p Distribution

The volume flow rate was increased from 4600 litres per minute to 7000 litres per minute in intervals of 400 litres per minute and the corresponding momentum coefficient was calculated, based upon theoretical approximations of the jet velocity.

Figure 128 shows the effect of C_μ on the surface static pressure distribution over the takeoff configuration at α=8°. As expected, the influence of tangential slot blowing on the developing flow field was most prominent over the trailing edge flap but its influence also extended upstream, modifying the C_p distribution over the aft $0.4c_{main}$ of the main element upper surface.

Recall that for the baseline takeoff configuration at α=8°, the boundary layer over the upper surface of the flap separated at $0.35c_{flap}$. In contrast, with the application of tangential slot blowing, the C_p distributions in Figure 128 indicated that boundary layer attachment was maintained to within close proximity of the trailing edge for all test C_μ implemented.

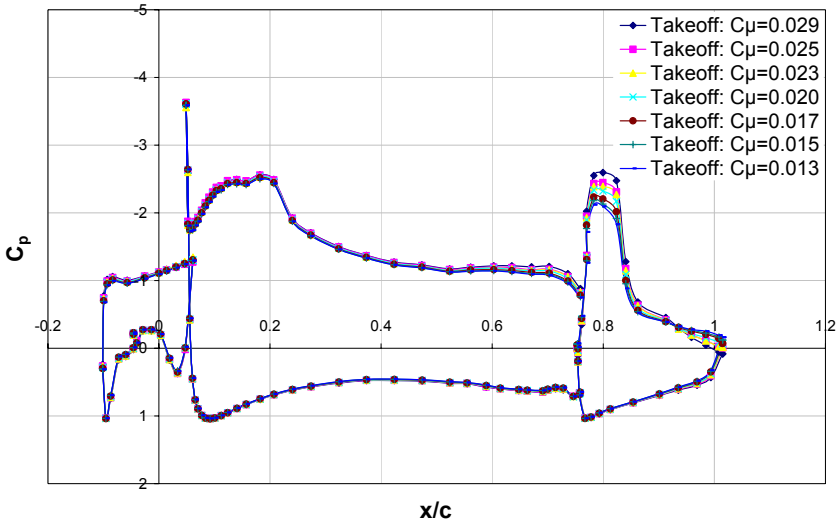

Figure 128: Effect of C_μ on C_p distribution for takeoff configuration at α=8°

Increasing C_μ from 0.013 to 0.029 progressively heightened the suction over the aft $0.4c_{main}$ of the main element upper surface and over the fore $0.6c_{flap}$ of the flap upper surface, although ΔC_p decreased in magnitude aft of $0.3c_{flap}$ on the flap upper surface. Aft of $0.6c_{flap}$, the trailing edge static pressure was progressively increased with successive increments in C_μ, with the increment increasing in magnitude with distance downstream for any given test C_μ. This increment in static pressure was indicative of decreasing boundary layer thickness with increasing C_μ. An increment in static pressure was also evident over the aft $0.4c_{flap}$ of the flap lower surface, again increasing in magnitude both with distance downstream for any given C_μ and with successive increments in C_μ. Similarly, this increment in static pressure on the lower surface was indicative of a reduction in trailing edge boundary layer thickness with successive increments in C_μ.

Finally, integration of the respective surface static pressure distributions indicated that, as expected, increasing C_μ from 0.013 to 0.029 increased the resultant C_l from 2.02 to 2.15, respectively, accounting for a 6% increment in C_l over the range of C_μ tested. Accordingly, tangential slot blowing at a C_μ of 0.013 and 0.029 correlated to an increment in C_l of 0.13 and 0.25, respectively, in comparison to the corresponding baseline configuration. Recalling that the boundary layer separation was prevented at a the lower test C_μ of 0.013, the trends in C_l corroborated Dods and Watson's (1956) observations, namely that once the value of C_μ necessary to maintain boundary layer attachment was achieved, further increments in C_μ only resulted in moderate increments in C_l.

There was a also tendency for the corresponding pressure drag to decrease in magnitude with successive increments in C_μ between 0.013 and 0.023, varying from a maximum of 0.108 to a minimum of 0.103 and correlating to a 4% decrement in pressure drag over the range of C_μ tested. However, a further increment in C_μ to 0.025 resulted in a marginal increment in C_d to 0.105, although with a final increment in C_μ to 0.029, C_d was once again decreased in magnitude to 0.104.

7.9 Effect of Reynolds Number

Figure 129 shows the effect of Reynolds number on the C_p distribution for the baseline takeoff configuration without tangential slot blowing at α=8°. The nominal freestream velocity was increased from $25m/s$ to $45m/s$ in intervals of $5m/s$, corresponding to Reynolds numbers (Re) of 9.94×10^5, 1.20, 1.40, 1.61 and 1.79×10^6, based upon the

stowed reference chord. The corresponding surface static pressure measurements indicated that Reynolds number effects were appreciable for the specified high-lift configuration, corroborating Ljungström's (1976) observations when optimising a high-lift multi-element configuration over a comparable range of Reynolds numbers. These deviations in the C_p distributions were attributed to the highly complex flow field developing over the high-lift configuration and the subsequent interactions of the confluent boundary layer/wake development, which were sensitive to variations in *Re*. Note that this was not a pure Reynolds number variation as the corresponding Mach number was also increasing, which Ljungström suggested may have resulted in a slight underestimation of the Reynolds number effects.

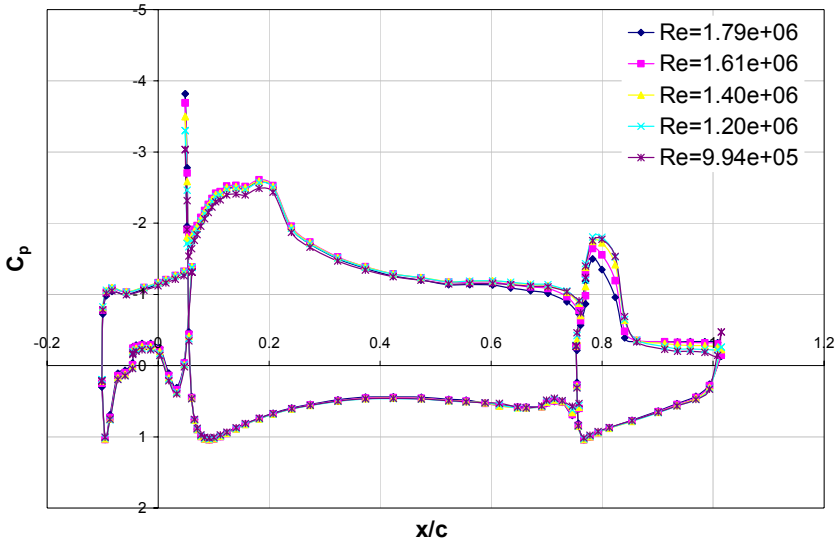

Figure 129: Effect of Reynolds number on C_p distribution for takeoff configuration without tangential slot blowing at α=8°

Quantifying these fluctuations for the takeoff configuration in the absence of tangential slot blowing at α=8°, integration of the surface static pressure distributions indicated that the lift and pressure drag coefficients initially increased in magnitude with increments in *Re* between 9.94×10^5 and 1.40×10^6 but decreased with further increments in *Re* to the upper test limit of 1.79×10^6. Consequently, the variation in C_l with *Re* for the specified configuration was only consistent with trends observed by Ljungström – namely that of C_l increasing with *Re* – for $9.94\times10^5 \leq Re \leq 1.40\times10^6$. Specifically, C_l and C_d varied by 4% and 5%, respectively, over the range of test *Re* for the specified configuration. Thus, the results presented herein were only completely valid for the test Reynolds number and further study of Reynolds number effects, particularly in the presence of tangential slot blowing, are required to enable a reasonable extrapolation of the boundary layer control results.

7.10 Chapter Summary

Air was blown tangentially over the upper surface of the flap from a conventional slot at the trailing edge of a main element for three specified high-lift configurations. Analysis of surface static pressure measurements, resultant aerodynamic forces and surface oil flow visualisation indicated that:

- When optimised, blowing tangentially at a nominal C_μ of 0.025 from a slot at the trailing edge of the main element over the upper surface of the flap was a highly effective means of maintaining boundary layer attachment to within close proximity of the trailing edge
- For the takeoff configuration, tangential slot blowing delayed boundary layer separation from $0.35c_{flap}$ to within close proximity of the flap trailing edge for all test α
- Effectiveness of tangential slot blowing as a means of preventing boundary layer separation was diminished for the landing and extended flap configurations, with separation typically delayed further aft
- For the takeoff and extended flap configurations, tangential slot blowing increased C_l for all test α
- For the landing configuration, the favourable effect of tangential slot blowing upon C_l was limited to $\alpha \leq 14°$
- Tangential slot blowing increased the pressure drag for all configurations and test α
- Further optimisation with regard to the impingement of the jet of air upon the flap upper surface, relative to the point of minimum pressure, for all test α may improve the effectiveness of tangential slot blowing as a means of preventing boundary layer separation for the landing and extended flap configurations
- Flow field development over the takeoff configuration was sensitive to variations in Reynolds number and hence, further studies of Reynolds number effects, particularly in the presence of tangential slot blowing, are required to enable a reasonable extrapolation of the boundary layer control results

8 Numerical Modelling: Tangential Slot Blowing

This chapter details the numerical modelling of blowing tangentially from a slot at the trailing edge of the main element over the upper surface of a deflected flap in a three-element high-lift configuration.

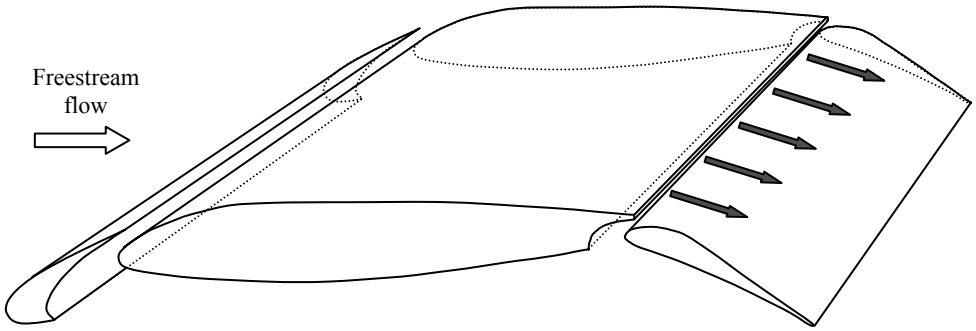

8.1 Introduction

The numerical study consisted of modelling tangential slot blowing over the upper surface of a deflected flap within a two-dimensional three-element takeoff configuration for angles of incidence between 0° and 20° (see inset in schematic on page xv for further details of blowing slot). The aim of the numerical investigation was, primarily, to establish a set of computational data correlating directly to the wind-tunnel tests for comparative purposes.

The grid for the two-dimensional high-lift configuration was provided by Instituto Nacional de Técnica Aeroespacial (INTA), a member of the HELIX consortium. Thirty layers of structured quadrilateral cells encircled each component of the aerofoil, encapsulating and extending beyond the expected boundary layer thickness for the designated freestream conditions. The final layer of structured cells interfaced with triangular cells, which formed the unstructured domain and extended to the circular far field boundary, with a radius of 30 chord lengths.

FLUENT was chosen as the commercial code for the numerical study, to ensure successful synthesis of the data with that of additional studies within the HELIX project.

8.2 FLUENT

FLUENT solves the governing partial differential equations of fluid flows, which represent mathematical statements for the conservation of mass, momentum and energy

and, where appropriate, additional scalars. An implicit segregated solver was specified, which solved the non-linear governing equations sequentially. Closure of the system of time-averaged mean flow equations was provided by one of four different classical turbulence models available in FLUENT, namely:

- Spalart-Allmaras
- k-ε
- k-ω
- Reynolds stress equation

As the numerical study was initially instigated to supplement the computational investigations within the HELIX project, the model implemented was consistent with that previously determined by INTA's rigorous validation of the available turbulence models. Accordingly, they proposed that the Spalart-Allmaras model was most favourable, as it was the least computationally expensive model which adequately captured the region of trailing edge boundary layer separation over the upper surface of the flap within a specified multi-element high-lift configuration.

The FLUENT user manual defined the Spalart-Allmaras model as a relatively simple one-equation model, specifically designed for aerospace applications involving wall-bounded flows. The modelled transport equations were solved for the kinematic turbulent eddy viscosity, omitting the necessity to calculate the length scale related to the local shear layer thickness. Furthermore, it noted that the model was advantageous in its simplicity and relatively small demand on computational resources, whilst demonstrative of favourable results for boundary layers subject to adverse pressure gradients.

The boundary conditions were defined by the freestream conditions observed for the corresponding wind-tunnel tests, which were corrected for blockage as applicable. Furthermore, the surface forming the slot at the trailing edge of the main element was either defined as a solid wall for the configurations without tangential slot blowing or as a mass flow inlet for the configurations with tangential slot blowing. Note that with regard to the latter, the mass flow rate was determined from the volume flow rate and the corrected freestream density observed from the corresponding wind-tunnel experiments.

Second order discretisation was maintained for all variables, with the exception of the modified turbulent viscosity, where first order discretisation was implemented to improve the stability of the computations, without unduly affecting the accuracy of the results. A SIMPLE (Semi-Implicit Method for Pressure-Linked Equations) pressure-velocity coupling was specified, which used an initial value for the pressure field to solve the discretised momentum equations and hence, yield the components of velocity. Default under-relaxation factors were implemented during the iterative process, controlling the updated variables generated by the approximate solution of the finite difference equations, promoting a stable computation and converged solution. The residuals – measures of the overall conservation of the flow properties – were monitored by default convergence criteria, based upon each residual being reduced to a value less than 10^{-3}, with the exception of the energy residual, for which the default convergence criterion was less than 10^{-6}. Whilst convergence was typically satisfied by the reduction of the residual values, it was not necessary condition. Accordingly, the lift and drag force coefficients were also monitored, with numerical consistency to the third decimal place for C_l and fourth decimal place for C_d inferring convergence. Subsequent studies by INTA confirmed that the simulation was grid independent.

8.3 Comparison of Experimental and Computational Data

Figure 130 compares the C_p distributions from the wind-tunnel measurements with the corresponding numerical solution for the takeoff configuration at a given angle of incidence. Data is presented for the baseline configurations without tangential slot blowing and for the corresponding configurations with tangential slot blowing applied at a nominal C_μ[1] of 0.025.

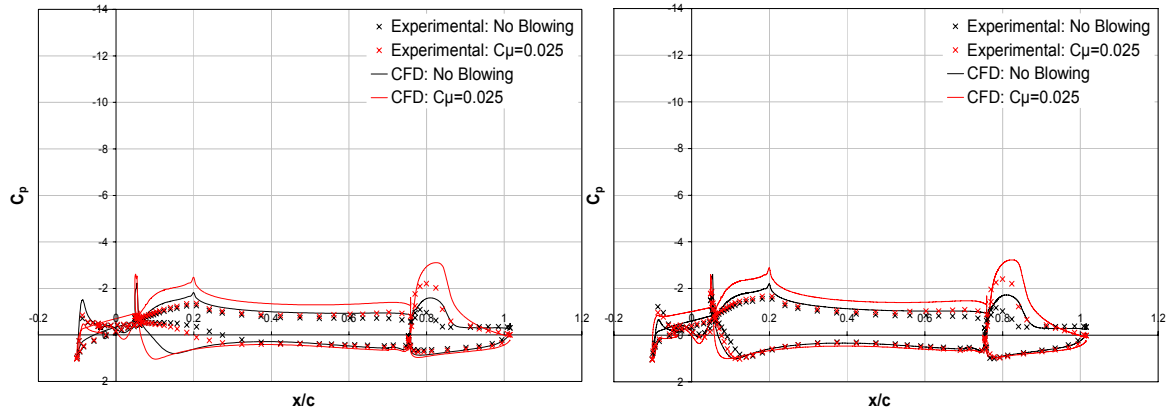

(a) α=0° **(b) α=2°**

[1] Note that C_μ refers to the momentum coefficient and not the eddy viscosity constant

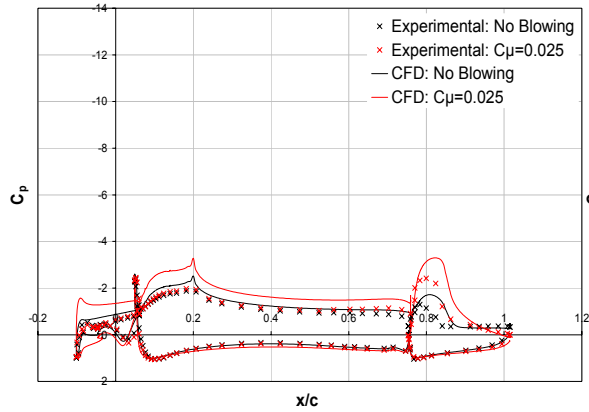

(c) α=4°

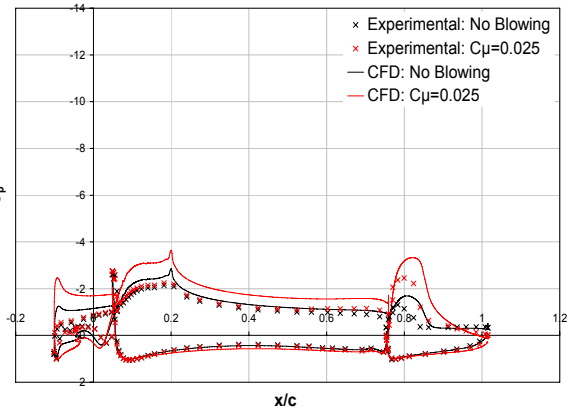

(d) α=6°

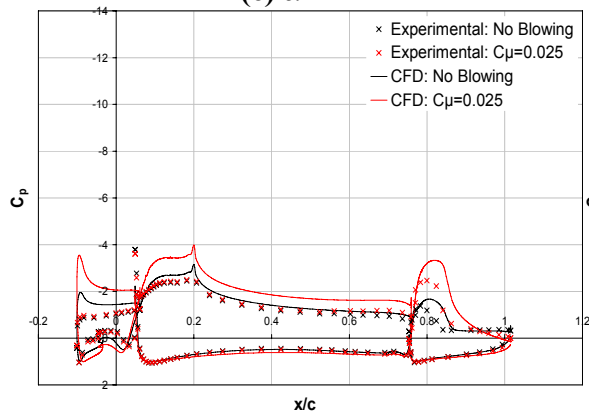

(e) α=8°

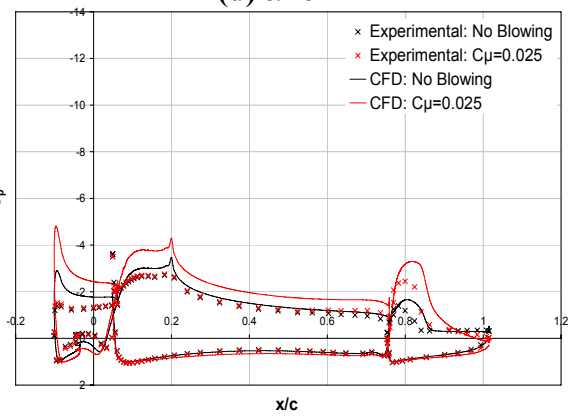

(f) α=10°

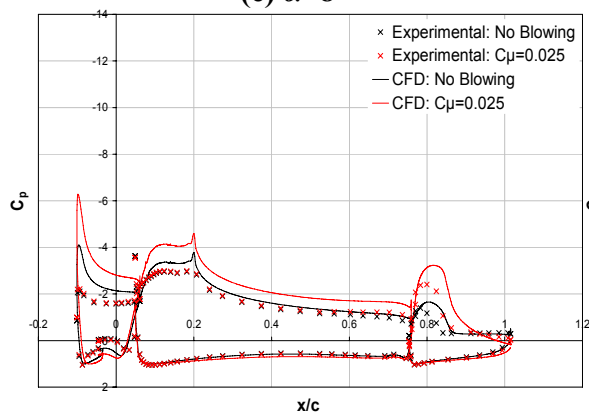

(g) α=12°

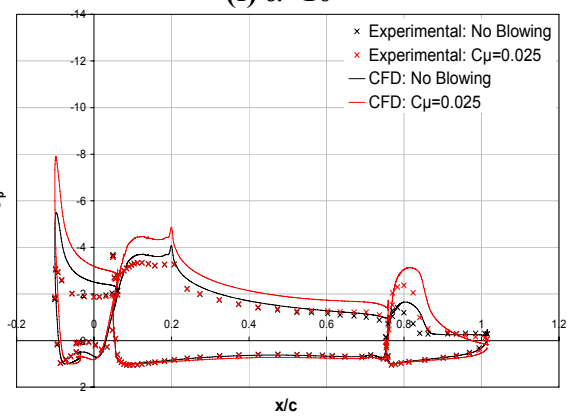

(h) α=14°

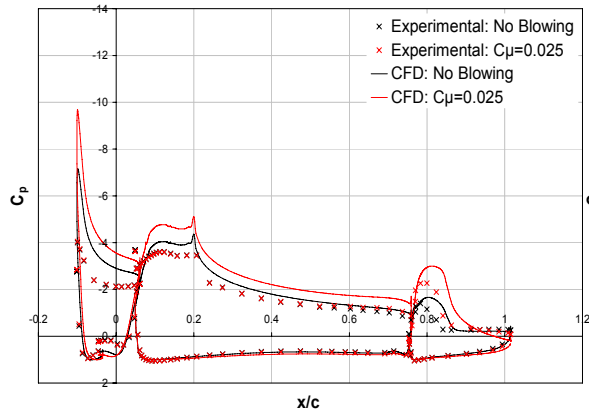

(i) α=16°

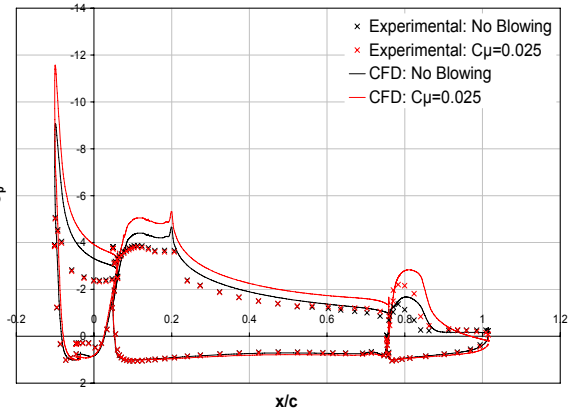

(j) α=18°

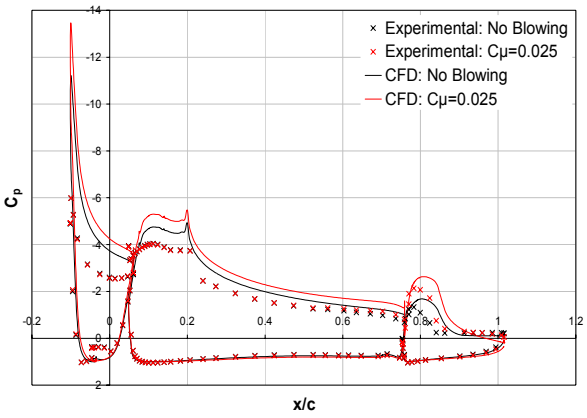

(k) α=20°

Figure 130(a)-(k): Comparison of experimental and numerical C_p distributions for takeoff configuration, with and without tangential slot blowing

8.3.1 Comparison of C_p Distributions without Tangential Slot Blowing

In the absence of tangential slot blowing, the salient attributes of the takeoff configuration identified in the experimental C_p distributions were also typically evident in the numerical solution. Considering the leading edge slat, the numerical C_p distribution was only in agreement with the experimental data at the leading edge. Immediately aft of the leading edge, the computational simulation tended to over-predict the pressure on the lower surface of the slat in comparison to the wind-tunnel data. However, over the aft region of the slat lower surface, the computations indicated a marked reduction in C_p in comparison to the experiments, although this decrement in C_p decreased in extent and magnitude with increments in α, such that any deviation in C_p was negated over the aft $0.25c_{slat}$ for $\alpha \geq 18°$. As expected, the anomalies in the computed C_p distribution over the mid-chord region of the slat lower surface were indicative of the complex reversed flow field, evident from the surface oil flow visualisation over the wind-tunnel model, which the turbulent model was unable to accurately resolve. Over the upper surface of the slat, the prominent features of the C_p distributions from the numerical simulations were comparable to the wind-tunnel data. However, the computations substantially over-predicted the suction on the upper surface of the slat in comparison to the experimental data, with the numerical solution displaying a notable improvement in the flow field over the leading edge slat for all $\alpha \geq 4°$.

Correlation of the computational and experimental data was improved over the main element of the takeoff configuration. This was particularly evident over the lower surface, where the C_p distribution generated by the numerical simulation was in good

agreement with the corresponding wind-tunnel data, although slight anomalies arose over the leading edge for $\alpha \leq 2°$. Over the upper surface of the main element, the salient attributes of the flow field development corroborated the wind-tunnel data, although the numerical model heightened the suction over the entire upper surface, particularly over the fore $0.3c_{main}$. An anomaly to this trend coincided with the first suction peak located at the foremost point of the upper surface leading edge, which was typically diminished in magnitude in comparison to the corresponding experimental data, particularly for $8° \leq \alpha \leq 14°$. In accordance with the observations of Foster et al (1970), this deviation in the magnitude of the first suction peak was attributed to the modified flow field over the leading edge slat exhibited by the numerical solution and the influence of the aft developing wake on the flow field development over the fore region of the main element. Furthermore, the computational solution exhibited a distinct spike in the upper surface pressure distribution at approximately $0.2c_{main}$ for all test α. This was attributed to a discontinuity in the geometry, which coincided with the locale of the slat trailing edge when retracted in its stowed position and was thus evident in the numerical C_p distribution, irrespective of whether or not tangential slot blowing was applied. Due to the distribution of the static pressure orifices, this irregularity was not captured by the wind-tunnel data. Note that a similar geometric discontinuity was also evident in the A300 wing profile – upon which the configuration geometry was based – generating a corresponding spike in the upper surface C_p distribution.

Regarding the trailing edge flap, the computational solution was in good agreement with the wind-tunnel data over the lower surface, only over-predicting C_p over the fore $0.5c_{flap}$ at $\alpha = 0°$. Over the upper surface of the flap, the numerical solution typically over-predicted both the extent and magnitude of the suction peak. The point of upper surface boundary layer separation also differed between the wind-tunnel observations and the numerical solution, with the experimental data indicating that the upper surface boundary layer separated aft of $0.35c_{flap}$ irrespective of variations in α. Whilst recognising that the accuracy of this was clearly limited by the distribution of the static pressure orifices, the computational simulation indicated that the upper surface boundary layer separated aft of $0.5c_{flap}$ for $0° \leq \alpha \leq 18°$, increasing to $0.6c_{flap}$ at $\alpha = 20°$. The delay of boundary layer separation at the upper test limit of α was inconsistent with expectation and the reason for this remained unclear. Note that whilst the numerical solution simulated a uniform flap lap/gap, the wind-tunnel tests indicated a certain degree of deformation of the flap under freestream conditions. Quantifying the deviation in the lap and gap was infeasible, although visual inspection suggested that the deformation was magnified at high angles of incidence. Accordingly, the disparities

between the experimental and computational flap lap/gap must be considered when comparing the respective C_p distributions, particularly as previous wind-tunnel tests for the takeoff configuration highlighted the sensitivity of the upper surface C_p distribution over the trailing edge flap to marginal variations in flap lap (see Section 7.2). Finally, the spike in the computational C_p distribution at the trailing edge of the flap indicated that the turbulent model was unable to resolve the boundary layer separation at the finite trailing edge.

8.3.2 Comparison of C_p Distributions with Tangential Slot Blowing

With the application of tangential slot blowing, the deviation between the experimental and computational data was most evident over the leading edge slat. From Figure 130 it was evident that whilst the wind-tunnel data indicated that blowing tangentially at a C_μ of 0.025 had no appreciable effect upon the C_p distribution, the numerical solution indicated that tangential slot blowing significantly heightened the suction over the entire upper surface of the slat for all test α. Over the lower surface, the computational simulation indicated that tangential slot blowing transposed the stagnation point marginally aft. Upstream of this stagnation point and over the aft $0.25c_{slat}$ of the slat lower surface, the static pressure was decreased by active boundary layer control, with the decrement in C_p heightened with successive increments in α. Although the static pressure over the mid-chord region of the slat lower surface tended to increase in magnitude with tangential slot blowing, anomalies in the computed C_p distribution were once again indicative of the complex reverse flow field which the turbulent model was unable to accurately resolve, inferring a degree of ambiguity in the simulated flow field over the lower surface of the slat.

With regard to the main element, Figure 130 showed that the computational solution corroborated the experimental data and predicted an increment in static pressure due to tangential slot blowing over the lower surface leading edge at low α. Although the magnitude of the increment generated by the numerical simulation was more pronounced, any deviation in static pressure over the fore region of the lower surface was negated for $\alpha \geq 6°$ and was thus in good agreement with the wind-tunnel data. However, contrary to the experimental data, the numerical C_p distribution indicated that tangential slot blowing increased the static pressure aft of the stagnation point and heightened the suction over the entire upper surface for all test α. Similarly to the baseline configuration without tangential slot blowing, an anomaly to this trend arose at the first suction peak, located at the foremost point on the upper surface leading edge,

whereby the magnitude was typically lower than that of the experiment, particularly for $8° \leq \alpha \leq 14°$. Again this was attributed to the influence of the modified wake developing aft of the leading edge slat. An additional spike in the upper surface C_p distribution coincided with the location of the slot at the trailing edge of the main element and accordingly, the decrement in C_p was attributed to the high velocities of the jet of air.

With regard to the trailing edge flap, the numerical simulation indicated that tangential slot blowing typically had no appreciable effect upon the lower surface C_p distribution over the fore $0.25c_{flap}$ and thus, was in good agreement with the wind-tunnel data, see Figure 130. Aft of this point, an increase in static pressure was evident, increasing in magnitude with successive distance downstream. Not only did the computational simulation extend the region over which tangential slot blowing influenced the lower surface C_p distribution in comparison to the experimental data but it also heightened the magnitude of the increment in comparison to the corresponding baseline configuration. Accordingly, the numerical solution over-predicted C_p over the aft $0.75c_{flap}$ of the lower surface in comparison to the experimental data, although the magnitude of this deviation was diminished at high test α. Over the upper surface of the flap, the numerical solution over-predicted the suction peak, both in extent and magnitude, transposing the location of C_{pmin} aft by approximately $0.1c_{flap}$ in comparison to that measured experimentally. Again, the influence of a uniform lap/gap in the numerical model must be considered, despite there being no quantifiable experimental data for corroboration. Despite the disparities between the computational and experimental data for upper surface pressure distribution, the numerical simulation corroborated the wind-tunnel measurements and indicated that tangential slot blowing maintained boundary layer attachment to the trailing edge for all test α.

8.3.3 Comparison of Aerodynamic Forces

The disparities between the experimental and computational C_p distributions were manifested in the contrasting magnitudes of the lift and drag forces generated over the three-element takeoff configuration. Note that the numerical solution computed the aerodynamic forces based upon both pressure and viscous forces acting upon the surface.

Considering the baseline takeoff configuration in the absence of tangential slot blowing, Figure 131 shows that, in comparison to the wind-tunnel data, the computational solution over-predicted the lift force generated for $\alpha \leq 16°$. The disparity between the

experimental and computation prediction of C_l for the baseline takeoff configuration without tangential slot blowing was greatest at low α, with the numerical solution overestimating C_l by 0.5 at α=0°, accounting for a 60% increment. A single increment in α to 2° markedly reduced this deviation to 0.39, indicating that the computational solution overestimated C_l by 31% in comparison to the experimental data. The deviation in C_l progressively diminished with subsequent increments in α, such that the numerical simulation only overestimated C_l by 2% at α=16°. With further increments in $\alpha \geq 18°$, the computational solution marginally underestimated C_l by ≤2% in comparison to the corresponding wind-tunnel data for the takeoff configuration without tangential slot blowing.

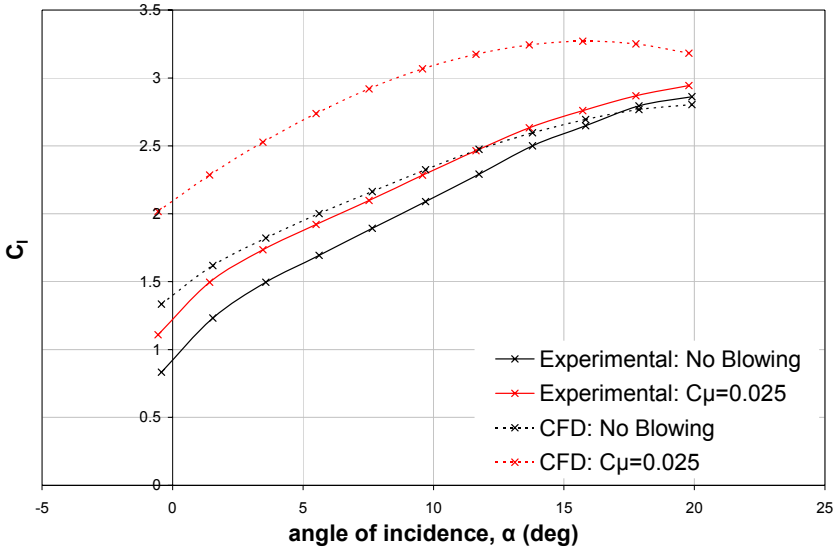

Figure 131: Comparison of experimental and computational C_l-α curves for the takeoff configuration, with and without tangential slot blowing

Whilst the increment in C_l due to tangential slot blowing predicted by the computational simulation for any given test α was consistent with trend identified from the wind-tunnel data, i.e. tangential slot blowing increased C_l in comparison to the corresponding baseline configuration, Figure 131 showed that the magnitude of the increment was significantly magnified by the numerical solution. This disparity between the experimental and computational data for the takeoff configuration with tangential slot blowing was greatest at low α with a ΔC_l of 0.91 accounting for 82% increment at α=0° and reducing to 0.79, equating to a 53% increase at α=2°. With subsequent increments in α, the magnitude by which the numerical simulation overestimated C_l initially increased to 0.82 at α=8°, although the corresponding percentage increment continued to progressively decrease, correlating to a 39% increment. For $10° \leq \alpha \leq 20°$, the discrepancy between the computational and experimental data diminished in magnitude, as did the corresponding percentage increment, such that the numerical solution

overestimated C_l for the takeoff configuration with tangential slot blowing by 0.24 or 8% at the upper test limit of α=20°.

Recalling that the experimental data indicated that ΔC_l due to tangential slot blowing decreased in magnitude with successive increments in α, the numerical solution indicated that ΔC_l due to tangential slot blowing initially increased in magnitude with successive increments in $\alpha \leq 8°$ from a ΔC_l of 0.68 at α=0° to a maximum value of 0.76 at α=8°, correlating to a 51% and 35% increment, respectively, when compared to the baseline takeoff configuration without tangential slot blowing. With subsequent increments in $\alpha \geq 10°$, the numerical solution indicated that ΔC_l due to tangential slot blowing progressively decreased in magnitude to a minimum value of 0.38 at the upper test limit of α=20°, representing a 13% increment in comparison to the corresponding baseline configuration. Thus, whilst the wind-tunnel data suggested that tangential slot blowing was most effective at low α in terms of increasing C_l, the numerical simulation indicated that tangential slot blowing was most favourable over the low- to mid-range of test α.

Furthermore, whilst the wind-tunnel data indicated that tangential slot blowing had negligible effect upon the stall angle, which exceeded the upper test limit of α=20°, the computational simulation indicated that tangential slot blowing reduced the stall angle from 20° to 16°.

Figure 132 shows the drag polar determined from the computational simulation for the takeoff configuration both with and without tangential slot blowing. Note that in determining C_d, the numerical solution computed both the pressure drag and skin friction drag. Over a comparable range of C_l, the numerical solution indicated that tangential slot blowing had no appreciable effect upon C_d for $2 \leq C_l \leq 2.1$ but with further increments in $2.1 < C_l \leq 2.8$, tangential slot blowing decreased C_d in comparison to the corresponding baseline configuration. The decrement increased in magnitude with successive increments in C_l and thus, corroborated the trends identified in Turner's (1964) two-dimensional study.

However, this decrement in C_d due to tangential slot blowing, evident in the numerical solution, contradicted the trend identified from the experimental data, whereby tangential slot blowing increased the pressure drag in comparison to the baseline configuration for any given C_l over a comparable range. Furthermore, integration of the surface static pressure distributions yielded pressure drag coefficients of significantly

greater magnitude than the profile drag coefficient determined from the numerical solution (see Figure 132).

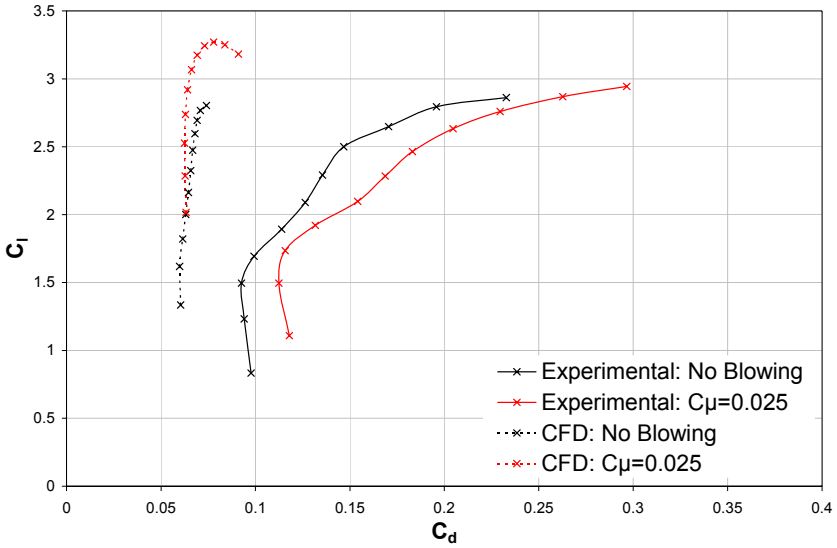

Figure 132: Comparison of experimental and computational drag polars for the takeoff configuration, with and without tangential slot blowing

Accordingly, it was by considering the drag force generated by individual components of the takeoff configuration that these discrepancies were better understood. Whilst it was recognised that in the absence of skin friction drag estimations for the experimental model, the wind-tunnel data could not be compared directly with the profile drag predictions of the numerical simulation, Figure 133 highlighted that it was the flow field development over the leading-edge slat which provoked the dominant source of error between the experimental and computational drag predictions.

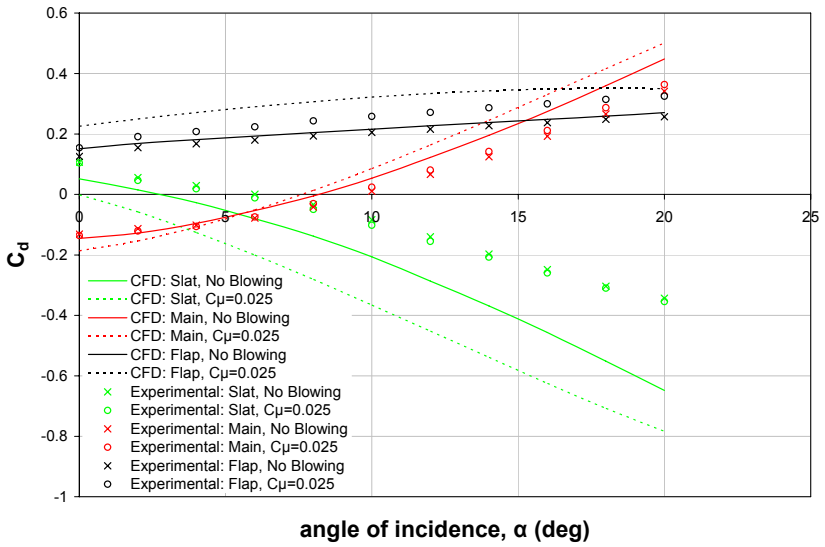

Figure 133: Comparison of experimental and computational drag forces acting on each element of the takeoff configuration, with and without tangential slot blowing

Further analysis of the C_p distributions over the leading-edge slat in Figure 130 identified two dominant sources of discrepancy. Firstly, by considering the takeoff configuration in the absence of tangential slot blowing, it was evident that the computational simulation considerably heightened the suction over the upper surface of the leading edge slat in comparison to that observed experimentally. Such discrepancies were fundamentally attributed to the boundary layer development over the leading edge slat, specifically the point of transition. Whilst the computational simulation assumed development of a fully turbulent boundary layer over the leading edge slat, free transition was maintained on the wind-tunnel model. Accordingly, the existence of a laminar boundary layer prior to transition over the fore region of the slat would critically influence the respective surface static pressure distributions. By virtue of the complex boundary layer/wake interaction, typified by high-lift configurations, the boundary layer development over the leading edge slat would, in turn, influence the boundary layer development over the downstream elements of the configuration. Thus, it is proposed that further experimental studies with transition fixed are required to ensure that the computational simulation was representative of the boundary layer development over the wind-tunnel model.

Secondly, the wind-tunnel measurements indicated that tangential slot blowing had no appreciable effect upon the C_p distribution over the leading edge slat. In contrast, the numerical simulation predicted a significant increment in suction over the upper surface of the slat due to tangential slot blowing, which suggested that the application of active boundary layer control increased the circulation about the takeoff configuration and hence, modified the flow field developing over the leading edge slat. This increase in circulation was typically associated with increased momentum coefficients (Lachmann, 1961) and hence suggested a disparity between the effective momentum coefficient of the wind-tunnel tests and that defined computationally. Whilst the blowing jet in the numerical solution was defined by a mass flow rate at the slot exit, the nominal momentum coefficient for the wind-tunnel tests was based upon theoretical assumptions of continuity and failed to take into account both losses within the boundary layer control system and spanwise variations in jet velocity.

Both sources of discrepancy clearly influenced the numerical predictions of C_l and C_d. Thus, until such potential sources of discrepancy between the experimental and computational data are resolved, such that the flow field simulated numerically is representative of the wind-tunnel model, it is neither possible to quantify the accuracy with which the computational simulation predicted the resultant aerodynamic forces,

nor is it possible to reconcile the discrepancies evident between the computational and experimental predictions of C_l and C_d.

Whilst recognising these sources of discrepancy between the experimental and computational data, the variation of L/D with α is presented in Figure 134, for completeness.

The favourable effect of tangential slot blowing upon both C_l and C_d, predicted by the computational simulation, resulted in a substantial increment in L/D for any given test α, in comparison to the corresponding baseline configuration. For the baseline configuration, the numerical solution indicated that L/D progressively increased with α from 22.1 at α=0° to a maximum value of 39.1 at α=18°, marginally decreasing in magnitude to 37.9 with a final increment in α to 20°. Application of tangential slot blowing modified the angle of incidence, and hence C_l, at which the maximum L/D was attained. Accordingly, the computational solution indicated that for the takeoff configuration with tangential slot blowing, L/D increased in magnitude from 52.7 at α=0° to a maximum value of 74.3 at α=8° and decreased in magnitude thereafter, attaining a minimum value of 47.2 at α=20°. Thus, for the numerical solution, the corresponding increment in L/D due to tangential slot blowing progressively decreased in magnitude from nearly a 140% increment at α=0° and a 110% increment at α=10° to a 25% increment in L/D at α=20°.

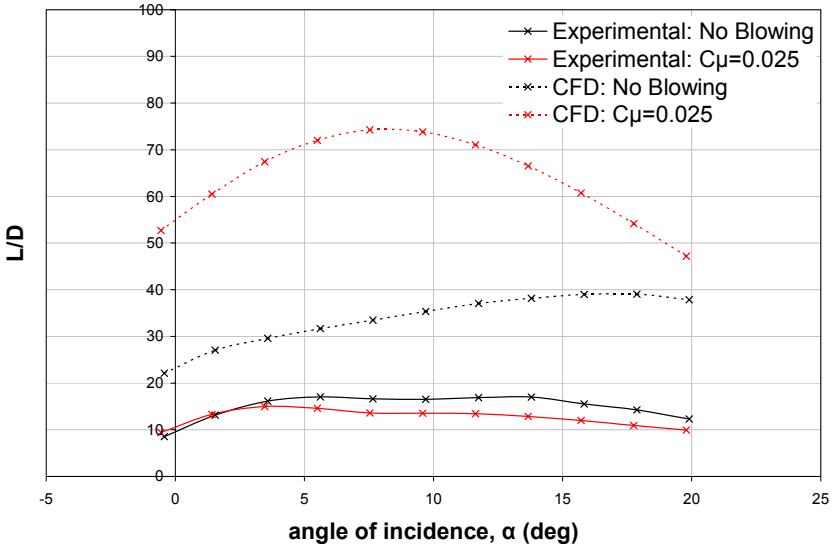

Figure 134: Comparison of experimental and computational *L/D* for takeoff configuration, with and without tangential slot blowing

Whilst the trends identified in the numerical prediction of L/D contradicted those of the experimental data, it was recognised that consideration of the pressure drag alone,

determined purely from the integration of the C_p distributions, was insufficient to accurately evaluate the aerodynamic performance of the configuration in terms of L/D and, when combined with the apparent discrepancies in transition modelling and effective momentum coefficient, it was evident that the experimental data could not be directly compared to the computational predictions. Thus, further studies are required to ensure that the computational solution accurately represents the experimental conditions and to determine whether such substantial gains in L/D evident in the numerical simulation are realistic and achievable for the given experimental setup.

8.3.4 Effect of Small Perturbations in Angle of Incidence

The effect of small perturbations in α on the developing flow field was investigated for the takeoff configuration at α=10°, both with and without tangential slot blowing. Whether or not tangential slot blowing was implemented, varying α by ±0.5° – representative of the magnitude of fluctuation for the wind-tunnel model – influenced the upper surface C_p distribution over the leading edge slat. This influence also extended to the fore $0.2c_{main}$ of the main element upper surface, aft of which any deviation in static pressure due to small perturbations in α was essentially negated. Fluctuations in α had no appreciable effect upon the lower surface pressure distribution. As expected, a perturbation increasing α to 10.5° heightened the suction over the upper surface of the slat and over the leading edge of the main element. This increment was greatest at the leading edge of the slat and decreased in magnitude with distance downstream. Conversely, decreasing α to 9.5° reduced the suction over the upper surface of the slat and over the leading edge of the main element, with the magnitude of the decrement decreasing with distance downstream. Accordingly, a perturbation increasing α to 10.5° marginally increased C_l and marginally decreased C_d, whereas a perturbation decreasing α to 9.5° marginally decreased C_l and marginally increased C_d. Whilst these trends were identified, the variation in C_l and C_d due to small perturbations in α accounted for less than ±2% deviation in the aerodynamic forces generated over the takeoff configuration, whether or not tangential slot blowing was applied.

8.3.5 Variation of Critical Parameters Defining the Jet of Air for the Numerical Simulation

The numerical simulation required the boundary conditions to be designated for the jet of air blown tangentially over the upper surface of the trailing edge flap. The critical

parameters were the mass flow rate, the direction of the jet at the slot origin, the temperature of the jet and the turbulence intensity.

The critical parameters for the jet of air were modified for the takeoff configuration at an angle of incidence comparable to that at the takeoff phase of the flight envelope. Studies showed that variations in the jet temperature and turbulence intensity had no appreciable effect upon the surface static pressure distributions or the resultant aerodynamic forces.

8.3.5.1 Effect of Varying the Jet Momentum Coefficient

Figure 135 shows the effect of varying the jet momentum coefficient on the C_p distribution over the takeoff configuration at α=10°. Typically, the C_μ corresponded to uniform increments in the mass flow rate between 0.125*kg*/*s* and 0.25*kg*/*s*, although the test C_μ of 0.025 was included for comparative purposes.

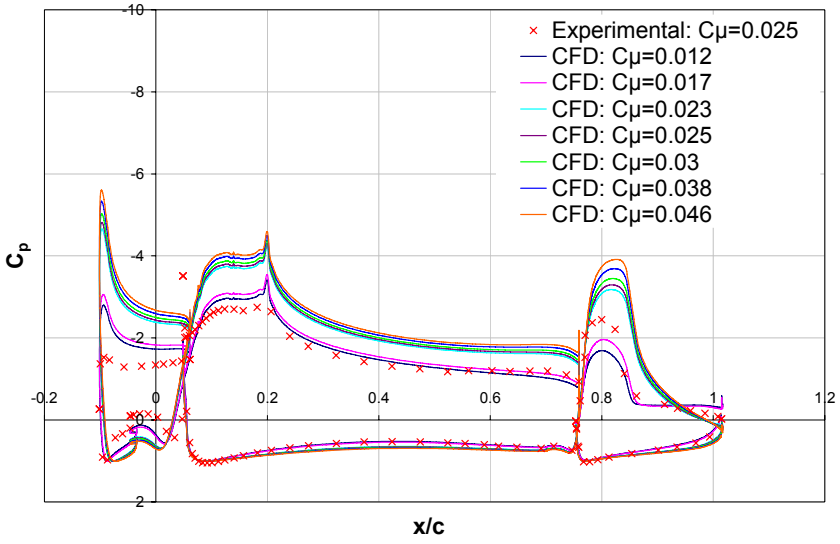

Figure 135: Effect of C_μ on the C_p distribution for the takeoff configuration at α=10°

Figure 135 showed that the suction over the upper surface of the takeoff configuration was progressively heightened with successive increments in C_μ. Note that the most marked increment in suction coincided with the increment in C_μ from 0.017 to 0.023, the latter of which defined the lowest test C_μ for which boundary layer attachment was maintained over the flap upper surface of the configuration.

With regard to the leading edge slat, the numerical solution over-predicted the suction over the upper surface of the slat for all test C_μ implemented in comparison to the experimental data, which once again confirmed the need to resolve discrepancies in

terms of the point of boundary layer transition over the leading edge slat and the effective momentum coefficient, so as to computationally simulate a flow field representative of the experimental setup. Over the lower surface of the slat, the computational solution over-predicted the pressure for all test C_μ, with anomalies over the mid-chord region once again indicative of the complex reverse flow field which the turbulent model was unable to accurately resolve.

Over the upper surface of the main element, implementing a C_μ of 0.012 or 0.017 only marginally heightened the suction over the fore region in comparison to the experimental data and was in good agreement with the wind-tunnel data over the aft $0.5c_{main}$. In contrast, increasing $C_\mu \geq 0.023$ significantly heightened the suction over the entire upper surface of the main element in comparison to the experimental data. Over the lower surface of the main element, the numerical solutions with a C_μ of 0.012 or 0.017 were in good agreement with the wind-tunnel data, although with further increments in $C_\mu \geq 0.023$, an increment in pressure was evident over the mid-chord region when compared to the experimental data.

The influence of C_μ on the flow field development was most prominent over the trailing edge flap. At C_μ of 0.012 or 0.017, the numerical solution underestimated the magnitude of the leading edge suction peak and more critically, was insufficient to prevent boundary layer separation, which occurred over the aft $0.6c_{flap}$. A single increment in C_μ to 0.023 substantially improved the flow field developing over the upper surface of the deflected flap, notably heightening the magnitude of the leading edge suction peak in comparison to the experimental data and delaying boundary layer separation to the trailing edge. Further increments in C_μ, heightened the magnitude of the leading edge suction peak whilst maintaining boundary layer attachment to the trailing edge. Note that the increased static pressure over the aft $0.25c_{flap}$ of the flap upper surface for all $0.023 \leq C_\mu \leq 0.046$ was indicative of a thinner trailing edge boundary layer in comparison to the experimental data. Over the lower surface of the flap, the numerical solutions with a C_μ of 0.012 or 0.017 were in good agreement with the wind-tunnel data, although with further increments in $C_\mu \geq 0.023$, the computations exhibited increased static pressure over the aft $0.5c_{flap}$. The increment in static pressure increased in magnitude with distance downstream and was indicative of a thinner trailing edge boundary layer in comparison to the experimental test data. Significantly, whilst the numerical solution indicated that for test $0.012 \leq C_\mu \leq 0.017$, the jet of blown air was insufficient to maintain boundary layer attachment over the upper surface of the flap, the wind-tunnel data indicated that boundary layer attachment was maintained to the

trailing edge for all test $C_\mu \geq 0.013$. Although, establishing the precise C_μ necessary to achieve boundary layer attachment was limited by the incremental values of C_μ tested, both experimentally and numerically. Recalling that whilst both the experimental and computational solutions indicated that blowing tangentially from a slot at a C_μ of 0.025 prevented boundary layer separation over the upper surface of the flap, the numerical solution suggested that the influence of the active boundary layer control on the developing flow field was far greater than that observed in the wind-tunnel measurements. Accordingly, it was unclear as to the reason why the numerical solution displayed diminished effectiveness of tangential slot blowing at low test C_μ in terms of maintaining boundary layer attachment.

In terms of the lift and drag forces predicted by the numerical simulation, Figure 136 shows that incrementing C_μ from 0.012 to 0.046 increased C_l and decreased C_d. As noted in the C_p distribution, the most marked variation in C_l and C_d coincided with the increment in C_μ from 0.017 to 0.023, correlating to the test C_μ required to prevent boundary layer separation over the upper surface of the flap and accounting for a 25% increment in C_l and a 35% decrement in C_d. With further increments in C_μ between 0.023 and 0.046, C_l was increased by a further 10% and C_d was reduced by a further 8%, corroborating Dods and Watson's (1956) observations that once the value of C_μ necessary to maintain boundary layer attachment was achieved, further increments in C_μ only resulted in moderate increments in C_l.

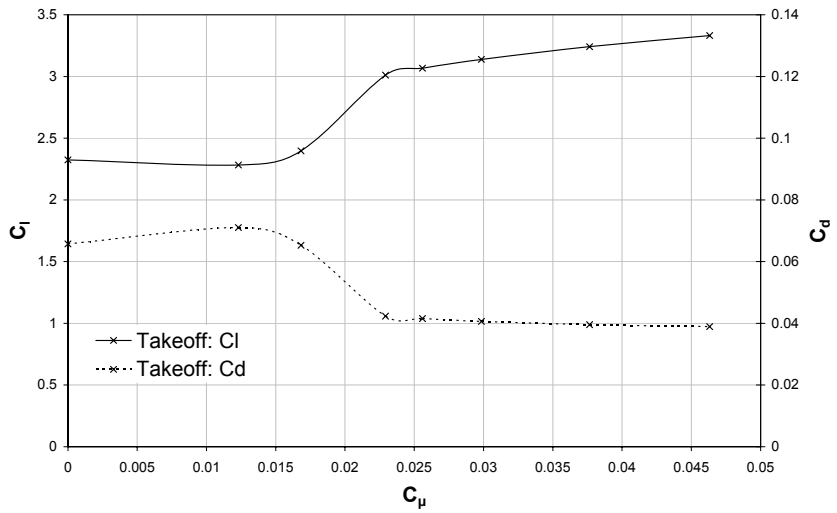

Figure 136: Effect of C_μ on numerically predicted C_l and C_d generated over takeoff configuration at α=10°

8.3.5.2 Effect of Varying the Inclination of the Jet of Air

The numerical simulation required the inclination of the jet of air to be specified, enabling a further element of investigation, not feasible within the limits of the present wind-tunnel study. Typically, the direction of the jet was designated normal to the slot. However, in order to establish whether directional fluctuations of the jet influenced the flow field development over the upper surface of the deflected flap, the orientation of the jet was modified.

Utilising the conventional jet direction normal to the slot as the point of reference, the jet was inclined by −10°, −20° and −30° relative to the normal, towards the upper surface of the flap. Figure 137 shows the effect of inclining the jet of air on the C_p distribution over the takeoff configuration at α=10°.

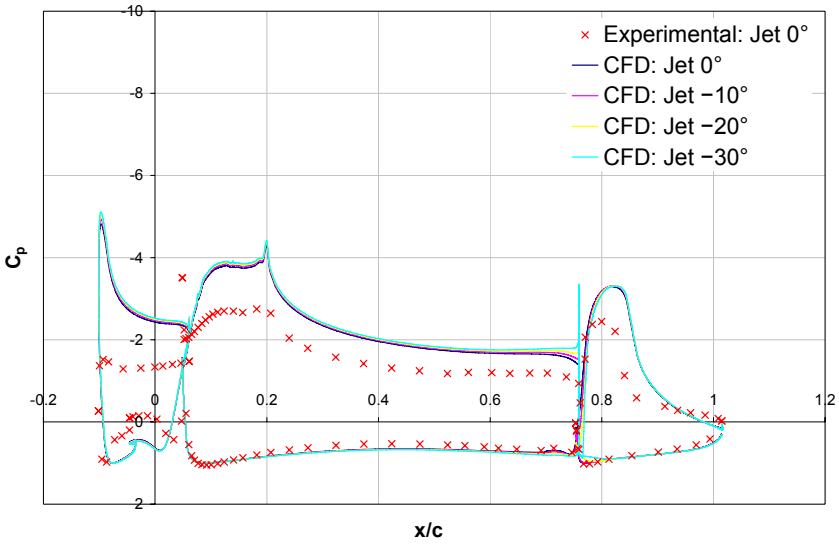

Figure 137: Effect of jet inclination on the C_p distribution for the takeoff configuration at α=10°

From Figure 137 it was evident that inclining the jet towards the flap upper surface tended to progressively heighten the suction over the upper surface of the leading edge slat and main element. This deviation in static pressure due to the jet inclination was most prominent over the aft $0.25c_{main}$ of the main element and was duly attributed to the proximity of the jet source. The spike in the C_p distribution at the trailing edge of the main element upper surface increased in magnitude with increments in jet inclination, correlating to the increasing jet velocities at the slot, predicted by the computational solution. Over the upper surface of the deflected flap, increasing the inclination of the jet towards the upper surface transposed the point of minimum pressure for the leading edge suction peak marginally aft. Accordingly, the suction upstream of C_{pmin} was

marginally decreased with successive increments in the jet inclination from −10° to −30°. Aft of C_{pmin}, variations in the jet inclination had no appreciable effect upon the C_p distribution, with the respective adverse pressure gradients coincident to the trailing edge. Inclination of the jet towards the flap upper surface typically had negligible effect upon the lower surface C_p distribution over the leading edge slat and main element, although marginal discrepancies arose at the trailing edge of the main element, with the static pressure marginally increasing with successive increments in jet inclination. In contrast, increasing the jet inclination towards the flap upper surface progressively reduced the static pressure over the fore $0.2c_{flap}$ of the flap lower surface. However, inclination of the jet of air had negligible effect upon the C_p distribution over the aft $0.8c_{flap}$ of the flap lower surface.

These variations in the C_p distribution due to inclination of the jet of blown air were more tangibly evaluated in terms of the effect upon C_l and C_d. Maintaining a C_μ of 0.025, C_l was increased from 3.07 with the jet trajectory normal to the surface to 3.14 when inclined by −30° to the flap upper surface, accounting for a 3% increment. Conversely C_d was progressively reduced from 0.041 when the jet trajectory was normal to the surface to 0.036 when inclined by −30° to the flap upper surface, correlating to a 13% decrement.

Accordingly, this highlighted the importance of optimising the impingement of the jet of air upon the flap upper surface for all test α. Furthermore, as tangential slot blowing favourably influenced boundary layer development for all jet inclination angles tested this suggested that, based upon the observations of Dods and Watson (1956) and Kelly et al (1958), the point at which the jet of air impinged upon the upper surface of the flap either coincided with or was upstream of the point of minimum pressure on the flap for all test α.

8.4 Chapter Summary

A two-dimensional numerical study was conducted simulating blowing air tangentially from a slot at the trailing edge of the main element over the upper surface of a trailing edge flap within the three-element takeoff configuration. Comparison of the computational simulation with the experimental data indicated that:

- The numerical simulation over-predicted the suction over the upper surface of all three-elements of the takeoff configuration, both with or without tangential slot blowing
- In the absence of tangential slot blowing, the numerical simulation delayed boundary layer separation marginally aft from $0.35c_{flap}$ to $0.5\text{-}0.6c_{flap}$, dependent upon α
- Both the numerical and experimental data indicated that tangential slot blowing prevented boundary layer separation for all test α
- The numerical solution typically over-predicted C_l for the takeoff configuration, both with and without tangential slot blowing, although the increment in C_l due to tangential slot blowing was significantly heightened for the numerical solution
- Unlike the wind-tunnel data, the computational simulation indicated that tangential slot blowing reduced the stall angle from 20° to 16°
- Tangential slot blowing decreased the computationally predicted drag, whereas the experimental data showed that tangential slot blowing increased the pressure drag
- Discrepancies between the computational solution and the experimental data highlighted the need to accurately represent the effective C_μ and accurately simulate the flow field over the leading edge slat of the wind-tunnel model, particularly with regard to the point of boundary layer transition
- $C_\mu \geq 0.023$ were required to prevent boundary layer separation for the numerical model but in contrast, boundary layer attachment was maintained to the trailing edge of the wind-tunnel model for all test $C_\mu \geq 0.013$
- Inclination of jet of air had a favourable effect upon C_l and C_d, highlighting the need to optimise the point of impingement of the jet of air upon the flap upper surface for all test α

9 High-Lift Configuration: Discrete Blowing

This chapter considers the effect of blowing air tangentially from discrete orifices at the trailing edge of the main element over the upper surface of a single slotted flap within a three-element high-lift configuration.

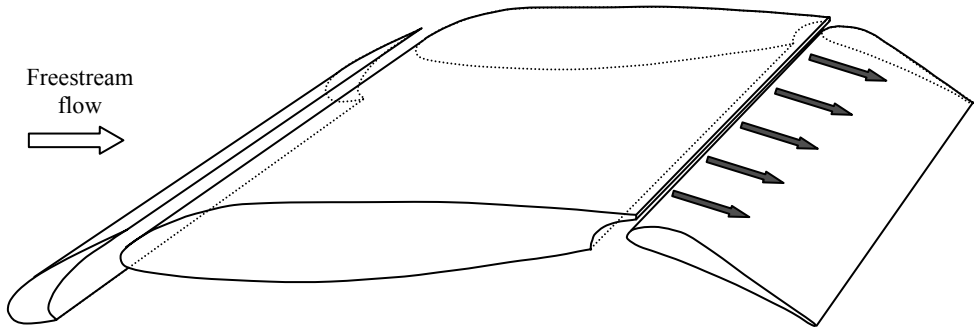

9.1 Introduction

Having established the aerodynamic benefits of conventional tangential slot blowing as a means of preventing boundary layer separation over the upper surface of a single slotted flap within the three-element takeoff configuration in Chapter 7, the trailing edge geometry through which the air was ejected was modified in order to determine whether the mass flow rate and hence, the momentum coefficient, could be reduced without compromising the favourable effect upon the boundary layer control. Due to facility and time limitations, the investigation was not extended to the landing and extended flap configurations, although it would have been interesting to determine whether blowing through discrete trailing edge holes would be more effective in preventing boundary layer separation than conventional tangential slot blowing (see inset in schematic on page xv for further details of discrete hole geometry).

With the lap, gap and deflection angle of the leading- and trailing-edge high-lift devices fixed, the configuration angle of incidence was incremented, both with and without discrete blowing. In the first instance, all discrete orifices at the trailing edge of the main element were left open and the ensuing flow field developing over the high-lift configuration was analysed, primarily by means of the surface static pressure measurements, supplemented by oil flow visualisation over the upper surface of the trailing edge flap. The effectiveness of discrete blowing as a means of delaying boundary layer separation was evaluated relative to the corresponding baseline takeoff configuration in the absence of discrete blowing. Free transition was maintained throughout on each of the three elements and unless otherwise stated, all experiments

were conducted at a nominal freestream velocity of 40m/s, corresponding to a Reynolds number of 1.64×10^6, based upon stowed reference chord.

Similarly to the baseline takeoff configuration in the absence of tangential slot blowing, the surface static pressure distributions for the baseline takeoff configuration in the absence of discrete blowing indicated that the C_p measurements were typically repeatable to within ±0.1. Implementation of discrete blowing marginally reduced the repeatability of the measurements, such that the corrected C_p values were typically repeatable to within ±0.2. However, it should be noted that greater deviation in repeated measurements occurred over the leading edge of the flap upper surface and was hence, directly attributed to the errors incurred by fluctuations in the volume flow rate throughout the data acquisition. In terms of the resultant aerodynamic forces generated over the three-element configuration, C_l was repeatable to within ±1% and C_d was typically repeatable to within ±2%.

9.2 Baseline Takeoff Configuration

Figure 138 shows the C_p distribution for the takeoff configuration at α=4°, 12° and 20°, in the absence of discrete blowing.

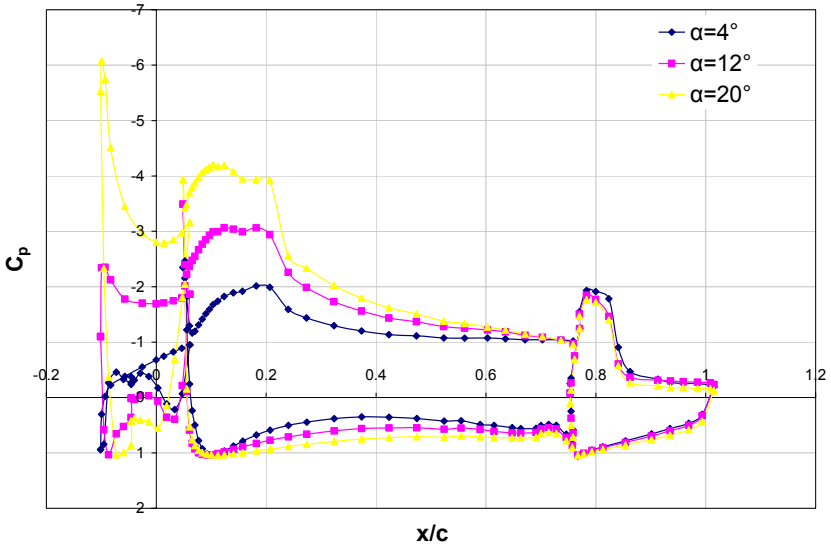

Figure 138: Effect of angle of incidence on C_p distribution for baseline takeoff configuration without discrete blowing

Similarly to the baseline tangential slot blowing takeoff configuration, the C_p distributions for the baseline discrete blowing takeoff configuration indicated that in the absence of blowing, increasing α from 0° to 20° had a marked effect upon the static

pressure distribution over the leading edge slat and the main element, although the C_p distribution over the trailing edge flap appeared relatively insensitive to increments in α.

Whilst the salient attributes of the C_p distributions across the incremental range of α were analogous to those previously identified for the baseline tangential slot blowing takeoff configuration (see Section 7.2 for more details), manufacturing and installation tolerances, together with contrasting surface finishes for the modular trailing edge component, rendered the precise magnitude of the static pressure distributions distinct. Installation of the discrete blowing modular component heightened the suction over the upper surface of all three elements of the takeoff configuration, which was particularly evident over the fore region of the flap upper surface, highlighting the sensitivity of the flow field development to slight inconsistencies in the configuration detail.

Accordingly, the resultant aerodynamic forces determined from integration of the C_p distributions over the three-element baseline takeoff configuration without discrete blowing deviated from those of the baseline takeoff configuration without tangential slot blowing. Specifically, the heightened suction over the upper surface of the baseline configuration without discrete blowing typically yielded greater values of C_l and smaller values of pressure drag than that of the corresponding baseline tangential slot blowing configuration.

Figure 139 shows the C_l-α curve for baseline takeoff configuration without discrete blowing.

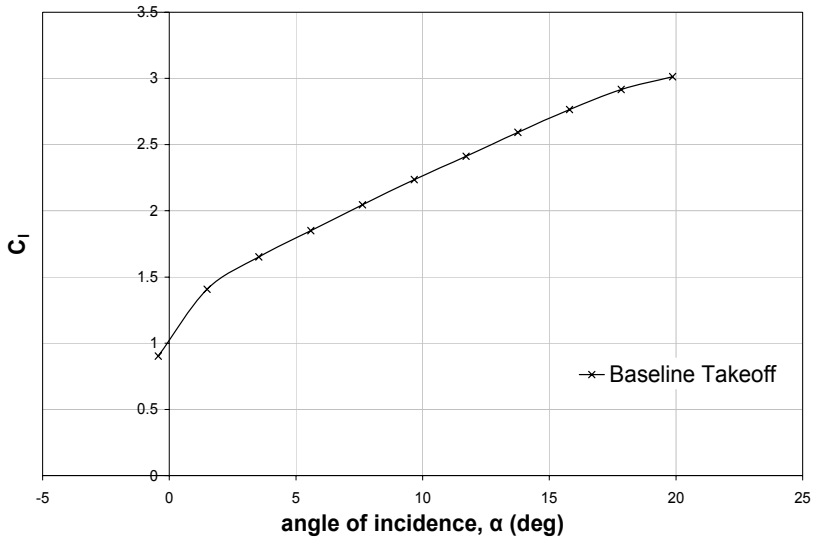

Figure 139: C_l-α curve for baseline takeoff configuration without discrete blowing

A single increment in α from 0° to 2° increased C_l from 0.90 to 1.41, respectively. With further increments in $2° \leq \alpha \leq 16°$, C_l increased approximately linearly with α attaining a C_l of 2.76 at α=16°. Again, the non-linearity of the lift curve at α=0° was attributed to the marked degradation of the flow field over the leading edge slat and main element and the marginal reduction in the lift-curve gradient for $\alpha \geq 18°$ was characteristic of the onset of stall.

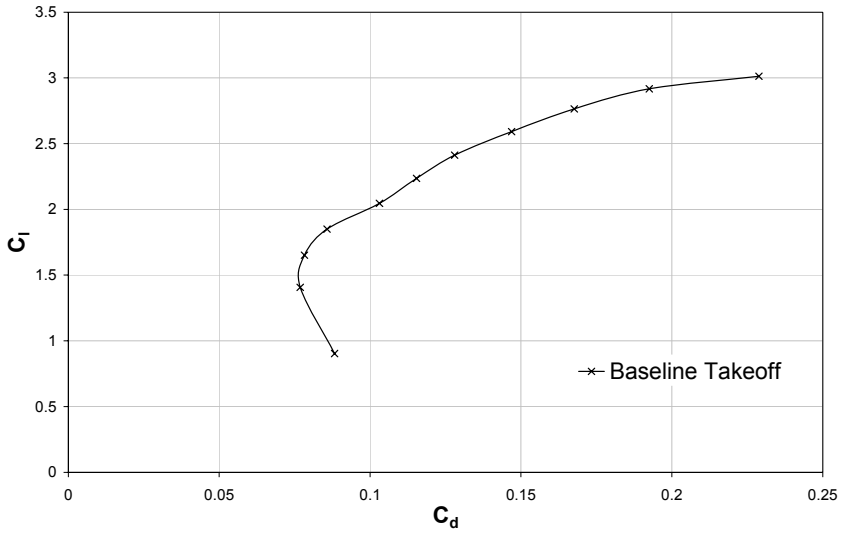

Figure 140: Drag polar for baseline takeoff configuration without discrete blowing

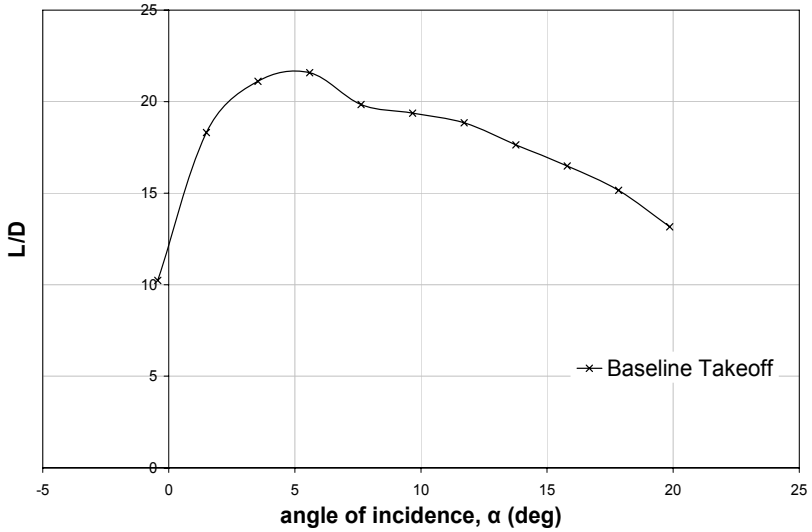

Figure 141: Variation of *L*/*D* with angle of incidence for baseline takeoff configuration without discrete blowing

From Figure 140 it was evident that for increments in $0.9 \leq C_l \leq 1.4$, the pressure drag initially decreased in magnitude from 0.09 to a minimum of 0.08. With further increments in $1.4 < C_l \leq 2.0$, C_d progressively increased in magnitude to 0.11 and with

further increments in C_l>2.0, the increment in C_d was notably heightened, attaining a maximum value of 0.23 at the measured C_{lmax} of 3.0, coinciding with the upper test limit of α=20°. Note that the pressure drag was determined purely from the integration of the surface static pressure distribution. Amalgamation of C_l and C_d in terms of L/D indicated that by incrementing α from 0° to 6°, L/D increased from 10.2 to a maximum of 21.6, see Figure 141. With further increments in α>6°, L/D progressively decreased in magnitude to 13.2 at α=20°.

9.3 Takeoff Configuration with Discrete Blowing

Although measurements confirmed that the temperature of the jet of air at the orifice exit was approximately ambient, attempts to establish the velocity of the jet of air were thwarted by the sensitivity of the measurement to the precise position of the total pressure probe relative to the discrete orifices. Thus, assuming no appreciable variation in density, the velocity of the jet of air was determined theoretically by means of the equation of continuity, based upon the known volume flow rate. Accordingly, a nominal C_μ of 0.025 was maintained, corresponding to a freestream velocity of 40m/s. Once again, the losses incurred within the system and variations in the jet velocity across the span of the model were not taken into consideration.

9.3.1 Effect of Discrete Blowing on C_p Distribution

Figure 142(a)-(k) shows the effect of blowing from discrete orifices at the trailing edge of the main element over a deflected single slotted flap in the three-element takeoff configuration.

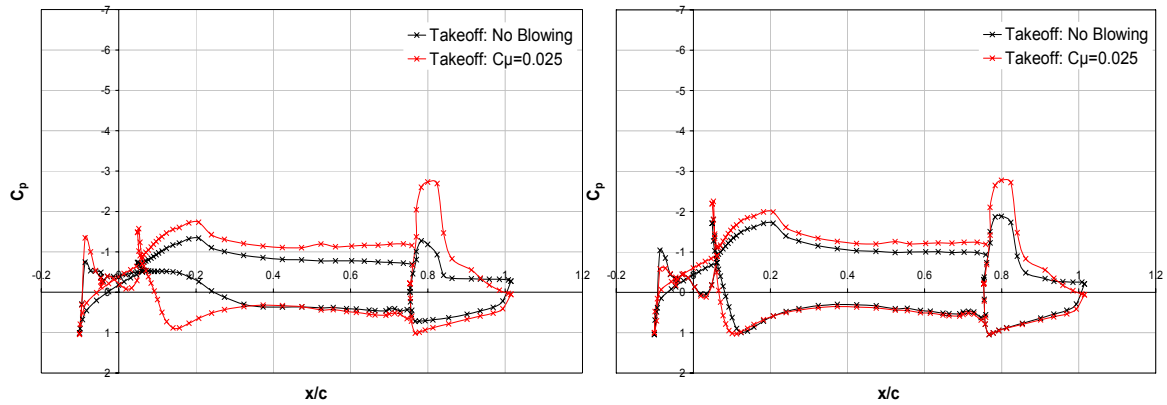

(a) α=0° **(b) α=2°**

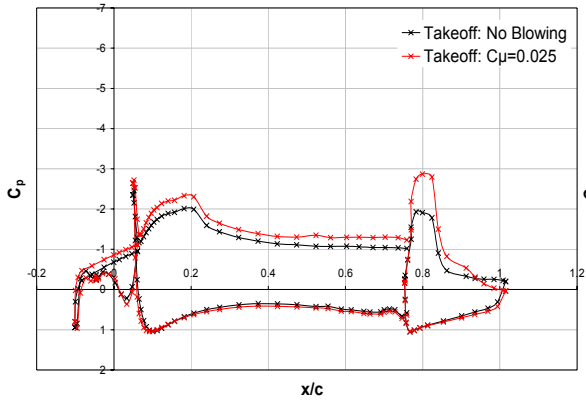

(c) α=4°

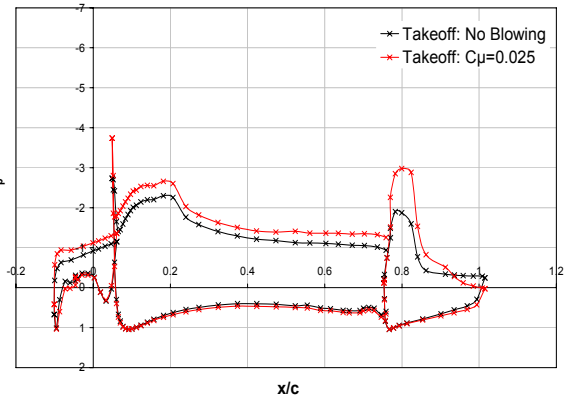

(d) α=6°

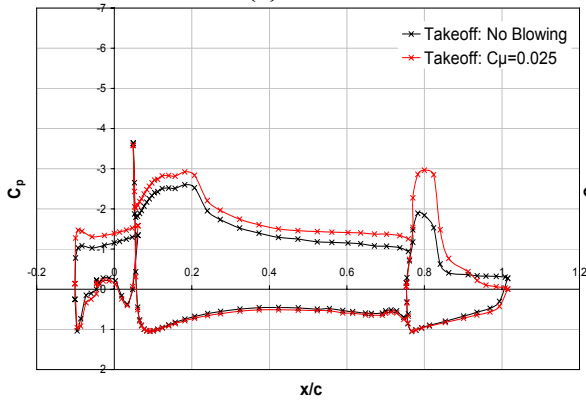

(e) α=8°

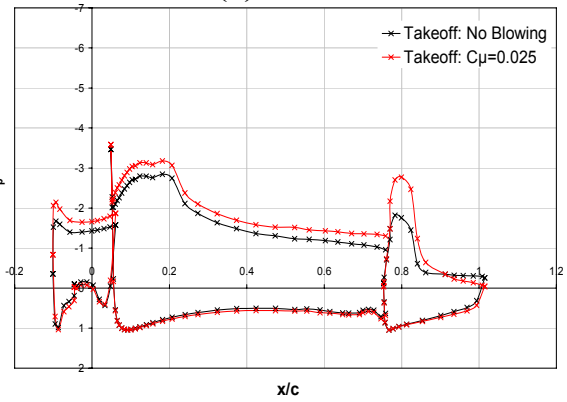

(f) α=10°

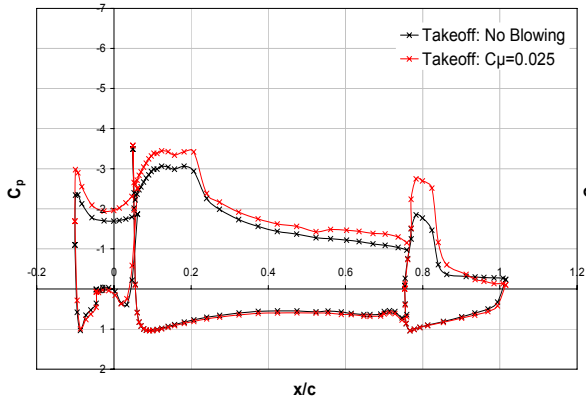

(g) α=12°

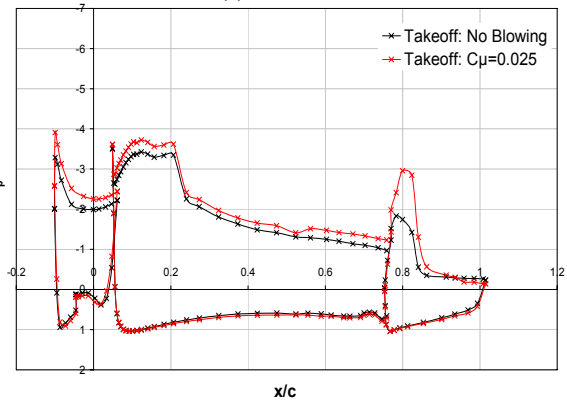

(h) α=14°

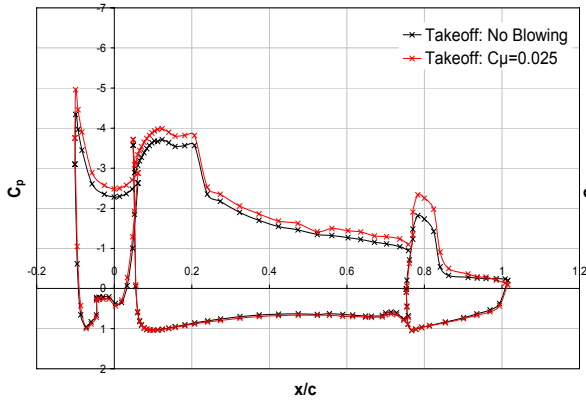

(i) α=16°

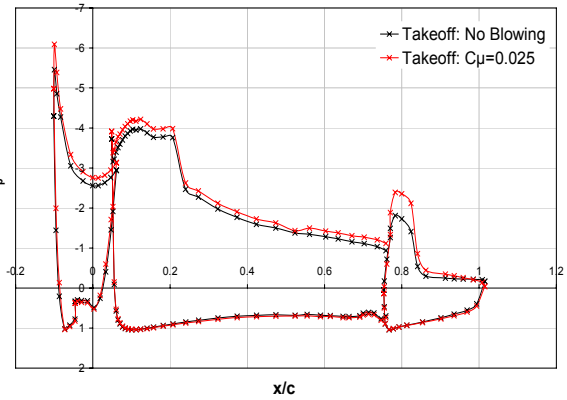

(j) α=18°

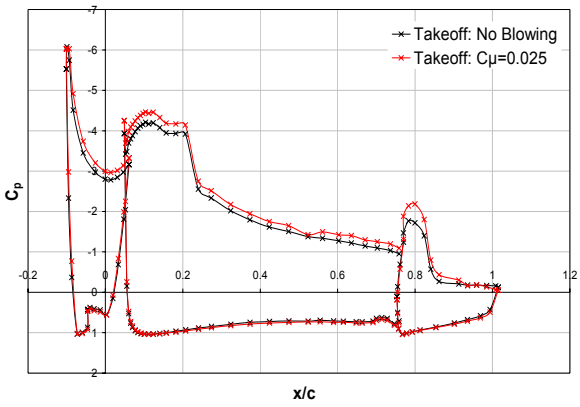

(k) α=20°

Figure 142(a)-(k): Effect of discrete blowing on the C_p distribution over the takeoff configuration, 0°≤α≤20°

As expected, the application of discrete blowing significantly influenced the flow field developing over the fore region of the flap upper surface. However, the influence of the discrete blowing extended upstream, modifying the surface static pressure distribution over both the main element and leading edge slat. Note that the latter was contrary to that exhibited by the application of tangential slot blowing, which had no appreciable effect upon the flow field developing over the leading edge slat, for all test α.

Figure 142(a) and (b) showed that due to the degradation in the flow field developing over the leading edge slat for 0°≤α≤2°, distinct trends regarding the effect of discrete blowing were difficult to ascertain, although it was evident that the flow field was modified by the application of discrete blowing. However for α≥4°, Figure 142(c) through to Figure 142(k) showed that discrete blowing distinctly heightened the suction over the upper surface of the leading edge slat in comparison to the baseline configuration. Over the lower surface of the leading edge slat, discrete blowing typically had no appreciable effect upon the C_p distribution, with the exception of marginal increments in static pressure over the mid-chord region for 4°≤α≤14°.

Considering the main element, discrete blowing markedly heightened the suction over the upper surface in comparison to the baseline configuration at α=0°, see Figure 142(a). Whilst the magnitude of the increment was relatively consistent across the extent of the chord, ΔC_p was marginally heightened over the aft $0.2c_{main}$. In addition to the suction peak at $0.2c_{main}$, discrete blowing modified the flow field such that an additional distinct suction peak was generated at the foremost point on the upper surface leading edge at α=0° – an attribute which only became apparent on the baseline configuration at α=2°. The location of the first suction peak was independent of α,

whereas the location of the local C_{pmin} for the second suction peak was transposed upstream from $0.2c_{main}$ for $0° \leq \alpha \leq 10°$ to $0.1c_{main}$ for $\alpha \geq 12°$. Discrete blowing heightened the suction over the entire upper surface for $\alpha \geq 2°$ (see Figure 142(b) through to Figure 142(k)). For $2° \leq \alpha \leq 10°$, ΔC_p was relatively consistent across the extent of the chord, although with further increments in $\alpha \geq 12°$, the increment in suction was greatest over the fore $0.3c_{main}$ of the main element upper surface and decreased in magnitude thereafter. The reduction in static pressure over the upper surface suggested that discrete blowing increased the trailing edge boundary layer thickness in comparison to the baseline configuration.

Over the lower surface of the main element, discrete blowing increased the static pressure at $\alpha=0°$, generating a distinct stagnation point at $0.15c_{main}$, see Figure 142(a). The increment in pressure was greatest over the fore $0.4c_{main}$ and was marginalised over the mid-chord region, although the increment in static pressure increased in magnitude over the aft $0.4c_{main}$, suggesting that the discrete blowing reduced the trailing edge boundary layer thickness in comparison to the corresponding baseline configuration. Whilst at $\alpha=2°$, Figure 142(b) showed that discrete blowing transposed the stagnation point marginally upstream from $0.1c_{main}$ to $0.07c_{main}$, with further increments in $\alpha \geq 4°$, Figure 142(c) through to Figure 142(k) showed that discrete blowing had no appreciable effect upon the location of the stagnation point on the lower surface of the main element. Upstream of the stagnation point, discrete blowing increased the leading edge static pressure for $2° \leq \alpha \leq 4°$, although any deviation in static pressure due to discrete blowing was negated for $\alpha \geq 6°$. Aft of the stagnation point, discrete blowing typically had no appreciable effect upon the lower surface C_p distribution for $\alpha \geq 2°$ (see Figure 142(b) through to Figure 142(k)).

As expected, the effect of discrete blowing was most prominent over the upper surface of the trailing edge flap for any given test α, considerably heightening the leading edge suction over the fore $0.4c_{flap}$. Quantifying the increment in suction by means of the measured C_{pmin}, it was evident that discrete blowing had maximum effect upon the leading edge suction at $\alpha=0°$, heightening C_{pmin} from -1.27 for the baseline configuration to -2.73, see Figure 142(a). With further increments in $\alpha \geq 2°$, there was a tendency for the decrement in leading edge static pressure to progressively reduce in magnitude such that at $\alpha=20°$, blowing tangentially from the discrete orifices at the trailing edge of the main element only accounted for a ΔC_{pmin} of -0.4, see Figure 142(k). For any given $\alpha \leq 14°$, Figure 142(a) through to Figure 142(h) showed that discrete blowing transposed the location of the measured C_{pmin} marginally aft from

$0.1c_{flap}$ to $0.2c_{flap}$, although with subsequent increments in $\alpha \geq 16°$, Figure 142(i) through to Figure 142(k) showed that the location of the measured C_{pmin} was unaffected by discrete blowing. Aft of $0.4c_{flap}$, the increment in suction due to the discrete blowing was marginalised in magnitude. For $\alpha \leq 10°$, discrete blowing typically increased the static pressure over the aft $0.3c_{flap}$ in comparison to the corresponding baseline configuration, with the increment increasing in magnitude with distance downstream for any given α. This increment in trailing edge static pressure for any given $\alpha \leq 10°$ was indicative of discrete blowing promoting an attached thinner boundary layer to within close proximity of the trailing edge, although the trailing edge boundary layer increased in thickness with successive increments in α. Most significantly, blowing from discrete orifices at a nominal C_μ of 0.025 delayed boundary layer separation from $0.35c_{flap}$ to within close proximity of the trailing edge for $\alpha \leq 10°$, see Figure 142(a) through to Figure 142(f).

This delay in boundary layer separation, from $0.35c_{flap}$ to within close proximity of the trailing edge for $\alpha \leq 10°$, was corroborated by the corresponding oil surface flow visualisation over the upper surface of the trailing edge flap. Note that the direction of the flow (denoted by U_∞) was from right to left in all photographs. Figure 143 is representative of these results.

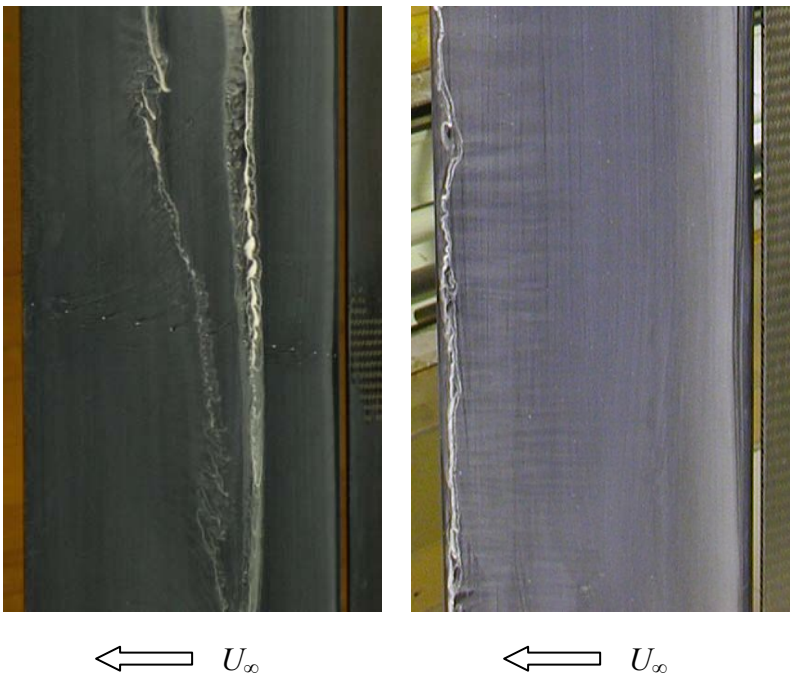

Figure 143(a) and (b): Oil flow visualisation over the flap upper surface for the takeoff configuration at α=6°, (a) without and (b) with discrete blowing

At α=6°, Figure 143(a) showed that in the absence of blowing boundary layer control, the upper surface boundary layer separated at approximately $0.3c_{flap}$, aft of which, a highly three-dimensional region of recirculating flow was evident. Figure 143(b) substantiated the C_p distributions and provided further evidence that discrete blowing delayed boundary layer separation to within close proximity of the trailing edge.

It should be noted that for any given α, the flow field development over the upper surface of the flap, when subject to discrete blowing, was highly sensitive to variations in the jet velocity and inconsistencies in the model surface finish, resulting in localised regions of premature boundary layer separation across the span. This sensitivity was heightened with successive increments in test α and exacerbated at locations coincident with the internal spars, the latter of which obstructed the jet of air. Furthermore, by the process of manufacture, drilling discrete orifices into the solid section at the trailing edge of the modular main element component rendered the internal surfaces of the orifices uneven. Whilst attempts were made to smooth the surface of each internal orifice cavity, irregularities were still evident, particularly in the form of obstructive material fibres. The cumulative effect was to locally diminish the effectiveness of discrete blowing as a means of maintaining boundary layer attachment. In addition, three-dimensional anomalies, induced by separation over the outer span regions, were also heightened at high test α, entraining fluid into localised regions of recirculating flow. With all discrete orifices open, such anomalies were observed along the spanwise centreline for all test α and accordingly, the photographs presented herein illustrate spanwise extents typifying the flow field development. Similarly to the tangential slot blowing configuration, the flow visualisation suggested that by addressing the defects within the boundary layer control system to ensure uniform jet velocity and eliminating orifice/surface irregularities to within manufacturing tolerances, boundary layer attachment could be maintained to within close proximity of the trailing edge over a significant proportion of the span, thereby reducing the extent of localised regions of boundary layer separation.

At α=10°, the oil flow visualisation over the upper surface of the trailing edge flap highlighted that the region of trailing edge separation began to extend marginally upstream, typically encompassing the aft $0.05\text{-}0.1c_{flap}$ when discrete blowing was applied, see Figure 144.

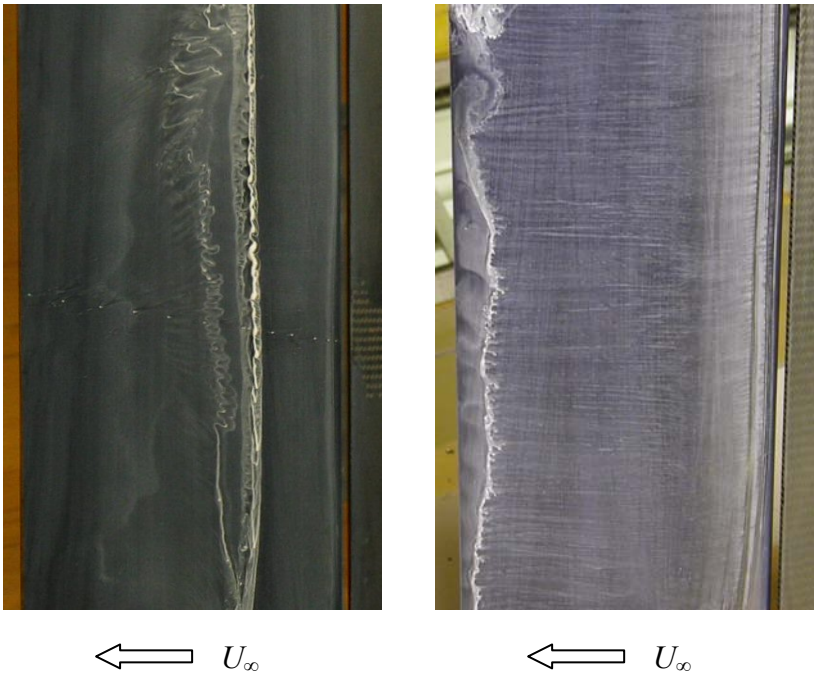

Figure 144(a) and (b): Oil flow visualisation over the flap upper surface for the takeoff configuration at α=10°, (a) without and (b) with discrete blowing

With further increments in $\alpha \geq 12°$, the discrete blowing at a momentum coefficient of 0.025 was insufficient to maintain boundary layer attachment to within close proximity of the trailing edge. Whilst this extension of the region of trailing edge boundary layer separation was not definitive from the C_p distributions, the corresponding oil flow visualisation explicitly illustrated the increased region of boundary layer separation at high test α. Accordingly, the point of boundary layer separation was progressively transposed upstream with successive increments in α, from $0.9c_{flap}$ at α=12° to $0.7c_{flap}$ at α=20°.

Figure 145 illustrates the flow field development over the upper surface of the trailing edge flap in the takeoff configuration at α=16°. Figure 144(a) and Figure 145(a) show that in the absence of discrete blowing, the salient features of the flow field were comparable to those previously described, with separation occurring at approximately $0.3c_{flap}$. However the increased region of trailing edge separation was clearly evident in Figure 144(b) and Figure 145(b), when compared to Figure 143(b).

Thus, at high test α, discrete blowing merely delayed the point of boundary layer separation. Note that for both configurations, the point of boundary layer separation varied along the span, which may be attributed to local variations in the jet velocity previously described.

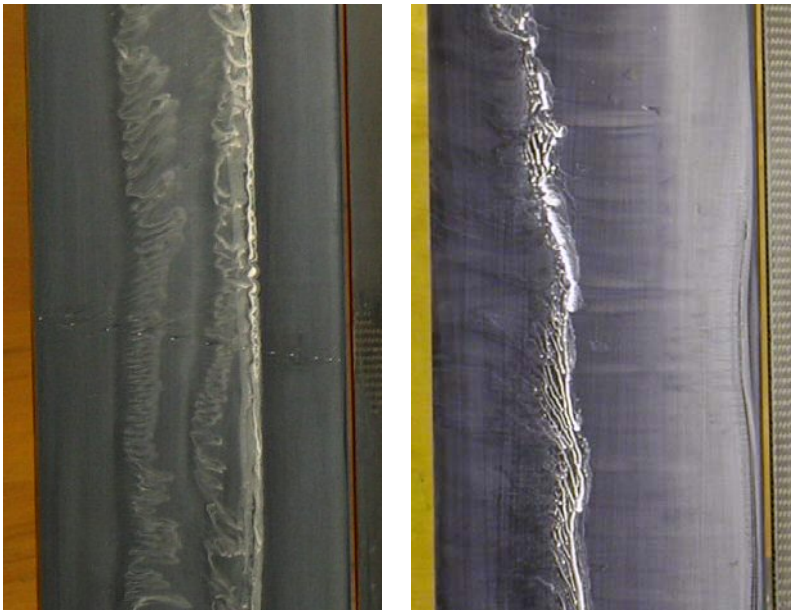

Figure 145(a) and (b): Oil flow visualisation over the flap upper surface for the takeoff configuration at α=16°, (a) without and (b) with discrete blowing

Over the lower surface of the trailing edge flap, discrete blowing notably increased the static pressure in comparison to the baseline configuration at α=0°, corresponding to a thinner boundary layer as a result of the blowing boundary layer control, see Figure 142(a). However, Figure 142(b) through to Figure 142(k) showed that subsequent increments in $\alpha \geq 2°$ essentially negated any variation in static pressure due to discrete blowing over the fore $0.4c_{flap}$ of the flap lower surface, although the static pressure was increased over the aft $0.6c_{flap}$, with ΔC_p increasing in magnitude with distance downstream towards the trailing edge for any given α and once again, indicative of a reduced boundary layer thickness in comparison to the corresponding baseline configuration.

In terms of maintaining boundary layer attachment over the upper surface of the flap, comparison of the effectiveness of discrete blowing and tangential slot blowing was difficult to accurately evaluate for the given experimental setup due to the spanwise variations in the local jet velocity, particularly for the tangential slot blowing configuration. Accordingly, based upon the present quantitative and qualitative data, it was concluded that tangential blowing either from a slot or discrete holes at the trailing edge of the main element over the upper surface of a single slotted flap at a nominal C_μ of 0.025 prevented boundary layer separation aft of $0.35c_{flap}$ and maintained boundary layer attachment to within close proximity of the trailing edge flap for $\alpha \leq 10°$. With

further increments in $\alpha \geq 12°$, discrete blowing at a nominal C_μ of 0.025 was insufficient to prevent boundary layer separation over the upper surface of the flap and trailing edge separation extended upstream with successive increments in α. In contrast, the C_p distributions and surface oil flow visualisation indicated that tangential slot blowing maintained boundary layer attachment to within close proximity of the trailing edge along the spanwise centreline. This suggested that for $\alpha \geq 12°$, tangential slot blowing was more effective in preventing boundary layer separation over the upper surface of the flap than blowing from the discrete holes. However, the substantial regions of separation developing over the upper surface of the flap when subject to tangential slot blowing, often within relatively close proximity to the spanwise centreline, cannot be ignored. Thus, in order to definitively confirm that tangential slot blowing could effectively prevent boundary layer separation across a significant spanwise extent, the defects within the tangential slot blowing boundary layer control system need to be addressed and the experiments repeated with near uniform spanwise jet velocity across the slot.

9.3.2 Effect of Discrete Blowing on the Aerodynamic Forces

Figure 146 shows that blowing over the flap upper surface from discrete holes at the trailing edge of the main element with a C_μ of 0.025 had a favourable effect upon C_l for all test α.

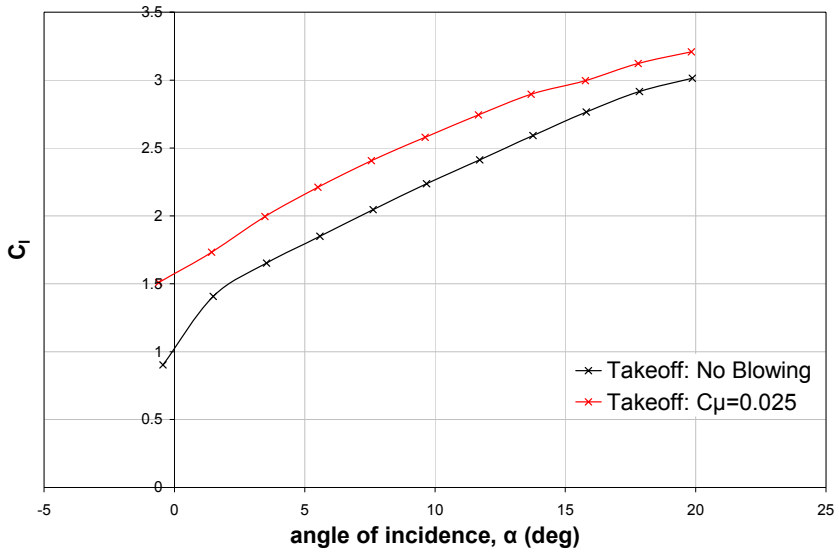

Figure 146: C_l-α curve for takeoff configuration, with and without discrete blowing

ΔC_l attained a maximum value of 0.61 at α=0°, accounting for a 67% increment in comparison to the corresponding baseline configuration. For $2° \leq \alpha \leq 12°$, ΔC_l due to discrete blowing was relatively consistent in magnitude, varying between 0.33 and 0.36,

see Figure 147 for further clarification. The corresponding percentage increments progressively decreased in magnitude from 23% at α=2° to a 14% increment at α=12°. With successive increments in $\alpha \geq 14°$, ΔC_l due to discrete blowing steadily decreased in magnitude from 0.30 at α=14° to 0.20 at α=20°, accounting for a 12% and 6% increment, respectively, in comparison to the corresponding baseline configuration without blowing boundary layer control.

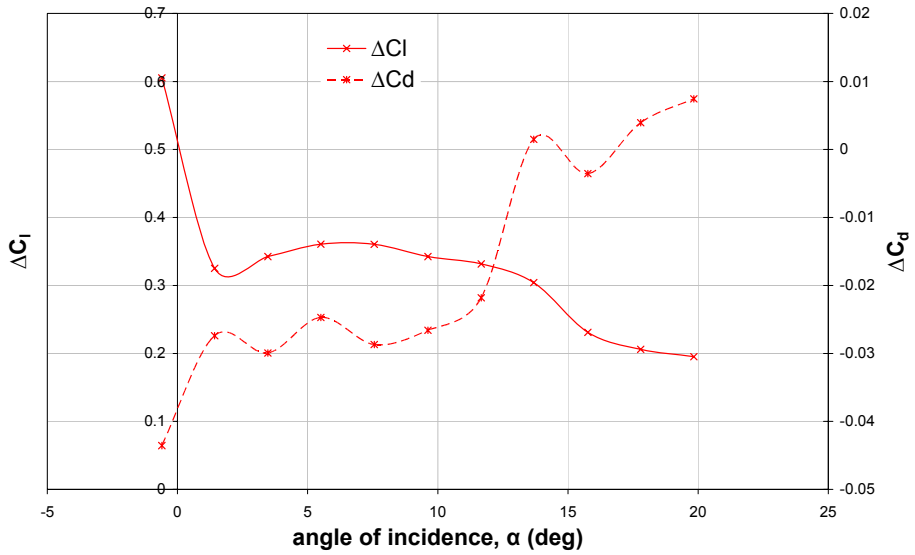

Figure 147: Variation of ΔC_l and ΔC_d with angle of incidence due to discrete blowing for takeoff configuration

Note that at a C_μ of 0.025, the increment in C_l due to discrete blowing for any given test α was of greater magnitude than that generated by blowing air tangentially from a trailing edge slot over the upper surface of the flap. Furthermore, the increment in C_l due to discrete blowing was far more consistent across the range of α tested than that for tangential slot blowing, whereby ΔC_l progressively decreased in magnitude with successive α. Thus, the preliminary evaluation indicated that modifying the trailing edge geometry through which the jet of air was ejected, from a conventional slot to discrete orifices, had a highly favourable effect upon the resultant lift force generated over the takeoff configuration for any given $0° \leq \alpha \leq 20°$.

In contrast to the configuration with tangential slot blowing, blowing air from discrete orifices at the trailing edge of the main element decreased the pressure drag in comparison to the corresponding baseline configuration for any given C_l over a comparable range, see the drag polar in Figure 148.

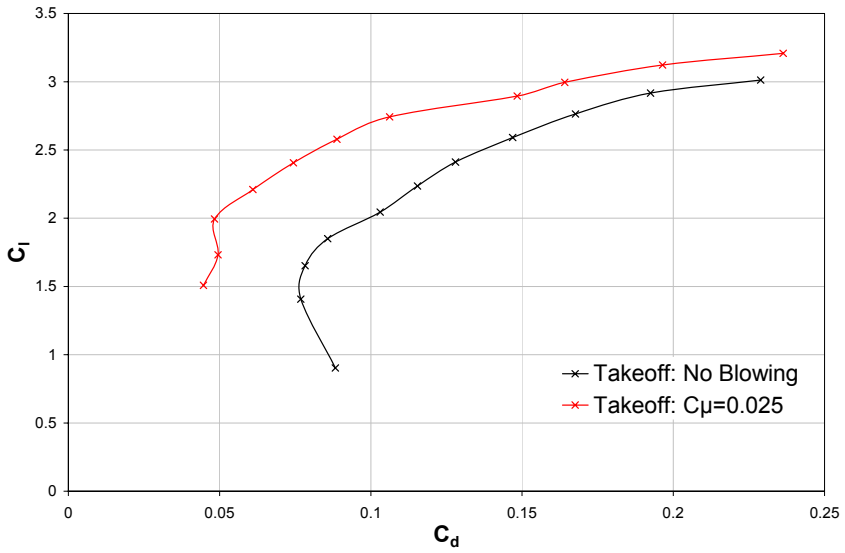

Figure 148: Drag polar for takeoff configuration, with and without discrete blowing

The decrement in pressure drag due to discrete blowing is clarified in Figure 147. Accordingly, Figure 147 showed that the decrement in pressure drag due to discrete blowing tended to decrease in magnitude with successive increments in α from −0.044 at α=0° to −0.022 at α=12°, correlating to a 50% and 17% decrement in C_d, respectively, in comparison to the baseline configuration. With further increments in $\alpha \geq 14°$, any variation in pressure drag due to discrete blowing was near negligible, accounting for less than a 2% variation in comparison to the baseline configuration.

Thus, based upon the pressure drag, Figure 149 shows that discrete blowing increased L/D in comparison to the baseline configuration for any given test α. The increment in L/D due to discrete blowing was greatest at low test α, varying between 16.7 and 23.5 for $0° \leq \alpha \leq 4°$. For $\alpha \geq 4°$, the increment in L/D due to discrete blowing progressively decreased in magnitude, such that the increment in L/D was 7.0 at α=12°, accounting for a 37% increment in comparison to the corresponding baseline configuration. With further increments in $\alpha \geq 14°$, the increment in L/D was markedly reduced in magnitude, decreasing from 1.9 α=14° to 0.4 at α=20°, corresponding to an 11% and 3% increment in comparison to the corresponding baseline takeoff configurations, respectively. However, it was once again recognised that consideration of the pressure drag alone, obtained purely from the integration of the surface static pressure distribution, limited the accuracy with which the aerodynamic performance of the configuration could be evaluated in terms of L/D.

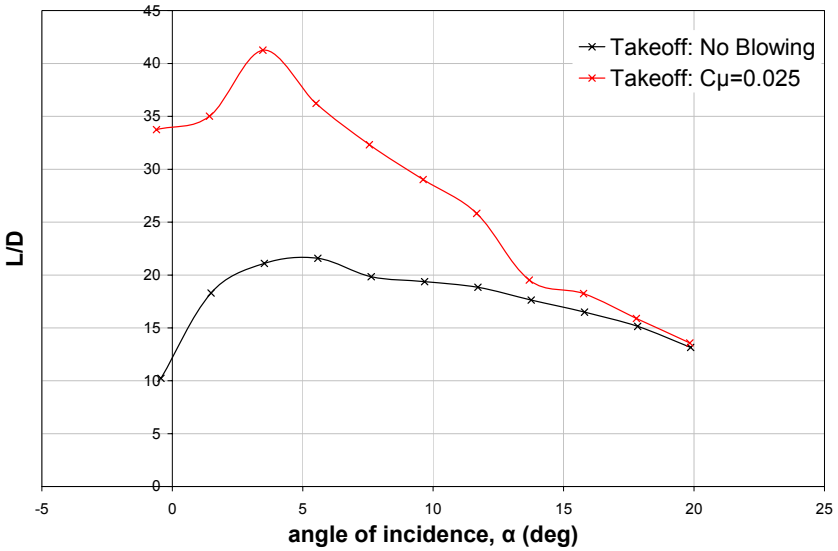

Figure 149: Variation of *L*/*D* with angle of incidence for takeoff configuration, with and without discrete blowing

9.3.3 Effect of C_μ on C_p Distribution

The volume flow rate was increased from 4600 litres per minute to 6600 litres per minute in intervals of 400 litres per minute and the corresponding momentum coefficient was calculated, based upon theoretical approximations of the jet velocity.

Figure 150 shows the effect of C_μ on the surface static pressure distribution over the takeoff configuration at α=8°. As expected, the influence of discrete blowing on the developing flow field was most prominent over the upper surface of the trailing edge flap. However, the influence of the active boundary layer control extended upstream, heightening the suction over the upper surface of the main element and the leading edge slat with successive increments in C_μ.

Recall that for the baseline takeoff configuration at α=8°, the boundary layer separated at $0.35c_{flap}$ over the upper surface of the flap. In contrast, the C_p distributions in Figure 150 indicated that discrete blowing maintained boundary layer attachment to within close proximity of the trailing edge for all test $0.012 \leq C_\mu \leq 0.025$. Furthermore, the suction was progressively heightened over the fore $0.7c_{flap}$ of the flap upper surface with successive increments in C_μ, although ΔC_p decreased in magnitude aft of $0.3c_{flap}$. Aft of $0.7c_{flap}$ on the flap upper surface, the trailing edge static pressure was progressively increased with successive increments in C_μ when compared to the baseline configuration, with the increment increasing in magnitude with distance downstream for

any given test C_μ. This increment in static pressure was indicative of a reduction in trailing edge boundary layer thickness with successive increments in C_μ. An increment in static pressure was also evident over the aft $0.4c_{flap}$ of the lower surface of the flap, again increasing in magnitude both with distance downstream for any given C_μ and with successive increments in C_μ. Similarly to the upper surface, this increment in static pressure on the lower surface was indicative of a reduction in trailing edge boundary layer thickness with successive increments in C_μ. Thus, whether discrete blowing or tangential slot blowing was applied, the C_p distributions indicated that boundary layer attachment was maintained to within close proximity of the trailing edge for all test C_μ.

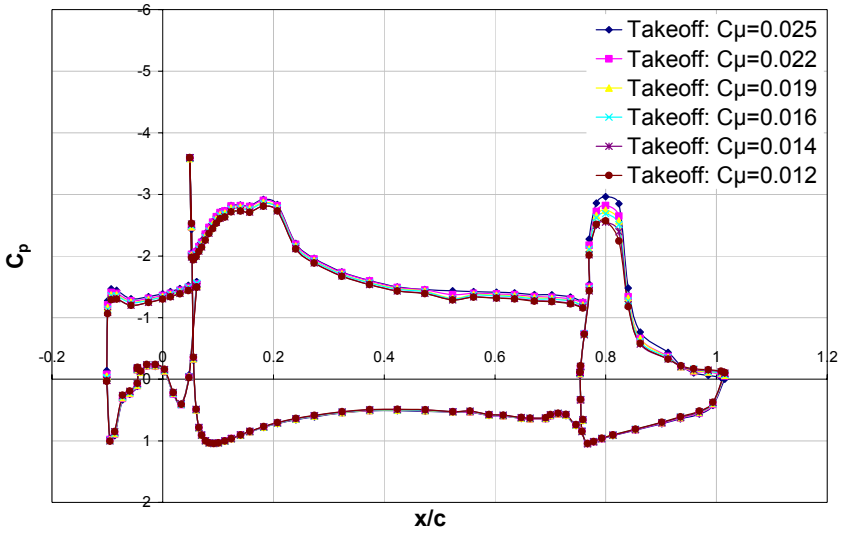

Figure 150: Effect of C_μ on C_p distribution for takeoff configuration at α=8°

Integration of the respective surface static pressure distributions indicated that C_l increased from 2.26 at a C_μ of 0.012 to a C_l of 2.41 at a C_μ of 0.025, accounting for a 6% increment in C_l, which was comparable to the percentage increment in C_l achieved by tangential slot blowing for $0.013 \leq C_\mu \leq 0.029$. Furthermore, there was a tendency for the corresponding pressure drag to decrease in magnitude with successive increments in C_μ between 0.012 and 0.025, varying from a maximum of 0.08 to a minimum of 0.074 and correlating to a 7% decrement in pressure drag over the range of C_μ tested.

In comparison to the corresponding baseline configuration, discrete blowing at a C_μ of 0.012 and 0.025 correlated to an increment in C_l of 0.22 and 0.36, respectively. Thus, the increment in C_l achieved by discrete blowing at the lower test C_μ of 0.012 was comparable to the increment in C_l attained by tangential slot blowing at a C_μ of 0.025. Whilst it was recognised that the data was limited to a single test configuration at α=8°, this suggested that the mass flow rate – and hence the momentum coefficient – could be

reduced for the discrete blowing configuration and whilst there would be attendant decrement in ΔC_l, discrete blowing would still prove more favourable than tangential slot blowing in terms of increasing the resultant C_l generated over the takeoff configuration.

9.3.4 Effect of Varying the Distance between Successive Discrete Orifices

Noting that the results obtained thus far for discrete blowing comprised orifices with 4*mm* between successive centres, a limited study was conducted to determine whether the favourable effect of discrete blowing on the flow field development over the upper surface of the trailing edge flap was thwarted by increasing the distance between successive discrete orifices.

Scaling the distance between two successive discrete orifices upon the orifice diameter (d), the distance between two successive orifices was initially increased from 2d to 4d. Similarly to the configuration with 2d between successive orifice centres,
Figure 151(a) shows that discrete blowing prevented boundary layer separation at $0.35c_{flap}$ and maintained boundary layer attachment to within close proximity of the flap trailing edge for $0° \leq \alpha \leq 2°$.

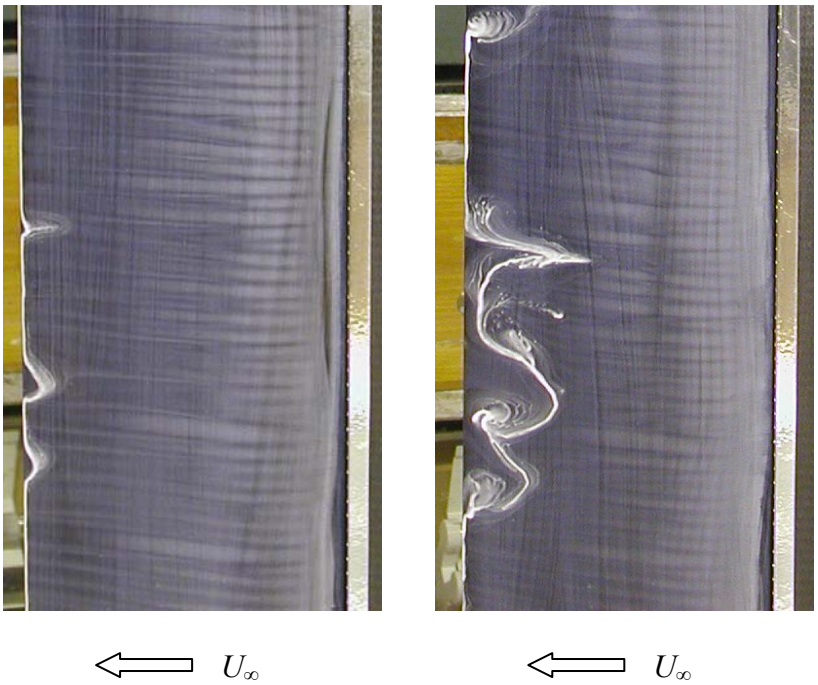

Figure 151(a) and (b): Oil flow visualisation over the flap upper surface for the takeoff configuration with discrete blowing, 4*d* between orifice centres, at (a) α=2° and (b) α=6°

However, increasing α to 4° provoked distinct regions of localised trailing edge separation, which were duly exacerbated with successive increments in α.
Figure 151(b) demonstrates the upper surface flow field of the flap at α=6°, with isolated regions of separation encompassing the aft $0.3c_{flap}$ at its maximum extent.

Noting that marginal fluctuations in the separation line were evident at α=2° at comparable spanwise locations to those at α=6°, it was plausible that the localised regions of trailing edge boundary layer separation coincided with a degradation in the local jet velocity, previously identified. Whether the degradation in the discrete blowing jet arose from surface irregularities of the internal orifice cavity or due to an obstruction from an internal strengthening spar, it was proposed that increasing the distance between successive discrete orifices from 2*d* to 4*d* heightened the sensitivity of the developing flow field to variations in the discrete jets of blown air.

Increasing the distance between successive discrete orifices to 6*d* heightened the degradation in the developing flow field over the upper surface of the flap for any given α. Figure 152(a) shows that whilst discrete blowing was able to maintain boundary layer attachment to within close proximity of the flap trailing edge across a limited spanwise extent at α=2°, the effectiveness of discrete blowing as a means of promoting boundary layer attachment was diminished with further increments in α. Accordingly, Figure 152(b) illustrates that at α=6°, blowing through discrete orifices, positioned at intervals of 6*d*, was insufficient to maintain boundary layer attachment to within close proximity of the trailing edge at any spanwise location. This dramatically contrasted the flow field over the upper surface of the flap in Figure 143(b), the latter of which showed that with 2*d* between successive orifices, discrete blowing maintained boundary layer attachment to within close proximity of the trailing edge across the comparable spanwise extent at α=6°.

Increasing the distance between successive discrete trailing edge orifices to 8*d* rendered the application of discrete blowing insufficient to maintain boundary layer attachment for any given test α. Flow visualisation at α=0° indicated that the boundary layer typically separated aft of approximately $0.5c_{flap}$.

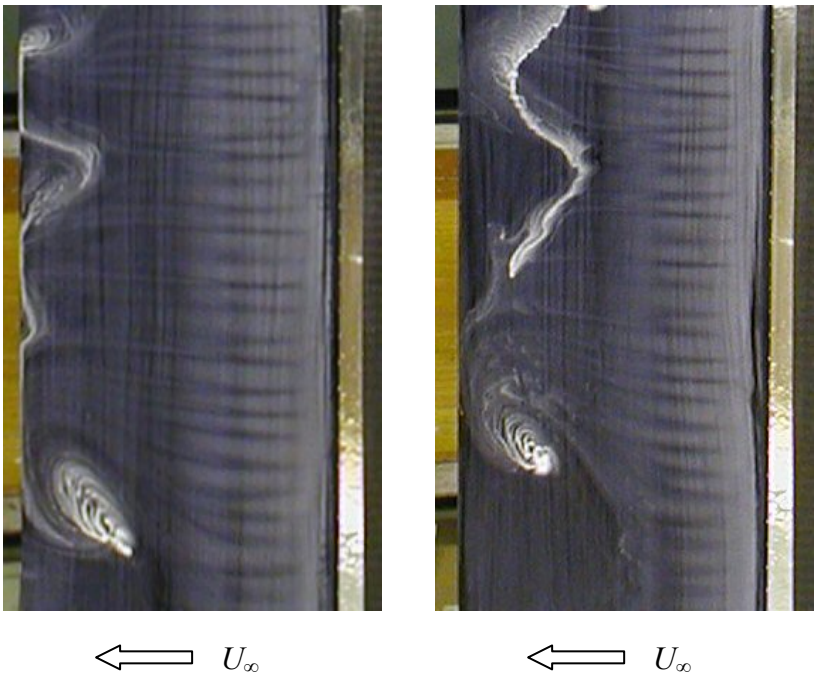

Figure 152 (a) and (b): Oil flow visualisation over the flap upper surface for the takeoff configuration with discrete blowing, 6*d* between orifice centres, at (a) α=2° and (b) α=6°

Comparison of the flow field developing over the upper surface of the flap indicated that discrete blowing as a means of preventing/delaying boundary layer separation was most effective with 2*d* between successive orifices centres. Whilst local flow field anomalies were still evident, the proximity of the discrete orifices typically negated the adverse effects of local fluctuations in the blown jet across significant proportions of the span. In contrast, increasing the distance between successive discrete orifices tended to heighten the sensitivity of the boundary layer separation to spanwise variations in the jet velocity.

9.3.5 Effect of Reynolds Number

Figure 153 shows the effect of Reynolds number on the C_p distribution for the takeoff configuration at α=8° with discrete blowing at a C_μ of 0.025. The nominal freestream velocity was increased from 25*m*/*s* to 45*m*/*s* in intervals of 5*m*/*s*, corresponding to Reynolds numbers (*Re*) of 9.67×10^5, 1.16, 1.35, 1.54 and 1.74×10^6, based upon stowed reference chord. Similarly to the tangential slot blowing configuration, the corresponding surface static pressure measurements indicated that Reynolds number effects were appreciable for the specified high-lift configuration, corroborating Ljungström's (1976) observations when optimising a high-lift multi-element

configuration over a comparable range of Reynolds numbers. These deviations in the C_p distributions were attributed to the highly complex flow field developing over the high-lift configuration and the subsequent interactions of the confluent boundary layer/wake development, which were sensitive to variations in *Re*. Note that once again, this was not a pure Reynolds number variation as the corresponding Mach number was also increasing, which Ljungström suggested may have resulted in a slight underestimation of the Reynolds number effects.

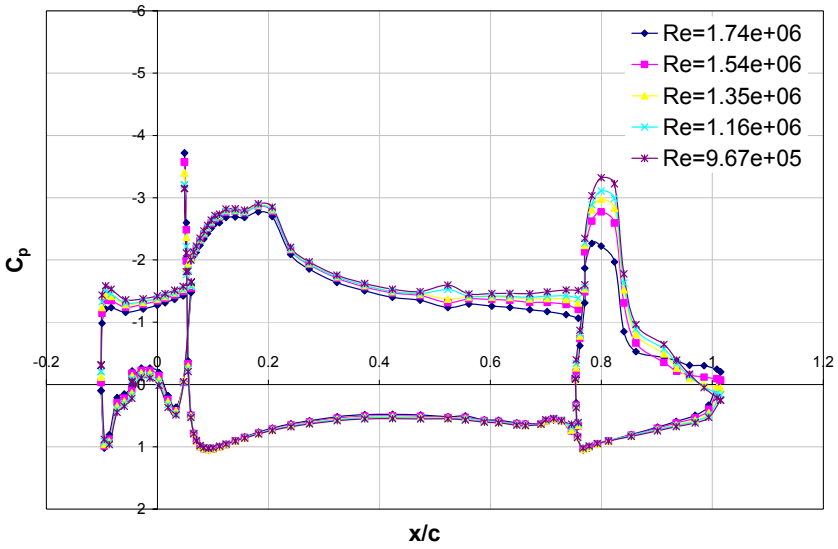

Figure 153: Effect of Reynolds number on C_p distribution for takeoff configuration with discrete blowing at α=8°

Quantifying these fluctuations for the takeoff configuration with discrete blowing at α=8°, integration of the surface static pressure distributions indicated that the lift force decreased in magnitude with successive increments in $9.67\times10^5 \leq Re \leq 1.74\times10^6$, accounting for a 12% decrement over the range of *Re* tested. This contradicted Ljungström's observed trend of increasing C_l with *Re* over a comparable range of *Re*. It was also evident that the pressure drag coefficient initially decreased in magnitude with increments in *Re* between 9.67×10^5 and 1.54×10^6 but increased in magnitude with a final increment in *Re* to the upper test limit of 1.74×10^6, correlating to a 23% variation in pressure drag over the range of *Re* tested.

Comparison with the Reynolds number tests for the baseline takeoff configuration without tangential slot blowing highlighted that the application of blowing boundary layer control heightened the sensitivity of the flow field development to variations in Reynolds number and thus confirmed that the results presented herein were only completely valid for the test Reynolds number. Further study of Reynolds number

effects, particularly in the presence of discrete blowing, were required to enable a reasonable extrapolation of the boundary layer control results.

9.4 Chapter Summary

Air was blown tangentially over the upper surface of the flap from discrete orifices at the trailing edge of a main element within the takeoff configuration. Analysis of the surface static pressure measurements, resultant aerodynamic forces and surface oil flow visualisation indicated that:

- Modifying the trailing edge geometry, through which the jet of air was ejected, from a conventional slot to discrete orifices, proved highly favourable for low to mid test α and hence, demonstrated a novel means of blowing boundary layer control with the potential eliminate or delay boundary layer separation
- Discrete blowing influenced the flow field developing over all three elements of the takeoff configuration
- For $\alpha \leq 10°$, discrete blowing delayed boundary layer separation over the upper surface of the flap from $0.35c_{flap}$ to within close proximity of the trailing edge
- For $\alpha \geq 12°$, the effectiveness of discrete blowing as a means of preventing boundary layer separation over the upper surface of the flap was progressively diminished
- In comparison to the baseline configuration, discrete blowing at a C_μ of 0.025 increased C_l for all test α, accounting for a ΔC_l between 0.20 and 0.61, dependent upon α
- At a C_μ of 0.025, ΔC_l due to discrete blowing for any given test α was of greater magnitude than that generated by blowing air tangentially from a conventional trailing edge slot
- At α=8°, the increment in C_l achieved by discrete blowing at the lower test C_μ of 0.012 was comparable to the increment in C_l attained by tangential slot blowing at a C_μ of 0.025
- Discrete blowing decreased the pressure drag in comparison to the baseline configuration for any given comparable C_l
- Limited investigations suggested the optimal distance tested between successive discrete orifice centres was $2d$
- Flow field development over the takeoff configuration was highly sensitive to variations in Reynolds number and hence, further study of Reynolds number effects, particularly in the presence of discrete blowing, are required to enable a reasonable extrapolation of the boundary layer control results

10 Conclusions & Recommendations for Further Work

10.1 Conclusions

A research programme was initiated to examine three candidate high-lift technologies, which would, if employed, simplify the mechanical complexity of the multiple component trailing-edge high-lift devices traditionally employed on civil transport aircraft. Each technology was examined in terms of its potential to favourably influence boundary layer development and improve the aerodynamic characteristics of a high-lift configuration.

Preliminary two-dimensional experiments were conducted on a modified flat plate with 10mm or 20mm 60° triangular serrations implemented at the trailing edge, positioned upstream of a single slotted flap. Establishing a comprehensive set of aerodynamic data, quantifying the effectiveness of the serrated trailing edge geometries over an incremental range of flap lap/gap and δ_f, the experimental investigations showed that:

- The effectiveness of the serrated geometries in delaying boundary layer separation over the upper surface of the single slotted flap and/or favourably influencing C_l and L/D was dependent upon the flap lap/gap, δ_f and serration length.

- In terms of increasing C_l and L/D, both the 10mm and 20mm serrations were most effective at a flap lap/gap of (0, −0.07), although this did not correlate to the optimum flap lap/gap in terms of maximising the overall C_l or L/D. However at the optimum flap lap/gap, the 20mm serrations proved more favourable than the baseline and 10mm serrated configurations for $\delta_f \leq 15°$, although the plain geometry attained the maximum value of C_l and L/D for $20° \leq \delta_f \leq 25°$.

- The 20mm serrations, corresponding to a nominal serration length of 13%c_{flap}, typically increased C_l and L/D at any given test lap/gap for $\delta_f \leq 15°$. In contrast, the 20mm serrations were often detrimental to the flow field development over the single slotted flap for $20° \leq \delta_f \leq 25°$, significantly heightening the severity of the stall in comparison to the baseline – and often, also the 10mm serrated – configuration(s). This heightened severity of the stall was particularly evident when the flap leading edge was positioned aft of the flat plate trailing edge.

- However in terms of reducing the profile drag, the 10mm serrations, corresponding to a nominal serration length of 7%c_{flap}, were more favourable than the 20mm serrations.

- Significantly, with the flap leading edge positioned upstream of the flat plate trailing edge, at a lap of −0.13, both the 10mm and 20mm serrations prevented boundary layer separation aft of 0.5c and promoted boundary layer attachment to the trailing edge of the single slotted flap at δ_f=25°.

Thus, these studies provided clear, quantitative evidence that the 20mm serrations favourably influenced boundary layer development and improved the aerodynamic characteristics over an aft positioned simple single slotted flap for low δ_f. However, with no available data to indicate the effect of employing serrated geometries within a representative multi-element high-lift configuration, 10mm and 20mm 60° triangular serrations were implemented at the trailing edge of main element, upstream of a single slotted flap, within a two- or three-element high-lift configuration. Note that the distinct cove geometry, which formed the aft lower surface of the main element, facilitated the retraction of the trailing-edge high-lift device in cruise conditions. Whilst limited, the ensuing two-dimensional experimental study indicated that:

- Over the limited range of flap lap/gap and δ_f tested, both the 10mm and 20mm serrations typically had a detrimental effect upon C_l and although the serrated geometries tended to reduce C_d, the magnitude of decrement was typically insufficient to offset a corresponding decrement in C_l. This suggested that the effectiveness of the serrations was highly sensitive to the precise configuration geometry.

- A single lap/gap of (−0.26, −0.2) was identified at which both the 10mm and 20mm serrations increased C_l for all test α and $\delta_f \leq 10°$, with the 20mm serrations, corresponding to a nominal serration length 11%c_{flap}, proving more effective than the 10mm serrations, corresponding to a nominal serration length 6%c_{flap}.

- Oil flow visualisation over the upper surface of the flap at a lap/gap of (−0.26, −0.2) exhibited wake structures emanating from individual vertices of the 20mm serrations for α=4°, 8° and 12° at δ_f=5° and for α=4° at δ_f=10°. This suggested evidence of the vortical structures generated from each serration vertex, corroborating previous research on single element aerofoils. The 10mm serrations exhibited no evidence of the wake structures emanating from the

serration vertices. The absence of wake structures evident over the upper surface of the flap did not counter their existence but instead, suggested that such flow field attributes were weak in terms of their impact upon the surface characteristics of the developing flow field. However, this did not necessarily infer diminished capability to prevent boundary layer separation.

- Limited data suggested that the effects of the serrated geometries upon the aerodynamic characteristics of a representative high-lift configuration were highly sensitive to the deployment of a leading-edge high-lift device, indicating the need to optimise the serration geometry for the complete configuration under consideration.

Although limited, these experiments provided initial evidence that serrations had the potential to favourably influence the flow field development within a high-lift configuration. Further flow visualisation studies are required in order to gain an in-depth understanding of the flow field mechanisms by which the serrations improve/degrade the boundary layer development, with the intention of aiding configuration optimisation.

With tangential slot blowing successfully integrated in production aircraft, the conventional method of active boundary layer control was evaluated within three multi-element high-lift configurations, so defined by distinct deflection angles of the leading-edge slat and the trailing-edge flap. The two-dimensional experiments showed that:

- When optimised, blowing tangentially from a slot at the trailing edge of the main element over the upper surface of the flap at a nominal C_μ of 0.025 was a highly effective means of maintaining boundary layer attachment to within close proximity of the trailing edge for all test α, increasing C_l but also increasing the pressure drag.

Comparing the wind-tunnel data with a corresponding two-dimensional computational simulation of tangential slot blowing within a multi-element high-lift configuration showed that:

- The numerical simulation corroborated the favourable effect of tangential slot blowing, preventing boundary layer separation and increasing C_l for all α, although the computational data also indicated that tangential slot blowing decreased the profile drag in comparison to the baseline configuration.

- The numerical solution over-predicted the suction over the upper surface of all three-elements of the takeoff configuration, both with and without tangential slot blowing. Such discrepancies between the computational and experimental data highlighted the need to accurately model the effective C_μ and accurately simulate the flow field over the leading edge slat of the wind-tunnel model, particularly with regard to the point of boundary layer transition.

Modifying the trailing edge geometry, through which the jet of air was ejected, from a conventional slot to discrete orifices proved highly favourable, with the two-dimensional wind-tunnel tests indicating that:

- Discrete blowing at a C_μ of 0.025 increased C_l for all test α and, unlike the conventional tangential slot blowing, decreased the pressure drag in comparison to the baseline configuration for any given comparable C_l.

- ΔC_l due to discrete blowing for any given test α was of greater magnitude than that generated by blowing air tangentially from a conventional trailing edge slot.

- For $\alpha \leq 10°$, discrete blowing prevented boundary layer separation over the upper surface of the flap, although the effectiveness of discrete blowing as a means of preventing boundary layer separation was progressively diminished for $\alpha \geq 12°$.

- Increasing the distance between successive discrete orifice centres degraded the effectiveness of discrete blowing in preventing or delaying boundary layer separation.

Thus, initial investigations of blowing through discrete orifices at the trailing edge of main element over the upper surface of a single slotted flap demonstrated that discrete blowing was a novel means of active boundary layer control within a multi-element high-lift configuration, with the potential to eliminate or delay boundary layer separation. Accordingly, further optimisation of the discrete orifices and momentum coefficient are suggested to yield its full potential.

10.2 Recommendations for Further Work

Based upon the results of the present research programme, the following recommendations can be made:

- From the present serrated trailing edge experiments, it is evident that there is a need to gain an in-depth understanding of the flow mechanisms by which the serrations favourably influence or degrade the boundary layer developing over an aft positioned single slotted flap. By utilising flow visualisation techniques able to capture the streamwise progression of the vortical structures, postulated to be emanating aft of the serration vertices, an enhanced awareness of the flow field development would be provided and hence, aid optimisation of the serrated trailing edge configuration. The two configurations of particular interest are: (a) the flat plate and trailing edge flap combination at a flap lap of −0.13, whereby both the 10mm and 20mm serrations delayed boundary layer separation from 0.5*c* to the trailing edge and (b) the high-lift configuration at a lap/gap of (−0.26, −0.2), with the latter complementing the surface oil flow visualisation.

- Noting that Vijgen et al (1989) scaled the length of the trailing edge serrations upon the local trailing edge boundary layer thickness, it was recognised that there were marked disparities between the upper-to-lower-surface-boundary-layer-thickness ratio at the trailing-edge of the flat plate (where the serrations often favourably influenced the developing flow field) and that at the trailing edge of the main element in the two-element high-lift configuration (where the serrations were typically detrimental to the flow field). Accordingly, further investigations are required to determine the influence of the local boundary layer thickness, including the upper-surface-to-lower-surface-boundary-layer-thickness ratio, on the effectiveness of the serrated geometries.

- Recognising that the practical implementation of serrations at the trailing edge of a main element would require corresponding "convergent" grooves in the flap upper surface to ensure a flush surface in cruise conditions, any development of a practical high-lift device would necessitate the investigation of how the postulated vortices, emanating aft of each serration vertex, interacted with and/or influenced the pairs of counter-rotating vortices, generated by the convergent grooves (for more details on convergent grooves, see Ciavatti, 2003 and Shah, 2004).

- Both the tangential slot blowing and discrete blowing experiments highlighted the need to address the defects within the blowing boundary layer control system to ensure near uniform spanwise jet velocity.

- The diminished effectiveness of tangential slot blowing in preventing boundary layer separation within the landing and extended flap configurations suggests the need to optimise the trajectory of the jet of blown air with regard to its impingement upon the flap upper surface. In accordance with the observations of Dods and Watson (1956) and Kelly et al (1958), the impingement of the jet of air upon the flap upper surface must either be upstream of or coincident with the point of minimum pressure for all test α. Further investigations into the benefits of inclining the nozzle jet towards the flap upper surface are also suggested.

- Both the tangential slot blowing and discrete blowing experiments highlighted that the flow field development over the takeoff configuration was highly sensitive to variations in Reynolds number and hence, further studies of Reynolds number effects, particularly in the presence of blowing boundary layer control, are required to enable a reasonable extrapolation of the boundary layer control results.

- Recognising the potential of the discrete blowing as a means of active boundary layer control within a high-lift configuration, further optimisation of the discrete orifices is recommended, in terms of discrete orifice diameter, spacing between successive orifices and orifice geometry. Further optimisation in terms of the impingement of the jet upon the flap upper surface, relative to the point of minimum pressure, is also recommended.

- Finally, optimisation of these passive or active boundary layer control technologies necessitates their evaluation at representative takeoff and/or landing configurations and conditions, to establish the critical performance characteristics associated with the high-lift phases of the flight envelope.

Bibliography

Amant, S. (2001), 'Drag prediction and decomposition, from wake surveys and calculations, in subsonic flows', *AIAA 2001-2446*.

Anderson, J.D. (1991), *Fundamentals of aerodynamics* (2nd edition), McGraw Hill.

Anderson, J.D. (2000), *Introduction to flight* (4th edition), McGraw-Hill.

Anderson, S.B., Quigley, H.C. and Innis, R.C. (1956), 'Flight measurements of the low-speed characteristics of a 35° swept-wing airplane with blowing-type boundary-layer control on the trailing-edge flaps', *NACA RM A56G30*.

Anscombe, A., Butler, S.F.J. and Guyett, M.B. (1963), 'Low-speed wind-tunnel tests on the Vickers-Supermarine N. 113 (Schimitar) with blowing over trailing-edge flaps', *RAE TN 2905*.

Aoyagi, K. and Hickey, D.H. (1963), 'Large-scale wind-tunnel tests in ground effect of a 35 degree sweptback wing jet transport model equipped with blowing boundary-layer-control trailing- and leading-edge devices', *NASA TN D-1884*.

Ashill, P.R., Fulker, J.L. and Hackett, K.C. (2001), 'Research at DERA on sub boundary layer vortex generators (SBVGs)', *AIAA 2001-0887*.

Bamber, I.M. (1931), ' Wind tunnel tests on aerofoil boundary layer control using a backward-opening slot', *NACA Report No 385*.

Barlow, J.B., Rae, W.H. and Pope, A. (1999), *Low-speed wind tunnel testing* (3rd edition), Wiley-Interscience.

Bertelrud, A. and Ljungstrom, B.L.G. (1974), 'The viscous flow around a two dimensional high lift wing', *FFA Technical Note AU-1155*.

Bollay, W. (1938), 'Determination of profile drag from measurements in the wake of a body', *Journal of the Aerospace Sciences,* Vol. 5, pp. 245-248.

Bray, T.P. (1998), 'A parametric study of vane and air-jet vortex generators', *EngD Thesis, Cranfield University*.

Brennan, S. (2002), 'A wind tunnel investigation into the effect of a serrated trailing edge forward of a deployed flap', *MSc Thesis, Cranfield University*.

Brune, G.W. (1994), 'Quantitative low-speed wake surveys', *Journal of Aircraft,* Vol. 31, No. 2, pp. 249-255.

Cebeci, T., Besnard, E. and Chen, H.H. (1996), 'Calculation of multielement airfoil flows, including flap wells', *AIAA 96-0056*.

Chao, D.D. and van Dam, C.P. (1999), 'Airfoil drag prediction and decomposition', *Journal of Aircraft,* Vol. 36, No. 4, pp. 675-681.

Chin, V.D., Peters, D.W., Spaid, F.W. and McGhee, R.J. (1993), 'Flowfield measurements about a multi-element airfoil at high Reynolds numbers', *AIAA 93-3137*.

Ciavatti, C. (2003), ' The effects of indentations on trailing edge flap performance', *MSc Thesis, College of Aeronautics, Cranfield University*.

Collins, F.G. (1981), 'Boundary-layer control on wings using sound and leading-edge serrations', *AIAA Journal,* Vol. 19, No. 2, pp. 129-130.

Dillner, B., May, F.W. and McMasters, J.H. (1984), 'Aerodynamic issues in the design of high-lift systems for transport aircraft', *AGARD CP 365 on Improvement of aerodynamic performance through boundary layer control and high lift systems,* pp. 9:1-9:21.

Dods, J.B. and Watson, E.C. (1956), 'The effects of blowing over various trailing-edge flaps on a NACA 0006 airfoil section, comparisons with various types of flaps on other airfoil sections, and an analysis of flow and power relationships for blowing systems', *NACA RM A56C01*.

Duncan, W.J., Thom, A.S. and Young, A.D. (1970), *Mechanics of fluids* (2nd edition), Edward Arnold.

ESDU 'Increment in aerofoil profile drag coefficient due to the deployment of a single-slotted flap', *Data Item 87005*.

ESDU 'Lift-interference and blockage corrections for two-dimensional subsonic flow in ventilated and closed wind-tunnels', *Data Item 76028*.

Fage, A. and Jones, L.J. (1925), 'On the drag of an aerofoil for two-dimensional flow', *ARC R&M 1015*.

Foster, D.N., Ashill, P.R. and Williams, B.R. (1972), 'The nature, development and effect of the viscous flow around an aerofoil with high-lift devices', *ARC CP 1258*.

Foster, D.N., Irwin, H.P.A.H. and Williams, B.R. (1970), 'The two dimensional flow around a slotted flap', *RAE TR 70164*.

Gai, S.L. and Palfrey, R. (2003), 'Influence of trailing-edge flow control on airfoil performance', *Journal of Aircraft,* Vol. 40, No. 2, pp. 332-337.

Gai, S.L. and Sharma, S.D. (1981), 'Experiments on the reduction of base drag of a blunt trailing edge aerofoil in subsonic flow', *Aeronautical Journal,* pp. 206-210.

Giguere, P., Dumas, G. and Lemay, J. (1997), 'Gurney flap scaling for optimum lift-to-drag ratio', *AIAA Journal,* Vol. 35, No. 12, pp. 1888-1890.

Goett, H.J. (1939), 'Experimental investigation of the momentum method for determining profile drag', *NACA Report 660*.

Graham, R.R. (1932), ' Safety devices in wings of birds', *Journal of Royal Aeronautical Society,* Vol. 36, pp. 24-58.

Graham, R.R. (1934), ' The silent flight of owls', *Journal of Royal Aeronautical Society,* Vol. 38, pp. 837-843.

Hanselman, D. and Littlefield, B. (2001), *Mastering Matlab 6: a comprehensive tutorial and reference*, Prentice Hall.

Hersh, A.S., Soderman, P.T. and Hayden, R.E. (1974), 'Investigation of acoustic effects of leading edge serrations on airfoils', *Journal of Aircraft,* Vol. 11, No. 4, pp. 197-202.

Hickey, D.H. and Aoyagi, K. (1958), 'Large-scale wind-tunnel tests of an airplane model with a 45° sweptback wing of aspect ratio 2.8 employing high-velocity blowing over the leading- and trailing-edge flaps', *NACA RM A58A09*.

Houghton, E.L. and Carpenter, P.W. (2003), *Aerodynamics for engineering students* (5th edition), Butterworth Heinmann.

Jones, B.M. (1936), 'The measurement of profile drag by the pitot-traverse method', *ARC R&M 1688*.

Kelly, M.W., Anderson, S.B. and Innis, R.C. (1958), 'Blowing-type boundary-layer control as applied to the trailing-edge flaps of a 35° swept-wing airplane', *NACA Report 1369*.

Kelly, M.W. and Tolhurst, W.H. (1955), 'Full-scale wind-tunnel tests of a 35 degree sweptback wing airplane with high-velocity blowing over the trailing-edge flaps', *NACA RM A55I09*.

Kelly, M.W. and Tucker, J.H. (1956), 'Wind-tunnel tests of blowing boundary-layer control with jet pressure ratios up to 9.5 on the trailing edge flaps of a 35° sweptback wing airplane', *NACA RM A56G19*.

Korbacher, G.K. and Sridhar, K. (1960), 'A review of the jet flap', *University of Toronto, Institute of Aerophysics, Review No 14*.

Lachmann, G.V. (1932), 'Slots and the wings of birds', *Journal of Royal Aeronautical Society,* Vol. 36, pp. 374-379.

Lachmann, G.V. (1961), *Boundary layer and flow control: its principles and application,* Vol. 1, Pergamon Press.

Lawford, J.A. (1968), 'Low-speed wind-tunnel tests on an unswept wing-fuselage model of aspect ratio 9.8, with tangential blowing over the trailing-edge flaps and ailerons, including the effect of slipstream', *RAE Technical Report 68111*.

Liebeck, R.H. (1978), 'Design of subsonic airfoils for high lift', *Journal of Aircraft,* Vol. 15, No. 9, pp. 547-561.

Lin, J.C., Robinson, S.K. and McGhee, R.J. (1992), 'Separation control on high Reynolds number multi-element airfoils', *AIAA 92-2636*.

Ljungstrom, B. (1976), 'Wind tunnel high lift optimization of a multiple element airfoil', *FFA Technical Note AU-778*.

McCormick, B.W. (1995), *Aerodynamics, aeronautics and flight mechanics* (2nd edition), Wiley.

Moir, I.R.M., Foster, D.N. and Holt, D.R. (1972), 'The measurement and analysis of the profile drag of a wing with a slotted flap', *ARC CP 1233*.

Nakayama, A., Kreplin, H.P. and Morgan, H.L. (1990), 'Experimental investigation of flowfield about a multielement airfoil', *AIAA Journal,* Vol. 28, No. 1, pp. 14-21.

Neuhart, D.H. and Pendergraft, O.C. (1988), 'A water tunnel study of gurney flaps', *NASA TM 4071*.

Powell, L.K.A. (2000), 'An investigation into the use of boundary layer and wake air for propulsion', *MSc Thesis, Cranfield University*.

Pratap, R. (2002), *Getting started with Matlab: a quick introduction for scientists and engineers*, Oxford University Press.

Prust, H.W. and Moffitt, T.P. (1976), 'Two-dimensional cold-air cascade study of a film-cooled turbine stator blade: III - effect of hole size on single-row and multirow ejection', *NASA TM X-3442*.

Quigley, H.C., Anderson, S.B. and Innis, R.C. (1958), 'Flight investigation of the low-speed characteristics of a 45° swept-wing fighter-type airplane with blowing boundary-layer control applied to the trailing-edge flaps', *NACA RM A58E05*.

Quigley, H.C., Hom, R.W.K. and Innis, R.C. (1957), 'A flight investigation of area-suction and blowing boundary layer control on the trailing-edge flaps of a 35° swept-wing carrier-type airplane', *NACA RM A57B14*.

Rogers, S.E. (1993), ' Progress in high-lift aerodynamic calculations', *AIAA 93-0194*.

Rolls, L.S. and Innis, R.C. (1956), 'A flight evaluation of a wing-shroud-blowing boundary-layer control system applied to the flaps of an F94F-4 airplane', *NACA RM A55K01*.

Schlichting, H. and Gersten, K. (2000), *Boundary layer theory* (8th edition), Springer.

Schwind, R.G. and Allen, H.J. (1973), 'The effects of leading-edge serrations on reducing flow unsteadiness about airfoils - an experimental and analytical investigation', *NASA CR-2344*.

Shah, N. (2004), 'Boundary layer flow control using surface indentations', *MSc Thesis, School of Engineering, Cranfield University*.

Smith, A.M.O. (1974), 'High-lift aerodynamics', *AIAA 74-939*.

Smith, A.M.O. (1975), 'High-lift aerodynamics', *Journal of Aircraft,* Vol. 12, No. 6, pp. 501-530.

Smith, E.G. and Sowers, H.D. (1974), 'Cascade tests of serrated leading edge blading at high subsonic speeds', *NASA CR-2472*.

Soderman, P.T. (1972), 'Aerodynamic effects of leading-edge serrations on a two-dimensional airfoil', *NASA TM X-2643*.

Soderman, P.T. (1973), 'Leading-edge serrations which reduce the noise of low-speed rotors', *NASA TN D-7371*.

Spaid, F.W. and Lynch, F.T. (1996), 'High Reynolds number, multi-element airfoil flowfield measurements', *AIAA 96-0682*.

Stevens, W.A., Goradia, S.H. and Braden, J.A. (1971), 'Mathematical model for two-dimensional multi-component airfoils in viscous flow', *NASA CR-1843*.

Szanca, E.M., Schum, H.J. and Behning, F.P. (1970), 'Cold-air investigation of a turbine with transpiration-cooled stator blades: II - stage performance with discrete hole stator blades', *NASA TM X-2133*.

Takeda, K., Ashcroft, G.B. and Zhang, X. (2001a), 'Unsteady aerodynamics of flap cove in a high-lift device configuration', *AIAA 2001-0707*.

Takeda, K., Ashcroft, G.B. and Zhang, X. (2001b), 'Unsteady aerodynamics of slat cove flow in a high-lift device configuration', *AIAA 2001-0706*.

Tanner, M. (1971), 'Experimental investigation of the drag of wings with a blunt trailing edge at transonic speeds', *AGARD CP 83-71 on Facilities and techniques for aerodynamic testing at transonic speeds and high Reynolds number,* pp. 8:1-8:6.

Tanner, M. (1972), 'A method for reducing the base drag of wings with blunt trailing edge', *The Aeronautical Quarterly,* Vol. 23, pp. 15-23.

Tanner, M. (1973), 'New investigations for reducing the base drag of wings with a blunt trailing edge', *AGARD Conference Proceedings No 124 on Aerodynamic Drag, 10-13 April 1973, Turkey,* pp. 12-1-12-9.

Tanner, M. (1975), 'Reduction of base drag', *Progress in Aerospace Sciences,* Vol. 16, No. 4, pp. 369-384.

Tolhurst, W.H. and Kelly, M.W. (1956), 'Full-scale wind-tunnel test of a 35° sweptback-wing airplane with high-velocity blowing over the trailing-edge flap - longitudinal and lateral stability and control', *NACA RM A56E24*.

Turner, T.R. (1964), 'Wind-tunnel investigation of boundary-layer control by blowing on an NACA 65_5-424 airfoil to effect drag reduction', *NASA TN D-2374*.

van den Berg, B. (1979), 'Boundary layer measurements on a two-dimensional wing with flap', *NLR TR 79009 U*.

Vanhoutte, F.G. (2001), 'Intrusion effects of pressure sensitive paint on the external flow field', *PhD Thesis, Cranfield University*.

Vijgen, P.M.H.W., Howard, F.G., Bushnell, D.M. and Holmes, B.J. (1992), 'Serrated trailing edge for improving lift and drag characteristics of lifting surfaces', *Patent US 5,088,665*.

Vijgen, P.M.H.W., van Dam, C.P., Holmes, B.J. and Howard, F.G. (1989), 'Wind-tunnel investigations of wings with serrated sharp trailing-edges', *Low Reynolds Number Aerodynamics,* Vol. 54, pp. 295-313.

Vlaenderen, J.M.M. (1959), 'Some aspects of the application of blown flaps on aircraft', *NLR Technical Report V-1859*.

White, F.M. (1991), *Viscous fluid flow* (2nd edition), McGraw-Hill.

Whittle, E.F. and Lipson, S. (1954), 'Effect of low-speed aerodynamic characteristics of a 49° sweptback wing having an aspect ratio of 3.78 of blowing air over the trailing-edge flap and aileron', *NACA RM L54C05*.

Williams, C.B. (2001), 'Experimental investigation of the unsteady flow on diamond and lambda planform wings', *PhD Thesis, Cranfield University*.

Williams, J. (1955), ' An analysis of aerodynamic data on blowing over trailing edge flaps for increasing lift', *ARC CP No 209*.

Appendix A

Non-Dimensional Flap Coordinates, Brough Wind-Tunnel

Lower Surface	
x/c_{flap}	y/c_{flap}
1.0000	0.0000
0.9999	-0.0133
0.9792	-0.0107
0.9585	-0.0081
0.9379	-0.0056
0.9172	-0.0031
0.8965	-0.0008
0.8758	0.0014
0.8551	0.0034
0.8343	0.0052
0.8136	0.0067
0.7928	0.0081
0.7720	0.0093
0.7512	0.0104
0.7304	0.0113
0.7096	0.0121
0.6888	0.0127
0.6680	0.0132
0.6472	0.0135
0.6264	0.0138
0.6055	0.0139
0.5847	0.0139
0.5639	0.0138
0.5431	0.0136
0.5223	0.0132
0.5014	0.0128

Lower Surface	
x/c_{flap}	y/c_{flap}
0.4806	0.0122
0.4598	0.0115
0.4390	0.0107
0.4182	0.0098
0.3974	0.0088
0.3766	0.0076
0.3558	0.0064
0.3351	0.0050
0.3143	0.0035
0.2936	0.0018
0.2728	0.0001
0.2521	-0.0018
0.2313	-0.0038
0.2106	-0.0059
0.1899	-0.0081
0.1692	-0.0105
0.1486	-0.0129
0.1279	-0.0155
0.1072	-0.0181
0.0866	-0.0209
0.0660	-0.0235
0.0454	-0.0266
0.0246	-0.0267
0.0057	-0.0194
0.0000	0.0000

Upper Surface	
x/c_{flap}	y/c_{flap}
0.0000	0.0000
0.0075	0.0193
0.0206	0.0355
0.0366	0.0486
0.0546	0.0592
0.0736	0.0675
0.0934	0.0741
0.1135	0.0795
0.1339	0.0836
0.1545	0.0867
0.1752	0.0890
0.1959	0.0906
0.2167	0.0917
0.2375	0.0924
0.2583	0.0929
0.2792	0.0932
0.3000	0.0933
0.3208	0.0934
0.3416	0.0933
0.3624	0.0931
0.3833	0.0927
0.4041	0.0922
0.4249	0.0914
0.4457	0.0902
0.4664	0.0888
0.4872	0.0871

Upper Surface	
x/c_{flap}	y/c_{flap}
0.5079	0.0855
0.5287	0.0839
0.5495	0.0822
0.5701	0.0798
0.5907	0.0768
0.6112	0.0731
0.6317	0.0692
0.6521	0.0652
0.6726	0.0613
0.6930	0.0574
0.7135	0.0535
0.7339	0.0496
0.7544	0.0458
0.7748	0.0419
0.7953	0.0380
0.8158	0.0342
0.8362	0.0303
0.8567	0.0265
0.8772	0.0227
0.8976	0.0188
0.9181	0.0150
0.9386	0.0112
0.9590	0.0075
0.9795	0.0037
1.0000	0.0000

Non-Dimensional Surface Static Pressure Orifice Coordinates for Flap, Brough Wind-Tunnel

Lower Surface	
x/c_{flap}	y/c_{flap}
0.0000	0.0000
0.0327	-0.0257
0.0660	-0.0235
0.0993	-0.0192
0.1660	-0.0109
0.2327	-0.0037
0.3327	0.0048

Lower Surface	
x/c_{flap}	y/c_{flap}
0.4660	0.0117
0.6327	0.0137
0.7993	0.0077
0.9853	-0.0115

Upper Surface	
x/c_{flap}	y/c_{flap}
0.0000	0.0000
0.0320	0.0452
0.0653	0.0641
0.0987	0.0757
0.1333	0.0835
0.1993	0.0908
0.2667	0.0930

Upper Surface	
x/c_{flap}	y/c_{flap}
0.3340	0.0933
0.4007	0.0923
0.4673	0.0887
0.5673	0.0802
0.6667	0.0624
0.8333	0.0309

Non-Dimensional Surface Static Pressure Orifice Coordinates for High-Lift Configuration, 8'×6' Wind-Tunnel

23° Slat	
x/c	y/c
0.019	-0.0078
0.0031	-0.0223
-0.0136	-0.0401
-0.0291	-0.0603
-0.0399	-0.0795
-0.0457	-0.0968
-0.0458	-0.1127
-0.046	-0.1228
-0.0598	-0.1241
-0.0727	-0.1248
-0.0868	-0.1234
-0.0955	-0.1174
-0.1013	-0.1019
-0.0997	-0.0885
-0.0933	-0.0765
-0.0832	-0.0655
-0.0572	-0.0451
-0.0256	-0.0242
-0.0004	-0.0092

27° Slat	
x/c	y/c
-0.0007	-0.023
-0.0156	-0.0386
-0.031	-0.0575
-0.0449	-0.0784
-0.0545	-0.0985
-0.0591	-0.1163
-0.0582	-0.1318
-0.0575	-0.1422
-0.0713	-0.1445
-0.0839	-0.146
-0.0982	-0.1456
-0.1074	-0.1403
-0.1142	-0.1252
-0.1136	-0.1117
-0.108	-0.0993
-0.0986	-0.0876
-0.0742	-0.0655
-0.0445	-0.0427
-0.0207	-0.0262

Main Element: Lower Surface	
x/c	y/c
0.5238	-0.0397
0.4742	-0.047
0.4238	-0.0528
0.3738	-0.0567
0.3239	-0.0589
0.2739	-0.0591
0.2405	-0.0582
0.2072	-0.0563
0.1822	-0.0544
0.1572	-0.0518
0.1405	-0.0497
0.1238	-0.0473
0.1121	-0.0455
0.1005	-0.0434
0.0921	-0.0419
0.0838	-0.0402
0.0771	-0.0387
0.0704	-0.0372
0.0654	-0.036
0.0604	-0.0348
0.0554	-0.0335
0.0521	-0.0312
0.0488	-0.0259

Main Element: Upper Surface	
x/c	y/c
0.0488	-0.0259
0.052	-0.0112
0.0553	-0.0058
0.0603	0.0004
0.0653	0.0055
0.0703	0.01
0.0769	0.0153
0.0836	0.0199
0.0902	0.0241
0.0969	0.028
0.1035	0.0316
0.1119	0.0357
0.1235	0.0407
0.1402	0.047
0.1568	0.0524
0.1818	0.0591
0.2068	0.0633
0.2401	0.0654
0.2734	0.067
0.3234	0.0685
0.3734	0.0692
0.4234	0.069
0.4734	0.0682
0.5234	0.0666

Non-Dimensional Surface Static Pressure Orifice Coordinates for High-Lift Configuration, 8'×6' Wind-Tunnel (Continued)

Modular Component	
x/c	y/c
0.5612	0.065
0.6029	0.0626
0.6353	0.0603
0.671	0.0573
0.7026	0.054
0.7364	0.0496
0.7463	0.0386
0.7281	0.0326
0.714	0.0246
0.7001	0.0071
0.6912	-0.0115
0.6633	-0.016
0.6477	-0.0186
0.6148	-0.0243
0.5893	-0.0287
0.5549	-0.0346

38° Flap	
x/c	y/c
1.0149	-0.1202
0.9937	-0.1069
0.969	-0.0897
0.9351	-0.0684
0.9012	-0.0489
0.8538	-0.0243
0.8129	-0.0052
0.7928	0.0035
0.7781	0.0097
0.7672	0.0142
0.7572	0.0185
0.7547	0.0207
0.7534	0.0234
0.7547	0.0291
0.7612	0.0355
0.7703	0.0393
0.7701	0.0393
0.783	0.0412
0.7996	0.0406
0.8238	0.0351
0.8407	0.0278
0.8623	0.0119
0.9127	-0.0312
0.9358	-0.051
0.9589	-0.0706
0.985	-0.0926
1.0083	-0.1121

48° Flap	
x/c	y/c
0.9901	-0.1584
0.9715	-0.1417
0.9502	-0.1204
0.9205	-0.0935
0.8905	-0.0684
0.8481	-0.0359
0.8111	-0.01
0.7929	0.002
0.7794	0.0106
0.7695	0.0169
0.7606	0.0228
0.7583	0.0256
0.7575	0.0285
0.7599	0.034
0.7674	0.039
0.7768	0.0412
0.7897	0.0408
0.8063	0.0373
0.8291	0.0276
0.8442	0.0176
0.8628	-0.0018
0.8843	-0.0279
0.9048	-0.0528
0.9242	-0.0765
0.9435	-0.0999
0.9652	-0.1258
0.9848	-0.1491

58° Flap	
x/c	y/c
0.9487	-0.1918
0.9332	-0.1721
0.916	-0.1474
0.8914	-0.1158
0.8662	-0.0859
0.8305	-0.047
0.7981	-0.0146
0.7823	0.0004
0.7706	0.0113
0.7618	0.0192
0.754	0.0267
0.7523	0.0297
0.7521	0.0327
0.7554	0.0376
0.7637	0.0413
0.7733	0.0418
0.7859	0.0392
0.8016	0.0328
0.8222	0.0195
0.8356	0.0069
0.8505	-0.0154
0.8671	-0.0449
0.883	-0.073
0.898	-0.0997
0.913	-0.1261
0.9298	-0.1554
0.9451	-0.1817

Appendix B

Integration of the Surface Pressure Distributions to Obtain the Aerodynamic Forces

For simplicity, an infinitesimal area on the upper surface of a flap was considered. As a result of the pressure distribution, the infinitesimal area was subject to a normal force acting perpendicularly to the flap chord. Summation of all the contributions from these areas on the upper surface, from the leading edge to the trailing edge, resulted in a force in the normal direction due to the pressure exerted on the upper surface of the aerofoil (subscript *u*). A similar term was obtained for the resultant pressure in the normal direction acting on the lower surface (subscript *l*). Thus, the total normal force per unit span (*N*) acting on an aerofoil was given by:

$$N = \int_0^c p_l dx - \int_0^c p_u dx \qquad [B.1]$$

Adding and subtracting a reference pressure and normalising by the dynamic pressure, the normal force coefficient per unit span (C_n) was:

$$C_n = \frac{1}{c}\int_0^c \left(\frac{p_l - p_{ref}}{q_{w/s}} \right) dx - \frac{1}{c}\int_0^c \left(\frac{p_u - p_{ref}}{q_{w/s}} \right) dx \qquad [B.2]$$

Recalling equation [3.3], C_n was simplified to:

$$C_n = \int_0^1 \left(C_{p,l} - C_{p,u} \right) d\left(\frac{x}{c} \right) \qquad [B.3]$$

Applying a similar argument, the axial force coefficient per unit span (C_a) was given by:

$$C_a = \int_{z_{\min}}^{z_{\max}} \Delta C_p \, d\left(\frac{z}{c} \right) \qquad [B.4]$$

where ΔC_p was the difference between the values of C_p acting on the fore and aft sections of the aerofoil and z_{min} and z_{max} were the minimum and maximum values of z, respectively.

Thus, estimations of the normal and axial force coefficients, resulting from the pressure distribution, were obtained by integrating the respective pressure coefficients over the flap surface.

With the pressure distributions represented by a set of discrete data, numerical integration was limited. However, by defining the data as continuous mathematical expressions, the integrands could be evaluated analytically.

In the first instance, a cubic spline function within Matlab was used to approximate the curve between each pair of successive data points, in each set of discrete data. For *n* discrete data points of the form:

$$(x_i, y_i) \quad where \ i = 1, 2, ..., n \qquad [B.5]$$

there were (*n*-1) cubic polynomials of the form

$$f_i(x) = a_i(x - x_i)^3 + b_i(x - x_i)^2 + c_i(x - x_i) + d_i, \quad i = 1, 2, ..., n-1 \qquad [B.6]$$

Application of the piecewise polynomial form of the cubic splines within Matlab explicitly assigned all the necessary information to evaluate the integral over a given interval to a convenient data structure, including the polynomial coefficients.

Analytical integration of each interval yields the area under a given cubic polynomial:

$$\int_{x_i}^{x_{i+1}} f_i(x)dx = \frac{a_i}{4}(x_{i+1} - x_i)^4 + \frac{b_i}{3}(x_{i+1} - x_i)^3 + \frac{c_i}{2}(x_{i+1} - x_i)^2 + d_i(x_{i+1} - x_i) \qquad [B.7]$$

Thus, the area under each piecewise polynomial representing the upper/lower surfaces or the fore/aft regions of the aerofoil was easily computed by means of summation:

$$\int_{x_1}^{x_n} f(x)dx = \sum_{i=1}^{n-1}\left(\frac{a_i}{4}(x_{i+1} - x_i)^4 + \frac{b_i}{3}(x_{i+1} - x_i)^3 + \frac{c_i}{2}(x_{i+1} - x_i)^2 + d_i(x_{i+1} - x_i)\right) \qquad [B.8]$$

Recalling equations [B.3] and [B.4] above, the normal and axial force coefficients resulting from the pressure distribution on the aerofoil were thus determined.

Appendix C

Two-Dimensional Blockage Corrections

Based upon Allen and Vincenti's estimation for solid blockage (ε_{sb}):

$$\varepsilon_{sb} = \Lambda\sigma \quad \text{where} \quad \Lambda = 4\lambda_2\left(\frac{t}{c}\right)^2 \text{ and } \quad \sigma = \frac{\pi^2}{48}\left(\frac{c}{h}\right)^2 \qquad [C.1]$$

where λ_2 was the body shape factor, (t/c) was the thickness-to-chord ratio and (c/h) was the model-chord-to-tunnel-height ratio and combined with Maskell's estimation for wake blockage (ε_{wb}):

$$\varepsilon_{wb} = \frac{c/h}{2} C_{du} \qquad [C.2]$$

the total blockage (ε) was defined as:

$$\varepsilon = \varepsilon_{sb} + \varepsilon_{wb} \qquad [C.3]$$

As detailed in Barlow et al (1999), the corrections to the freestream quantities, angle of incidence, non-dimensional coefficients and Reynolds number were given by:

$$U_c = U_u(1+\varepsilon) \qquad [C.4]$$

$$q_c = q_u(1+2\varepsilon) \qquad [C.5]$$

$$\alpha_c = \alpha_u + \frac{57.3\sigma}{2\pi}\left(C_{lu} + 4C_{m_{\frac{1}{4}}u}\right) \qquad [C.6]$$

$$C_{p_c} = 1 - \frac{\left(1 - C_{p_u}\right)}{\left(\frac{q_c}{q_u}\right)} \qquad [C.7]$$

$$C_{lc} = C_{lu}(1-\sigma-2\varepsilon) \qquad [C.8]$$

$$C_{dc} = C_{du}(1-3\varepsilon_{sb}-2\varepsilon_{wb}) \qquad [C.9]$$

$$C_{m_{\frac{1}{4}}c} = C_{m_{\frac{1}{4}}u}(1-2\varepsilon) + \frac{1}{4}\sigma C_{lc} \qquad [C.10]$$

$$R_{\infty c} = R_{\infty u}(1+\varepsilon) \qquad [C.11]$$

Appendix D

C_p Distributions over Single Slotted Flap for Plain, 10mm and 20mm Serrated Trailing-Edge Configurations, Brough Wind-Tunnel

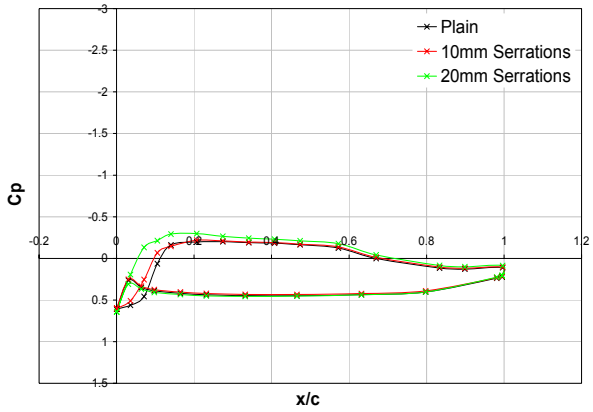

(a) Lap/Gap: (−0.13, −0.07), δ_f=5°

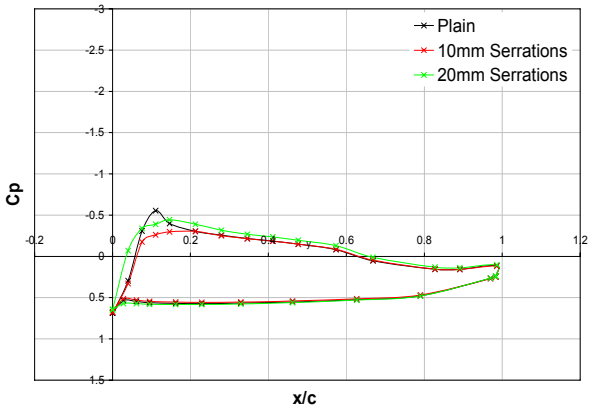

(b) Lap/Gap: (−0.13, −0.07), δ_f=10°

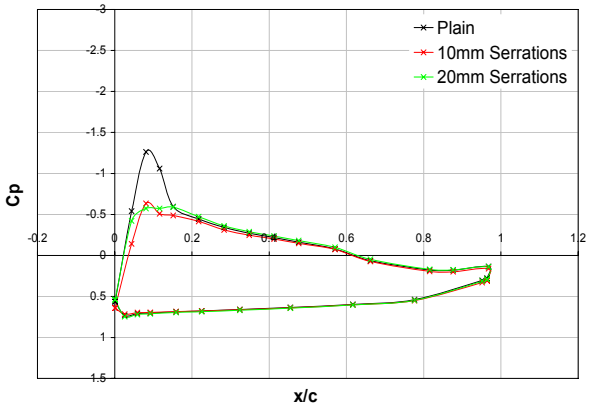

(c) Lap/Gap: (−0.13, −0.07), δ_f=15°

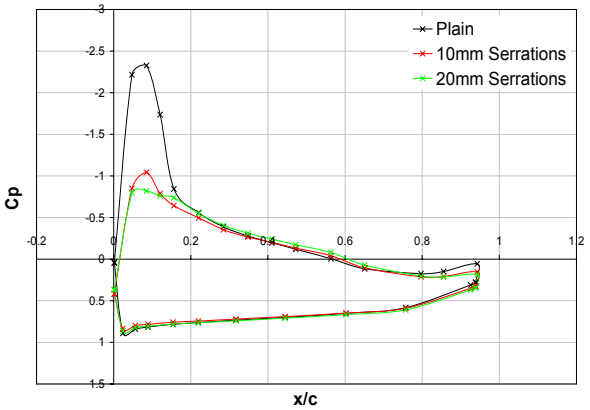

(d) Lap/Gap: (−0.13, −0.07), δ_f=20°

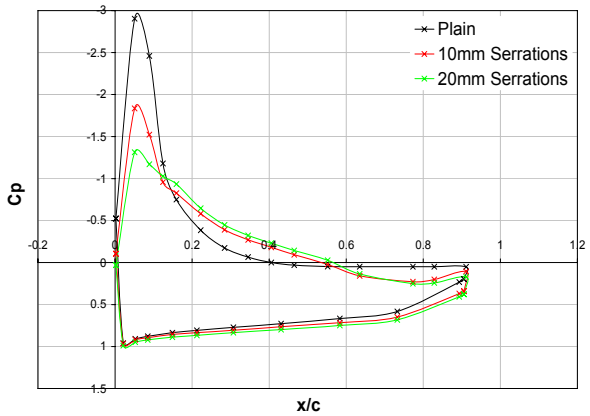

(e) Lap/Gap: (−0.13, −0.07), δ_f=25°

Figure 154(a)-(e): C_p distributions at a flap lap/gap of (−0.13, −0.07), 5°≤δ_f≤25°

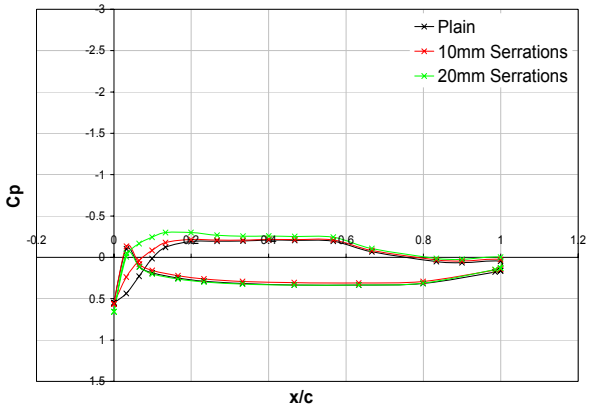

(a) Lap/Gap: (−0.07, −0.07), δ_f=0°

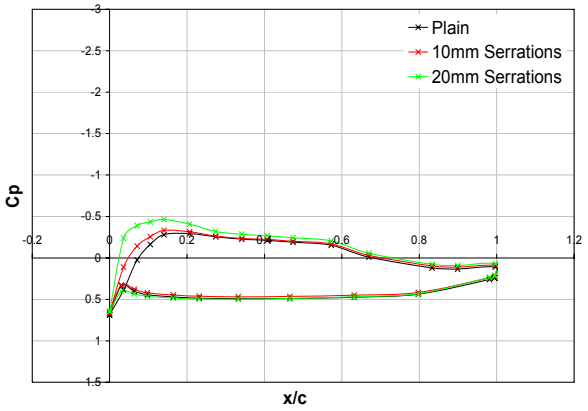

(b) Lap/Gap: (−0.07, −0.07), δ_f=5°

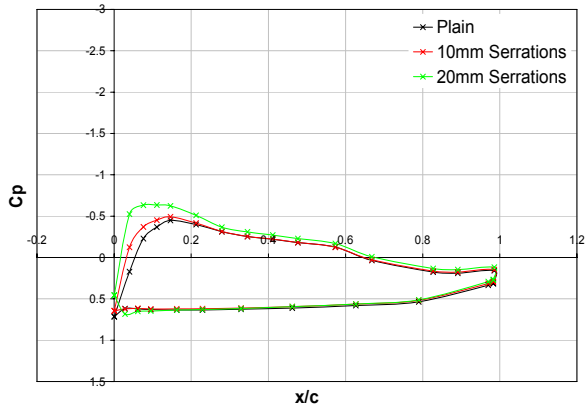

(c) Lap/Gap: (−0.07, −0.07), δ_f=10°

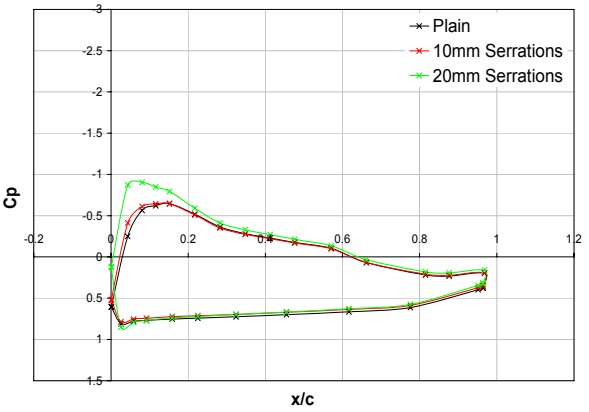

(d) Lap/Gap: (−0.07, −0.07), δ_f=15°

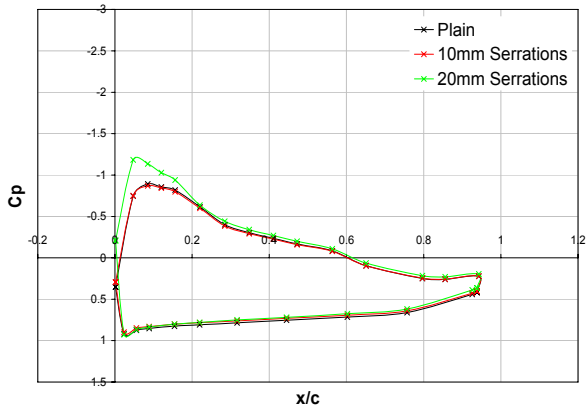

(e) Lap/Gap: (−0.07, −0.07), δ_f=20°

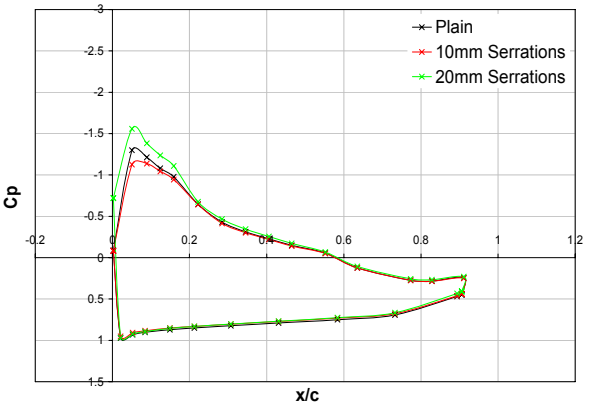

(f) Lap/Gap: (−0.07, −0.07), δ_f=25°

Figure 155(a)-(f): C_p distributions at a flap lap/gap of (−0.07, −0.07), 0°≤δ_f≤25°

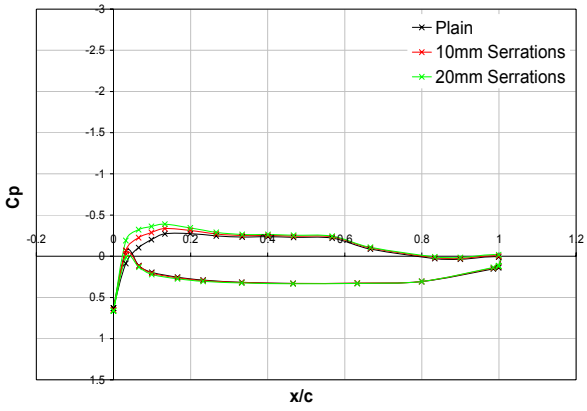

(a) Lap/Gap: (0, −0.07), δ_f=0°

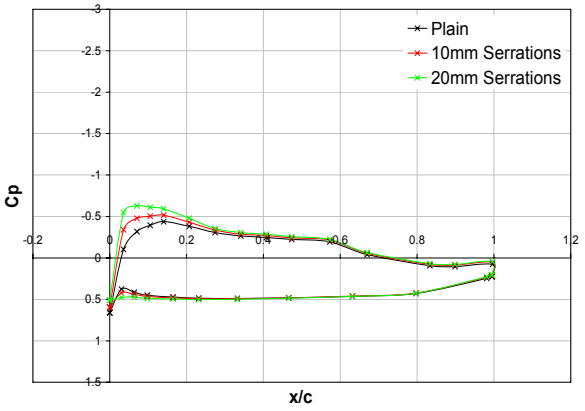

(b) Lap/Gap: (0, −0.07), δ_f=5°

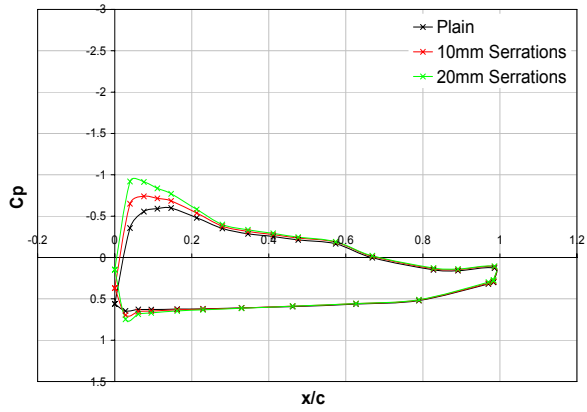

(c) Lap/Gap: (0, −0.07), δ_f=10°

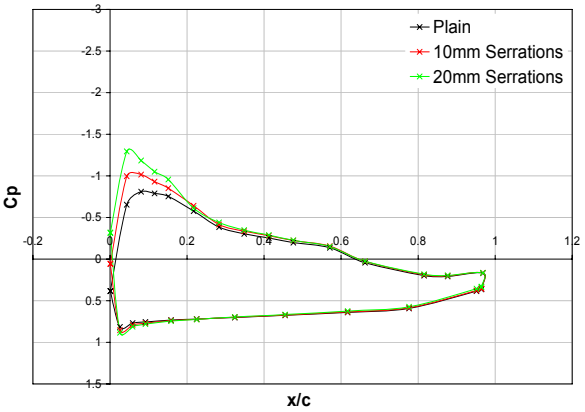

(d) Lap/Gap: (0, −0.07), δ_f=15°

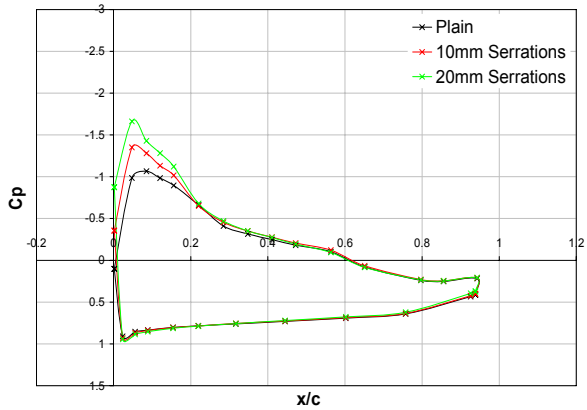

(c) Lap/Gap: (0, −0.07), δ_f=20°

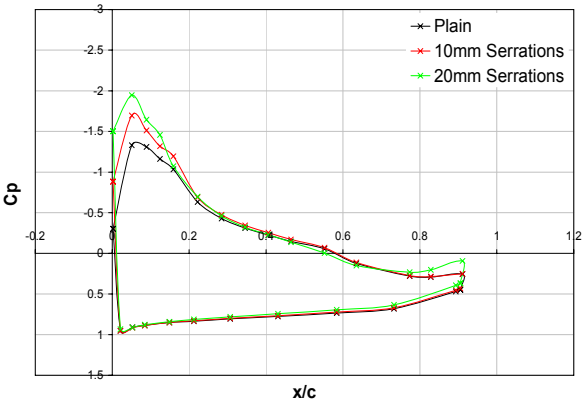

(d) Lap/Gap: (0, −0.07), δ_f=25°

Figure 156(a)-(f): C_p distributions at a flap lap/gap of (0, −0.07), 0°≤δ_f≤25°

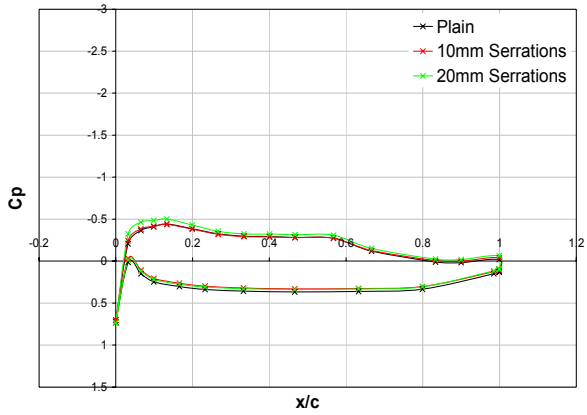

(a) Lap/Gap: (0.07, −0.07), δ_f=0°

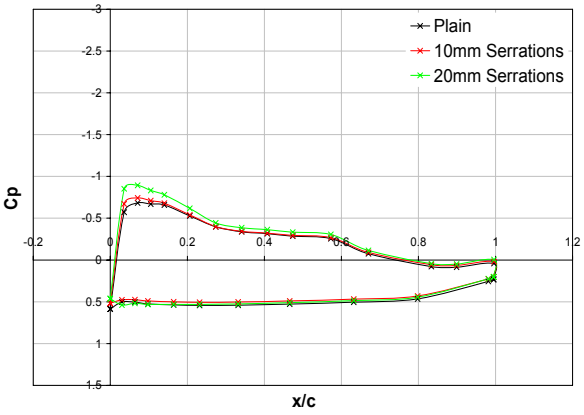

(b) Lap/Gap: (0.07, −0.07), δ_f=5°

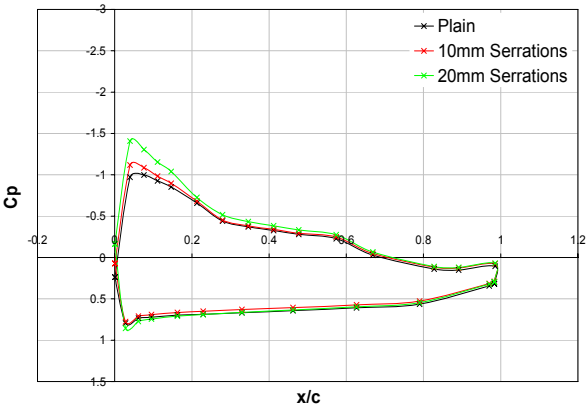

(c) Lap/Gap: (0.07, −0.07), δ_f=10°

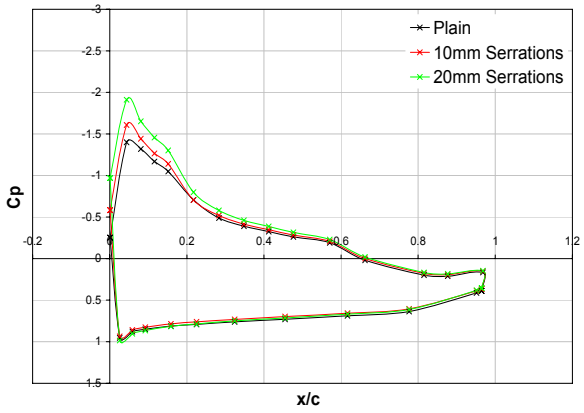

(d) Lap/Gap: (0.07, −0.07), δ_f=15°

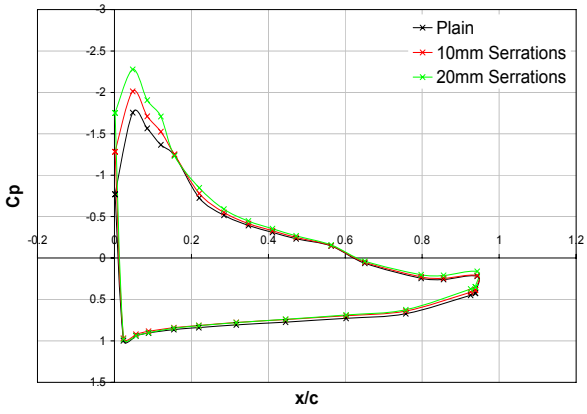

(e) Lap/Gap: (0.07, −0.07), δ_f=20°

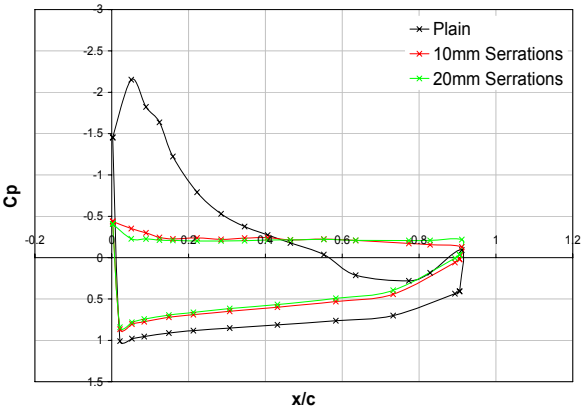

(f) Lap/Gap: (0.07, −0.07), δ_f=25°

Figure 157(a)-(f): C_p distributions at a flap lap/gap of (0.07, −0.07), 0°≤δ_f≤25°

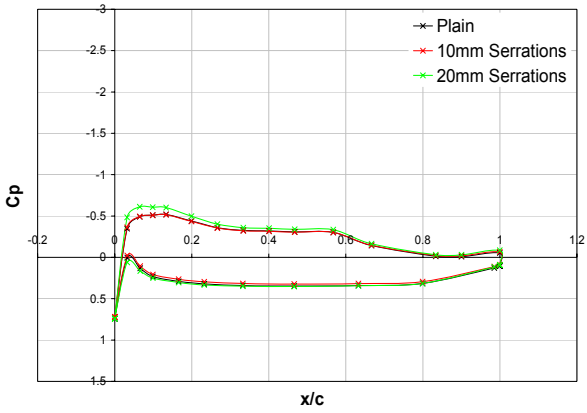

(a) Lap/Gap: (0.13, −0.07), δ_f=0°

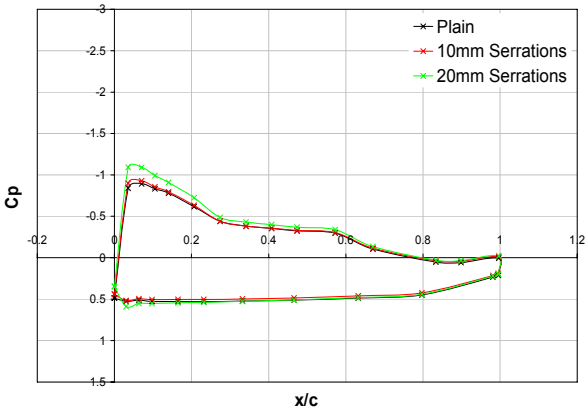

(b) Lap/Gap: (0.13, −0.07), δ_f=5°

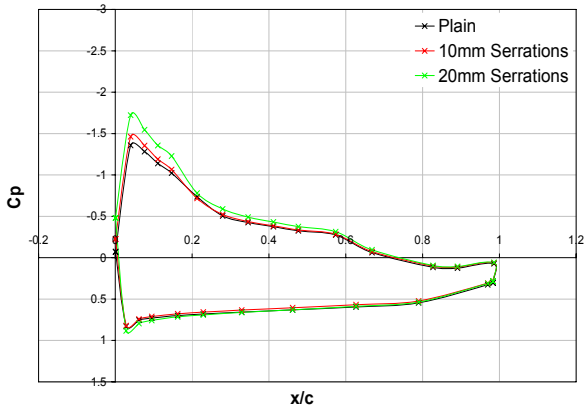

(c) Lap/Gap: (0.13, −0.07), δ_f=10°

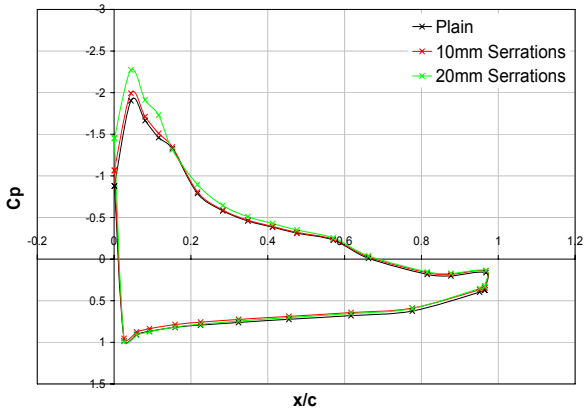

(d) Lap/Gap: (0.13, −0.07), δ_f=15°

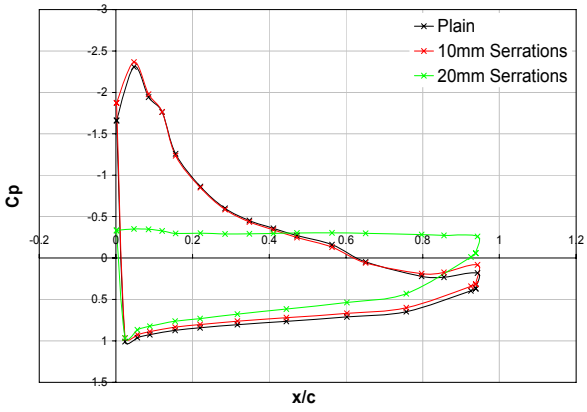

(e) Lap/Gap: (0.13, −0.07), δ_f=20°

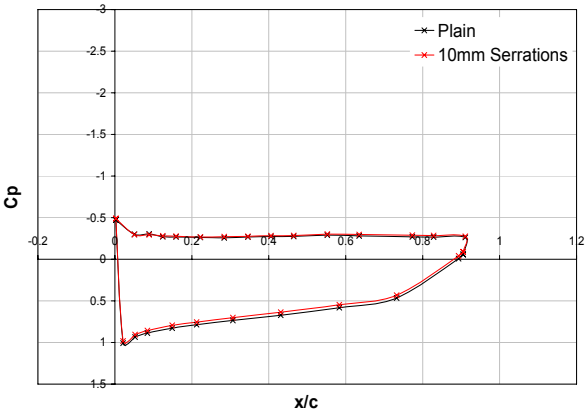

(f) Lap/Gap: (0.13, −0.07), δ_f=25°

Figure 158(a)-(f): C_p distributions at a flap lap/gap of (0.13, −0.07), 0°≤δ_f≤25°

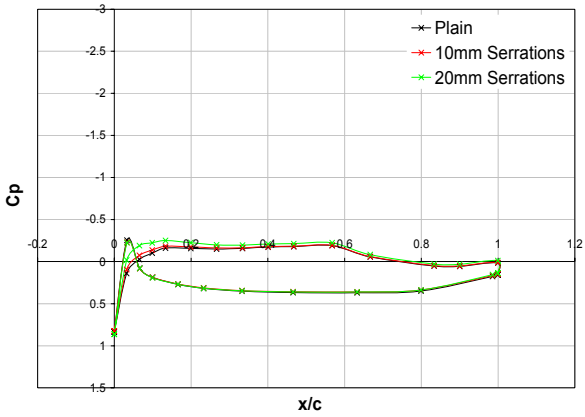

(a) Lap/Gap: (−0.13, −0.13), δ_f=0°

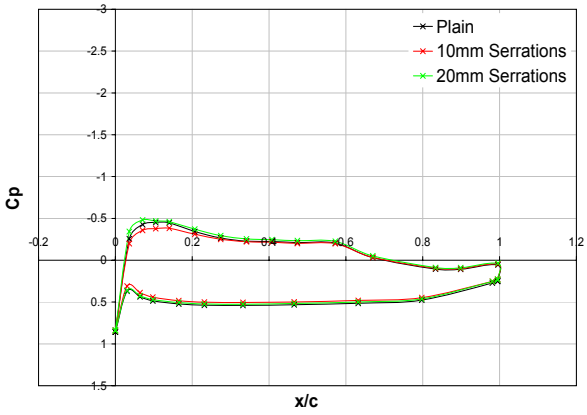

(b) Lap/Gap: (−0.13, −0.13), δ_f=5°

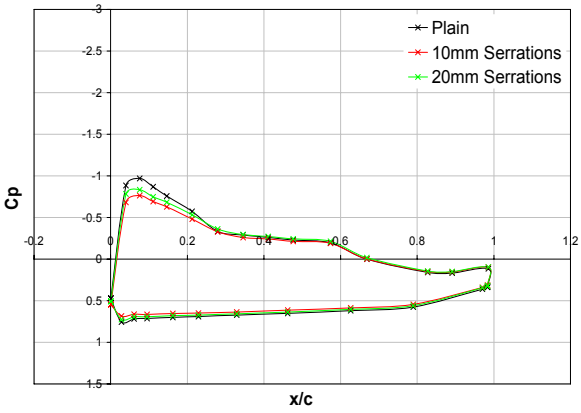

(c) Lap/Gap: (−0.13, −0.13), δ_f=10°

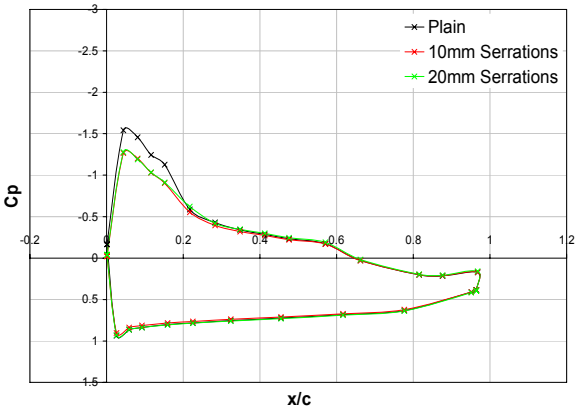

(d) Lap/Gap: (−0.13, −0.13), δ_f=15°

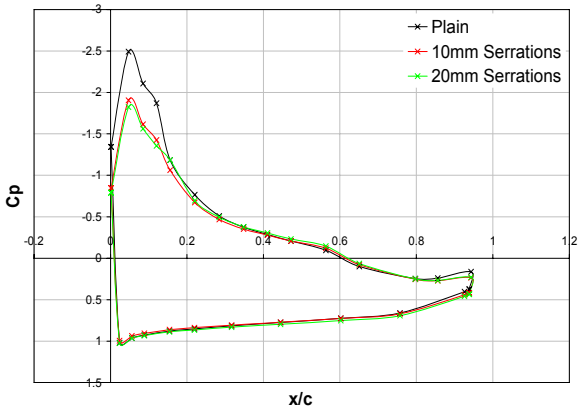

(e) Lap/Gap: (−0.13, −0.13), δ_f=20°

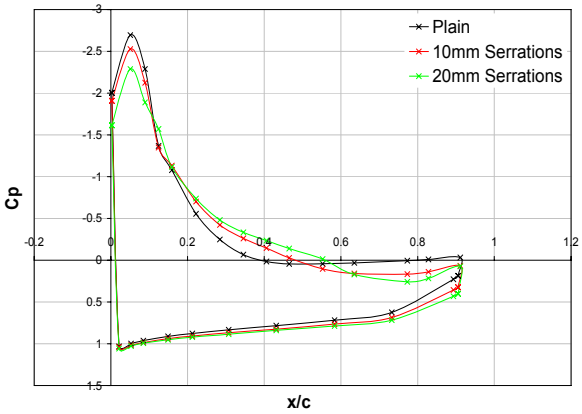

(f) Lap/Gap: (−0.13, −0.13), δ_f=25°

Figure 159(a)-(f): C_p distributions at a flap lap/gap of (−0.13, −0.13), 0°≤δ_f≤25°

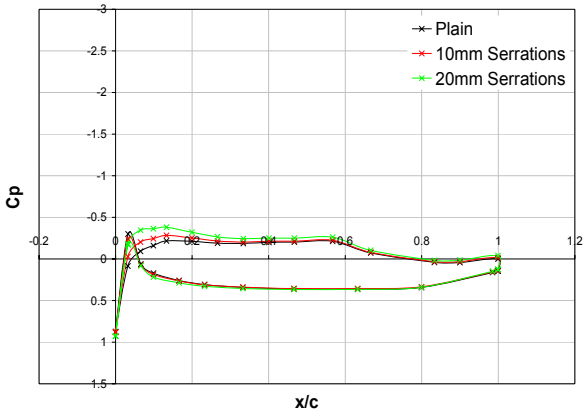

(a) Lap/Gap: (−0.07, −0.13), δ_f=0°

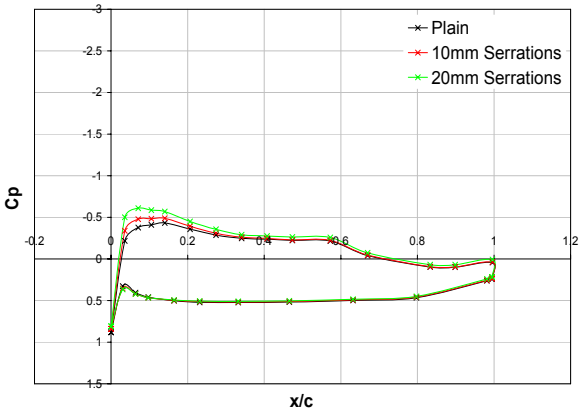

(b) Lap/Gap: (−0.07, −0.13), δ_f=5°

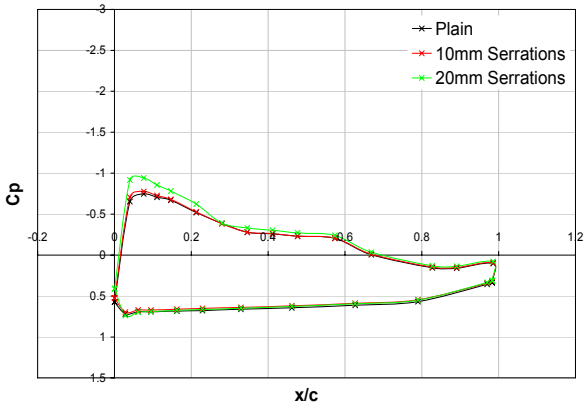

(c) Lap/Gap: (−0.07, −0.13), δ_f=10°

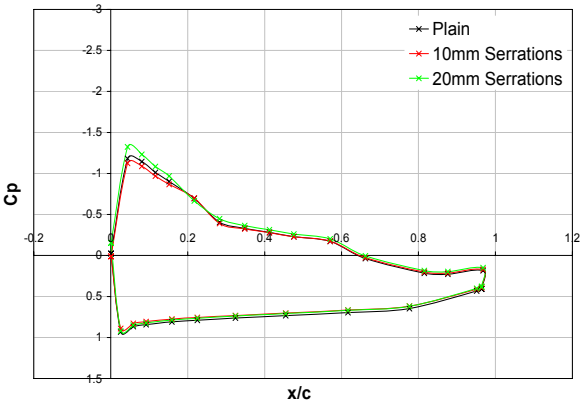

(d) Lap/Gap: (−0.07, −0.13), δ_f=15°

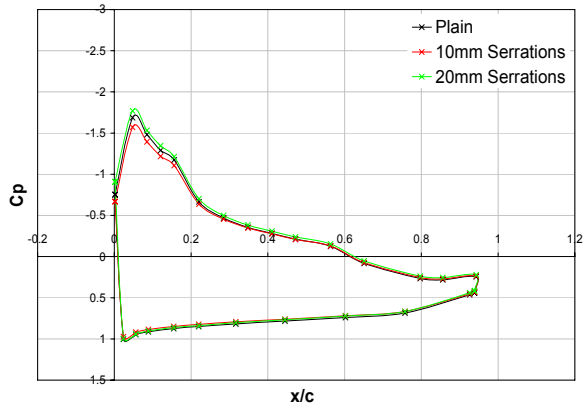

(e) Lap/Gap: (−0.07, −0.13), δ_f=20°

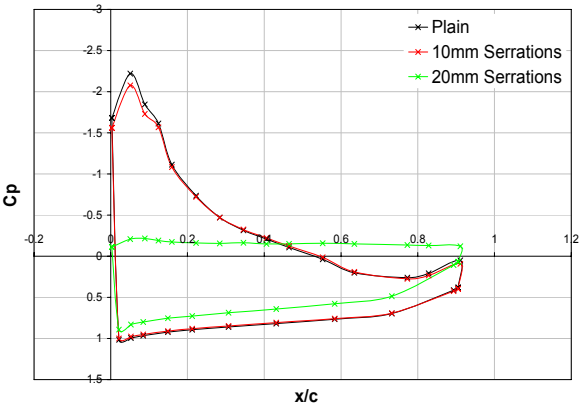

(f) Lap/Gap: (−0.07, −0.13), δ_f=25°

Figure 160(a)-(f): C_p distributions at a flap lap/gap of (−0.07, −0.13), 0°≤δ_f≤25°

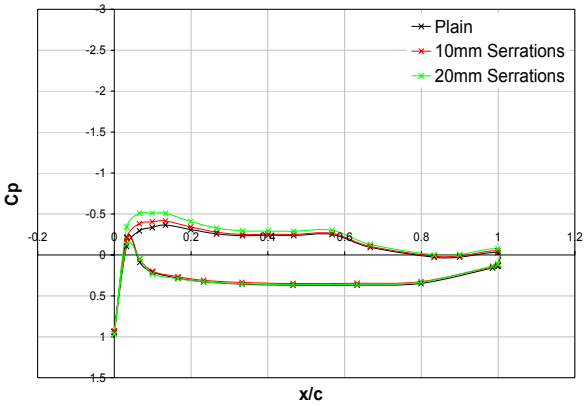

(a) Lap/Gap: (0, −0.13), δ_f=0°

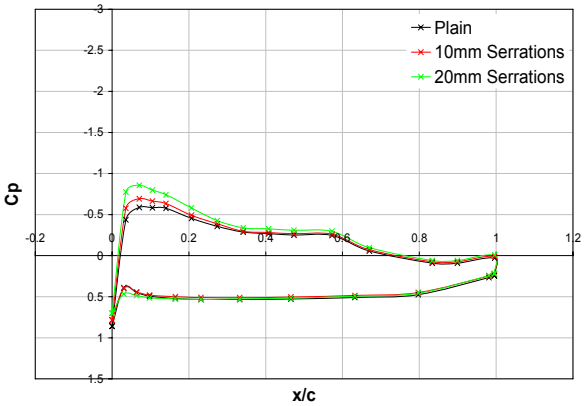

(b) Lap/Gap: (0, −0.13), δ_f=5°

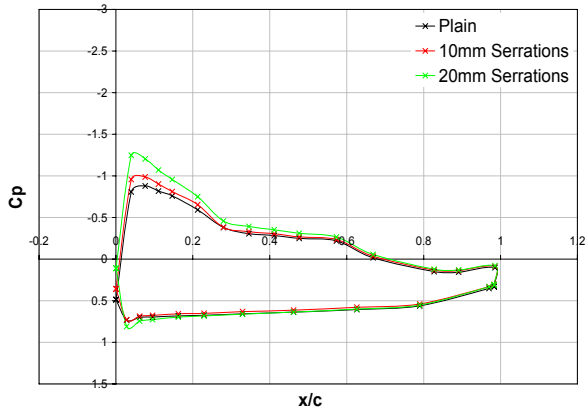

(c) Lap/Gap: (0, −0.13), δ_f=10°

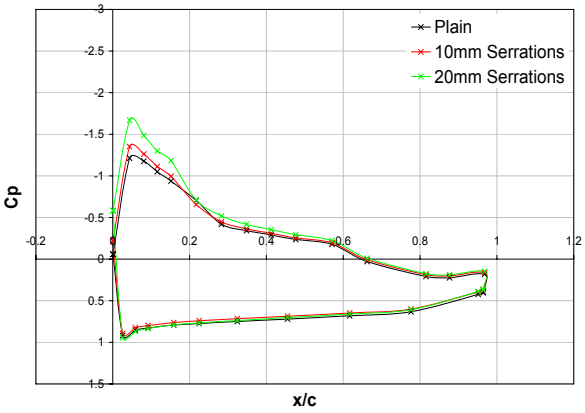

(d) Lap/Gap: (0, −0.13), δ_f=15°

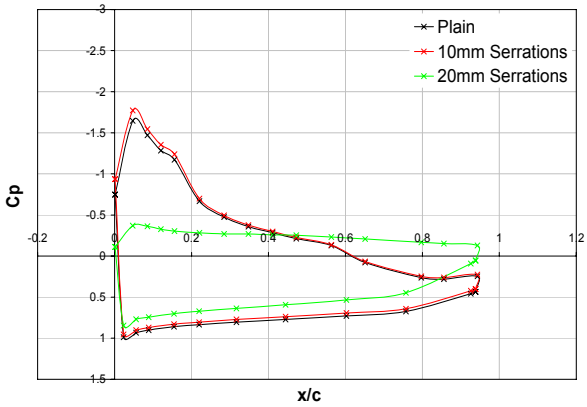

(e) Lap/Gap: (0, −0.13), δ_f=20°

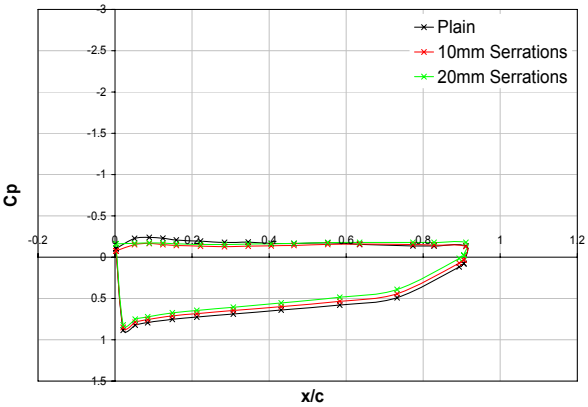

(f) Lap/Gap: (0, −0.13), δ_f=25°

Figure 161(a)-(f): C_p distributions at a flap lap/gap of (0, −0.13), 0°≤δ_f≤25°

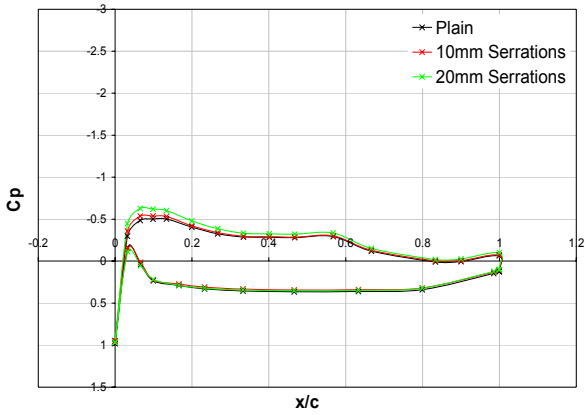

(a) Lap/Gap: (0.07, −0.13), δ_f=0°

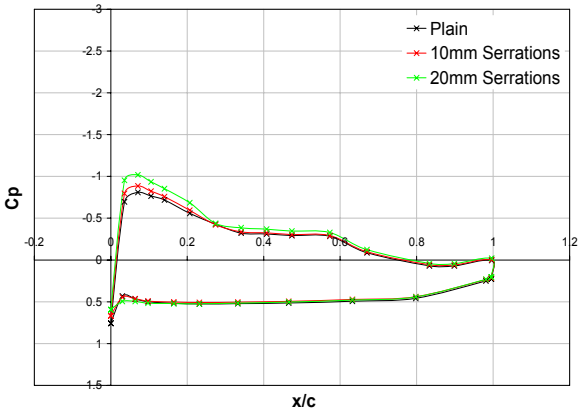

(b) Lap/Gap: (0.07, −0.13), δ_f=5°

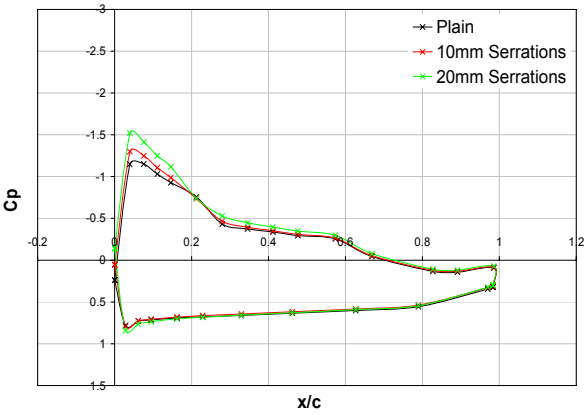

(c) Lap/Gap: (0.07, −0.13), δ_f=10°

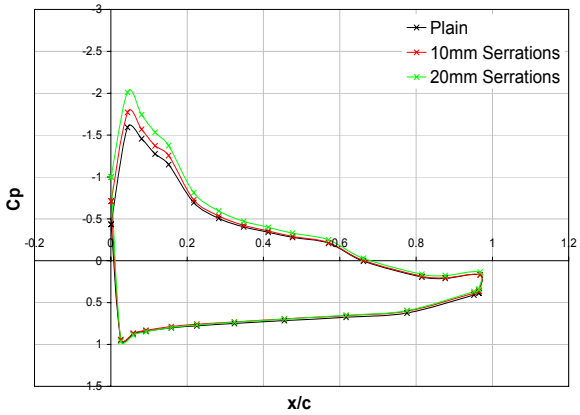

(d) Lap/Gap: (0.07, −0.13), δ_f=15°

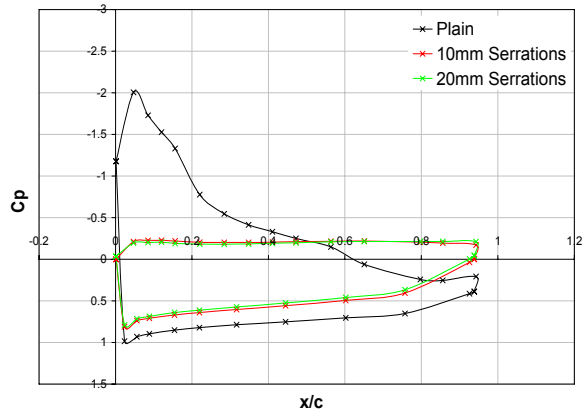

(e) Lap/Gap: (0.07, −0.13), δ_f=20°

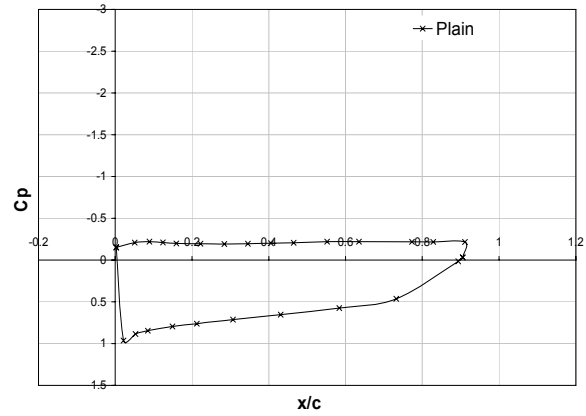

(f) Lap/Gap: (0.07, −0.13), δ_f=25°

Figure 162(a)-(f): C_p distributions at a flap lap/gap of (0.07, −0.13), 0°≤δ_f≤25°

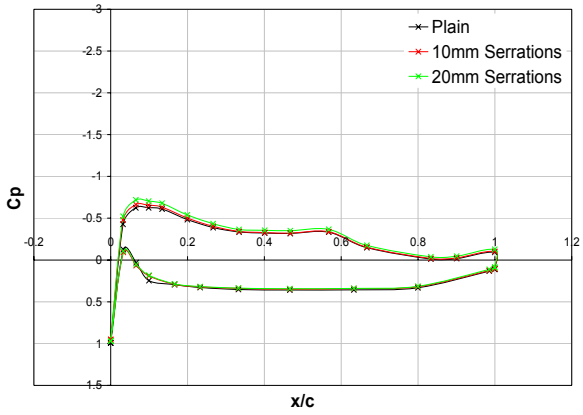

(a) Lap/Gap: (0.13, −0.13), δ_f=0°

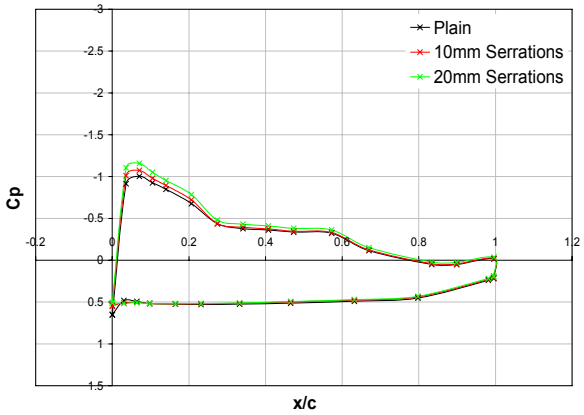

(b) Lap/Gap: (0.13, −0.13), δ_f=5°

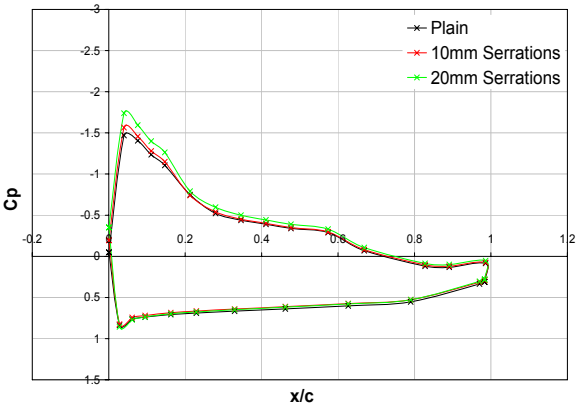

(c) Lap/Gap: (0.13, −0.13), δ_f=10°

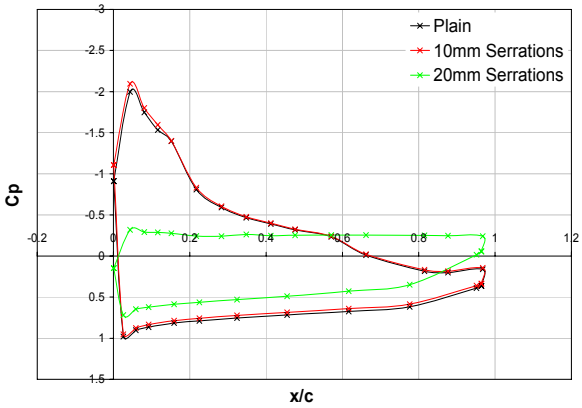

(d) Lap/Gap: (0.13, −0.13), δ_f=15°

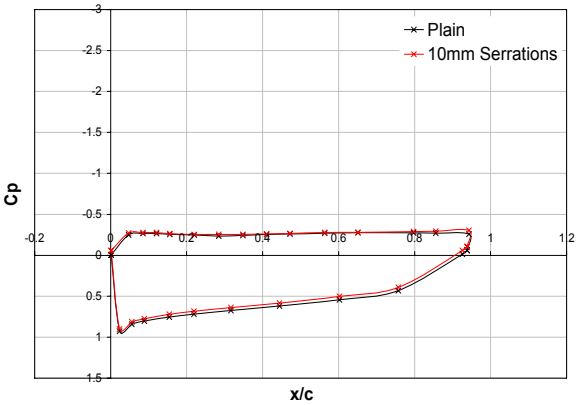

(e) Lap/Gap: (0.13, −0.13), δ_f=20°

Figure 163(a)-(e): C_p distributions at a flap lap/gap of (0.13, −0.13), 0°≤δ_f≤20°

Appendix E

Non-Dimensional Wake Surveys Aft of Flat Plate and Single Slotted Flap for Plain, 10mm and 20mm Serrated Trailing-Edge Configurations, Brough Wind-Tunnel

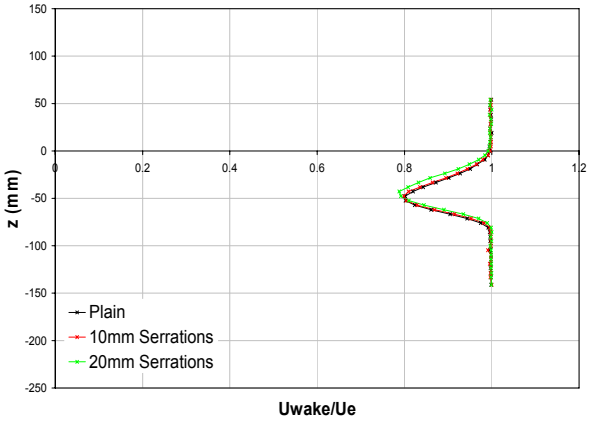

(a) Lap/Gap: (−0.13, −0.07), δ_f=5°

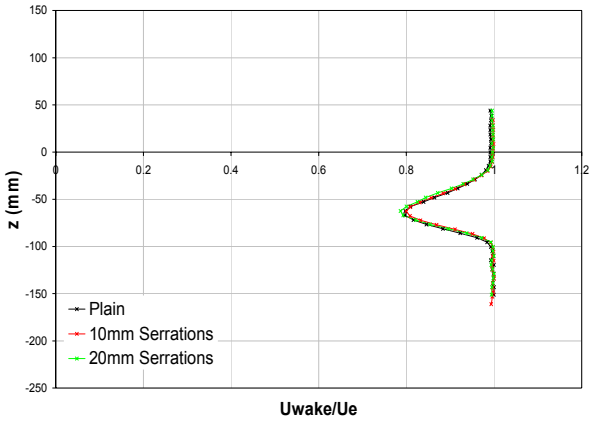

(b) Lap/Gap: (−0.13, −0.07), δ_f=10°

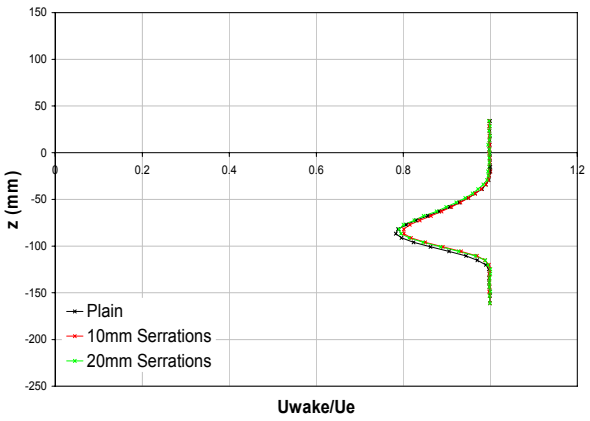

(c) Lap/Gap: (−0.13, −0.07), δ_f=15°

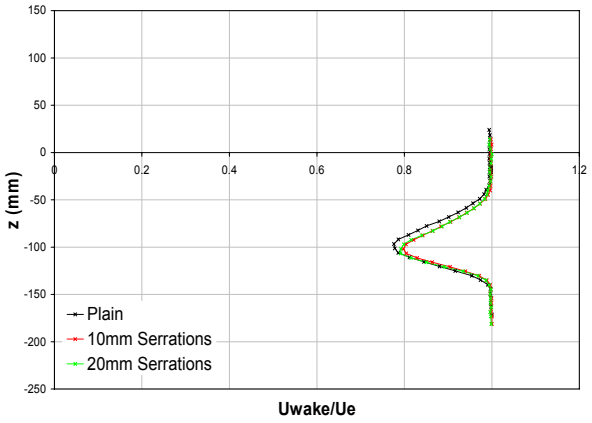

(d) Lap/Gap: (−0.13, −0.07), δ_f=20°

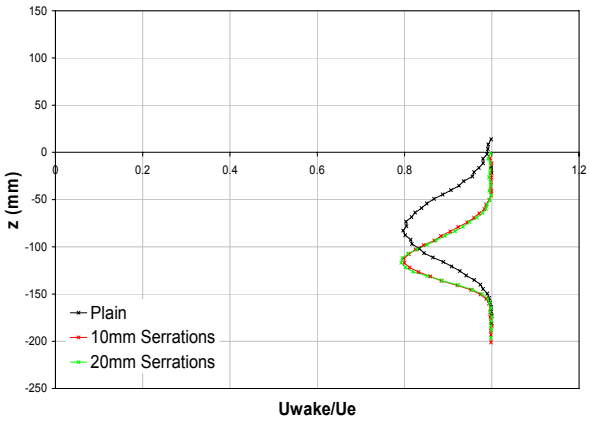

(e) Lap/Gap: (−0.13, −0.07), δ_f=25°

Figure 164(a)-(e): Wake surveys aft of flat plate and single slotted flap combination at a flap lap/gap of (−0.13, −0.07), 5°≤δ_f≤25°

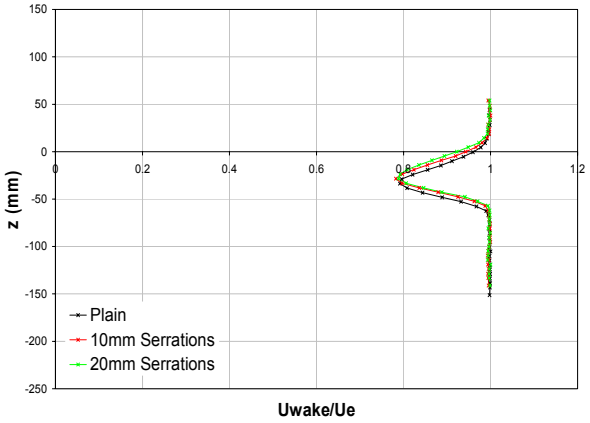

(a) Lap/Gap: (−0.07, −0.07), δ_f=0°

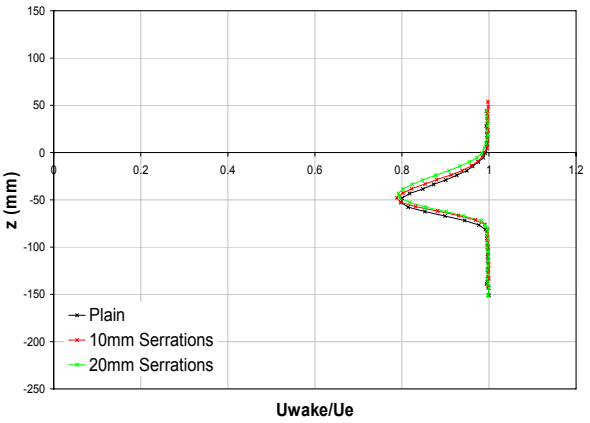

(b) Lap/Gap: (−0.07, −0.07), δ_f=5°

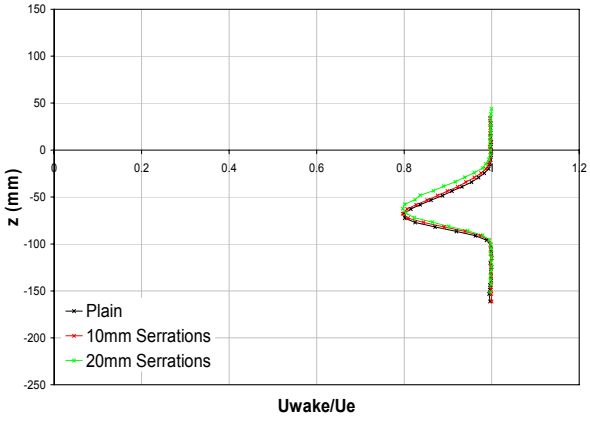

(c) Lap/Gap: (−0.07, −0.07), δ_f=10°

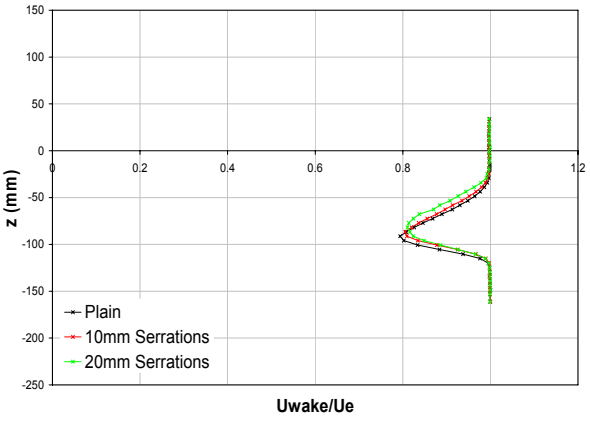

(d) Lap/Gap: (−0.07, −0.07), δ_f=15°

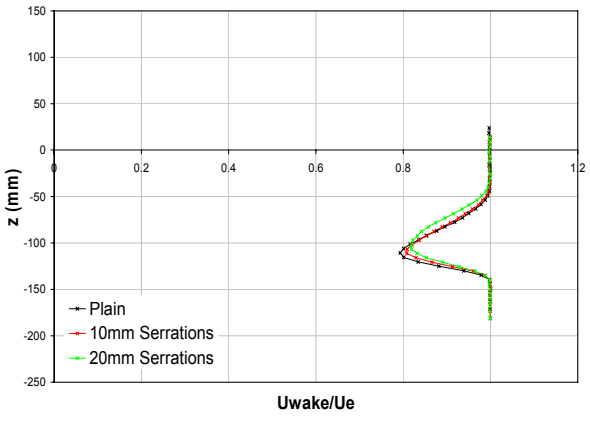

(e) Lap/Gap: (−0.07, −0.07), δ_f=20°

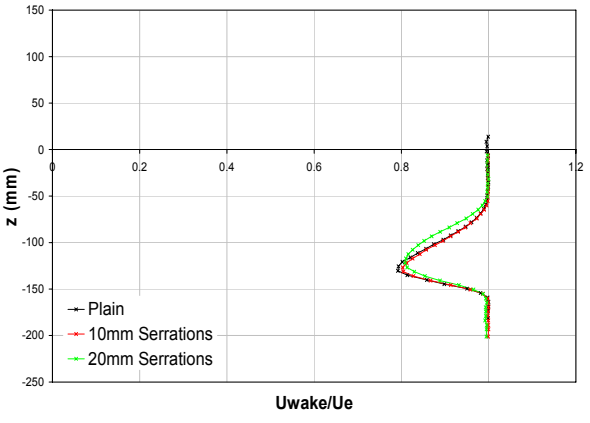

(f) Lap/Gap: (−0.07, −0.07), δ_f=25°

Figure 165(a)-(f): Wake surveys aft of flat plate and single slotted flap combination at a flap lap/gap of (−0.07, −0.07), 0°≤δ_f≤25°

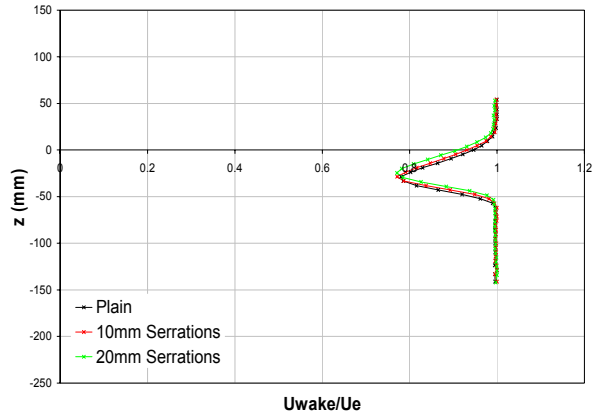

(a) Lap/Gap: (0, −0.07), δ_f=0°

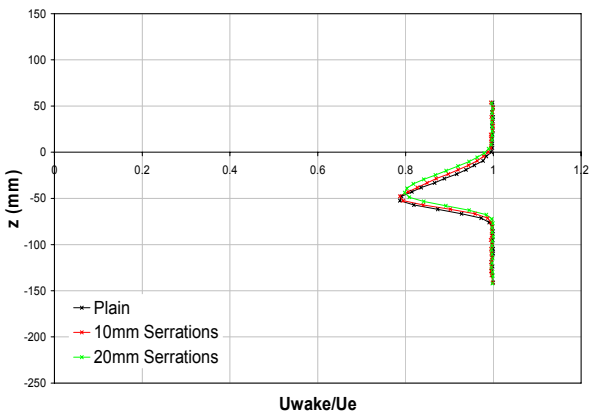

(b) Lap/Gap: (0, −0.07), δ_f=5°

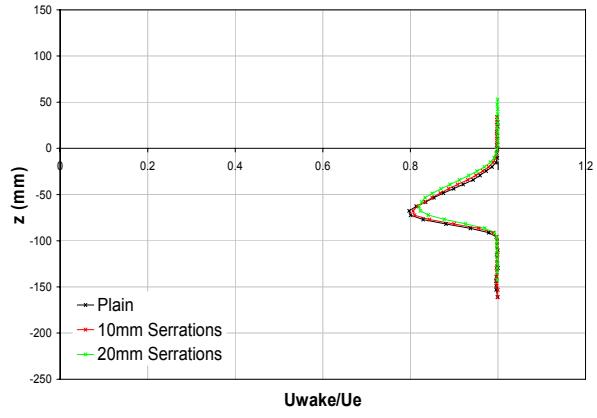

(c) Lap/Gap: (0, −0.07), δ_f=10°

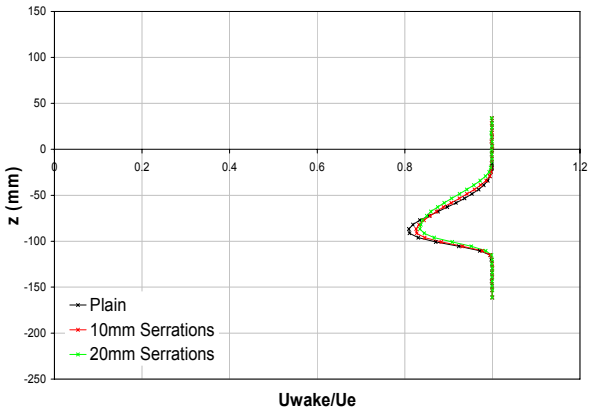

(d) Lap/Gap: (0, −0.07), δ_f=15°

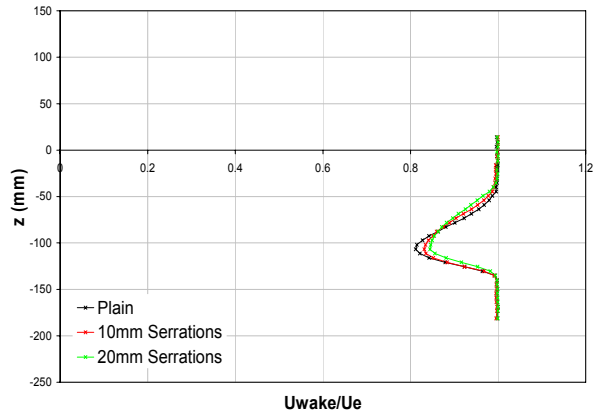

(e) Lap/Gap: (0, −0.07), δ_f=20°

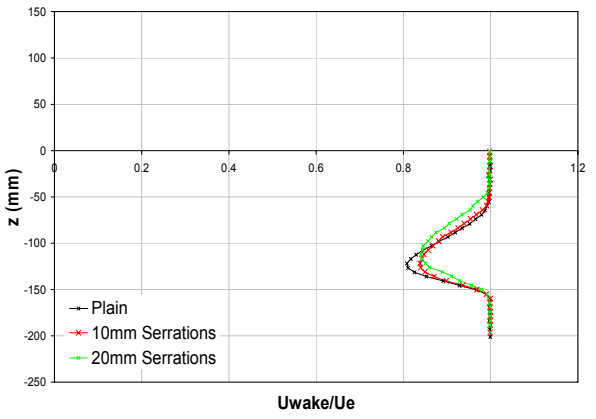

(f) Lap/Gap: (0, −0.07), δ_f=25°

Figure 166(a)-(f): Wake surveys aft of flat plate and single slotted flap combination at a flap lap/gap of (0, −0.07), 0°≤δ_f≤25°

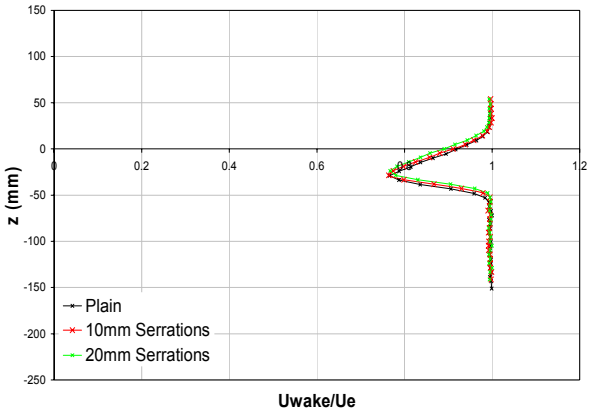

(a) Lap/Gap: (0.07, −0.07), δ_f=0°

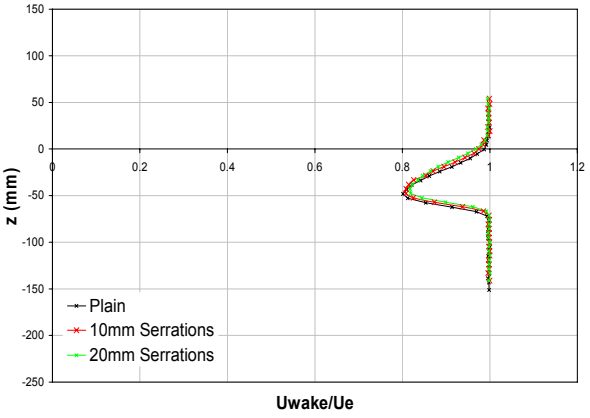

(b) Lap/Gap: (0.07, −0.07), δ_f=5°

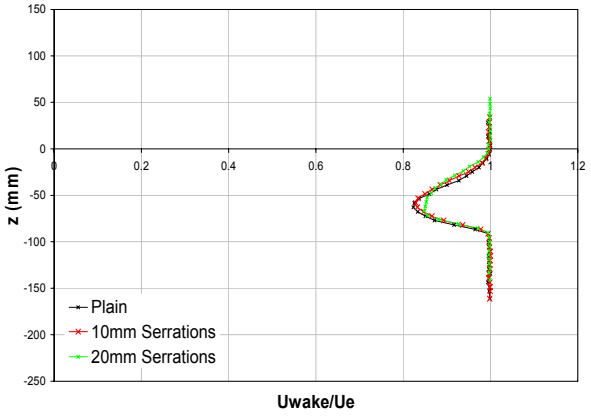

(c) Lap/Gap: (0.07, −0.07), δ_f=10°

(d) Lap/Gap: (0.07, −0.07), δ_f=15°

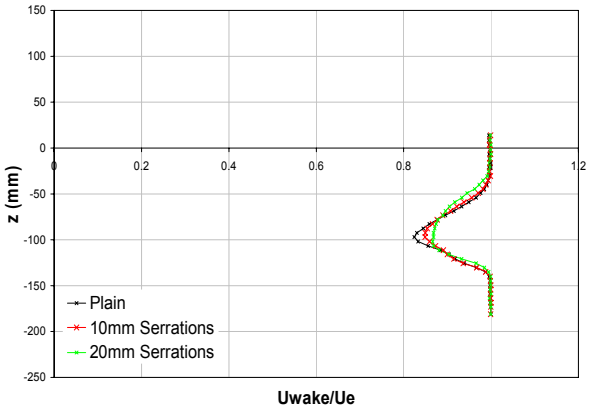

(e) Lap/Gap: (0.07, −0.07), δ_f=20°

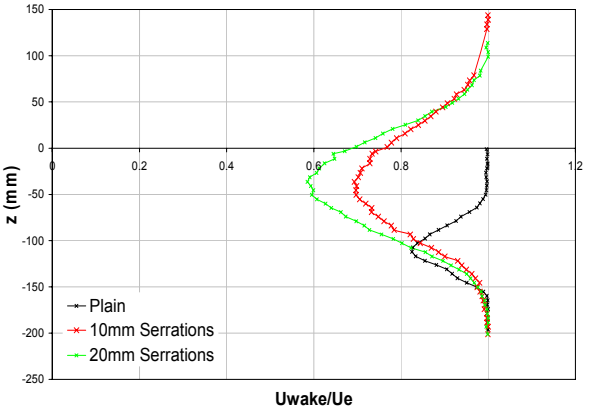

(f) Lap/Gap: (0.07, −0.07), δ_f=25°

Figure 167(a)-(f): Wake surveys aft of flat plate and single slotted flap combination at a flap lap/gap of (0.07, −0.07), 0°≤δ_f≤25°

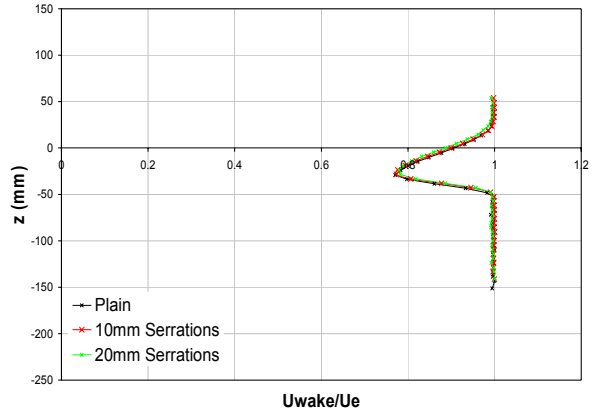

(a) Lap/Gap: (0.13, −0.07), δ_f=0°

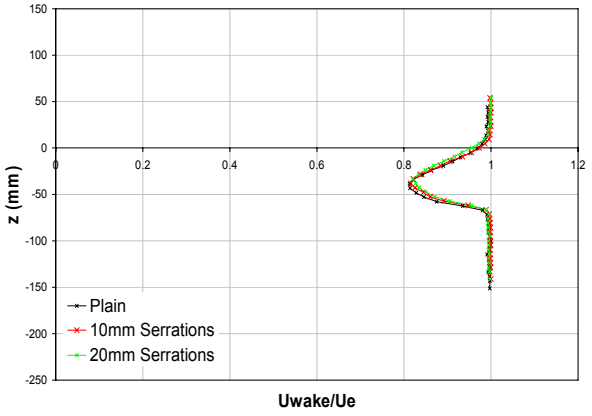

(b) Lap/Gap: (0.13, −0.07), δ_f=5°

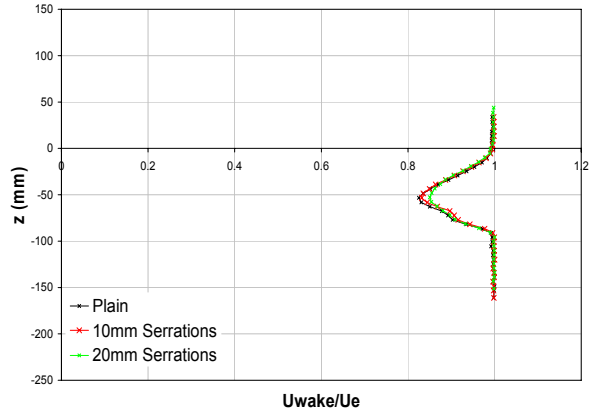

(c) Lap/Gap: (0.13, −0.07), δ_f=10°

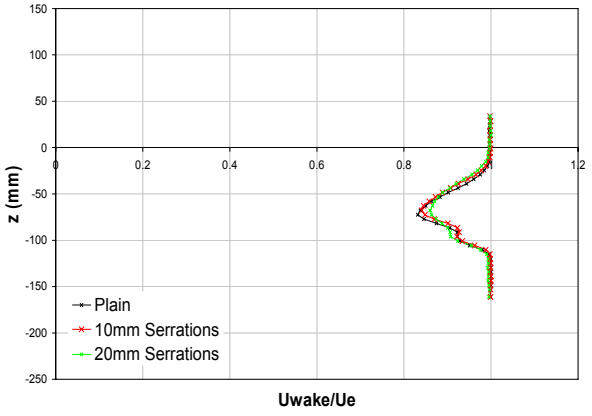

(d) Lap/Gap: (0.13, −0.07), δ_f=15°

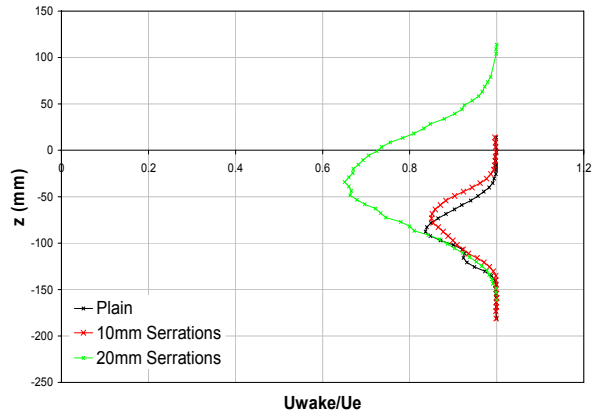

(e) Lap/Gap: (0.13, −0.07), δ_f=20°

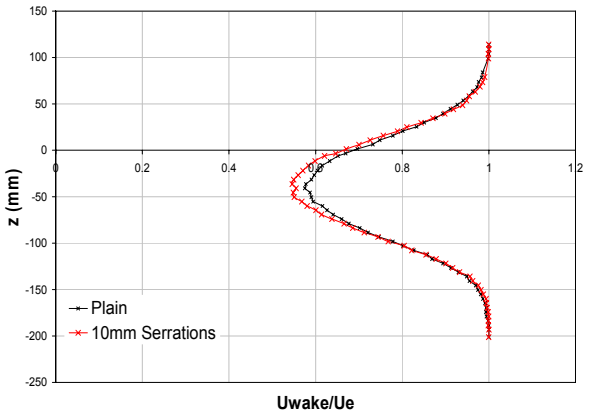

(f) Lap/Gap: (0.13, −0.07), δ_f=25°

Figure 168(a)-(f): Wake surveys aft of flat plate and single slotted flap combination at a flap lap/gap of (0.13, −0.07), 0°≤δ_f≤25°

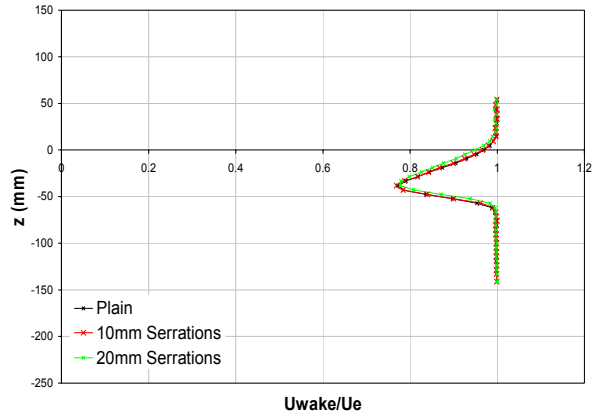

(a) Lap/Gap: (−0.13, −0.13), δ_f=0°

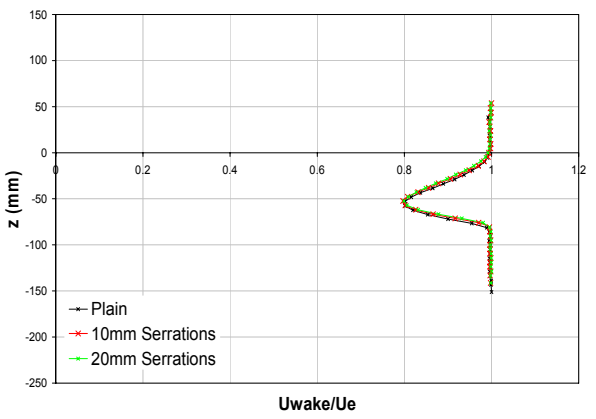

(b) Lap/Gap: (−0.13, −0.13), δ_f=5°

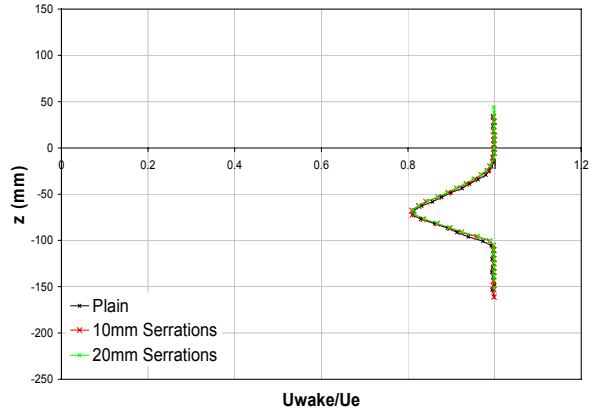

(c) Lap/Gap: (−0.13, −0.13), δ_f=10°

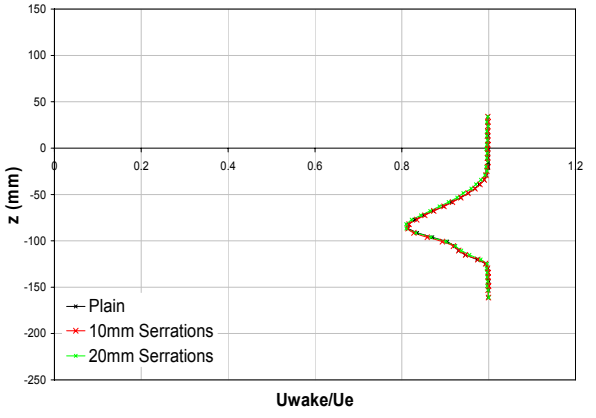

(d) Lap/Gap: (−0.13, −0.13), δ_f=15°

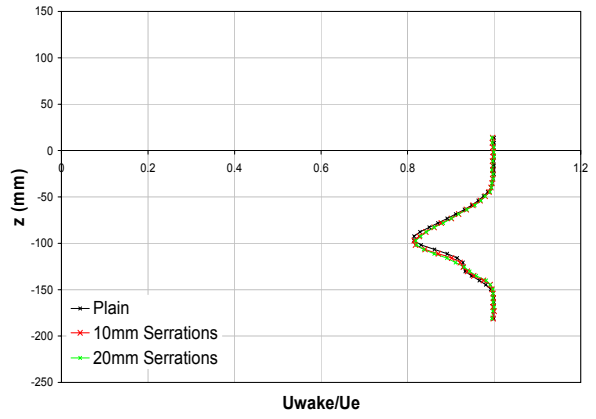

(e) Lap/Gap: (−0.13, −0.13), δ_f=20°

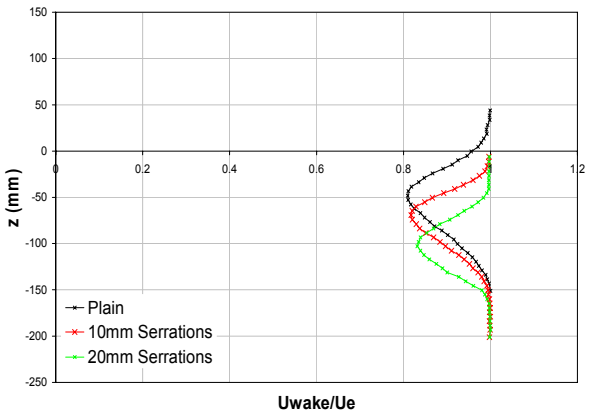

(f) Lap/Gap: (−0.13, −0.13), δ_f=25°

Figure 169(a)-(f): Wake surveys aft of flat plate and single slotted flap combination at a flap lap/gap of (−0.13, −0.13), 0°≤δ_f≤25°

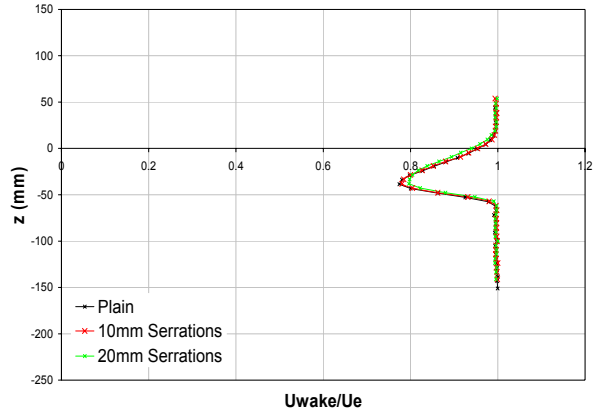

(a) Lap/Gap: (−0.07, −0.13), δ_f=0°

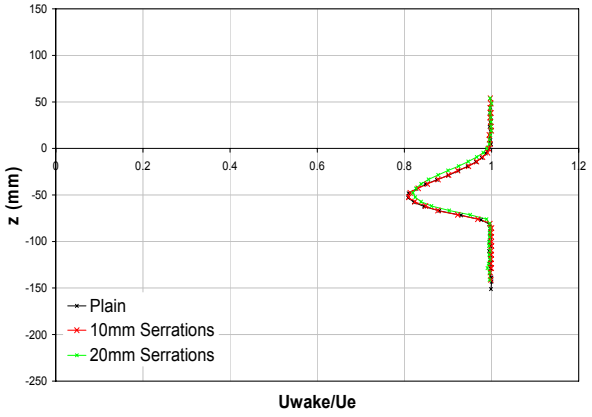

(b) Lap/Gap: (−0.07, −0.13), δ_f=5°

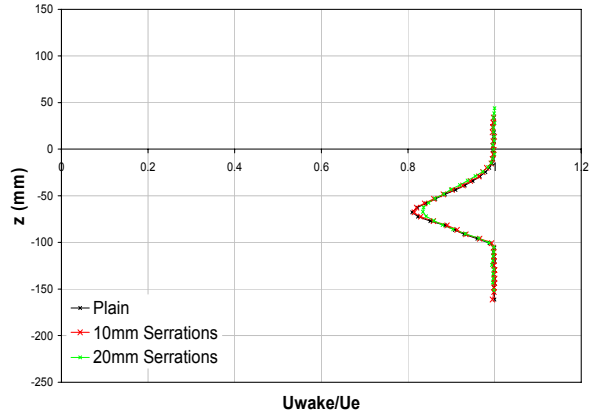

(c) Lap/Gap: (−0.07, −0.13), δ_f=10°

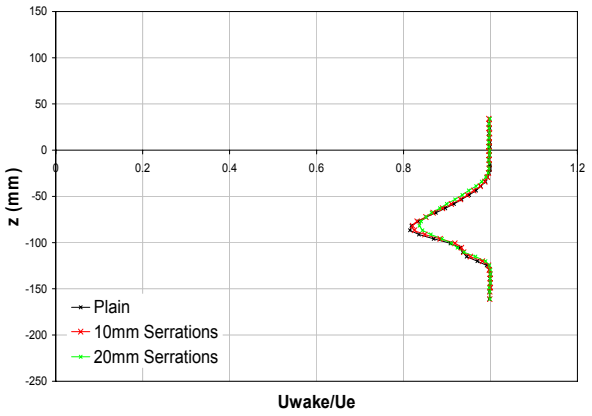

(d) Lap/Gap: (−0.07, −0.13), δ_f=15°

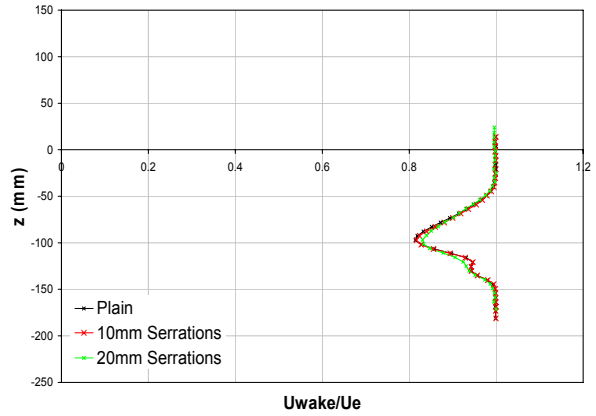

(e) Lap/Gap: (−0.07, −0.13), δ_f=20°

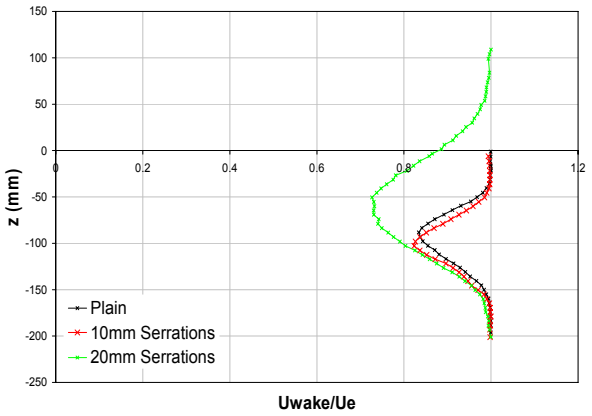

(f) Lap/Gap: (−0.07, −0.13), δ_f=25°

Figure 170(a)-(f): Wake surveys aft of flat plate and single slotted flap combination at a flap lap/gap of (−0.07, −0.13), 0°≤δ_f≤25°

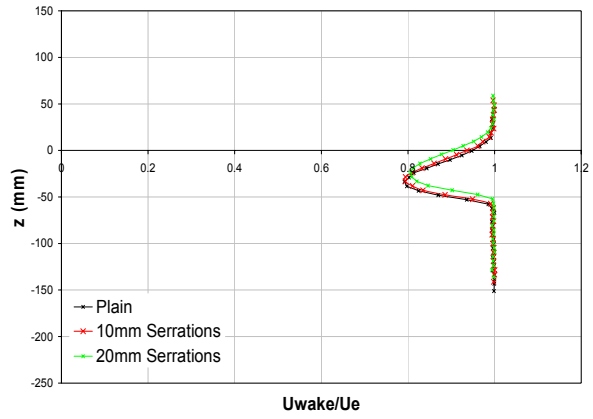

(a) Lap/Gap: (0, −0.13), δ_f=0°

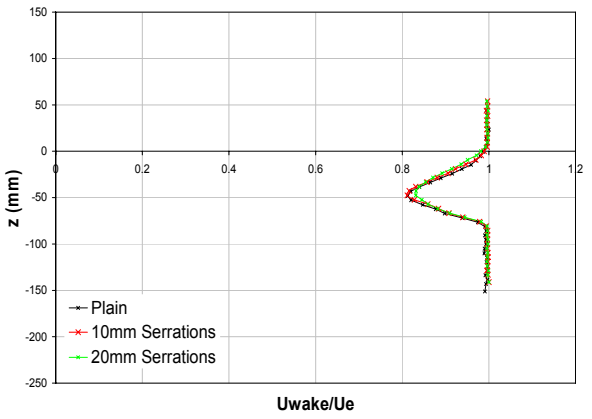

(b) Lap/Gap: (0, −0.13), δ_f=5°

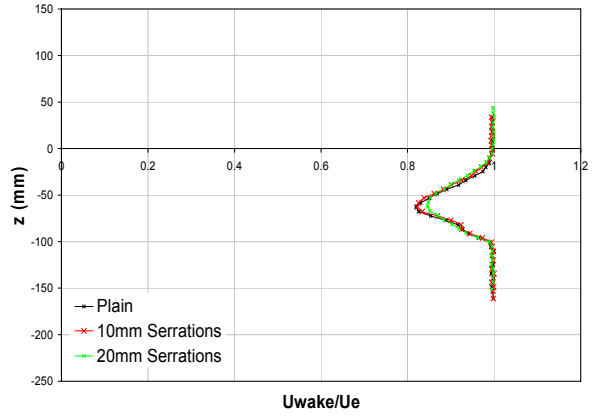

(c) Lap/Gap: (0, −0.13), δ_f=10°

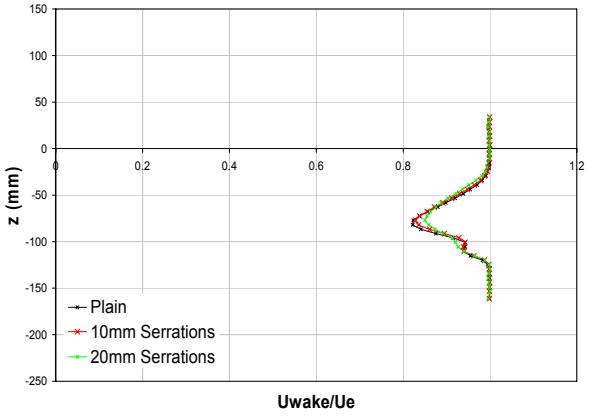

(d) Lap/Gap: (0, −0.13), δ_f=15°

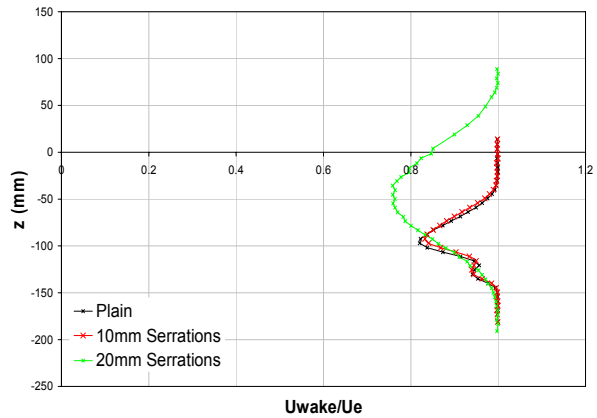

(e) Lap/Gap: (0, −0.13), δ_f=20°

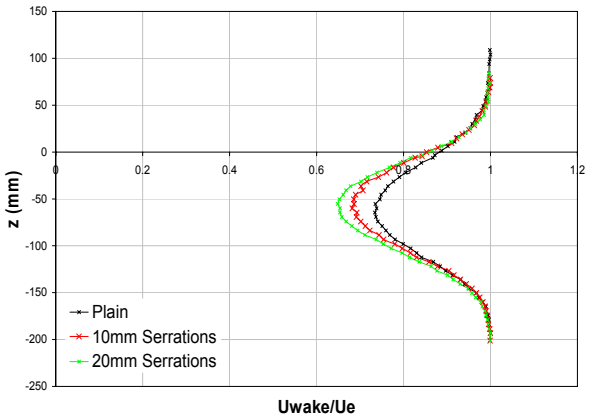

(f) Lap/Gap: (0, −0.13), δ_f=25°

Figure 171(a)-(f): Wake surveys aft of flat plate and single slotted flap combination at a flap lap/gap of (0, −0.13), 0°≤δ_f≤25°

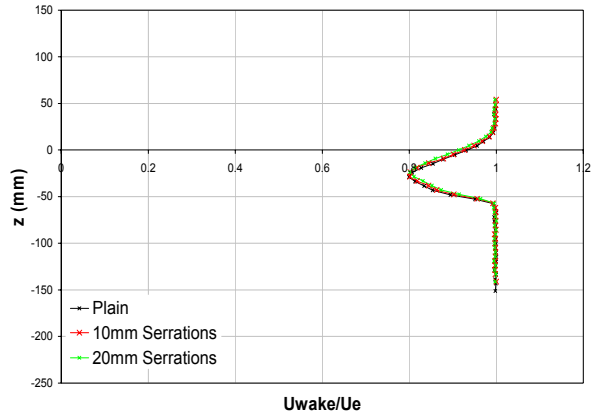

(a) Lap/Gap: (0.07, −0.13), δ_f=0°

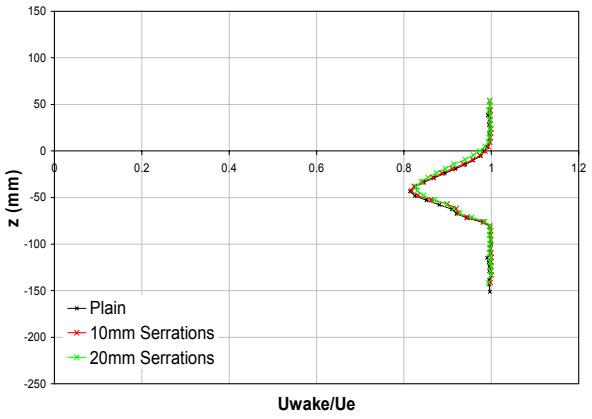

(b) Lap/Gap: (0.07, −0.13), δ_f=5°

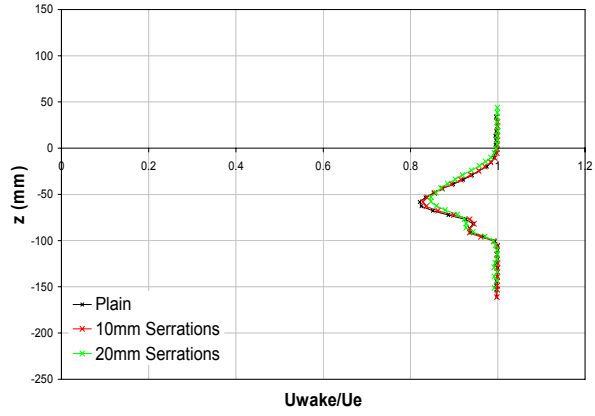

(c) Lap/Gap: (0.07, −0.13), δ_f=10°

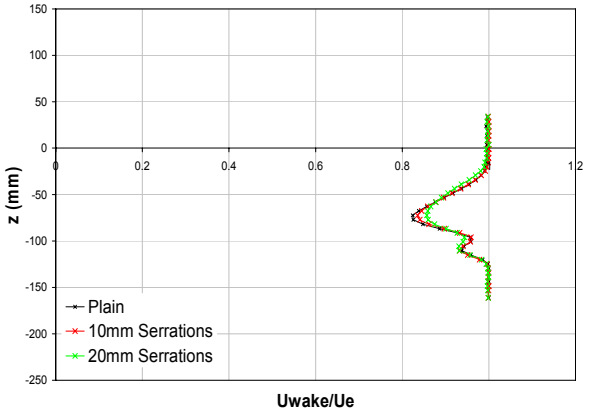

(d) Lap/Gap: (0.07, −0.13), δ_f=15°

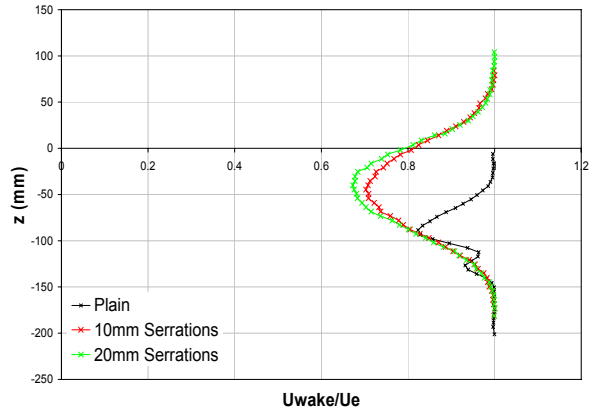

(e) Lap/Gap: (0.07, −0.13), δ_f=20°

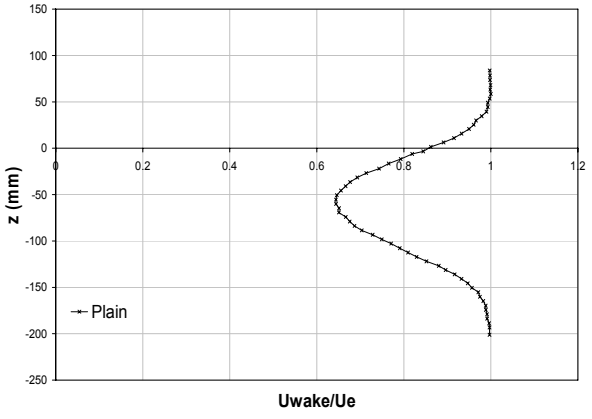

(f) Lap/Gap: (0.07, −0.13), δ_f=25°

Figure 172(a)-(f): Wake surveys aft of flat plate and single slotted flap combination at a flap lap/gap of (0.07, −0.13), 0°≤δ_f≤25°

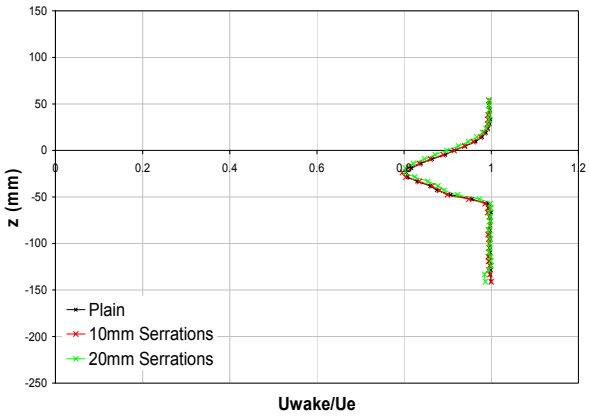

(a) Lap/Gap: (0.13, −0.13), δ_f=0°

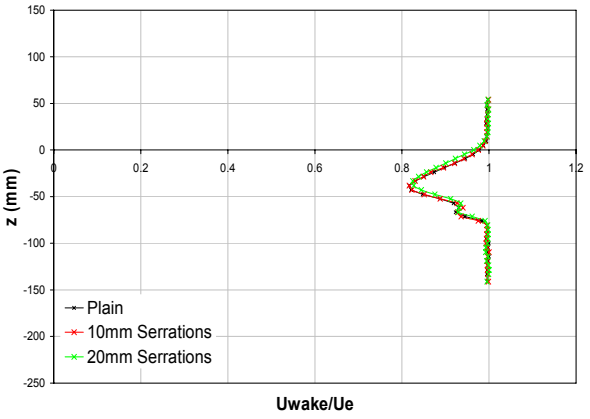

(b) Lap/Gap: (0.13, −0.13), δ_f=5°

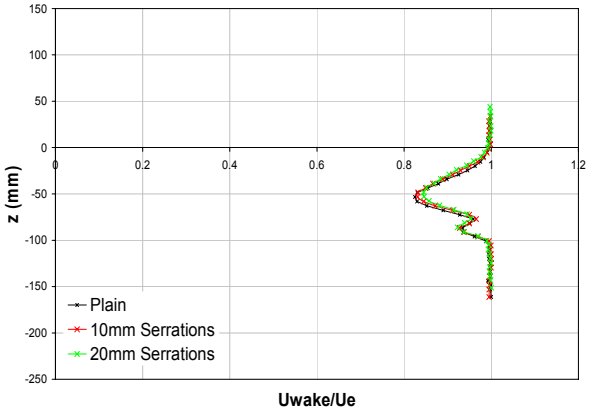

(c) Lap/Gap: (0.13, −0.13), δ_f=10°

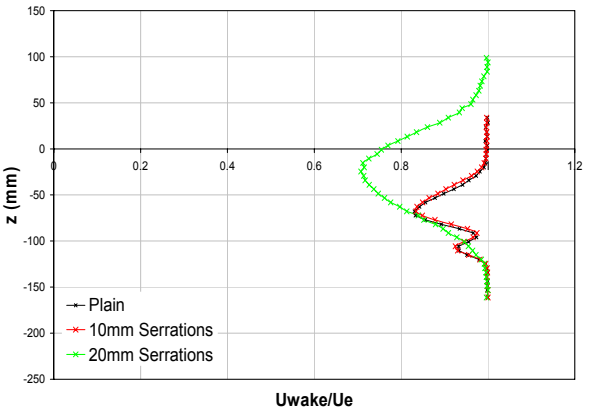

(d) Lap/Gap: (0.13, −0.13), δ_f=15°

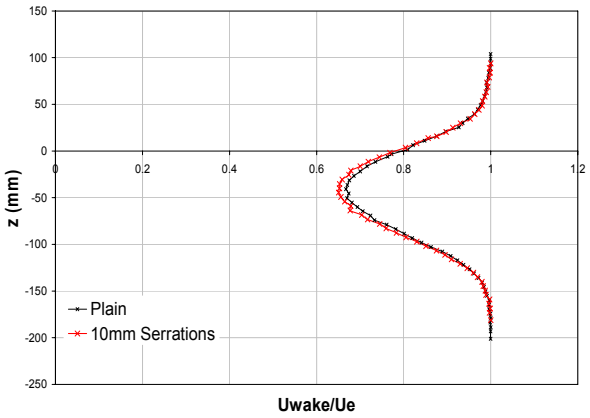

(e) Lap/Gap: (0.13, −0.13), δ_f=20°

Figure 173(a)-(e): Wake surveys aft of flat plate and single slotted flap combination at a flap lap/gap of (0.13, −0.13), 0°≤δ_f≤20°

Appendix F

Effect of Reynolds Number Variation on Single Slotted Flap Aft of Modified Flat Plate with Plain Trailing Edge, Brough Wind-Tunnel

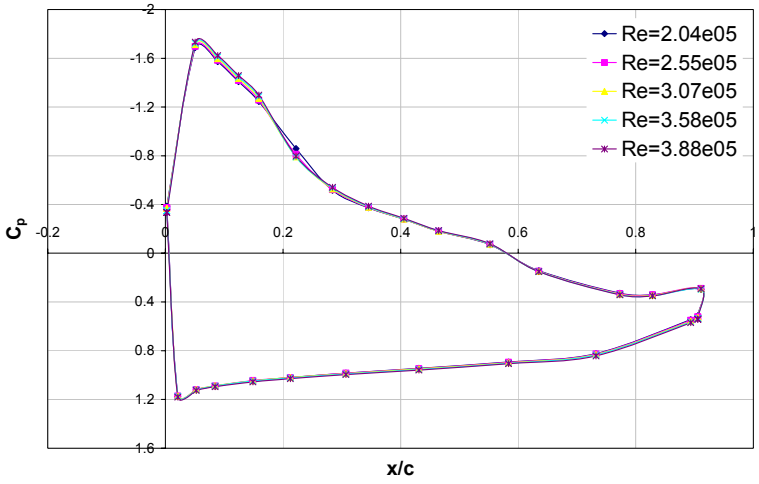

Figure 174: Effect of Reynolds number on C_p distribution over trailing edge flap at a flap lap/gap of (0, −0.07), δ_f=25°

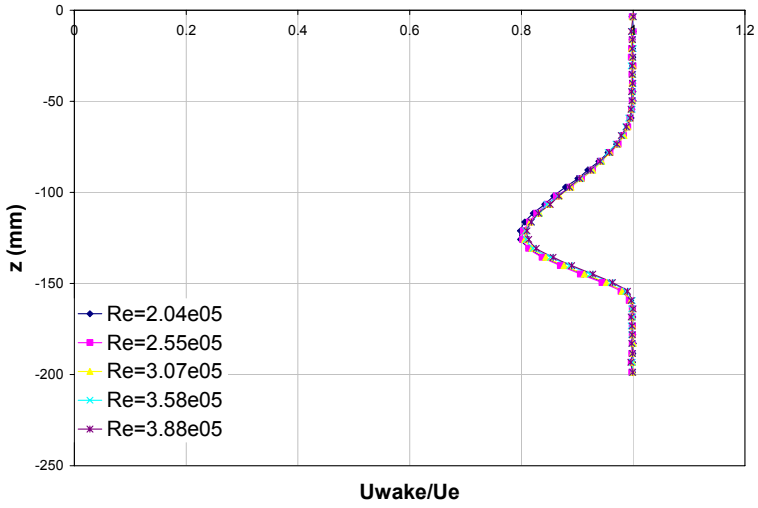

Figure 175: Effect of Reynolds number on wake aft of flat plate and trailing edge flap combination at a flap lap/gap of (0, −0.07), δ_f=25°

Appendix G

C_p Distributions for Takeoff Configuration with Plain, 10mm and 20mm Serrated Trailing Edges

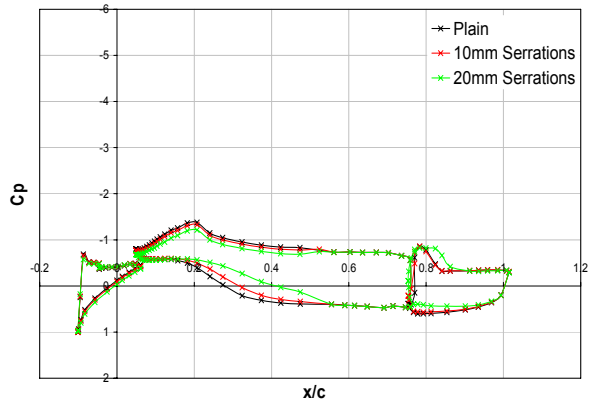

(a) α=0°

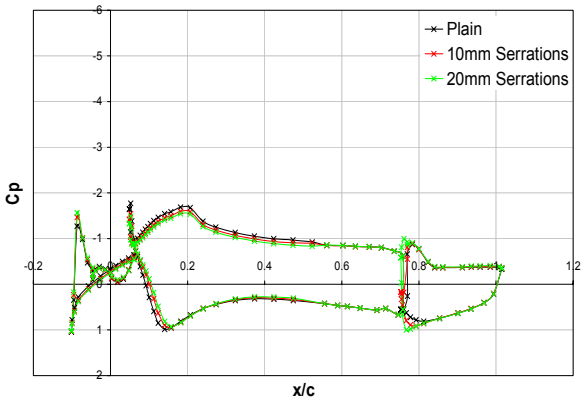

(b) α=2°

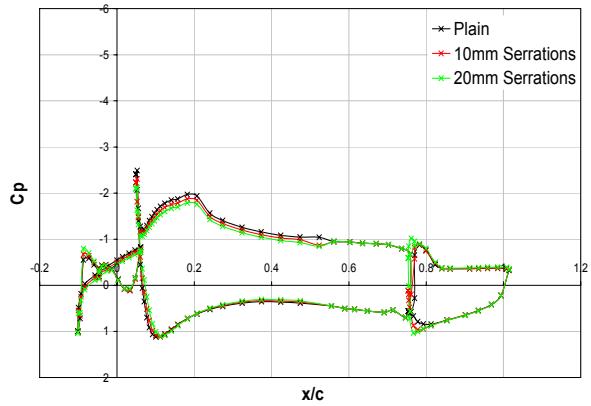

(c) α=4°

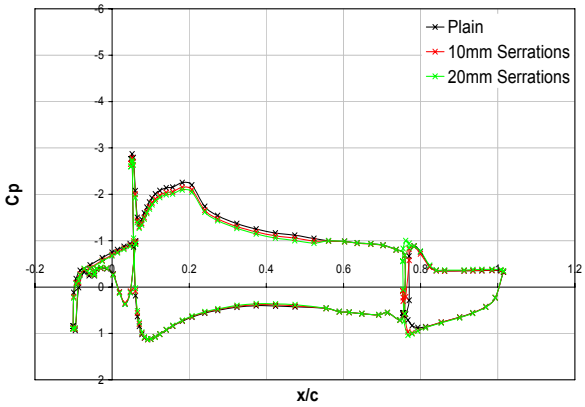

(d) α=6°

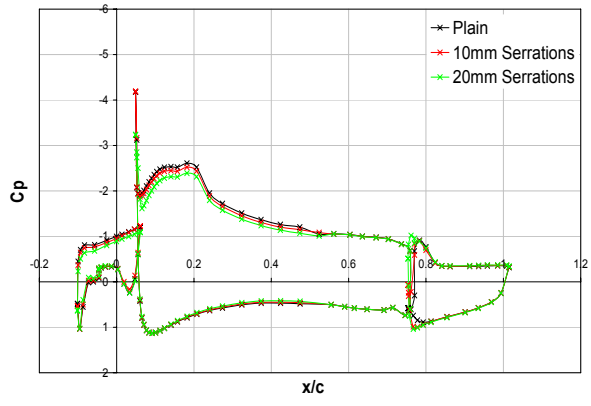

(e) α=8°

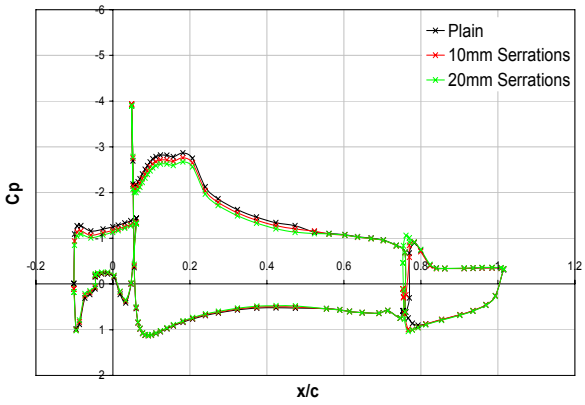

(f) α=10°

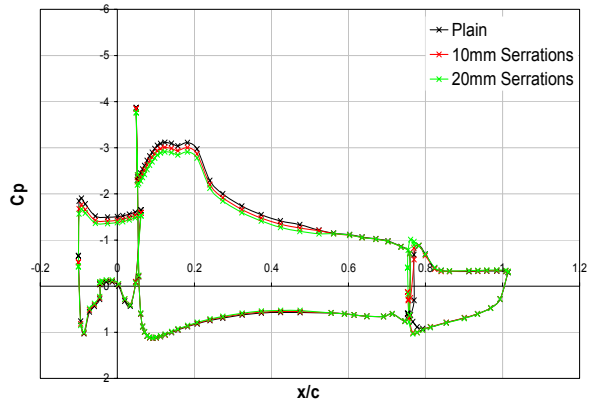

(g) α=12°

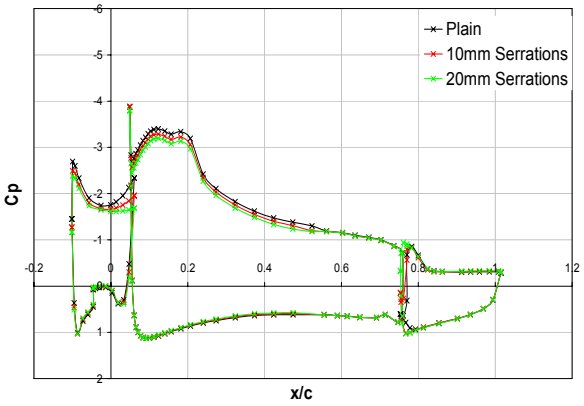

(h) α=14°

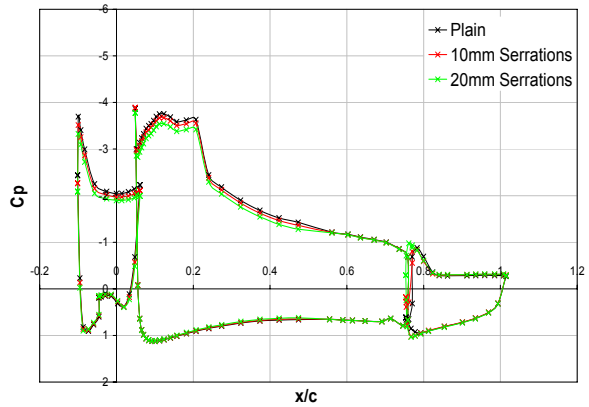

(i) α=16°

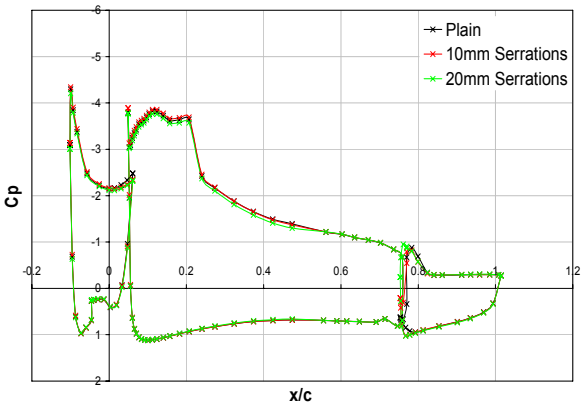

(j) α=18°

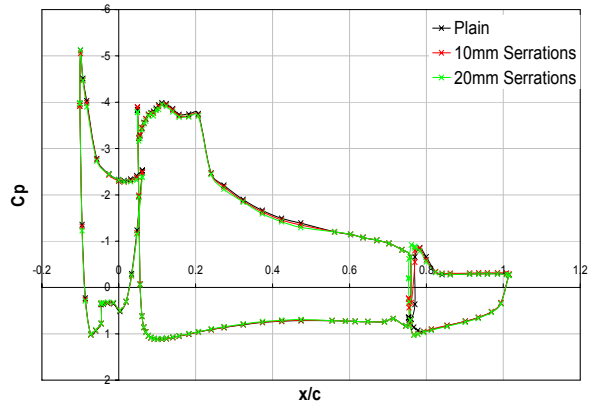

(k) α=20°

Figure 176(a)-(k): C_p distributions for takeoff configuration with plain, 10mm and 20mm serrated trailing edge geometries, 0°≤α≤20°

Appendix H

C_p Distributions for Landing Configuration with Plain, 10mm and 20mm Serrated Trailing Edges

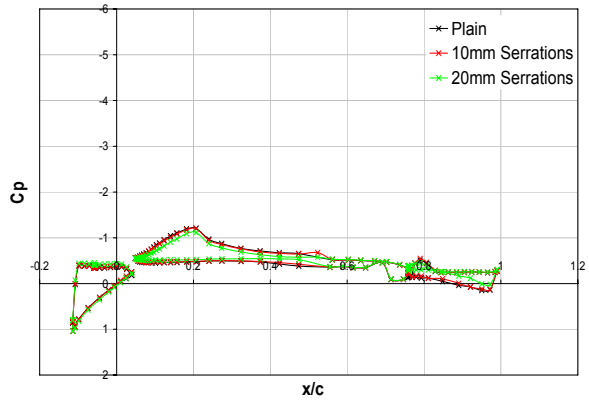

(a) α=0°

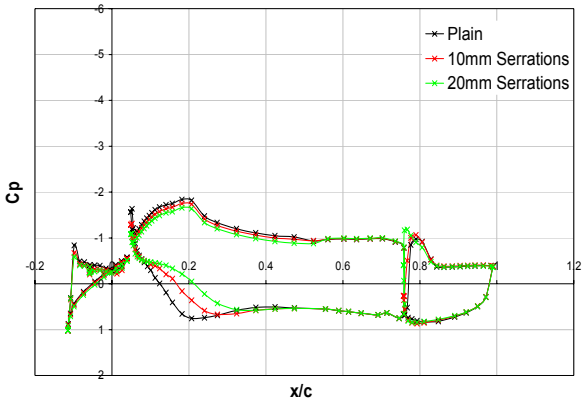

(b) α=2°

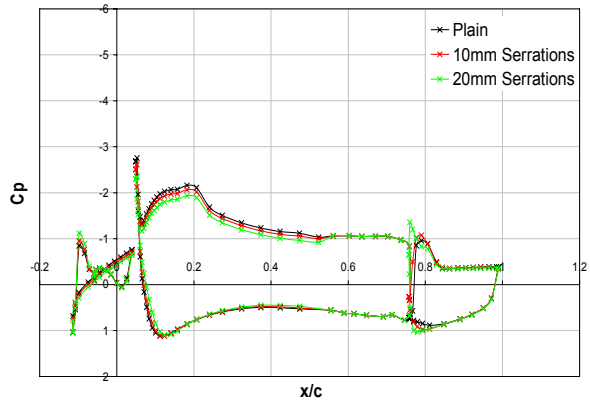

(c) α=4°

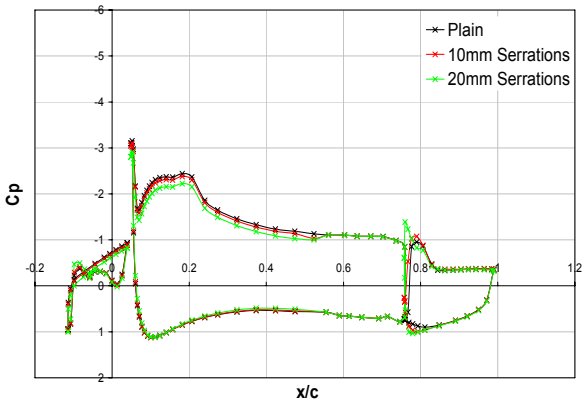

(d) α=6°

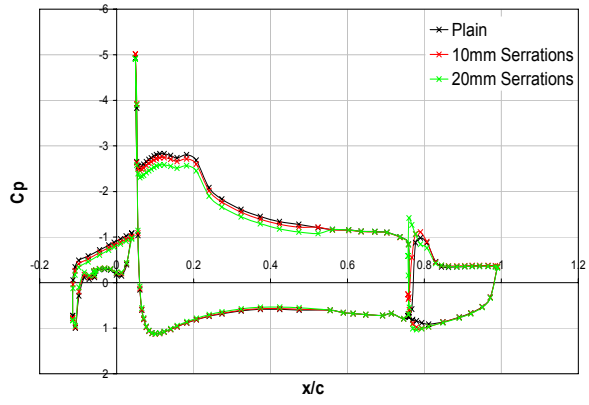

(e) α=8°

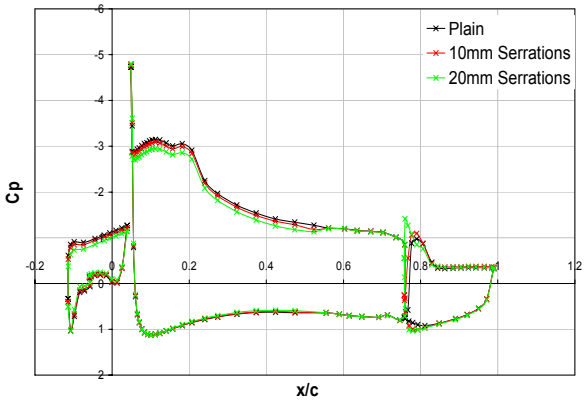

(f) α=10°

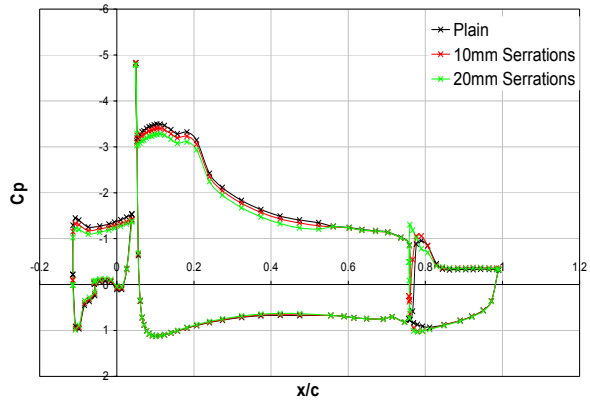

(g) α=12°

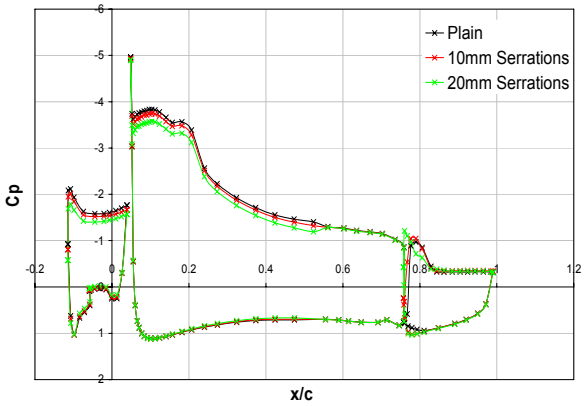

(h) α=14°

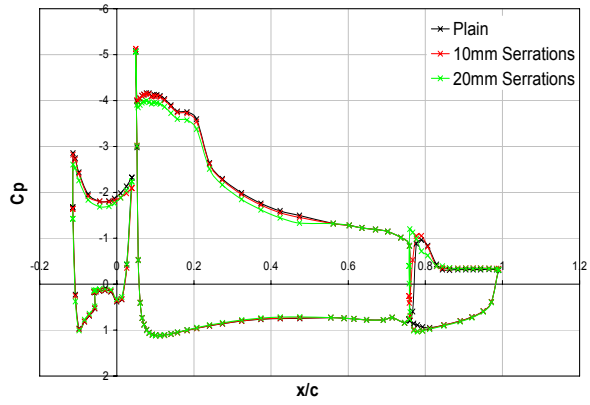

(i) α=16°

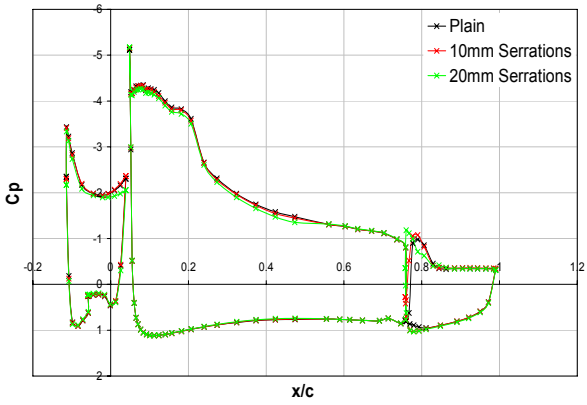

(j) α=18°

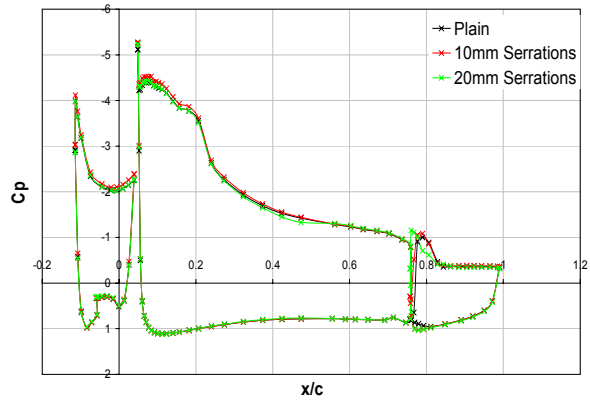

(k) α=20°

Figure 177(a)-(k): C_p distributions for landing configuration with plain, 10mm and 20mm serrated trailing edge geometries, 0°≤α≤20°

Appendix I

Two-Element Baseline High-Lift Configuration with Plain Trailing Edge: Coarse Flap Lap/Gap Grid

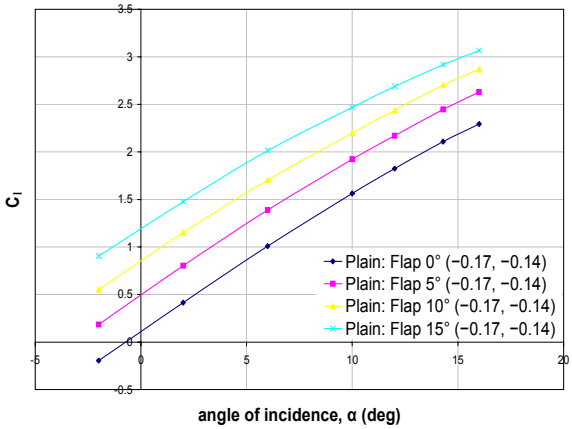

(a) Lap/Gap: (−0.17, −0.14), $0°\leq\delta_f\leq15°$

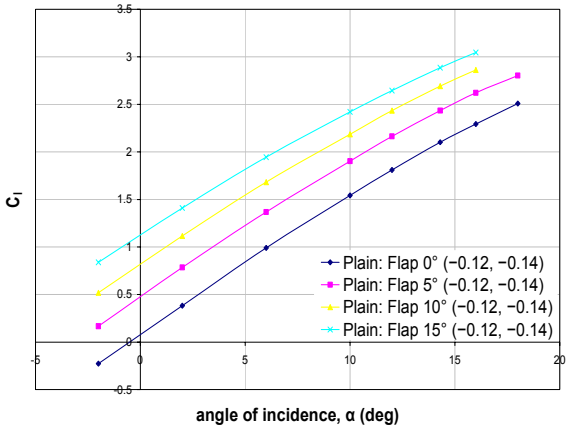

(b) Lap/Gap: (−0.12, −0.14), $0°\leq\delta_f\leq15°$

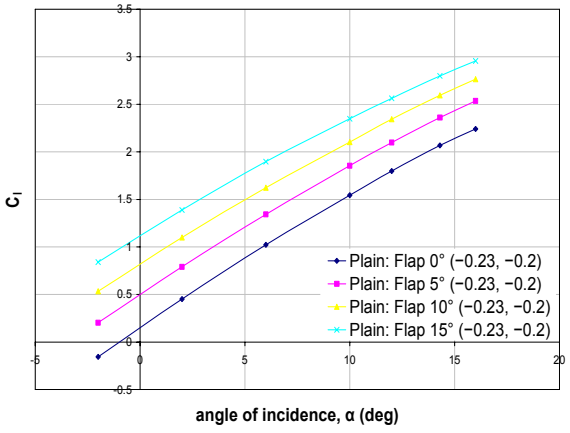

(c) Lap/Gap: (−0.23, −0.2), $0°\leq\delta_f\leq15°$

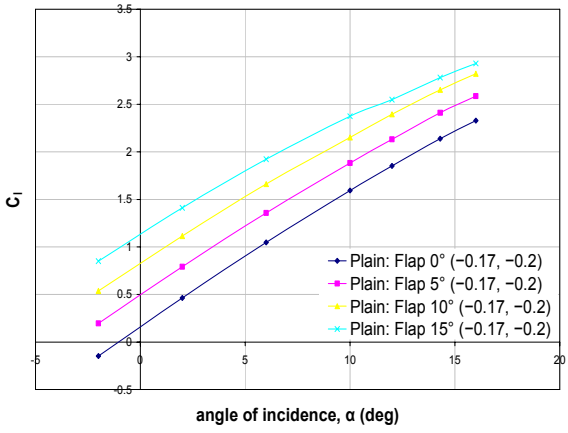

(d) Lap/Gap: (−0.17, −0.2), $0°\leq\delta_f\leq15°$

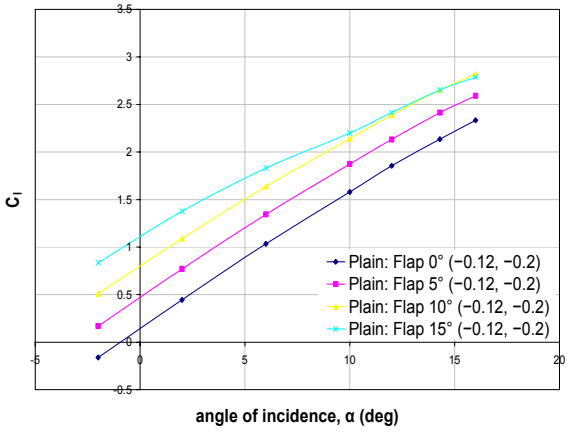

(e) Lap/Gap: (−0.12, −0.2), $0°\leq\delta_f\leq15°$

Figure 178(a)-(e): C_l-α curve for the two-element high-lift configuration with plain trailing edge at each coarse lap/gap grid, $\delta_s=0°$, $0°\leq\delta_f\leq15°$

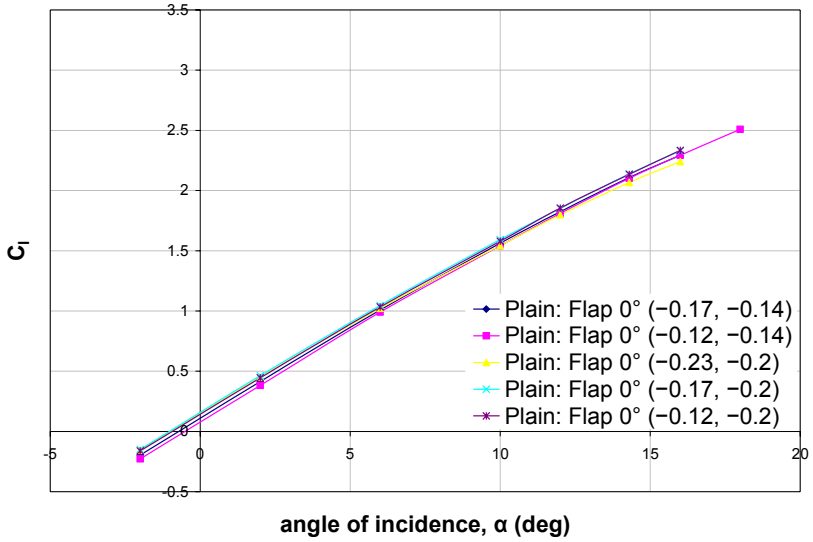

(a) Coarse Lap/Gap Grid: δ_f=0°

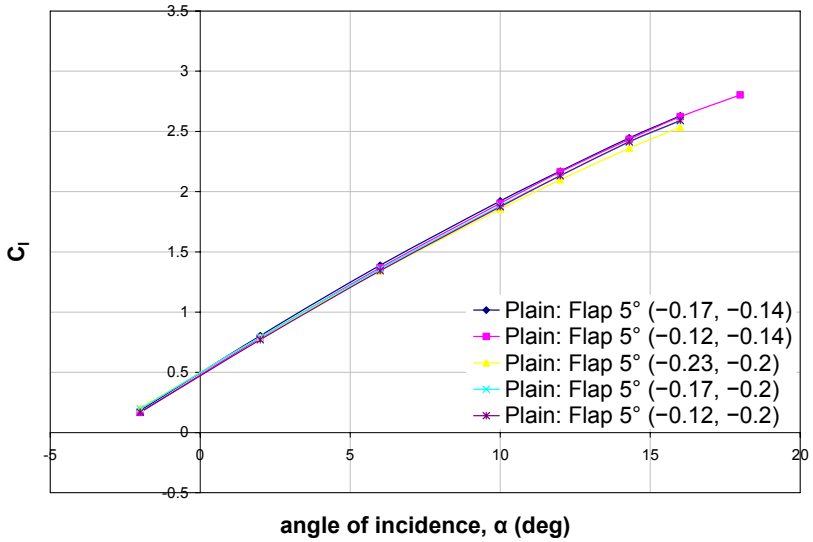

(b) Coarse Lap/Gap Grid: δ_f=5°

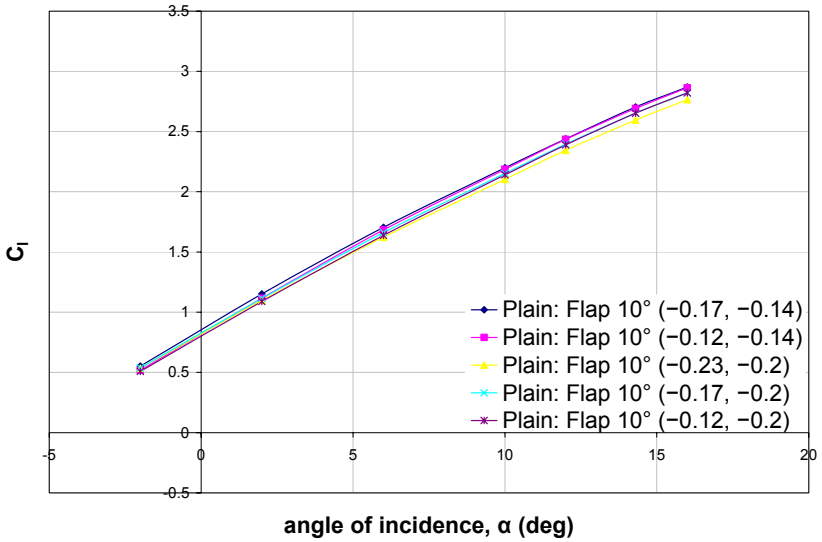

(c) Coarse Lap/Gap Grid: δ_f=10°

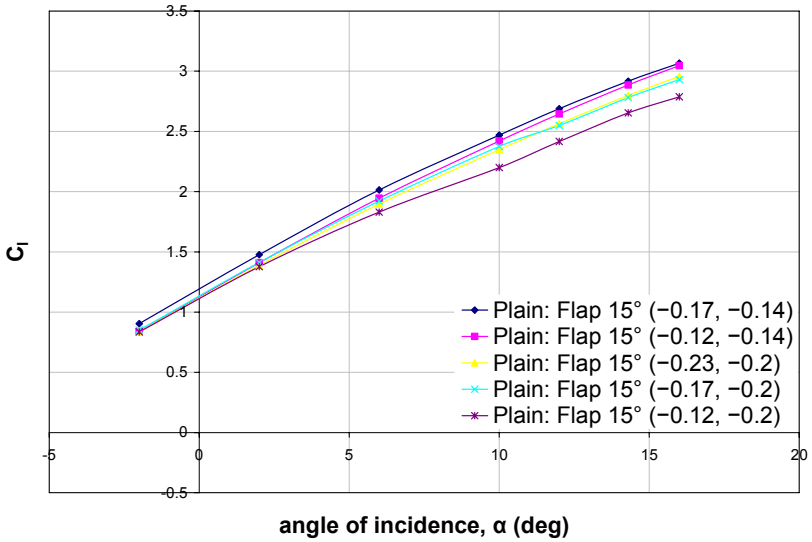

(d) Coarse Lap/Gap Grid: δ_f=15°

Figure 179(a)-(d): Comparison of C_l-α curves for two-element high-lift configuration with plain trailing edge for all coarse lap/gap grid positions at each test δ_f

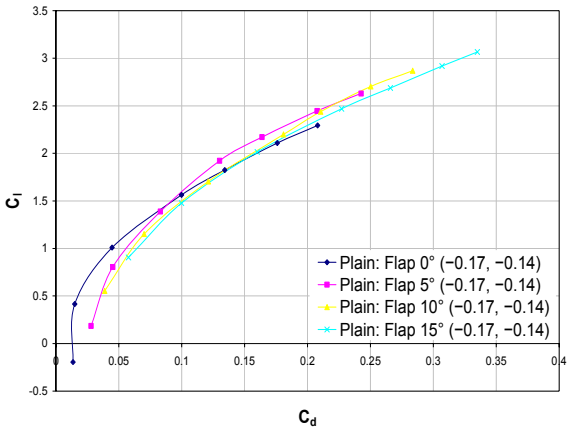

(a) Lap/Gap: (−0.17, −0.14), $0°\leq\delta_f\leq15°$

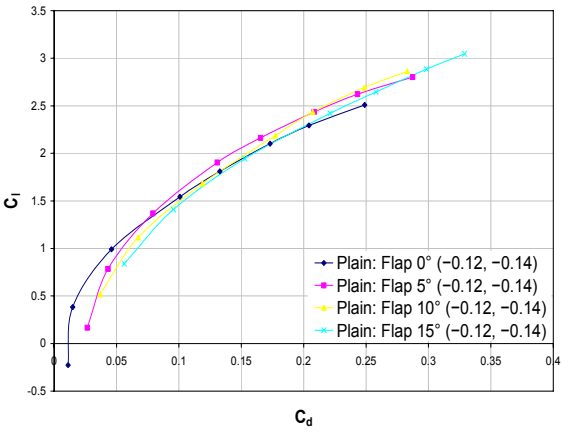

(b) Lap/Gap: (−0.12, −0.14), $0°\leq\delta_f\leq15°$

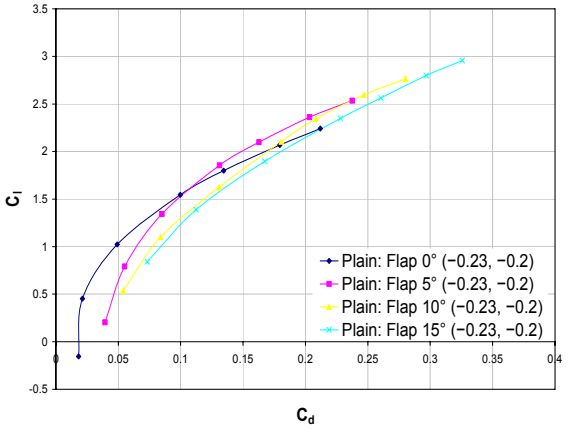

(c) Lap/Gap: (−0.23, −0.2), $0°\leq\delta_f\leq15°$

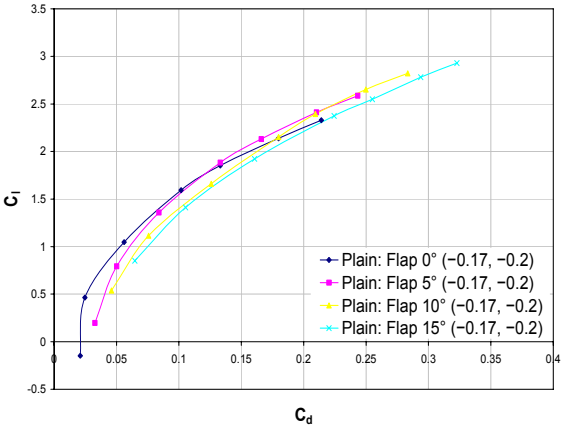

(d) Lap/Gap: (−0.17, −0.2), $0°\leq\delta_f\leq15°$

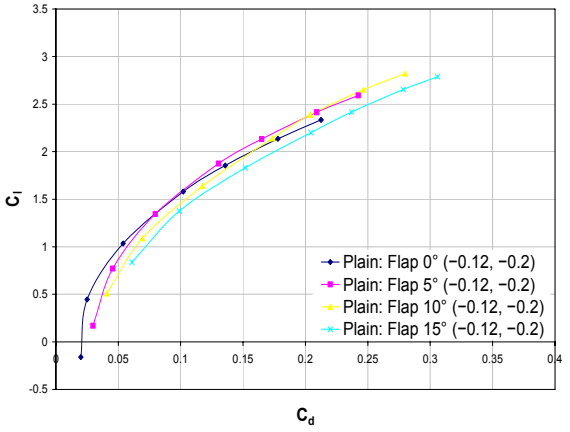

(e) Lap/Gap: (−0.12, −0.2), $0°\leq\delta_f\leq15°$

Figure 180(a)-(e): Drag polars for the two-element high-lift configuration with plain trailing edge at each coarse lap/gap grid, $\delta_s=0°$, $0°\leq\delta_f\leq15°$

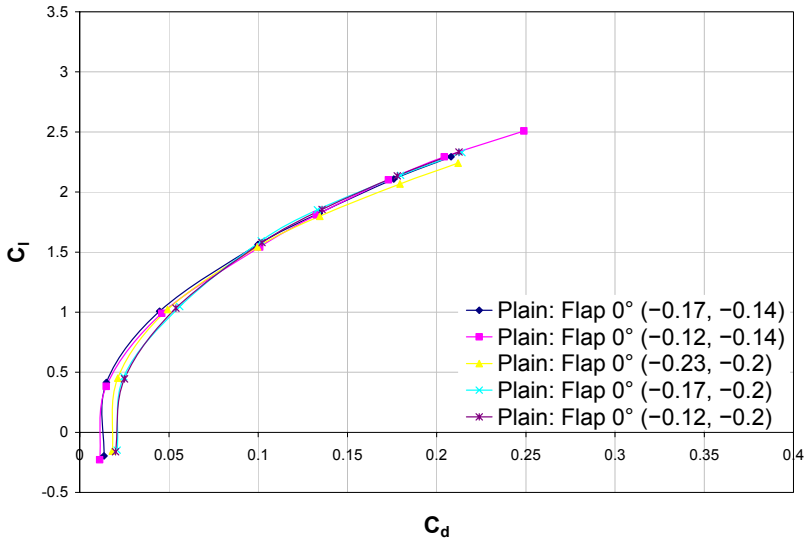

(a) Coarse Lap/Gap Grid: δ_f=0°

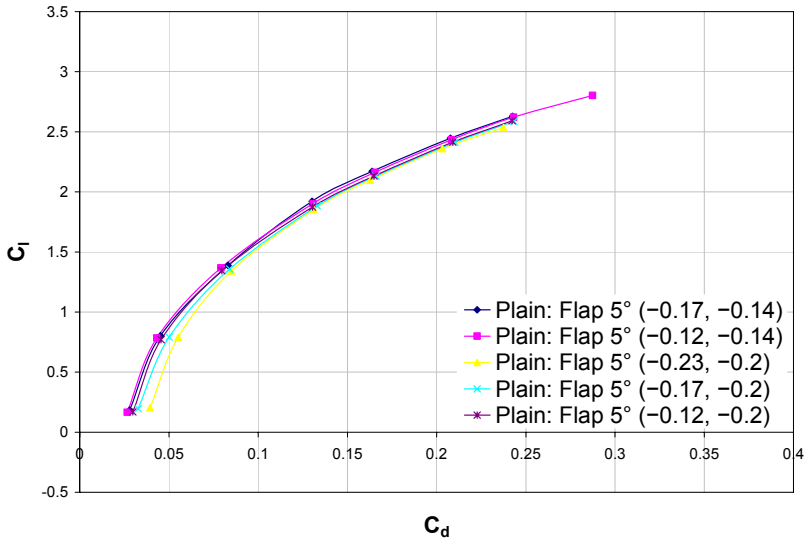

(b) Coarse Lap/Gap Grid: δ_f=5°

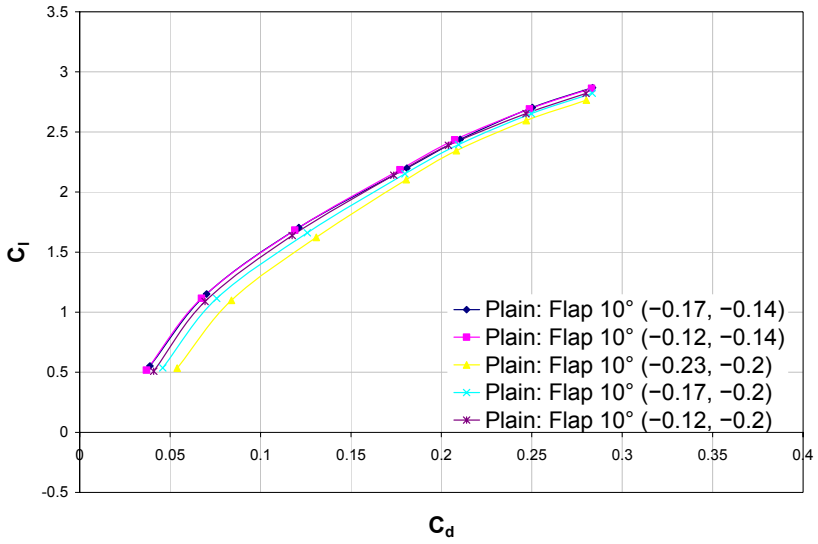

(c) Coarse Lap/Gap Grid: δ_f=10°

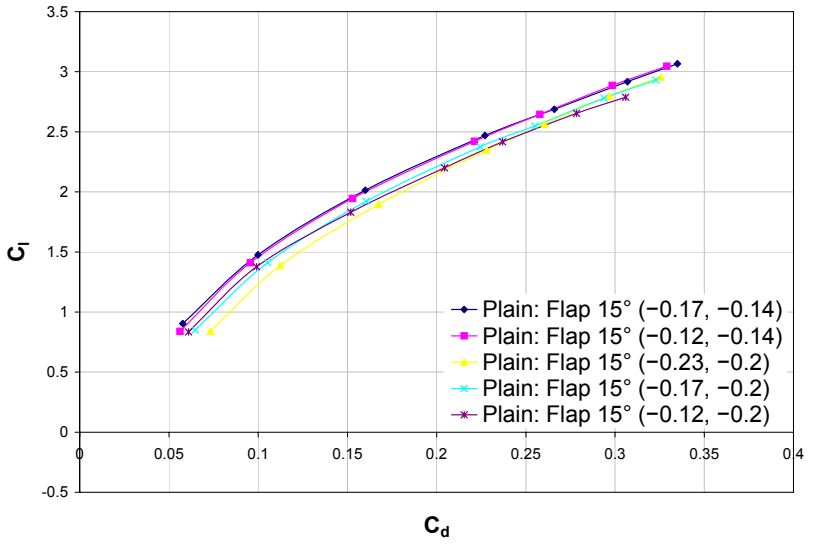

(d) Coarse Lap/Gap Grid: δ_f=15°

Figure 181(a)-(d): Comparison of drag polars for two-element high-lift configuration with plain trailing edge for all coarse lap/gap grid positions at each test δ_f

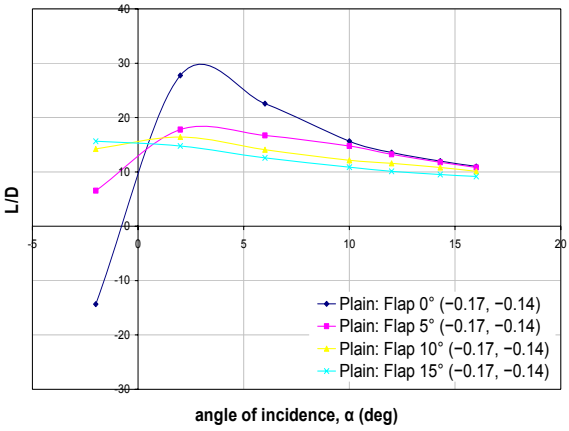

(a) Lap/Gap: (−0.17, −0.14), $0°\leq\delta_f\leq15°$

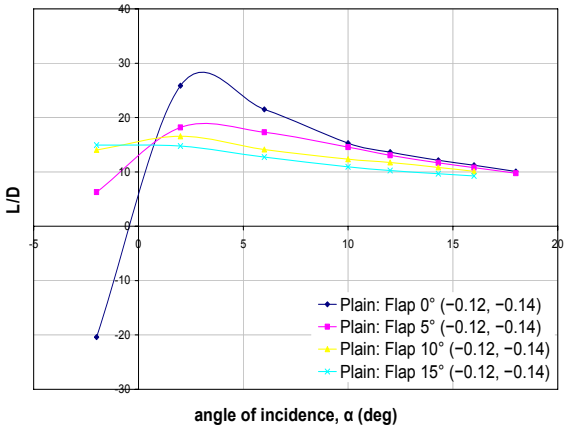

(b) Lap/Gap: (−0.12, −0.14), $0°\leq\delta_f\leq15°$

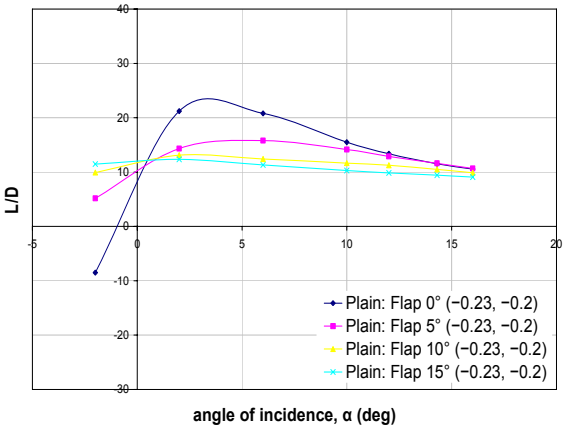

(c) Lap/Gap: (−0.23, −0.2), $0°\leq\delta_f\leq15°$

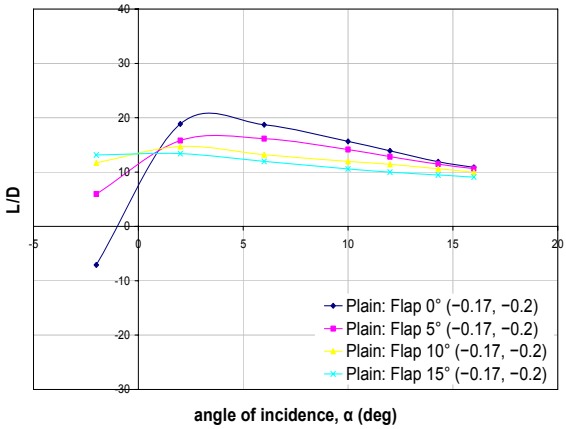

(d) Lap/Gap: (−0.17, −0.2), $0°\leq\delta_f\leq15°$

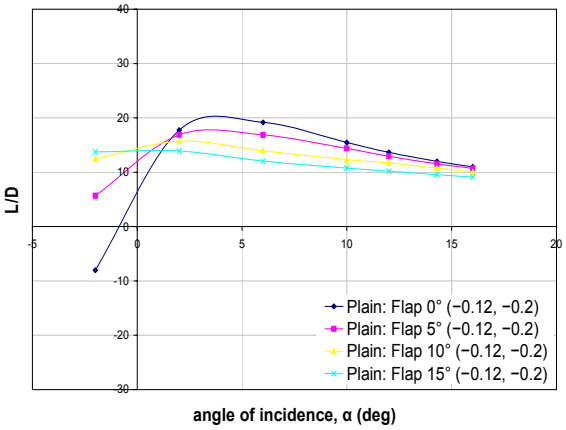

(e) Lap/Gap: (−0.12, −0.2), $0°\leq\delta_f\leq15°$

Figure 182(a)-(e): Variation of *L*/*D* with angle of incidence for the two-element high-lift configuration with plain trailing edge at each coarse lap/gap grid, $\delta_s=0°$, $0°\leq\delta_f\leq15°$

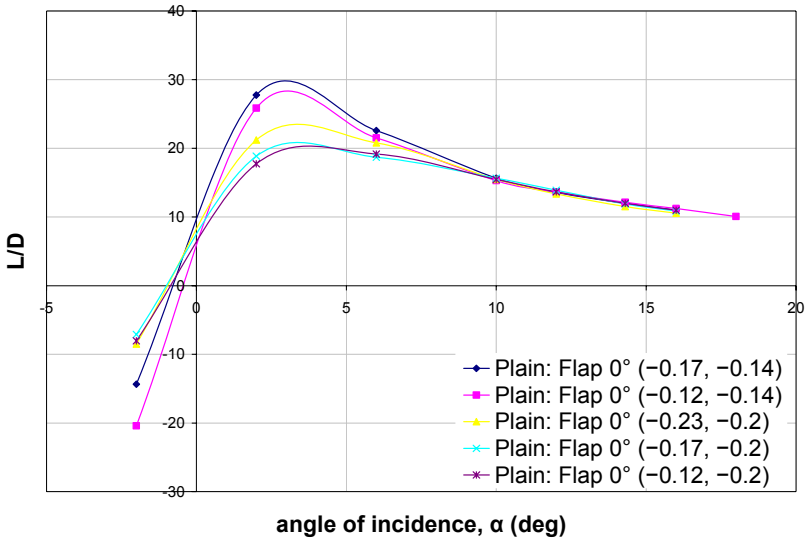

(a) Coarse Lap/Gap Grid: δ_f=0°

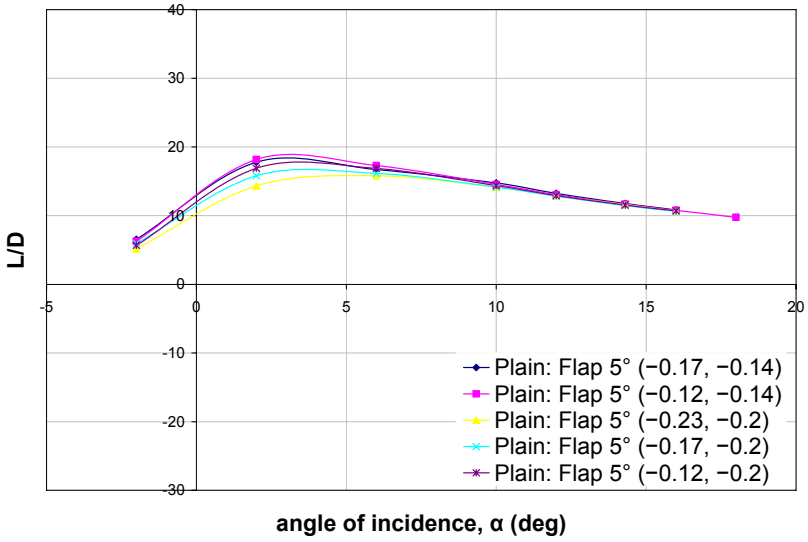

(b) Coarse Lap/Gap Grid: δ_f=5°

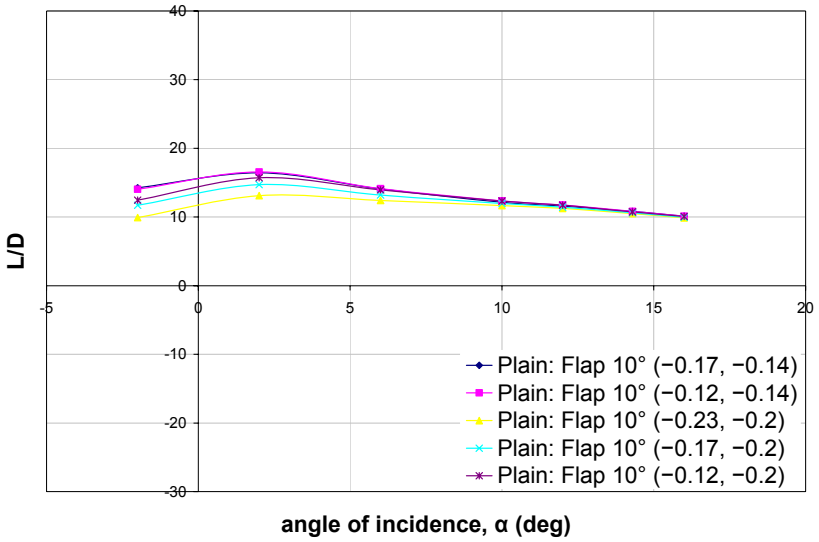

(c) Coarse Lap/Gap Grid: δ_f=10°

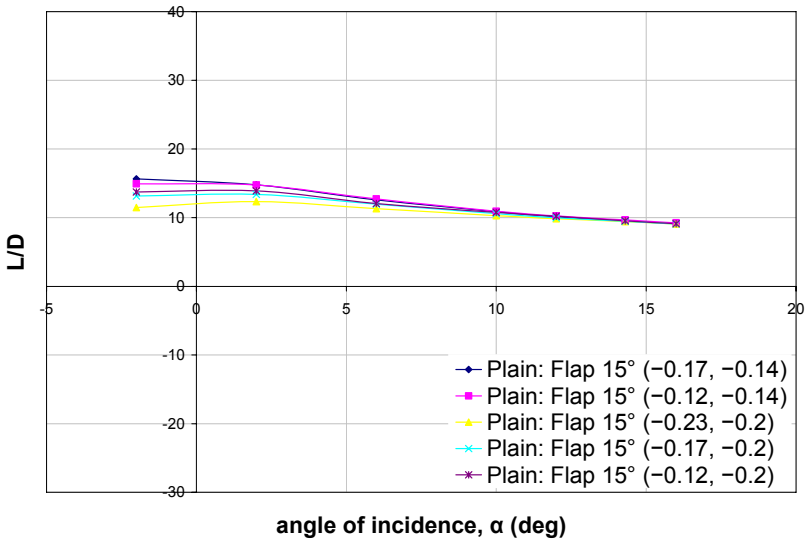

(d) Coarse Lap/Gap Grid: δ_f=15°

Figure 183(a)-(d): Comparison of *L*/*D* with angle of incidence for two-element high-lift configuration with plain trailing edge for all coarse lap/gap grid positions at each test δ_f

Appendix J

Two-Element High-Lift Configuration with Plain, 10mm and 20mm Serrated Trailing Edges: Coarse Flap Lap/Gap Grid

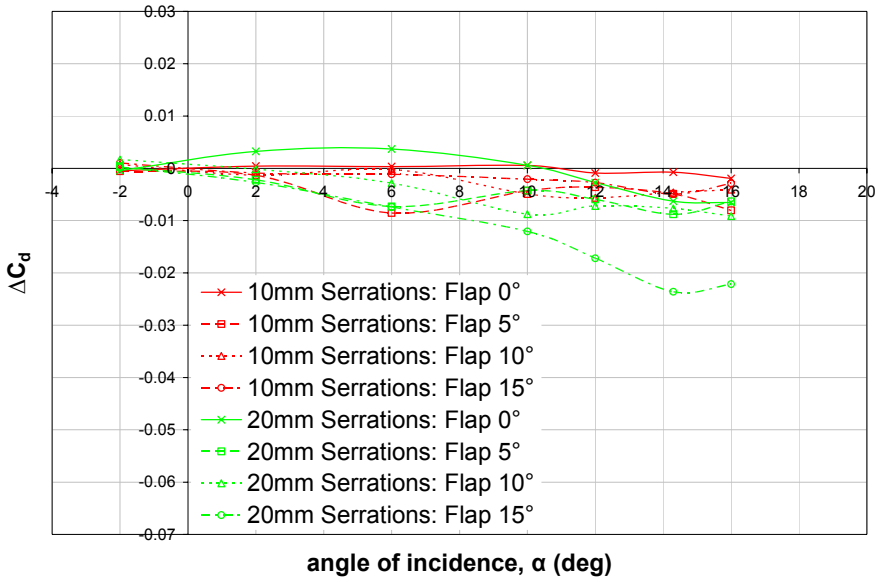

(a) Lap/Gap: (−0.17, −0.14), $0° \leq \delta_f \leq 15°$

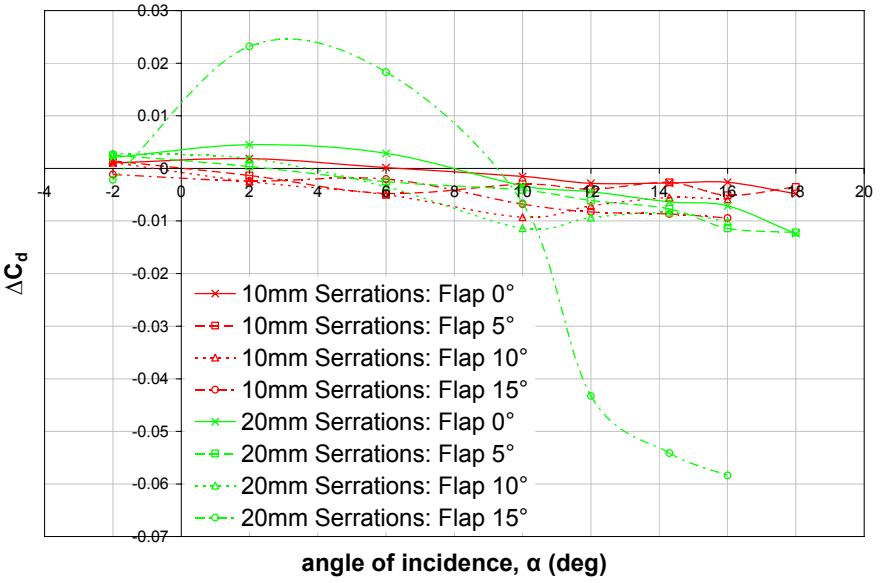

(b) Lap/Gap: (−0.12, −0.14), $0° \leq \delta_f \leq 15°$

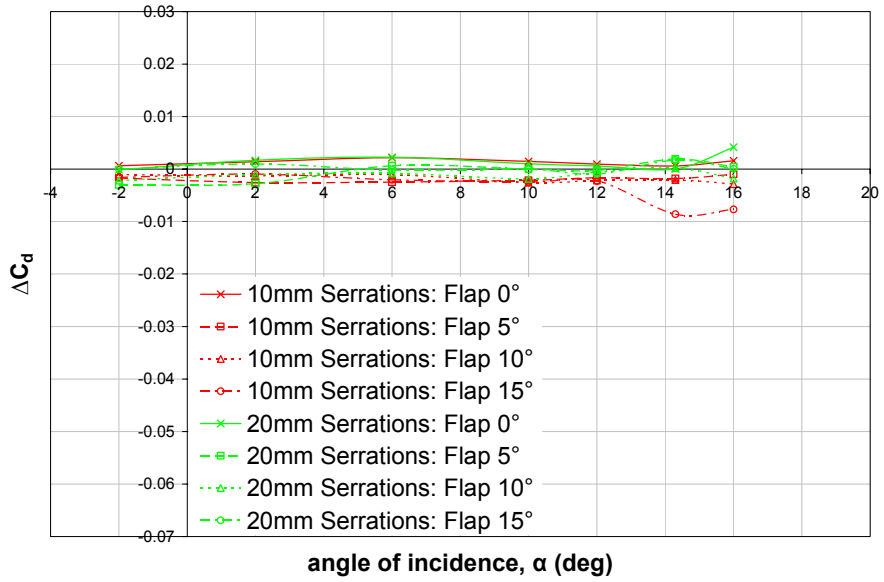

(c) Lap/Gap: (−0.23, −0.2), $0° \leq \delta_f \leq 15°$

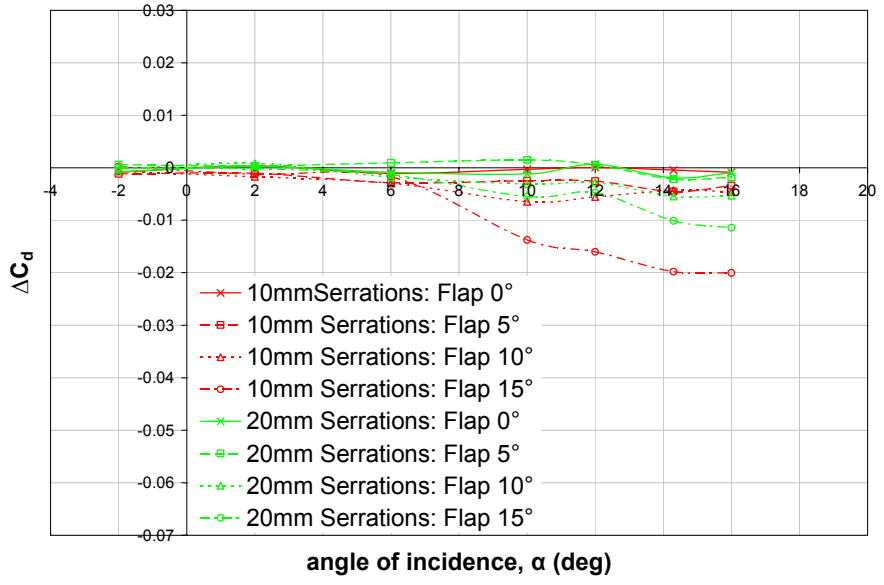

(d) Lap/Gap: (−0.17, −0.2), $0° \leq \delta_f \leq 15°$

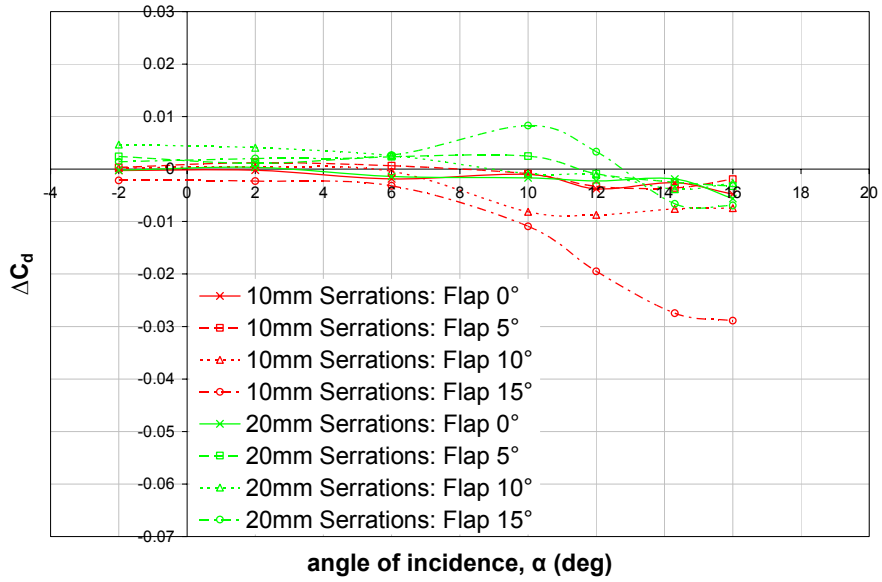

(e) Lap/Gap: (−0.12, −0.2), $0°\leq\delta_f\leq15°$

Figure 184(a)-(e): Variation of ΔC_d with angle of incidence due to 10mm and 20mm serrations for the two-element high-lift configuration at each coarse lap/gap grid, $\delta_s=0°$, $0°\leq\delta_f\leq15°$

Appendix K

Two-Element Baseline High-Lift Configuration with Plain Trailing Edge: Fine Flap Lap/Gap Grid

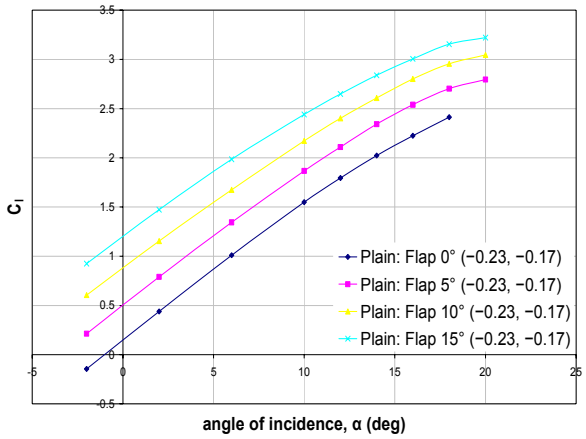

(a) Lap/Gap: (−0.23, −0.17), $0°\leq\delta_f\leq15°$

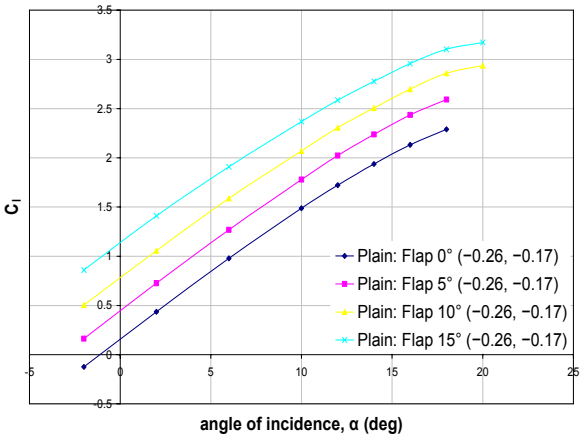

(b) Lap/Gap: (−0.26, −0.17), $0°\leq\delta_f\leq15°$

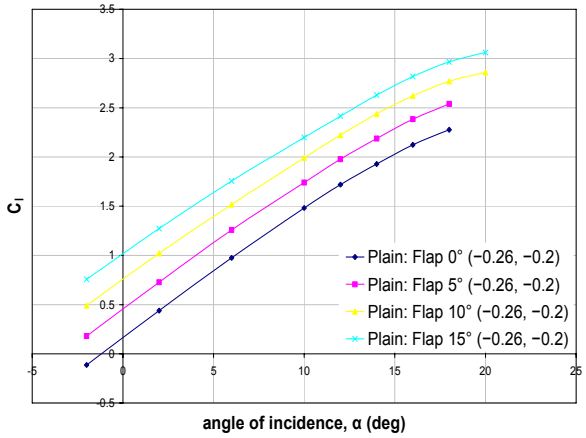

(c) Lap/Gap: (−0.26, −0.2), $0°\leq\delta_f\leq15°$

Figure 185(a)-(c): C_l-α curve for the two-element high-lift configuration with plain trailing edge at each fine lap/gap grid, $\delta_s=0°$, $0°\leq\delta_f\leq15°$

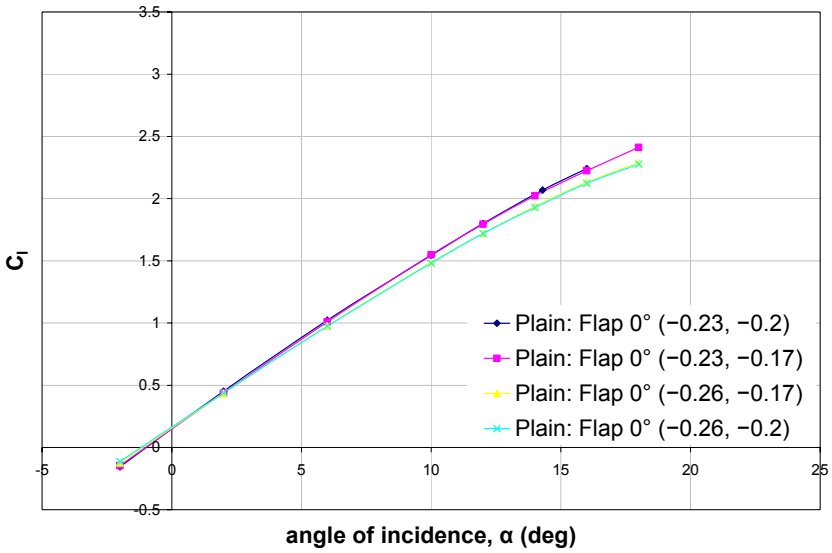

(a) Fine Lap/Gap Grid: δ_f=0°

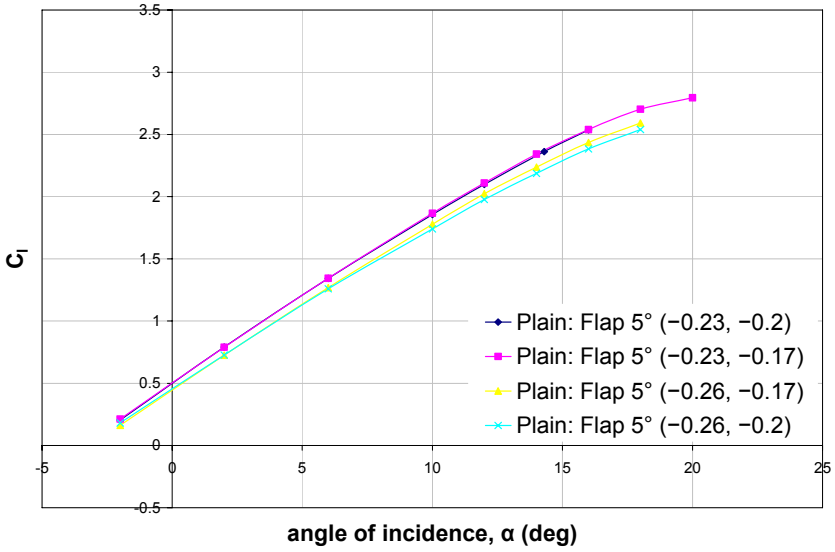

(b) Fine Lap/Gap Grid: δ_f=5°

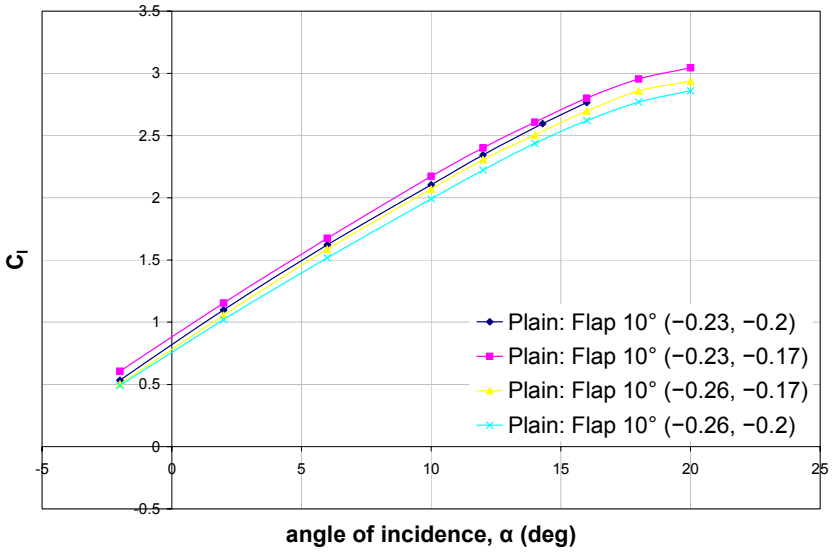

(c) Fine Lap/Gap Grid: δ_f=10°

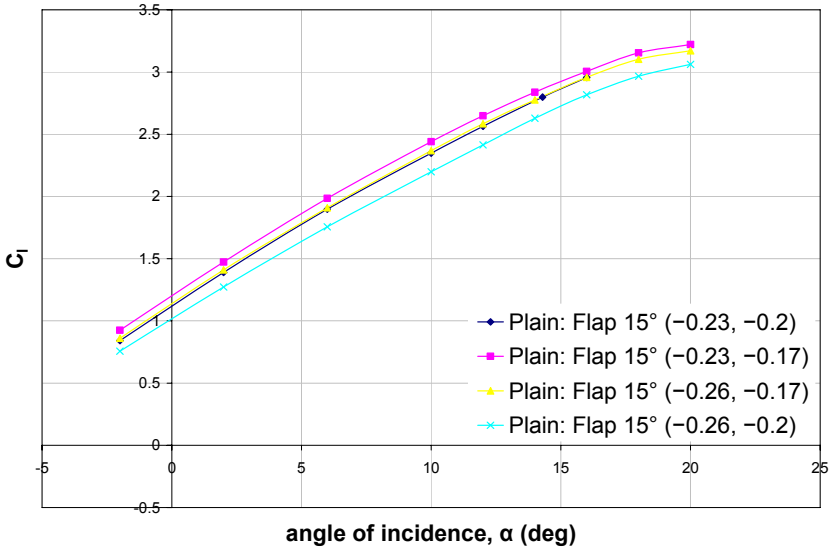

(d) Fine Lap/Gap Grid: δ_f=15°

Figure 186(a)-(d): Comparison of C_l-α curves for two-element high-lift configuration with plain trailing edge for all fine lap/gap grid positions at each test δ_f

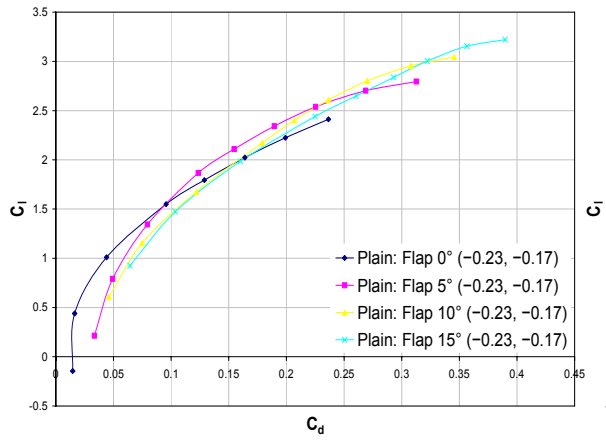

(a) Lap/Gap: (−0.23, −0.17), $0°\leq\delta_f\leq15°$

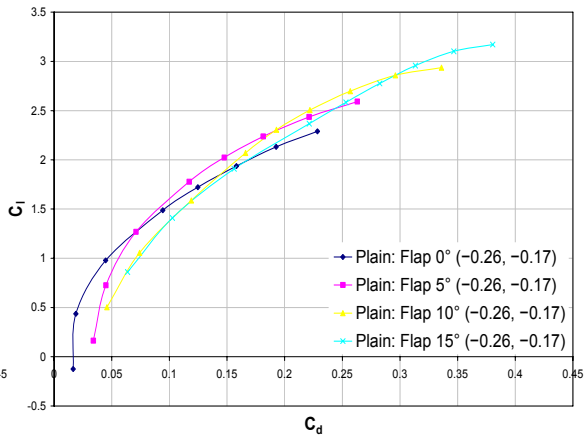

(b) Lap/Gap: (−0.26, −0.17), $0°\leq\delta_f\leq15°$

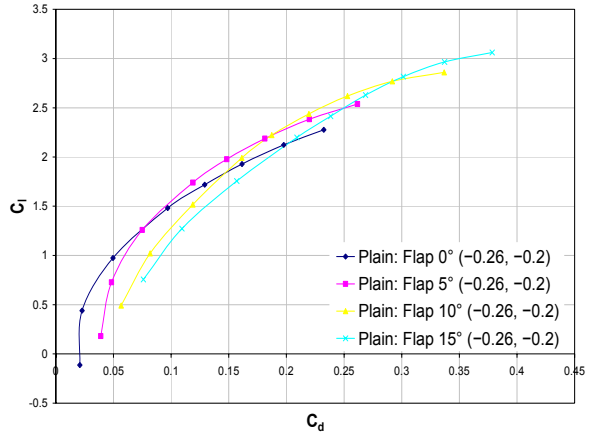

(c) Lap/Gap: (−0.26, −0.2), $0°\leq\delta_f\leq15°$

Figure 187(a)-(c): Drag polars for the two-element high-lift configuration with plain trailing edge at each fine lap/gap grid, $\delta_s=0°$, $0°\leq\delta_f\leq15°$

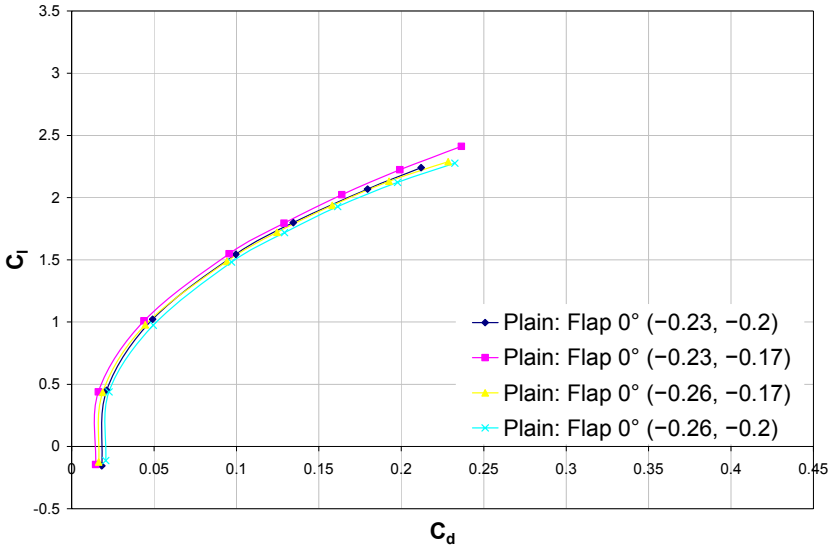

(a) Fine Lap/Gap Grid: δ_f=0°

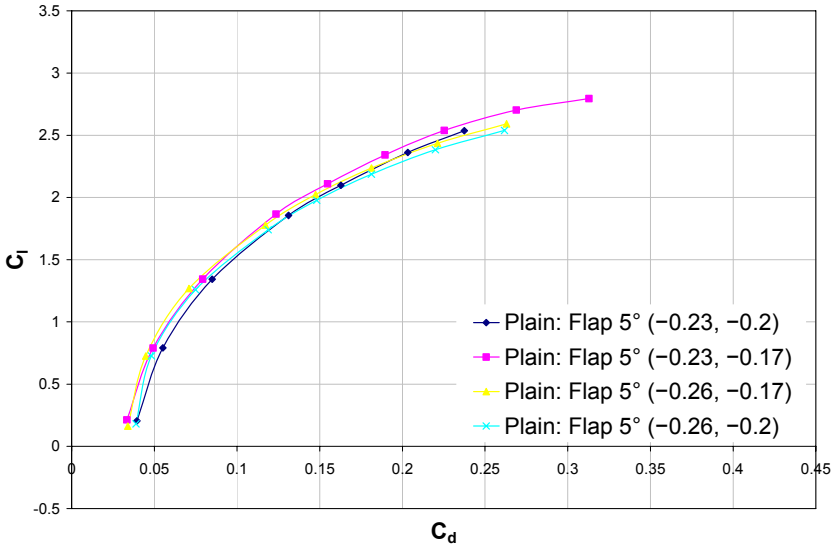

(b) Fine Lap/Gap Grid: δ_f=5°

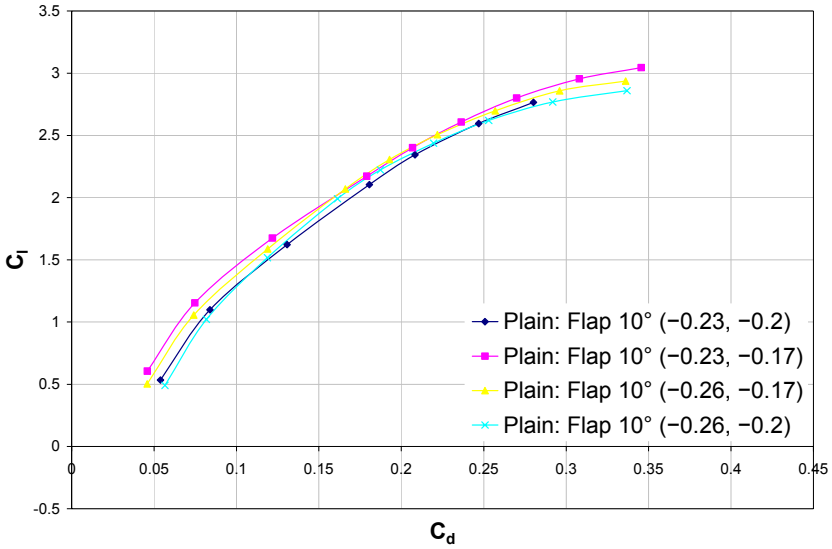

(c) Fine Lap/Gap Grid: δ_f=10°

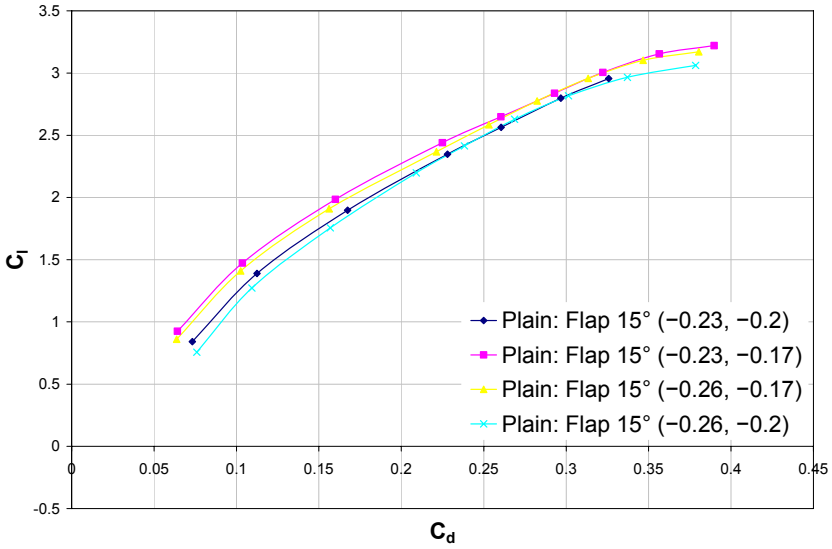

(d) Fine Lap/Gap Grid: δ_f=15°

Figure 188(a)-(d): Comparison of drag polars for two-element high-lift configuration with plain trailing edge for all fine lap/gap grid positions at each test δ_f

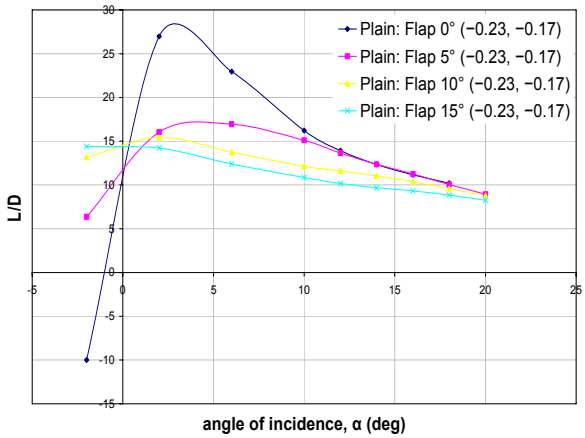

(a) Lap/Gap: (−0.23, −0.17), $0°\leq\delta_f\leq15°$

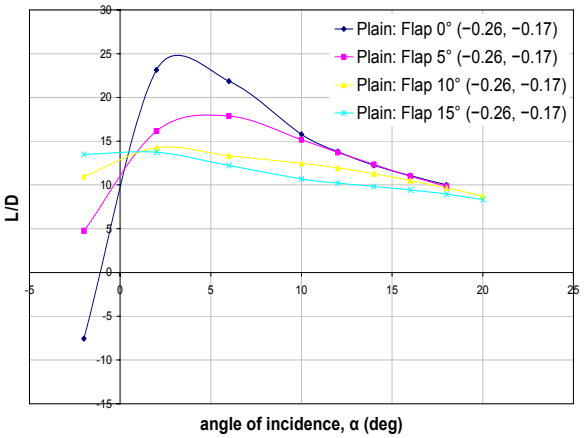

(b) Lap/Gap: (−0.26, −0.17), $0°\leq\delta_f\leq15$

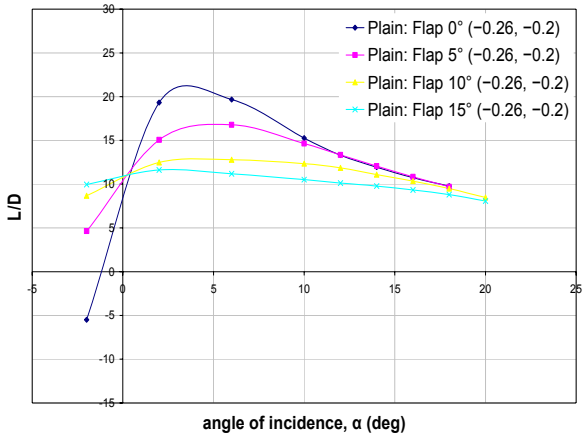

(c) Lap/Gap: (−0.26, −0.2), $0°\leq\delta_f\leq15°$

Figure 189(a)-(c): Variation of *L*/*D* with angle of incidence for the two-element high-lift configuration with plain trailing edge at each fine lap/gap grid, $\delta_s=0°$, $0°\leq\delta_f\leq15°$

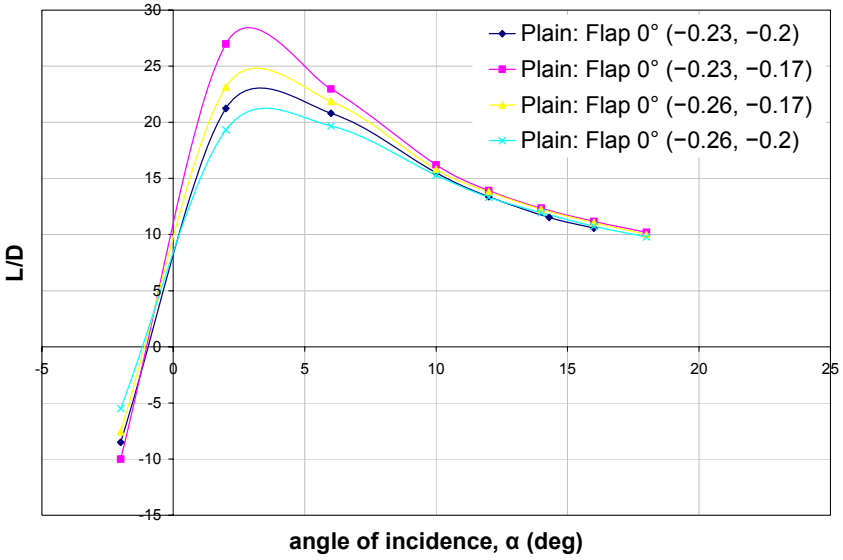

(a) Fine Lap/Gap Grid: δ_f=0°

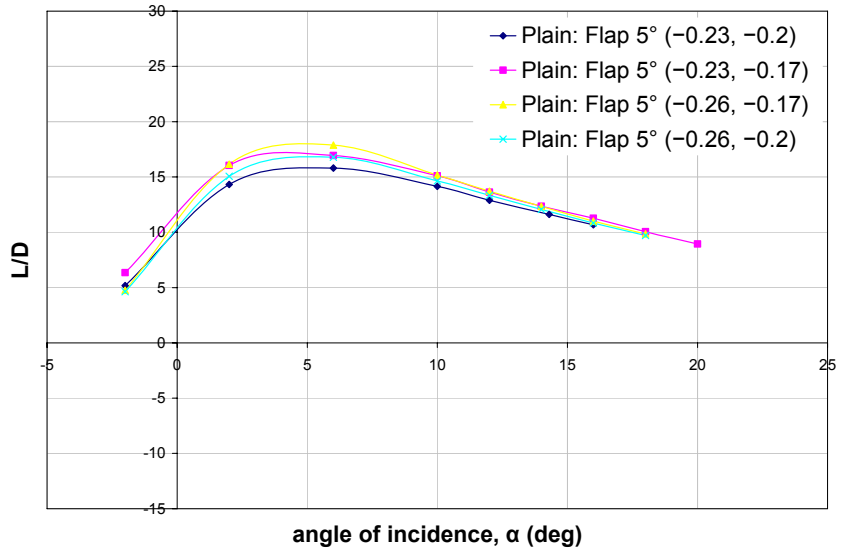

(b) Fine Lap/Gap Grid: δ_f=5°

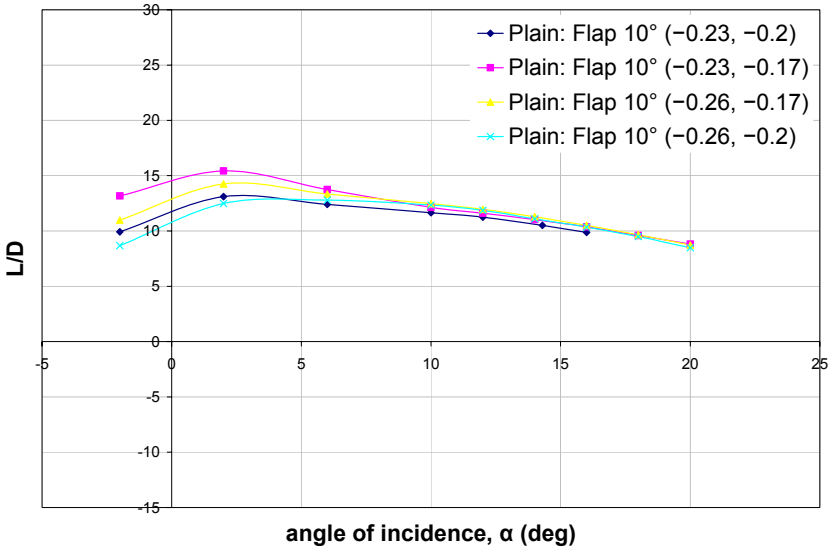

(c) Fine Lap/Gap Grid: δ_f=10°

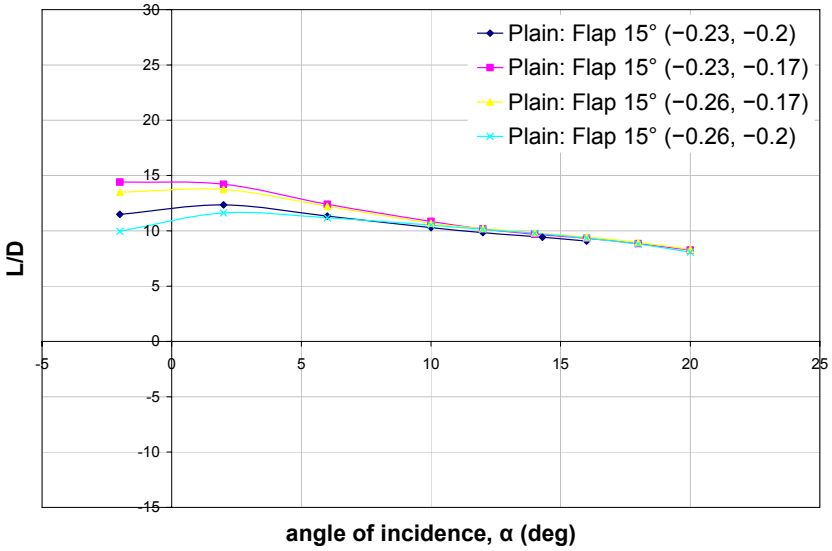

(d) Fine Lap/Gap Grid: δ_f=15°

Figure 190(a)-(d): Comparison of *L*/*D* with angle of incidence for two-element high-lift configuration with plain trailing edge for all fine lap/gap grid positions at each test δ_f

Appendix L

Two-Element High-Lift Configuration with Plain, 10mm and 20mm Serrated Trailing Edges: Fine Flap Lap/Gap Grid

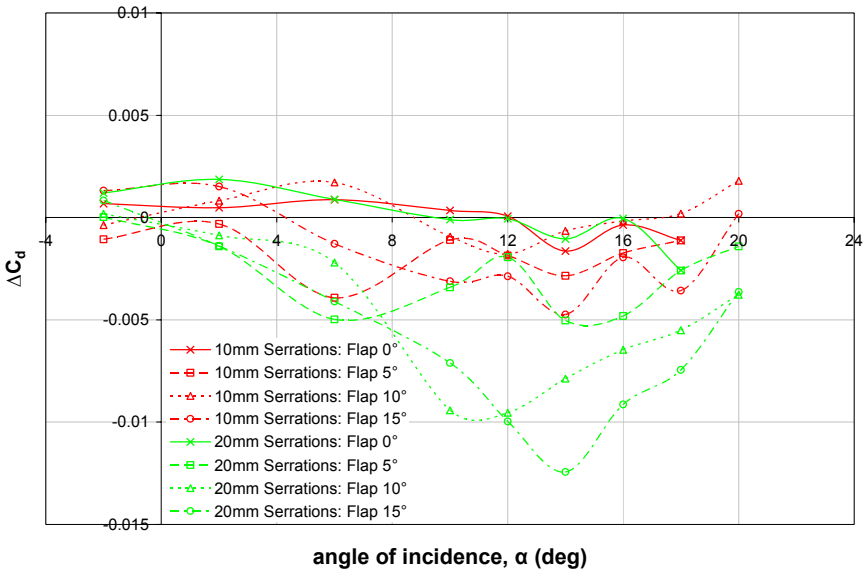

(a) Lap/Gap: (−0.23, −0.17), $0° \leq \delta_f \leq 15°$

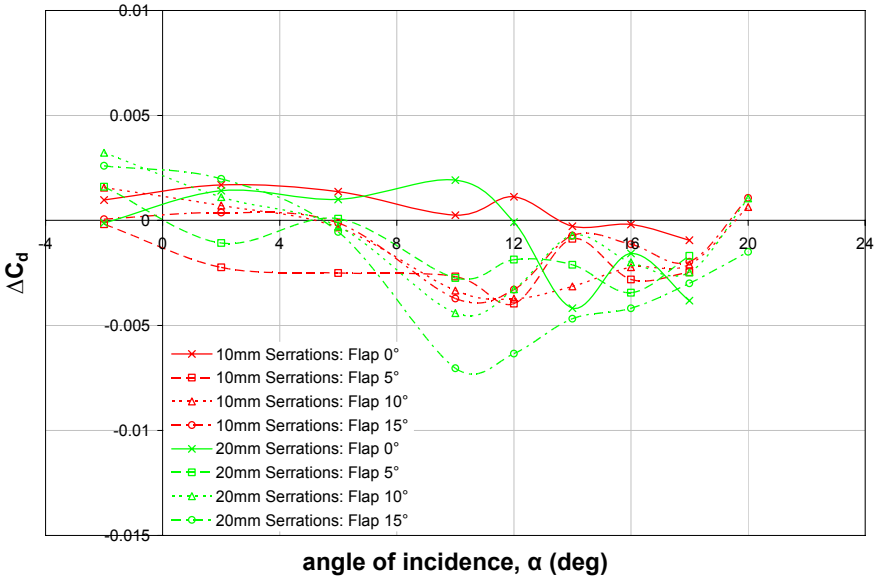

(b) Lap/Gap: (−0.26, −0.17), $0° \leq \delta_f \leq 15°$

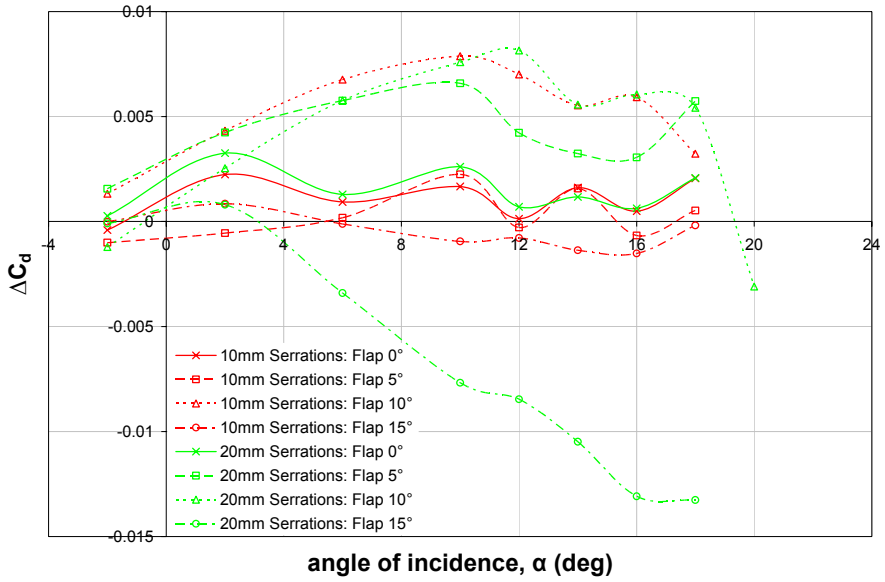

(c) Lap/Gap: (−0.26, −0.2), $0°\leq\delta_f\leq15°$

Figure 191(a)-(c): Variation of ΔC_d with angle of incidence due to 10mm and 20mm serrations for the two-element high-lift configuration at each fine lap/gap grid, $\delta_s=0°$, $0°\leq\delta_f\leq15°$